Reactivity studies of pincer metal complexes stabilized by a bis(1,2,3-triazol-5-ylidene)carbazolide ligand scaffold

by

George Kleinhans

Submitted in partial fulfilment of the requirements for the degree

PHILOSOPHIAE DOCTOR

Chemistry

In the Faculty of Natural and Agricultural Sciences

Department of Chemistry

University of Pretoria

Pretoria

February 2018

© University of Pretoria

Declaration

I, George Kleinhans declare that the thesis, which I hereby submit for the degree PhD. Chemistry at the University of Pretoria, is my own work and has not previously been submitted by me for a degree at this or any other tertiary institution.
The study is a continuation of the MSc. project preceding this degree, and all data from my MSc. dissertation have been clearly referenced and cited in this thesis.

Contributions to this thesis are hereby acknowledged:
Collection and refinement of single crystal X-ray diffraction data were performed by Mr. David C. Liles, University of Pretoria.

The crystal of compound **11**$_a$ (chapter 2) was prepared by Ms. Tyra L. Horngren during her BSc. Honours project under my supervision at the University of Pretoria.

The transfer hydrogenation catalysis (chapter 3) was completed by me in the laboratories of Prof. Eduardo Peris at Universitat Jaume I in Castellón de la Plana, Spain. Useful discussions with Dr. Gregorio Guisado-Barrios and Prof. Josè A. Mata are gratefully acknowledged.

The catalytic study performed by myself in chapter 4 was conducted in collaboration with Prof. Guy Bertrand, University of California, San Diego, USA and Dr. Gregorio Guisado-Barrios, Jaume I University, Spain.

In chapter 5, the cyclic voltammetry experiment was conducted by Dr. Mohand Melaimi and the computational calculations were performed by Dr. Max Hansmann, from the University of California, San Diego, USA in the research group of Prof. Guy Bertrand. Invaluable discussions with Prof. Guy Bertrand are gratefully acknowledged.

The experimental work of chapter 6 was performed in the laboratories of Prof. Alexander A. Trifonov, in collaboration with Dr. Dmitry M. Lyubov at the Institute of Organometallic Chemistry of the Russian Academy of Sciences, Russia, during a research visit.

© University of Pretoria

I hereby gratefully acknowledge the University of Pretoria for a post-graduate study abroad travel grant towards the funding of this research visit.

The financial assistance of the National Research Foundation (NRF) toward this research is hereby acknowledged. Opinions expressed and conclusions arrived at, are those of the author and are not necessarily to be attributed to the NRF.

I also gratefully acknowledge the financial support by Sasol Technology R&D Pty. Ltd. South Africa, towards this research project.

Appreciatively, I acknowledge my supervisor Prof. Daniela I. Bezuidenhout for her assistance, motivation and guidance.

Results from this PhD Thesis have been published in:

Rhodium(I) Oxygen Adduct as a Selective Catalyst for One-Pot Sequential Alkyne Dimerization-Hydrothiolation Tandem Reactions

George Kleinhans, Gregorio Guisado-Barrios, David C. Liles, Guy Bertrand, Daniela I. Bezuidenhout, *Chem. Commun.*, **2016**, *52*, 3504-3507.

Nucleophilic T-shaped (LXL)Au(I)-Pincer Complexes: Protonation and Alkylation

George Kleinhans, Max M. Hansmann, Gregorio Guisado-Barrios, David C. Liles, Guy Bertrand, Daniela I. Bezuidenhout, *J. Am. Chem. Soc.*, **2016**, *138*, 15873-15876.

(featured as a "Spotlight article" in J. Am. Chem. Soc., 138, 16567*)*

Ruthenium(II) pincer complexes featuring an anionic CNC bis(1,2,3-triazol-5-ylidene)carbazolide ligand coordinated in a meridional fashion

George Kleinhans, Gregorio Guisado-Barrios, Eduardo Peris, Daniela I. Bezuidenhout, *Polyhedron*, **2017**, https://doi.org/10.1016/j.poly.2017.07.010. *(Invited paper for Polyhedron Special Issue: Pincer Ligands)*

SIGNATURE:

DATE: 28 February 2018

© University of Pretoria

Table of Contents

Summary viii
List of Complexes x
List of Abbreviations xviii

Chapter 1 1
Introduction
1.1 Triazolylidene ligands 2
1.1.1 Brief overview of 1,2,3-triazol-5-ylidenes 3
1.1.2 Selected recent highlights of 1,2,3-triazol-5-ylidene compounds 5
1.2 The carbazole ligand scaffold 7
1.3 Bis(1,2,3-triazol-5-ylidene)carbazolide 10
1.4 Aim 14
1.5 References 15

Chapter 2 18
Reversible carbon dioxide activation mediated by a nickel hydride complex
2.1 Background 18
2.1.1 CO_2 activation by nickel hydrides 25
2.1.2 CO_2 activation by main group elements 28
2.2 Aim 30
2.3 Results and Discussion 31
2.3.1 Reversible carbon dioxide activation 31
2.4 Conclusion 41
2.5 Experimental 43
2.5.1 (CNC_{Dipp})Ni(II)H (8_a) 43
2.5.2 Synthesis of (CNC_{Dipp})Ni(II)OCOH (10_a) 43
2.5.3 Synthesis of (CNC_{Dipp})Ni(II)$OCOCH_3$ (11_a) 44
2.5.4 Synthesis of (CNC_{Dipp})Ni(II)Cl (12_a) 45
2.6 References 46

Chapter 3 48
Meridional ruthenium(II) pincer complexes towards catalytic hydrogenation reactions

© University of Pretoria

3.1 Background 48
3.1.1 Triazolylidene ruthenium(II) complexes 53
3.1.2 General consideration of the transfer hydrogenation reaction 57
3.2 Aim 59
3.3 Results and Discussion 60
3.3.1 Synthesis of CNC-ruthenium(II) chlorido complex 60
3.3.2 Synthesis of CNC-ruthenium(II) hydride complexes 64
3.4 Conclusion 67
3.5 Experimental 68
3.5.1 Synthesis of [(CNC_{Mes})Ru(II)$(CO)_2$Cl] (13_b) 68
3.5.2 Synthesis of intermediate [(CNC_{Mes})Ru(II)($AsPh_3$)(CO)H] (14_b) 68
3.5.3 Synthesis of [(CNC_{Mes})Ru(II)$(CO)_2$H] (15_b) 69
3.5.4 Catalytic transfer hydrogenation reaction catalyzed by 13_b 70
3.6 References 70

Chapter 4 72
A rhodium(I)-oxygen adduct as a selective catalyst for one-pot sequential alkyne dimerization-hydrothiolation tandem reactions
4.1 Background 72
4.1.1 Alkyne dimerization 74
4.1.2 Alkyne hydrothiolation 79
4.1.3 Rhodium(I)-oxygen adducts 86
4.2 Aim 88
4.3 Results and Discussion 89
4.3.1 Rhodium(I)-oxygen adduct synthesis 89
4.3.2 Homo-dimerization of terminal alkynes 90
4.3.3 Alkyne hydrothiolation 93
4.3.4 Sequential alkyne dimerization-hydrothiolation tandem reaction 98
4.4 Conclusion 101
4.5 Experimental 102
4.5.1 Synthesis of (CNC_{Dipp})Rh(I)O_2 (16_a) 102
4.5.2 Synthesis of (CNC_{Mes})Rh(I)O_2 (17_b) 104
4.5.3 Synthesis of (CNC_{Dipp})Rh(I)CO (18_a) 106
4.5.4 Synthesis of (CNC_{Mes})Rh(I)CO (19_b) 108
4.5.5 Optimization of alkyne dimerization reaction conditions 109
4.5.6 Dimerization of terminal alkynes 110
4.5.7 Optimization of alkyne hydrothiolation reaction conditions 114
4.5.8 Hydrothiolation of terminal alkynes 114
4.5.9 Sequential bis-hydrothiolation 119
4.5.10 Sequential bis-hydrothiolation under preparative conditions 125
4.5.11 Sequential alkyne dimerization-hydrothiolation catalytic details 125

© University of Pretoria

4.6 References 129

Chapter 5 132
Nucleophilic T-shaped Au(I) pincer complexes: electrophilic oxidation
5.1 Background 132
5.1.1 Transmetallation 134
5.1.2 Migratory insertion 137
5.1.3 Reductive elimination 141
5.1.4 Oxidative addition 144
5.1.4.1 Monocoordinate cationic gold(I) 145
5.1.4.2 Neutral two coordinate gold(I) complexes 147
5.1.4.3 Chelate-assisted oxidative addition 148
5.1.4.4 Bent two coordinate gold(I) complexes 149
5.1.5 The Lewis basic gold question 151
5.2 Aim 152
5.3 Results and Discussion 153
5.3.1 Gold(I) complex formation 153
5.3.2 Protonation of T-shaped (CNC)Au(I) 155
5.3.3 Electrophilic alkylation of T-shaped gold(I) complexes 163
5.3.4 Towards a cationic gold(III) fluoride complex 167
5.4 Conclusion 168
5.5 Experimental 169
5.5.1 Synthesis of (CNC_{Dipp})Au(I) (20_a) 169
5.5.2 Synthesis of (CNC_{Mes})Au(I) (21_b) 172
5.5.3 Synthesis of [(CNC_{Dipp})Au(III)H]OTf (22_a) 174
5.5.4 Synthesis of [(CNC_{Dipp})Au(III)H]OAc^F (23_a) 176
5.5.5 Synthesis of [($CNHC_{Dipp}$)Au(I)]OTf (24_a) 178
5.5.6 Synthesis of [($CNMeC_{Dipp}$)Au(I)]OTf (26_a) 180
5.5.7 Synthesis of [($CNMeC_{Dipp}$)Au(I)]I (27_a) 182
5.5.8 Synthesis of [(CNC_{Mes})Au(III)CH_3]I (28_b) 184
5.5.9 Synthesis of [(CNC_{Mes})Au(III)CH_2Cl]Cl (29_b) 185
5.5.10 Synthesis of [(CNC_{Dipp})Au(III)F]BF_4 (30_a) 187
5.5.11 Solvent dependent redox reaction of 20_a with acetic acid 189
5.5.12 Deprotonation and reduction of 22_a with sodium hydride 190
5.5.13 Reaction of 22_a with hydrochloric acid 190
5.6 References 191

Chapter 6 193
An exploratory study towards the first yttrium triazolylidene complex

© University of Pretoria

6.1 Background 193
6.1.1 Yttrium carbenes 196
6.1.2 Lanthanides for efficient catalysis 200
6.2 Aim 203
6.3 Results and Discussion 204
6.4 Conclusion 217
6.5 Experimental 218
6.5.1 Synthesis of (CNC_{Dipp})Li (31_a) 218
6.5.2 Synthesis of [(CNC_{Dipp})$YCl_2(thf)_2$](LiCl) (32_a) 218
6.5.3 Synthesis of (CNC_{Mes})Li (33_b) 219
6.5.4 Synthesis of [(CNC_{Mes})$YCl_2(thf)_2$](LiCl) (34_b) 220
6.5.5 Synthesis of [(CNC_{Mes})$Y(thf)_2$] (35_b) 220
6.5.6 Synthesis of [(CNC_{Mes})$Y(C_8H_5)_2(thf)_2$] (36_b) 221
6.5.7 Catalytic hydrophosphination of styrene with diphenylphosphine 221
6.6 References 221

Chapter 7 223
Conclusion

Chapter 8 229
Experimental
8.1 Standard operating procedures 229
8.1.1 Method 229
8.1.2 Materials 229
8.2 Characterization techniques 230
8.2.1 Nuclear magnetic resonance spectroscopy 230
8.2.2 Fourier-transform infrared spectroscopy 230
8.2.3 Mass Spectroscopy 231
8.2.4 X-ray diffraction analysis 231
8.3 Computational details 235
8.4 References 253

© University of Pretoria

Summary

by

George Kleinhans

Supervisor: Prof. D. I. Bezuidenhout

Submitted in partial fulfilment of the requirements for the degree,

PHILOSOPHIAE DOCTOR

Department of Chemistry, University of Pretoria

The stability and reactivity of two analogous bis(1,2,3-triazol-5-ylidene)carbazolide ligand scaffolds were exploited during the preparation and characterization of a range of novel metal complexes. The CNC-pincer supported metal complexes demonstrated various unique reactivity patterns, while the ligands stabilized complexes believed to be only transient intermediates in catalysis.

A nickel hydride complex mediated the reversible CO_2 insertion across the metal hydrogen bond at ambient temperatures, with the reaction ensuing to form a nickel formate complex which, when exposed to negative pressures at room temperature, resulted in the facile regeneration of the hydride product. The *in situ* generated formate complex was reacted with various chloride containing trapping reagents resulting to the isolation of the corresponding nickel chloride product, but more importantly, evidenced the reversible nature of the reaction.

Catalytically active metal complexes of ruthenium and rhodium could also be prepared and it was demonstrated that the atmospherically stable ruthenium complex catalyzed the transfer hydrogenation reaction of acetophenone to the corresponding alcohol with *iso*-propanol as sacrificial hydrogen atom donor, albeit with unsatisfactory catalytic activity.

© University of Pretoria

The air-stable rhodium oxygen adduct prepared, was found to catalyze the alkyne dimerization and hydrothiolation reactions with a high degree of selectivity for one product, out of a possible three isomers. The selective and step-wise double hydrothiolation of a dithiol with two non-equivalent alkynes were also readily catalyzed by the same complex. Moreover, the two different catalytic reactions (dimerization and hydrothiolation) could be performed as a one-pot tandem process. Accordingly, the *gem*-enyne prepared *in situ* from the Rh-catalyzed dimerization of a terminal alkyne was subjected to hydrothiolation with an alkyl thiol. This resulted in the *syn* addition of the thiol across the internal alkyne of the enyne, yielding the 1,3- and 1,4-*gem*-ene-β-*E*-vinyl sulfide products with a ratio of 1:1.

Coordination of the ligands to (tht)AuCl yielded the corresponding neutral, three coordinate gold(I) complexes featuring an unusual T-shaped geometry. The redox potential of the Au(I)/Au(III) couple was determined through cyclic voltammetry, indicating reversible oxidation even at potentials negative relative to ferrocene. In addition, computational analysis predicted a gold(I) complex with Lewis basic character. The gold(I) products could therefore be reacted with electrophiles, which directly contrasts with classical gold(I) species. The unique reactivity allowed for the preparation of the first example of a cationic gold(III) hydride complex, with protic and not hydridic character. Additionally, treatment of the gold(I) species with alkylating electrophiles resulted in alkylation of the amido nitrogen to yield the cationic gold(I) complex, or alkylation and oxidation of the metal center to form the gold(III) methyl product. The first example of an atmospherically stable cationic gold(III) fluoride complex could also be isolated, after reacting the gold(I) product with Selectfluor. The results, in addition to some very recent literature reports, disprove the long-standing belief that gold cannot mimic the reactivity of the platinum group metals.

Finally, the first example of a triazolylidene-coordinated lanthanide complex has also been reported. The exploratory study suggested that specific ligand geometry is required during the isolation of the highly reactive species; the ligand featuring the bulky 2,6-diisopropylphenyl wingtip groups did not yield stable complexes, contrasting intuitive reasoning. However, the use of the smaller 2,4,6-trimethylphenyl functionalized pincer ligand did lead to isolation of the CNC-pincer coordinated yttrium product featuring benzyl bonds due to the C-H activation of two of the 2,4,6-trimethylphenyl wingtip substituents.

© University of Pretoria

List of Compounds

In the numbering of the compounds, subscript '$_a$' will be used throughout the thesis to indicate substitution of the ligand scaffold with 2,6-diisopropylphenyl (Dipp) groups, while a compound number followed by subscript '$_b$' denotes 2,4,6-trimethylphenyl (Mes) substitution of the triazoliums/triazolylidenes.

Chapter 1

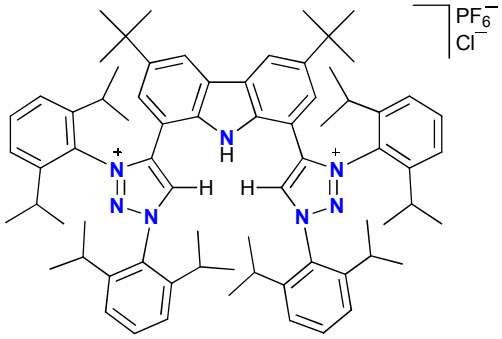

[(CNC$_{Dipp}$)](PF$_6$)(Cl) (L$_a$)

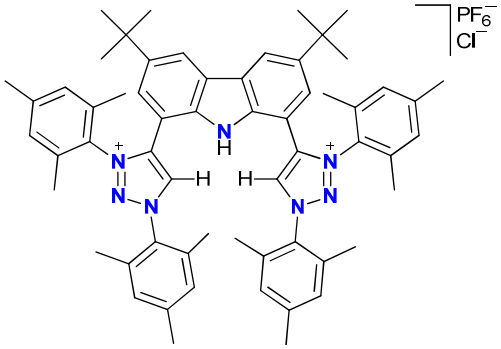

[(CNC$_{Mes}$)](PF$_6$)(Cl) (L$_b$)

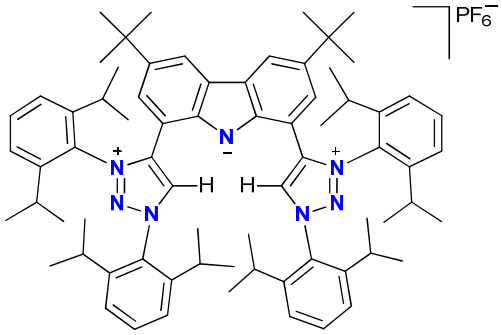

[(CNC$_{Dipp}$)]PF$_6$ (1$_a$)

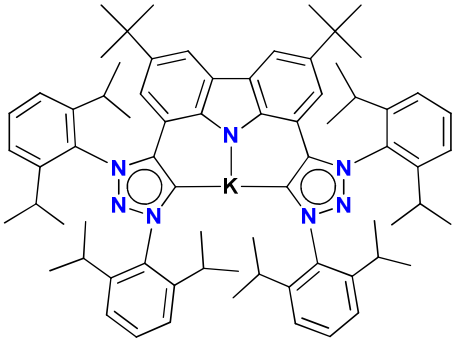

(CNC$_{Dipp}$)K (2$_a$)

© University of Pretoria

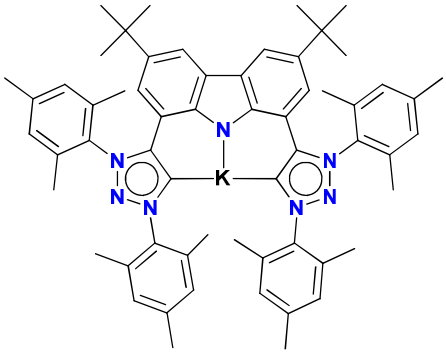

(CNC$_{Mes}$)K (3$_b$)

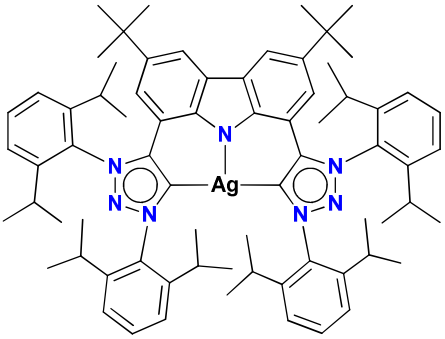

(CNC$_{Dipp}$)Ag(I) (4$_a$)

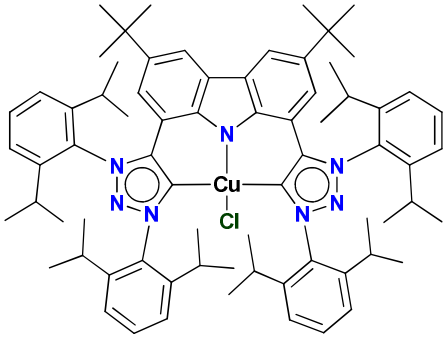

(CNC$_{Dipp}$)Cu(II)Cl (5$_a$)

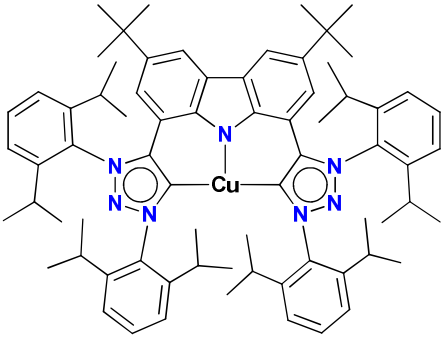

(CNC$_{Dipp}$)Cu(I) (6$_a$)

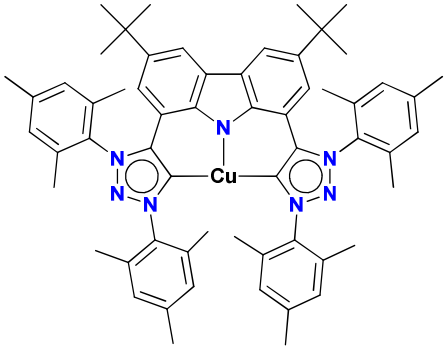

(CNC$_{Mes}$)Cu(I) (7$_b$)

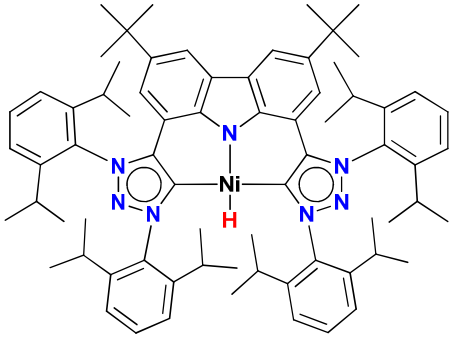

(CNC$_{Dipp}$)Ni(II)H (8$_a$)

© University of Pretoria

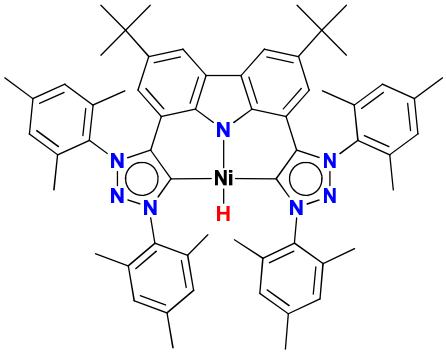

$(CNC_{Mes})Ni(II)H$ (9_b)

Chapter 2

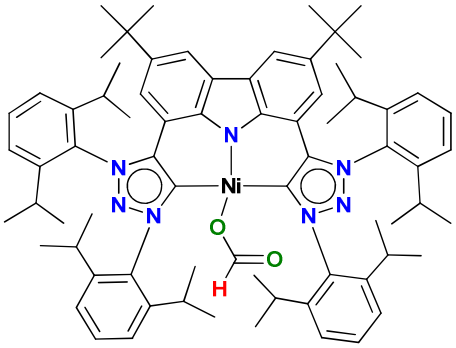

$(CNC_{Dipp})Ni(II)OCOH$ (10_a)

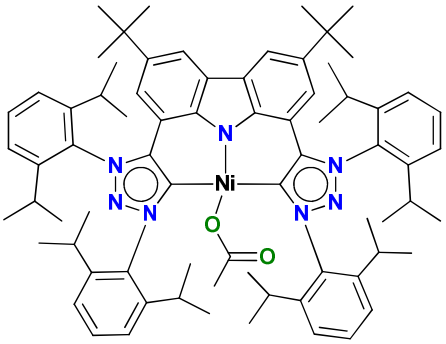

$(CNC_{Dipp})Ni(II)OCOCH_3$ (11_a)

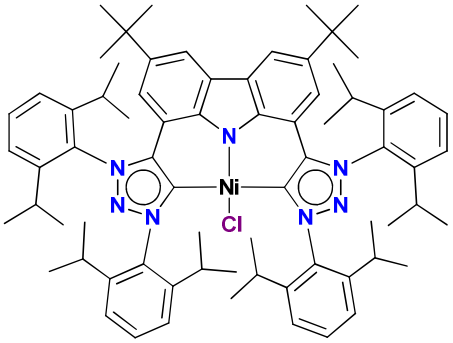

$(CNC_{Dipp})Ni(II)Cl$ (12_a)

© University of Pretoria

Chapter 3

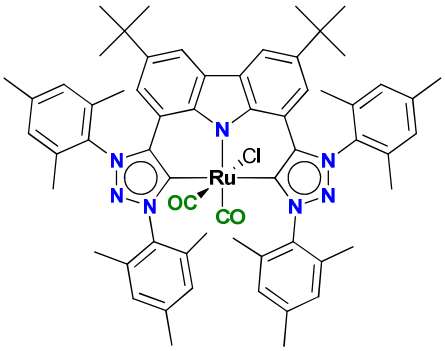

[(CNC$_{Mes}$)Ru(II)(CO)$_2$Cl] (13$_b$)

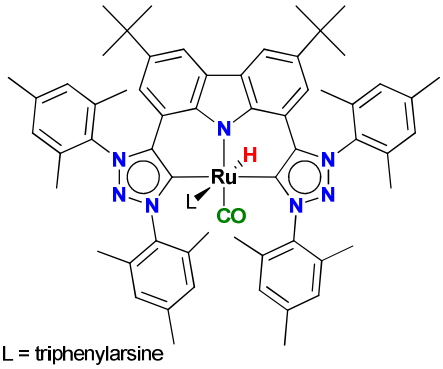

[(CNC$_{Mes}$)Ru(II)(AsPh$_3$)(CO)H] (14$_b$)

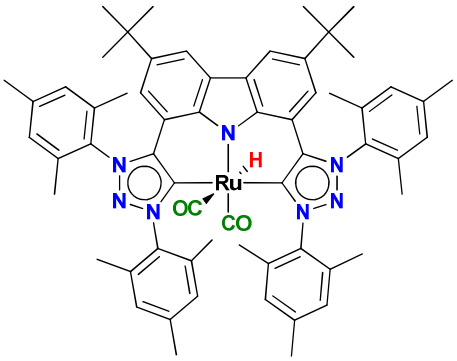

[(CNC$_{Mes}$)Ru(II)(CO)$_2$H] (15$_b$)

Chapter 4

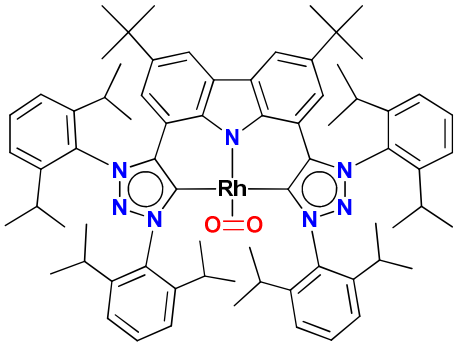

(CNC$_{Dipp}$)Rh(I)O$_2$ (16$_a$)

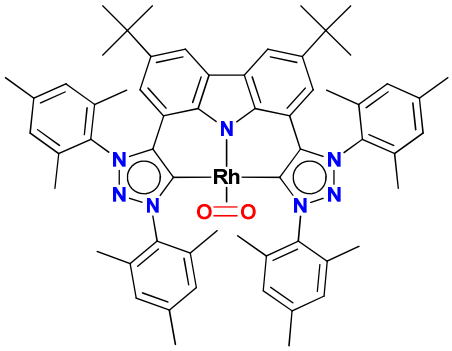

(CNC$_{Mes}$)Rh(I)O$_2$ (17$_b$)

© University of Pretoria

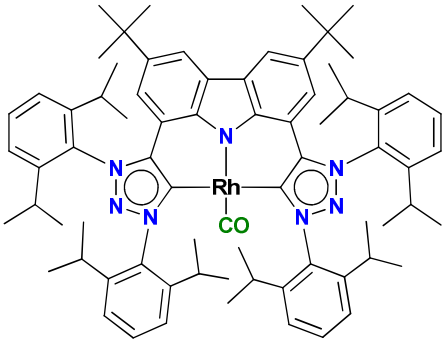

(CNC$_{Dipp}$)Rh(I)CO (18$_a$)

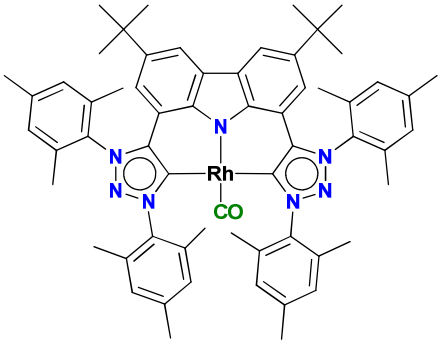

(CNC$_{Mes}$)Rh(I)CO (19$_b$)

Chapter 5

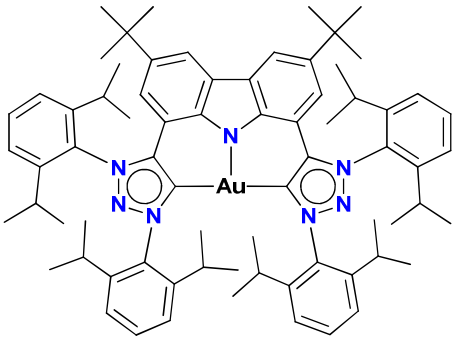

(CNC$_{Dipp}$)Au(I) (20$_a$)

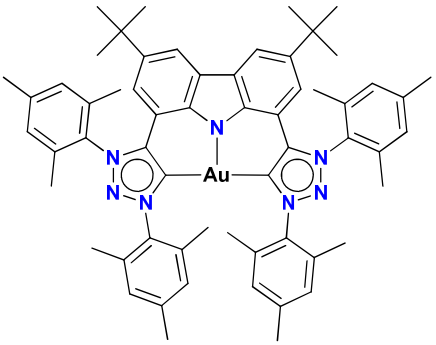

(CNC$_{Mes}$)Au(I) (21$_b$)

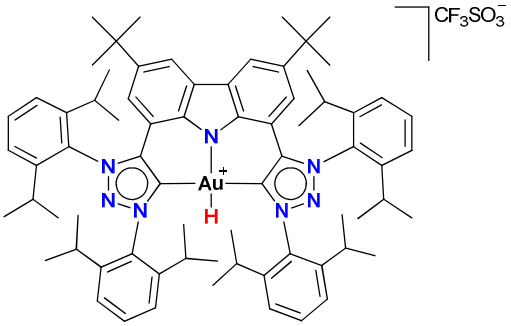

[(CNC$_{Dipp}$)Au(III)H]OTf (22$_a$)

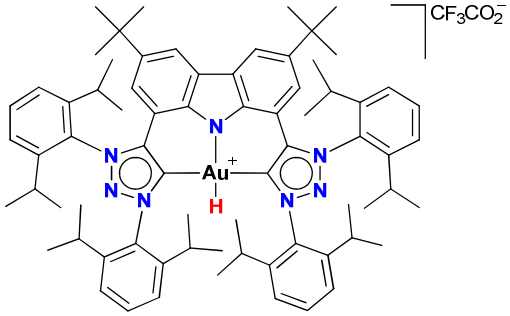

[(CNC$_{Dipp}$)Au(III)H]OAc^F (23$_a$)

© University of Pretoria

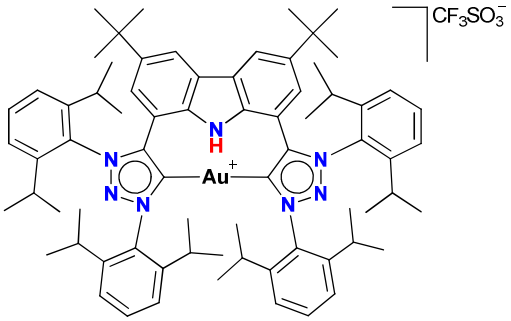

[(CNHC$_{Dipp}$)Au(I)]OTf (24$_a$)

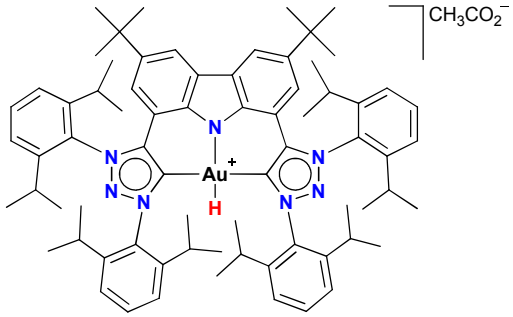

[(CNC$_{Dipp}$)Au(III)H]OAc (25$_a$)

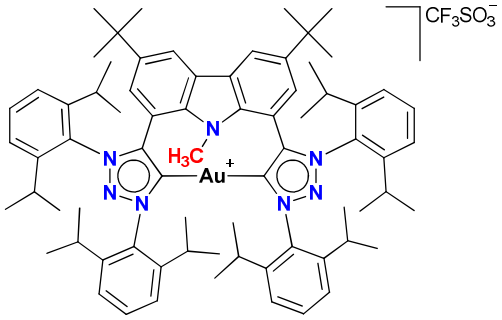

[(CNMeC$_{Dipp}$)Au(I)]OTf (26$_a$)

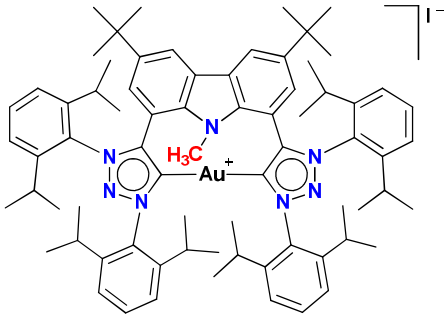

[(CNMeC$_{Dipp}$)Au(I)]I (27$_a$)

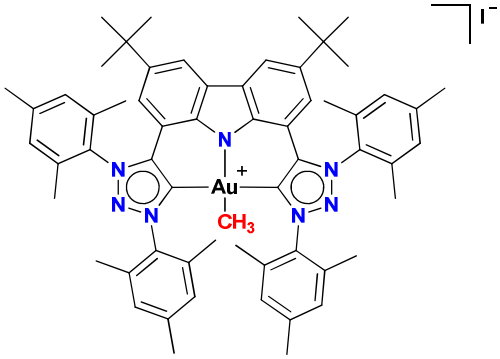

[(CNC$_{Mes}$)Au(III)CH$_3$]I (28$_b$)

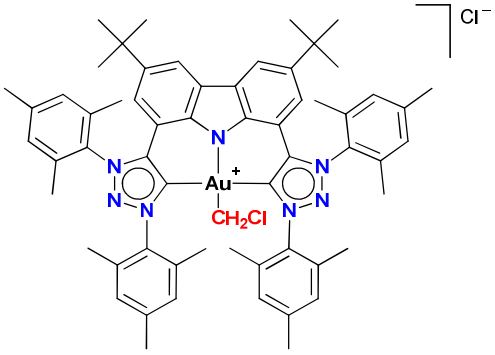

[(CNC$_{Mes}$)Au(III)CH$_2$Cl]Cl (29$_b$)

© University of Pretoria

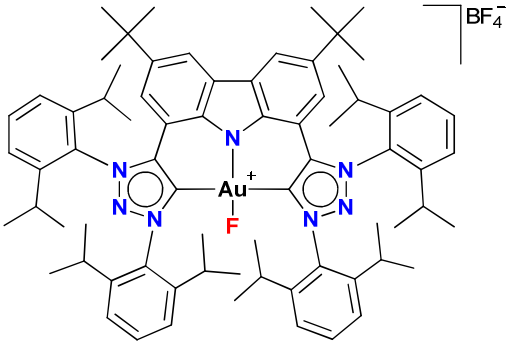

[(CNC$_{Dipp}$)Au(III)F]BF$_4$ (30$_a$)

Chapter 6

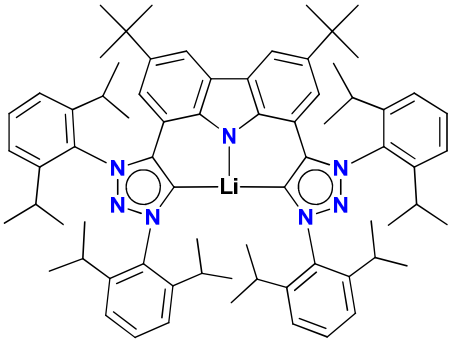

(CNC$_{Dipp}$)Li (31$_a$)

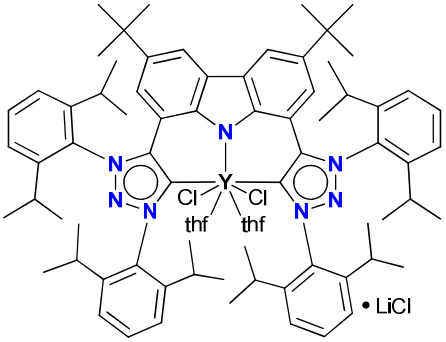

[(CNC$_{Dipp}$)YCl$_2$(thf)$_2$](LiCl) (32$_a$)

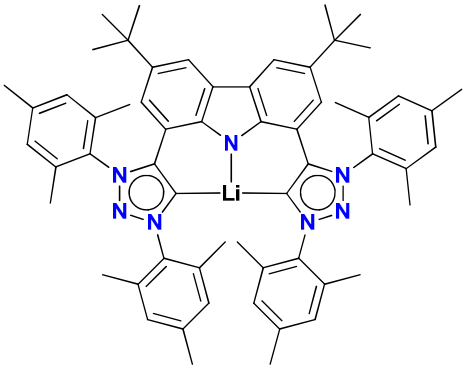

(CNC$_{Mes}$)Li (33$_b$)

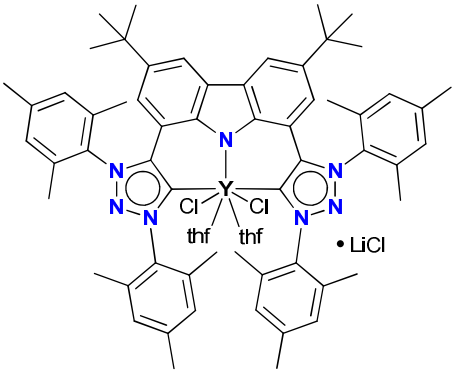

[(CNC$_{Mes}$)YCl$_2$(thf)$_2$](LiCl) (34$_b$)

© University of Pretoria

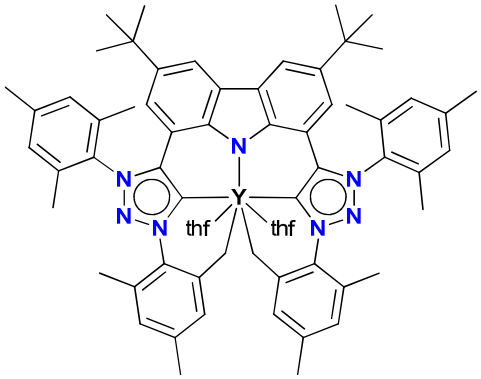

[(CNC$_{Mes}$)Y(thf)$_2$] (35$_b$)

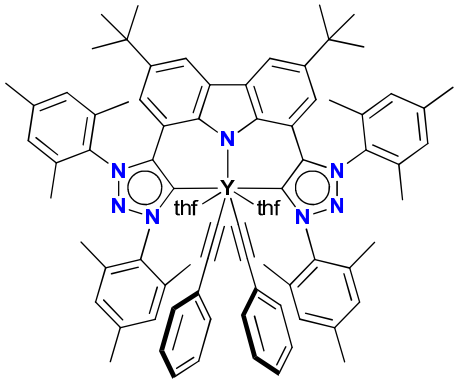

[(CNC$_{Mes}$)Y(C$_8$H$_5$)$_2$(thf)$_2$] (36$_b$)

© University of Pretoria

List of Abbreviations

aNHC	abnormal *N*-heterocyclic carbene
OAc	acetate
acac	acetylacetonato
Ad	adamantyl
R	alkyl/aryl
All	allyl
Å	angstrom
Ar	aryl
atm	atmosphere
ν_{av}	average stretching frequency
Bz	benzyl
nbd	bicyclo[2.2.1]hepta-2,5-diene or norbornadiene
IPr	*N*,*N'*-bis(2,6-diisopropylphenyl)imidazole-2-ylidene
bimca	1,8-bis(imidazolin-2-yliden-1-yl)carbazolide
BBN	9-borabicyclo[3.3.1]nonane
Bu	butyl
^{t}Bu	*tert*-butyl
Boc	*tert*-butyloxycarbonyl
HBcat	catecholborane
δ	Chemical shift
CuAAc	copper catalysed cycloaddition of alkynes with azides
J	coupling constant
CAAC	cyclic (alkyl)(amino) carbenes
COD	1,5-cyclooctadiene
coe	cyclooctene

© University of Pretoria

Cp	cyclopentadiene
DFT	density functional theory
°C	degrees Celsius
DBU	1,8-diazabicyclo[5.4.0]undec-7-ene
DCM	dichloromethane
Dipp	2,6-diisopropylphenyl
dme	dimethoxyethane
DMF	*N,N*-dimethylformamide
DMSO	dimethylsulfoxide
EPR	electron paramagnetic resonance
ESI-TOFMS	electrospray ionization-time of flight-mass spectrometry
E	entgegen
eq./equiv.	equivalent
Et	ethyl
fac	facial
FIA-ESI-MS	flow injection analysis-electrospray ionization-mass spectrometry
FT-IR	Fourier-transform infrared
g	gram
GC	gas chromatography
gem	geminal
NHC	*N*-heterocyclic carbene
HRMS	high resolution mass spectrometry
HOMO	highest occupied molecular orbital
Tp*	hydrotris(3,5-dimethylpyrazolyl)borate
Tp	hydrotris(3,5-di-2-propylpyrazolyl)borate
h	hour
IR	infrared

© University of Pretoria

int./interm.	intermediate
kcal	kilocalories
kg	kilogram
Ln	lanthanide
LA	Lewis acid
LB	Lewis base
LED	light emitting diode
LDA	lithium diisopropylamide
LUMO	lowest unoccupied molecular orbital
MS	Mass spectrometry
MP	Melting point
mer	meridional
MIC	mesoionic carbene
MC	metal centered
MLCT	metal-to-ligand charge transfer
Me	methyl
µL	microliter
µs	microsecond
mg	milligram
mL	milliliter
min	minute
MO	molecular orbital
nm	nanometer
ns	nanosecond
nNHC	normal/classical *N*-heterocyclic carbene
n.o.	not observed
NMR	nuclear magnetic resonance

© University of Pretoria

o	*ortho*
p	*para*
ppm	parts per million
Cp*	pentamethylcyclopentadienyl
Ph	phenyl
ps	picosecond
OPiv	pivalate
PVC	polyvinyl chloride
KHMDS	potassium bis(trimethylsilyl)amide
^{i}Pr	*iso*-propyl
py	pyridine
RT	Room temperature
s	seconds
SET	single-electron transfer
v	stretching frequency
tpy	terpyridine
thf/THF	tetrahydrofuran
tht	tetrahydrothiophene
$BArF_{24}$	tetrakis[bis(3,5-trifluoromethyl)phenyl]borate
TMEDA	*N,N,N',N'*-tetramethylethylenediamine
thd	tetramethylheptanedioate
IMe_4	tetra(methyl)imidazole-2-ylidene
TEP	Tolman Electronic Parameter
TH	transfer hydrogenation
*trz***H**	triazolium
trz	1,2,3-triazol-5-ylidene
OAc^F	trifluoroacetate

© University of Pretoria

OTf	trifluoromethanesulfonate or triflate
HOTf	trifluoromethanesulfonic acid or triflic acid
Vkd	2,8,9-triisopropyl-2,5,8,9-tetraaza-1-phosphabicyclo[3.3.3]undecane (Verkade's base)
Mes	2,4,6-trimethylphenyl or mesityl
TMS	trimethylsilyl
TDMPP	tris(2,6-dimethoxyphenyl)phosphine
tpz	trispyrazolylborate
TOF	turnover frequency
TON	turnover number
UV	ultraviolet
UV-vis	ultraviolet-visible
cm^{-1}	wavenumber
XRD	X-ray diffraction
Z	zusammen

© University of Pretoria

Chapter 1

Introduction

Ever increasing global challenges exhort a greater demand for an atom-economy driven climate, with methods for decreasing energy input and waste production finding an increasing preference over the rate of product fabrication.[1] In addition, modern day factors such as carbon tax, elaborate purification methods, the use of expensive and/or hazardous chemicals, as well as the production of dangerous by-products during a chemical process, govern the library of synthetic techniques available towards the production of valuable chemicals needed to sustain society on a daily basis. The above-mentioned problems can be addressed by appropriate ***catalyst*** design.[1] Complexes for catalysis have become the answer to a range of problematic questions such as: selectivity, which also directly affects purification procedures; costly energy input and waste production; use of stoichiometric amounts of hazardous chemicals; and, most importantly, environmentally benign chemical processes.[1,2]

The selectivity outcome of a catalyzed reaction greatly affects the atom-economy of that reaction.[1,2] In numerous catalytic processes, selectivity for a desired isomer remains a challenge. Fortunately, catalyst fine-tuning can yield a complex able to catalyze a reaction with good to perfect selectivity.[1,2,3] The choice of coordinating ligand plays a crucial role during catalyst optimization. Ligand manipulation has resulted in catalysts performing with increased selectivity and activity, whilst stabilizing the active complex and hampering catalyst decomposition.[1,2,3] One such family of ligands which has firmly cemented its position as one of the favoured amongst the range of ligand classes to choose from, are the κ^1-C carbene-based ligands.[4] Carbene ligands have been coordinated to metals for decades (see Figure 1.1 for selected cases representing first reported examples of various carbene types and carbene supported complexes),[5] but have only recently been extensively used as supporting ligands (innocent or non-innocent) during catalyst design.[6]

© University of Pretoria

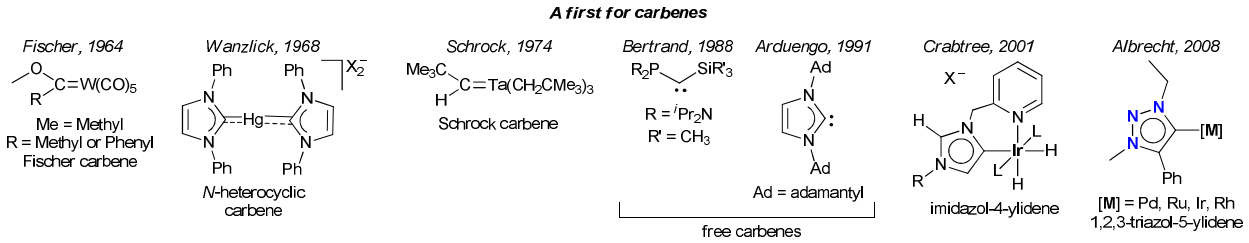

Figure 1.1: Selected cases representing first reported examples of various carbene classes[5]

Generally, coordination of a carbene ligand to a metal center not only yields a stable complex as desired catalyst, but also allows for the fundamental investigation of the reactivity profile of that complex and the catalytic reaction mechanism by which the catalyst operates.[3,4,6]

The study of the synthesis and complexation of triazolylidene ligands, a class of carbene-based ligands still underdeveloped at the time, has been a focus area in our research group. The current research project, the topic of this PhD thesis, was initiated during a Master's degree,[7] and has since been continued by the author of the study towards the completion of a PhD degree. Several of the complexes synthesized during the MSc study will be encountered throughout this thesis. Both triazolylidene and pincer-based ligands have been reviewed.[7] This include the synthetic methodologies concerning 1,2,3-tiazol-5-ylidenes, both their electronic properties and bonding considerations, as well as the effect of steric variation on the synthesized complexes. An overview of the pincer class of ligands was also included. Consequently, only a short review of triazolylidene ligands is given here, including some selected highlights within the field. For the tridentate pincer class of ligands, focus will be directed only towards carbazole-based ligands. In each of the subsequent chapters, a focused literature background on the state-of-the-art of the outlined study will be presented.

1.1 Triazolylidene ligands

It has not been ten years since the first reported example of a 1,2,3-triazol-5-ylidene (*trz*)-supported organometallic complex,[5g] yet this carbene ligand subclass has generated a surge in interest due to several game-changing developments.[8] These developments are not only attributed to their strong donor properties, but also to the facile preparation of the precursor triazolium salts (*trz***H**) and ease of ligand fine-tuning. Additionally, *trz* ligands are renowned for the stabilization it confers to metals in both high and low oxidation states. We can therefore, as intuitively expected, access organometallic

© University of Pretoria

complexes manifesting a range of oxidation states, which is extremely beneficial, especially during catalysis.[8] Triazolylidene-supported metal complexes for catalytic endeavors are resultantly very appealing, but these *trz* organometallic species are not limited to catalysis only. Both photophysical[9] and biological[10] disciplines have been boosted by metal complexes coordinated by *trz* ligands. These attributes and applications have rendered these organic compounds comparable to traditional NHC ligands in their usefulness, justifying further investigation of this class of persistent carbenes.

1.1.1 Brief overview of 1,2,3-triazol-5-ylidenes

Triazolylidene ligands can be obtained from their triazolium precursor salts (Scheme 1.1). In turn, these salts are generally synthesized through two methods, which includes the more popular copper catalyzed cycloaddition of an alkyne and an azide (CuAAC method, also known as the 'click' reaction), followed by alkylation of the isolated triazole (**I**, Scheme 1.1).[8] This method is simple, robust, and high-yielding and the work-up procedure is straight forward. In addition, two different regioisomers can be synthesized selectively by exchange of the copper catalyst for a ruthenium catalyst (**I**, Scheme 1.1).[8a] Preparation of *trz***H** precursors has been dominated by the CuAAC method based on the abovementioned advantages. The second, less explored method, involves the cycloaddition of 1,3-diaryl-2-azoniaallene salts with alkynes in the presence of *tert*-butyl hypochlorite (^{t}BuOCl) and KPF_6 or $SbCl_5$ (**II**, Scheme 1.1).[11] This method is more difficult and also not as high-yielding, but it does not require an alkylation step and the *trz***H** salt precursors can be isolated after the reaction. This synthetic route introduces a second bulky aryl substituent at the N-3 position. Therefore, a more sterically hindered ligand system is accessed that can especially be applied during synthesis and isolation of reactive complexes.[11] The corresponding *trz* metal complexes, or just the free *trz*, can be obtained through various synthetic protocols such as deprotonation and/or metallation, transmetallation from the pre-prepared silver or copper complexes, or simply direct metallation of the *trz***H** salt (**III**, Scheme 1.1).[8,11,12]

© University of Pretoria

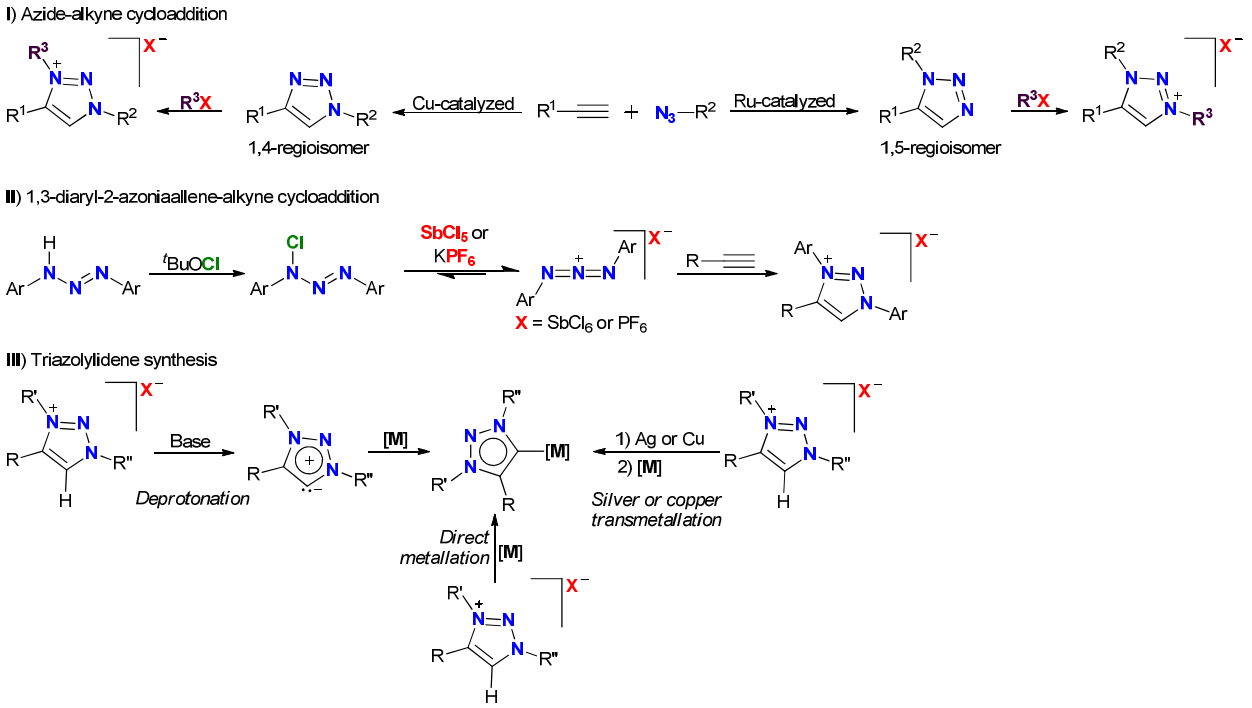

Scheme 1.1: Synthetic methods for **I**, **II**) *trz***H** and **III**) *trz* preparation

The donor properties of *trz* have been extensively evaluated. All of the data obtained correspond with a stronger donor ligand system compared to classical NHCs.[8,13] Triazolylidene ligands are therefore stronger donors compared to basic phosphine and NHC ligands, but still not as strong a donor as the imidazole-4-ylidene class of carbene ligands (Figure 1.2). Also, *trz* are weaker π-donor ligands compared to NHC ligands. Nonetheless, these stronger donor ligands have yielded metal complexes outperforming their NHC analogues in various catalyzed processes.[8] Another important feature of *trz,* is the possibility of these ligands to facilitate charge separations within the five-membered heterocycle, as is the case for imidazole-4-ylidenes (*vide infra*),[13] consequently leading to the dubbing of these carbenes as "mesoionic carbenes" or MICs.[8,11,12] A probable explanation for the ability of *trz* ligands to stabilize metals in various oxidation states can be based on the aforementioned intramolecular charge separation. Neutral *trz* ligands would readily stabilize metals with a low oxidation number, while a vinylic carbon metal bond, a direct result of charge separation, would stabilize metals in higher oxidation states. The strong σ- and weak π-donor properties of *trz* ligands, in addition to their facile preparation and the high stability imparted to metal complexes, have brought about both interesting and exceptional results owing to the use of these ligands.

© University of Pretoria

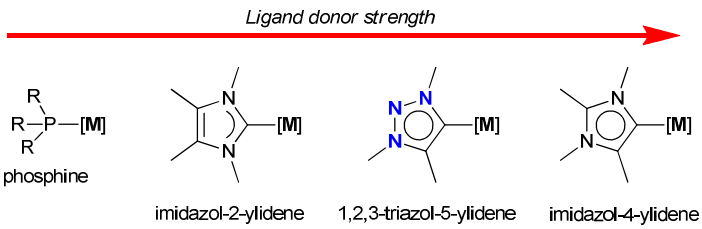

Figure 1.2: Simplified representation of ligand donor strength scale[13]

1.1.2 Selected recent highlights of 1,2,3-triazol-5-ylidene compounds

The synthesis of a triazolium salt featuring bulky substituents around the heterocycle permitted the isolation of the first free triazolylidene (Figure 1.3).[12] Less bulky substituents resulted to decomposition within a few hours at elevated temperature (50 °C), but the increased steric bulk inhibited bond rearrangement as well as the Wanzlick dimerization pathway, a decomposition route encountered for NHCs but not triazolylidenes.[12] The first example of a triazolylidene supported cobalt(III) complex was recently disclosed (Figure 1.3).[14] It was demonstrated that the cobalt catalyst was an effective electrocatalyst for hydrogen production, with turnover numbers at very low overpotential. It was further reported that the analogous triazole complexes did not exhibit any electrocatalytic activity, while the *trz* supported complex was robust against excess acids.[14] A triazolylidene-stabilized borenium ion was prepared for the hydrogenation of imines and N-heterocycles (Figure 1.3).[15] Remarkably, the organocatalyst mediated this catalyzed reaction at ambient temperature, and at low hydrogen gas pressure. This is a marked improvement from the corresponding NHC analogue, which required high temperatures and hydrogen gas pressure.[15] The hydrosilylation of aldehydes was efficiently catalyzed by a cyclometallated, *trz* supported nickel complex (Figure 1.3).[16] The catalytic reduction reaction reached very high turnover numbers, with only 0.05 mol % catalyst loading after just 20 minutes. The catalyst exhibited a high selectivity for the aldehyde functionality, even in the presence of other carbonyl moieties, such as ketones.[16] Very recently a cationic iron(III) complex, supported by three bidentate triazolylidene coordinating ligands, was prepared (Figure 1.3).[17] The unique properties of *trz* ligands directly resulted in an iron complex demonstrating a long-lived excited state life-time of 100 ps, in addition to room temperature photoluminescence.[17] These examples illustrate the unique advantages accessed through the use of *trz* ligands (Figure 1.3).

© University of Pretoria

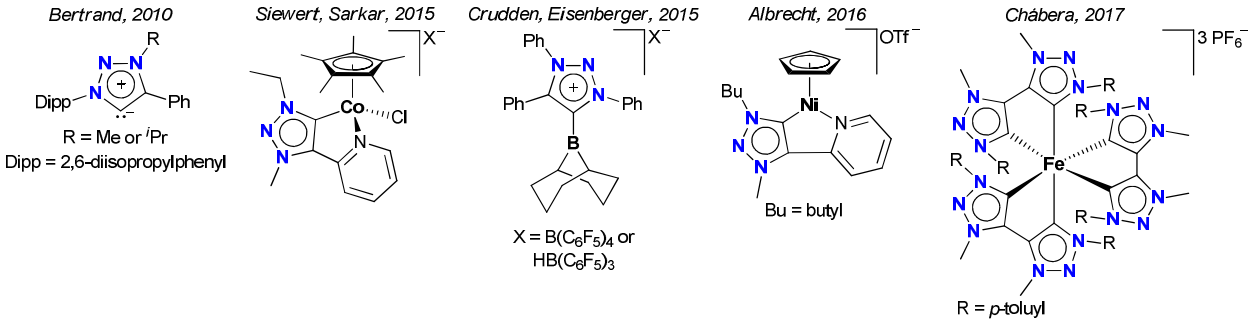

Figure 1.3: Selected highlights in the field of *trz* organometallic complexes

The mentioned stabilization conveyed to metals in various oxidation states (through intramolecular charge separation), was demonstrated by Albrecht and co-workers.[8d] Charge separation was reported to be one of main factors directly responsible for the excellent catalytic activity of iridium[18] (**I**, Figure 1.4) and ruthenium[19] water oxidation catalysts (for the example of the ruthenium water oxidation catalyst, see chapter 3). The *trz* supported catalyst mediated the challenging water oxidation reaction with efficient oxygen evolution, reaching high turnover numbers in the presence of a sacrificial Ce(IV) oxidant.[18] Intramolecular charge separation not only improves stability of the intermediate complexes, but also acts as a reservoir for positive and negative charges (such as hydrogen ions). This feature of *trz* ligands is exploited during the water oxidation process, whereby proton transfer from the bound water molecule to the olefinic fragment drives the multielectron process (**II**, Figure 1.4).[13] We can therefore propose that *trz* ligands have an inherent non-innocent ligand behavior, further enhancing their role in catalysis.

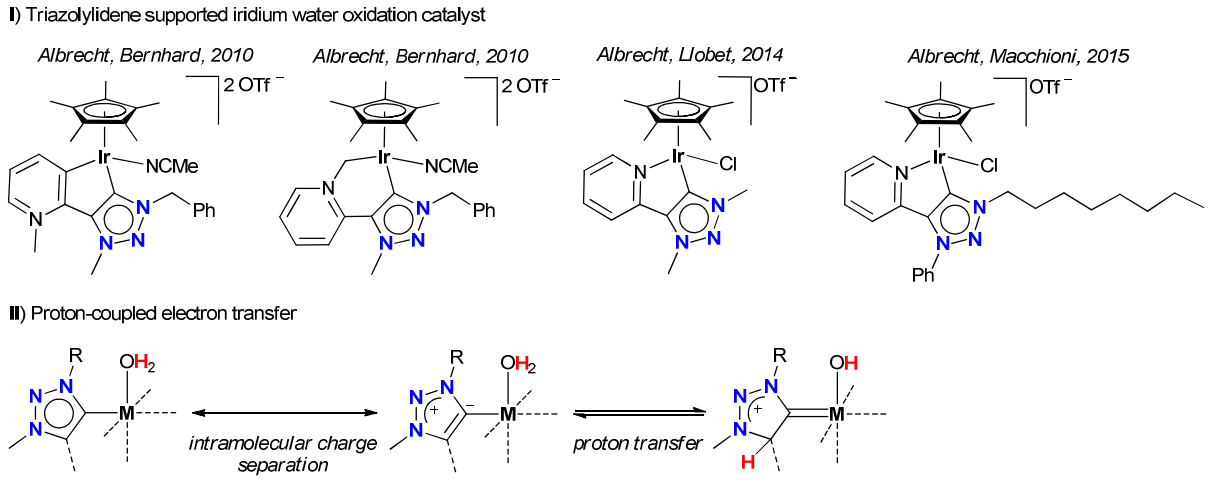

Figure 1.4: Highly efficient **I**) iridium water oxidation catalyst and **II**) the proton-coupled electron transfer process[13,18]

© University of Pretoria

1.2 The carbazole ligand scaffold

The carbazole-scaffold has materialized as one of the privileged class of ligands; the pincer ligands. Indeed, the pincer class of ligands has emerged as a powerful tool in general chemistry and especially within the realms of catalysis,[20] while seminal achievements within various disciplines, such as organometallic chemistry, biology, photoluminescence, etc. have also been reported. The huge success attained by pincer ligands is not only ascribed to the formation of stable complexes upon coordination of the ligand to the metal, but also due to their electronic and steric properties. Both properties can be readily fine-tuned to access a tailor-made pincer ligand that, upon coordination to a metal center (or even main-group and rare-earth elements), yields the desired complex catalyst.[20] This custom-made catalyst can mediate a catalytic reaction with marked improvement in both rate of catalysis and selectivity outcome, compared to classical catalytic or synthetic procedures. The same holds for the carbazole ligand scaffold (Figure 1.5). Isolation of both reactive species/intermediates and catalytically active metal complexes has been permitted through the use of functionalized carbazole ligands.

The carbazole platform is a rigid, aromatic scaffold.[21] A range of functionalization strategies enable the incorporation of various functional groups around the carbazole scaffold. Indeed, substitution of positions 1 and 8, as well as positions 3 and 6, has resulted in the formation of a plethora of carbazole-based pincer ligands (see Figure 1.6, *vide infra*). In most instances, alkyl substituents are introduced at positions 3 and 6. It serves two purposes: *1*) functional group size variation at this position allows for remote steric control and; *2*) alkylation protects the position *para* to the amido moiety, permitting further functionalization of position 1 and 8 without the possibility of undesired polysubstitution reactions occurring (Figure 1.5). As is evident from Figure 1.5, metallation of the carbazole ligand would result in either five- or six-membered metallacycle formation, depending on the introduction, or lack thereof, of a linker atom (represented as **X** in Figure 1.5).[20,21] The carbazole scaffold is a prime example of electronic variation permitted around pincer ligands. The central basic, hard X-type amido moiety serves not only as an anchor between the metal and the ligand, but is likewise directly responsible for increased electron donation towards the metal.[20,21] The donor atom **D** (Figure 1.5), directly bonded to the metal, can be varied for either soft or hard and weak or strong donor atoms. Typically, both strong and weak, soft donor atoms readily coordinate to late transition metals anchored in the pincer pocket, forming favourable bonds and therefore stabilizing the isolated complex. Lewis acidic metals enjoy favourable interactions with hard basic donor functionalities, either weak or, preferably, strong donors. The electronic situation can further be altered at indirect sites. Both the linker atom **X** (Figure 1.5) and

© University of Pretoria

the **R'** substituents directly bonded to the donor atom **D** (Figure 1.5), can be changed to either increase electron donation to the donor atom (ultimately leading to increased electron density at the metal), or decrease electron density at the donor atom (and therefore at the metal) through incorporating electron withdrawing functionalities.[20,21] The steric properties of the envisaged ligand can also be varied at the **R'** substituents (Figure 1.5). Sterically encumbering substituents permit isolation of reactive species, while small **R'** groups yield catalysts with improved catalytic performance due to increased access of the incoming substrates to the catalytically active metal center.[20,21]

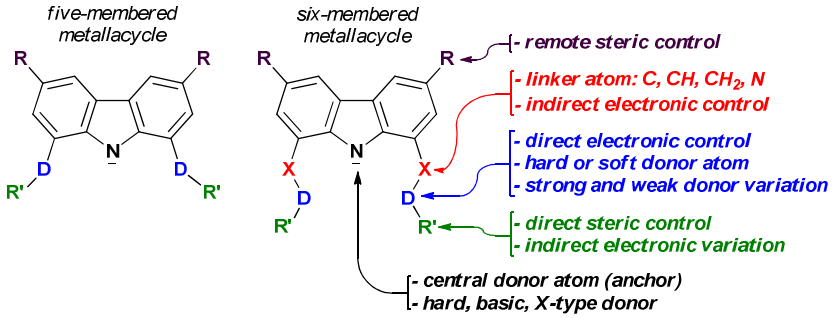

Figure 1.5: DND-anionic carbazole pincer platform

The large degree of freedom with regards to the variation of both steric and electronic properties, has enabled the preparation of a wide range of carbazole-based PNP-[22] and NNN-pincer[23] ligands, which were successfully coordinated to an assortment of metals (see Figure 1.6 for examples of PNP- and NNN-pincer ligands).

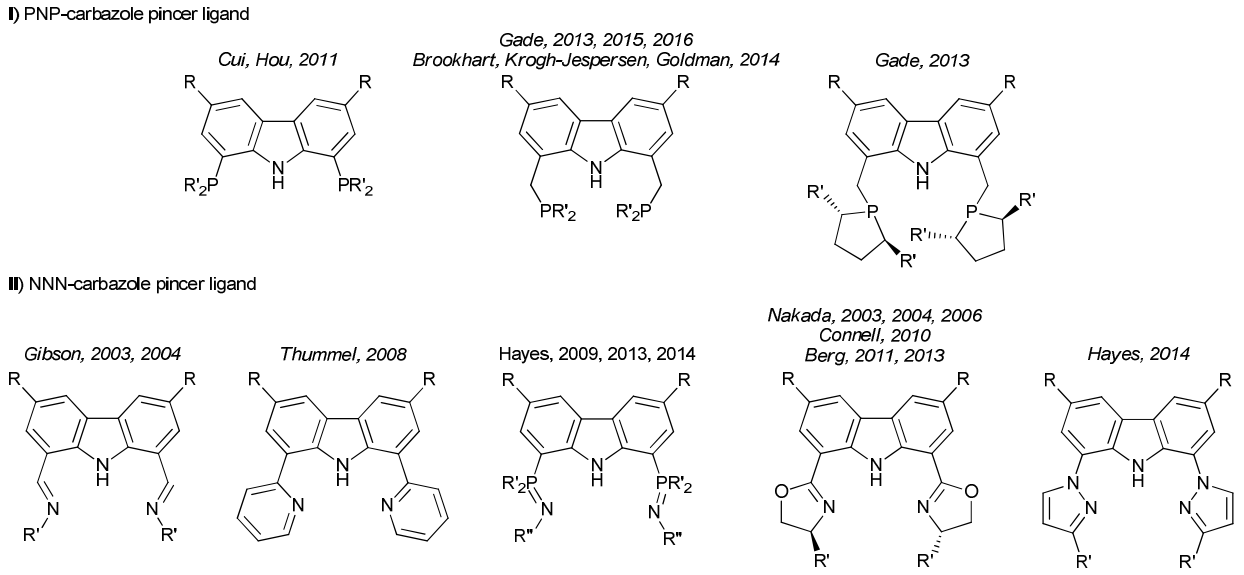

Figure 1.6: Representative examples of **I**) PNP- and **II**) NNN-carbazole pincer ligands

© University of Pretoria

An NHC-based CNC-carbazole pincer ligand (bimca) was reported by Kunz and co-workers (Scheme 1.2).[24] The soft-hard-soft donor ligand proved sufficient to stabilize various reactive late transition metals. The lithium carbene adduct could readily be synthesized employing three equivalents of MeLi or LDA (lithium diisopropylamide).[24,25] Salt metathesis reactions from the *in situ* generated lithium carbene adduct with $CuCl_2$, resulted in the formation of the (bimca)CuCl complex (Scheme 1.2).[26] The [(bimca)AuCl]Cl was synthesized through a transmetallation reaction, from the *in situ* generated silver complex (Scheme 1.2).[26] Both rhodium[24] and iridium[27] carbonyl complexes, supported by the bimca ligand, could also be obtained through a salt metathesis reaction with the appropriate metal precursor (Scheme 1.2). The rhodium and iridium carbonyl products readily facilitated the oxidative addition reaction of allyl chlorides,[27,28] while the rhodium analogue additionally mediated the oxidative addition of iodomethane (Scheme 1.2).[24] A one-pot synthetic route, employing Ni(0), Pd(0) or Pt(0) in addition to two equivalents of MeLi, resulted to *in situ* deprotonation and formal oxidative addition, with concomitant formation of the corresponding metal hydrides (Scheme 1.2).[29] Both Pd and Pt hydrides were reported to be stable, while the (bimca)Ni-H complex decomposed after several hours.[29] A (bimca)Ru(Cp*) complex was also reported by Kunz and co-workers,[30] and is further discussed in chapter 3.

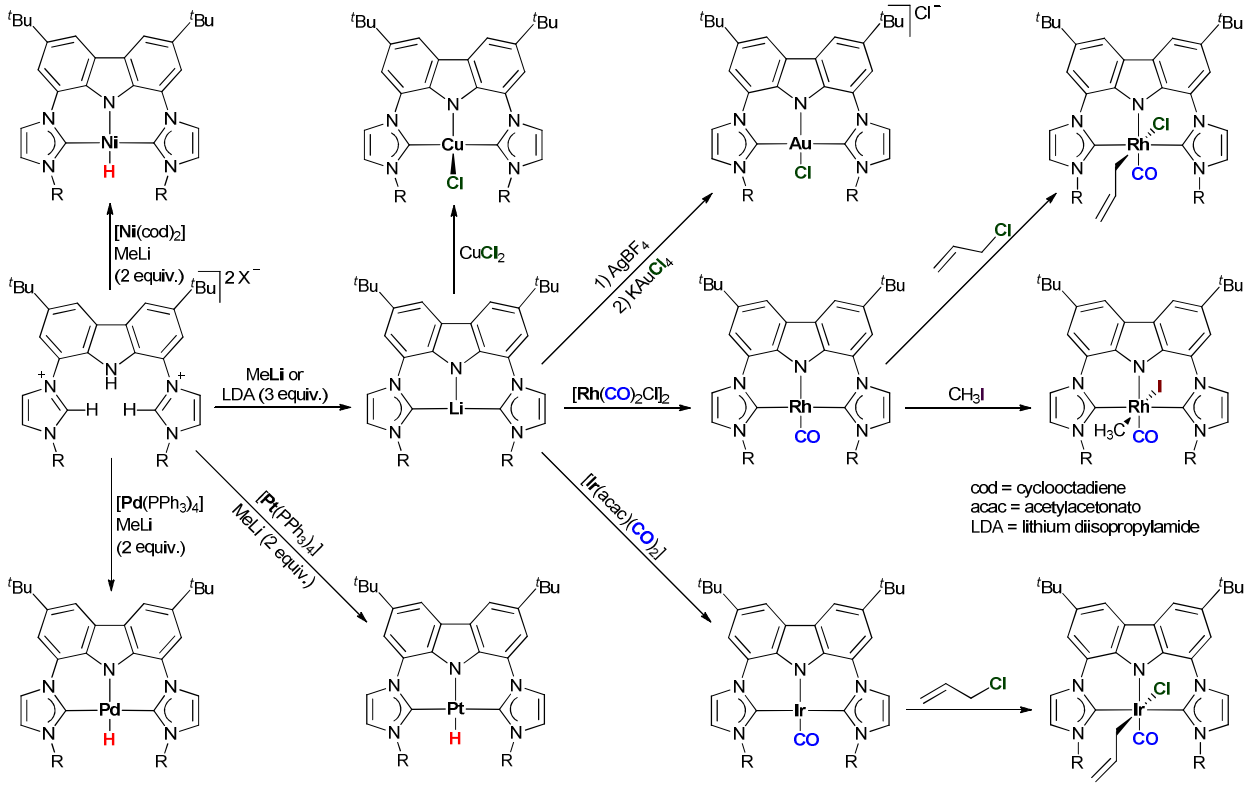

Scheme 1.2: Various bimca supported transition metal complexes[24-29]

© University of Pretoria

As is evident from the various abovementioned examples, the incorporation of strong donor carbene ligands leads to the isolation of metals with a high nucleophilic character, while the carbazole ligand framework provides a scaffold to adequately stabilize a range of transition and lanthanide organometallic complexes. Substitution of the NHC ligands with *trz*, would therefore result in a stronger donor ligand scaffold. As such, we set out to prepare a CNC-pincer ligand similar to the bimca ligand, but with the incorporation of *trz* as carbene donor ligands (Figure 1.7). The *trz* moieties would be prepared *via* the cycloaddition of 1,3-diaryl-2-azoniaallene salts with alkynes, in order to obtain the diarylated heterocycles (Figure 1.7). We had reasoned that both the carbazole scaffold and the increased steric bulk around the *trz* donors, would allow for the isolation of reactive species due to increased steric stabilization.[31] The strongly donating *trz* and amido moieties will increase the electron density at the metal center, thereby yielding metal complexes with higher nucleophilic character, which could be beneficial for catalytic applications.

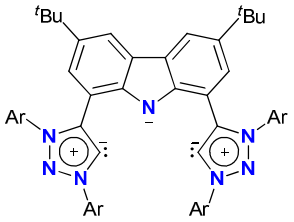

Ar = 2,6-diisopropylphenyl or 2,4,6-trimethylphenyl

Figure 1.7: Targeted *trz* CNC-pincer ligand featuring a carbazole backbone

1.3 Bis(1,2,3-triazol-5-ylidene)carbazolide[31]

The targeted dicationic triazolium salts (see Figure 1.7, *vide supra*) could be prepared through the cycloaddition of 1,3-diaryl-2-azoniaallene salts with 1,8-diethynylcarbazole. The products could be isolated with high purity and in moderate yields (Scheme 1.3). Both ligands $\mathbf{L_a}$ and $\mathbf{L_b}$ were fully characterized, which includes structure determination through X-ray diffraction (XRD) analysis of suitable crystals.[7] It was determined that deprotonation of $\mathbf{L_a}$ with three equivalents of base (which includes the use of either $KN[Si(CH_3)_3]_2$ or ^{n}BuLi), did not lead to deprotonation of all three acidic protons, even when working under strict inert conditions (Scheme 1.3). Rather, the mono-deprotonated salt $\mathbf{1_a}$ was isolated as a bright orange solid in high yields. Fortunately, the free carbene ligands could be isolated as the potassium salts $\mathbf{2_a}$ and $\mathbf{3_b}$ (Scheme 1.3), after treating the dicationic ligand salts $\mathbf{L_a}$ and $\mathbf{L_b}$ with five equivalents of $KN[Si(CH_3)_3]_2$ in either THF or Et_2O, respectively. Both solvent systems permitted the synthesis of $\mathbf{2_a}$ and $\mathbf{3_b}$, but the products were isolated with higher yields when using Et_2O as the

© University of Pretoria

solvent of choice. Slow evaporation of a benzene solution of **2**$_a$ yielded crystals suitable for XRD analysis. The free carbene adduct exists as a dimer in the solid state, with two potassium counterions coordinated by two free carbene ligands (Figure 1.8). Interestingly, the potassium salts **2**$_a$ and **3**$_b$ were indefinitely stable in the solid state and in solution, under inert conditions. Additionally, a THF solution of **2**$_a$ was refluxed for several hours in the absence of air and moisture, with no sign of decomposition. This is a testament of the high degree of stabilization imparted by the bulky and rigid ligand scaffold, and the incorporation of two aryl substituents at both *trz* nitrogen positions.

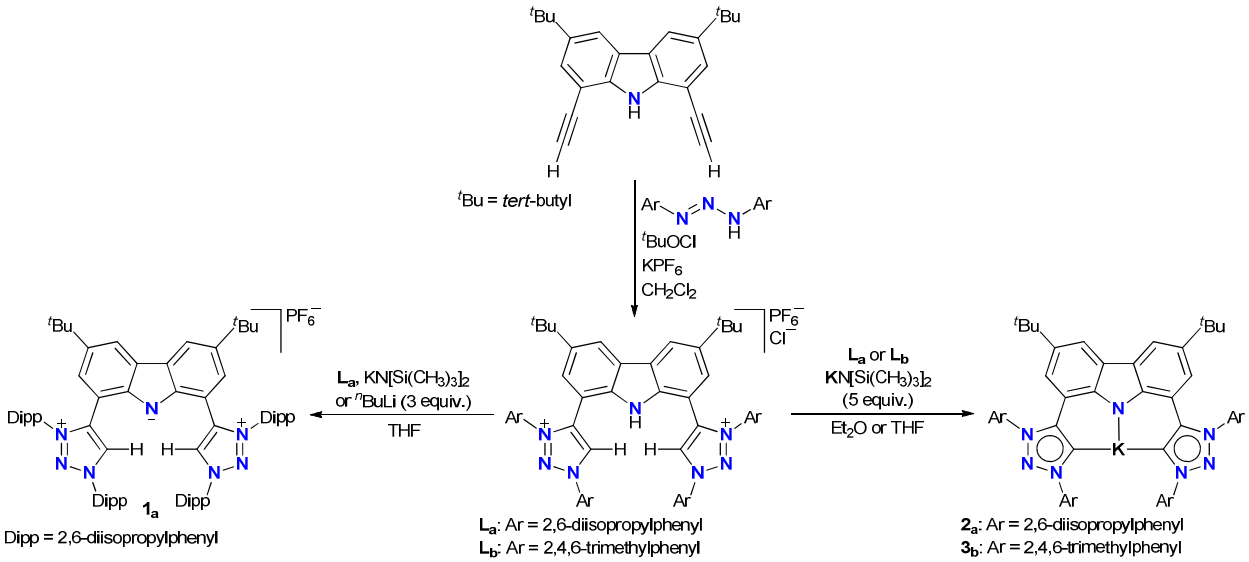

Scheme 1.3: *Trz***H** and *trz* salt synthesis

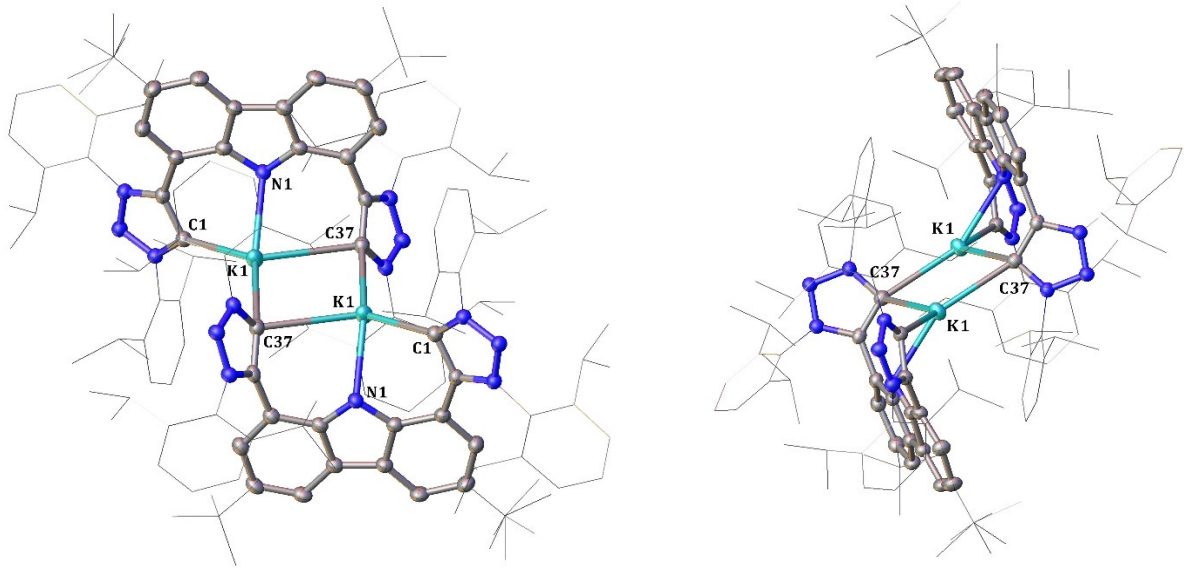

Figure 1.8: Crystal structure of **2**$_a$ (Hydrogens and solvent molecules omitted for clarity. The wingtip substituents and the *tert*-butyl groups have been drawn as wireframes for ease of viewing).[7,31]

© University of Pretoria

The dicationic salt $\mathbf{L_a}$ was reacted with silver oxide in CH_2Cl_2, in the presence of KBr (Scheme 1.4). The corresponding silver carbene complex $\mathbf{4_a}$ was isolated as an orange solid. The (CNC_{Dipp})Ag(I) complex has a unique T-shaped geometry around the metal center (Figure 1.9). This is indeed a unique result as coinage metals generally adopt a two-coordinate, linear complex geometry. Surprisingly, the planned transmetallation reaction with $CuCl_2$ was unsuccessful (Scheme 1.4). The absence of a reaction is in all probability a result of the formation of a highly stable silver carbene complex upon pincer coordination. Fortunately, the targeted copper(II) carbene complex could be synthesized through a one-pot deprotonation and metallation reaction (Scheme 1.4). The (CNC_{Dipp})CuCl complex $\mathbf{5_a}$ was isolated as a brown solid. The paramagnetic nature of $\mathbf{5_a}$ was evidenced during NMR experiments. Resultantly, formation of $\mathbf{5_a}$ was unequivocally verified through XRD studies (see Figure 1.9 for crystal structure of $\mathbf{5_a}$) and mass spectrometric analysis. Copper(II) carbene complexes are postulated intermediates in various copper carbene catalyzed reactions, warranting their synthesis and isolation.[32] However, these species are generally too reactive to isolate, while their paramagnetic nature further complicates characterization of isolable species.[26,32] It therefore comes as no surprise that there are only a handful of copper(II) carbene examples reported to date.[26,32,33]

To further exploit the stabilizing ability of the pincer ligand, we attempted to synthesize the elusive copper(II) hydride carbene complex. To access the proposed hydride complex, $\mathbf{5_a}$ was treated with stoichiometric amounts of $LiHB(CH_2CH_3)_3$ (Scheme 1.4). Unfortunately, the targeted copper hydride was not isolated. Instead, the reaction of $\mathbf{5_a}$ with the hydride source resulted in the reduction of Cu(II) to the corresponding Cu(I) complex $\mathbf{6_a}$. Complex $\mathbf{6_a}$ could also be obtained through a one-pot deprotonation and metallation reaction, employing CuI as the metal precursor (Scheme 1.4). The reaction progressed readily, and after purification procedures, products $\mathbf{6_a}$ or $\mathbf{7_b}$ (if $\mathbf{L_a}$ or $\mathbf{L_b}$ was used as ligand salt precursors, respectively) were isolated as brown solids. Crystals of $\mathbf{6_a}$ suitable for X-ray analysis could be obtained through slow evaporation of a benzene solution (Figure 1.9). As was the case for the silver complex $\mathbf{4_a}$, the coinage metal adopts a T-shaped geometry around the copper center. Both copper(I) carbene complexes were remarkably stable, even when stored under atmospheric conditions for several years. Deprotonation of both ligands $\mathbf{L_a}$ and $\mathbf{L_b}$ in the presence of $[NiCl_2(dme)]$ (dme = dimethoxyethane) resulted in the unexpected formation of the corresponding nickel hydride products $\mathbf{8_a}$ and $\mathbf{9_b}$, respectively, instead of the nickel chloride complexes (Scheme 1.4). It was suggested that hydride formation occurs through either a C-H bond insertion reaction, similar to the reported example by Cavell and co-workers,[34] or *via* an N-H insertion mechanism.[29] The nickel hydride complexes $\mathbf{8_a}$ and $\mathbf{9_b}$ were remarkably stable, even under atmospheric conditions. In fact, bubbling (un-dried) oxygen through a

© University of Pretoria

deuterated benzene solution of **8a** did not lead to any detectable signs of decomposition products after several days. It was only when the aforementioned solution saturated with oxygen was heated up to 80 °C for two days that a change was noted, as determined by NMR analysis. Crystal structure determination of **8a** allowed for the unambiguous localization of the hydride atom in the square-planar complex (Figure 1.9). It is interesting to note that only a few examples of nickel hydride carbene complexes have been reported to date; a result of their high reactivity.[29,34,35]

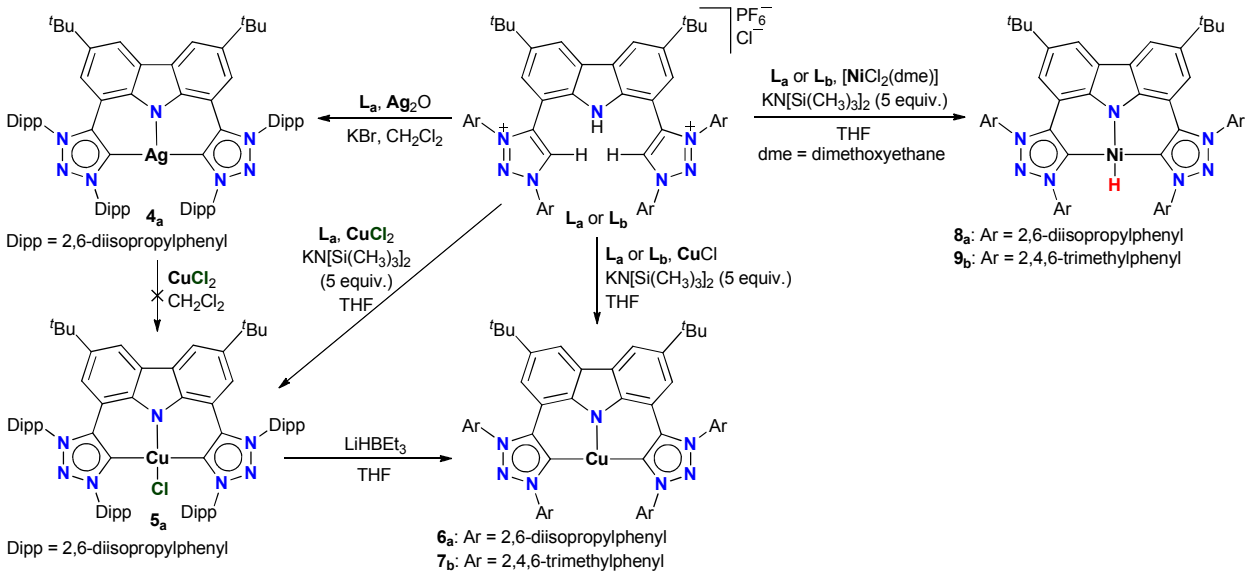

Scheme 1.4: Coordination of ligands derived from salt precursors **La** and **Lb** to various late transition metals

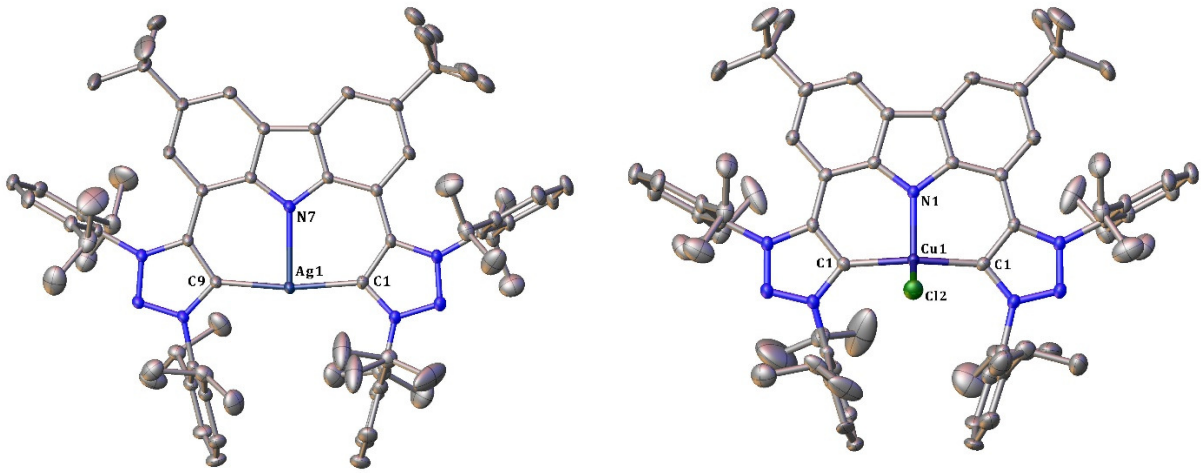

4a **5a**

© University of Pretoria

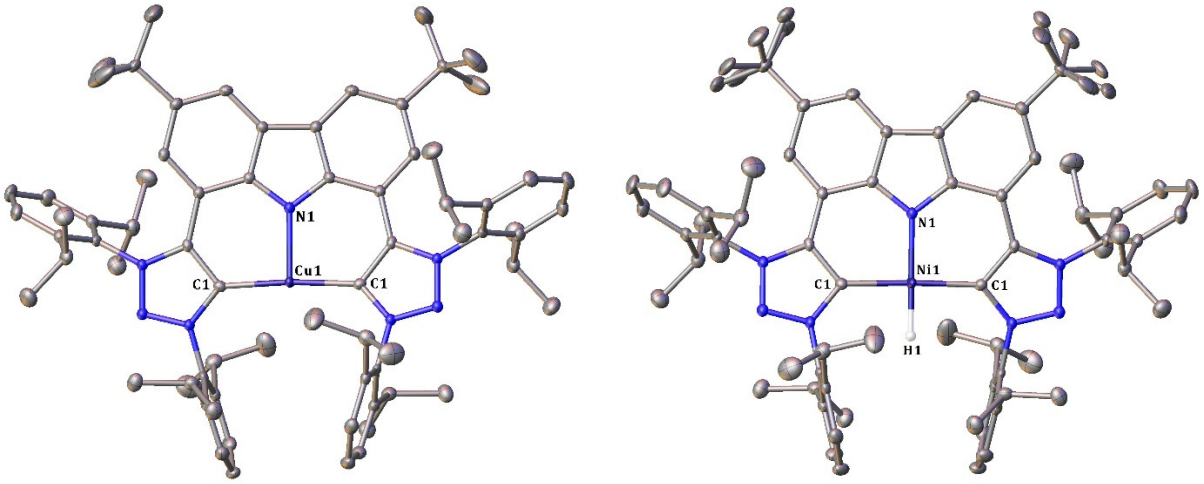

6_a **8_a**

Figure 1.9: Crystal structures of bis(1,2,3-triazol-5-ylidene)carbazolide supported late transition metal complexes (hydrogens and solvent molecules omitted for clarity)[7,31]

1.4 Aim

The bis(1,2,3-triazol-5-ylidene)carbazolide ligand scaffold has permitted the facile isolation of reactive complexes, which has been traditionally viewed as not isolable. The aforementioned complexes feature unique properties that could lead to complexes mediating various stoichiometric and/or catalytic reactions. Accordingly, the reactivity of the complexes synthesized will be investigated; including the reactivity of the nickel hydride complex **8_a** towards small molecule activation in a range of stoichiometric reactions.

The ligand precursor salts **L_a** and **L_b** will furthermore be coordinated to other late transition metals, which are known 'heavy weights' within the field of catalysis. Successful isolation of the targeted complexes will be followed by catalytic investigation of the aforementioned products.

Ligand coordination will also be expanded to heavier metals. This includes late transition metals as well as rare earth metals. The ligand stabilizing factor could mediate the isolation of such highly reactive complexes. On the other hand, the unique properties of the ligand, such as its strong electron donating ability and the soft-hard-soft donor sites, could lead to heavy metal complexes with novel fundamental reactivity patterns.

© University of Pretoria

1.5 References

[1] See book chapter, review articles and reference therein: *a*) I. Delidovich, R. Palkovits, *Green Chem.*, **2016**, *18*, 590 – 593; *b*) S. L. Suib, ed., *New and Future Developments in Catalysis*, Elsevier, Amsterdam, **2013**; *c*) R. A. Sheldon, *Chem. Soc. Rev.*, **2012**, *41*, 1437 – 1451; *d*) B. M. Trost, Atom Economy: a Challenge for Enhanced Synthetic Efficiency. *Handbook of Green Chemistry*, *7*, 1 – 35, **2012**; *e*) C.-J. Li, B. M. Trost, *PNAS*, **2008**, *105*, 13197 – 13202; *f*) B. M. Trost, *Acc. Chem. Res.*, **2002**, *35*, 695 – 705; *g*) B. M. Trost, *Angew. Chem. Int. Ed.*, **1995**, *34*, 259 – 281.

[2] See review articles and references therein: *a*) Q.-W. Song, Z.-H. Zhou, L.-N. He, *Green Chem.*, **2017**, *19*, 3707 – 3728; *b*) Y.-F. Liang, N. Jiao, *Acc. Chem. Res.*, **2017**, *50*, 1640 – 1653; *c*) V. F. Batista, D. C. G. A. Pinto, A. M. S. Silva, *ACS Sustainable Chem. Eng.*, **2016**, *4*, 4064 – 4078; *d*) N. Kumagai, M. Shibasaki, *Chem. Eur. J.*, **2016**, *22*, 15192 – 15200; *e*) R. Castarlenas, A. D. Giuseppe, J. J. Pérez-Torrente, L. A. Oro, *Angew. Chem. Int. Ed.*, **2013**, *52*, 211 – 222; *f*) B. Li, P. H. Dixneuf, *Chem. Soc. Rev.*, **2013**, *42*, 5744 – 5767; *g*) K. Godula, D. Sames, *Science*, **2006**, *312*, 67 – 72.

[3] See review articles and references therein: *a*) J. F. Hartwig, *Acc. Chem. Res.*, **2017**, *50*, 549 – 555; *b*) N. Funken, Y.-Q. Zhang, A. Gansäuer, *Chem. Eur. J.*, **2017**, *23*, 19 – 32; *c*) N. V. Tzouras, I. K. Stamatopoulos, A. T. Papastavrou, A. A. Liori, G. C. Vougioukalakis, *Coord. Chem. Rev.*, **2017**, *343*, 25 – 138; *d*) H. Li, C. Mazet, *Acc. Chem. Res.*, **2016**, *49*, 1232 – 1241; *e*) N. D. Ca', M. Fontana, E. Motti, M. Catellani, *Acc. Chem. Res.*, **2016**, *49*, 1389 – 1400; *f*) Y. Wei, X. Zeng, *Synlett*, **2016**, *27*, 650 – 655; *g*) L. E. Hanna, E. R. Jarvo, *Angew. Chem. Int. Ed.*, **2015**, *54*, 15618 – 15620; *h*) G. Song, X. Li, *Acc. Chem. Res.*, **2015**, *48*, 1007 – 1020; *i*) W.-H. Zhang, S. W. Chien, T. S. A. Hor, *Coord. Chem. Rev.*, **2011**, *255*, 1991 – 2024; *j*) J. I. van der Vlugt, *Chem. Soc. Rev.*, **2010**, *39*, 2302 – 2322; *k*) L. H. Gade, S. Bellemin-Laponnaz, *Chem. Eur. J.*, **2008**, *14*, 4142 – 4152; *l*) L. H. Gade, S. Bellemin-Laponnaz, *Coord. Chem. Rev.*, **2007**, *251*, 718 – 725.

[4] See review articles and references therein: *a*) H. G. Raubenheimer, *Dalton Trans.*, **2014**, *43*, 16959 – 16973; *b*) R. H. Crabtree, *Coord. Chem. Rev.*, **2013**, *257*, 755 – 766; *c*) D. Martin, M. Melaimi, M. Soleilhavoup, G. Bertrand, *Organometallics*, **2011**, *30*, 5304 – 5313; *d*) D. Martin, M. Soleilhavoup, G. Bertrand, *Chem. Sci.*, **2011**, *2*, 389 – 399; *e*) M. Melaimi, M. Soleilhavoup, G. Bertrand, *Angew. Chem. Int. Ed.*, **2010**, *49*, 8810 – 8849; *f*) J. Vignolle, X. Cattoën, D. Bourissou, *Chem. Rev.*, **2009**, *109*, 3333 – 3384; *g*) P. de Frémont, N. Marion, S. P. Nolan, *Coord. Chem. Rev.*, **2009**, *253*, 862 – 892; *h*) A. J. Arduengo, G. Bertrand, *Chem. Rev.*, **2009**, *109*, 3209 – 3210; *i*) F. E. Hahn, *Angew. Chem. Int. Ed.*, **2006**, *45*, 1348 – 1352; *j*) R. H. Crabtree, *J. Organomet. Chem.*, **2005**, *690*, 5451 – 5457; *k*) W. Kirmse, *Angew. Chem. Int. Ed.*, **2004**, *43*, 1767 – 1769; *l*) Y. Canac, M. Soleilhavoup, S. Conejero, G. Bertrand, *J. Organomet. Chem.*, **2004**, *689*, 3857 – 3865; *m*) D. Bourissou, O. Guerret, F. P. Gabbaï, G. Bertrand, *Chem. Rev.*, **2000**, *100*, 39 – 91; *n*) W. A. Herrmann, C. Köcher, *Angew. Chem. Int. Ed.*, **1997**, *36*, 2162 – 2187.

[5] Order of references reflects order of examples as illustrated in Figure 1.1: *a*) E. O. Fischer, A. Maasböl, *Angew. Chem. Int. Ed. Engl.*, **1964**, *3*, 580; *b*) H. W. Wanzlick, H. J. Schönherr, *Angew. Chem. Int. Ed. Engl.*, **1968**, *7*, 141 – 142; *c*) R. R. Schrock, *J. Am. Chem. Soc.*, **1974**, *96*, 6796; *d*) A. Igau, H. Grutzmacher, A. Baceiredo, G. Bertrand, *J. Am. Chem. Soc.*, **1988**, *110,* 6463 – 6466; *e*) A. J. Arduengo, R. L. Harlow, M. Kline, *J. Am. Chem.* Soc., **1991**, *113*, 361 – 363; *f*) S. Gründemann, A. Kovacevic, M. Albrecht, J. W. Faller, R. H. Crabtree, *Chem. Commun.*, **2001**, 2274 – 2275; *g*) P. Mathew, A. Neels, M. Albrecht, *J. Am. Chem. Soc.*, 2008, **130**, 13534 – 13535.

[6] See books and references therein: *a*) S. Díez-González, *N-Heterocyclic Carbenes: From Laboratory Curiosities to Efficient Tools*, RSC, **2011**; *b*) F. Glorius, ed., *Top. Organomet. Chem.*, Springer: Heidelberg, **2007**; *c*) S. P. Nolan, ed., *N-Heterocyclic Carbene in Synthesis*, John Wiley and Sons, **2006**. See review articles and references therein: *d*) F. Wang, L.-J. Liu, W. Wang, S. Li, M. Shi, *Coord. Chem. Rev.*, **2012**, *256*, 804 – 853; *e*) M. Poyatos, J. A Mata, E. Peris, *Chem. Rev.*, **2009**, *109*, 3677 – 3707; *f*) F. E. Hahn, M. C. Jahnke, *Angew. Chem. Int. Ed.*, **2008**, *47*, 3122 – 3172; *g*) J. A. Mata, M. Poyatos, E. Peris, *Coord. Chem. Rev.*, **2007**, *251*, 841 – 859; *h*) V. César, S. Bellemin-Laponnaz, L. H. Gade, *Chem. Soc. Rev.*, **2004**, *33*, 619 – 636; *i*) C. M. Crudden, D. P. Allen, *Coord. Chem. Rev.*, **2004**, *248*, 2247 – 2273; *j*) E. Peris, R. H. Crabtree, *Coord. Chem. Rev.*, **2004**, *248*, 2239 – 2246; *k*) W. A. Herrmann, *Angew. Chem. Int. Ed.*, **2002**, *41*, 1290 – 1309; *l*) T. Weskamp, V. P. W. Böhm, W. A. Herrmann, *J. Organomet. Chem.*, **2000**, *600*, 12 – 22.

[7] G. Kleinhans, *MSc Dissertation*, University of Pretoria, **2014**.

[8] See book chapter, review articles and reference therein: *a*) D. Schweinfurth, L. Hettmanczyk, L. Suntrup, B. Sarkar, *Z. Anorg. Allg. Chem.*, **2017**, *643*, 554 – 584; *b*) P. I. P. Elliott, *Organomet. Chem.*, **2014**, *39*, 1 – 25; *c*) M. Albrecht, *Adv. Organomet. Chem.*, **2014**, *62*, 111 – 158; *d*) K. F. Donnely, A. Petronilho, M. Albrecht, *Chem. Commun.*, **2013**, *49*, 1145 – 1159; *e*) O. Schuster, L. Yang, H. G. Raubenheimer, M. Albrecht, *Chem. Rev.,* **2009**, *109*, 3445 – 3478.

© University of Pretoria

[9] *a*) M. Navarro, S. Wang, H. Müller-Bunz, G. Redmond, P. Farràs, M. Albrecht, *Organometallics*, **2017**, *36*, 1469 – 1478; *b*) J. Soellner, M. Tenne, G. Wagenblast, T. Strassner, *Chem. Eur. J.*, **2016**, *22*, 9914 – 9918; *c*) A. Baschieri, F. Monti, E. Matteucci, A. Mazzanti, A. Barbieri, N. Armaroli, L. Sambri, *Inorg. Chem.*, **2016**, *55*, 7912 – 7919; *d*) D. G. Brown, N. Sanguantrakun, B. Schulze, U. S. Schubert, C. P. Berlinguette, *J. Am. Chem. Soc.*, **2012**, *134*, 12354 – 12357.

[10] *a*) K. J. Kilpin, S. Crot, T. Riedel, J. A. Kitchen, P. J. Dyson, *Dalton Trans.*, **2014**, *43*, 1443 – 1448; *b*) R. Lalrempuia, H. Müller-Bunz, M. Albrecht, *Angew. Chem. Int. Ed.*, **2011**, *50*, 9969 – 9972.

[11] J. Bouffard, B. K. Keitz, R. Tonner, G. Guisado-Barrios, G. Frenking, R. H. Grubbs, G. Bertrand, *Organometallics*, 2011, **30**, 2617 – 2627.

[12] *a*) G. Guisado-Barrios, J. Bouffard, B. Donnadieu, G. Bertrand, *Organometallics*, **2011**, *30*, 6017 – 6021; *b*) G. Guisado-Barrios, J. Bouffard, B. Donnadieu, G. Bertrand, *Angew. Chem. Int. Ed.*, **2010**, *49*, 4759 – 4762.

[13] A. Krüger, M. Albrecht, *Aust. J. Chem.*, **2011**, *64*, 1113 – 1117.

[14] M. van der Meer, E. Glais, I. Siewert, B. Sarkar, *Angew. Chem. Int. Ed.*, **2015**, *54*, 13792 – 13795.

[15] P. Eisenberger, B. P. Bestvater, E. C. Keske, C. M. Crudden, *Angew. Chem. Int. Ed.*, **2015**, *54*, 2467 – 2471.

[16] Y. Wei, S.-X. Liu, H. Müeller-Bunz, M. Albrecht, *ACS Catal.*, **2016**, *6*, 8192 – 8200.

[17] P. Chábera, Y. Liu, O. Prakash, E. Thyrhaug, A. E. Nahhas, A. Honarfar, S. Essén, L. A. Fredin, T. C. B. Harlang, K. S. Kjær, K. Handrup, F. Ericson, H. Tatsuno, K. Morgan, J. Schnadt, L. Häggström, T. Ericsson, A. Sobkowiak, S. Lidin, P. Huang, S. Styring, J. Uhlig, J. Bendix, R. Lomoth, V. Sundström, P. Persson, K. Wärnmark, *Nature*, **2017**, *543*, 695 – 699.

[18] *a*) I. Corbucci, A. Petronilho, H. Müller-Bunz, L. Rocchigiani, M. Albrecht, A. Macchioni, *ACS Catal.*, **2015**, *5*, 2714 – 2718; *b*) A. Petronilho, A. Llobet, M. Albrecht, *Inorg. Chem.*, **2014**, *53*, 12896 – 12901; *c*) J. A. Woods, R. Lalrempuia, A. Petronilho, N. D. McDaniel, H. Müller-Bunz, M. Albrecht, S. Bernhard, *Energy Environ. Sci.*, **2014**, *7*, 2316 – 2328; *d*) A. Petronilho, M. Rahman, J. A. Woods, H. Al-Sayyed, H. Müller-Bunz, J. M. D. MacElroy, S. Bernhard, M. Albrecht, *Dalton Trans.*, **2012**, *41*, 13074 – 13080; *e*) R. Lalrempuia, N. D. McDaniel, H. Müller-Bunz, S. Bernhard, M. Albrecht, *Angew. Chem. Int. Ed.*, **2010**, *49*, 9765 – 9768.

[19] L. Bernet, R. Lalrempuia, W. Ghattas, H. Müeller-Bunz, L. Vigara, A. Llobet, M. Albrecht, *Chem. Commun.*, **2011**, *47*, 8058 – 8060.

[20] See books and references therein: *a*) K. J. Szabó, O. F. Wendt, ed., *Pincer and Pincer-Type complexes*, John Wiley and Sons, **2014**; *b*) G. Van Koten, D. Milstein, ed., *Organometallic Pincer Chemistry*, Springer: Heidelberg, **2013**. See review articles and references therein: *c*) H. Valdés, L. González-Sebastián, D. Morales-Morales, *J. Organomet. Chem.*, **2017**, *845*, 229 – 257; *d*) R. E. Andrew, L. González-Sebastián, A. D. Chaplin, *Dalton Trans.*, **2016**, *45*, 1299 – 1305; *e*) S. Murugesan, K. Kirchner, *Dalton Trans.*, **2016**, *45*, 416 – 439; *f*) M. Asay, D. Morales-Morales, *Dalton Trans.*, **2015**, *44*, 17432 – 17447; *g*) S. Chakraborty, P. Bhattacharya, H. Dai, H. Guan, *Acc. Chem. Res.*, **2015**, *48*, 1995 – 2003; *h*) S. Werkmeister, J. Neumann, K. Junge, M. Beller, *Chem. Eur. J.*, **2015**, *21*, 12226 – 12250; *i*) Q.-H. Deng, R. L. Melen, L. H. Gade, *Acc. Chem. Res.*, **2014**, *47*, 3162 – 3173; *j*) G. Van Koten, *J. Organomet. Chem.*, **2013**, *730*, 156 – 164; *k*) D. Gelman, S. Musa, *ACS Catal*., **2012**, *2*, 2456 – 2466; *l*) G. Van Koten, R. J. M. K. Gebbink, *Dalton Trans.*, **2011**, *40*, 8731 – 8732; *m*) J. Choi, A. H. Roy MacArthur, M. Brookhart, A. S. Goldman, *Chem. Rev.*, **2011**, *111*, 1761 – 1779; *n*) M. Albrecht, M. M. Lindner, *Dalton Trans.*, **2011**, *40*, 8733 – 8744; *o*) D. Pugh, A. A. Danopoulos, *Coord. Chem. Rev.*, **2007**, *251*, 610 – 641; *p*) M. E. van der Boom, D. Milstein, *Chem. Rev.*, **2003**, *103*, 1759 – 1792; *q*) M. Albrecht, G. van Koten, *Angew. Chem. Int. Ed.*, **2001**, *40*, 3750 – 3781.

[21] See review article and references therein: S. J. Malthus, S. A. Cameron, S. Brooker, *Coord. Chem. Rev.*, **2016**, *316*, 125 – 161.

[22] For selected examples of PNP-carbazole pincer ligands and their coordination to various metals, see (order of references reflects order of examples as illustrated in Figure 1.6): *a*) L. Wang, D. Cui, Z. Hou, W. Li, Y. Li, *Organometallics*, **2011**, *30*, 760 – 767; *b*) N. Grüger, L.-I. Rodríguez, H. Wadepohl, L. H. Gade, *Inorg. Chem.*, **2013**, *52*, 2050 – 2059; *c*) Y. Xu, C. A. Rettenmeier, G. T. Plundrich, H. Wadepohl, M. Enders, L. H. Gade, *Organomettalics*, **2015**, *34*, 5113 – 5118; *d*) N. Grüger, H. Wadepohl, L. H. Gade, *Eur. J. Inorg. Chem.*, **2013**, *2013*, 5358 – 5365; *e*) C. Cheng, B. G. Kim, D. Guironnet, M. Brookhart, C. Guan, D. Y. Wang, K. Krogh-Jespersen, A. S. Goldman, *J. Am. Chem. Soc.*, **2014**, *136*, 6672 – 6683; *f*) G. T. Plundrich, H. Wadepohl, L. H. Gade, *Inorg. Chem.*, **2016**, *55*, 353 – 365; *g*) G. T. Plundrich, H. Wadepohl, E. Clot, L. H. Gade, *Chem. Eur. J.*, **2016**, *22*, 9283 – 9292.

© University of Pretoria

[23] For selected examples of NNN-carbazole pincer ligands and their coordination to various metals, see (order of references reflects order of examples as illustrated in Figure 1.6): *a*) G. J. P. Britovsek, V. C. Gibson, O. D. Hoarau, S. K. Spitzmesser, A. J. P. White, D. J. Williams, *Inorg. Chem.*, **2003**, *42*, 3454 – 3465; *b*) V. C. Gibson, S. K. Spitzmesser, A. J. P. White, D. J. Williams, *Dalton Trans.*, **2003**, 2718 – 2727; *c*) J. A. Gaunt, V. C. Gibson, A. Haynes, S. K. Spitzmesser, A. J. P. White, D. J. Williams, *Organometallics*, **2004**, *23*, 1015 – 1023; *d*) M. S. Mudadu, A. N. Singh, R. P. Thummel, *J. Org. Chem.*, **2008**, *73*, 6513 – 6520; *e*) K. R. D. Johnson, P. G. Hayes, *Organometallics*, **2009**, *28*, 6352 – 6361; *f*) K. R. D. Johnson, P. G. Hayes, *Organometallics*, **2013**, *32*, 4046 – 4049; *g*) K. R. D. Johnson, P. G. Hayes, *Dalton Trans.*, **2014**, *43*, 2448 – 2457; *h*) M. Inoue, M. Nakada, *Org. Lett.*, **2004**, *6*, 2977 – 2980; *i*) M. Inoue, T. Suzuki, M. Nakada, *J. Am. Chem. Soc.*, **2003**, *125*, 1140 – 1141; *j*) M. Inoue, M. Nakada, *Angew. Chem. Int. Ed.*, **2006**, *45*, 252 – 255; *k*) M. Durán-Galván, S. A. Worlikar, B. T. Connell, *Tetrahedron*, **2010**, *66*, 7707 – 7719; *l*) M. Durán-Galván, J. R. Hemmer, B. T. Connell, *Tetrahedron*, **2010**, *51*, 5080 – 5082; *m*) M. Duran-Galvan, B. T. Connell, *Eur. J. Org. Chem.*, **2010**, *13*, 2445 – 2448; *n*) J. Zou, D. J. Berg, D. Stuart, R. McDonald, B. Twamley, *Organometallics*, **2011**, *30*, 4958 – 4967; *o*) J. Zou, D. J. Berg, A. Oliver, B. Twamley, *Organometallics*, **2013**, *32*, 6532 – 6540; *p*) K. R. D. Johnson, B. L. Kamenz, P. G. Hayes, *Organometallics*, **2014**, *33*, 3005 – 3011.

[24] M. Moser, B. Wucher, D. Kunz, F. Rominger, *Organometallics*, **2007**, *26*, 1024 – 1030.

[25] E. Jürgens, K. N. Buys, A.-T. Schmidt, S. K. Furfari, M. L. Cole, M. Moser, F. Rominger, D. Kunz, *New J. Chem.*, **2016**, *40*, 9160 – 9169.

[26] E. Jürgens, O. Back, J. J. Mayer, K. Heinze, D. Kunz, *Z. Naturforsch. B*, **2016**, *71*, 1011 – 1018.

[27] A. Seyboldt, B. Wucher, M. Alles, F. Rominger, C. Maichle-Mössmer, D. Kunz, *J. Organomet. Chem.*, **2015**, *775*, 202 – 208.

[28] B. Wucher, M. Moser, S. A. Schumacher, F. Rominger, D. Kunz, *Angew. Chem. Int. Ed.*, **2009**, *48*, 4417 – 4421.

[29] A. Seyboldt, B. Wucher, S. Hohnstein, K. Eichele, F. Rominger, K. W. Törnroos, D. Kunz, *Organometallics*, **2015**, *34*, 2717 – 2725.

[30] E. Jürgens, D. Kunz, *Eur. J. Inorg. Chem.*, **2017**, 233 – 236.

[31] D. I. Bezuidenhout, G. Kleinhans, G. Guisado-Barrios, D. C. Liles, G. Ung, G. Bertrand, *Chem. Commun.*, **2014**, *50*, 2431 – 2433.

[32] See articles and references therein: *a*) J. Yun, D. Kim, H. Yun, *Chem. Commun.*, **2005**, 5181 – 5183; *b*) J. J. Van Veldhuizen, J. E. Campbell, R. E. Giudici, A. H. Hoveyda, *J. Am. Chem. Soc.*, **2005**, *127*, 6877 – 6882; *c*) A. O. Larsen, W. Leu, C. N. Oberhuber, J. E. Campbell, A. H. Hoveyda, *J. Am. Chem. Soc.*, **2004**, *126*, 11130 – 11131; *d*) J. M. Fraile, J. I. Garcia, V. Matínez-Merino, J. A. Mayoral, L. Salvatella, *J. Am. Chem. Soc.*, **2001**, *123*, 7616 – 7625; *e*) M. P. Doyle, D. C. Forbes, *Chem. Rev.*, **1998**, *98*, 911 – 936.

[33] See articles and references therein: *a*) D. J. O'Hearn, R. D. Singer, *Organometallics*, **2017**, *36*, 3175 – 3177; *b*) B. R. M. Lake, C. E. Willans, *Organometallics*, **2014**, *33*, 2027 – 2038; *c*) E. L. Kolychev, V. V. Shuntikov, V. N. Khrustalev, A. A. Bush, M. S. Nechaev, *Dalton Trans.*, **2011**, *40*, 3074 – 3076; *d*) J. M. Smith, J. R. Long, *Inorg. Chem.*, **2010**, *49*, 11223 – 11230; *e*) B. Liu, B. Liu, Y. Zhou, W. Chen, *Organometallics*, **2010**, *29*, 1457 – 1464; *f*) P. L. Arnold, M. Rodden, K. M. Davis, A. C. Scarisbrick, A. J. Blake, C. Wilson, *Chem. Commun.*, **2004**, 1612 – 1613; *g*) X. Hu, I. Castro-Rodriguez, K. Meyer, *J. Am. Chem. Soc.*, **2003**, *125*, 12237 – 12245.

[34] N. D. Clement, K. J. Cavell, C. Jones, C. J. Elsevier, *Angew. Chem. Int. Ed.*, **2004**, *43*, 1277 – 1279.

[35] N. A. Eberhardt, H. Guan, *Chem. Rev.*, **2016**, *116*, 8373 – 8426.

© University of Pretoria

Chapter 2

Reversible carbon dioxide activation mediated by a nickel hydride complex

2.1 Background

Increasing carbon dioxide levels, resulting from energy generation through the burning of fossil fuels, necessitates research on greener methods towards clean energy as well as advancement in the procedures for carbon dioxide utilization.[1] Consequently, sequestration of carbon dioxide from the atmosphere through its fixation into value-added commodity chemicals could lead to a decrease of the CO_2 concentration in the atmosphere.[1,2] Additionally, CO_2 is a cheap, earth-abundant and non-toxic C1-building block rendering it an attractive choice for the preparation of simple or elaborate fine-chemicals.[1,2] Unfortunately, utilization of CO_2 is hampered by the fact that it is a small inert molecule with stable bonds featuring both considerable thermodynamic stability and a high ionization potential, even higher compared to water or ammonia.[2] In this regard, transition metal-based catalysts have proven feasible tools to overcome the high energy barrier of the carbon-oxygen double bond and therefore ''activate'' the small inert molecule for exploitation as a C1 source.[3] Furthermore, hydrogenation of CO_2 to formic acid, formaldehyde and/or methanol *via* a metal complex/catalyst (Scheme 2.1), yields valuable feedstock chemicals in proficient hydrogen storage/release processes. This allows for the direct and safe access to hydrogen as a clean energy source, compared to the direct transport and use of hydrogen gas.[1-3,4]

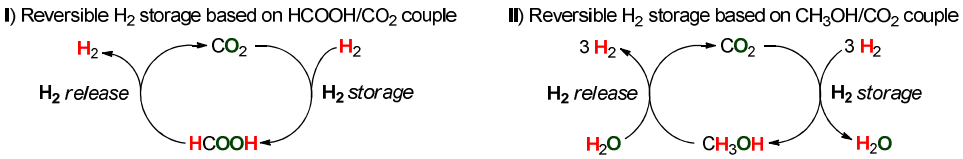

Scheme 2.1: Reversible hydrogen storage based on the formic acid or methanol and CO_2 couple[1,4]

A range of CO_2 activation modes have been disclosed (Figure 2.1).[1-4,5] In general, these mechanisms revolve around nucleophilic attack at the electron deficient carbon center.[2b] To be more specific, the lowest unoccupied molecular orbital (LUMO) is situated at the carbon atom, rendering it susceptible

© University of Pretoria

towards nucleophilic attack.[2] As such, a Lewis base (LB) can donate electron density into the LUMO of CO_2, yielding a LB adduct (**I**, Figure 2.1).[5] Addition of both a LB and a Lewis acid (LA), such as in the case of frustrated Lewis acid-base pairs, would yield the corresponding Lewis acid-base formate product (**II**, Figure 2.1). Main-group hydrides have also been demonstrated to be proficient in cleaving the carbon-oxygen double bond of CO_2 (**III**, Figure 2.1).[5] These methods of CO_2 activation are certainly appealing, as they are metal-free.[6] However, they are both scarcely reported and not as efficient, when compared to metal-mediated CO_2 activation strategies.[6] Transition metal-based complexes/catalysts activate carbon dioxide by facilitating insertion of one of the carbon-oxygen double bonds of CO_2 across a polarized M-X (X = H, C, N, O) bond (**IV**, Figure 2.1).[2,3] Carbon dioxide insertion across a metal hydride bond gives direct access to metal formates, which constitutes the first step towards reduction of CO_2 to the acid, aldehyde or alcohol level (**V**, Figure 2.1). Consequently, metal hydrides are, in all probability, the most attractive transition metal species for CO_2 activation.[2] The rest of this section will focus on metal hydride CO_2 bond activation, which includes a simplified mechanism of the reaction. However, due to both its elegance and/or relevance, CO_2 activation with main-group elements (specifically, main-group *p*-block hydrides) will also be included (*vide infra*).

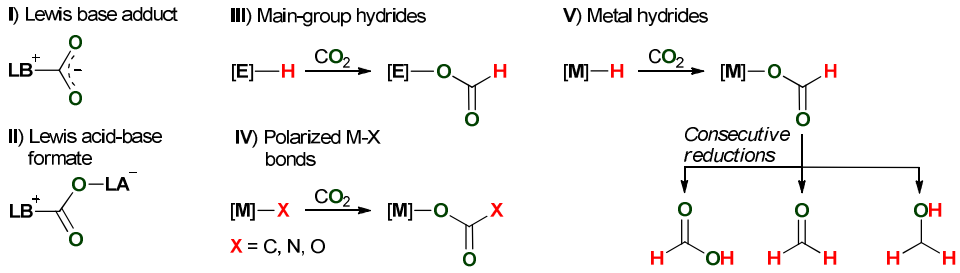

Figure 2.1: Various CO_2 activation strategies[2,5]

Only a handful of reports regard the direct hydrogenation of CO_2 to methanol under homogeneous catalyzed conditions, with metal hydrides at the forefront. In all cases, the reactions were catalyzed by ruthenium-based catalysts (Scheme 2.2).[3a] The key step of hydrogenating CO_2 to formic acid is proposed to be the primary barrier during the reduction of CO_2 to methanol.[3a] The solution was brought about by trapping the formic acid through an additive alcohol[7] or amine.[8] The formed amide[8] or ester[7] would subsequently be hydrogenated to methanol with reformation of the active catalyst and the additive trapping agent (Scheme 2.2). This example demonstrates the possibility of hydrogenating CO_2 to methanol. However, further research is needed, as these catalytic systems have low catalytic activity with unsatisfactory TON (turnover number).[3a] A viable alternative is formate trapping, isolation and subsequent hydrogenation of the formate to the aldehyde or methanol level. This is a more tedious

© University of Pretoria

approach, as it entails a multipot synthetic protocol, but well-defined catalysts have been developed for the hydrogenation of CO_2 and trapping of formate exhibiting high catalytic efficiency (*vide infra*).

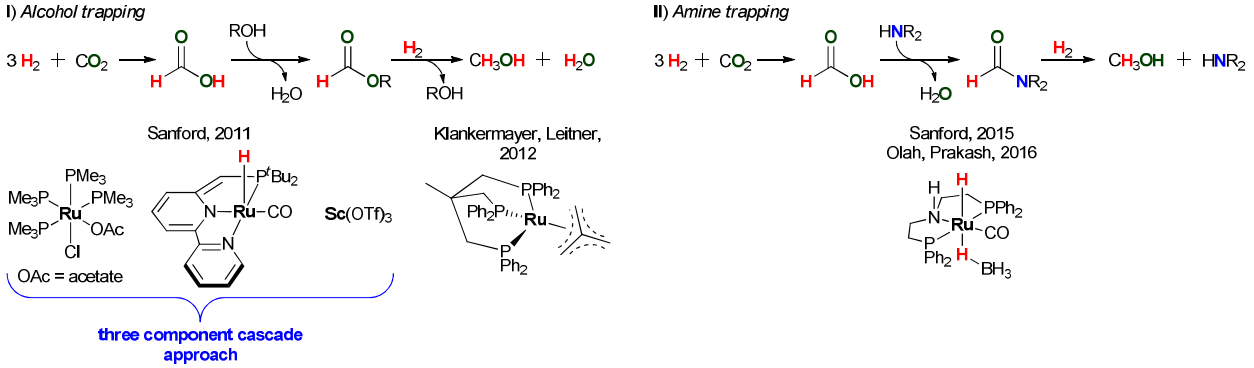

Scheme 2.2: CO_2 hydrogenation to CH_3OH *via* formate trapping with **I**) alcohols[7] or **II**) amines[8]

Iridium-based catalysts for CO_2 reduction have been enthusiastically studied. The onset of this interest was arguably initiated by the report of Nozaki and co-workers regarding the preparation of an iridium(III) trihydride complex (Scheme 2.3), catalyzing the hydrogenation of CO_2 to potassium formate with exceptionally high TOF (turnover frequency) and TON.[9] The catalytic activity of the trihydride was superior compared to the chloride analogue, with TON and TOF reaching 3 500 000 and 150 000 h^{-1}, respectively, in the presence of KOH as a formate trapping reagent (Scheme 2.3). A catalytic reaction mechanism was elucidated based on experimental investigations. The hydride *trans* to the other hydride will have a higher nucleophilic character, which explains CO_2 insertion at the aforementioned bond and not across the iridium hydride bond where the hydride is *trans* to the nitrogen.[9] Deprotonative dearomatization leads to rapid dissociation of the formato ligand, followed by hydrogenation to yield the active catalyst (Scheme 2.3). The high catalytic activity of the trihydride catalyst was attributed to both the strong *trans* donor hydride ligand and the aromatization/dearomatization of the ligand backbone.

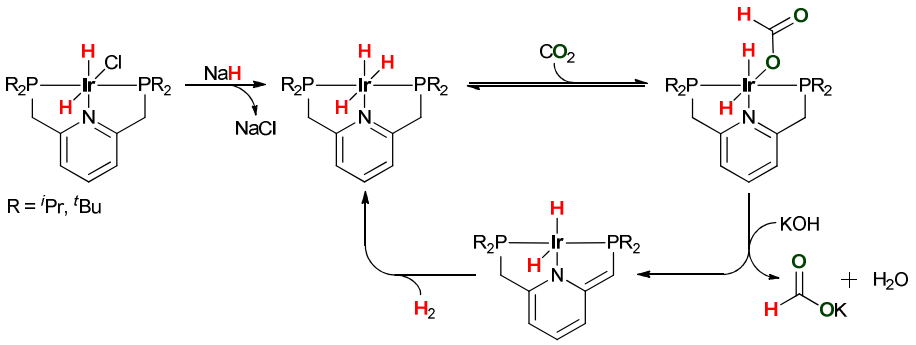

Scheme 2.3: Fast catalytic hydrogenation of CO_2 mediated by an iridium trihydride catalyst[9]

© University of Pretoria

Leading the charge towards fast CO_2 hydrogenation was the ruthenium pincer catalyst described by Pidko and co-workers,[10] the only catalyst to surpass the catalytic activity of the iridium trihydride complex[9] (see above, Scheme 2.3) during the reduction of CO_2 with hydrogen gas to the corresponding formate salt (Scheme 2.4).[10] The ruthenium PNP-pincer catalyst catalyzed the hydrogenation of CO_2 to formate with a TOF of 1 100 000 h^{-1} in the presence of DBU (1,8-diazabicyclo[5.4.0]undec-7-ene) as base (Scheme 2.4). The dehydrogenation of formic acid to CO_2, with the liberation of hydrogen gas was also catalyzed with a very high TOF of 257 000 h^{-1}. Additionally, the catalyst operated at improved catalytic activity at certain temperatures, which can be beneficial during temperature controlled experiments. A mechanism for both hydrogenation and dehydrogenation catalyzed reactions were proposed (Scheme 2.4). The improved nucleophilicity of the hydride *trans* to another hydride ligand, coordinates and activates CO_2. Formic acid dissociates as the formate salt, while molecular hydrogen coordinates to the vacant site at the cationic ruthenium metal center. Subsequent base-assisted hydrogen cleavage yields the active catalyst, that re-enters another catalytic cycle. The reverse reaction entails hydrogen gas evolution through the reaction of the conjugate acid with the hydride ligand. The cationic ruthenium complex resultantly coordinates the formate salt, with liberation of CO_2 and regeneration of the active dihydride catalyst *via* β-hydride elimination (Scheme 2.4).[10] This seminal report leads us one step closer to the realization of an efficient and cheap protocol for the storage, transfer and on-demand release of hydrogen in a safe, controlled environment.

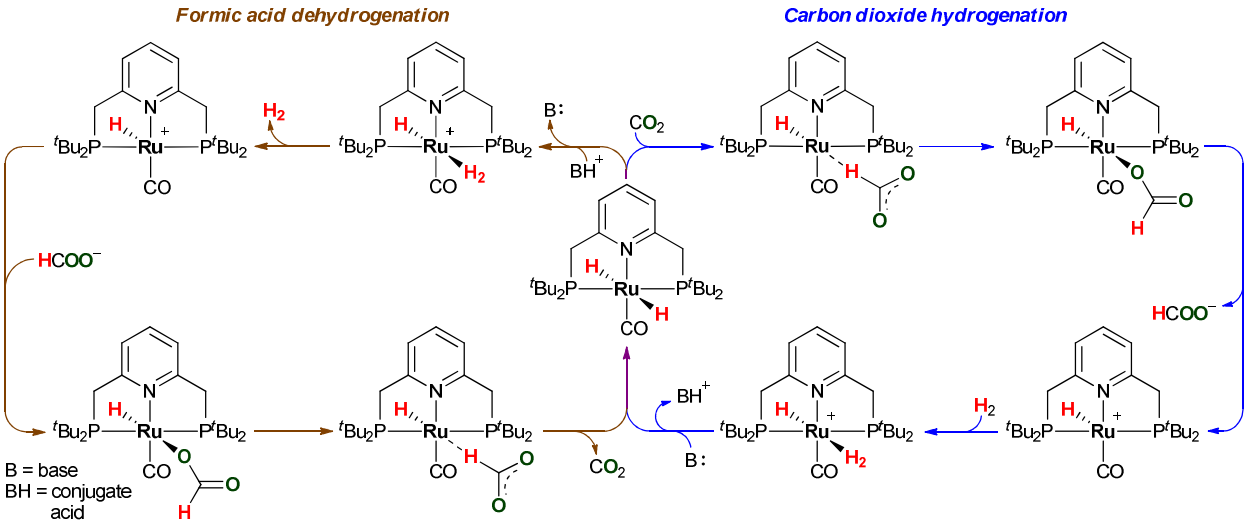

Scheme 2.4: CO_2 hydrogenation and formic acid dehydrogenation *via* a ruthenium catalyst[10]

From the above examples, as well as a compilation of reports regarding CO_2 activation, a general trend through which metal hydrides mediate the bond cleavage process could be realized. As such, two

© University of Pretoria

common mechanisms generally encountered for CO_2 insertion across a metal hydride bond was elucidated from experimental investigation supported by theoretical calculations (Scheme 2.5).[2a] The more generally encountered mechanism involves nucleophilic attack on the CO_2 by the hydride, yielding the H-bound metal formate (**I**, Scheme 2.5). Subsequent rearrangement of the H-bound formate yields the O-bound formate product, as is experimentally observed. The stepwise insertion process has two transition state intermediates, proposed to be the rate-determining steps. The reaction follows an outer-sphere mechanism if the first transition state is the rate-determining step (**I**, Scheme 2.5). An inner-sphere reaction mechanism is implied if the rate of the reaction is controlled by the second transition state (**I**, Scheme 2.5). The concerted CO_2 insertion reaction mechanism also follows an inner-sphere reaction pathway, and involves CO_2 coordination and bond rearrangement yielding the O-bound formate product (**II**, Scheme 2.5).

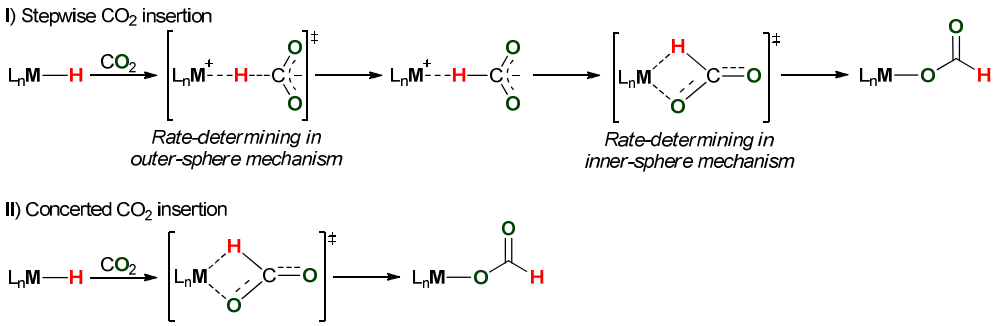

Scheme 2.5: Proposed mechanistic protocols for CO_2 insertion across metal hydrides[2a]

Non-noble metal hydrides for CO_2 activation with accompanying high catalytic efficiency in the holy grail catalyzed CO_2 hydrogenation reaction, is vigorously pursued.[1a,2a,3] A few recent reports describe the use of late 3*d*-transition metal hydrides mediating the activation of CO_2. In some cases, the complexes exhibited catalytic efficiency during the conversion of CO_2 to the formate salt. It is worth mentioning that most of these complexes were supported by a pincer ligand.[1a,2a,3] As a case in point, an iron(II) complex coordinated by an aliphatic PNP-pincer ligand catalyzed the hydrogenation of CO_2 to the formate salt, reaching turnover numbers of up to 60 000.[11] Two Fe(II) catalysts were reported, one being coordinated by a aliphatic PNP-pincer ligand featuring a secondary amine as the central donor atom (**I**, Scheme 2.6). The second iron-containing catalyst was also supported by an aliphatic PNP-pincer ligand, but in this case the ligand featured a tertiary amine as the central donor atom (**II**, Scheme 2.6).[11] Although the catalyst could mediate hydrogenation of CO_2 with H_2 to the formate salt in the presence of a base, only moderate TONs where achieved. However, upon the addition of a Lewis acid, in this case a lithium salt, a significant improvement of the catalytic activity for the complexes was noted. For the

© University of Pretoria

secondary amine ligand supported iron catalyst, the catalytic CO_2 hydrogenation reaction proceeds through a 1,2-addition of H_2 across the Fe-N bond. Molecular hydrogen coordinates in the vacant site, which is followed by H_2 cleavage to generate the dihydride intermediate. Resultantly, the hydride has sufficient nucleophilic character (being *trans* to another hydride) to coordinate and insert CO_2, generating the iron formate intermediate.[11] The extensive experimental data indicated that formate extrusion and N-H deprotonation were the rate-limiting steps. The addition of a lithium salt accelerated the rate-determining step by coordinating the anionic formate and disrupting the intramolecular hydrogen bond, which enhances the deprotonation of the secondary amine by the base (**I**, Scheme 2.6).[11] The tertiary amine supported iron catalyst inserts CO_2 in the same way as did the secondary amine coordinated catalyst (**II**, Scheme 2.6). Lithium salt mediates the extrusion of the formate anion with coordination of molecular hydrogen at the formed vacant site. The iron dihydride active catalyst is regenerated by the deprotonation of the iron dihydrogen intermediate and release of the conjugate acid (**II**, Scheme 2.6).[11]

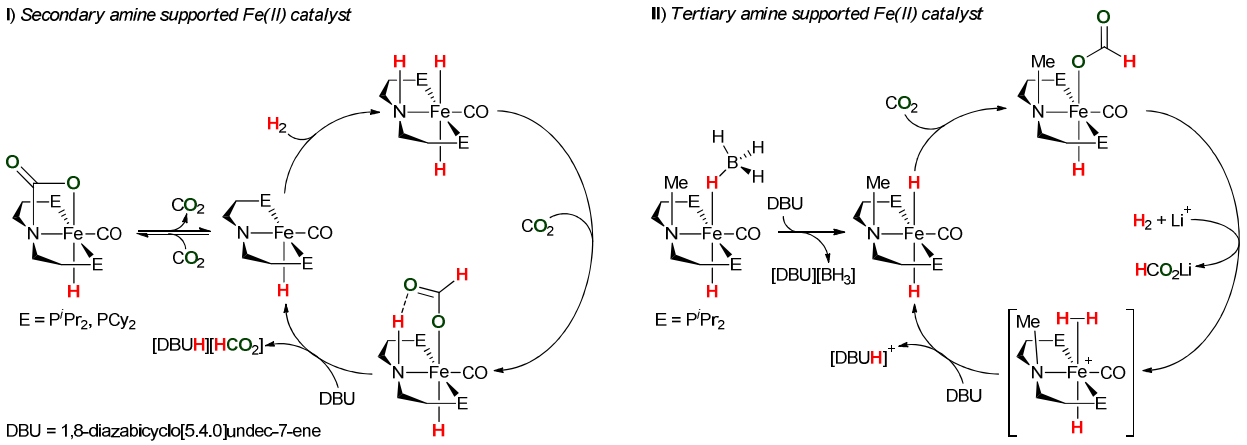

Scheme 2.6: Iron(II) complexes as efficient CO_2 hydrogenation catalyst[11]

Another seminal report regarding the reduction of CO_2 with hydrogen to the formate level employing earth-abundant metals, came from the group of Linehan.[12] A bis(diphosphine)cobalt hydride was prepared, and it was demonstrated that the complex sufficiently catalyzes the hydrogenation of CO_2 (Scheme 2.7) in the presence of 2,8,9-triisopropyl-2,5,8,9-tetraaza-1-phosphabicyclo[3.3.3]undecane (also known as Verkade's base, Vkd).[12,13] Only mild reaction conditions were required to reach appreciable TONs,[12,13] albeit not as high as the iron catalyst disclosed above (see Scheme 2.6).[11] The sufficient hydridic character of the cobalt hydride complex mediated the carbon oxygen double bond cleavage, with concomitant release of the formate salt and the cationic cobalt complex (**I**, Scheme

© University of Pretoria

2.7).[12,13] Oxidative addition of molecular hydrogen yields the cationic cobalt dihydride intermediate. The active monohydride cobalt catalyst is regenerated through reductive deprotonation of the dihydride by Verkade's base, which is the rate-limiting step of the reaction if weaker bases are employed, but not with Verkade's base (**I**, Scheme 2.7). In the presence of Verkade's base, transfer of the hydride to the CO_2 becomes the rate-limiting step.[12,13] This encouraged the group of Appel and Raugei to elucidate the mechanism of CO_2 insertion through extensive theoretical calculations.[14] Two mechanistic scenarios were considered, namely the direct transfer of the hydride ligand or an associative pathway in which CO_2 coordination is followed by oxidative addition, yielding the intermediate Co(III) hydride complex with reductive elimination regenerating the active catalyst and releasing the formate anion (**II**, Scheme 2.7). Calculations suggested that the direct transfer of the hydride ligand to CO_2 is endergonic, favouring an associative pathway that was calculated to be 1.4 kcal.mol^{-1} lower in energy compared to the direct transfer pathway. This rate-limiting pre-coordination of CO_2 to the metal center is indeed interesting, as this mode of CO_2 activation is generally not encountered for metal hydrides.[14]

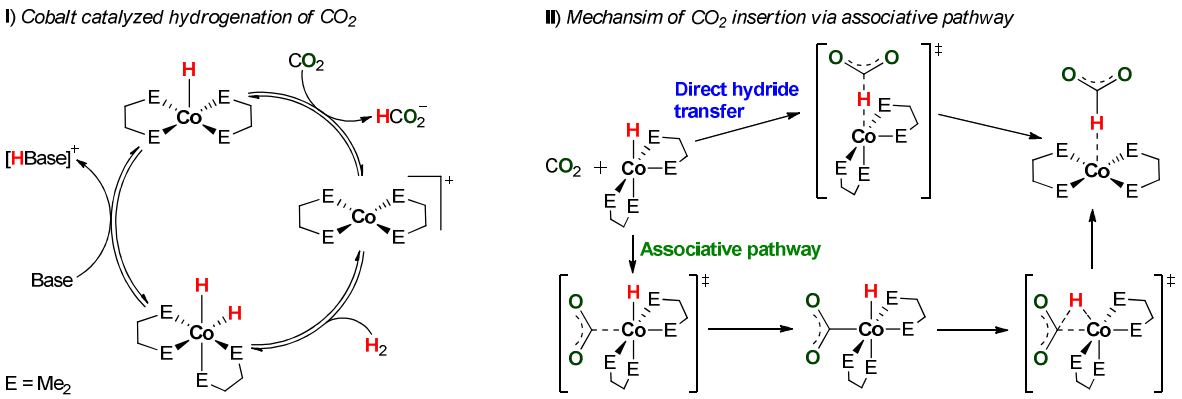

Scheme 2.7: Cobalt catalyzed **I**) hydrogenation of CO_2[12,13] and **II**) mechanistic consideration of CO_2 insertion[14]

Carbon dioxide activation is not only limited to iron and cobalt non-noble metals.[2,15] Nickel hydrides have also been reported as efficient complexes for CO_2 activation. Carbon dioxide bond cleavage has been demonstrated to occur under stoichiometric and catalytic reaction conditions. Nickel is also a cheap, earth abundant metal and less toxic compared to the heavier, late-transition metals. More importantly, functionalization of the *trans* donor ligand (*trans* to hydride) greatly affects the reactivity of the complex, or lack thereof, towards CO_2 activation.[2,15] The abovementioned principles therefore warrant the investigation of nickel hydrides for carbon dioxide activation and utilization, as the reactivity pattern can be readily altered by functionalization of the *trans* donor atom.

© University of Pretoria

2.1.1 CO_2 activation by nickel hydrides

A stronger *trans* donor atom decreases the nickel hydride bond strength and therefore increases the nucleophilic character of the hydride ligand, resulting in faster and more efficient CO_2 insertion across the metal hydride bond.[2,15] The influence of the *trans* donor ligand was not only evidenced through experimental data, but also *via* computational calculations.[16] The theoretical data suggested that CO_2 insertion is greatly dependent on the amount of destabilization of the nickel hydride bond. The relative energy of the various transition states is also lower when strong *trans* donor ligands are employed, as they are better suited for stabilizing the four-centered transition states.[16a] It therefore comes as no surprise that nickel hydrides supported by strongly donating anionic PCP-,[16b,17] POCOP-,[18] PNCNP-[19], PSiP-[16b] and PBP-pincer[20] ligands have been avidly studied, as they generally activate and insert CO_2 at room temperature in a few minutes (Figure 2.2). The various case studies also referred to the influence of the donor strength of the ligand with a *cis* disposition to the hydride, on CO_2 activation.[16b] As can be expected, a stronger ligand donor 'arm' enhances the rate of CO_2 insertion. In some instances, the stoichiometric CO_2 activation reactions were extrapolated to catalytic reactions, where the nickel hydride mediated the reduction of CO_2 to the methoxide level, in the presence of an appropriate reducing agent (*vide infra*).[18a,18c,18d]

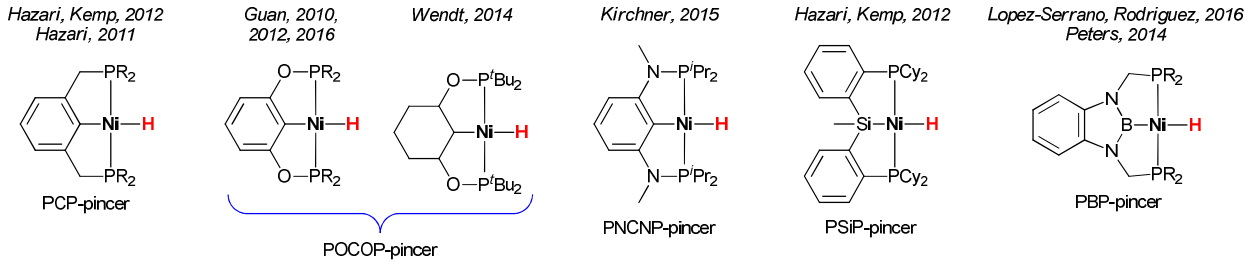

Figure 2.2: Pincer nickel hydrides facilitating fast CO_2 insertion

The reduction of CO_2 with a nickel hydride was elegantly illustrated by the group of Guan (Scheme 2.8).[18a,18c,18d,21] Reacting the POCOP-pincer supported nickel hydride with CO_2 resulted in quantitative formation of the nickel formate in 5 minutes at room temperature (**I**, Scheme 2.8). It was further reported that CO_2 insertion was reversible. The reversible reaction was substantiated by mixing a ^{13}C-labeled nickel formate solution with non-labeled CO_2, yielding the non-labeled nickel formate complex. Alternatively, heating up a solution of the nickel formate to 60 °C under negative pressure for 5 hours regenerated the nickel hydride complex (**I**, Scheme 2.8).[18d] Addition of catecholborane (HBcat) to a nickel formate solution regenerated the hydride complex and released the formate HCO_2Bcat product.

© University of Pretoria

More intriguing, was the addition of excess HBcat to the nickel formate complex, which yielded the nickel hydride and the methanol derivative CH_3OBcat. The nickel hydride complex also proved to be catalytically active, reducing CO_2 to the methoxide level with a TOF of 495 h^{-1}.[18c,18d] A catalytic reaction mechanism for the reduction of CO_2 with HBcat was elucidated, based on extensive theoretical investigations (**II**, Scheme 2.8).[22] The calculations suggested that three catalytic cycles describes the reduction of CO_2 to HCO_2Bcat, HCHO and finally CH_3OBcat. The first catalytic cycle involves CO_2 activation and insertion, followed by hydride regeneration and formation of the formate HCO_2Bcat (**II**, Scheme 2.8). A second insertion step yields the nickel alkoxide that leads to formation of formaldehyde through β-alkoxy elimination. Subsequent nickel hydride regeneration is mediated through the reaction of Ni-OBcat with another equivalent of HBcat, with formation of catBOBcat as the by-product of the reaction (**II**, Scheme 2.8).[22] The third and final catalytic cycle leads to generation of the targeted CH_3OBcat and reformation of the nickel hydride through formaldehyde insertion and nickel methoxide bond cleavage with HBcat (**II**, Scheme 2.8).

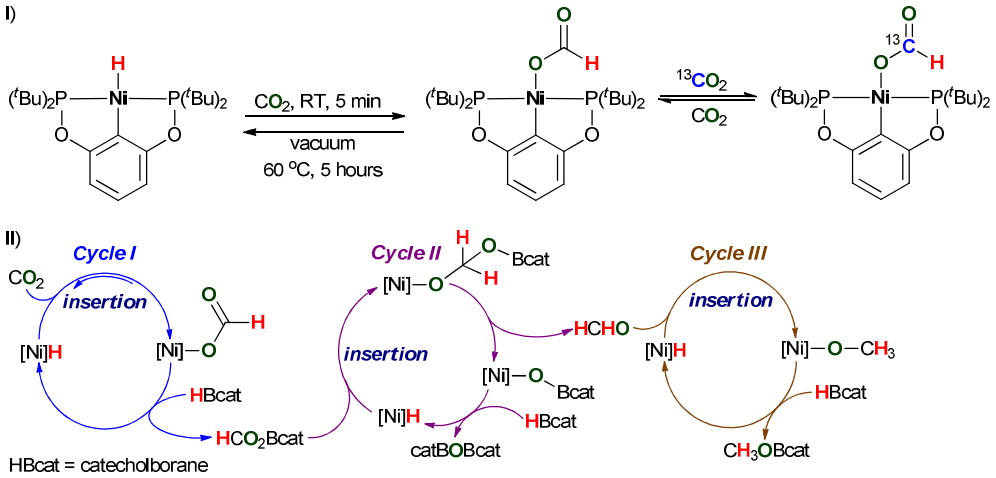

Scheme 2.8: POCOP-pincer supported nickel hydride for reversible CO_2 **I**) activation and **II**) reduction to MeOH[18a,18c,18d,21,22]

Anionic PNP-supported nickel hydrides have also been considered for CO_2 activation and insertion yielding the corresponding nickel formate complexes (Figure 2.3).[2,3] However, various case studies all confirm a much slower rate of insertion, if any, across the nickel hydride bond featuring the weaker, anionic nitrogen donor *trans* to the hydride ligand. This is in all probability a direct result of a more stable complex with a shorter nickel hydride bond length, due to the weaker anionic nitrogen *trans* donor ligand. This also results to a decrease in the nucleophilic character of the hydride ligand, which ultimately requires a bigger contribution from the metal towards CO_2 activation. Nonetheless, a handful

© University of Pretoria

of examples has been reported regarding CO_2 activation with nickel hydrides featuring the weaker *trans* donor ligands (Figure 2.3). One such report concerns the synthesis of a diphenyl substituted PNP-pincer complex which activates and inserts CO_2 across the nickel hydride bond.[16b,23] However, very long reaction times (10 days) were required for full conversion to the corresponding nickel formate in C_6D_6 as solvent (Figure 2.3).[23] In the more polar CH_3CN solvent, the reaction proceeded smoothly, although 7 hours where required for complete conversion at room temperature. The increased rate of insertion was attributed to stabilization of the transition state by the more polar solvent. Heating up a solution of the aforementioned nickel formate complex in C_6D_6 to 60 °C for 20 hours, resulted in regeneration of the nickel hydride through β-hydride elimination (Figure 2.3).[23] Similar results were also reported for an analogous nickel complex featuring an anionic nitrogen donor *trans* to the hydride. The PNP-pincer nickel hydride featuring a pyrrole backbone, was independently reported by the groups of Tonzetich[24] and of Bernskoetter and Walter (Figure 2.3), for CO_2 insertion.[25] The reports confirmed CO_2 insertion across the nickel hydride bond, but again, long reaction times were required for quantitative formation of the nickel formate product.[24,25] No CO_2 insertion was observed if the phosphine donor ligands were substituted with bulky *tert*-butyl substituents (Figure 2.3).[25] Interestingly, a reversible CO_2 insertion was noted for the *iso*-propyl substituted nickel hydride analogue. Full conversion to the nickel formate required a day, but when the nickel formate solution was heated up to 100 °C, the nickel hydride was regenerated through decarboxylation of the nickel formate complex. If the same solution was left to cool down to room temperature, reinsertion of CO_2 occurred to yield the nickel formate complex (Figure 2.3).[25] Decarboxylation at elevated temperatures (110 °C) was also reported for an analogous pyrrole coordinated nickel formate complex, yielding the nickel hydride product.[26]

These examples validate the necessity for a strong, anionic central donor atom for efficient CO_2 activation and insertion.[23-25] However, the weaker anionic nitrogen donor ligand (compared to the anionic B, Si or C pincer ligands) allows for CO_2 insertion and spontaneous decarboxylation at elevated temperatures.

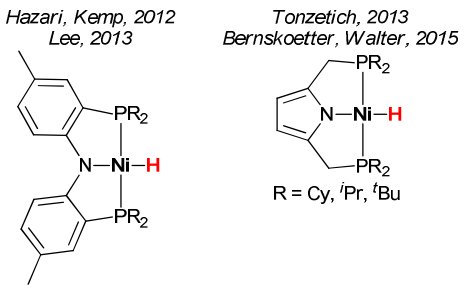

Figure 2.3: CO_2 insertion across nickel hydrides supported by anionic PNP-pincer ligands

© University of Pretoria

An interesting example was reported regarding the unique reactivity of an anionic PNP-pincer supported nickel hydride complex with CO_2 (Scheme 2.9).[27] Several days were required for complete insertion of CO_2 across a nickel hydride bond coordinated by a PSiNSiP-pincer ligand. However, instead of the expected nickel formate complex, formation of a complex featuring a hydride ligand occurred. An XRD study disclosed a nitrogen transposition with one of the oxygen atoms from CO_2. This yielded a nickel hydride complex supported by a PSiOSiP-pincer ligand, in addition to being coordinated by an N-bound cyanate ligand (Scheme 2.9).[27] A postulation, supported by a previous study,[28] included nucleophilic attack at the electrophilic CO_2 by the amide, which weakens the carbon oxygen bonds.[27] This was substantiated by the fact that the nickel nitrogen bond was already weakened due the *trans* influence of the hydride ligand. However, the driving force of the reaction was stated to be the favourable formation of silicon-oxygen bonds. This suggests that in some cases, the central anionic donor *trans* to the hydride ligand does not merely determine the nucleophilic character of the hydride, but can in fact act as a non-innocent ligand (Scheme 2.9).[27]

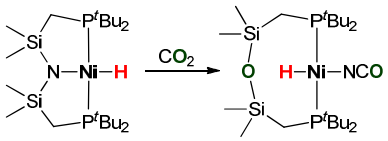

Scheme 2.9: CO_2 activation *via* nitrogen-oxygen transposition[27]

The abovementioned examples illustrate that earth-abundant metal hydrides, such as nickel hydrides, are efficient molecular tools for cleaving the carbon oxygen double bond of CO_2. However, ligand design plays a pivotal role during CO_2 activation, with the biggest influence on reactivity, or lack thereof, imparted by the *trans* donor ligand. However, the 'side-arm' donor atoms of a pincer ligand can also affect the reactivity outcome. Stronger donor atoms with small wingtip substituents could favour CO_2 insertion, especially if the *trans* donor atom is not sufficient in itself to mediate the reaction being scrutinized.

2.1.2 CO_2 activation by main group elements

Main group *p*-block elements have also been successfully investigated as potential candidates for CO_2 activation (see Figure 2.1).[5,6] The frustrated Lewis-base pairs have been instrumental in the development of main group compounds for CO_2 activation (**II**, Figure 2.1).[29] Frustrated Lewis-base pairs readily activate CO_2 and reduce the inert molecule with the appropriate substrate and/or co-catalyst.

© University of Pretoria

Another class of main group complexes of specific relevance are the main group hydrides as viable tools for CO_2 activation (**III**, Figure 2.1).[30] These hydride species have sufficient nucleophilic character and polarized bonds to allow insertion of CO_2 across the aforementioned bond. The group 13 and group 14 elements have received considerable attention during the preparation of the hydride species. In contrast, the group 15 elements have not been investigated as enthusiastically, as they yield complexes that are less reactive towards CO_2 activation.

Nonetheless, a seminal contribution from the laboratory of Kinjo demonstrated the relevance of group 15 hydrides for CO_2 activation and reduction. The insertion reaction of CO_2 across a P-H bond was mediated by a 1,2,3-diazaphospholene. The five-membered heterocycle, with its electrophilic phosphor atom and hydridic hydrogen,[31] rapidly reacts with and inserts CO_2 at room temperature in acetonitrile as solvent (**I**, Scheme 2.10).[5] The experimental data indicated that a zwitterionic complex prevailed in solution, rather than a neutral formate product (**I**, Scheme 2.10). It was reasoned that an anionic formate functionality would be readily transferred to an acceptor substrate. The authors supported their hypothesis of a zwitterionic complex and fast formate transfer by trapping the formate anion with the addition of a silane. Resultantly, the targeted silyl formate product was obtained through reacting the zwitterionic complex with diphenylsilane (**I**, Scheme 2.10). In addition to the silyl formate product, the formation of siloxane was also reported. Finally, the starting 1,2,3-diazaphospholene was not detected, only the zwitterionic formate complex due to the immediate reaction of the *in situ* generated 1,2,3-diazaphospholene with excess CO_2 (**I**, Scheme 2.10).[5] Over an extended period of time, all of the silyl formate had converted to the siloxane by-product (**I**, Scheme 2.10). Nevertheless, formation of the silyl formate confirmed a zwitterionic formate complex in solution. The 1,2,3-diazaphospholene, with diphenylsilane as co-catalyst, could mediate the N-formylation of primary and secondary amines with CO_2 under catalytic conditions. A proposed catalytic reaction mechanism involved CO_2 insertion followed by formate transfer to diphenylsilane and regeneration of 1,2,3-diazaphospholene (**II**, Scheme 2.10). This resulted in formation of the intermediate formatosilane, which transferred a formate moiety to the added amine (**II**, Scheme 2.10).[5]

© University of Pretoria

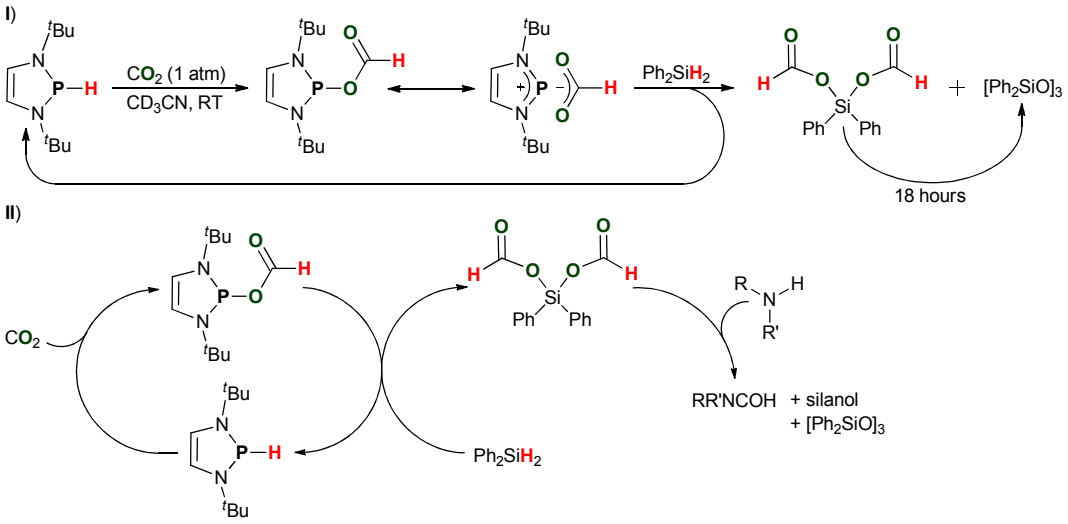

Scheme 2.10: 1,2,3-diazaphospholene facilitating CO_2 **I**) insertion and **II**) catalytic transfer to amines[5]

2.2 Aim

It was postulated that the nickel hydride complex $\mathbf{8_a}$ (see chapter 1), prepared during the preceding MSc study of the author, could mediate the carbon oxygen double bond cleavage of carbon dioxide (Figure 2.4).[32] Even though the donor atom *trans* to the hydride ligand is not a strongly donating anionic B, Si, or C-based ligand, the combined electronic effect of the pincer ligand from precursor $\mathbf{L_a}$ could render the metal center with sufficient nucleophilic character to activate CO_2. Based on the examples discussed above, especially the nickel complexes featuring an anionic nitrogen donor ligand *trans* to the hydride moiety (see Figure 2.3), it was reasoned that CO_2 insertion could be reversible if $\mathbf{8_a}$ is reactive towards CO_2.

The nickel hydride complex $\mathbf{8_a}$ is surprisingly stable under various conditions (Figure 2.4). The stability can be attributed to the rigid backbone and steric bulk of the ligand. The enhanced stability could also originate from the hydride ligand with decreased nucleophilic character compared to the average nickel hydride complex.[15] The decreased nucleophilic character is a direct result of a weaker *trans* donor atom. This is further evidenced in the short nickel hydride bond length of $\mathbf{8_a}$, determined to be 1.45(2) Å from the crystal structure (see Figure 1.9, chapter 1).[32] The facile manipulation of $\mathbf{8_a}$ can therefore be attributed to the above mentioned properties of the complex.

© University of Pretoria

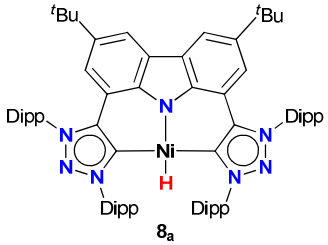

8a

Dipp = 2,6-diisopropylphenyl

Figure 2.4: Nickel hydride pincer complex scrutinized towards the CO_2 activation

2.3 Results and Discussion

2.3.1 Reversible carbon dioxide activation

The reactivity of **8a** towards CO_2 activation was investigated. Consequently, a high pressure NMR tube was loaded with **8a** and dissolved in either C_6D_6 or *d8*-thf. The solution was cooled down, followed by the addition of CO_2 (s). The reaction changed colour from dark red to orange upon warming up of the reaction mixture to room temperature (Scheme 2.11). NMR analysis of the solution indicated that roughly 80% of **8a** reacted and was converted to **10a** (Scheme 2.11). Resultantly, more CO_2 (s) was added to the same reaction mixture, and NMR analysis confirmed full conversion of **8a** to **10a** (Scheme 2.11). Heating up the solution of **10a** to 55 °C in the same high pressure NMR tube resulted in an immediate colour change from orange to dark red, with regeneration of **8a**. Cooling the solution back down to room temperature was accompanied by a colour change from dark red back to orange. This is similar to the previously reported example regarding CO_2 insertion across a nickel hydride bond and CO_2 elimination at elevated temperatures.[16b,18d,23-25] The above observations lead us to postulate that formation of **10a** from **8a** was both reversible and dependent on the concentration of CO_2 in solution. As such, the reaction vessel was placed under vacuum. The solution gradually changed colour from orange to dark red, and NMR analysis evidenced the formation of **8a** from **10a** (*vide infra*). Confirming CO_2 insertion and therefore formation of **10a** with MS (mass spectrometry) and XRD (X-ray diffraction) characterization techniques were not possible, due to the requirement for a CO_2 atmosphere. To unequivocally prove reversible CO_2 activation and therefore formation of **10a,** a series of stoichiometric and formate trapping experiments was conducted.

© University of Pretoria

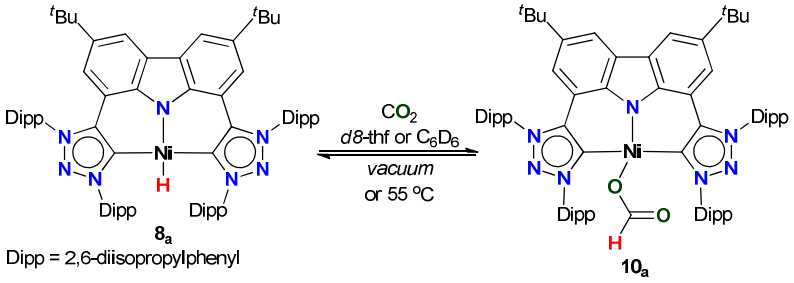

Scheme 2.11: Reversible carbon dioxide activation

Figures 2.5 and 2.6 display the ^{1}H and ^{13}C NMR spectra of **10$_a$** (small inserts in both figures represent the ^{1}H and ^{13}C NMR spectra of **8$_a$**, respectively). The ^{1}H NMR spectrum (Figure 2.5) corroborates the ^{13}C NMR spectrum, confirming CO_2 insertion across the nickel hydride bond. The hydride signal resonating at δ_H -6.34 ppm has completely disappeared, while the characteristic aromatic carbazole CH proton resonances have shifted upfield, from δ_H 8.28 for **8$_a$** to 8.17 ppm for **10$_a$** (Figure 2.5). The nickel formate proton resonance was not detected. Various resonance structures or hydrogen bonding interactions could account for the absence of the formate proton signal in the ^{1}H NMR spectrum. Low temperature ^{1}H NMR studies were also performed to shed light on the nickel formate complex structure (*vide infra*). As is evident from Figure 2.6, the carbene carbon resonance has shifted upfield, from $\delta_{Ccarbene}$ 159.8 to 153.8 ppm for **8$_a$** and **10$_a$**, respectively. In addition to the excess free CO_2 in solution (resonating at δ_{CO_2} 124.9 ppm), another additional signal is detected which resonates at δ_C 156.0 ppm and corresponds to the nickel formate carbonyl carbon. This value is slightly upfield from the reported values for analogues nickel formate complexes, but still within an acceptable range for a Ni-OCOH complex.[16,23-25]

© University of Pretoria

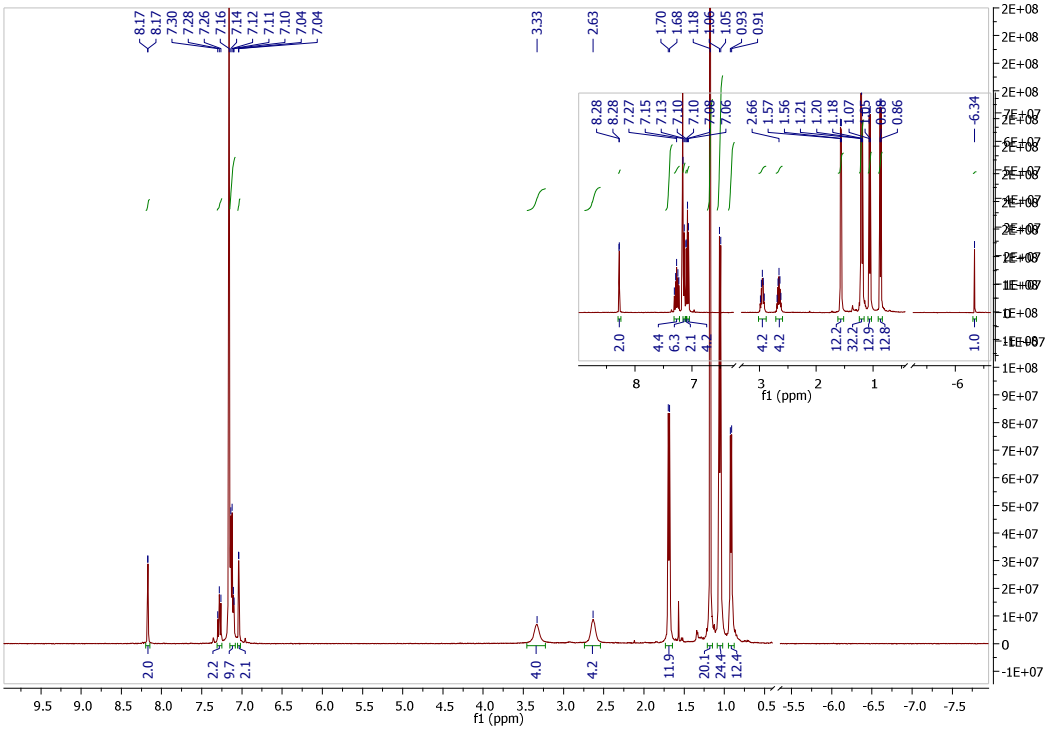

Figure 2.5: ^{1}H NMR spectrum of **10$_a$** (small insert represent ^{1}H NMR spectrum of **8$_a$**) in solvent C_6D_6

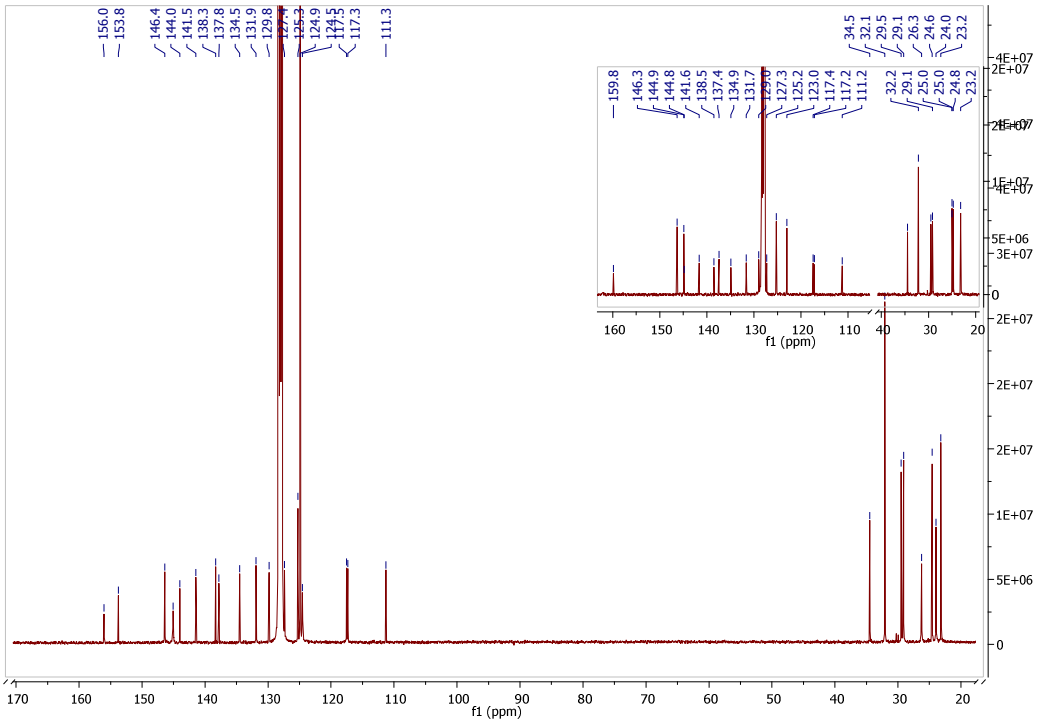

Figure 2.6: ^{13}C NMR spectrum of **10$_a$** (small insert represent ^{13}C NMR spectrum of **8$_a$**) in solvent C_6D_6

© University of Pretoria

A low temperature ^{1}H NMR study was executed in order to determine the formate proton resonance. The red solid **8$_a$** was dissolved, in a high pressure NMR tube, through the addition of *d8*-thf. The vessel was cooled down to -78 °C, followed by the addition of CO_2 (s). The reaction immediately changed colour upon warming up to room temperature. The ^{1}H NMR spectrum of the solution was recorded at room temperature and at -70 °C. At room temperature, only one product was detected in the solution, as before. However, at -70 °C, two acidic protons are noted in the ^{1}H NMR spectrum (Figure 2.7). The proton resonating at δ_H 9.50 ppm corresponds to the nickel formate complex **10$_a$**, further evidencing nickel formate formation and therefore reversible CO_2 activation and insertion. The resonance value is slightly downfield compared to literature reported values for analogues complexes, but still within the acceptable range for nickel formates.[16,18,20a,23-25] A second peak is also detected at δ_H 15.84 ppm (Figure 2.7). This resonance corresponds to a second product, as two products are noted and the acidic protons are in a ratio of 1:1 with regards to each other (both overlapping aromatic carbazole CH signals at δ_H 8.08-8.05 ppm are integrated to 4H, giving an integration of 1 for each acidic proton). Unfortunately, all the signals resonating upfield from δ_H 9.50 ppm broadened considerably at -70 °C and the spectrum is too complex to analyze further (Figure 2.7). We can however speculate on the structural conformation of the second product.

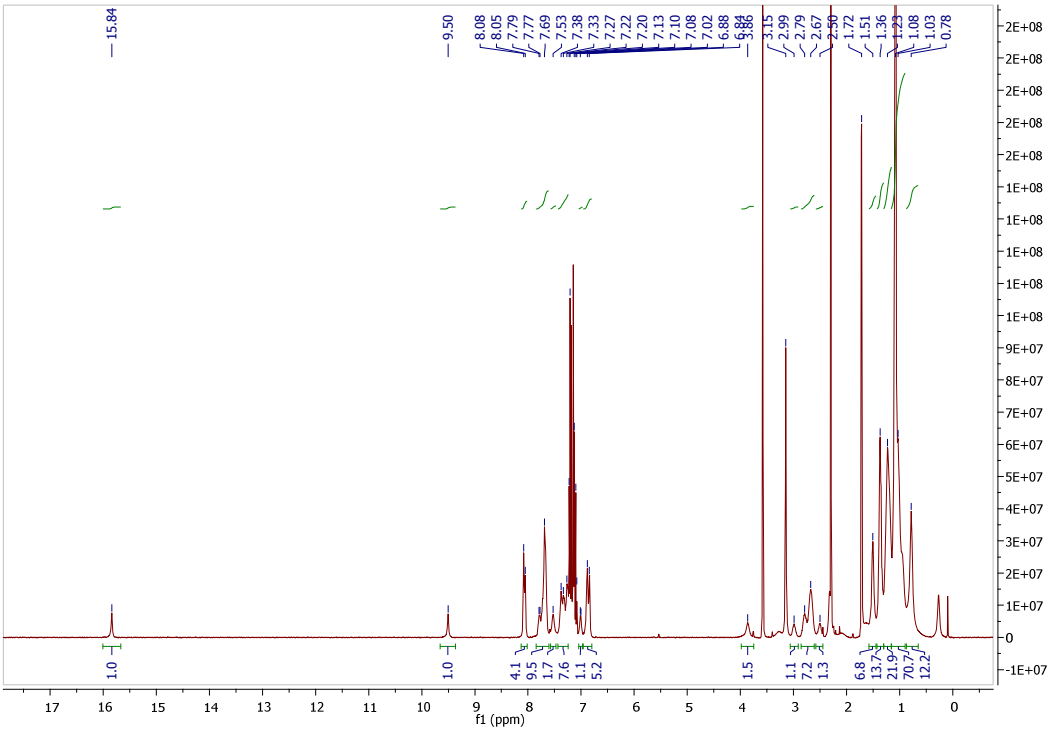

Figure 2.7: ^{1}H NMR spectrum of **10$_a$** in *d8*-thf at -70 °C

© University of Pretoria

At -70 °C, bond rotation becomes increasingly restricted. Therefore, the kinetically stable products will be favoured over the thermodynamic product. It can be suggested that the second product at -70 °C is a resonance structure of **10$_a$**, which accounts for the second product detected during the low temperature NMR studies. Alternatively, various hydrogen bonding interactions or the realization of a partial negative nickel center, a result of the electron releasing effect of the carbene ligands, could also explain the downfield proton chemical shift of δ_H 15.84 ppm (Scheme 2.12). The postulation of a negatively charged nickel center and/or hydrogen bonding could also be supported by the fact that these interactions could be present during β-hydride elimination. β-hydride elimination results in regeneration of the nickel hydride complex and elimination of CO_2 (Scheme 2.12). At very low temperatures, the various intermediate complexes during β-hydride elimination can be stabilized to such an extent that it can be observed spectroscopically (Scheme 2.12). The acidic formate hydrogen can form favourable bonding interactions with both the metal and the basic amido moiety. A five-membered metallacycle will form if coordination is through the amido nitrogen, which further enhances the stability of the intermediate product (Scheme 2.12). Consequently, the hydrogen resonance will be shifted considerably downfield if coordination occurs as proposed. At higher temperatures or at lower CO_2 concentration, the classical four-membered metallacycle will lead to β-hydride elimination after bond rearrangement and therefore reformation of **8$_a$** and CO_2 (Scheme 2.12).

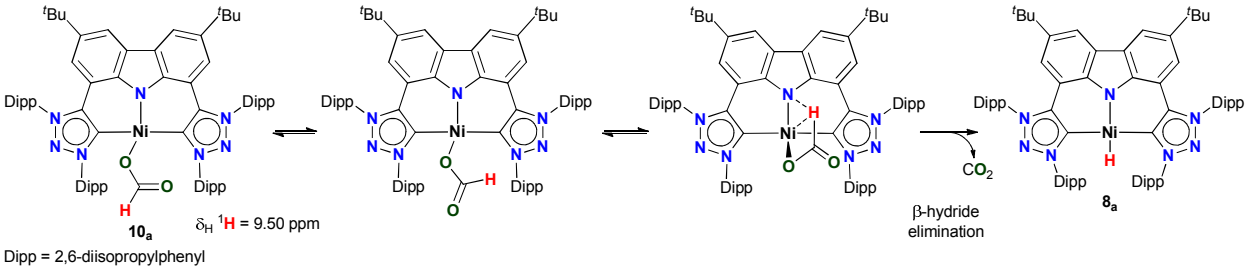

Scheme 2.12: Possible resonance structures and hydrogen bonding interactions towards β-hydride elimination and regeneration of **8$_a$**

To demonstrate reversible CO_2 insertion at room temperature (see Scheme 2.11), a C_6D_6 solution of **10$_a$** was placed under vacuum for 2 minutes (Scheme 2.11). After 2 minutes under reduced pressure, approximately 50% of **10$_a$** converted back to **8$_a$** (see green spectrum, Figure 2.8). Complete evaporation of the solvent (in this case C_6D_6) followed by re-dissolving of the solid in C_6D_6, resulted in near complete regeneration of **8$_a$** with 10% of **10$_a$** remaining (see blue spectrum, Figure 2.8). The cycle was repeated once more, yielding **8$_a$** as the only product in solution (see purple spectrum, Figure 2.8). This further evidences facile CO_2 insertion and elimination at room temperature under reduced pressure. Elimination

© University of Pretoria

of CO_2 was also recorded to occur immediately at 55 °C or under ambient conditions, albeit longer reaction times were required for the latter process. This constitutes another rare example of reversible CO_2 activation under very mild conditions.

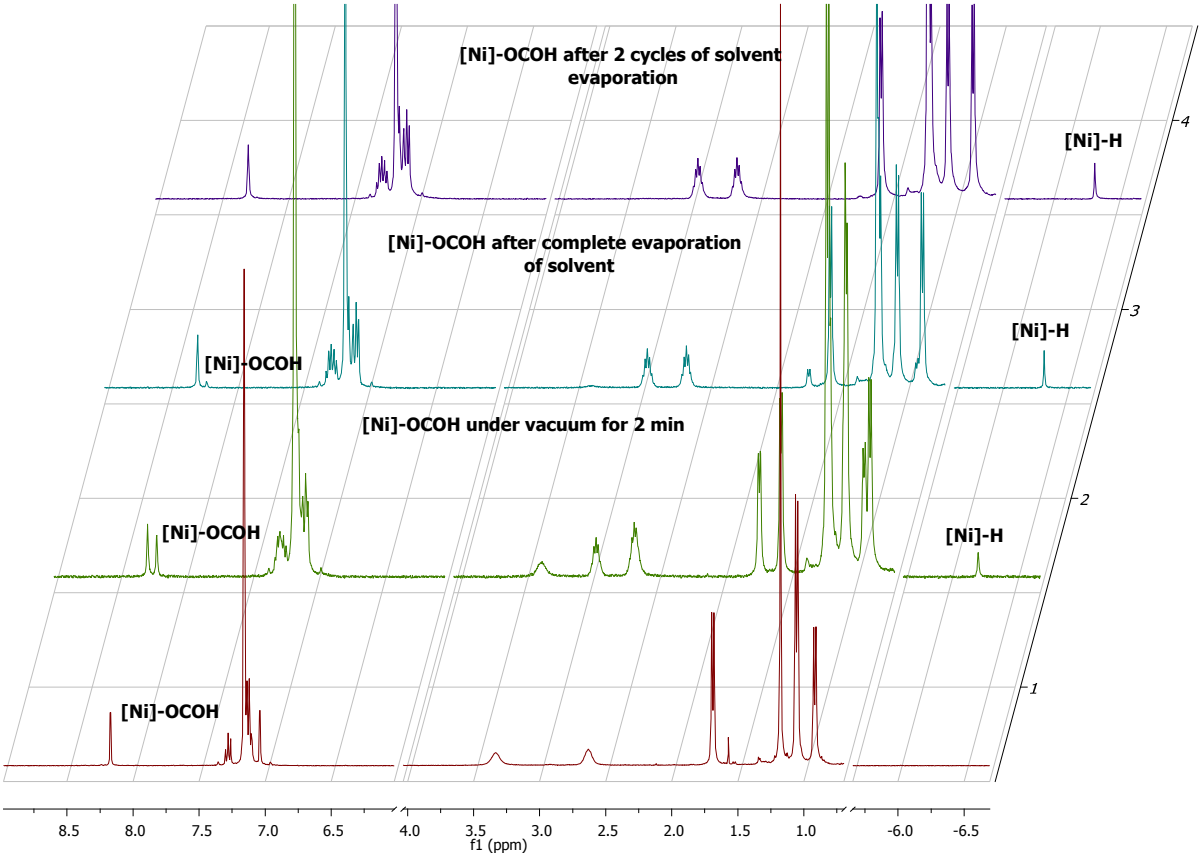

Figure 2.8: Stacked ^1H NMR spectra of CO_2 elimination from **10$_a$** at room temperature *in vacuo* (solvent C_6D_6)

The reaction between **8$_a$** and acetic acid was investigated to further substantiate CO_2 insertion across the nickel hydride bond and therefore formation of the nickel formate complex **10$_a$** (Scheme 2.13). Treatment of **8$_a$** with a stoichiometric amount of acetic acid at -80 °C resulted in an immediate colour change and formation of the targeted nickel acetate complex **11$_a$** (Scheme 2.13). Spectroscopic analysis of **11$_a$** revealed various similarities between **11$_a$** and **10$_a$**. The aromatic carbazole CH protons of **11$_a$** resonated at δ_H 8.20 ppm (Figure 2.9), which is only 0.03 ppm downfield from the corresponding resonance of **10$_a$** at δ_H 8.17 ppm (see Figure 2.5). The acetate methyl resonance of **11$_a$** was detected at δ_H 0.51 ppm (Figure 2.9). The carbene carbon resonance of the two products were also determined to be very similar. The carbene carbon chemical shift of **11$_a$** was observed at $\delta_{Ccarbene}$ 154.0 ppm (Figure 2.10), which resonates downfield from **10$_a$** by just 0.2 ppm. The above spectroscopic values signify that

© University of Pretoria

the bonding situation of **11$_a$** and **10$_a$** is very similar. The only marked spectroscopic difference between **11$_a$** and **10$_a$**, in addition to an extra methyl group instead of just a hydrogen, is at the carbonyl carbon which resonates downfield at δ_C 177.7 ppm (Figure 2.10) for **11$_a$** compared to the upfield NMR shift of **10$_a$** at δ_C 156.0 ppm (see Figure 2.6).

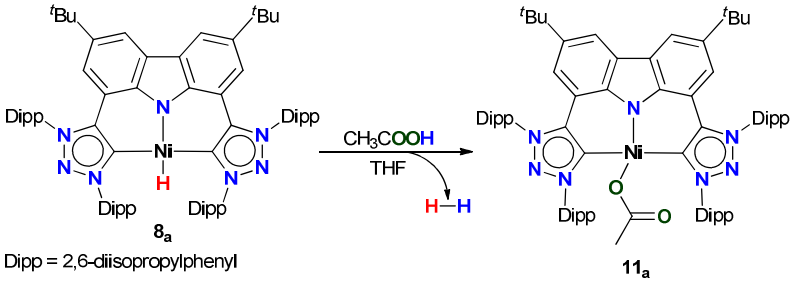

Scheme 2.13: Nickel acetate preparation through H_2 elimination

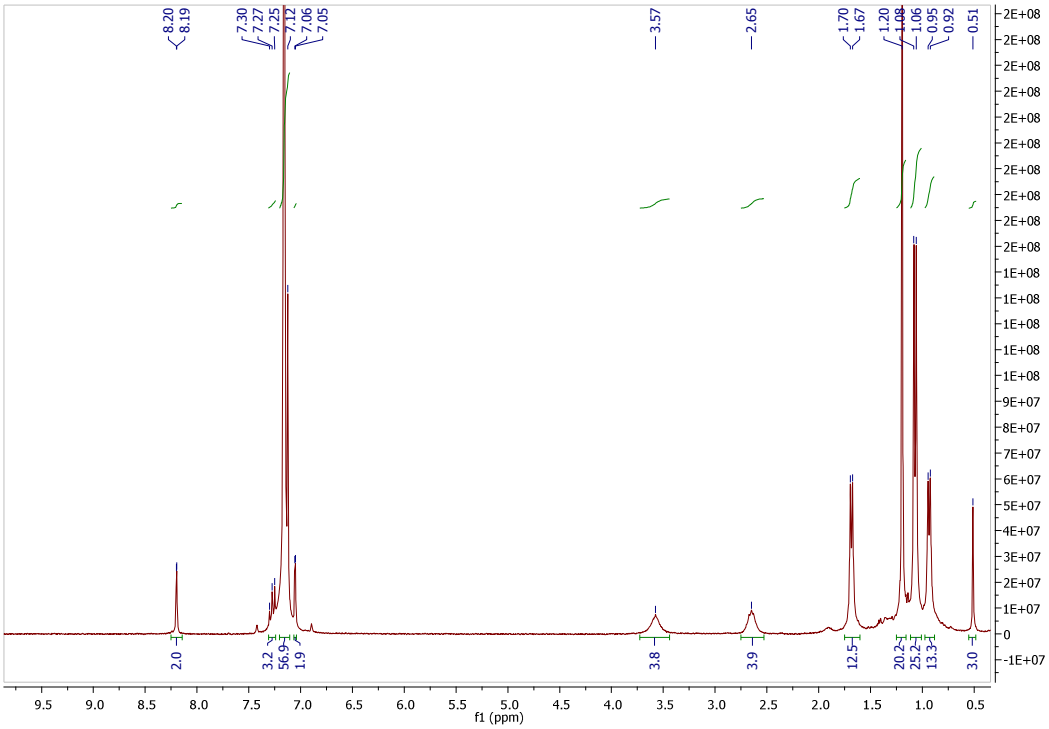

Figure 2.9: ^{1}H NMR spectrum of nickel acetate **11$_a$** in solvent C_6D_6

© University of Pretoria

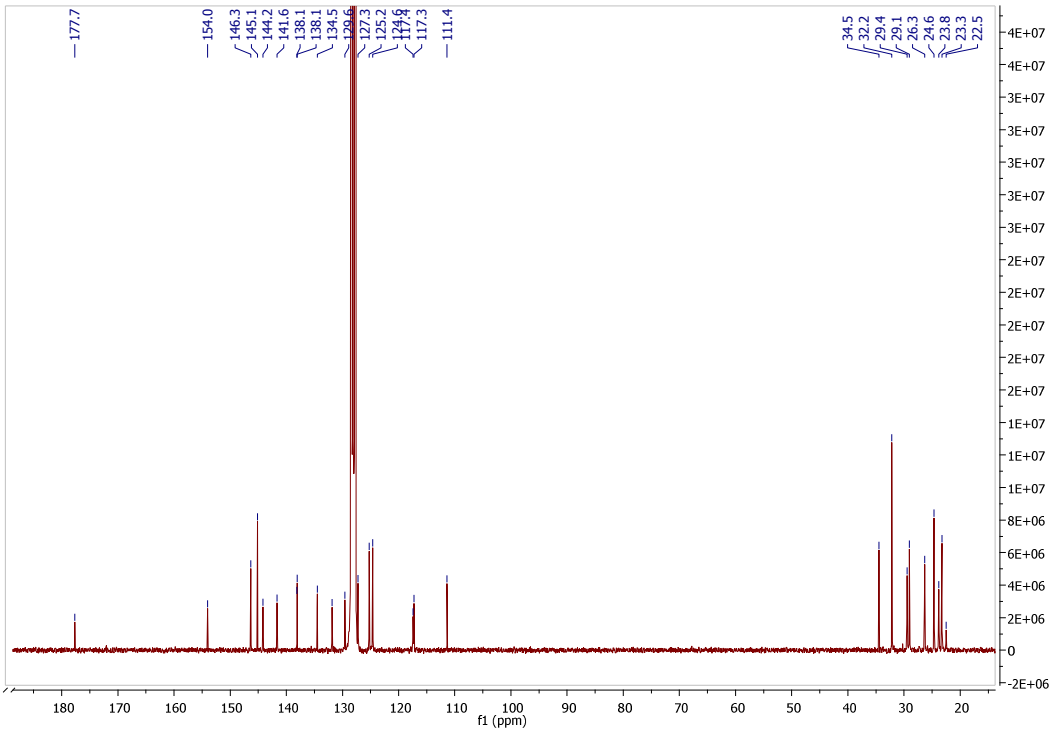

Figure 2.10: ^{13}C NMR spectrum of nickel acetate **11$_a$** in solvent C_6D_6

Slow evaporation of a C_6D_6 solution of **11$_a$** yielded crystals suitable for an X-ray diffraction study (Figure 2.11). The nickel carbene bond lengths of **11$_a$** are similar to the corresponding bond lengths of complex **8$_a$** (nickel carbene bond lengths for **11$_a$** are 1.927(4) and 1.915(4) Å, for the Ni1-C16 and Ni1-C14 bonds, respectively).[32] The carbene-nickel-carbene bond angle of **11$_a$** deviates slightly from the expected 180°, at 173.62(13)°. The nickel-amido bond length at 1.897(3) Å is also similar to the equivalent bond length for **8$_a$**, at 1.9016(18) Å.[32] The Ni1-O1 bond length was determined to be 1.867(3) Å, while the N1-Ni1-O1 bond angle is almost linear (177.71(11)°). The bond properties of **11$_a$** allows for further insight into the bonding situation concerning **10$_a$**.

© University of Pretoria

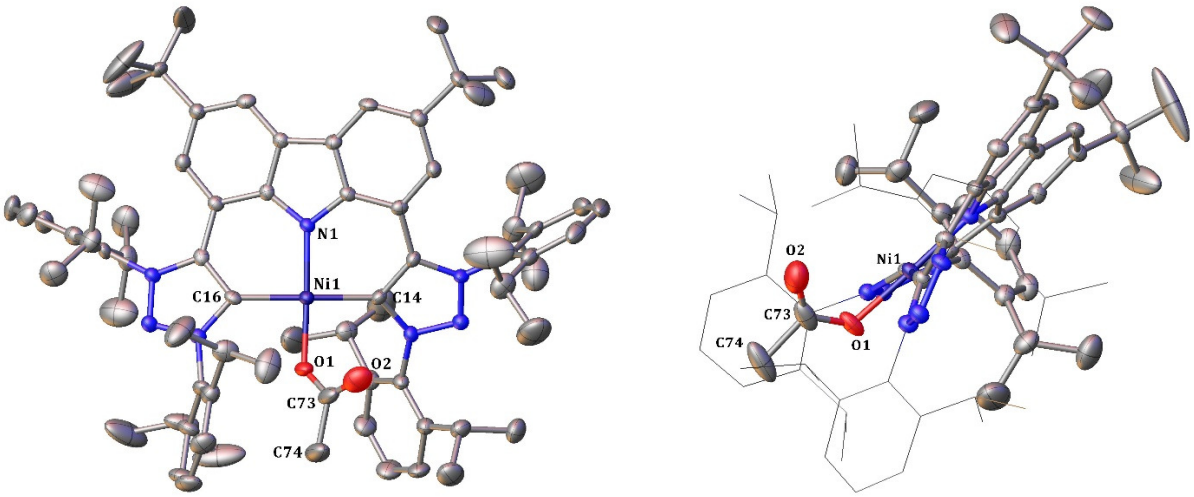

Figure 2.11: Crystal structure of **11$_a$** (Frontal and side-on views. Hydrogens and solvent molecules omitted for clarity.)

Additional evidence for the formation of **10$_a$** *via* CO_2 insertion across the nickel hydride bond, providing further confirmation of reversible room temperature CO_2 activation, was acquired by formate trapping experiments.[5] Complex **10$_a$** was treated with different chloride containing reagents, which reacts with and eliminates the formate moiety, while the formed vacant site at the nickel metal center is saturated by the chloride anion present in solution. Two reagents were used to trap the formate functional group (Scheme 2.14). First, the nickel formate complex **10$_a$** was reacted with an excess amount of trimethylsilyl chloride (TMSCl), which resulted in a slight colour change from orange to dark orange (Scheme 2.14). The progress of the reaction was monitored by NMR spectroscopy, which confirmed immediate formation of a new product, namely the targeted nickel chloride complex **12$_a$** (Scheme 2.14). The formation of hexamethyldisiloxane was also noted, in addition to **12$_a$**. This is similar to the observations reported by Kinjo and co-workers during their respective formate trapping experiment.[5] Also, no trimethylsilane was observed during extensive NMR spectroscopic characterization, indicating that TMSCl did not react with **8$_a$** as there is no hydride present in solution. The nickel formate complex was likewise treated with excess tetrabutylammonium chloride (Scheme 2.14). The softer reagent reacted more slowly with **10$_a$** compared to the TMSCl reagent. The reaction progress was scrutinized with NMR techniques, which indicated that complete conversion of the nickel formate to the nickel chloride complex had occurred after two hours. The reaction mixture was purified and spectroscopic analysis of the isolated products confirmed the formation of the two products, namely the nickel chloride complex **12$_a$** and tetrabutylammonium formate (Scheme 2.14). MS spectroscopic analysis of **12$_a$** also confirmed

© University of Pretoria

formation of the targeted product (see Section 2.5). No reaction was observed between the nickel hydride complex and tetrabutylammonium chloride in a control experiment.

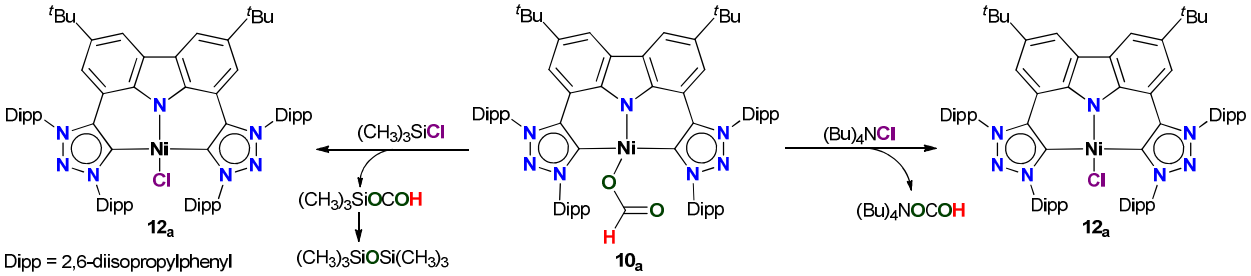

Scheme 2.14: Nickel chlorido complex formation through formate trapping with chloride-containing reagents

The aromatic carbazole CH protons of **12$_a$** resonate at δ_H 8.25 ppm (Figure 2.12), downfield from the nickel formate complex **10$_a$** (δ_H 8.17 ppm) and slightly upfield from the nickel hydride product **8$_a$** (δ_H 8.28 ppm). The carbene carbon resonance of **12$_a$** at $\delta_{Ccarbene}$ 153.1 ppm (Figure 2.13) is significantly upfield from the corresponding resonance of **8$_a$** ($\delta_{Ccarbene}$ 159.8 ppm), but is different from **10$_a$** ($\delta_{Ccarbene}$ 153.8 ppm) by only 0.7 ppm. However, no carbonyl resonance is detected, confirming elimination of the formate functionality.

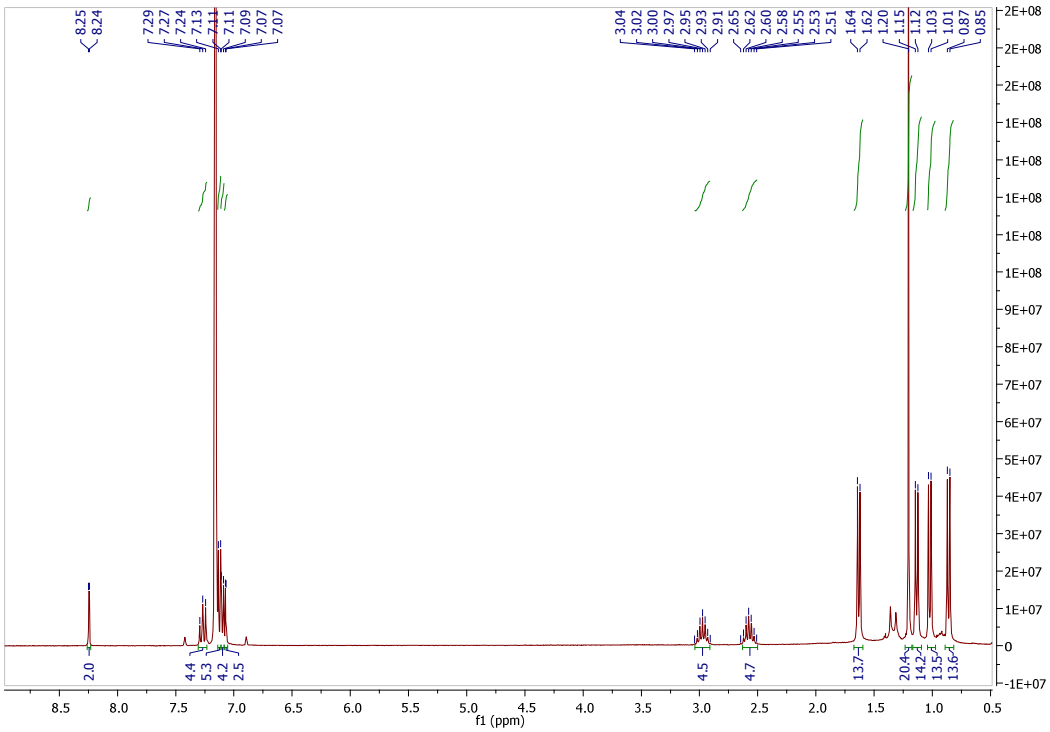

Figure 2.12: ^{1}H NMR spectrum of **12$_a$** in solvent C_6D_6

© University of Pretoria

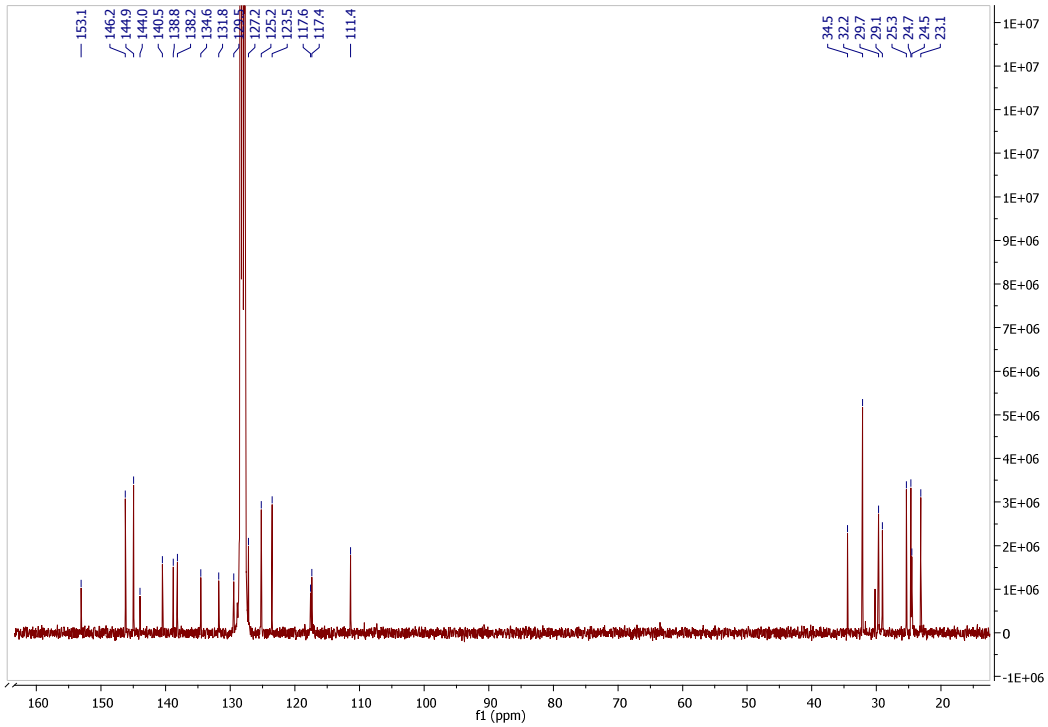

Figure 2.13: ^{13}C NMR spectrum of **12$_a$** in solvent C_6D_6

The nickel chlorido complex **12$_a$** was independently synthesized by H_2 elimination. In this case, treatment of **8$_a$** with HCl at -80 °C resulted in an immediate colour change from dark red to dark orange, with concomitant formation of **12$_a$** (Scheme 2.15). Analysis of both ^1H and ^{13}C NMR spectra of **12$_a$** through hydrogen gas elimination (Scheme 2.15), confirmed the formation of the nickel chlorido complex through formate trapping, as both sets of NMR spectra are identical.

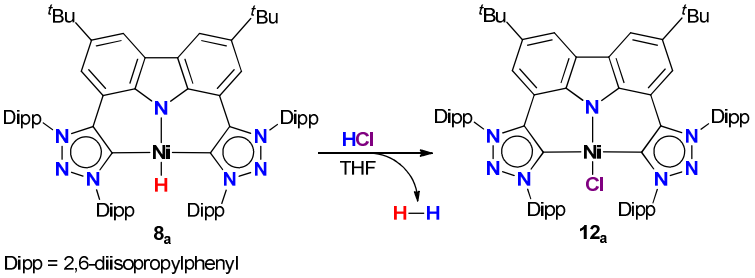

Scheme 2.15: Synthesis of **12$_a$** *via* H_2 elimination

2.4 Conclusion

The atmospherically stable nickel hydride complex activates and inserts CO_2 instantaneously at room temperature. This is contrary to nickel hydride complexes featuring anionic nitrogen donor ligands *trans*

© University of Pretoria

to the hydride moiety, which generally requires several hours or even days to insert CO_2 across the respective nickel hydride bonds. The reactivity of **8$_a$** towards CO_2 can be substantiated by the strong donor properties of the pincer ligand decorated with triazolylidene functionalities. Even though the triazolylidenes are *cis* to the hydride ligand, these donor ligands impart sufficient electron density to the metal to allow for CO_2 activation. Synthesis of the nickel formate complex could only be verified by NMR spectroscopy, due to the reversible nature of the Ni-O bond formed. As such, the nickel hydride complex was treated with acetic acid. The corresponding nickel acetate **11$_a$** was isolated, with spectroscopic data determined to be very similar to that of **10$_a$**. A crystal structure of **11$_a$** could also be obtained, which gives insight into the bonding situation of **10$_a$**.

More intriguing is the reversible nature of the insertion reaction. Generally, high temperatures under a constant vacuum for prolonged periods of time are required for nickel formate decarboxylation. However, the nickel formate complex **10$_a$** readily mediates β-hydride elimination at room temperature under a negative pressure to regenerate the nickel hydride complex and release CO_2. The spontaneous nickel formate decarboxylation can be attributed to the weaker amido moiety *trans* to the hydride ligand, which does not yield a nickel formate complex upon irreversible CO_2 insertion, as is the case for stronger anionic donor ligands *trans* to the hydride moiety.

Formation of the nickel formate complex was further evidenced by formate trapping experiments with TMSCl and tetrabutylammonium chloride. Treatment of the nickel formate with the trapping reagents yielded the nickel chloride complex **12$_a$** and the formate product. In the case of TMSCl, the hexamethyldisiloxane was detected during NMR experiments, while the tetrabutylammonium formate salt was isolated upon reaction of **10$_a$** with tetrabutylammonium chloride. The trapping experiments clearly substantiate the preparation of the nickel formate complex. The nickel chloride complex was independently synthesized by reacting the hydride complex with HCl, to confirm the isolation of the nickel chlorido complex during the formate trapping experiments.

The catalytic activity of the nickel hydride complex could further be scrutinized towards the reduction of CO_2. Specifically, the reduction of CO_2 with various silanes and boranes to the formaldehyde and/or methanol level could be investigated. Finally, if the abovementioned reactions are successful, the hydrogenation of CO_2 with hydrogen could be attempted.

© University of Pretoria

2.5 Experimental

2.5.1 (CNC_{Dipp})Ni(II)H (8_a)

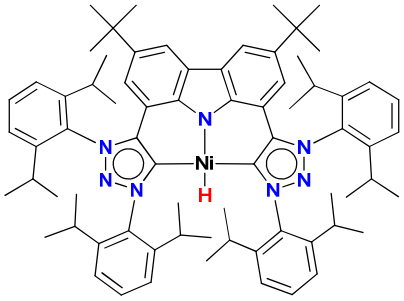

Compound **8_a** was synthesized as previously reported.[32] The NMR characterization and spectra are included here for direct comparison to derivatized nickel(II) complexes. **^{1}H NMR** δ_H (C_6D_6, 300 MHz) 8.28 (d, *J* = 1.6 Hz, 2H, Ar**H**$_{carb}$), 7.29 (dd, *J* = 8.0 Hz, 7.6 Hz, 2H, Ar**H**$_{Dipp}$ overlaps with ArH_{Dipp}), 7.25 (dd, *J* = 8.0 Hz, 7.6 Hz, 2H, Ar**H**$_{Dipp}$ overlaps with ArH_{Dipp}), 7.14 (d, *J* = 8.0 Hz, 4H, Ar**H**$_{Dipp}$ overlaps with C_6D_6), 7.10 (d, *J* = 2.0 Hz, 2H, Ar**H**$_{carb}$), 7.07 (d, *J* = 7.6 Hz, 4H, Ar**H**$_{Dipp}$), 2.95 (sept, *J* = 6.8 Hz, 4H, C**H**$(CH_3)_2$), 2.66 (sept, *J* = 6.8 Hz, 4H, C**H**$(CH_3)_2$), 1.56 (d, *J* = 6.8 Hz, 12H, CH(C**H**$_3)_2$), 1.21 (s, 18H, C(C**H**$_3)_3$), 1.19 (d, *J* = 6.8 Hz, 12H, CH(C**H**$_3)_2$), 1.06 (d, *J* = 6.8 Hz, 12H, CH(C**H**$_3)_2$), 0.87 (d, *J* = 6.8 Hz, 12H, CH(C**H**$_3)_2$), -6.34 (s, 1H, Ni**H**). **^{13}C NMR** δ_C (C_6D_6, 75 MHz) 159.8 (**C**$_{Carbene}$), 146.3 (Ar**C**$_q$), 144.9 (Ar**C**$_q$), 144.8 (Ar**C**$_q$), 141.6 (Ar**C**$_q$), 138.5 (Ar**C**$_q$), 137.4 (Ar**C**$_q$), 134.9 (Ar**C**$_q$), 131.7 (Ar**C**H), 129.0 (Ar**C**H), 127.3 (Ar**C**$_q$), 125.2 (Ar**C**H), 123.0 (Ar**C**H), 117.4 (Ar**C**H), 117.2 (Ar**C**H), 111.3 (Ar**C**$_q$), 34.5 (**C**$(CH_3)_3$), 32.2 (C(**C**$H_3)_3$), 29.5 (**C**H$(CH_3)_2$), 29.1 (**C**H$(CH_3)_2$), 25.1 (CH(**C**$H_3)_2$), 25.0 (CH(**C**$H_3)_2$), 24.8 (CH(**C**$H_3)_2$), 23.2 (CH(**C**$H_3)_2$).

2.5.2 Synthesis of (CNC_{Dipp})Ni(II)OCOH (10_a)

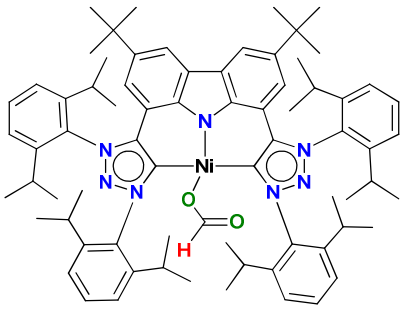

Addition of excess CO_2 (s) in a high pressure NMR tube containing a red solution of **8_a** (15.0 mg, 1.3 x 10^{-5} mol) in either C_6D_6 or *d8*-thf, at -78 °C under Ar (g), was quickly followed by capping the high pressure NMR tube. The reaction was warmed up to room temperature, with a concomitant colour change from dark red to orange. NMR analysis indicated quantitative conversion of **8_a**, to yield **10_a** as the only product of the reaction. Due to the requirement for a CO_2 atmosphere to ensure formation of **10_a**, the product could not be isolated. **^{1}H NMR** δ_H (C_6D_6, 400 MHz) 8.17 (d, *J* = 1.6 Hz, 2H, Ar**H**$_{carb}$), 7.28 (dd, *J* = 8.0 Hz, 7.6 Hz, 2H, Ar**H**$_{Dipp}$), 7.16 – 7.10 (m, 10H, Ar**H**$_{Dipp}$ overlaps with ArH_{Dipp} and C_6D_6), 7.04 (d, *J* = 1.6 Hz, 2H, Ar**H**$_{carb}$), 3.33 (br s, 4H, C**H**$(CH_3)_2$), 2.63 (br s, 4H, C**H**$(CH_3)_2$), 1.69 (d, *J* = 6.4 Hz, 12H, CH(C**H**$_3)_2$), 1.18 (s, 18H, C(C**H**$_3)_3$), 1.05 (d, *J* = 6.4 Hz, 24H, CH(C**H**$_3)_2$), 0.92 (d, *J* = 6.8 Hz, 12H, CH(C**H**$_3)_2$), NiOCO**H** (n.o.). **^{13}C NMR** δ_C (C_6D_6, 100 MHz) 156.0 (NiO**C**OH), 153.8 (**C**$_{Carbene}$), 146.4 (Ar**C**$_q$),

© University of Pretoria

145.1 (Ar**C**$_q$), 144.0 (Ar**C**$_q$), 141.5 (Ar**C**$_q$), 138.3 (Ar**C**$_q$), 137.8 (Ar**C**$_q$), 134.5 (Ar**C**$_q$), 131.9 (Ar**C**H), 129.9 (Ar**C**H), 127.4 (Ar**C**$_q$), 125.3 (Ar**C**H), 124.9 (excess free **C**O_2), 124.5 (Ar**C**H), 117.5 (Ar**C**H), 117.3 (Ar**C**H), 111.3 (Ar**C**$_q$), 34.5 (**C**$(CH_3)_3$), 32.1 (C(**C**$H_3)_3$), 29.5 (**C**H$(CH_3)_2$), 29.1 (**C**H$(CH_3)_2$), 26.3 (CH(**C**$H_3)_2$), 24.6 (CH(**C**$H_3)_2$), 24.0 (CH(**C**$H_3)_2$), 23.2 (CH(**C**$H_3)_2$).

2.5.3 Synthesis of (CNC$_{Dipp}$)Ni(II)OCOCH$_3$ (**11$_a$**)

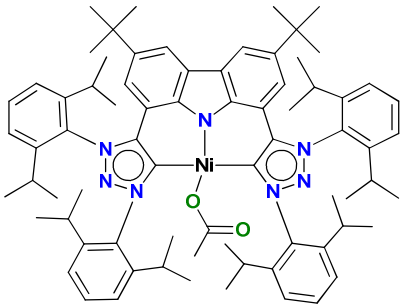

A Schlenk tube was charged with **8$_a$** (15.0 mg, 1.3 x 10^{-5} mol), evacuated and purged with Ar (g). The solids were dissolved through the addition of THF (10 mL). The solution was cooled down to -80 °C, followed by the addition of acetic acid (0.8 µL, 1.3 x 10^{-5} mol). The colour of the solution changed immediately upon addition of the acid, from dark-red to orange. The solution was evaporated under reduced pressure. The complex was extracted with hexanes (3 x 10 mL). The solvent was evaporated *in vacuo*, to yield **11$_a$** (7.0 mg, 6.0 x 10^{-6} mol, 44%) as an orange solid. Slow evaporation of a C_6D_6 solution of **11$_a$** yielded crystals suitable for an X-ray diffraction study. **^{1}H NMR** δ_H (C_6D_6, 300 MHz) 8.20 (d, *J* = 1.8 Hz, 2H, Ar**H**$_{carb}$), 7.28 (t, *J* = 7.8 Hz, 2H, Ar**H**$_{Dipp}$ overlaps with C_6D_6), 7.16 – 7.10 (m, 10H, Ar**H**$_{Dipp}$ overlaps with ArH_{Dipp} and C_6D_6), 7.05 (d, *J* = 1.8 Hz, 2H, Ar**H**$_{carb}$), 3.57 (br s, 4H, C**H**$(CH_3)_2$), 2.65 (br s, 4H, C**H**$(CH_3)_2$), 1.68 (d, *J* = 6.6 Hz, 12H, CH(C**H**$_3)_2$), 1.20 (s, 18H, C(C**H**$_3)_3$), 1.07 (d, *J* = 6.6 Hz, 24H, CH(C**H**$_3)_2$), 0.93 (d, *J* = 6.6 Hz, 12H, CH(C**H**$_3)_2$), 0.51 (s, 3H, NiOCOC**H**$_3$). **^{13}C NMR** δ_C (C_6D_6, 75 MHz) 177.7 (NiO**C**OCH$_3$), 154.0 (**C**$_{Carbene}$), 146.3 (Ar**C**$_q$), 145.1 (Ar**C**$_q$), 144.2 (Ar**C**$_q$), 141.6 (Ar**C**$_q$), 138.1 (Ar**C**$_q$), 138.1 (Ar**C**$_q$), 134.5 (Ar**C**$_q$), 131.8 (Ar**C**H), 129.6 (Ar**C**H), 127.3 (Ar**C**$_q$), 125.2 (Ar**C**H), 124.6 (Ar**C**H), 117.4 (Ar**C**H), 117.3 (Ar**C**H), 111.4 (Ar**C**$_q$), 34.5 (**C**$(CH_3)_3$), 32.2 (C(**C**$H_3)_3$), 29.4 (**C**H$(CH_3)_2$), 29.1 (**C**H$(CH_3)_2$), 26.3 (CH(**C**$H_3)_2$), 24.6 (CH(**C**$H_3)_2$), 23.8 (CH(**C**$H_3)_2$), 23.3 (CH(**C**$H_3)_2$), 22.5 (NiOCO**C**H_3).

© University of Pretoria

2.5.4 Synthesis of (CNC_{Dipp})Ni(II)Cl (12_a)

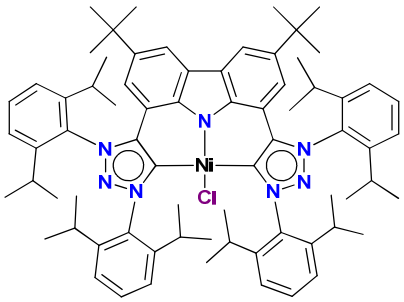

Method 1: A high pressure NMR tube was charged with **8_a** (15.0 mg, 1.3 x 10^{-5} mol) under a nitrogen gas atmosphere. The solids were dissolved through the addition of *d8*-thf (0.4 mL). The solution was cooled down to -78 °C, followed by the addition of excess CO_2 (s) to achieve 1 bar CO_2 (g) atmosphere. The reaction vessel was warmed up to room temperature, with a concomitant colour change from dark red to orange. The solution was cooled down to -78 °C. Trimethylsilyl chloride (3.8 µL, 3.0 x 10^{-5} mol) was added to the cold solution. Upon warming of the reaction mixture, the colour changed from orange to dark orange. The product was not isolated, but NMR analysis confirmed quantitative conversion of **10_a** to **12_a**. **Method 2**: A high pressure NMR tube was loaded with **8_a** (15.0 mg, 1.3 x 10^{-5} mol) and tetrabutylammonium chloride (11.2 mg, 4.0 x 10^{-5} mol), under a nitrogen gas atmosphere. To the solid mixture was added *d8*-thf (0.4 mL). The colour of the solution remained dark red. The solution was cooled down to -78 °C and CO_2 (s) added to the reaction vessel, followed by warming up of the reaction mixture. The colour of the solution changed from dark red to orange, and after 2 hours, the solution darkened in colour, to dark orange as above. The reaction was followed by NMR analysis and it was determined that after 2 hours, complete conversion of **10_a** to **12_a** had occurred. The solution was quantitatively decanted to a Schlenk tube. The solvent was evaporated under reduced pressure, yielding an orange residue. The product was extracted with hexanes (3 x 15 mL), followed by evaporation of the solvent under reduced pressure to yield **12_a** (5.0 mg, 4.4 x 10^{-6} mol, 32%) as an orange solid. The remaining residue was extracted with DCM (2 x 10 mL), followed by evaporation of the solvent under reduced pressure to yield tetrabutylammonium formate as a pale yellow-orange solid. Tetrabutylammonium formate formation was confirmed with NMR analysis. **^{1}H NMR** δ_H (CD_2Cl_2, 300 MHz) 7.51 (s, 1H, [$(CH_3CH_2CH_2CH_2)_4NOCO\mathbf{H}$]), 3.11 – 3.05 (m, 8H, [$(CH_3CH_2CH_2C\mathbf{H}_2)_4NOCOH$]), 1.64 – 1.59 (m, 8H, [$(CH_3CH_2C\mathbf{H}_2CH_2)_4NOCOH$]), 1.42 – 1.30 (m, 8H, [$(CH_3C\mathbf{H}_2CH_2CH_2)_4NOCOH$]), 0.97 (t, *J* = 7.2 Hz, 12H, [$(C\mathbf{H}_3CH_2CH_2CH_2)_4NOCOH$]). **Method 3**: A Schlenk tube was charged with **8_a** (15.0 mg, 1.3 x 10^{-5} mol), evacuated and purged with Ar (g). The solids were dissolved by the addition of THF (10 mL) and the solution was cooled down to -80 °C, followed by the addition of 1M HCl in Et_2O (14.8 µL, 1.5 x 10^{-5} mol). The colour of the solution changed immediately upon addition of HCl, from dark-red to dark-orange. The solution was evaporated under reduced pressure and the complex was extracted with hexanes (3 x 10 mL). The solvent was evaporated *in vacuo*, to yield **12_a** (6.5 mg, 5.7 x 10^{-6} mol, 42%) as

© University of Pretoria

an orange solid. **^{1}H NMR** δ_H (C_6D_6, 300 MHz) 8.25 (d, *J* = 1.8 Hz, 2H, Ar**H**$_{carb}$), 7.27 (dd, *J* = 7.8 Hz, 7.6 Hz, 4H, Ar**H**$_{Dipp}$), 7.12 (d, *J* = 7.5 Hz, 4H, Ar**H**$_{Dipp}$ overlaps with ArH_{Dipp}), 7.10 (d, *J* = 7.5 Hz, 4H, Ar**H**$_{Dipp}$ overlaps with ArH_{Dipp}), 7.07 (d, *J* = 1.8 Hz, 2H, Ar**H**$_{carb}$), 2.97 (sept, *J* = 6.9 Hz, 4H, C**H**$(CH_3)_2$), 2.58 (sept, *J* = 6.9 Hz, 4H, C**H**$(CH_3)_2$), 1.63 (d, *J* = 6.9 Hz, 12H, CH(C**H**$_3)_2$), 1.20 (s, 18H, C(C**H**$_3)_3$), 1.13 (d, *J* = 6.9 Hz, 12H, CH(C**H**$_3)_2$), 1.02 (d, *J* = 6.9 Hz, 12H, CH(C**H**$_3)_2$), 0.86 (d, *J* = 6.9 Hz, 12H, CH(C**H**$_3)_2$). **^{13}C NMR** δ_C (C_6D_6, 75 MHz) 153.1 (**C**$_{Carbene}$), 146.2 (Ar**C**$_q$), 144.9 (Ar**C**$_q$), 144.0 (Ar**C**$_q$), 140.5 (Ar**C**$_q$), 138.8 (Ar**C**$_q$), 138.2 (Ar**C**$_q$), 134.6 (Ar**C**$_q$), 131.8 (Ar**C**H), 129.5 (Ar**C**H), 127.2 (Ar**C**$_q$), 125.2 (Ar**C**H), 123.5 (Ar**C**H), 117.6 (Ar**C**H), 117.4 (Ar**C**H), 111.4 (Ar**C**$_q$), 34.5 (**C**$(CH_3)_3$), 32.2 (C(**C**$H_3)_3$), 29.7 (**C**$H(CH_3)_2$), 29.1 (**C**$H(CH_3)_2$), 25.3 (CH(**C**$H_3)_2$), 24.7 (CH(**C**$H_3)_2$), 24.5 (CH(**C**$H_3)_2$), 23.1 (CH(**C**$H_3)_2$). Calculated for $C_{72}H_{90}N_7Ni^+$ $[Ni]^+$: 1110.6611, found: 1110.6590.

2.6 References

[1] *a*) K. Sordakis, C. Tang, L. K. Vogt, H. Junge, P. J. Dyson, M. Beller, G. Laurenczy, *Chem. Rev.*, **2017**, Accepted for publication; *b*) K. L. Skubi, T. R. Blum, T. P. Yoon, *Chem. Rev.*, **2017**, Accepted for publication; *c*) P. Zimmermann, C. Limberg, *Chem. Rev.*, **2017**, Accepted for publication; *d*) W.-H. Wang, Y. Himeda, J. T. Muckerman, G. F. Manbeck, E. Fujita, *Chem. Rev.*, **2015**, *115*, 12936 – 12973; *e*) M. Beller, U. T. Bornscheuer, *Angew. Chem. Int. Ed.*, **2014**, *53*, 4527 – 4528; *f*) M. Cokoja, C. Bruckmeier, B. Rieger, W. A. Herrmann, F. E. Kühn, *Angew. Chem. Int. Ed.*, **2011**, *50*, 8510 – 8537; *g*) C. Federsel, R. Jackstell, M. Beller, *Angew. Chem. Int. Ed.*, **2010**, *49*, 6254 – 6257.

[2] *a*) N. Hazari, J. E. Heimann, *Inorg. Chem.*, **2017**, Accepted for publication; *b*) A. M. Appel, J. E. Bercaw, A. B. Bocarsly, H. Dobbek, D. L. DuBois, M. Dupuis, J. G. Ferry, E. Fujita, R. Hille, P. J. A. Kenis, C. A. Kerfeld, R. H. Morris, C. H. F. Peden, A. R. Portis, S. W. Ragsdale, T. B. Rauchfuss, J. N. H. Reek, L. C. Seefeldt, R. K. Thauer, G. L. Waldrop, *Chem. Rev.*, **2013**, *113*, 6621 – 6658; *c*) J. Schneider, H. Jia, J. T. Muckerman, E. Fujita, *Chem. Soc. Rev.*, **2012**, *41*, 2036 – 2051; *d*) D. J. Darensbourg, *Inorg. Chem.*, **2010**, *49*, 10765 – 10780.

[3] *a*) W. H. Bernskoetter, N. Hazari, *Acc. Chem. Res.*, **2017**, *50*, 1049 – 1058; *b*) Y. Li, X. Cui, K. Dong, K. Junge, M. Beller, *ACS Catal.*, **2017**, *7*, 1077 – 1086; *c*) K. Natte, H. Neumann, M. Beller, R. V. Jagadeesh, *Angew. Chem. Int. Ed.*, **2017**, *56*, 6384 – 6394; *d*) J. Klankermayer, S. Wesselbaum, K. Beydoun, W. Leitner, *Angew. Chem. Int. Ed.*, **2016**, *55*, 7296 – 7343; *e*) F. J. Fernández-Alvarez, A. M. Aitani, L. A. Oro, *Catal. Sci. Technol.*, **2014**, *4*, 611 – 624; *f*) Q. Liu, L. Wu, R. Jackstell, M. Beller, *Nature Commun.*, **2015**, 1 – 15; *g*) I. Omae, *Coord. Chem. Rev.*, **2012**, *256*, 1384 – 1405; *h*) M. Peters, B. Köhler, W. Kuckshinrichs, W. Leitner, P. Markewitz, T. E. Müller, *ChemSusChem*, **2011**, *4*, 1216 – 1240; *i*) S. N. Riduan, Y. Zhang, *Dalton Trans.*, **2010**, *39*, 3347 – 3357.

[4] *a*) D. Mellmann, P. Sponholz, H. Junge, M. Beller, *Chem. Soc. Rev.*, **2016**, *45*, 3954 – 3988; *b*) B. Loges, A. Boddien, F. Gärtner, H. Junge, M. Beller, *Top. Catal.*, **2010**, *53*, 902 – 914.

[5] C. C. Chong, R. Kinjo, *Angew. Chem. Int. Ed.*, **2015**, *54*, 12116 – 12120.

[6] *a*) S. Bontemps, *Coord. Chem. Rev.*, **2016**, *308*, 117 – 130; *b*) L. J. Murphy, K. N. Robertson, R. A. Kemp, H. M. Tuononen, J. A. C. Clyburne, *Chem. Commun.*, **2015**, *51*, 3942 – 3956; *c*) F.-G. Fontaine, M.-A. Courtemanche, M.-A. Légaré, *Chem. Eur. J.*, **2014**, *20*, 2990 – 2996; *d*) P. P. Power, *Nature*, **2010**, *463*, 171 – 177.

[7] *a*) S. Wesselbaum, T. vom Stein, J. Klankermayer, W. Leitner, *Angew. Chem. Int. Ed.*, **2012**, *51*, 7499 – 7502; *b*) C. A. Huff, M. S. Sanford, *J. Am. Chem. Soc.*, **2011**, *133*, 18122 – 18125.

[8] *a*) J. Kothandaraman, A. Goeppert, M. Czaun, G. A. Olah, G. K. S. Prakash, *J. Am. Chem. Soc.*, **2016**, *138*, 778 – 781; *b*) N. M. Rezayee, C. A. Huff, M. S. Sanford, *J. Am. Chem. Soc.*, **2015**, *137*, 1028 – 1031.

[9] R. Tanaka, M. Yamashita, K. Nozaki, *J. Am. Chem. Soc.*, **2009**, *131*, 14168 – 14169.

[10] G. A. Filonenko, R. van Putten, E. N. Schulpen, E. J. M. Hensen, E. A. Pidko, *ChemCatChem*, **2014**, *6*, 1526 – 1530.

© University of Pretoria

[11] Y. Zhang, A. D. MacIntosh, J. L. Wong, E. A. Bielinski, P. G. Williard, B. Q. Mercado, N. Hazari, W. H. Bernskoetter, *Chem. Sci.*, **2015**, *6*, 4291 – 4299.
[12] M. S. Jeletic, M. T. Mock, A. M. Appel, J. C. Linehan, *J. Am. Chem. Soc.*, **2013**, *135*, 11533 – 11536.
[13] M. S. Jeletic, M. L. Helm, E. B. Hulley, M. T. Mock, A. M. Appel, J. C. Linehan, *ACS Catal.*, **2014**, *4*, 3755 – 3762.
[14] N. Kumar, D. M. Camaioni, M. Dupuis, S. Raugei, A. M. Appel, *Dalton Trans.*, **2014**, *43*, 11803 – 11806.
[15] N. A. Eberhardt, H. Guan, *Chem. Rev.*, **2016**, *116*, 8373 – 8426.
[16] *a*) P. Ríos, A. Rodríguez, J. López-Serrano, *ACS Catal.*, **2016**, *6*, 5715 – 5723; *b*) H.-W. Suh, T. J. Schmeier, N. Hazari, R. A. Kemp, M. K. Takase, *Organometallics*, **2012**, *31*, 8225 – 8236.
[17] T. J. Schmeier, N. Hazari, C. D. Incarvito, J. A. Raskatov, *Chem. Commun.*, **2011**, *47*, 1824 – 1826.
[18] *a*) Q.-Q. Ma, T. Liu, A. Adhikary, J. Zhang, J. A. Krause, H. Guan, *Organometallics*, **2016**, *35*, 4077 – 4082; *b*) K. J. Jonasson, O. F. Wendt, *Chem. Eur. J.*, **2014**, *20*, 11894 – 11902; *c*) S. Chakraborty, Y. J. Patel, J. A. Krause, H. Guan, *Polyhedron*, **2012**, *32*, 30 – 34; *d*) S. Chakraborty, J. Zhang, J. A. Krause, H. Guan, *J. Am. Chem. Soc.*, **2010**, *132*, 8872 – 8873.
[19] S. Murugesan, B. Stöger, M. Weil, L. F. Veiros, K. Kirchner, *Organometallics*, **2015**, *34*, 1364 – 1372.
[20] *a*) P. Ríos, N. Curado, J. López-Serrano, A. Rodríguez, *Chem. Commun.*, **2016**, *52*, 2114 – 2117; *b*) T.-P. Lin, J. C. Peters, *J. Am. Chem. Soc.*, **2014**, *136*, 13672 – 13683.
[21] S. Chakraborty, P. Bhattacharya, H. Dai, H. Guan, *Acc. Chem. Res.*, **2015**, *48*, 1995 – 2003.
[22] F. Huang, C. Zhang, J. Jiang, Z.-X. Wang, H. Guan, *Inorg. Chem.*, **2011**, *50*, 3816 – 3825.
[23] C. Yoo, J. Kim, Y. Lee, *Organometallics*, **2013**, *32*, 7195 – 7203.
[24] G. T. Venkanna, S. Tammineni, H. D. Arman, Z. J. Tonzetich, *Organometallics*, **2013**, *32*, 4656 – 4663.
[25] M. Kreye, M. Freytag, P. G. Jones, P. G. Williard, W. H. Bernskoetter, M. D. Walter, *Chem. Commun.*, **2015**, *51*, 2946 – 2949.
[26] C. A. Rettenmeier, H. Wadepohl, L. H. Gade, *Chem. Sci.*, **2016**, *7*, 3533 – 3542.
[27] M. F. Laird, M. Pink, N. P. Tsvetkov, H. Fan, K. G. Caulton, *Dalton Trans.*, **2009**, 1283 – 1285.
[28] B. C. Fullmer, H. Fan, M. Pink, K. G. Caulton, *Inorg. Chem.*, **2008**, *47*, 1865 – 1867.
[29] *a*) D. W. Stephan, G. Erker, *Angew. Chem. Int. Ed.*, **2015**, *54*, 6400 – 6441; *b*) D. W. Stephan, G. Erker, *Angew. Chem. Int. Ed.*, **2010**, *49*, 46 – 76.
[30] See examples and references therein: *a*) I. Knopf, C. C. Cummins, *Organometallics*, **2015**, *34*, 1601 – 1603; *b*) K. Fujiwara, S. Yasuda, T. Mizuta, *Organometallics*, **2014**, *33*, 6692 – 6695; *c*) C. D. N. Gomes, E. Blondiaux, P. Thuéry, T. Cantat, *Chem. Eur. J.*, **2014**, *20*, 7098 – 7106; *d*) M.-A. Courtemanche, M.-A. Légaré, L. Maron, F.-G. Fontaine, *J. Am. Chem. Soc.*, **2013**, *135*, 9326 – 9329; *e*) A. Berkefeld, W. E. Piers, M. Parvez, *J. Am. Chem. Soc.*, **2010**, *132*, 10660 – 10661; *f*) A. Jana, G. Tavčar, H. W. Roesky, M. John, *Dalton Trans.*, **2010**, *39*, 9487 – 9489; *g*) A. E. Ashley, A. L. Thompson, D. O'Hare, *Angew. Chem. Int. Ed.*, **2009**, *48*, 9839 – 9843; *h*) A. Jana, H. W. Roesky, C. Schulzke, A. Döring, *Angew. Chem. Int. Ed.*, **2009**, *48*, 1106 – 1109; *i*) A. Jana, D. Ghoshal, H. W. Roesky, I. Objartel, G. Schwab, D. Stalke, *J. Am. Chem. Soc.*, **2009**, *131*, 1288 – 1293.
[31] S. Burck, D. Gudat, M. Nieger, W.-W. Du Mont, *J. Am. Chem. Soc.*, **2006**, *128*, 3946 – 3955.
[32] *a*) G. Kleinhans, *MSc Dissertation*, University of Pretoria, **2014**, 73 – 105; *b*) D. I. Bezuidenhout, G. Kleinhans, G. Guisado-Barrios, D. C. Liles, G. Ung, G. Bertrand, *Chem. Commun.*, **2014**, *50*, 2431 – 2433.

© University of Pretoria

Chapter 3

Meridional ruthenium(II) pincer complexes towards catalytic hydrogenation reactions

3.1 Background

The interest in the coordination of tridentate pincer type ligands to ruthenium(II) metal centers has resulted in a plethora of complexes being developed for end use in various photophysical, biological, and to the largest extent, catalytic applications. The balance between reactivity *versus* stability renders the ruthenium pincer complexes viable tools with regards to catalytic endeavors. Intrinsically, ruthenium pincer complexes are highly proficient in catalysis, providing access to organic transformation reactions of utmost importance.

When discussing ruthenium catalyzed reactions, one has to mention the groundbreaking discoveries made by Schrock and Grubbs (even though not supported by tridentate pincer ligands). The synthesis of the well-defined olefin metathesis catalyst and its applications further cemented the prominent role of organometallic ruthenium complexes in the field of homogeneous catalysis. The independent reports by Schrock in 1990[1] and Grubbs in 1992[2] disclosed the molybdenum and ruthenium metathesis catalyst, respectively (Figure 3.1). The drawback of these catalysts was the lack of stability, but it was the necessary spark needed. The stability and improved catalytic activity were addressed by the introduction of NHC and/or chelating ligands to stabilize the ruthenium catalyst. Hoveyda and co-workers substituted a phosphine ligand for a chelating phenyl-oxygen moiety, which markedly improved the stability of the olefin metathesis catalyst (Figure 3.1).[3] The stability, catalytic activity and functional group tolerance was further enhanced by the introduction of unsaturated NHC ligands.[4] This finally lead to the synthesis of the now famous, second generation Grubbs catalyst, supported by a saturated NHC ligand (Figure 3.1).[5]

© University of Pretoria

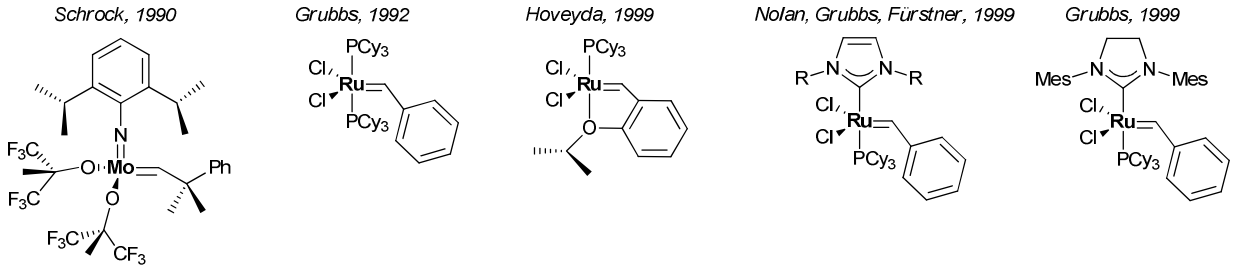

Figure 3.1: Milestones in the development of ruthenium olefin metathesis catalysts

As is evident from above, carbene-supported ruthenium catalysts have found a prominent position in organometallic chemistry. Alongside the ever growing field of ruthenium carbene catalysts, the preparation of tridentate pincer ruthenium complexes has also witnessed exceptional developments, especially in the last two decades. Coordination of a tridentate ligand to a ruthenium metal yields a more stable complex when compared to mono- and bidentate ligands.[6] This results in the formation of a complex, in general, with a meridional geometry around the ruthenium metal center. Both electronic and steric factors can be readily controlled, at various positions on the ligand, as was discussed in chapter 1. Manipulation of the aforementioned properties and therefore catalyst fine-tuning has rendered pincer ruthenium complexes highly influential in catalysis.[7] In addition, metal-ligand cooperativity has been ingeniously exploited in a range of ruthenium pincer catalyzed reactions.[8] Due to the significance of the mentioned benefits, the seminal contributions made by Milstein and Gusev with regards to ruthenium pincer catalyzed reactions, are worth discussing briefly.

The ruthenium pincer complex reported by Milstein and co-workers was demonstrated to catalyze a range of challenging reactions.[9] These reactions included, amongst others, hydrogenation of esters to alcohols (see **II**, Scheme 3.1),[10] dehydrogenative coupling of alcohols yielding esters,[11] hydrogenation of amides to alcohols and amines,[12] and mild synthesis of amides from esters and amines.[13] The reactions are facilitated by ligand cooperativity, with aromatization and dearomatization of the ligand backbone being the driving force behind the wide spread success of the ruthenium pincer complex.[9] The pyridinylmethylenic carbon plays a pivotal role during the aromatization/dearomatization process. Deprotonation of the methylenic carbon leads to dearomatization of the pyridine backbone (**I**, Scheme 3.1).[10] Activation of the incoming substrate results in Y-H (where Y = H, OH, OR, NH_2, NR_2, C) bond scission and therefore protonation and rearomatization of the pyridine backbone (see **II**, Scheme 3.1 for representative ester hydrogenation example). It is important to note that the bond activation process occurred without a change in the oxidation state of the ruthenium(II) metal. The catalytic reaction subsequently continuous through substitution of the hemilabile ligand arm and coordination of the

© University of Pretoria

second substrate. Y-ligand (hydride represents Y-ligand in **II**, Scheme 3.1) transfer ensues, followed by substitution of the targeted product and re-coordination of the hemilabile arm to re-generate the active dearomatized catalyst (**II**, Scheme 3.1).[10]

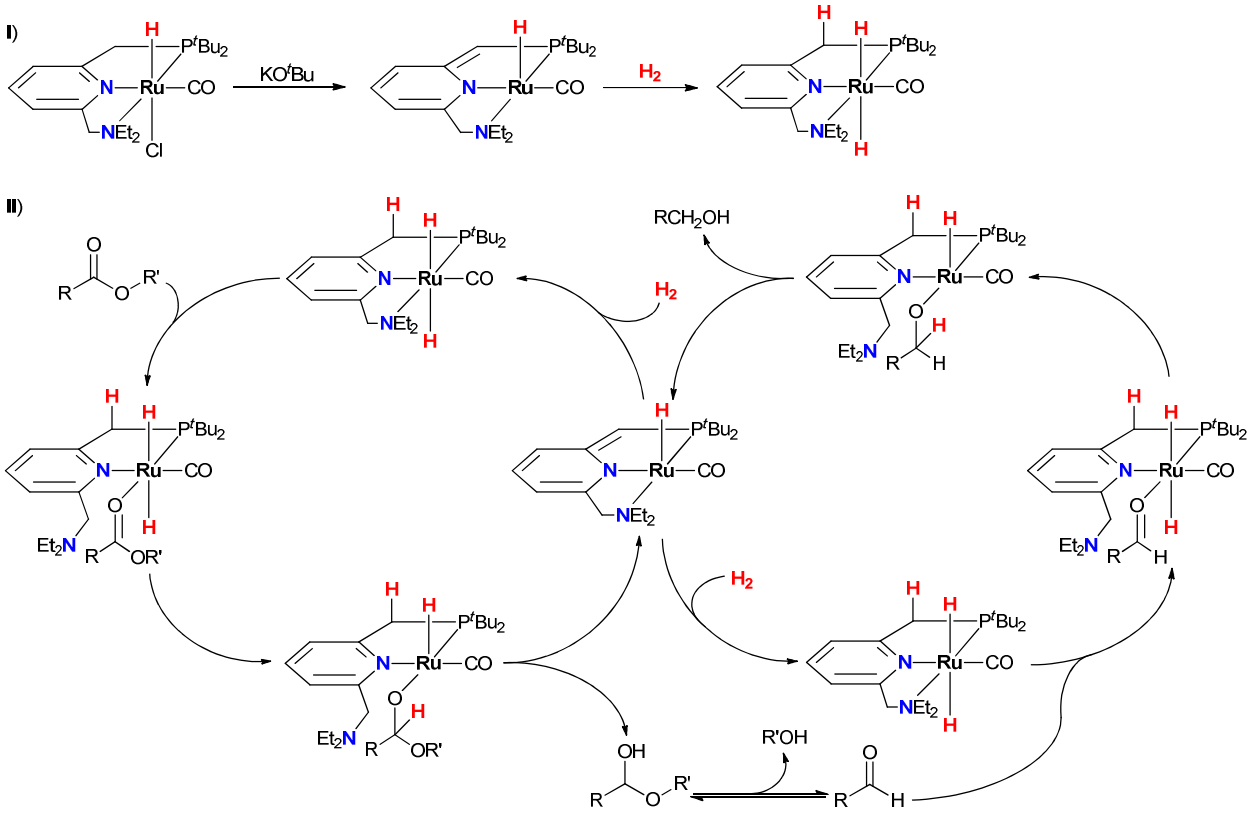

Scheme 3.1: Mechanistic consideration of ester hydrogenation reaction catalyzed by Milstein's catalyst[10]

The group of Gusev reported on the synthesis of pincer ruthenium and osmium complexes, with the metal supported by a tridentate PNN-pincer ligand.[14] The air-stable complexes displayed good catalytic activity in the ester hydrogenation catalyzed reaction. However, as is the case with the Milstein catalyst, the phosphine substituted complexes are expensive. The problem was solved by the same group a year later, through the introduction of SNS-pincer ligands.[15] The SNS supported ruthenium pincer complex was prepared at a fraction of the cost, all the while exhibiting excellent catalytic efficiency in the ester hydrogenation catalyzed reaction (Scheme 3.2). For instance, hydrogenation of ethyl acetate afforded a TON (turnover number) of 58400 after 21 hours at 40 °C. A high selectivity for esters, imines and ketones in the presence of olefins was also noted. Finally, the acceptorless dehydrogenative coupling of ethanol to ethyl acetate was also readily catalyzed by the SNS-tridentate ruthenium complex. Synthesis of the analogous ether bridged SOS- or methyl protected SN(Me)S-ligands, their complexation to ruthenium and the reactivity of the resulting complexes were also tested. It was established that the N-

© University of Pretoria

H functionality was imperative for catalysis, as the aforementioned ether-bridged and N-protected analogues were shown to be inactive in the catalytic reactions. A mechanism for the catalyzed reaction was proposed and it did not involve free organic intermediates (Scheme 3.2).[15] The octahedral ruthenium(II)-dihydride complex was the proposed active catalyst. Ethyl acetate insertion into the Ru-H bond is followed by intramolecular nucleophilic substitution yielding the bis(ethoxide) intermediate. Rearrangement of the intermediate complex vacates a coordination site for hydrogen coordination. Heterolytic splitting of H_2 results in elimination of ethanol and coordination of another H_2 molecule. Finally, a second hydrogen heterolytic cleavage reaction yields the second ethanol molecule and the active ruthenium(II)-dihydride catalyst.[15]

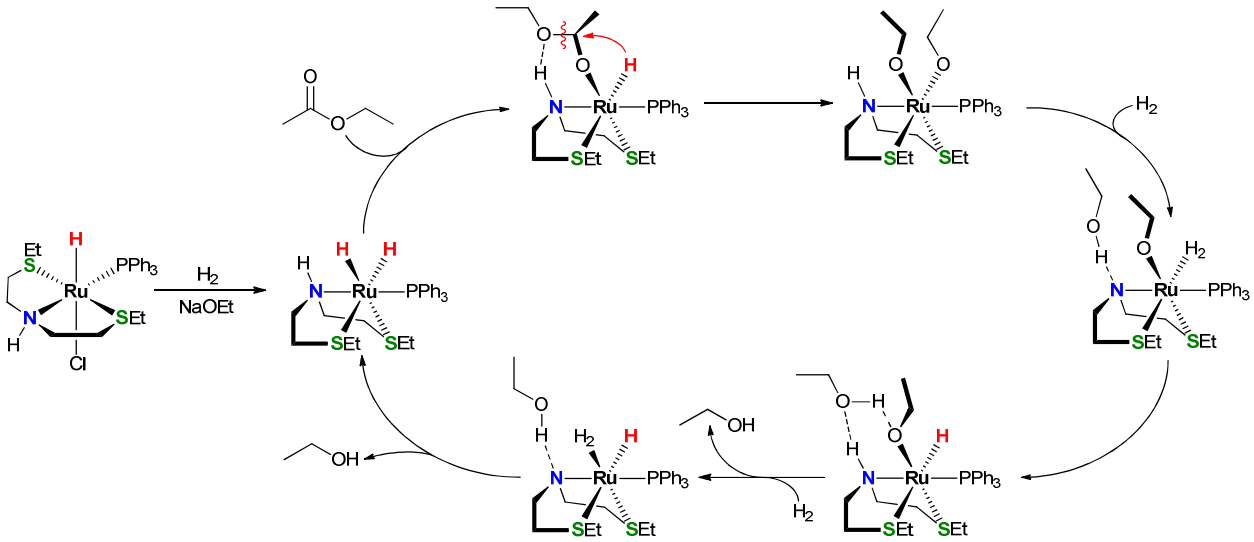

Scheme 3.2: Proposed mechanism for the ester hydrogenation reaction catalyzed by Gusev's SNS-ruthenium catalyst[15]

The incorporation of NHC donor functionalities into tridentate ligands has been less explored than the phosphine analogues. Nonetheless, success has been achieved in this field, and a few relevant examples are disclosed below. Danopoulos and co-workers made use of an analogue of the aforementioned privileged ligand class.[16] A bis(imidazolium) ligand salt with a central pyridine scaffold was readily deprotonated to generate the free biscarbene ligand. Coordination of the pincer biscarbene ligand to a ruthenium(II) precursor yielded the targeted $[(CNC)Ru(Cl)_2(PPh_3)]$ complex featuring a meridional geometry around the metal center (Figure 3.2). The catalyst was subjected to the transfer hydrogenation reaction, exhibiting good catalytic activity at low catalyst loading.[16] A year later, Peris et al. described the synthetic methodology towards a similar ruthenium(II) complex (Figure 3.2).[17] The relaxed requirements (compared to isolation of the air-sensitive free carbene) to complex formation

© University of Pretoria

involved refluxing of the bis(imidazolium) ligand salt in EtOH, in the presence of Et_3N and a $[RuCl_2(nbd)]_n$ precursor (nbd = norbornadiene). The isolated dibromo-ruthenium carbonyl CNC-pincer complex featured the expected meridional geometry around the ruthenium coordination sphere. The $[(CNC)Ru(Br)_2(CO)]$ complex was catalytically active with regards to the transfer hydrogenation reaction. Additionally, changing the metal precursor to $RuCl_3 \cdot 3H_2O$ allowed for the synthesis of the dicationic ruthenium(II) product with coordination of two CNC-pincer ligands, also in a meridional fashion.[17] The challenging ester hydrogenation reaction was tamed with the Milstein and Gusev catalyst, amongst others (*vide supra*). However, an NHC supported ruthenium complex highly active in the ester hydrogenation reaction had not been realized, until the seminal report by Pidko and co-workers in 2015 (Figure 3.2).[18] The octahedral ruthenium(II) complex coordinated by two neutral CNC-pincer biscarbene ligands, displaying a facial geometry with the ligands coordinating in a tripodal fashion, was readily obtained *via* transmetallation form the silver precursor complex with $[Ru(DMSO)_4(Cl)_2]$ (DMSO = dimethylsulfoxide) (Figure 3.2). The complex demonstrated a high catalytic activity in the ester hydrogenation reaction yielding alcohols. The reactions were catalyzed with a high turnover frequency and a high chemoselectivity whilst catalyzing a range of esters substituted with various functional groups.[18] Very recently, the group of Hor and Luo disclosed on a pyridine supported bis(imidazolylidene)ruthenium(II) complex as an active catalyst in the hydroboration of carbon dioxide.[19] The silver transmetallation route proved useful once again. The silver carbene complex was transmetallated with $[Ru(CO)_2Cl_2]_n$ yielding the $[(CNC)Ru(CO)_2Cl]PF_6$ product that was further reacted with sodium borohydride. This resulted to the formation of the ruthenium hydride complex (Figure 3.2), reported to be the complex with the highest catalytic activity for the hydroboration reaction, out of the series of ruthenium(II) complexes disclosed. Crystal structure analysis confirmed the expected meridional complex geometry around the ruthenium metal center (Figure 3.2).[19]

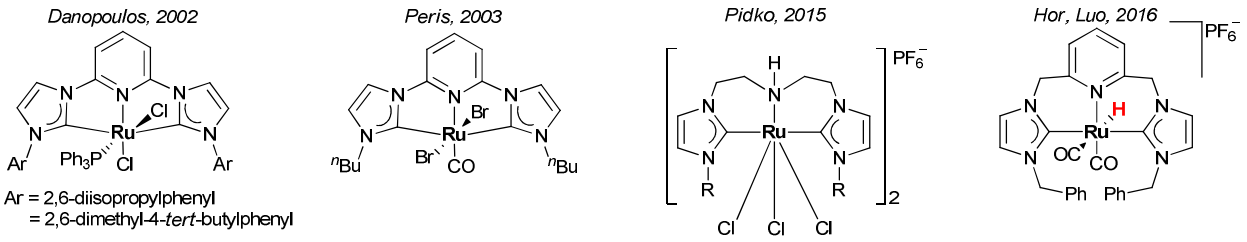

Figure 3.2: Examples of tridentate bis(imidazolylidene) ruthenium(II) complexes featuring a meridional geometry

The group of Kunz synthesized an analogue of the bimca ligand (see chapter 1) in order to coordinate to a ruthenium metal center.[20] The homoallyl derivatized bis(imidazolium)carbazole ligand salt readily

© University of Pretoria

reacted with MeLi generating the lithium carbene adduct, that was subsequently treated with $[Ru(CH_3CN)_3(Cp^*)]PF_6$ (Cp* = pentamethylcyclopentadienyl) (Scheme 3.3). This yielded the Cp*Ru(II) complex with the two carbene carbons and the amido moieties coordinating to the ruthenium center in a tripodal fashion. As such, the complex geometry was reported to exhibit a facial coordination mode around the metal center. ^{13}C NMR analysis confirmed coordination of the carbene carbons (Scheme 3.3). The carbene carbons resonated downfield at $\delta_{Ccarbene}$ 195.3 ppm.[20] It was further reported, after crystal structure analysis, that the ruthenium metal positioned itself as close as possible to the amido nitrogen (Ru-N = 2.062(6) Å) for increased bond overlap. This case study proved that rigid pincer ligands, consisting mostly of sp^2-hybridized atoms, can bend and twist to allow for an unorthodox coordination mode.

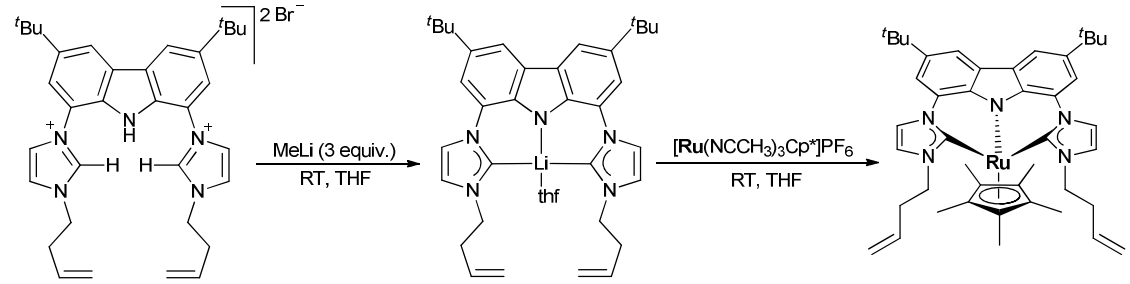

Scheme 3.3: Synthesis of a CNC-pincer ligand acting as a tripodal Cp analogue[20]

3.1.1 Triazolylidene ruthenium(II) complexes

Ruthenium complexes supported by triazolylidene (*trz*) ligands have been documented on a regular basis, since the first reported example of such a complex by Albrecht and co-workers in 2008 (Figure 3.3).[21] In most cases, the documented examples revolve around the stabilization of ruthenium(II) *para*-cymene (*p*-cymene) complexes through coordination of a mono- or bidentate ligand with one coordinating ligand being a triazolylidene carbene moiety. Various groups have reported on the synthesis of triazolylidene supported ruthenium(II) *para*-cymene complexes, with these organometallic species generally being used in a range of catalytic reactions.[22] The laboratory of Albrecht has made significant contributions with respect to (*trz*)Ru(*p*-cymene) complexes and their applications, specifically towards catalysis.[23] Through a compilation of articles, the authors again demonstrated the stabilization imparted by triazolylidene ligands to metals, and in these cases, towards ruthenium species both in a high oxidation state as well as a low oxidation state. Triazolylidene coordination stabilized a low-valent Ru(0) dicarbonyl complex (Figure 3.3).[24] On the other side of the spectrum, triazolylidene coordination

© University of Pretoria

stabilized a ruthenium(II) metal center during the catalyzed water oxidation reaction (Figure 3.3).[25] Contrary to the mono- and bidentate triazolylidene supported ruthenium complexes, the use of tridentate pincer ligands decorated with triazolylidene ligands and their coordination to ruthenium has been underexplored. To the best of our knowledge, only three examples have been reported regarding ruthenium triazolylidene pincer complex formation (*vide infra*).

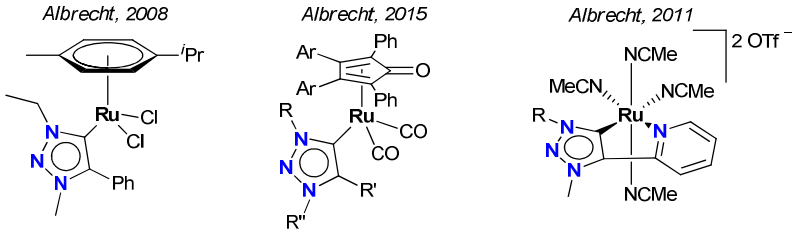

Figure 3.3: Selected examples of triazolylidene supported ruthenium complexes disclosed by Albrecht et al.

The first reported example regarding ruthenium triazolylidene pincer complex formation surfaced in 2011. Bis(triazolylidene)ruthenium(II) complexes for use as photosensitizers and derivatives thereof, were reported by the group of Schubert.[26] The success, and also the shortcomings, of ruthenium(II) polypyridyl complexes with regards to photosensitizing applications prompted the study of bis(*trz*)Ru(II) complexes as possible alternatives to the well-known ruthenium polypyridyl complexes. It was further realized that the stronger σ-donor and weak π-accepting abnormal carbene ligands would lead to a destabilized triplet metal-centered state (^{3}MC), while maintaining or even lowering the energy of the triplet metal-to-ligand charge transfer state (^{3}MLCT). Transmetallation from the dinuclear silver carbene complex with *cis*-[Ru(tpy)(DMSO)Cl_2] (tpy = terpyridine, DMSO = dimethylsulfoxide) yielded the targeted dicationic [(CNC)Ru(tpy)](2BF_4) complex (Scheme 3.4).[26] The complex featured the expected meridional geometry around the metal center, with the carbene carbons resonating in the region of $\delta_{Ccarbene}$ 180 ppm. Both experimental data and theoretical calculations proved that the complex has very promising electrochemical and photophysical properties. This was evident from the reversible redox event and the fact that the triazolylidene ligands raised the energy of the ^{3}MC state by 32 kcal.mol^{-1} above the ^{3}MLCT state.[26] The raised energy of the ^{3}MC state repressed the deactivation pathway (*via* the energetically favourable low-lying ^{3}MC state) allowing for a long-lived excited state lifetime of 633 ns.[26] The same group further demonstrated that by various modifications to the ligand backbone, the excited state lifetime could be increased to the microsecond range (Scheme 3.4).[27] The mesityl wingtip functionalities substituted on the triazolylidene heterocycle were functionalized with either electron donating or electron withdrawing groups. The position *para* to the nitrogen of the tpy ligand was also substituted

© University of Pretoria

with the same functionalities. The presence of these added functionalities, in addition to the triazolylidene ligands, further separated the ^{3}MLCT and ^{3}MC states which increased the long-lived excited states lifetime into the range of 1.7 – 7.9 µs (Scheme 3.4).[27]

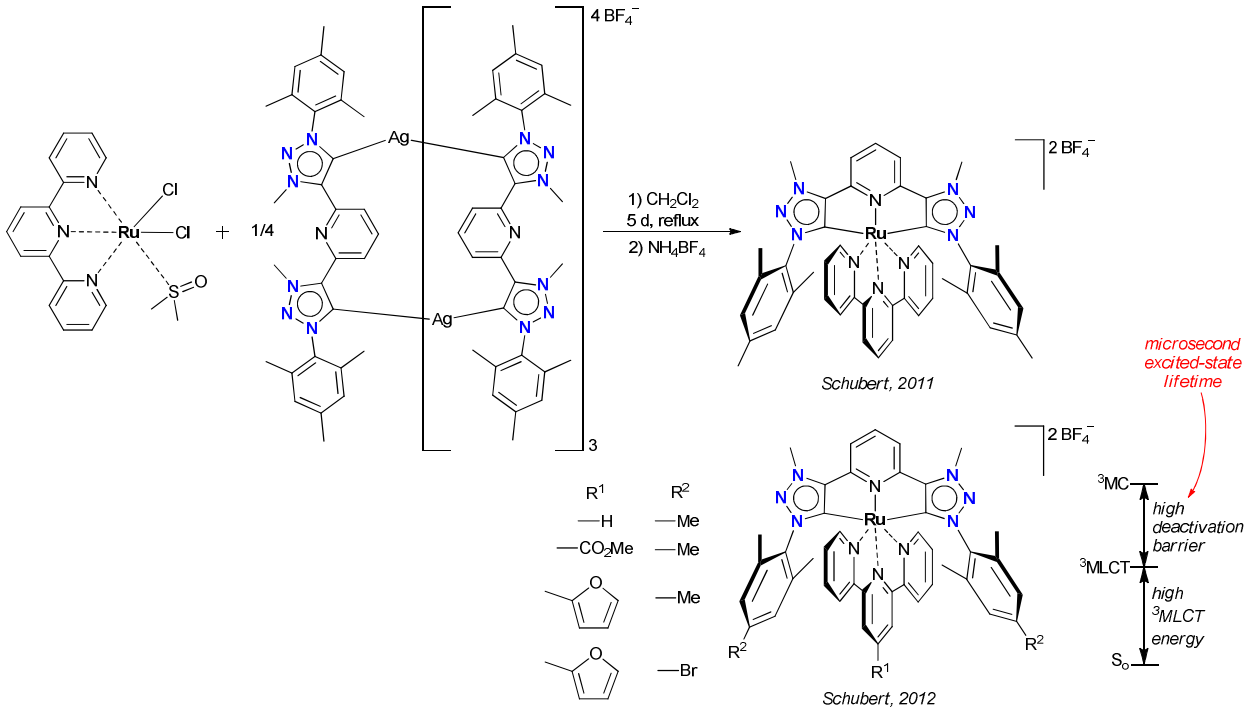

Scheme 3.4: Synthesis of bis(triazolylidene)ruthenium(II) pincer complexes with long-lived excited states[26,27]

Recently, Albrecht and Kühn disclosed on the synthesis of a pincer ligand with different carbene donor moieties coordinated to a ruthenium metal center.[28] The bis(triazole) ligand could readily be obtained through the copper-catalyzed dipolar [2 + 3] cycloaddition reaction of an azide and the corresponding alkyne. This yielded the precursor bis(triazole) functionalized NHC salt (Scheme 3.5). A one-pot silver transmetallation reaction with $[RuCl_2(p\text{-cymene})]_2$ metal precursor employing the triazole ligand yielded the ruthenium chloro complex with the ligand coordinating in a bidentate fashion. Further functionalization of the corresponding product with AgOTf allowed for pincer complex formation, with coordination of the second triazole resulting to a three-legged piano stool complex geometry (Scheme 3.5). In order to obtain a mixed multi-carbene complex, the two triazole substituents first had to be alkylated to yield the precursor bis(triazolium) ligand salt. The isolated tris-cationic precursor salt was then subjected to ruthenium complex formation. This was achieved through a one-pot microwave assisted reaction, whereby ruthenium pincer complex formation was preceded by *in situ* silver metallation, followed by transmetallation with $[RuCl_2(p\text{-cymene})]_2$ (Scheme 3.5). Various

© University of Pretoria

characterization techniques confirmed coordination of all three carbenes in a meridional configuration, with three acetonitrile ligands saturating the octahedral coordination sphere (Scheme 3.5).[28] The triazolylidene carbene carbons resonated upfield at $\delta_{Ccarbene}$ 172.6 ppm compared to the NHC carbene carbon, with a more downfield chemical shift of $\delta_{Ccarbene}$ 185.3 ppm. This is not surprising, as the basic triazolylidene carbene carbons experience greater shielding than classical NHC carbenes. Both complexes were found to be active in the transfer hydrogenation catalyzed reaction, with the tris-carbene complex exhibiting the highest catalytic activity. It was also reported that the tris-carbene complex was more robust than the mono-carbene complex.[28]

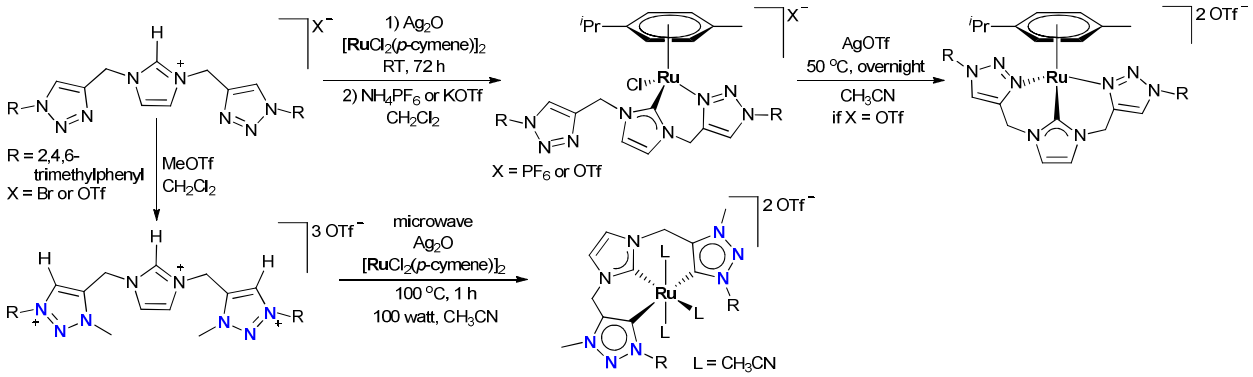

Scheme 3.5: Synthesis of mixed NHC/trz pincer carbene complexes[28]

Recently, van der Vlugt and Elsevier reported on the preparation of bis(triazolylidene)ruthenium(II) complexes, in addition to the ester hydrogenation reaction catalyzed by the aforementioned ruthenium pincer products.[29] Two ligands were employed during the study. Both ligands contained a central coordinating pyridine moiety, two flanking triazole functionalities and a methylene spacer between the triazole and pyridine (Scheme 3.6). Mono- and di-alkylation of the triazole substituents yielded the two ligand precursors, featuring either two triazoliums or a mixture of one triazolium and one triazole substituents. It was reported that deprotonation of the ligand with various bases followed by ruthenium coordination was unsuccessful. Fortunately, transmetallation with $[Ru(CO)(H)(Cl)(PPh_3)_3]$ from the corresponding pre-prepared silver complexes allowed for the isolation of the mono- and bis-carbene ruthenium(II) complexes (Scheme 3.6). Both complexes featured facial geometries and not the expected meridional coordination mode. The ruthenium-carbene carbons were reported to resonate at $\delta_{Ccarbene}$ 172.2 and 164.9 ppm for the bis-carbene product and at $\delta_{Ccarbene}$ 166.0 ppm for the mono-carbene complex.[29] The hydride signals resonated at δ_H –7.04 and –13.0 ppm, for the bis- and mono-carbene complexes, respectively. It was further demonstrated that deprotonation with KO^{t}Bu resulted in

© University of Pretoria

dearomatization of the pyridine backbone. This process was reversible, as the addition of HCl protonated the complex and rearomatization of the pyridine backbone ensued. The hydrogenation of esters was catalyzed by both complexes, with good catalytic activity achievable only after the addition of 20 mol % KO^{t}Bu. A mechanism for the catalyzed reaction was not proposed, due to the reported complexity of the reaction brought on specifically by the base. It was noted that the base participates in a number of reactions during catalysis, such as deprotonation of the ligand, trans-esterification reactions, induced metal-ligand cooperativity as well as possibly enhancing product expulsion from the catalyst.[29]

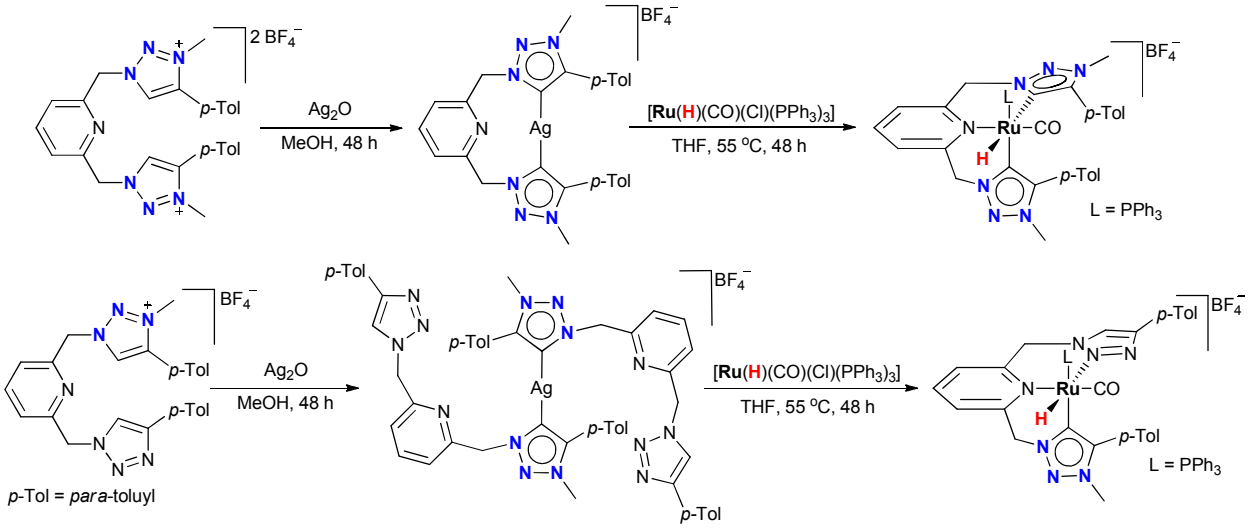

Scheme 3.6: Synthetic protocol towards *fac*-[(CNC)Ru(H)(CO)(PPh_3)]BF_4 and *fac*-[(CNN)Ru(H)(CO)(PPh_3)]BF_4[29]

3.1.2 General consideration of the transfer hydrogenation reaction

The transfer hydrogenation (TH) reaction is an extremely well-known method towards the reduction of organic compounds, with the first report by Knoevenagel dating back more than a century ago.[30] It involves the addition of a hydrogen atom from a non-H_2 source, to an organic molecule containing unsaturated bond/s.[31] It is a powerful and attractive alternative to the direct hydrogenation reaction with hydrogen gas, mainly because *i*) the catalyst involved is readily accessible and not sensitive towards atmospheric conditions, *ii*) the sacrificial H-donors are inexpensive, easy to handle and readily available, *iii*) the large quantities of by-products are readily recyclable and *iv*) the use of hazardous, hydrogen pressurized systems as well as the requirement for more advanced synthetic techniques, are not

© University of Pretoria

necessary. These attributes have given rise to the TH reaction finding industrial applications during the large scale production of various organic products, ranging from fine chemicals to pharmaceuticals.[31]

A range of catalyst has been developed to catalyze the TH reaction following different mechanisms.[31,32] This resulted to a range of mechanistic considerations disclosed to date. As such, only a few important and relevant examples are given (*vide infra*). One of the most well-known and most frequently encountered TH reaction mechanism is the inner-sphere monohydride reaction mechanism.[31,32,33] The first step is formation of the active catalyst, through deprotonation of the sacrificial H-donor leading to metal-alkoxide formation after X-ligand substitution (Scheme 3.7). Hydrogen transfer from the alkoxide to the metal yields the metal-hydride-intermediate, with dissociation of the carbonyl product. The incoming substrate coordinates to the metal, which is followed by metal-hydride insertion. The final step involves protonation of the metal-alkoxide intermediate by the sacrificial hydrogen donor to regenerate the active catalyst and yield the targeted product. A relevant mechanism of the TH reaction with *iso*-propanol as sacrificial H-donor is illustrated (Scheme 3.7). The inner-sphere dihydride reaction mechanism is another frequently encountered mechanism, and involves the formation of a metal dihydride as the active catalytic intermediate. The dihydride reacts with the incoming substrate, yielding the metal-alkoxide-hydride species with subsequent reductive elimination releasing the targeted product. The metal-alkoxide-hydride complex is re-formed by oxidative addition of the sacrificial H-donor molecule. β-hydride elimination ensues to re-generate the active dihydride catalyst (Scheme 3.7).

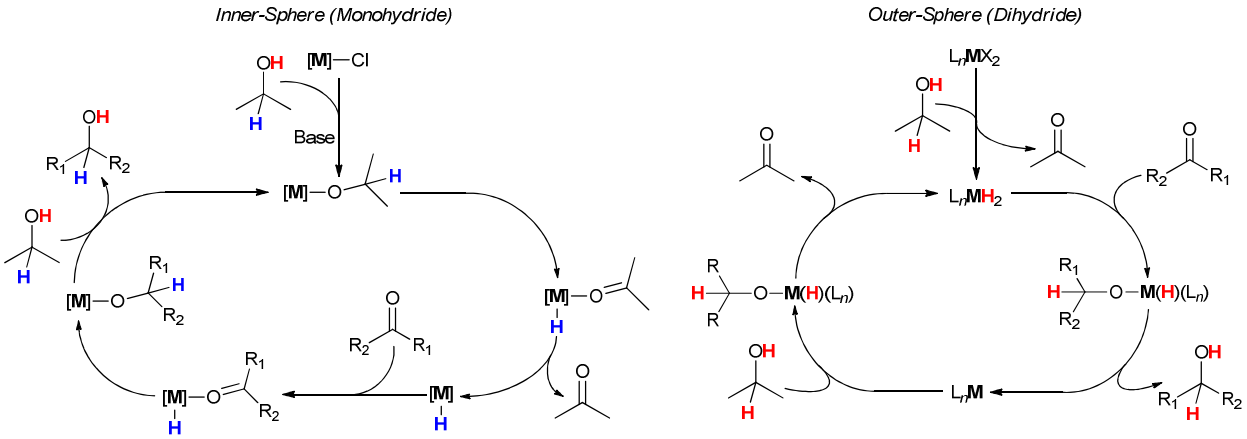

Scheme 3.7: Inner-sphere mono- and outer-sphere-dihydride mechanistic consideration for TH reactions[31,32,33]

Noyori's catalyst[34] is another exceptional hydrogenation catalyst and functions *via* a bifunctional mechanism.[35] Ligand cooperativity plays an important role in this mechanistic consideration, similar to the examples of Milstein and Gusev described above. Deprotonation and halide abstraction yields the

© University of Pretoria

active 16-electron catalyst (Scheme 3.8). Both hydrogen atoms from the sacrificial H-donor molecule are transferred to the catalyst in one step. This results in formation of the 18-electron metal-hydride intermediate, in turn transferring both hydrogen atoms to the incoming unsaturated substrate. This regenerates the active catalyst and yields the organic product that has been reduced (Scheme 3.8).[35]

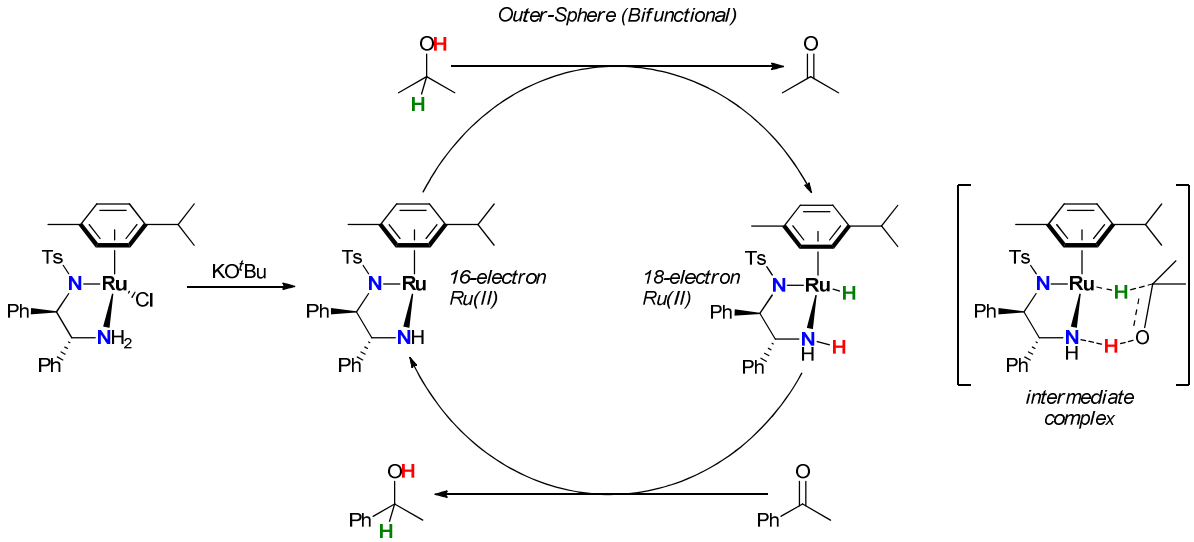

Scheme 3.8: TH reaction catalyzed by Noyori's bifunctional catalyst[35]

3.2 Aim

The success of ruthenium complexes in catalysis prompted us to investigate the possibility of preparing CNC-supported Ru(II) complexes. Successful coordination of the strongly donating pincer ligand could lead to a ruthenium complex with increased electron density located on the metal center. The catalytic activity of the more basic ruthenium complex can then be screened against hydrogenation reactions. As was noted in the preceding section, the tridentate ligands substituted with triazolylidene moieties yielded pincer ruthenium complexes active in the transfer hydrogenation and ester hydrogenation catalyzed reactions. The complexes also exhibited a high degree of stability, which can mainly be attributed to the coordination of a tridentate pincer ligand.

It can also be postulated that, once coordinated, the CNC-pincer ligand from precursor $\mathbf{L_b}$ could act as a non-innocent ligand during catalysis. The basic amido moiety next to the ruthenium metal center, could exhibit bifunctional character during a catalytic run. To be more specific, the amido moiety could coordinate the incoming substrate during catalysis, weakening bonds and lowering the energy of the substrate activation barrier, as was the case for Gusev's catalyst (*vide supra*). Alternatively, the basic

© University of Pretoria

amido moiety could assist in substrate coordination followed by deprotonation of the acidic proton during a hydrogenation catalyzed reaction, similar to Noyori's bifunctional catalyst. Another mechanistic scenario that has to be considered is a hydrogenation catalyzed reaction following the classical inner-sphere reaction pathway. This would involve metal-alkoxide formation through halide substitution, requiring the addition of base.

3.3 Results and Discussion

3.3.1 Synthesis of CNC-ruthenium(II) chlorido complex

A procedure reported by Peris and co-workers[17] was adapted towards the synthesis of **13$_b$**. The dicationic bis(triazolium)carbazole ligand salt **L$_b$** was therefore reacted with (bicyclo[2.2.1]hepta-2,5-diene)dichlororuthenium(II) polymer ([RuCl$_2$(nbd)]$_n$, nbd = norbornadiene) and Et$_3$N in EtOH, at 95 °C for 5 days in the absence of light (Scheme 3.9). Multiple filtrations and extractions allowed for the isolation of the complex **13$_b$** with high purity, albeit low yields (14%), similar to the previous report.[17] To our surprise, the dicarbonyl product was isolated, instead of the mono-carbonyl complex as was previously reported for a tridentate CNC-pincer carbene ligand.[17] The stronger donor anionic ligand could favour the formation of the dicarbonyl complex, due to a metal center with a higher nucleophilic character. A transmetallation reaction from the corresponding silver(I) precursor, as reported for the Ru-bis(triazolium)-pyridine/lutidine pincer complexes (see Section 3.1.1), was not required.

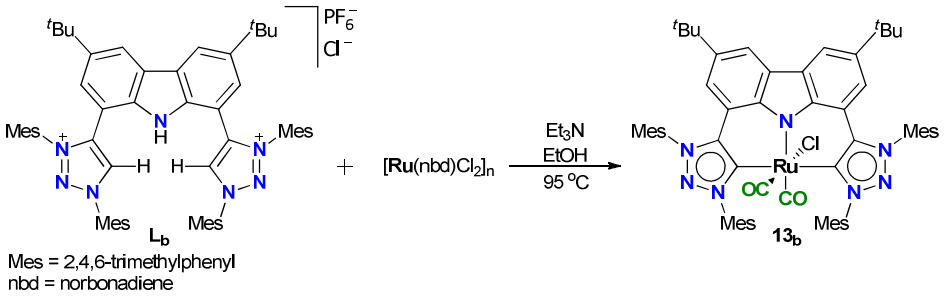

Scheme 3.9: Synthetic protocol towards [(CNC)Ru(CO)$_2$Cl]

NMR spectroscopic characterization confirmed successful complexation. Proton NMR (Figure 3.4) analysis revealed complete disappearance of all three **L$_b$** acidic protons (two triazolium CH and one carbazole NH protons). The carbene carbon resonance was detected at $\delta_{Ccarbene}$ 165.2 ppm in the carbon NMR spectra, with two additional signals resonating further downfield at δ_{CO} 196.0 ppm and δ_{CO} 198.7

© University of Pretoria

ppm, corresponding to the two carbonyl carbons (Figure 3.5). The carbene carbon resonance is upfield but still falls within the range of other reported triazolylidene carbene carbon resonance ($\delta_{Ccarbene}$ 161 to 185 ppm) (see Section 3.1.1). The strongly donating ligand and the overall neutral charge of the complex increases the shielding experienced by the carbene carbons. This results in the observed upfield NMR shift of **13_b** compared to the other Ru-trz complexes. The same reasoning can be applied to the observed upfield resonance of the carbonyl carbons, while their stretching frequencies were detected at 2028 cm^{-1} and 1957 cm^{-1} in the FT-IR spectrum.

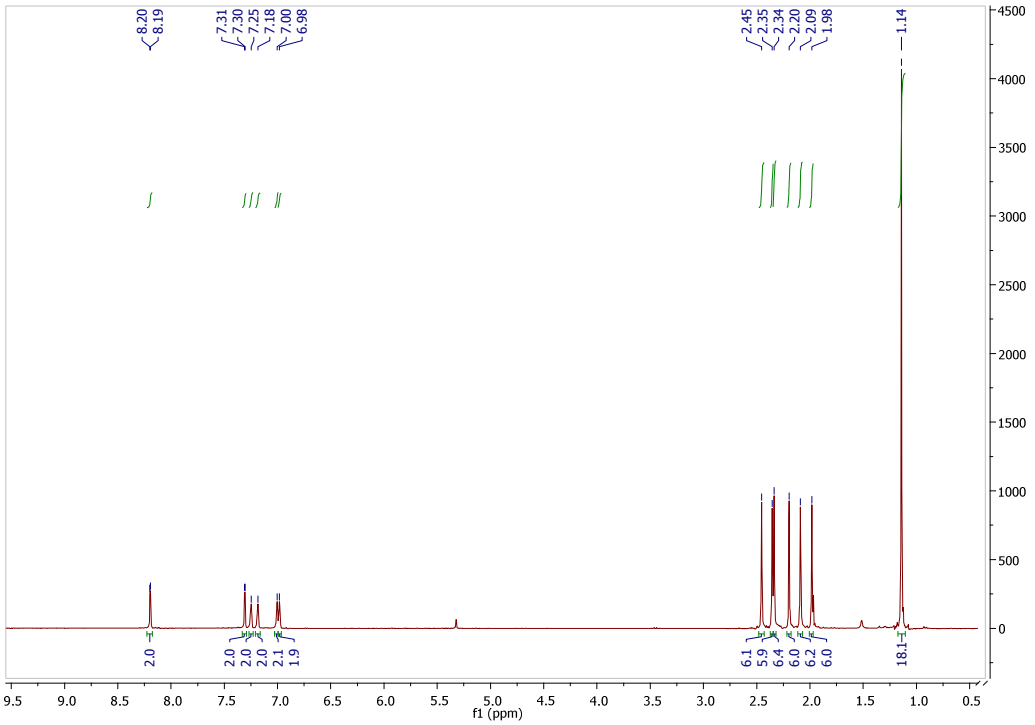

Figure 3.4: ^{1}H NMR spectrum of **13_b** in CD_2Cl_2

© University of Pretoria

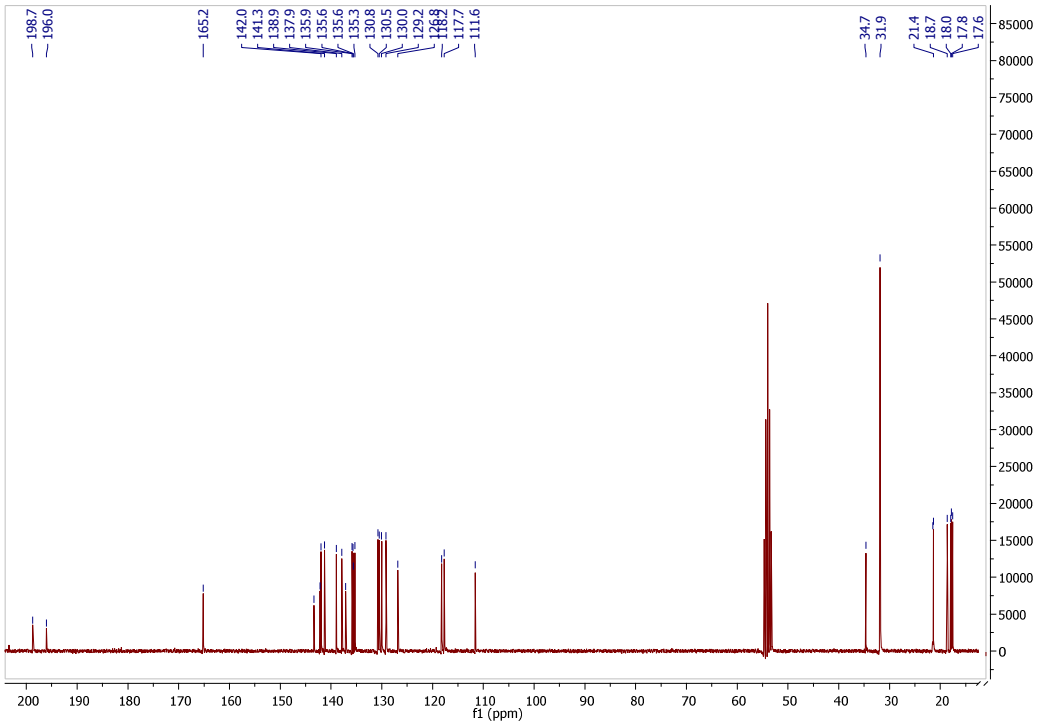

Figure 3.5: ^{13}C NMR spectrum of **13$_b$** in CD_2Cl_2

The molecular structure revealed a slightly distorted octahedral geometry for **13$_b$** (Figure 3.6). The complex further exhibits a meridional geometry similar to previous reported complex structures (see Section 3.1). The increased steric crowding around the ruthenium metal center of **13$_b$** can account for the increased bond lengths and a C(1)-Ru(1)-C(3) bond angle (169.4(8)°) deviating from ideal 180°. The Ru-$C_{Carbene}$ bond lengths of 2.132(2) and 2.119(2) Å for the Ru(1)-C(1) and Ru(3)-C(3) bonds of **13$_b$**, respectively, are longer compared to the Ru-NHC/trz pincer complexes (Ru-$C_{Carbene}$ = 1.97 – 2.09 Å) discussed in Section 3.1. Not surprising is the coordination position of the two carbonyl ligands, being *cis* with respect to each other and *trans* to the chlorido and amido moieties, respectively.

© University of Pretoria

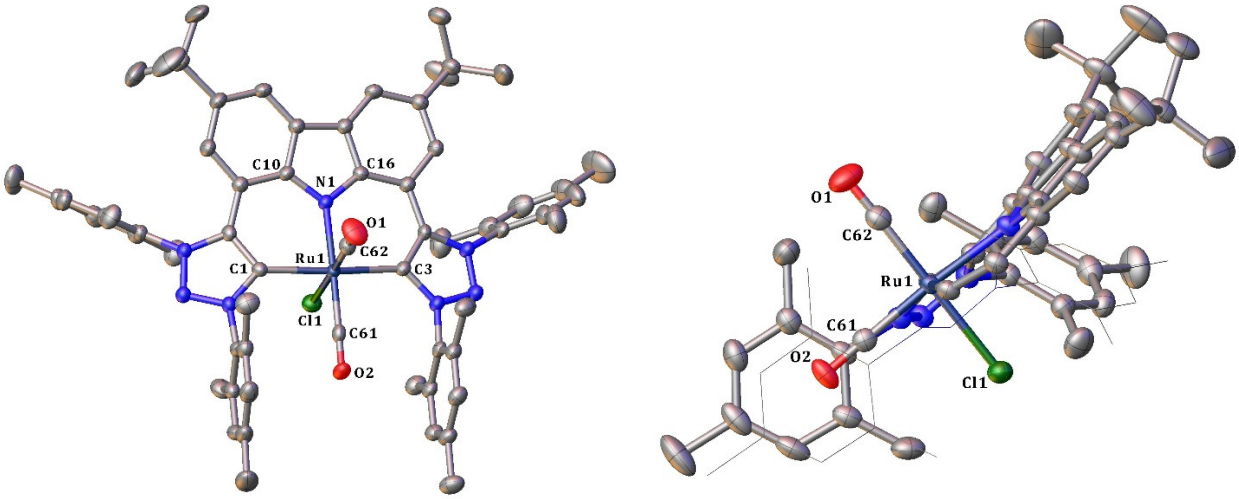

Figure 3.6: Crystal structure of **13$_b$** (Frontal and side-on views). Hydrogens and solvent molecules omitted for clarity.

Next, we investigated the hydrogenation reactions catalyzed by **13$_b$**. The catalytic ester hydrogenation of methyl benzoate with hydrogen gas catalyzed by **13$_b$** was first attempted. Unfortunately, the complex was found to be inactive in the hydrogenation catalyzed reaction, even with a catalyst loading of 5 mol %, hydrogen pressure of 20 bar and at 90 °C for 14 hours. Exploration of the transfer hydrogenation reaction ensued. The TH of acetophenone to 1-phenylethanol with *iso*-propanol as sacrificial hydrogen donor was chosen as the model reaction for optimization of the reaction conditions. The base, substrate:base:catalyst ratio, temperature and reaction time were all altered during the catalyst screening. Entry 6 in Table 3.1 indicates the optimal reaction conditions for the transfer hydrogenation reaction catalyzed by **13$_b$**. It was found that **13$_b$** did not catalyze the reaction of 4-bromoacetophenone, with the conversion a result of a base catalyzed reaction only. Steric factors were dismissed as the cause of the low catalytic activity. Rather, the complete octahedral coordination sphere of the catalyst with a chlorido and two carbonyl ligands and the absence of reactive hydride ligands can be ascribed to the low catalytic activity. This could, in all probability, point towards an inner-sphere catalytic mechanism

© University of Pretoria

Table 3.1: Optimization of transfer hydrogenation reaction conditions

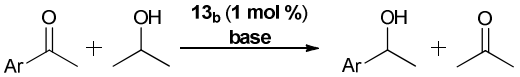

Entry	Base	Substrate	S/B/C[a]	Temperature (°C)	Time (h)	Conversion [b] (%)
1	^{t}BuOK	Acetophenone	100/20/1	80	14	50 [0]
2	^{t}BuOK	Acetophenone	100/20/1	80	86	99 [10]
3	Cs_2CO_3	Acetophenone	100/100/1	95	14	99 [50]
4	Cs_2CO_3	Acetophenone	100/20/1	80	14	75 [0]
5	Cs_2CO_3	Acetophenone	100/20/1	80	86	100 [5]
6	Cs_2CO_3	Acetophenone	100/10/1	95	14	95 [5]
7	Cs_2CO_3	Acetophenone	100/5/1	95	14	60 [0]
8	Cs_2CO_3	4-Bromoacetophenone	100/5/1	95	14	20 [20]

[a]S/B/C = ratio of substrate : base : catalyst **13b**. [b]% Conversion mediated by base, as determined from blank experiments.

3.3.2 Synthesis of CNC-ruthenium(II) hydride complexes

Changing the ruthenium metal precursor and the synthetic protocol, allowed for the synthesis and isolation of the Ru(II)-H complex **14b**. Deprotonation of all three **Lb** acidic protons with KHMDS in the presence of [Ru(H)(Cl)(CO)($AsPh_3$)$_3$] lead to the formation of the intermediate ruthenium hydride complex (Scheme 3.10). The intermediate triphenylarsine coordinated complex **14b** was always accompanied with excess $AsPh_3$ and all further purification attempts were unsuccessful. To solve this problem, the polarity of the complex had to be changed as both the intermediate complex and triphenylarsine exhibited similar solubility properties. As such, treatment of **14b** with CO (g) in Et_2O yielded the dicarbonyl ruthenium(II) hydride complex (Scheme 3.10). The complex **15b** was obtained, after work-up, with high purity albeit low yield (overall yield from triazolium precursor salt 17%).

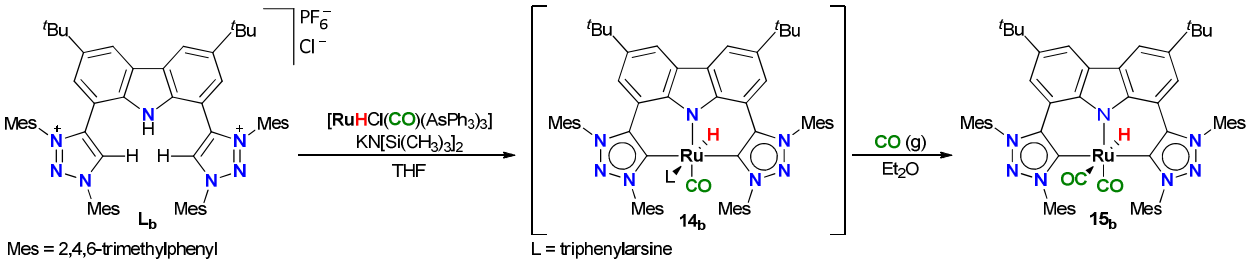

Scheme 3.10: Synthesis of [(CNC)Ru(CO)$_2$H] **15b** through intermediate **14b**

© University of Pretoria

Even though we could not isolate the intermediate complex, it was still characterized with NMR spectroscopy. Figure 3.7 depicts both the ^{1}H, as well as the ^{13}C NMR spectra (insert displaying the aromatic region of the ^{13}C NMR spectra) of the [(CNC)Ru(H)(CO)($AsPh_3$)] complex with accompanying excess triphenylarsine. The hydride signal of **14b** resonates at δ_H -8.82 ppm, while the carbene and carbonyl carbons feature a downfield chemical shift compared to the ruthenium chloride complex **13b** ($\delta_{Carbene}$ = 178.8 ppm and δ_{CO} = 205.9 ppm for **14b**, respectively). The NMR spectral data describes the metal center of **14b** having a higher nucleophilic character compared to **13b**. This is not surprising, as the presence of two π-accepting carbonyl ligands decreases the electron density located on the metal center. Figures 3.8 and 3.9 represent the proton and carbon NMR spectra of ruthenium dicarbonyl complex **15b**, respectively. The hydride resonance has shifted downfield, from δ_H -8.82 ppm for the intermediate complex hydride to δ_H -3.83 ppm for the dicarbonyl ruthenium(II) hydride (Figure 3.8). Figure 3.9 confirms that both the carbene and two carbonyl carbons also resonate upfield compared to the intermediate complex **14b**, as could be expected ($\delta_{Carbene}$ = 170.6 ppm and δ_{CO} = 196.4 and 201.3 ppm, respectively). FT-IR analysis of **15b** further supported [(CNC)Ru$(CO)_2$H] complex formation. The hydride band vibrates at higher wavenumbers (2040 cm^{-1}), but this high energy vibration is not unprecedented in literature.[10] The strong σ-donating hydride ligand induced a lower carbonyl stretching frequency for **15b** (ν_{CO} = 2008, 1944 cm^{-1}) compared to **13b**.

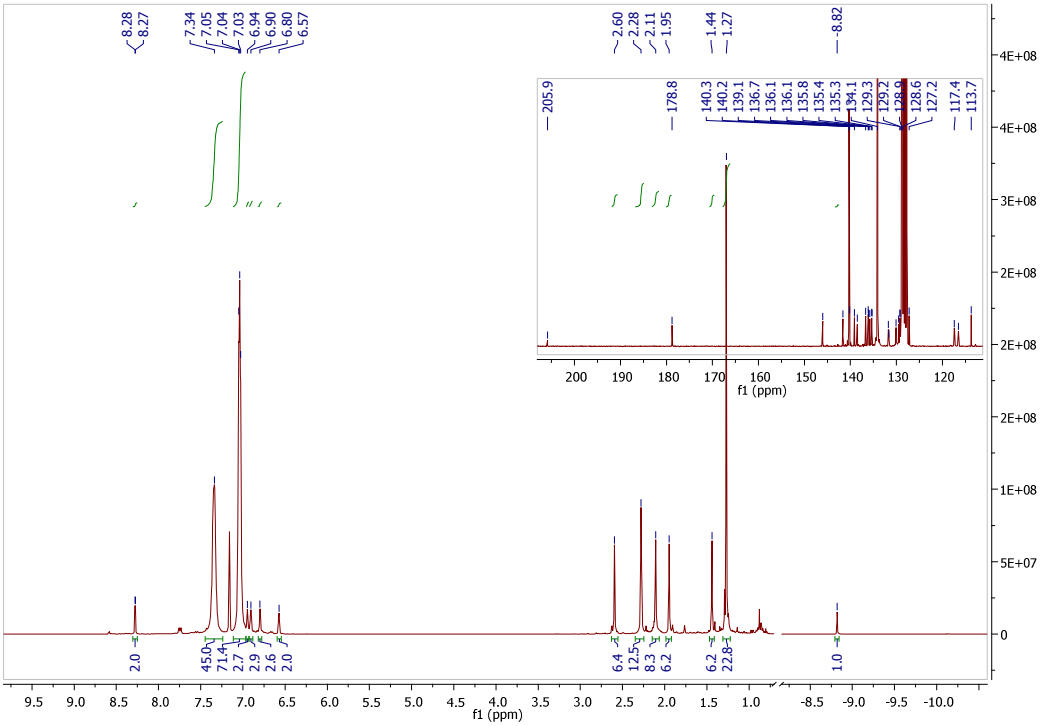

Figure 3.7: ^{1}H and ^{13}C (insert of aromatic region) NMR spectra of **14b** in C_6D_6

© University of Pretoria

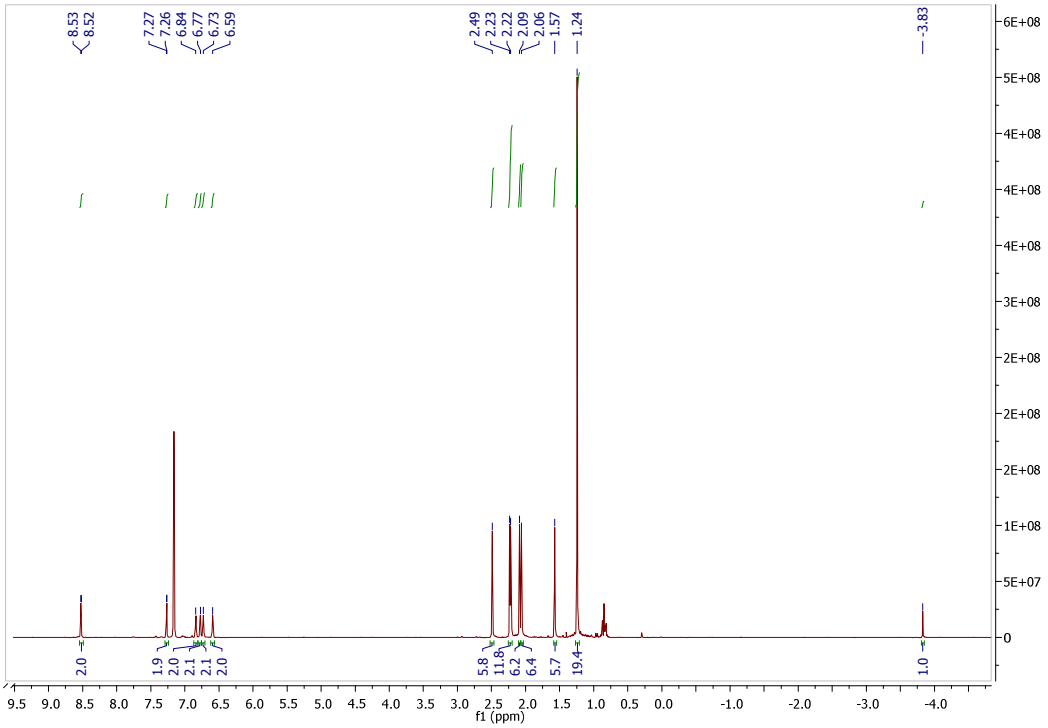

Figure 3.8: ^{1}H NMR spectrum of **15b** in C_6D_6

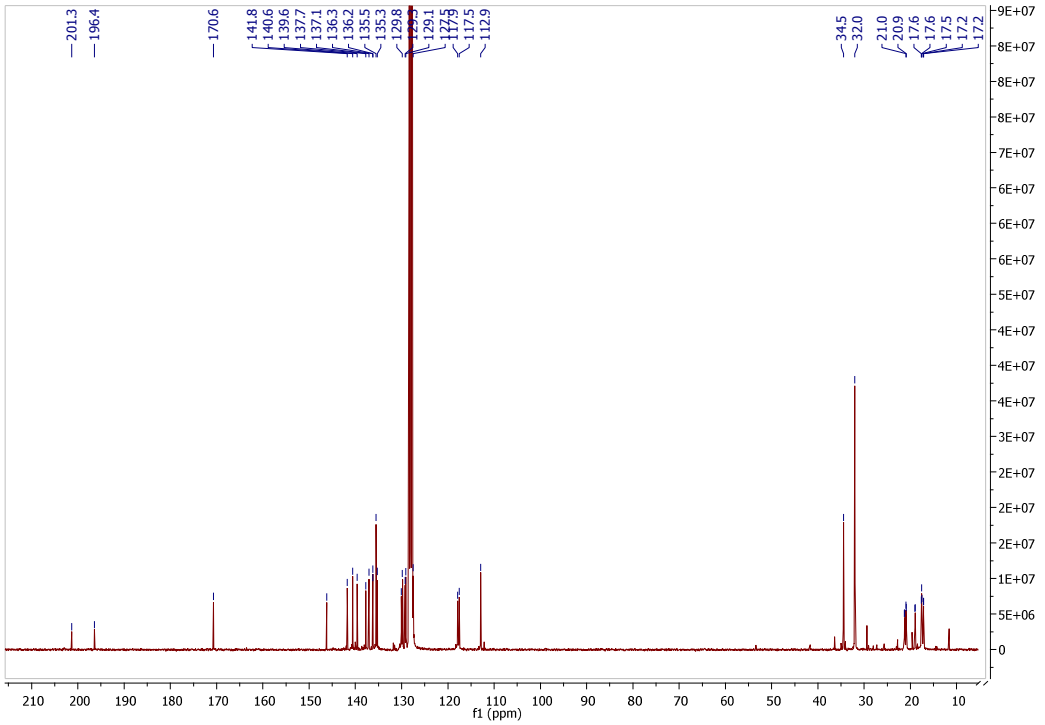

Figure 3.9: ^{13}C NMR spectrum of **15b** in C_6D_6

© University of Pretoria

3.4 Conclusion

Disclosed in this chapter is the synthesis of novel ruthenium(II) pincer complexes, coordinated by a bis(1,2,3-triazol-5-ylidene)carbazolide ligand. The use of a silver complex intermediate as a transmetallating agent is circumvented during the preparation of the novel complexes **13$_b$** - **15$_b$**, contrasting to the synthetic methodology towards the various triazolylidene supported ruthenium complexes discussed in Section 3.1.1. The isolated complexes exhibit a high degree of stability, as can be expected.

For complex **13$_b$**, the ancillary ligands constitute a chlorido in addition to two carbonyl ligands. The rigidity of the central carbazole moiety, together with the presence of bulky mesityl substituents at the triazolylidene rings, enforce a meridional geometry of the CNC pincer ligand. This finding contrasts with the recent example reported by Kunz and co-workers (see Section 3.1), in which a related CNC-bis(NHC) ligand with a carbazole scaffold forced a facial CNC conformation. In our case, the steric bulk produced by the mesityl fragments may disfavour coordination in the tripodal (*fac*) form. The complex constitutes the first example of a CNC-pincer complex of ruthenium where the central N-donor coordinates as a monoanionic X-type ligand flanked by 1,2,3-triazol-5-ylidene moieties.

The hydrido-analogue **15$_b$**, featuring two carbonyl ancillary ligands in addition to the CNC-pincer ligand, was accessed through *in situ* deprotonation of the ligand precursor with KHMDS, followed by metallation with a ruthenium(II) carbonyl hydrido precursor. The intermediate complex **14$_b$** was accompanied with excess triphenylarsine, and was characterized by NMR spectroscopy. Treatment of the intermediate ruthenium(II)-hydride complex with carbon monoxide afforded the [(CNC)RuH(CO)$_2$] product **15$_b$**.

The catalytic activity of the dicarbonyl chlorido Ru(II) pincer complex **13$_b$** in both the hydrogenation of methyl benzoate with hydrogen, as well as the transfer hydrogenation of ketones to alcohols, was investigated. Ester hydrogenation to primary alcohols was not catalyzed by **13$_b$**. Also, the transfer hydrogenation catalyzed reaction did not yield satisfactory results. This could be due to the difficulty for carbonyl dissociation, as well as the lack of reactive ancillary ligands. The possibility of these complexes as catalysts in other model organic transformations, including amination reactions, could be investigated, while the analogous hydrido complex **15$_b$** could be subjected to screening for activity in the TH reaction.

© University of Pretoria

3.5 Experimental

3.5.1 Synthesis of [(CNC$_{Mes}$)Ru(II)(CO)$_2$Cl] (13$_b$)

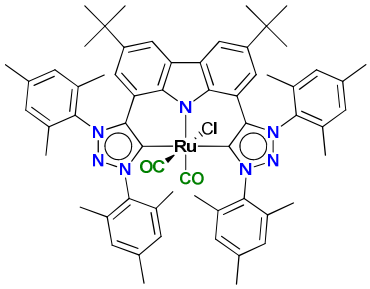

A Schlenk tube was loaded with **L$_b$** (1.00 g, 9.4 x 10^{-4} mol) and (bicyclo[2.2.1]hepta-2,5-diene)dichlororuthenium(II) polymer (352.9 mg, 1.4 x 10^{-3} mol). The tube was evacuated and purged with N_2 (g), with subsequent addition of degassed ethanol (60 mL). Degassed Et_3N (1.56 mL, 1.1 x 10 $^{-2}$ mol) was added to the mixture. The reaction mixture was then heated up and refluxed at 95 °C for 5 days in the absence of light. The solvent was evaporated under reduced pressure. The product was extracted with Et_2O (3 x 30 mL), and the solvent removed *in vacuo* to obtain a dark yellow solid. The solid was first washed with hexanes (5 x 30 mL), followed by CH_3CN (10 mL) and finally dried under reduced pressure to yield 145.0 mg of **13$_b$** (1.3 x 10^{-4} mol, yield 14%) as a yellow solid. Crystals suitable for XRD analysis was obtained through slow evaporation of a DCM solution of **13$_b$**. **^{1}H NMR** δ_H (CD_2Cl_2, 300 MHz) 8.20 (d, *J* = 2.1 Hz, 2H, Ar**H**$_{carb}$), 7.31 (d, *J* = 1.8 Hz, 2H, Ar**H**$_{carb}$), 7.25 (s, 2H, Ar**H**$_{Mes}$), 7.18 (s, 2H, Ar**H**$_{Mes}$), 7.00 (s, 2H, Ar**H**$_{Mes}$), 6.98 (s, 2H, Ar**H**$_{Mes}$), 2.45 (s, 6H, ArC**H**$_3$), 2.35 (s, 6H, ArC**H**$_3$), 2.34 (s, 6H, ArC**H**$_3$), 2.20 (s, 6H, ArC**H**$_3$), 2.09 (s, 6H, ArC**H**$_3$), 1.98 (s, 6H, ArC**H**$_3$), 1.14 (s, 18H, C(C**H**$_3$)$_3$). **^{13}C NMR** δ_C (CD_2Cl_2, 75 MHz) 198.7 (Ru**C**O), 196.0 (Ru**C**O), 165.2 (**C**$_{Carbene}$), 143.4, 142.2, 142.0, 141.3, 138.9, 137.9, 137.1, 135.9, 135.6, 135.6, 135.3, 130.8, 130.5, 130.0, 129.2, 126.8, 118.2, 117.7, 111.6, 34.7 (**C**(CH$_3$)$_3$), 31.9 (**C**(CH$_3$)$_3$), 21.5 (Ar**C**H$_3$), 21.4 (Ar**C**H$_3$), 18.7 (Ar**C**H$_3$), 18.0 (Ar**C**H$_3$), 17.8 (Ar**C**H$_3$), 17.6 (Ar**C**H$_3$). **FTIR** (KBr): 2028 cm^{-1} (υ**CO**), 1957 cm^{-1} (υ**CO**). **HRMS** (ESI-TOF): Calculated for $C_{62}H_{66}N_7O_2Ru^+$ [M]$^+$: 1042.4321, found: 1042.4343. **Elemental analysis calc. (%) for** $C_{62}H_{66}N_7O_2RuCl$: C 69.1, H 6.1, N 9.1; found: C 68.3, H 6.0, N 8.6.

3.5.2 Synthesis of intermediate [(CNC$_{Mes}$)Ru(II)(AsPh$_3$)(CO)H] (14$_b$)

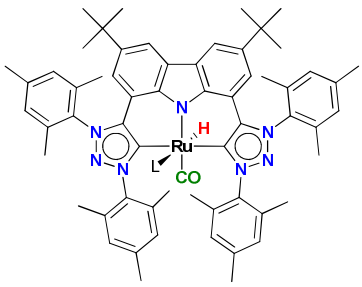

L = triphenylarsine

A Schlenk tube was charged with **L$_b$** (400.0 mg, 3.7 x 10^{-4} mol), [RuCl(H)(AsPh$_3$)$_3$(CO)] (487.0 mg, 4.5 x 10^{-4} mol) and KN[Si(CH$_3$)$_3$]$_2$ (373.3 mg, 1.9 x 10^{-3} mol) under a N_2 (g) atmosphere. The solids were cooled down to -78 °C, before the addition of THF (25 mL), which had also been cooled down to -78 °C. The mixture was stirred at -78 °C for one hour, before it was allowed to gradually warm up to room temperature whilst

© University of Pretoria

stirring the solution overnight in the absence of light. The solvent was evaporated *in vacuo* and compound **14_b** was extracted with hexanes (4 x 30 mL). The solvent was evaporated under reduced pressure to yield a red residue, which was characterized by NMR spectroscopy as being complex **14_b** accompanied by a residual amount of $AsPh_3$. **^{1}H NMR** δ_H (C_6D_6, 300 MHz) 8.28 (d, *J* = 1.8 Hz, 2H, Ar**H**$_{carb}$), 7.34 (br s, 45H, As(C_6**H**$_5$)$_3$), 7.05 - 7.03 (m, 15H, As(C_6**H**$_5$)$_3$, overlapping with uncoordinated $AsPh_3$), 6.94 (s, 2H, Ar**H**$_{Mes}$), 6.90 (s, 2H, Ar**H**$_{Mes}$), 6.80 (s, 2H, Ar**H**$_{Mes}$), 6.57 (s, 2H, Ar**H**$_{Mes}$), 2.60 (s, 6H, ArC**H**$_3$), 2.28 (s, 12H, ArC**H**$_3$), 2.11 (s, 6H, ArC**H**$_3$), 1.95 (s, 6H, ArC**H**$_3$), 1.44 (s, 6H, ArC**H**$_3$), 1.27 (s, 18H, C(C**H**$_3$)$_3$), -8.82 (s, 1H, Ru**H**). **^{13}C NMR** δ_C (C_6D_6, 75 MHz) 205.9 (Ru**C**O), 178.8 (**C**$_{Carbene}$), 146.0, 141.6, 140.3 (As(**C**$_6$H$_5$)$_3$), 140.2, 139.1, 138.5, 136.7, 136.1, 136.1, 135.8, 135.4, 135.3, 134.1 (As(**C**$_6$H$_5$)$_3$), 131.8, 131.6, 130.1, 129.5, 129.3, 129.2, 128.9 (As(**C**$_6$H$_5$)$_3$), 128.6 (As(**C**$_6$H$_5$)$_3$), 127.2, 117.4, 116.5, 113.7, 34.4 (**C**(CH$_3$)$_3$), 32.1 (C(**C**H$_3$)$_3$), 21.5 (Ar**C**H$_3$), 21.5 (Ar**C**H$_3$), 21.1 (Ar**C**H$_3$), 21.0 (Ar**C**H$_3$), 19.4 (Ar**C**H$_3$), 18.2 (Ar**C**H$_3$), 18.1 (Ar**C**H$_3$), 18.0 (Ar**C**H$_3$), 18.0 (Ar**C**H$_3$), 17.2 (Ar**C**H$_3$).

3.5.3 Synthesis of [(CNC$_{Mes}$)Ru(II)(CO)$_2$H] (15_b)

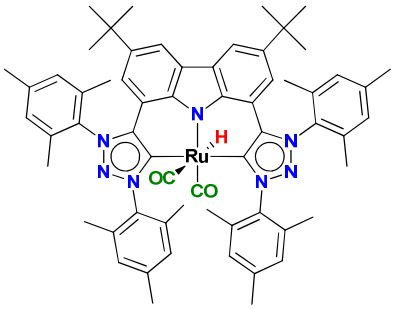

The red residue obtained from the reaction to prepare **14_b**, was dissolved in diethyl ether at room temperature. In the absence of light, CO (g) was bubbled through the red solution for 10 min. The vessel was sealed, and the reaction stirred overnight, at which point a slight colour change occurred from red to orange-brown. The reaction was left to settle, and the solution filtered off from the precipitate. The solvent was evaporated *in vacuo*, and the residue was washed with hexanes (4 x 20 mL). The solid was dried under reduced pressure, to yield **15_b** (68.0 mg, 6.5 x 10^{-5} mol, overall yield 17%) as a yellow brown solid. **^{1}H NMR** δ_H (C_6D_6, 300 MHz) 8.52 (d, *J* = 1.8 Hz, 2H, Ar**H**$_{carb}$), 7.27 (d, *J* = 2.1 Hz, 2H, Ar**H**$_{carb}$), 6.84 (s, 2H, Ar**H**$_{Mes}$), 6.77 (s, 2H, Ar**H**$_{Mes}$), 6.73 (s, 2H, Ar**H**$_{Mes}$), 6.59 (s, 2H, Ar**H**$_{Mes}$), 2.49 (s, 6H, ArC**H**$_3$), 2.23 (s, 6H, ArC**H**$_3$), 2.22 (s, 6H, ArC**H**$_3$), 2.09 (s, 6H, ArC**H**$_3$), 2.06 (s, 6H, ArC**H**$_3$), 1.57 (s, 6H, ArC**H**$_3$), 1.24 (s, 18H, C(C**H**$_3$)$_3$), -3.83 (s, 1H, Ru**H**). **^{13}C NMR** δ_C (C_6D_6, 75 MHz) 201.3 (Ru**C**O), 196.4 (Ru**C**O), 170.6 (**C**$_{Carbene}$), 146.2, 141.8, 140.6, 139.6, 137.7, 137.1, 136.3, 136.2, 135.5, 135.3, 130.1, 129.8, 129.3, 129.1, 127.5, 117.9, 117.5, 112.9, 34.5 (**C**(CH$_3$)$_3$), 32.0 (C(**C**H$_3$)$_3$), 21.3 (Ar**C**H$_3$), 21.3 (Ar**C**H$_3$), 21.0 (Ar**C**H$_3$), 20.9 (Ar**C**H$_3$), 19.0 (Ar**C**H$_3$), 19.0 (Ar**C**H$_3$), 17.6 (Ar**C**H$_3$), 17.6 (Ar**C**H$_3$), 17.5 (Ar**C**H$_3$), 17.2 (Ar**C**H$_3$), 17.2 (Ar**C**H$_3$). **FTIR** (CH_2Cl_2): 2040 cm^{-1} (υ-Ru**H**), 2008 cm^{-1} (υ-**CO**), 1944 cm^{-1} (υ-**CO**). **HRMS** (ESI-TOF):

© University of Pretoria

Calculated for $C_{62}H_{66}N_7O_2Ru^+$ $[M-H]^+$: 1042.4321, found: 1042.4374, and calculated for $C_{62}H_{67}N_7O_2Ru^+$ $[M]^+$: 1043.4399, found: 1043.4391.

3.5.4 Catalytic transfer hydrogenation reaction catalyzed by 13_b

In a typical run, a vessel was charged with **13_b** (3.0 mg, 1.4 x 10^{-6} mol), anisole (15.1 µL, 1.4 x 10^{-4} mol), substrate (32.5 µL, 1.4 x 10^{-4} mol), base and *iso*-propanol (2.0 mL). With regards to catalytic reaction employing 4-bromoacetophenone, 33.8 µL (1.4 x 10^{-4} mol) of the substrate was used (entry 8, Table 3.1). The vessel was capped, and heated up to the desired temperature for the duration as indicated in Table 3.1. The reaction progress was monitored *via* GC analysis. The yields of the catalytic reactions were calculated by GC using anisole as an internal standard (Shimadzu GC-2010, NF-5225, 30 m, 0.25 mm, 0.25 mm, He at 1.0 mL/min, constant Flow 40 °C for 2 min, ramp to 100 °C at 30 °C/min, ramp to 240 °C at 45 °C/min (hold 0.5 min)). Table 3.1: value in parenthesis under converted column is percentage conversion by base, as determined from blank experiments.

3.6 References

[1] R. R. Schrock, J. S. Murdzek, G. C. Bazan, J. Robins, M. DiMare, M. O'Regan, *J. Am. Chem. Soc.*, **1990**, *112*, 3875 – 3886.
[2] S. T. Nguyen, L. K. Johnson, R. H. Grubbs, *J. Am. Chem. Soc.*, **1992**, *114*, 3974 – 3975.
[3] J. S. Kingsbury, J. P. A. Harrity, P. J. Bonitatebus Jr., A. H. Hoveyda, *J. Am. Chem. Soc.*, **1999**, *121*, 791 – 799.
[4] *a*) J. Huang, E. D. Stevens, S. P. Nolan, J. L. Peterson, *J. Am. Chem. Soc.*, **1999**, *121*, 2674 – 2678; *b*) M. Scholl, T. M. Trnka, J. P. Morgan, R. H. Grubbs, *Tetrahedron Lett.*, **1999**, *40*, 2247 – 2250; *c*) L. Ackermann, A. Fürstner, T. Weskamp, F. J. Kohl, W. A. Herrmann, *Tetrahedron Lett.*, **1999**, *40*, 4787 – 4790.
[5] M. Scholl, S. Ding, C. W. Lee, R. H. Grubbs, *Org. Lett.*, **1999**, *1*, 953 – 956.
[6] G. Van Koten, D. Milstein, ed., *Organometallic Pincer Chemistry*, Springer: Heidelberg, **2013**.
[7] *a*) S. Werkmeister, J. Neumann, K. Junge, M. Beller, *Chem. Eur. J.*, **2015**, *21*, 12226 – 12250; *b*) C. Gunanathan, D. Milstein, *Chem. Rev.*, **2014**, *114*, 12024 – 12087; *c*) E. Balaraman, D. Milstein, *Top. Organomet. Chem.*, **2014**, *48*, 19 – 44.
[8] *a*) J. R. Khusnutdinova, D. Milstein, *Angew. Chem. Int. Ed.*, **2015**, *54*, 12236 – 12273, *b*) D. Milstein, *Top. Organomet. Chem.*, **2010**, *53*, 915 – 923.
[9] C. Gunanathan, D. Milstein, *Acc. Chem. Res.*, **2011**, *44*, 588 – 602.
[10] J. Zhang, G. Leitus, Y. Ben-David, D. Milstein, *Angew. Chem. Int. Ed.*, **2006**, *45*, 1113 – 1115.
[11] J. Zhang, G. Leitus, Y. Ben-David, D. Milstein, *J. Am. Chem. Soc.*, **2005**, *127*, 10840 – 10841.
[12] E. Balaraman, B. Gnanaprakasam, L. J. W. Shimon, D. Milstein, *J. Am. Chem. Soc.*, **2010**, *132*, 16756 – 16758.
[13] B. Gnanaprakasam, D. Milstein, *J. Am. Chem. Soc.*, **2011**, *133*, 1682 – 1685.
[14] D. Spasyuk, S. Smith, D. G. Gusev, *Angew. Chem. Int. Ed.*, **2012**, *51*, 2772 – 2775.
[15] D. Spasyuk, S. Smith, D. G. Gusev, *Angew. Chem. Int. Ed.*, **2013**, *52*, 2538 – 2542.
[16] A. A. Danopoulos, S. Winston, W. B. Motherwell, *Chem. Commun.*, **2002**, 1376 – 1377.
[17] M. Poyatos, J. A. Mata, E. Falomir, R. H. Crabtree, E. Peris, *Organometallics*, **2003**, *22*, 1110 – 1114.

© University of Pretoria

[18] G. A. Filonenko, M. J. B. Aguila, E. N. Schulpen, R. van Putten, J. Wiecko, C. Müller, L. Lefort, E. J. M. Hensen, E. A. Pidko, *J. Am. Chem. Soc.*, **2015**, *137*, 7620 – 7623.
[19] C. K. Ng, J. Wu, T. S. A. Hor, H.-K. Luo, *Chem. Commun.*, **2016**, *52*, 11842 – 11845.
[20] E. Jürgens, D. Kunz, *Eur. J. Inorg. Chem.*, **2017**, 233 – 236.
[21] P. Mathew, A. Neels, M. Albrecht, *J. Am. Chem. Soc.*, **2008**, *130*, 13534 – 13535.
[22] For relevant examples, see: *a*) J. Olguín, M. Á. Paz-Sandoval, *J. Organomet. Chem.*, **2017**, *Accepted for publication* (DOI: 10.1016/j.jorganchem.2017.08.012); *b*) L. Suntrup, S. Hohloch, B. Sarkar, *Chem. Eur. J.*, **2016**, *22*, 18009 – 18018; *c*) A. Bolje, S. Hohloch, M. van der Meer, J. Košmrlj, B. Sarkar, *Chem. Eur. J.*, **2015**, *21*, 6756 – 6764; *d*) B. Bagh, A. M. McKinty, A. J. Lough, D. W. Stephan, *Dalton Trans.*, **2015**, *44*, 2712 – 2723; *e*) K. J. Kilpin, S. Crot, T. Riedel, J. A. Kitchen, P. J. Dyson, *Dalton Trans.*, **2014**, *43*, 1443 – 1448; *f*) B. Bagh, A. M. McKinty, A. J. Lough, D. W. Stephan, *Dalton Trans.*, **2014**, *43*, 12842 – 12850; *g*) B. Bagh, D. W. Stephan, *Dalton Trans.*, **2014**, *43*, 15638 – 15645; *h*) S. Hohloch, L. Hettmanczyk, B. Sarkar, *Eur. J. Inorg. Chem.*, **2014**, 3164 – 3171; *i*) K. Ogata, S. Inomata, S. Fukuzawa, *Dalton Trans.*, **2013**, *42*, 2362 – 2365; *j*) J. Bouffard, B. K. Keitz, R. Tonner, G. Guisado-Barrios, G. Frenking, R. H. Grubbs, G. Bertrand, *Organometallics*, **2011**, *30*, 2617 – 2627; *k*) J. Cai, X. Yang, K. Arumugam, C. W. Bielawski, J. L. Sessler, *Organometallics*, **2011**, *30*, 5033 – 5037.
[23] *a*) R. Pretorius, Z. Mazloomi, M. Albrecht, *J. Organomet. Chem.*, **2017**, *845*, 196 – 205; *b*) S. Sabater, H. Müller-Bunz, M. Albrecht, *Organometallics*, **2016**, *35*, 2256 – 2266; *c*) K. F. Donnelly, C. Segarra, L.-X. Shao, R. Suen, H. Müller-Bunz, M. Albrecht, *Organometallics*, **2015**, *34*, 4076 – 4084; *d*) M. Delgado-Rebollo, D. Canseco-Gonzalez, M. Hollering, H. Mueller-Bunz, M. Albrecht, *Dalton Trans.*, **2014**, *43*, 4462 – 4473; *e*) V. Leigh, W. Ghattas, R. Lalrempuia, H. Müller-Bunz, M. T. Pryce, M. Albrecht, *Inorg. Chem.*, **2013**, *52*, 5395 – 5402; *f*) D. Canseco-Gonzalez, M. Albrecht, *Dalton Trans.*, **2013**, *42*, 7424 – 7432; *g*) A. Prades, E. Peris, M. Albrecht, *Organometallics*, **2011**, *30*, 1162 – 1167.
[24] C. Cesari, R. Mazzoni, H. Müller-Bunz, M. Albrecht, *J. Organomet. Chem.*, **2015**, *793*, 256 – 262.
[25] L. Bernet, R. Lalrempuia, W. Ghattas, H. Mueller-Bunz, L. Vigara, A. Llobet, M. Albrecht, *Chem. Commun.*, **2011**, *47*, 8058 – 8060.
[26] B. Schulze, D. Escudero, C. Friebe, R. Siebert, H. Görls, U. Köhn, E. Altuntas, A. Baumgaertel, M. D. Hager, A. Winter, B. Dietzek, J. Popp, L. González, U. S. Schubert, *Chem. Eur. J.*, **2011**, *17*, 5494 – 5498.
[27] D. G. Brown, N. Sanguantrakun, B. Schulze, U. S. Schubert, C. P. Berlinguette, *J. Am. Chem. Soc.*, **2012**, *134*, 12354 – 12357.
[28] M. Hollering, M. Albrecht, F. E. Kühn, *Organometallics*, **2016**, *35*, 2980 – 2986.
[29] S. N. Sluijter, T. J. Korstanje, J. I. van der Vlugt, C. J. Elsevier, *J. Organomet. Chem.*, **2017**, *845*, 30 – 37.
[30] E. Knoevenagel, B. Bergdolt, *Chem. Ber.*, **1903**, *36*, 2857 – 2860.
[31] See review article and references therein, D. Wang, D. Astruc, *Chem. Rev.*, **2015**, *115*, 6621 – 6686.
[32] *a*) B. Štefan, F. Požgan, *Cat. Rev.: Science and Engineering*, **2014**, *56*, 82 – 174; *b*) J. Ito, H. Nishiyama, *Tetrahedron Lett.*, **2014**, *55*, 3133 – 3146; *c*) J. G. de Vries, C. J. Elsevier, *The Handbook of Homogeneous Hydrogenation*, **2007**, 585 – 630; and references therein.
[33] See review article and references therein, F. Foubelo, C. Nájera, M. Yus, *Tetrahedron: Asymmetry*, **2015**, *26*, 769 – 790.
[34] R. Noyori, *Angew. Chem. Int. Ed.*, **2002**, *41*, 2008 – 2022.
[35] See review article and references therein: *a*) P. A. Dub, J. C. Gordon, *Dalton Trans.*, **2016**, *45*, 6756 – 6781; *b*) O. Eisenstein, R. H. Crabtree, *New J. Chem.*, **2013**, *37*, 21 – 27; *c*) W. S. Knowles, R. Noyori, *Acc. Chem. Res.*, **2007**, *40*, 1238 – 1239; *d*) R. Noyori, S. Hashiguchi, *Acc. Chem. Res.*, **1997**, *30*, 97 – 102.

© University of Pretoria

Chapter 4

A rhodium(I)-oxygen adduct as a selective catalyst for one-pot sequential alkyne dimerization-hydrothiolation tandem reactions

Rhodium complexes **16$_a$** and **18$_a$**, **17$_b$** and **19$_b$** have been previously reported in the MSc study preceding this PhD investigation.[1] However, an optimized procedure was employed for the preparation of these complexes for use as catalyst precursors as described in this study, and therefore the syntheses and characterization of the complexes were included in chapter 4 of this thesis.

4.1 Background

The metal catalyzed alkyne functionalization reaction, a pillar of the fine chemical production industry, has enjoyed wide spread attention due to this powerful atom economical approach for selective synthesis of elaborate organic compounds.[2] In particular, C-C[3], C-S[4] and C-N[5] bond formation strategies are of utmost importance and in great demand in general organic chemistry, the biological and pharmaceutical industry, as well as in the field of both polymer sciences and agricultural developments, to name but a few.[2,3,4,5] Various methodologies towards production of the aforementioned products have been extensively studied. The development of organometallic complexes able to catalyze these procedures has been the object of considerable interest due to the prominent advantages offered by metal catalyzed processes. One of the main advantages is access to a desired isomer in a selective manor. Acid, base or radical catalyzed reactions usually lead to the formation of a range of isomers, rendering a selective metal catalyzed reaction invaluable.[2,3,4,5] Lowering the energy barrier of the reaction, decreased waste production and improved atom-economy are just a few of the additional gains accessed through a metal catalyzed process.[6]

© University of Pretoria

As such, it was proposed that synthesis of a rhodium complex supported by the strong CNC donor ligand (from ligand precursors $\mathbf{L_a}$ and $\mathbf{L_b}$) could mediate the aforementioned reactions. Specifically, the hydroamination of unactivated alkynes with various primary and/or secondary amines catalyzed by the (CNC)Rh(I) complex was envisaged. The hydroamination of unactivated alkynes has been successfully catalyzed with various late transition metals, of which rhodium has been documented repeatedly.[5] These complexes feature, in most cases, strong donor ligands yielding a metal center with a high nucleophilic character that can resist the formation of inert Werner complexes.[7] Our efforts towards the attempted synthesis of a rhodium 14-electron complex supported by the CNC-pincer ligand resulted in the formation and isolation of a rhodium(I) oxygen adduct (see MSc dissertation of the author).[1] Nonetheless, substitution of molecular oxygen by the amine should be followed by oxidative addition, alkyne insertion and subsequent reductive elimination to yield either the Markovnikov or anti-Markovnikov amine products. To our surprise, the rhodium-oxygen adduct did not mediate the hydroamination reaction as planned, but did in fact catalyze the alkyne homo-dimerization reaction of 1-pentyne to yield the corresponding *gem*-enyne as the only product of the test reaction (Scheme 4.1).

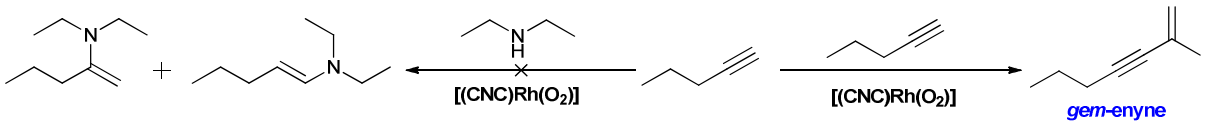

Scheme 4.1: Enyne formation instead of hydroamination of 1-pentyne catalyzed by the rhodium-oxygen adduct

With this preliminary result in hand, it was reasoned that the rhodium-oxygen adduct could also catalyze the alkyne hydrothiolation reaction, in addition to the dimerization of a range of terminal alkynes. Both dimerization[8] and hydrothiolation[9] reactions are known to be catalyzed by an array of compounds. Promoters of both reactions include main group elements, lanthanides and actinides, in addition to a wide range of transition metal species of which Pd, Rh, Ru, Ir and Ni has been documented numerously.[3,4,8,9] The mentioned 'heavy weights' of catalysis, especially the Pd- and Rh-containing organometallic catalysts, have been recognized as complex metals able to catalyze either dimerization or hydrothiolation reactions with good to perfect regio-, stereo-, and chemoselectivity. For both Pd and Rh metal complexes, it has additionally been noted that the selectivity outcome of the reactions can be altered through subtle modifications to the ligand or to the reaction conditions employed.[3,4,8,9]

Therefore, ligand design plays an extremely important role during catalyst perfection. It can not only stabilize the precatalyst, but also dictate the selectivity outcome of the catalyzed reaction as well as affecting the catalyst activity. Furthermore, a catalyst able to promote both alkyne dimerization and

© University of Pretoria

alkyne hydrothiolation reactions would certainly render such a complex indispensable. Therefore, the choice of palladium or rhodium as the active metal center along with the appropriate ligand could yield such a theoretical catalyst. The following sections follow on the mechanistic considerations, along with recent and relevant examples, on both alkyne dimerization and hydrothiolation reactions.

4.1.1 Alkyne dimerization

The atom economical terminal alkyne C_{sp}-H bond addition across another alkyne (either terminal or internal) has become a useful strategy for the synthesis of conjugated enynes, with their structural motif finding uses in the biological field, polymer industries, as photoactive derivatives, etc.[10] However, chemo-, regio-, and stereoselective control remains a challenge, with catalyst design focused particularly on selective enyne preparation instead of improved catalytic performance.[8,11] Three main isomers are usually formed, namely the *E*- or *Z*-enynes as well as the *gem*-enyne isomer, for which the preparation of the latter is more difficult and less reported compared to the *E*/*Z*-enyne isomers.[8] Alternatively, the formation of diynes, dienynes, butatrienes, cyclotrimers, oligomers and polymers has also been reported as possible by-product formation of the dimerization reaction, subject to the catalyst employed and the choice of reaction conditions.[8]

For the alkyne dimerization catalyzed reaction, two main mechanistic scenarios can be considered.[8,11] The first mechanism regards the oxidative addition of the acidic alkyne C-H bond generating the metal-hydride-alkynyl intermediate complex (Scheme 4.2). This is followed by migratory insertion of the second alkyne. The insertion can be across the metal-hydride (hydrometallation) or the metal-alkynyl bond (carbometallation). The orientation of the alkyne insertion across the aforementioned bonds also dictates *gem*- or *E*-enyne product formation.[8,11] The carbometallation pathway following a 1,2-insertion yields the *gem*-enyne, while a 2,1-insertion leads to *E*-enyne formation after reductive elimination, respectively. Metal-hydride 1,2-insertion results in *E*-enyne formation after reductive elimination, while the hydrometallation 2,1-insertion pathway yields the *gem*-enyne product after reductive elimination (Scheme 4.2). Therefore, carbometallation and hydrometallation mechanistic pathways generate the *gem*- and/or *E*-enynes and not the *Z*-enyne isomer.[8,11]

The second mechanistic scenario that has to be considered is metal-vinylidene complex formation.[8,11] Coordination of the alkyne is followed by isomerization yielding the metal-vinylidene intermediate (Scheme 4.2). The second alkyne oxidatively adds across the metal-vinylidene intermediate. Successive

© University of Pretoria

nucleophilic attack on the electrophilic C_α atom of the cumulene moiety by the hydride or alkynyl group is followed by reductive elimination yielding the *E*/*Z*-enynes. Additionally, an acid-base mediated mechanism can also account for *E*/*Z*-enyne production after vinylidene complex formation. The vinylidene catalyzed route is generally considered for ruthenium-metal based catalysts, although not limited to this specific metal (Scheme 4.2). Most importantly is the fact that, in general, the two mechanistic cycles deliver either *gem*/*E*- or *E*/*Z*-enynes.[8,11]

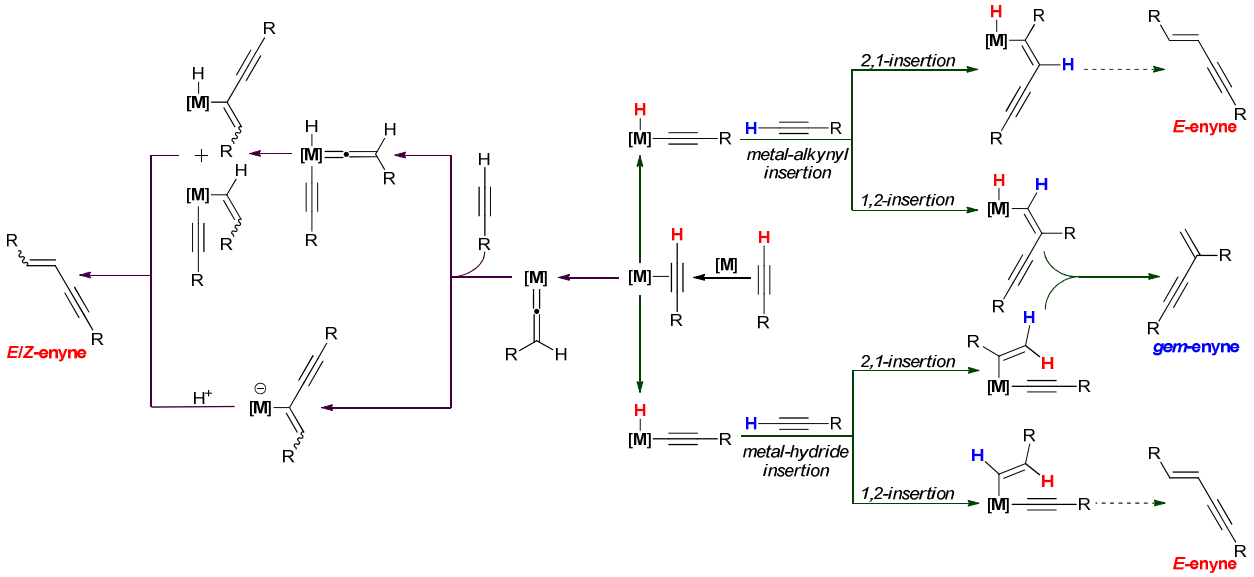

Scheme 4.2: Mechanistic consideration for the alkyne dimerization catalyzed reaction[8,11]

As was stated, selective *gem*-enyne formation (also known as the head-to-tail dimerization reaction) can be relatively problematic. Preparation of the *gem*-enyne isomer as the sole product of the reaction was recently reported. The groups of Han[12] and Guo[13] disclosed on the selective palladium catalyzed head-to-tail dimerization. In both studies, various acids such diphenylphosphonic acid and acetic acid were required for the catalyzed reactions.[12,13] Prior to these reports, was the example by Trost and co-workers in 1987 on the selective preparation of *gem*-enynes, also catalyzed by a palladium complex.[14] More recently was the seminal report by the group of Oro and co-workers, who developed a method for selective *gem*-enyne preparation through the addition of an additive pyridine.[8] Poor to no selectivity was noted for the *gem*-enyne isomer during the control experiments. Upon addition of ten equivalents of pyridine, more than 90% selectivity for the *gem*-enyne isomer was obtained in addition to the catalytic activity being markedly improved (Scheme 4.3). The experiment was duplicated with trimethylamine, with no formation of the targeted *gem*-enyne isomer. Therefore, the pyridine does not simply act as a base for improved catalytic performance, but suppresses the formation of *E*/*Z*-enynes in

© University of Pretoria

addition to the products of trimerization and cyclotrimerization. Extensive experimental and theoretical calculations supported a mechanistic scenario following a 2,1-insertion across the metal-hydride bond. This is surprising as the higher *trans* influence exhorted by the hydride ligand would lead to coordination of the second alkyne *trans* to the hydride and *cis* to the alkynyl ligand, that would then enter a carbometallation pathway.[8] However, the energy barrier was computationally predicted to be higher for the C-C bond formation reaction compared to the C-H bond construction process. After hydrometallation following a 2,1-insertion path, reductive elimination ensues to yield the *gem*-enyne (Scheme 4.3). In all mechanistic considerations, it was computationally shown that coordination of a second pyridine molecule stabilizes the complex intermediate after oxidative addition, and more importantly, does not render the intermediate complex inactive as the second incoming alkyne readily substitutes the pyridine ligand in question (Scheme 4.3).[8]

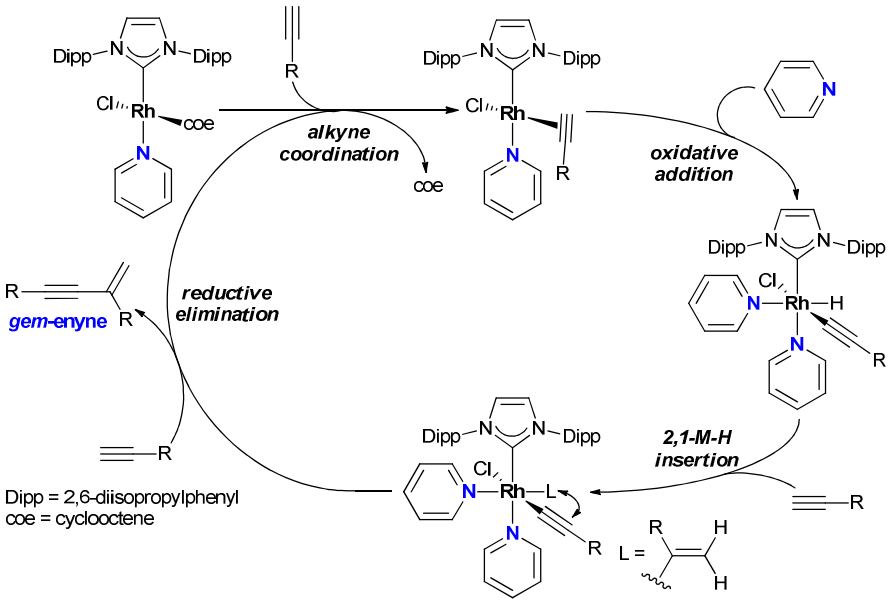

Scheme 4.3: Mechanistic proposal through which the (NHC)Rh complex catalyzes the dimerization reaction[8]

The group of Gevorgyan and Ananikov recently disclosed a palladium catalyzed dimerization reaction, with a selectivity switch between either *gem*- or *E*-enyne isomers (**II**, Scheme 4.4).[15] Previously, the group of Gevorgyan reported *E*-enyne preparation with complete selectivity for the one isomer (**I**, Scheme 4.4).[16] The reaction was catalyzed by an allyl palladium chloride dimer in the presence of a bulky electron rich phosphine ligand (TDMPP = tris(2,6-dimethoxyphenyl)phosphine) and Et_2NH (**I**, Scheme 4.4). It was demonstrated that the bulky phosphine ligand is required for complete selectivity as smaller phosphines yielded mixtures of products (**I**, Scheme 4.4).[16] With regards to their recent report, the *E*-

© University of Pretoria

enyne formation could also be catalyzed with complete selectivity while the introduction of an NHC coordinating ligand stabilized the catalytically active complex (**II**, Scheme 4.4).[15] The selectivity could be changed from the *E*-enyne to the *gem*-enyne isomer by the addition of an acetate anion and cesium pivalate, furnishing the head-to-tail isomer as the only product of the reaction.

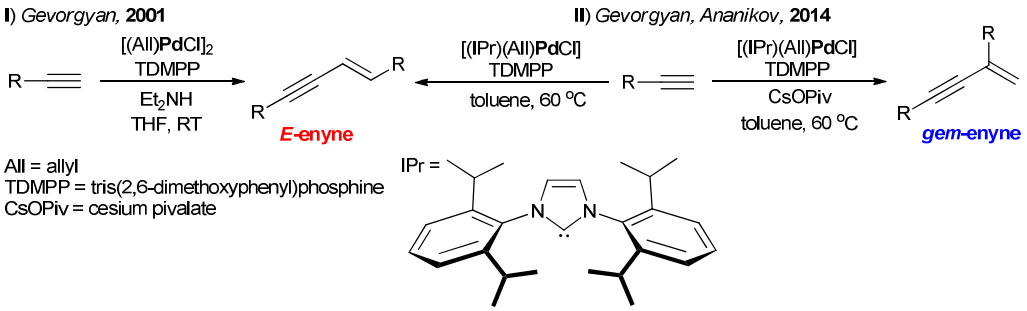

Scheme 4.4: Selective synthesis of **I**) *E*-enynes and **II**) selectivity switch for access to either *E*- or *gem*-enynes

A mechanism was postulated after extensive calculations to explain the switch between the two reactions and the observed selectivity (**II**, Scheme 4.4). Computational analysis predicted that a hydropalladation (hydrometallation) pathway is favoured in both head-to-head and head-to-tail synthetic routes over the carbopalladation insertion mechanism, before the addition of the acetate anion (Scheme 4.5).[15] For the hydropalladation mechanism, the energy differences between the head-to-head and head-to-tail reaction pathways were not significant. However, the energy barriers for the head-to-head pathway was still lower in energy in every step compared to the head-to-tail route, favouring *E*-enyne formation as was experimentally observed. As such, a carbopalladation mechanistic route is required to yield the *gem*-enyne isomer, with access to this route possible only after addition of the acetate anion. Proton removal from the palladium hydride complex intermediate by acetate was computationally predicted to be energetically favourable in a protic media, as the protic solvent can coordinate and stabilize the intermediate anionic Pd complex (Scheme 4.5). This forces a carbopalladation pathway to ensue over a hydropalladation route as there is no Pd-H bond to insert across. The relative energies of the intermediate complexes after coordination of the second alkyne suggested that the head-to-head pathway is still favoured over head-to-tail product formation. The elegance of this selectivity switch lies within the use of the acetate anion in an aprotic solvent media (Scheme 4.5).[15] Theoretical considerations suggested that formation of the palladium-acetate ion-pair in aprotic solvents is plausible since the differences in free energies are small. Calculations further predicted that coordination of the second alkyne leads to hydrogen migration from the palladium-hydride to the acetate anion yielding the anionic palladium complex intermediate with coordinated

© University of Pretoria

acetic acid and alkyne. In this complex, both alkynes remain coordinated to the metal favouring the carbopalladation head-to-tail insertion reaction. This is in contrast to the head-to-head carbopalladation reaction, where dissociation of the second alkyne occurs before insertion leading ultimately to the observed selectivity. The results suggest that the acetate anion has a dual role. First, the anion inhibits the hydropalladation pathway by abstracting the hydride ligand.[15] Finally, the acetate anion forms an ion-pair in aprotic solvents which increases the energy differences between the palladium complexes involved in head-to-head and head-to-tail dimerization reactions, with the head-to-tail intermediate complex being more stable due to less steric hindrance with the coordinated NHC ligand (Scheme 4.5).[15]

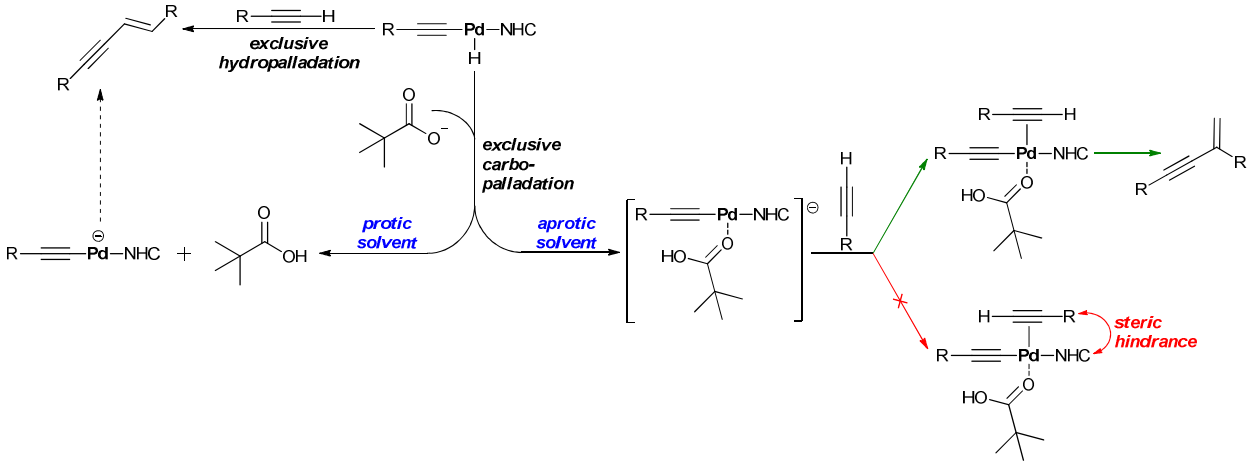

Scheme 4.5: Mechanistic consideration for selectivity switch between *E*- and *gem*-enyne formation[15]

As is evident from the abovementioned case studies, selectivity can be controlled through step-wise consideration of the reaction mechanism/conditions. Bulky phosphines can furnish enyne isomers with complete selectivity, with the addition of hydride scavengers changing the selectivity outcome completely. Additives can also act as directing or stabilizing ligands with direct consequence on the selectivity outcome. A few reports regard the selective synthesis of *gem*-enynes accessed through the addition of just metal precursor and ligand (usually phosphines) which coordinates *in situ* to yield the active catalyst.[14] The use of a well-defined mononuclear metal complex for selective *gem*-enyne preparation is also scarcely encountered. The advantages of employing such a mononuclear catalyst that does not require additive directing groups or base, render these complexes as warranting attention.

© University of Pretoria

4.1.2 Alkyne hydrothiolation

Direct access to the one-step incorporation of sulphur-containing moieties to alkyne substituted organic products has been extensively studied, as this route allows for the atom-economical preparation of vinyl sufides.[4,9] The structural motifs of these compounds have rendered these products very useful in a diverse range of applications.[17] As was the case with the alkyne dimerization reaction, the alkyne hydrothiolation reaction can be mediated by a wide range of processes.[9] The S-H addition reaction generally results in the formation of three major isomers, namely the β-*E*-, β-*Z*- and/or the α-vinyl sulfides. However, selectivity for a specific isomer still remains a challenge, especially with regards to the selective preparation of the α-vinyl sulfide product as its synthesis is more problematic.[9]

Several approaches have been reported towards the preparation of vinyl sulfides including radical catalyzed methods as well as metal catalyzed procedures.[4,9] Radical catalyzed methods can be readily promoted, especially when employing aromatic substituted substrates. Unfortunately, the selectivity outcome for a radical process is non-satisfactory, with no possibility of α-vinyl sulfide preparation in addition to a mixture of β-*E*- and β-*Z*-isomers generally encountered for these reactions. Metal catalyzed reactions have been documented as the foremost methodology for selective synthesis of vinyl sulfides, including α-vinyl sulfide preparation.[9] To this end, rhodium-containing organometallic complexes have received considerable attention as this chameleonic specie has been documented on several occasions as a selective catalyst towards α-vinyl sulfide synthesis. Unlike other metals such as Pd and Ni, rhodium complexes can oxidatively add the thiol substrate yielding the hydride thiolate intermediate complex. This in turn allows for a ligand-based control of the selectivity outcome of the reaction. Therefore, rhodium complexes can be manipulated *via* ligand fine-tuning to yield the desired isomer in a selective manner.[9] Rhodium has been shown to entertain three different mechanistic scenarios in terms of the hydrothiolation reaction of thiols with alkynes. These mechanistic considerations include metal-thiolate[9] or metal-hydride[9] insertion, as well as a metal-ligand cooperative catalyzed reaction were the non-innocent ligand serves a multipurpose role (Scheme 4.6).[18]

Reactions that are initiated by the oxidative addition of a thiol are followed by a metal-thiolate (M-SR) or a metal-hydride (M-H) insertion reaction (Scheme 4.6).[9] The insertion process can occur *via* a 1,2- or 2,1-insertion mechanism. For the metal-thiolate insertion reaction, a 2,1-insertion leads to β-*E*-vinyl sulfides while the 1,2-insertion process results to the formation of the α-vinyl sulfide, after reduction of the vinyl sulfide and hydride moieties (Scheme 4.6). A 2,1-M-H insertion reaction also yields the α-vinyl sulfide isomer, while the 1,2-M-H insertion process generates the β-*E*-vinyl sulfides, after reductive

© University of Pretoria

elimination.[9] Non-innocent ligands can catalyze the hydrothiolation reaction *via* first deprotonation of the acidic thiol proton by a basic functionality substituted on the ligand.[18] This opens up a coordination site for alkyne coordination, followed by migratory insertion and finally protonolysis yielding the targeted product and the starting catalyst (Scheme 4.6).[18] The three mechanistic considerations discussed are depicted in Scheme 4.6. The alkyne hydrothiolation catalyzed reaction has recently been extensively reviewed, and as such, only a few relevant examples as well as very recent reports will be discussed here.[9] The examples include the use of a rhodium catalyst towards the selective preparation of α-vinyl sulfides.

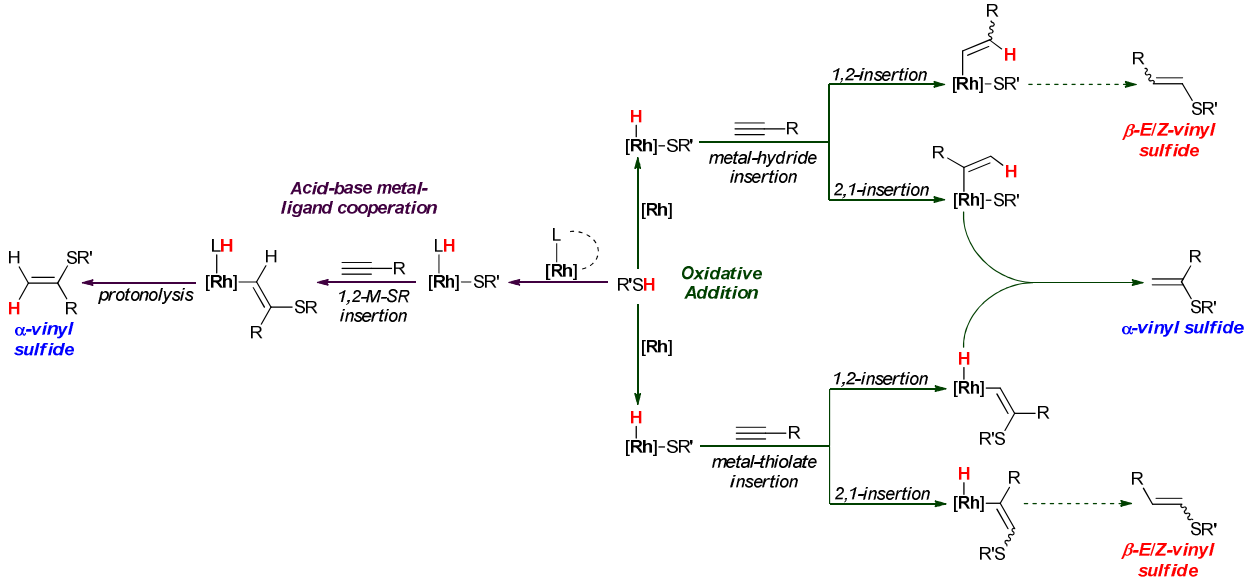

Scheme 4.6: Mechanistic consideration for the alkyne hydrothiolation catalyzed reaction

The group of Love contradicted the expectation that Group 9 metals only catalyze the formation of linear and not branched vinyl sulfides.[19] The rhodium metal was supported by a hydrotris(3,5-dimethylpyrazolyl)borate ligand (Tp*) yielding an electron rich metal center that could catalyze the hydrothiolation of aliphatic substituted substrates, a process which was reported at the time to be extremely difficult. Even more intriguing was the complete selectivity for the branched vinyl sulfide isomer when employing alkyl thiols and various alkynes. Additionally, the [Tp*Rh(PPh_3)$_2$] catalyst tolerated a broad range of functionalities while displaying a high catalytic activity. The use of aryl substituted thiols with alkynes was detrimental to the catalyst, with 100% conversion within reasonable time frames but with selectivity for the α-vinyl sulfide isomer being severely diminished. Nonetheless, the seminal report proved that electron rich Group 9 metal centers could facilitate the very challenging hydrothiolation of alkyl thiols with various alkynes, including aliphatic substituted alkynes yielding the

© University of Pretoria

branched vinyl sulfides selectively. An M-SR insertion mechanism has been proposed for the reaction, but a complete mechanistic cycle has not yet been elucidated.[19] A mechanism was, however, proposed for a related [Tp*Rh(coe)(CH_3CN)] complex by Mizobe and co-workers a year after the report by Love.[20] Substitution of the cyclooctene (coe) ligand with a thiol substrate, followed by oxidative addition of a second thiol, leads to elimination of hydrogen gas and the acetonitrile ligand (Scheme 4.7). Alkyne coordination to the vacant site of the rhodium(III) dithiolate complex is followed by a 1,2-M-SR insertion, with concomitant reductive elimination yielding the branched vinyl sulfide isomer and the active dithiolate catalyst (Scheme 4.7).[20] Steric hindrance dictates the geometry of the M-SR insertion reaction. A 2,1-M-SR insertion results in increased steric hindrance between the Tp* ligand and the substituent of the alkyne substrate. Therefore, the lower energy intermediate drives the 1,2-M-SR insertion reaction in generating the branched isomer.

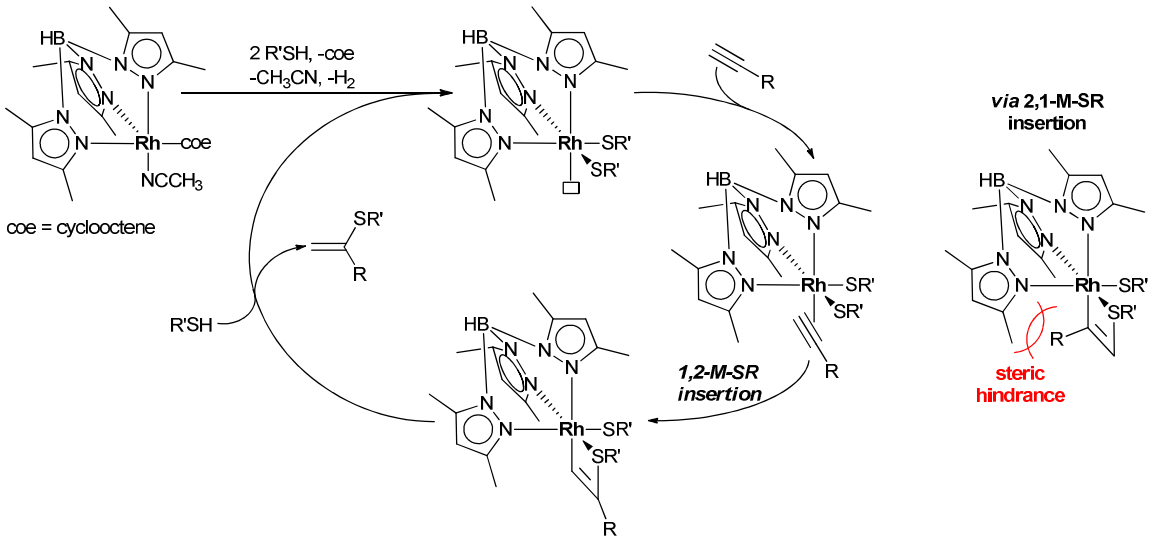

Scheme 4.7: [Tp*Rh(coe)(CH_3CN)] catalyzed hydrothiolation of alkynes *via* rhodium dithiolate formation[20]

More recently it was demonstrated that the selectivity towards the α-vinyl sulfide isomer could be improved through the addition of pyridine, as was the case for the alkyne dimerization reaction.[21] The poor selectivity of the very active dinuclear rhodium complex was switched to the *anti*-Markovnikov product by the addition of ten equivalents of pyridine, yielding the α-vinyl sulfide isomer with more than 94% selectivity (Scheme 4.8). As the NHC ligand is a strongly donor ligand, it directs the coordination of the first pyridine ligand *trans* with respect to itself. This inhibits coordination of the alkyne, after oxidative addition and attack of the incoming alkyne, at this position. Thiol coordination to the rhodium(I) metal center after substitution of the cyclooctene ligand, is followed by oxidative addition yielding the hydride thiolate rhodium(III) intermediate complex.[21] At the same time, a second equivalent

© University of Pretoria

of pyridine coordinates *trans* to the hydride directing ligand, saturating the metal complex (Scheme 4.8). Alkyne coordination is now restricted to one position only. Therefore, substitution of the pyridine *trans* to the hydride leads to coordination of the alkyne *cis* to the thiolate ligand. This restricts a M-H insertion reaction, with only a 1,2-M-SR or 2,1-M-SR insertion route possible. Finally, steric hindrance directs the insertion step with a 1,2-M-SR step being more favourable, as a 2,1-M-SR insertion has a higher energy barrier as a result of steric clashes between the alkyne substituent and the NHC ligand (Scheme 4.8). The 1,2-M-SR insertion reaction is then followed by reductive elimination and coordination of another thiol substrate to yield the active starting catalyst and the α-vinyl sulfide isomer.[21]

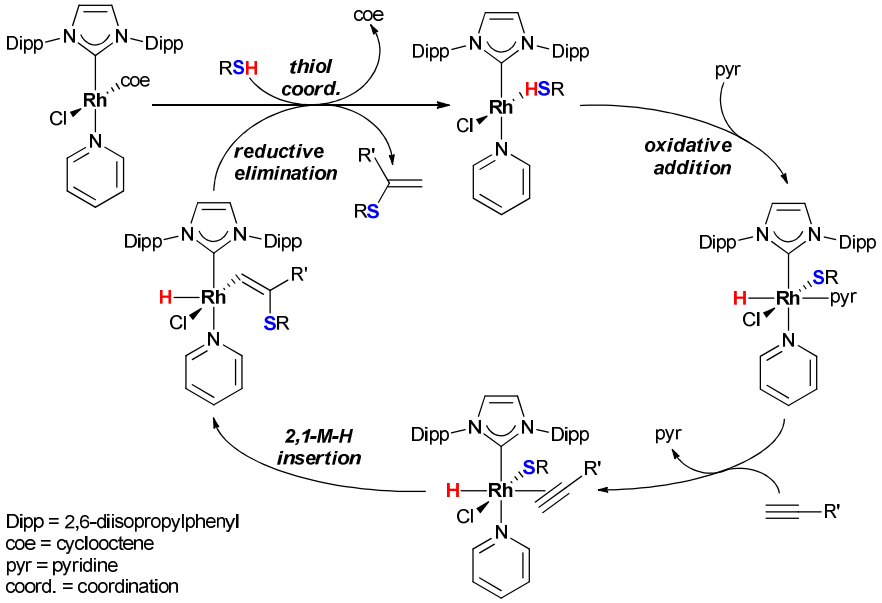

Scheme 4.8: Pyridine enhanced selectivity towards the α-vinyl sulfide isomer[21]

Also very recently, two different reports revolved around the acid-base rhodium-ligand cooperative catalyzed hydrothiolation reaction towards the preparation of α-vinyl sulfides. Oro and co-workers reported on the synthesis of rhodium alkoxopyridine carbonyl complexes supported by an NHC ligand.[18] The simple preparation involved deprotonation and coordination of hydroxymethylpyridine with the dinuclear rhodium hydroxo complex (Scheme 4.9). The same complex could also be synthesized by a salt elimination reaction from the corresponding dinuclear rhodium chlorido complex. Exposure to air yielded the stable rhodium dioxygen adduct coordination (*vide infra*). Both molecular oxygen and cyclooctene ligands could be substituted with CO yielding the rhodium carbonyl complex, used as the catalyst precursor. It was reasoned that the π-accepting CO ligand could stabilize the rhodium metal against oxidation reactions while the alkoxopyridine moiety would deprotonate the incoming thiol

© University of Pretoria

substrate. Indeed, deprotonation of the acidic thiol S-H by the alkoxopyridine moiety resulted to the formation of the active starting catalyst. Hydroxymethylpyridine substitution by the incoming alkyne is followed by a 1,2-M-SR insertion reaction (Scheme 4.9). Coordination of another thiol substrate with subsequent elimination of the α-vinyl sulfide isomer and re-coordination of the hydroxymethylpyridine ligand regenerate the active catalyst. Note that the metal did not undergo an oxidation or reduction event (Scheme 4.9).[18]

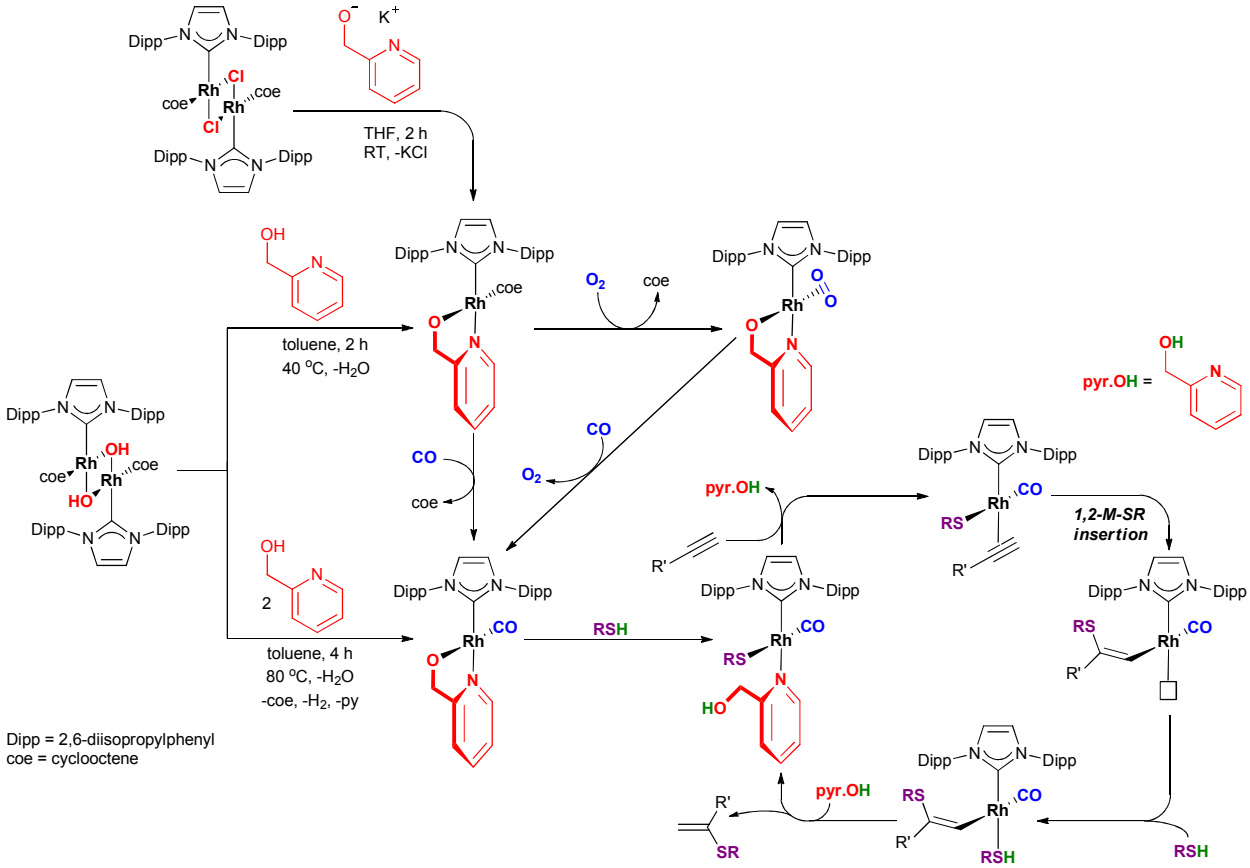

Scheme 4.9: Rh(I) hydrothiolation through acid-base metal-ligand cooperativity[18]

Another, prior example of acid-base metal-ligand cooperative catalyzed hydrothiolation of terminal alkynes originated from our group.[22] A series of cationic and neutral rhodium(I) complexes supported by triazolylidene ligands containing an N-donor functionalized pendant ligand were synthesized (Scheme 4.10). The N-donor (N = NMe_2, NH_2 or NHBoc) pendant functionality was demonstrated to either deprotonate the acidic thiol S-H (N = NBoc) or simply dissociate from the metal complex and vacate a coordination site (N = NMe_2, NH_2). The synthesis of the bidentate complexes were straightforward and accompanied with high yields. It was validated that all the complexes catalyzed the hydrothiolation

© University of Pretoria

reaction with good to excellent selectivity for the α-vinyl sulfide isomer. The N-donor pendant of the cationic complexes was reported to act as hemilabile ligands based on experimental data and theoretical calculations. The mechanism involves deprotonation of the thiophenol with catalytic amount of weak base. This is followed by substitution of the NMe_2 or NH_2 moiety and coordination of thiophenolate. Coordination of the attacking alkyne occurs *trans* to the strongly donating carbene carbon after dissociation of the carbonyl ligand (Scheme 4.10). Finally, 1,2-M-SR insertion is followed by protonolysis by another thiophenol substrate releasing the active catalyst and the branched vinyl sulfide.[22] The neutral rhodium(I) catalyst was reported to be the most selective catalyst of the series with excellent selectivities noted for the aryl substituted thiols and alkynes. The catalyst also displayed a high functional group tolerance, with the catalyst activity ranging from average to excellent. A different mechanism for the neutral NBoc (Boc = *tert*-butoxycarbonyl) rhodium catalyst involving non-innocent ligand behavior, was proposed. The coordinated NBoc acted as a base by deprotonating the thiol substrate. Subsequent carbonyl substitution by the incoming alkyne substrate generated the π-coordinated alkyne rhodium thiolate intermediate complex with a *cis* disposition of the alkyne with respect to the thiolate ligand. 1,2-M-SR insertion ensues together with carbonyl re-coordination. Finally, protonolysis by another thiophenol substrate yields the α-vinyl sulfide isomer selectively, with regeneration of the active catalyst (Scheme 4.10). For both neutral and cationic rhodium catalysts, no hydride formation during the catalysis was proposed based on experimental and theoretical data. This eliminates any possibility of an M-H insertion reaction and rules out a redox event.[22] A probable explanation for the lack of an S-H oxidative addition event could be based on the alkoxopyridine rhodum catalyst (see Scheme 4.9), where the presence of π-accepting CO ligands stabilizes the metal center against oxidation.[18]

© University of Pretoria

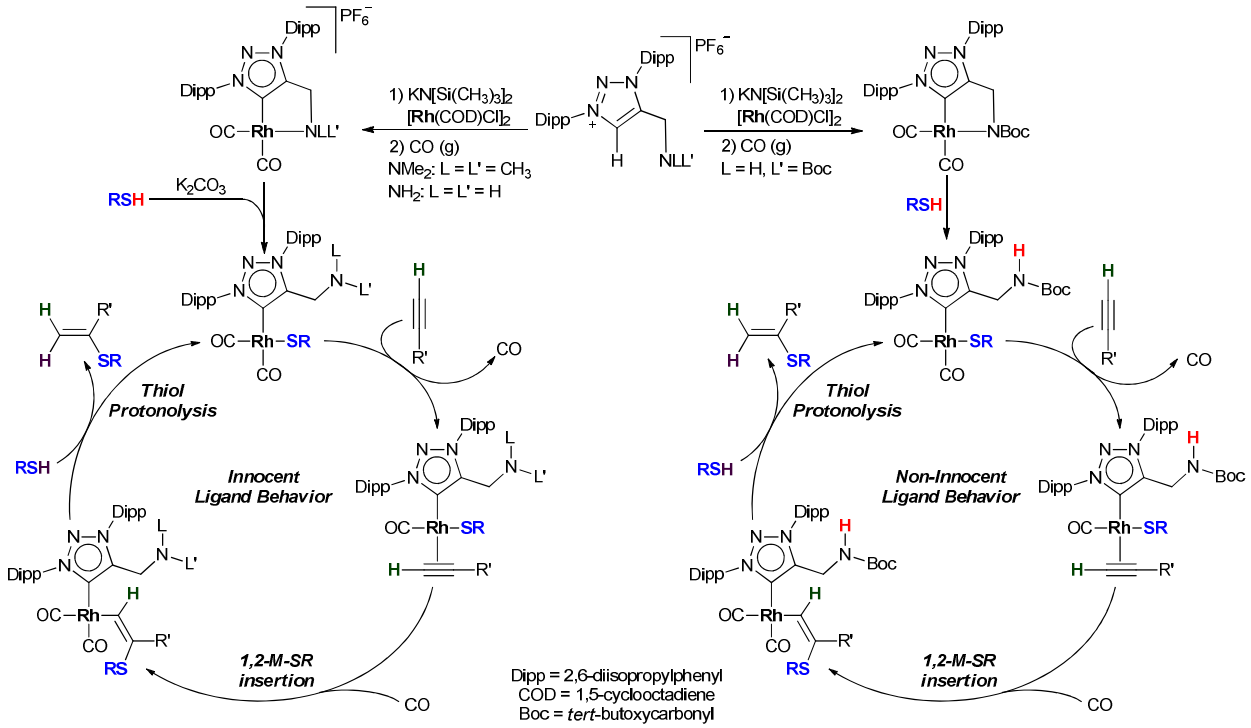

Scheme 4.10: Triazolylidene rhodium(I) catalyzed hydrothiolation with innocent and non-innocent ligand behavior[22]

As was the case for the alkyne dimerization reaction, ligand design constitutes an indispensable role towards the selectivity outcome of the hydrothiolation reaction, as is evident from the above discussed examples. The use of rhodium as the active metal center can allow for the selective synthesis of all possible isomers. Ligand fine-tuning drives the selectivity outcome of the reaction in one direction. Strong donor ligands readily facilitate and stabilize an oxidation event while less electron rich metal centers negate the oxidation event and remain in a Rh(I) oxidation state throughout the catalytic cycle. In addition, electron rich rhodium metal centers catalyze the hydrothiolation of aliphatic thiols with excellent selectivity, while less electron rich rhodium complexes perform better when catalyzing the S-H bond addition of aromatic thiols with aromatic alkynes. Finally, the use of additive directing ligands or increasing the steric bulk on the metal co-ligands also improves the selectivity outcome of the reaction towards a specific isomer.

© University of Pretoria

4.1.3 Rhodium(I)-oxygen adducts

As was stated earlier, coordination of our triazolylidene-based CNC pincer ligand allowed for the isolation of a rhodium(I)-oxygen adduct. Therefore, a brief consideration of such species is warranted. Rhodium-oxygen adducts are scarcely reported. This is not surprising as only certain ligands have allowed for its stabilization and therefore isolation.[23] In general, the rhodium metal undergoes oxidation in the presence of oxygen. This results in the formation of either the corresponding rhodium(III) complex, or simply products of decomposition. Fortunately, a limited number of supporting ligands have been coordinated successfully to a rhodium(I) metal center and permitted the isolation of rhodium(I)-oxygen adducts, where molecular oxygen is π-coordinated in a side-on fashion.[18,23,24,25,26] In most reported cases, NHC ligands were found to be adequately sufficient for stabilization of the reactive complexes. This is not attributed mainly to the robust metal-carbon bond governing oxidation and/or decomposition of the rhodium complexes. Various other subtle, yet imperative factors have to be considered when exploring the influences towards stabilization in order for successful isolation of the side-on L-type oxygen to rhodium coordination (*vide infra*).[26] To the best of our knowledge, all known examples representing rhodium(I)-oxygen adducts are presented in Figure 4.1.[18,23-26]

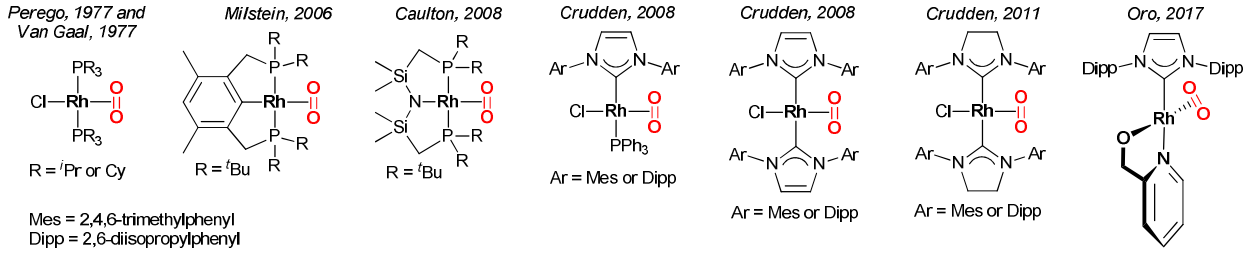

Figure 4.1: Various stable rhodium(I)-oxygen adducts reported to date[18,23-26]

The Rh(I)-O_2 adducts in general, feature square-planar geometries with unusually short oxygen-oxygen bond lengths.[18,23-26] The short oxygen-oxygen bond lengths for L-type coordinated O_2 moieties are generally in the range of 1.24 – 1.39 Å.[26] Longer oxygen-oxygen bond lengths of 1.43 – 1.50 Å are characteristic of η^2-peroxo bonding modes, encountered in metals with higher oxidation states. Vibrational and NMR (in the case of carbene-based ligands) spectroscopy are also useful tools to further substantiate the oxygen binding mode. Higher vibrational stretching frequencies are indicative of a η^2-superoxo binding motif, while lower stretching frequencies correspond to η^2-peroxo coordination geometries.[26] NMR spectroscopic analysis of the carbene carbon resonance (regarding the examples containing NHC ligands) can further give insight into the rhodium oxidation state.[23] In general, the

© University of Pretoria

rhodium(I) carbene carbons of unsaturated NHC ligands resonate at > $\delta_{Ccarbene}$ 170 ppm, while an upfield NMR shift of more than δ 20 ppm is usually accompanied with a rhodium carbene complex where the rhodium metal has an oxidation state of +3.[23]

A closer look at the bonding interaction is warranted. The bonding situation, based on extensive experimental an theoretical data, has been described as rhodium(I) coordinated by singlet oxygen in a side-on fashion, similar to the bonding scenario of metal-olefins.[25,26] Molecular oxygen coordination results in an σ-bonding interaction between the filled O_2 π-orbital and an empty Rh $4d_{x^2-y^2}$ orbital (Figure 4.2). Additionally, it has been reported that back-bonding arise between the Rh $4d_{xz}$ orbital into the empty O_2 π*-orbital. The back-bonding imparts stabilization towards the singlet oxygen in the ground state (Figure 4.2).[25,26]

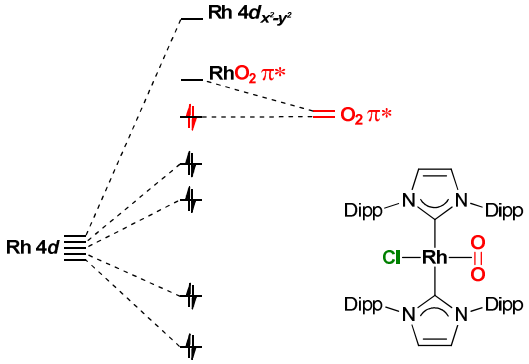

Figure 4.2: Valence MO diagram of bis(NHC)Rh(O_2)(Cl) complex[26]

It has been stated that the ability to stabilize low lying metal 4*d*-orbitals with an unsaturated coordination sphere allows for the isolation of rhodium(I)-oxygen adducts. The necessary stabilization can be achieved through appropriate ligand design. To be more specific, bulky electron rich ligands with π-donor moieties occupying the position *trans* to the molecular oxygen coordination site could be sufficient in terms of stabilization of the metal against oxidation and/or decomposition.[26] π-acceptor ligands can be viewed as having the ability to destabilize the Rh-O_2 bonding interaction which favours oxidation of the metal and reduction of the oxygen motif. The rhodium(I)-oxygen adduct featured a chlorido ligand *trans* to the oxygen moiety (Scheme 4.11). Halide abstraction with a silver salt in acetonitrile as solvent cleanly afforded the rhodium(III)-peroxo complex with two acetonitrile molecules coordinating at the position *trans* to both oxygen atoms. The experimental observation could be explained as follows.[26] The π-donor ligands occupy the coordination position directly *trans* to the center of mass of the O_2 moiety (Scheme 4.11). However, chloride abstraction results in coordination of one π-

© University of Pretoria

accepting acetonitrile ligand that prefers coordination directly *trans* to one oxygen atom. This yields an open coordination site *trans* to the second oxygen atom that is subsequently engaged by the second acetonitrile ligand. Finally, the oxygen-oxygen bond length increases to > 1.43 Å with concomitant oxidation of rhodium(I) to rhodium(III) and reduction of the O_2 double bond to the η^2-peroxo motif (Scheme 4.11).[26]

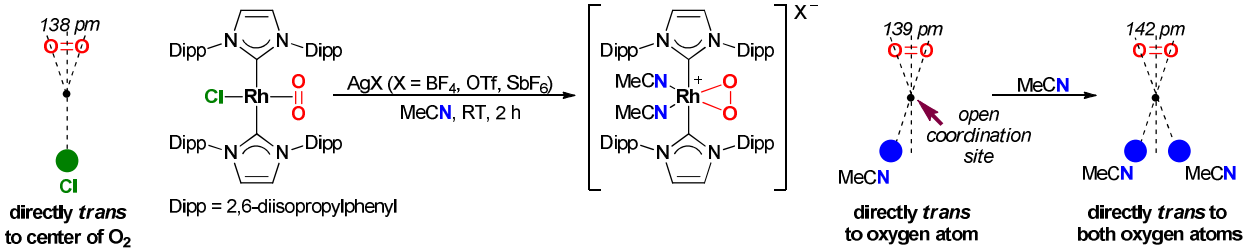

Scheme 4.11: Influence of ligand *trans* to the oxygen ligand[26]

4.2 Aim

It was proposed that the rhodium-oxygen adduct previously prepared by the author, with the strongly donating tridentate ligand could mediate the alkyne functionalization reaction (dimerization, hydrothiolation). For this, the complex synthesis first had to be optimized, as the existing methodology allowed for the preparation of the rhodium-oxygen adducts but with persistent accompanying impurities.

Optimization of the alkyne dimerization reaction, followed by a study on the scope of substrate tolerance is planned for a range of terminal alkynes. The complex reactivity towards the alkyne hydrothiolation reaction is also presented. The optimization of the reaction conditions will be followed by the hydrothiolation of various alkynes with thiols.

Finally, two novel one-pot synthetic procedures towards more elaborated organic products will be attempted. The first includes, if hydrothiolation is found to be successful, the S-H addition reaction of a dithiol across two non-equivalent terminal alkynes. This would result to the preparation of unsymmetrical bis-vinyl sulfides, a reaction that has not been reported to date. The second one-pot tandem reaction would involve a combination of both alkyne dimerization and hydrothiolation reactions. The complete alkyne dimerization reaction would be followed by the hydrothiolation of the formed internal alkyne, yielding the diene products.

© University of Pretoria

4.3 Results and Discussion

4.3.1 Rhodium(I)-oxygen adduct synthesis

The synthesis of the oxygen adducts has already been reported, in the Master's research study preceding this thesis.[1] However, the protocol was adapted to yield the complex with a higher purity after a more extensive work-up procedure. The cationic ligand precursors **L_a** and **L_b** were treated with five equivalents of base, in the presence of the rhodium metal precursor (rhodium dimer $[Rh(C_2H_4)_2Cl]_2$ was used) submerged in THF and cooled down to -78 °C (Scheme 4.12). The THF was evaporated after the reaction was stirred overnight at room temperature. After extraction of the product in hexane and evaporation of the solvent, the residue was re-dissolved in oxygenated toluene and left to settle for 2 days at room temperature. The two rhodium-oxygen-adducts were obtained with > 95% purity after evaporation of the toluene. The carbene carbon resonance is included in Scheme 4.12. Both carbene carbon NMR shifts are slightly upfield compared to the general carbene resonances observed for rhodium(I) NHC complexes (see Section 4.1.3). However, a difference of 2 ppm does not point to rhodium(III) complex formation, but rather a more nucleophilic carbene carbon as can be expected for the more basic triazolylidene ligands compared to classical NHCs. The complexes were then treated with CO in order to gain some insight into the electronic properties of the pincer ligand supported rhodium-oxygen adducts. Bubbling of CO (g) through a hexane solution of **17_b** or a CH_2Cl_2 solution of **16_a**, yielded the rhodium-carbonyl complexes **19_b** and **18_a**, respectively. The carbonyl stretching frequencies were determined to be of low energy, at 1941 cm^{-1} for **19_b** and 1955 cm^{-1} for **18_a** (Scheme 4.12). This suggested that the ligands have strong donor abilities, but not as strong as the NHC analogue (bimca ligand) with a stretching frequency of 1921 cm^{-1}.[27]

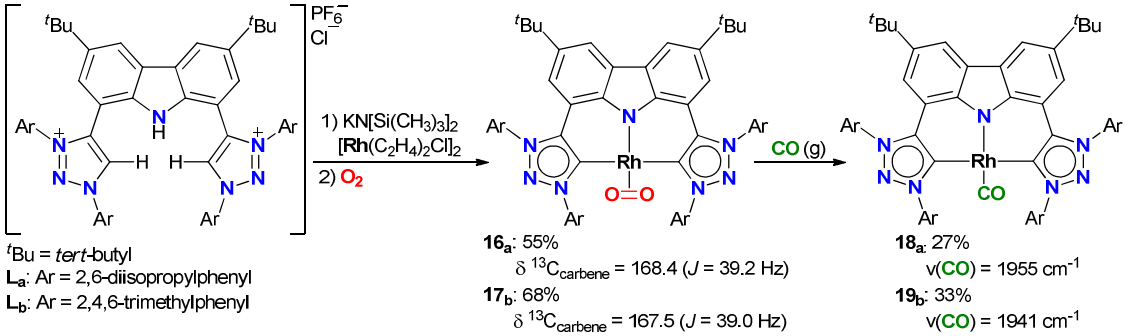

Scheme 4.12: Synthesis of rhodium-oxygen and carbonyl complexes

© University of Pretoria

Crystals suitable for X-ray diffraction analysis for the rhodium-oxygen adduct **16$_a$** were obtained by slow evaporation of a toluene solution (Figure 4.3). The square-planar rhodium metal is π-coordinated by molecular oxygen in a side-on fashion, similar to the rhodium-oxygen adducts discussed in Section 4.1.3. The O8-O9 bond length of 1.375(4) Å is slightly elongated from the oxygen-oxygen bond lengths reported by Crudden for rhodium-oxygen adducts.[23,26] However, this value still falls well within the range of O-O bond lengths for Rh(I)-O_2 adducts (see Section 4.1.3). It could be postulated, based on the studies reported by Crudden[26] and Caulton,[25] that rhodium-oxygen adduct formation is favoured over rhodium oxidation. The bulky electron rich ligand will stabilize the unsaturated rhodium(I) metal center and thus favour oxygen π-coordination in the side-on fashion. The strong π-donating amido moiety further enhances the stabilization of the Rh-O_2 π-interaction. These factors render the rhodium(I)-oxygen adducts resistant against spontaneous oxidation and/or decomposition, even after exposure towards atmospheric conditions for several months.

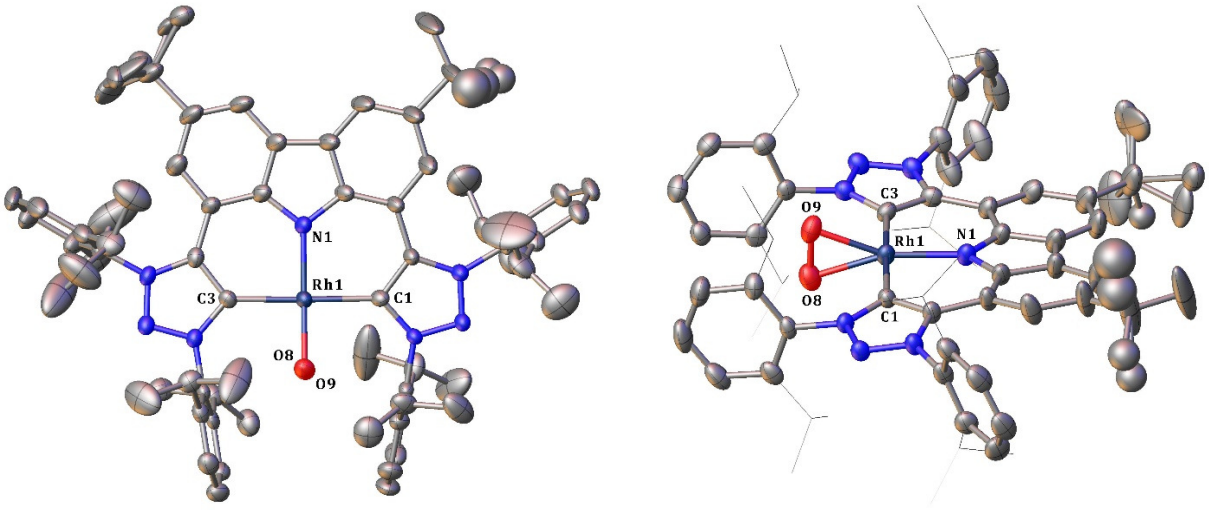

Figure 4.3: Frontal and side-on view of rhodium-oxygen adduct **16$_a$** (Hydrogens and solvent molecules omitted for clarity. The preliminary structure of **16$_a$** has previously been reported,[1] but the refined data set is reported here in the experimental section, chapter 8)

4.3.2 Homo-dimerization of terminal alkynes

The reaction conditions for the homo-dimerization of terminal alkynes catalyzed by **17$_b$** were first optimized. Dimerization of 1-hexyne to 7-methylene-undec-5-yne was chosen as the model reaction. Entry 7, Table 4.1 indicates the optimized reaction conditions for the homo-dimerization of terminal alkynes. Gratifyingly, dimerization of 1-hexyne catalyzed by **17$_b$** yielded the *gem*-enyne isomer with complete selectivity, in addition to complete conversion in less than an hour at 80 °C. This was in

© University of Pretoria

contrast with catalyst **16$_a$**, which showed no activity towards the dimerization reaction. As intuitively expected, the bulkier diisopropylphenyl wingtip substituents of catalyst **16$_a$** impede the coordination of the incoming alkyne, inhibiting catalysis (Table 4.1). It was further realized that no base was required for catalysis, while the addition of pyridine decreased the catalytic activity of **17$_b$** with no added benefit in terms of selectivity, contrasting to the catalyst reported by Oro and co-workers (see Section 4.1.1).[8] Finally, a mercury drop-test did not lead to a decrease of the catalytic activity or selectivity, indicative of a homogeneous reaction mechanism.

Table 4.1: Homo-dimerization of 1-hexyne promoted by **16$_a$** or **17$_b$**[a]

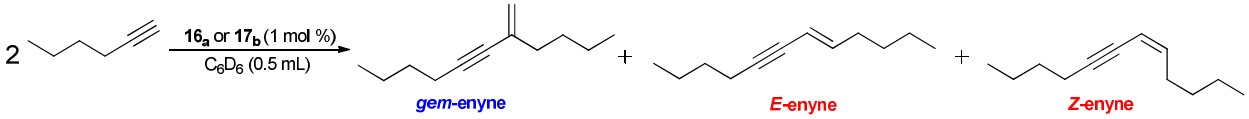

Entry	Catalyst	Base (mol %)	T (°C)	*t* (h)	Conversion[b] (%)	Yield[c] (%)	Product distribution		
							Gem-enyne	*E*-enyne	*Z*-enyne
1	**17$_b$**	K_2CO_3 (1)	80	> 1	> 99	99	100	-	-
2	**17$_b$**	K_2CO_3 (1)	40	> 1	6	4	100	-	-
3	**17$_b$**	KO^{t}Bu (1)	80	> 1	> 99	99	100	-	-
4	**17$_b$**	Pyridine (3)	80	> 1	88	88	100	-	-
5	**16$_a$**	K_2CO_3 (1)	80	> 1	0	0	-	-	-
6	**16$_a$**	K_2CO_3 (1)	80	20	9	3	100	-	-
7	**17$_b$**	None	80	> 1	> 99	99	100	-	-

[a]Reactions performed in C_6D_6 (0.5 mL) with internal standard 1,4-di-*tert*-butylbenzene, 1 mol % catalyst (3.5 x 10^{-6} mol) and 3.5 x 10^{-4} mol 1-hexyne. [b]Conversion as determined through NMR integration based on 1-hexyne referenced to 1,4-di-*tert*-butylbenzene. [c]Yield as determined from NMR integration based on 1-hexyne.

The catalytic activity of **17$_b$** was further scrutinized towards a range of terminal alkynes, featuring various functional groups (Table 4.2). Again, complete selectivity for the *gem*-enyne isomer, out of the possible three isomers, was noted when the substrate alkyne featured an aliphatic substituted terminal alkyne. The reaction with phenylacetylene yielded a mixture of both *gem*- and *E*-enynes, in addition to the yield of the reaction being low. Nonetheless, the air-stable catalyst displayed a high functional group tolerance and, even more appealing is the fact that additives are not required (Table 4.2).

© University of Pretoria

Table 4.2: Homo-dimerization of various terminal alkynes[a]

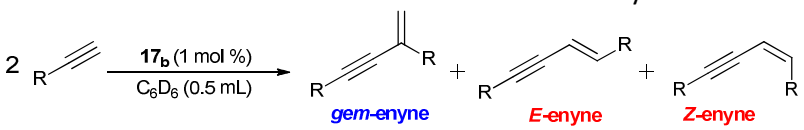

Entry	Substrate	*t* (h)	Conv.[b] (yield[c])	*gem*/*E*/*Z*
1	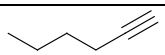	1	>99 (99[c])	100/-/-
2	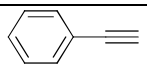	24	72 (11[c])	89/11/-
3	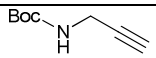	24	96 (89[c])	100/-/-
4	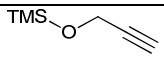	24	69 (62[c])	100/-/-
5	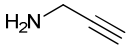	24	59 (42[c])	100/-/-
6	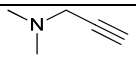	5	>99 (99[c])	100/-/-
7	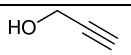	10	48 (21[c])	100/-/-
8	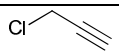	24	77 (11[c])	100/-/-

[a]Reactions performed at 80 °C, with 1 mol % of **17b** in 0.5 mL C_6D_6, and 1,4-di-*tert*-butylbenzene as internal standard. [b]Conversion based on NMR integration (%). [c]NMR yield (%).

A possible explanation for the complete selectivity (exception to this is the use of the aryl substituted alkyne) could be based on the mechanistic studies outlined in Section 4.1.1. Oxidative addition will give rise to the octahedral rhodium(III) intermediate complex, with the rigid pincer ligand closing off three coordination sites in the equatorial positions (Scheme 4.13). The alkynyl and hydride ligands will occupy two more coordination sites, leaving only one coordination site vacant (***int.* 17b**, Scheme 4.13). Based on their strong donor properties and high *trans* influence, the hydride and amido ligands will in all probability not coordinate *trans* with respect to each other. As such, the hydride becomes a directing functionality that directs the attack of the incoming alkyne *trans* into the vacant position (***int.* 17b'** and ***int.* 17b''**, Scheme 4.13). Carbometallation becomes the most probable catalytic route with either 1,2- or 2,1-insertion reactions possible. Based on the experimental observations, a 1,2-insertion is the most likely addition step as this will lead to *gem*-enyne formation. The preference for a 1,2- over 2,1-insertion can be based on steric considerations. The steric bulk of the ligand directs a 1,2- (***int.* 17b'**, Scheme 4.13) rather than a 2,1-insertion (***int.* 17b''**, Scheme 4.13), as this could alleviate steric strain between the substituent on the terminal alkyne and the ligand backbone. Consequently, a 1,2-carbometallation insertion route is followed, yielding the *gem*-enyne after reductive elimination with coordination of

© University of Pretoria

another alkyne to the open vacant site of the rhodium(I) active catalyst. The postulated mechanism is depicted in Scheme 4.13.

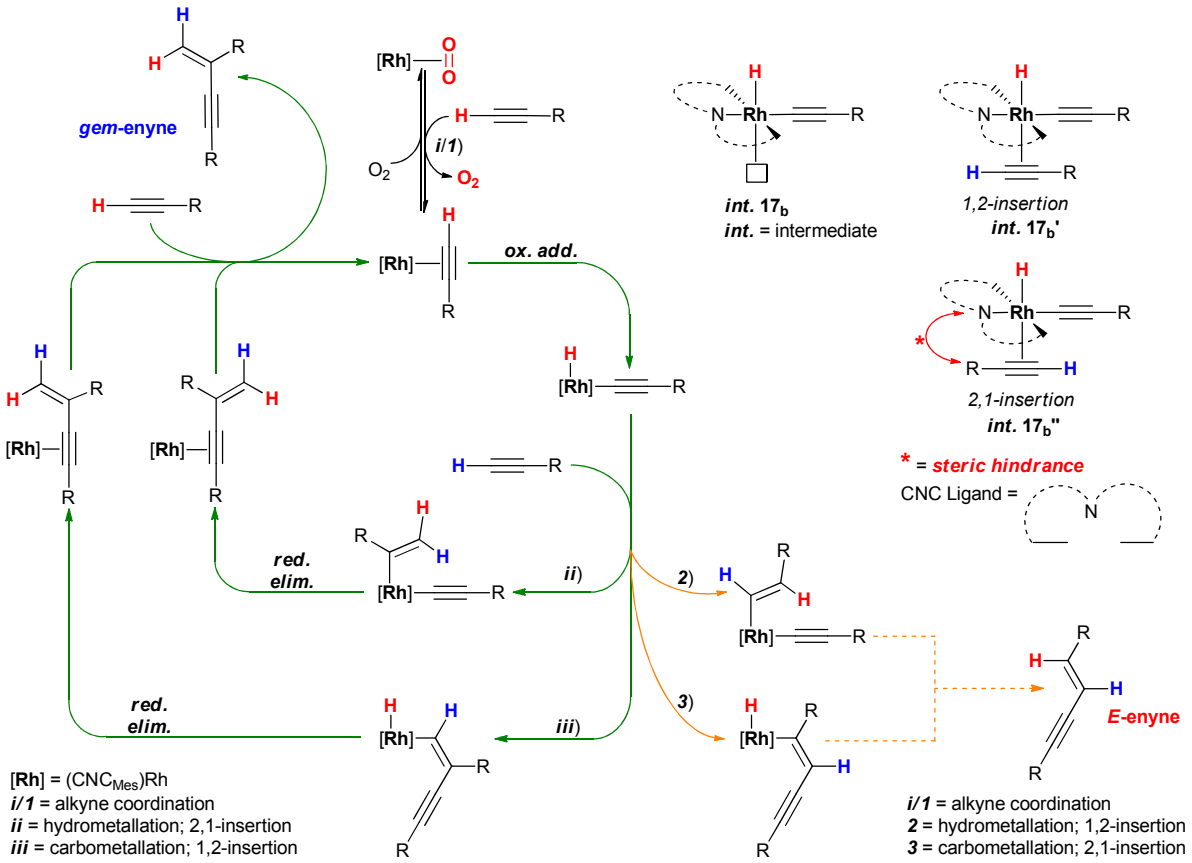

Scheme 4.13: Mechanistic considerations of the alkyne dimerization reaction catalyzed by **17b**

4.3.3 Alkyne hydrothiolation

The rhodium-oxygen adducts were then subjected to the catalytic hydrothiolation of alkynes with thiols. Hydrothiolation of 1-hexyne with thiophenol was used as the model reaction during the optimization of the reaction conditions (Table 4.3). Entry 4 in Table 4.3 indicates the optimized reaction conditions for the hydrothiolation reaction. Unlike the alkyne dimerization, the alkyne hydrothiolation reaction was catalyzed by both rhodium-oxygen adducts. While not surprising, the catalytic activity of **17b** was higher compared to **16a**. Thiol addition across the alkyne was catalyzed by **17b** with more than 90% selectivity for the α-vinyl sulfide isomer with satisfactory conversion and yields after 24 hours at 80 °C (Table 4.3). Again, no base was required while the addition of a directing pyridine additive decreased the catalytic activity of **17b** as well as the selectivity, contrasting to the catalyst reported by Oro and co-workers.[21]

© University of Pretoria

Table 4.3: Hydrothiolation of 1-hexyne (1 equiv.) with thiophenol (1 equiv.) promoted by **16$_a$** or **17$_b$**[a]

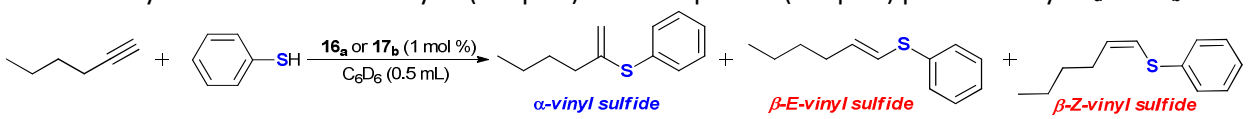

Entry	Catalyst	Base (mol %)	T (°C)	*t* (h)	Conversion (%)[b]	Yield (%)[c]	Product distribution		
							α-vinyl sulfide	β-*E*-vinyl sulfide	β-*Z*-vinyl sulfide
1	**17$_b$**	K_2CO_3 (1)	80	24	77	71	91[d]	6	3
2	**17$_b$**	K_2CO_3 (1)	40	24	14	11	91[d]	5	4
3	**17$_b$**	Pyridine (5)	80	24	74	64	89[d]	8	3
4	**17$_b$**	None	80	24	81	74	91[d]	6	3
5	**16$_a$**	K_2CO_3 (1)	80	24	58	49	92[d]	2	6

[a]Reactions performed in C_6D_6 (0.5 mL) with internal standard 1,4-di-*tert*-butylbenzene, 1 mol % catalyst (3.5 x 10^{-6} mol) and 3.5 x 10^{-4} mol 1-hexyne. [b]Conversion as determined through NMR integration based on 1-hexyne referenced to 1,4-di-*tert*-butylbenzene. [c]Yield of α-vinyl sulfide as determined from NMR integration based on 1-hexyne. [d]Plus unidentified products.

The scope of the catalytic hydrothiolation reaction catalyzed by **17$_b$** was expanded to a range of various terminal alkynes and thiols. Table 4.4 summarizes the different substrates used, as well as the outcome of the catalytic reactions. With regards to the hydrothiolation of aliphatic alkynes with aliphatic thiols, complete selectivity towards the α-vinyl sulfide isomer was noted, in addition to adequate conversion and yields. These results therefore demonstrate that the complex catalyst is comparable to some of the best catalysts reported to date.[19,21,28] A decrease in both catalytic activity and selectivity was noted when aryl substituted alkynes and thiols were employed as substrates, similar to previous reports.[19] Additionally, a radical catalyzed reaction can also be considered for the reaction between phenylacetylene and thiophenol, which would ultimately lead to a mixture of mostly β-*E* and β-*Z* isomers.[9]

© University of Pretoria

Table 4.4: Terminal alkyne hydrothiolation catalyzed by **17b**[a]

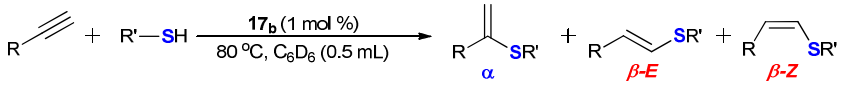

Entry	Alkyne	Thiol	*t* (h)	Conv.[b] (yield[c,d])	α/ β-*E*/ β-*Z*
1	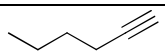	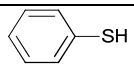	24	81 (74[c], 66[d])	91/6/3
2	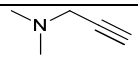	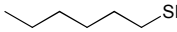	10	>99 (98[c])	100/-/-
3	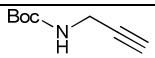	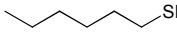	24	>99 (98[c])	100/-/-
4	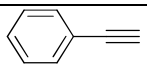	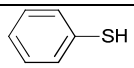	24	59 (23[c])	40/19/41

[a]Reactions performed at 80 °C with 1 mol % of **17b** in C_6D_6 (0.5 mL) with 1,4-di-*tert*-butylbenzene as internal standard. [b]Conversion based on NMR integration. [c]NMR calculated yield for α-vinyl sulfide (%). [d]Isolated yield (%).

The following has to be considered first before a mechanistic scenario can be postulated. No base is required for catalysis, ruling out an acid-base and/or metal-ligand cooperative hydrothiolation catalyzed reaction. A radical catalyzed reaction can also be discarded in the case of Entries 1 to 3 (Table 4.4), as there is complete or near-complete selectivity for the α-vinyl sulfide isomer. Finally, no product of alkyne dimerization is detected. This would imply that the catalyst has a higher affinity for the thiol substrate and S-H oxidative addition is favoured over C-H addition. Therefore, substitution of the oxygen moiety followed by thiol coordination yields the active starting catalyst (Scheme 4.14). Subsequent S-H bond oxidative addition results to the formation of the rhodium(III)-hydrido-thiolate complex. The hydride ligand, being a strong donor ligand, will direct the incoming alkyne to coordinate to the vacant site *trans* with respect to itself and *cis* with regards to the thiolate ligand. A metal-thiolate (M-SR) insertion is followed, with either a 1,2- or a 2-1-insertion reaction being plausible (Scheme 4.14). However, only a 1,2-M-SR insertion can be considered since selectivity is displayed towards the α-vinyl sulfide isomer, while a 2,1-M-SR insertion would have yielded the β-*E*-vinyl sulfide product. Again it can be speculated that the steric bulk of the ligand can account for the direction of the insertion step, with a 2,1-insertion leading to a complex intermediate with a higher energy value due to increased steric hindrance between the substituent on the substrate and the ligand scaffold. Reductive elimination of the 1,2-M-SR insertion product with the hydride ligand ensues, yielding the α-vinyl sulfide product and the active catalyst after coordination of another thiol substrate molecule (Scheme 4.14).

© University of Pretoria

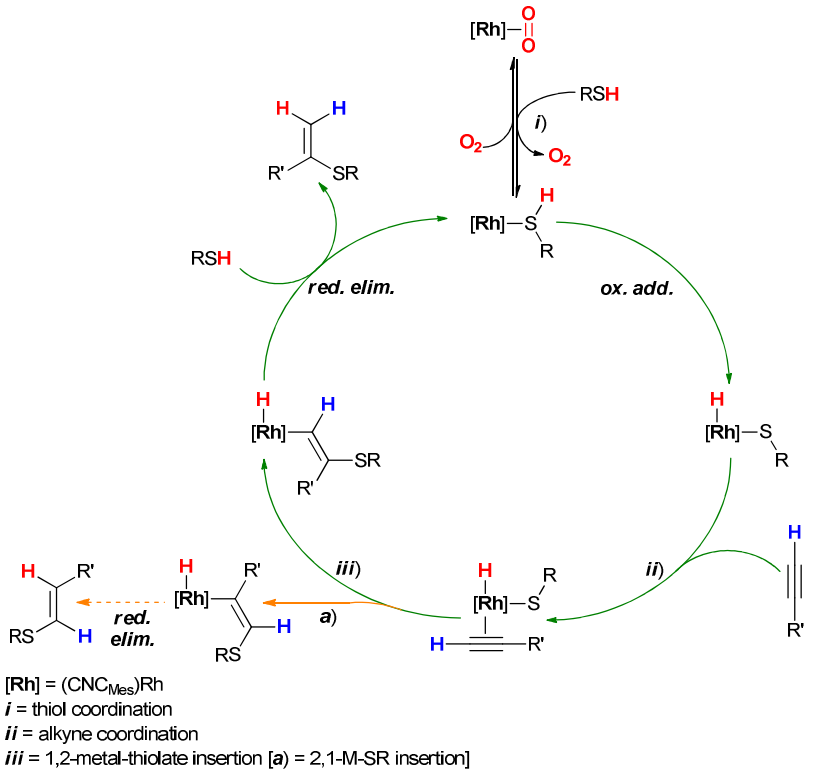

Scheme 4.14: Postulated mechanism for the catalytic hydrothiolation reaction

Encouraged by the catalytic activity and selectivity of the rhodium-oxygen adduct in the catalyzed hydrothiolation reaction, the possibility of preparing unsymmetrical bis-vinyl sulfides was explored. For this sequential bis-hydrothiolation reaction, a dithiol was used with the step-wise addition of different alkynes, which included a terminal and an internal alkyne. As such, one equivalent of a dithiol was treated with one equivalent of a terminal alkyne in the presence of **17$_b$**, dissolved in C_6D_6 at 80 °C (Table 4.5). The mono α-vinyl sulfide was furnished with complete selectivity. A second, different alkyne was then added to the same reaction mixture under atmospheric conditions, which again demonstrated the stability of the complex. The reaction vessel was capped and heated up and upon completion of the reaction the unsymmetrical bis-vinyl sulfide was obtained as the only product of the reaction (Table 4.5). Unsymmetrical bis-vinyl sulfide preparation has not been reported to date, with only a few examples describing the synthesis of symmetrical bis-vinyl sulfides through addition of two equivalents of the same alkyne to a reaction mixture containing one equivalent dithiol.[21] Employing two terminal alkynes resulted in the isolation of bis-α,α'-vinyl sulfides, while the use of an internal alkyne as the second alkyne substrate, yielded the bis-α,β-*E*-vinyl sulfide (Table 4.5).

© University of Pretoria

Table 4.5: Bis-hydrothiolation in a sequential one-pot reaction employing a dithiol and various alkynes[a]

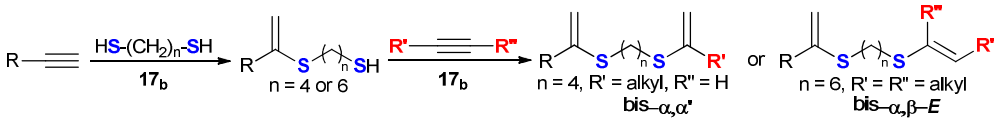

Entry	1st alkyne	Dithiol	*t* (h)	Intermediate Product	Conv.	2nd alkyne	*t* (h)	Final product	Overall conv. (Yield)[b]
1			10	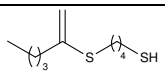	>99		16	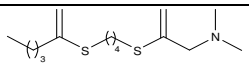	>99 (88)
2			9	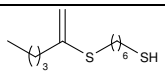	>99	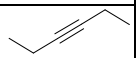	38	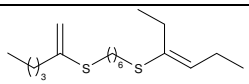	59 (50)

[a]Reaction performed in 0.5 mL C_6D_6, with 2 mol % of **17b** and 1,4-di-*tert*-butylbenzene as internal standard. [b]NMR calculated overall yield (%).

Stacked ^{1}H NMR spectra of the reaction outlined by Entry 1, Table 4.5 demonstrates the step-wise bis-hydrothiolation reaction (Figure 4.4). As is evident from the NMR spectra, the reactions are catalyzed with complete selectivity for one isomer. The blue spectrum portrays the initial time of the experiment (Figure 4.4). The green spectrum exhibits the complete formation of the mono-α-vinyl sulfide with the addition of the second non-equivalent alkyne. The red spectrum corresponds to the final time of the reaction (Figure 4.4). In order to illustrate the relevance of the unsymmetrical bis-hydrothiolation reaction under preparative conditions, the reaction portrayed in Table 4.5 as Entry 1, was scaled up tenfold. The bis-α,α'-vinyl sulfide was isolated as a pure product after elution of the reaction mixture through an aluminum oxide plug, with an overall isolated yield of 47%.

© University of Pretoria

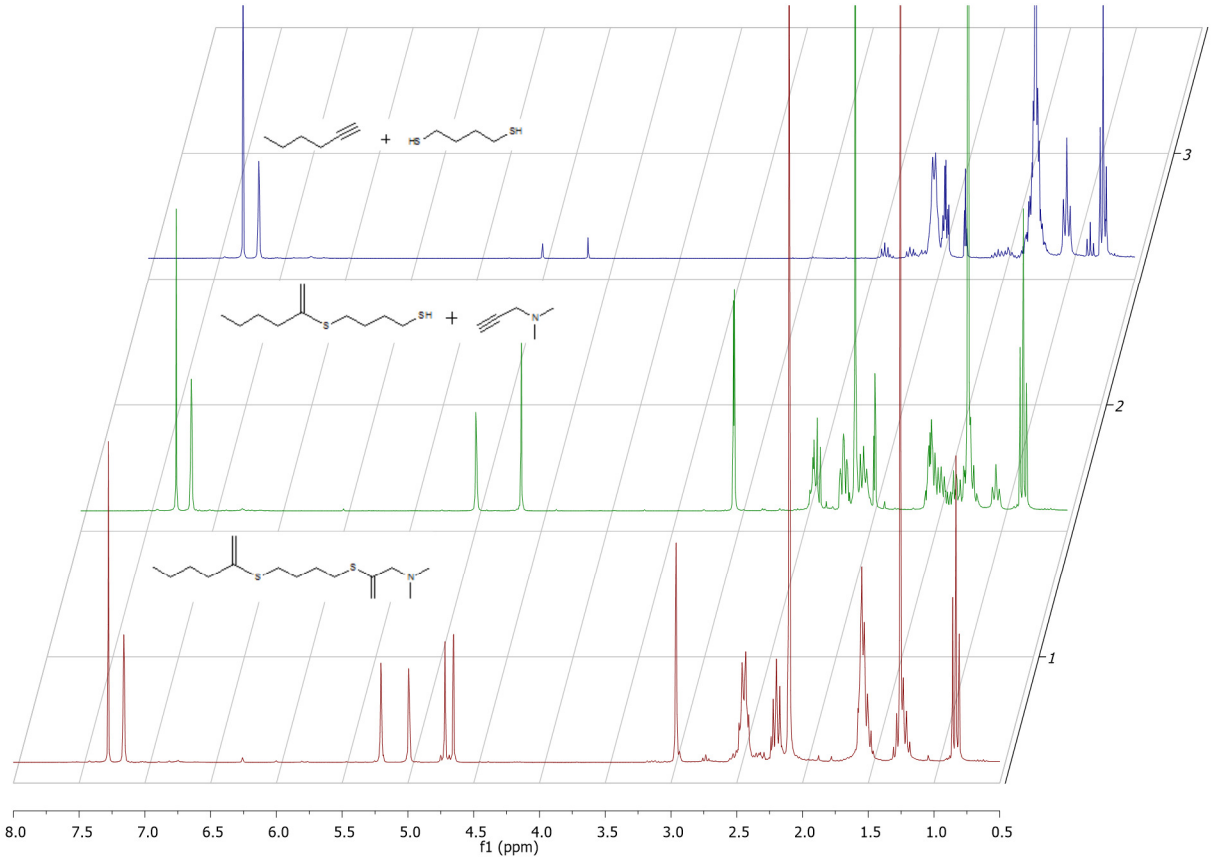

Figure 4.4: Stacked ^{1}H NMR spectra of unsymmetrical bis-hydrothiolation reaction depicted in Table 4.5, Entry 1

4.3.4 Sequential alkyne dimerization-hydrothiolation tandem reaction

Curiosity towards the possibility of a tandem dimerization and hydrothiolation catalyzed reaction was prompted by the success of the rhodium-oxygen adduct in both C-H and S-H addition reactions. As such, dimethylaminopropyne was first dimerized to the corresponding enyne (Table 4.6). As this reaction proceeds with complete selectivity for the *gem*-enyne, no purification is needed in addition to no possible cross-contamination reactions from minor impurities occurring during the sequential reaction. Subsequent addition of hexanethiol to the same reaction mixture containing the *gem*-enyne, yielded the product of a *syn*-addition reaction across the internal alkyne of the enyne (Table 4.6). Again, no attempts were made to exclude air or moisture during the addition of the hexanethiol substrate. Two major products were obtained, namely the 1,3-*gem*-ene-β-*E*-vinyl sulfide and the 1,4-*gem*-ene-β-*E*-vinyl sulfide. The geminal alkene was not affected by the added thiol. It could be concluded that discrimination between the sites of attack across the internal alkyne is not possible, as the two products obtained from the reaction were evenly distributed (overall NMR calculated yield for each product was

© University of Pretoria

29%, see Table 4.6). A minor product was also detected, namely the 1,4-*gem*-ene-β-*Z*-vinyl sulfide isomer. The amount of the *Z*-isomer increased at elevated temperatures and over prolonged periods of time (as determined from NMR spectroscopic analysis), which lead us to postulate an isomerization reaction as a plausible cause for the product formation. Nonetheless, such a cascade reaction has not been reported to date to the best of our knowledge, but only a few reports revolving around the hydrothiolation of pre-prepared enynes with diminished selectivity, while S-H addition occurred over the less challenging terminal alkynes.[21,29] The reaction was also scaled up tenfold, illustrating that the procedure can be completed under preparative conditions. Such a cascade reaction can allow for the mild and easy preparation of elaborate organic products from readily available and fairly inexpensive starting materials.

Table 4.6. Cascade alkyne dimerization/hydrothiolation to form *gem*-ene-vinyl sulfides promoted by **17b**[a]

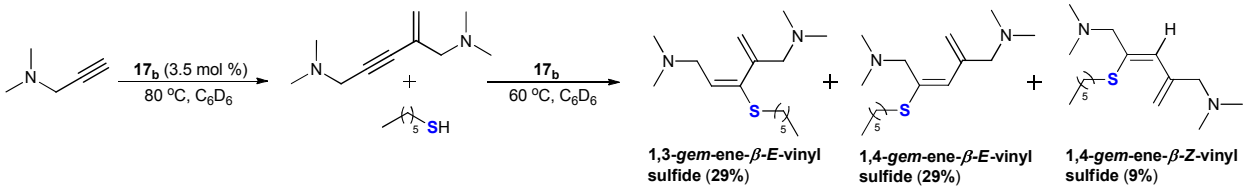

Step 1[b]			Step 2[d]					
T (°C)	*t* (h)	Conversion (%)[c]	T (°C)	*t* (h)	Conversion (%)[c]	Products	Yield (%)[e]	Product Distribution
80	3	> 99	60	48	82	**1,3-*gem*-ene-β-*E*-**	29	44
						1,4-*gem*-ene-β-*E*-	29	43
						1,4-*gem*-ene-β-*Z*-	9	13

[a]Reaction performed in 0.5 mL C_6D_6 with 1,4-di-*tert*-butylbenzene as internal standard and 3.5 mol % catalyst loading. [b]Homo-dimerization of dimethylaminopropyne yielding *N,N,N,N*-tetramethyl-4-methylenepent-2-yne-1,5-diamine. [c]Conversion as determined through NMR integration based on substrate and products referenced to internal standard. [d]Hydrothiolation of internal alkyne of enyne formed after step 1, with 1-hexanethiol. [e]NMR calculated yield.

The stacked ^{1}H NMR spectra of the reaction is displayed in Figure 4.5. The blue spectrum exhibits the reaction at initial time. The spectrum in green displays completion of the alkyne dimerization reaction and the addition of the hexanethiol to the enyne. The red spectrum shows the reaction at completion, with formation of the two major products, the *gem*-ene-β-*E* isomers as well as the *gem*-ene-β-*Z* minor product of isomerization.

© University of Pretoria

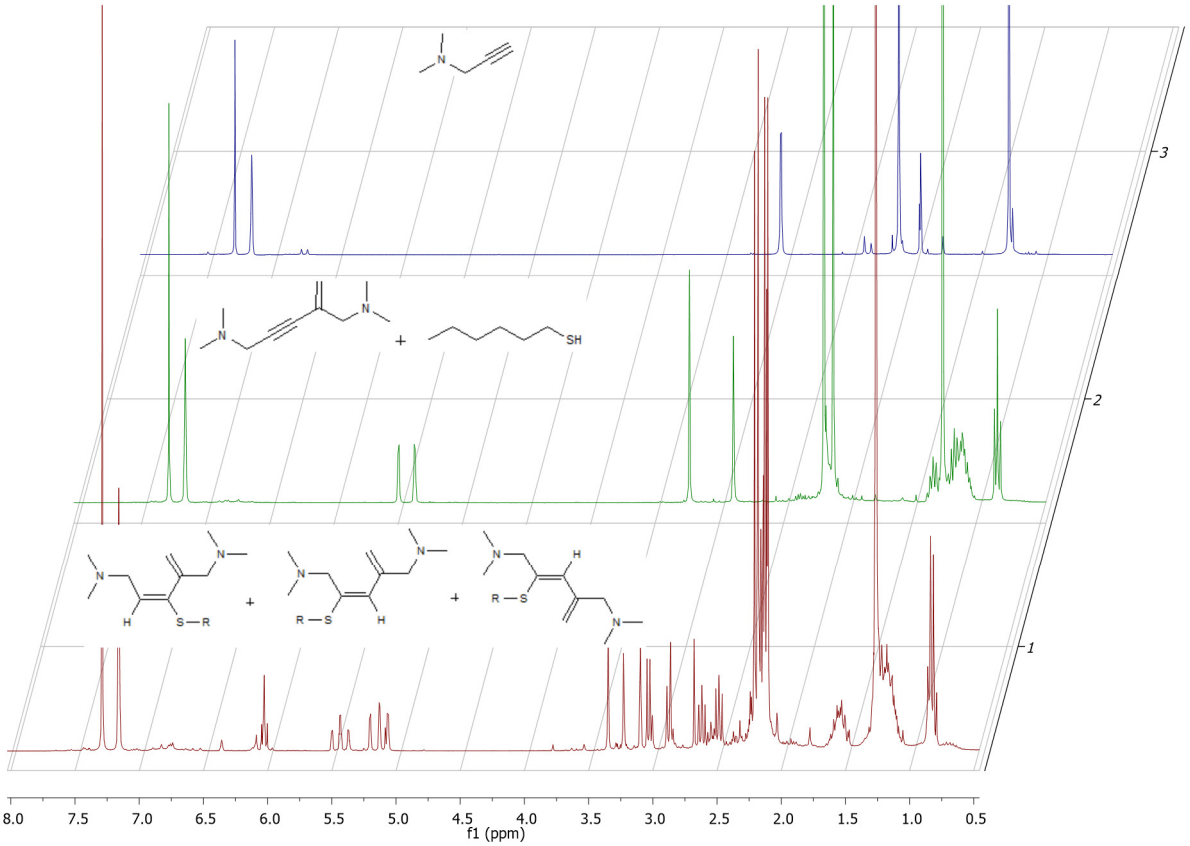

Figure 4.5: Stacked ^{1}H NMR spectra of tandem catalyzed dimerization and hydrothiolation reaction (formation of the minor *Z*-isomer was also noted)

A postulated mechanism is shown in Scheme 4.15 for the one-pot sequential alkyne dimerization-hydrothiolation reaction. After the alkyne dimerization reaction is complete, the coordinated enyne is substituted by the thiol. Thiol S-H oxidative addition is followed by π-coordination of the internal alkyne of the enyne substrate *trans* to the hydride directing ligand. The reaction then proceeds through both 1,2- and 2-1-metal-thiolate insertions. The product of insertion undergoes reductive elimination with the hydride ligand, yielding the *gem*-ene-β-*E*-vinyl sulfides (Scheme 4.15). The complex enters another catalytic cycle after substitution of the diene with an additional thiol substrate.

© University of Pretoria

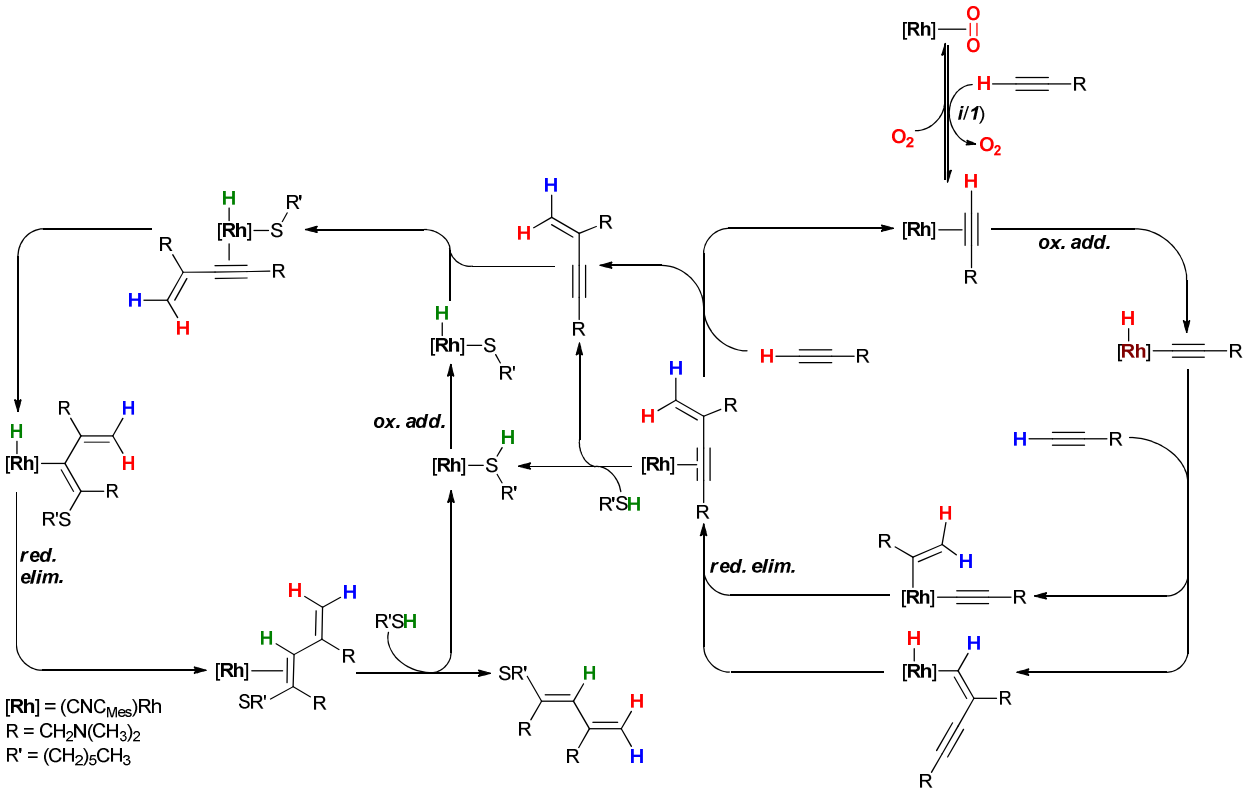

Scheme 4.15: Postulated mechanism for one-pot sequential alkyne dimerization-hydrothiolation tandem reaction

4.4 Conclusion

To summarize, two analogous air-stable rhodium-oxygen adducts **16**$_a$ and **17**$_b$ were synthesized applying an adapted procedure to isolate the products with high purity. Crystal structure determination of **16**$_a$ confirms the side-on π-coordination of molecular oxygen to the square-planar rhodium(I) metal. The rhodium carbonyl analogue complexes were also synthesized through simple treatment of a solution of the rhodium-oxygen adducts with carbon monoxide gas. The carbonyl stretching frequencies suggested that the ligands are strong donor ligands. The use of pincer ligands stabilized the rhodium-oxygen adducts against oxidation and decomposition. The molecular oxygen ligand in turn stabilized the vacant rhodium coordination site, in addition to being easily substituted by alkynes and thiols for the alkyne dimerization and alkyne hydrothiolation catalyzed reactions.

As such, it was shown that the rhodium complexes readily catalyzed the aforementioned alkyne functionalization reactions with excellent selectivity. For both dimerization and hydrothiolation catalyzed reactions, no base or additives were required with appreciable catalytic activity as only 1 mol % catalyst loading is needed for catalysis. For the alkyne dimerization reaction, the *gem*-enyne is the

© University of Pretoria

isomer obtained while the hydrothiolation reaction yields the α-vinyl sulfide product. In both reactions, complete selectivity was obtained when aliphatic substituted substrates were employed, while the selectivity diminished if aromatic substituted substrates were used. The possibility of unsymmetrical bis-hydrothiolation reactions was also explored. The step-wise treatment of a dithiol with non-equivalent alkynes allowed for the synthesis of the unsymmetrical bis-vinyl sulfides with complete selectivity in one-pot.

Finally, the two alkyne functionalization reactions were combined in the first example of a one-pot tandem catalyzed alkyne dimerization and hydrothiolation reaction. The alkyne was first dimerized to the corresponding *gem*-enyne. To the same reaction mixture was added hexanethiol, which resulted to formation of the 1,3-*gem*-ene-β-*E* and 1,4-*gem*-ene-β-*E* vinyl sulfide isomers as the two major isomers of the reaction with a 1:1 ratio. The minor product of isomerization was also obtained, namely the 1,4-*gem*-ene-β-*Z*-vinyl sulfide.

4.5 Experimental

4.5.1 Synthesis of $(CNC_{Dipp})Rh(I)O_2$ (16_a)

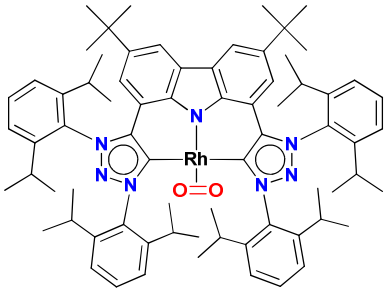

A flame dried Schlenk tube was loaded with $\mathbf{L_a}$ (200.0 mg, 1.6 x 10^{-4} mol), $[Rh(C_2H_4)_2Cl]_2$, (50.3 mg, 1.3 x 10^{-4} mol) and $KN[Si(CH_3)_3]_2$ (161.3 mg, 8.1 x 10^{-4} mol). The Schlenk tube was evacuated and purged with N_2 (g). The reaction vessel was cooled down to -78 °C, and the solids dissolved by addition of THF (20 mL) which was also cooled down to -78 °C. The solution was stirred for one hour at -78 °C. The reaction, after one hour, was slowly heated up to RT whilst stirring overnight. The solvents were evaporated *in vacuo* and the product was extracted with hexanes (4 x 15 mL). Evaporation of the hexane solvent, *in vacuo*, yielded a brown residue. The residue was re-dissolved in oxygenated dry toluene, and left to settle at RT for 48 hours. After 48 hours, the solution was filtered and the solvent evaporated *in vacuo* to obtain $\mathbf{16_a}$ (105.0 mg, 8.8 x 10^{-5} mol, 55%) as a brown solid. Slow evaporation of a toluene solution yielded single crystals suitable for XRD analysis. **^{1}H NMR** δ_H (C_6D_6, 400 MHz) 8.40 (d, *J* = 2.0 Hz, 2H, Ar**H**$_{carb}$), 7.49 (d, *J* = 2.0 Hz, 2H, Ar**H**$_{carb}$), 7.34 (t, *J* = 7.8 Hz, 2H, Ar**H**$_{Dipp}$), 7.30 (t, *J* = 7.8 Hz, 2H, Ar**H**$_{Dipp}$), 7.16 (d, 4H, Ar**H**$_{Dipp}$ overlaps with C_6D_6), 7.13 (d, *J* = 8.0 Hz, 4H, Ar**H**$_{Dipp}$), 2.98 (sept, *J* = 6.8 Hz, 4H,

© University of Pretoria

C**H**(CH_3)$_2$), 2.66 (sept, *J* = 6.8 Hz, 4H, C**H**(CH_3)$_2$), 1.65 (d, *J* = 6.8 Hz, 12H, CH(C**H**$_3$)$_2$), 1.23 (d, *J* = 7.2 Hz, 12H, CH(C**H**$_3$)$_2$), 1.21 (s, 18H, C(C**H**$_3$)$_3$), 1.05 (d, *J* = 6.8 Hz, 12H, CH(C**H**$_3$)$_2$), 0.78 (d, *J* = 6.8 Hz, 12H, CH(C**H**$_3$)$_2$). **^{13}C NMR** δ_C (C_6D_6, 100 MHz) 168.4 (d, *J* = 39.2 Hz, Rh-**C**$_{Carbene}$), 146.3 (Ar**C**$_q$), 145.4 (Ar**C**$_q$), 144.4 (Ar**C**$_q$), 141.6 (Ar**C**$_q$), 140.6 (Ar**C**$_q$), 137.5 (Ar**C**$_q$), 135.3 (Ar**C**$_q$), 131.7 (Ar**C**H), 129.1 (Ar**C**H), 125.5 (Ar**C**H), 121.6 (Ar**C**H), 119.6 (Ar**C**H), 116.7 (Ar**C**H), 113.2 (Ar**C**$_q$), 34.6 (**C**(CH_3)$_3$), 32.0 (C(**C**H$_3$)$_3$), 29.6 (**C**H(CH_3)$_2$), 29.1 (**C**H(CH_3)$_2$), 26.0 (CH(**C**H$_3$)$_2$), 24.8 (CH(**C**H$_3$)$_2$), 24.3 (CH(**C**H$_3$)$_2$), 23.2 (CH(**C**H$_3$)$_2$). **HRMS** (FIA-ESI): Calculated for $C_{72}H_{90}N_7RhO_2^{2+}$ $[M]^{2+}$: 593.8105, found: 593.8127. **Elemental analysis calc.** (%) for $RhC_{72}H_{90}N_7O_2$: C, 72.77; H, 6.53; N, 8.25. Found: C, 71.65; H, 7.40; N, 7.76.

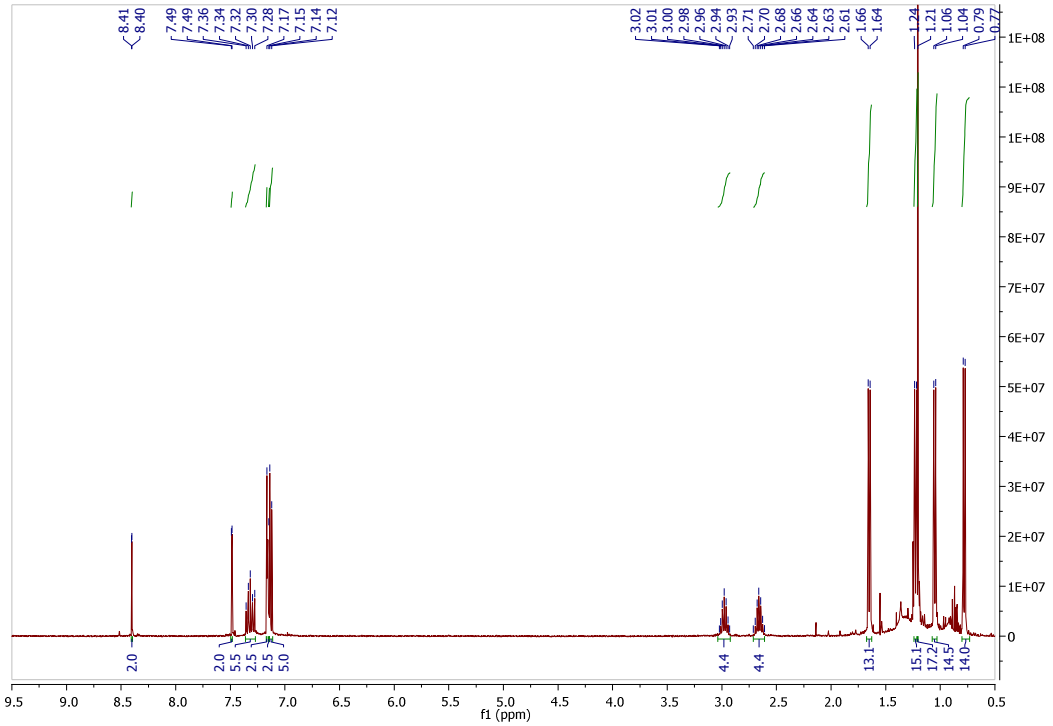

Figure 4.6: ^{1}H NMR spectrum of **16$_a$** in C_6D_6 solvent

© University of Pretoria

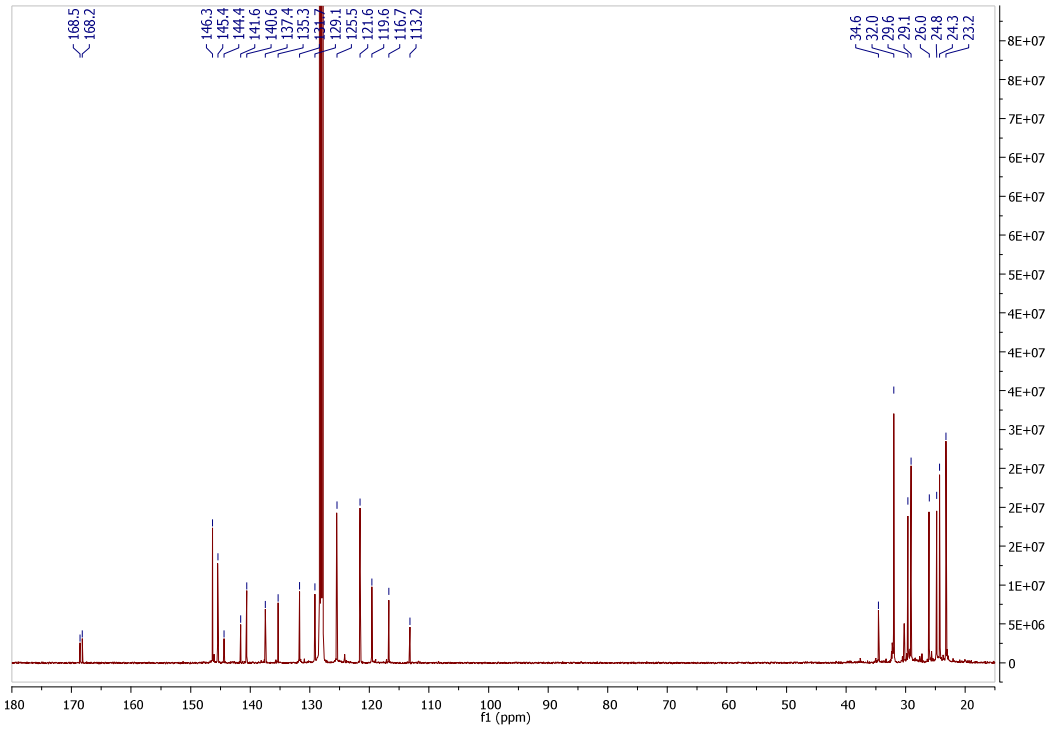

Figure 4.7: ^{13}C NMR spectrum of **16$_a$** in C_6D_6 solvent

4.5.2 Synthesis of (CNC$_{Mes}$)Rh(I)O$_2$ (17$_b$)

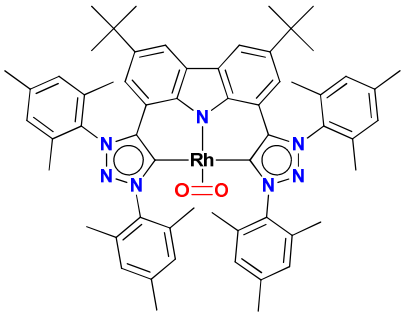

A flame dried Schlenk tube was charged with **L$_b$** (200.0 mg, 1.9 x 10^{-4} mol), $[Rh(C_2H_4)_2Cl]_2$ (58.2 mg, 1.5 x 10^{-4} mol) and $KN[Si(CH_3)_3]_2$ (186.7 mg, 9.4 x 10^{-4} mol). The reaction vessel was evacuated, purged with N_2 (g), and cooled down to -78 °C. The solids were dissolved by addition of THF (20 mL) which was also cooled down to -78 °C. The solution was stirred for one hour at -78 °C. After one hour, the reaction was slowly heated up to RT whilst stirring overnight. The solvent was evaporated *in vacuo* and the product was extracted with hexanes (4 x 15 mL). Hexane was evaporated, *in vacuo*, yielding a brown residue. The residue was re-dissolved in oxygenated dry toluene, and left to settle at RT for 48 hours. After 48 hours, the solution was filtered and the solvent evaporated *in vacuo* to obtain **17$_b$** (130.0 mg, 1.3 x 10^{-4} mol, 68%) as a brown solid. Crystal suitable for X-ray diffraction could not be obtained. **^{1}H NMR** δ_H (C_6D_6, 300 MHz) 8.55 (d, *J* = 1.8 Hz, 2H, Ar**H**$_{carb}$), 7.55 (d, *J* = 1.8 Hz, 2H, Ar**H**$_{carb}$), 6.78 (s, 4H, Ar**H**$_{Mes}$), 6.71 (s, 4H, Ar**H**$_{Mes}$), 2.43 (s, 12H, ArC**H**$_3$), 2.34 (s, 6H, ArC**H**$_3$), 2.08 (s, 6H, ArC**H**$_3$), 1.77 (s, 12H, ArC**H**$_3$), 1.25 (s, 18H, C(C**H**$_3$)$_3$). **^{13}C NMR** δ_C (C_6D_6, 75 MHz) 167.5 (d, *J* = 39.0 Hz, Rh-**C**$_{Carbene}$), 144.4

© University of Pretoria

(Ar**C**$_q$), 141.1 (Ar**C**$_q$), 140.8 (Ar**C**$_q$), 140.4 (Ar**C**$_q$), 138.3 (Ar**C**$_q$), 137.2 (Ar**C**$_q$), 135.7 (Ar**C**$_q$), 135.7 (Ar**C**$_q$), 134.9 (Ar**C**$_q$), 130.0 (Ar**C**H), 127.2 (Ar**C**H), 118.1 (Ar**C**H), 116.4 (Ar**C**H), 113.9 (Ar**C**$_q$), 113.9 (Ar**C**$_q$), 34.7 (**C**(CH$_3$)$_3$), 31.9 (C(**C**H$_3$)$_3$), 21.4 (Ar**C**H$_3$), 21.3 (Ar**C**H$_3$), 21.0 (Ar**C**H$_3$), 21.0 (Ar**C**H$_3$), 18.4 (Ar**C**H$_3$), 18.4 (Ar**C**H$_3$), 17.2 (Ar**C**H$_3$), 17.2 (Ar**C**H$_3$). **HRMS** (FIA-ESI): Calculated for $C_{60}H_{66}N_7RhO_2^{2+}$ [M + CH_3CN + 2H]$^{2+}$: 531.2377, found: 531.2393. **Elemental analysis calc.** (%) for $RhC_{60}H_{66}N_7O_2$: C, 70.64; H, 6.52; N, 9.61. Found: C, 68.52; H, 6.42; N, 9.01.

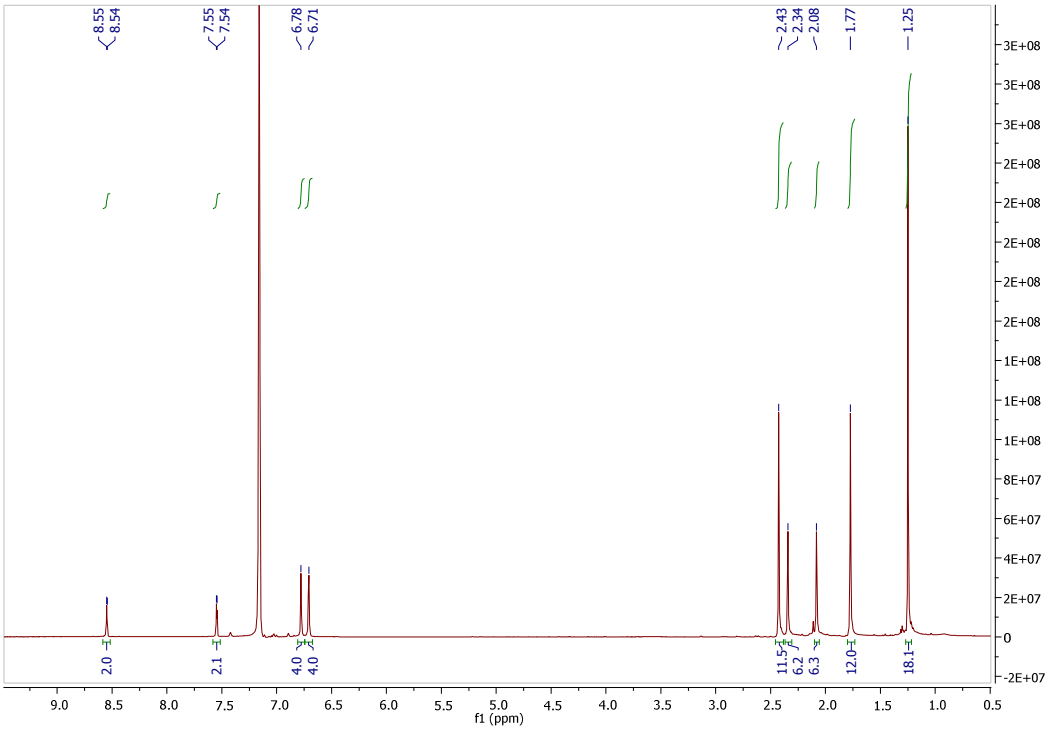

Figure 4.8: ^{1}H NMR spectrum of **17$_b$** in C_6D_6 solvent

© University of Pretoria

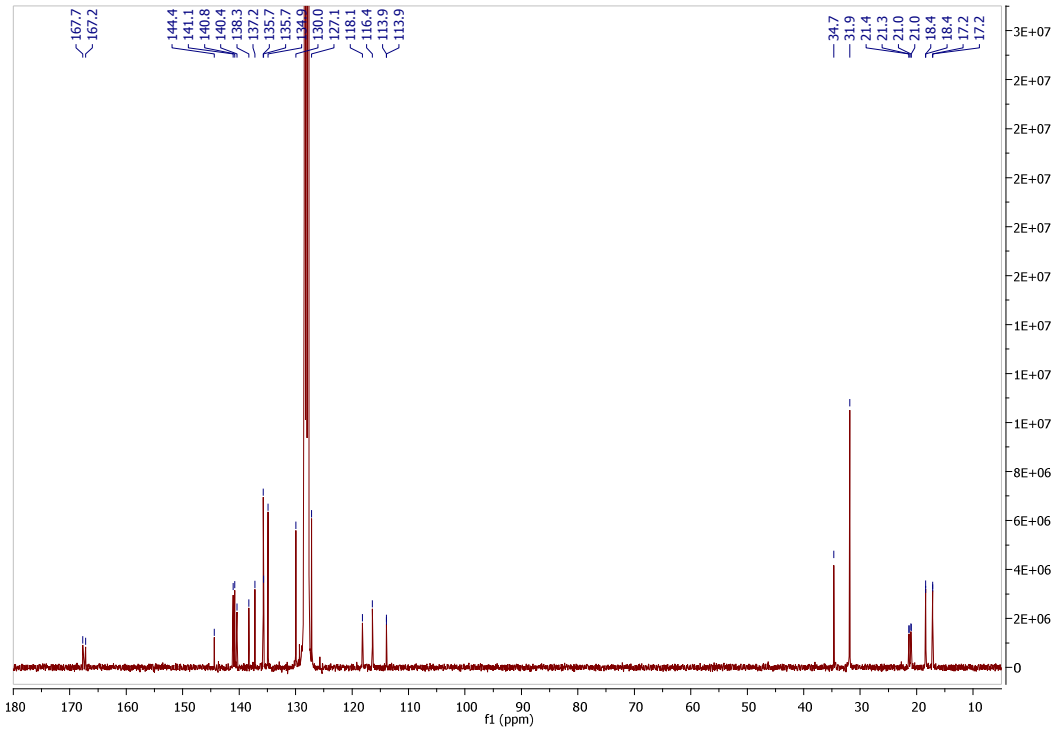

Figure 4.9: ^{13}C NMR spectrum of **17$_b$** in C_6D_6 solvent

4.5.3 Synthesis of (CNC$_{Dipp}$)Rh(I)CO (18$_a$)

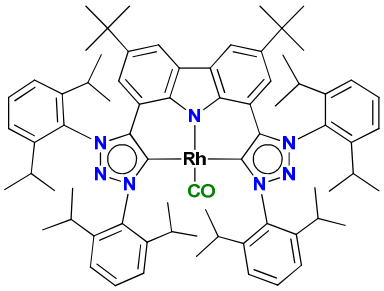

To a Schlenk tube was added **16$_a$** (30.0 mg, 2.5 x 10^{-5} mol), and dissolved by adding CH_2Cl_2 (2 mL) resulting in a brown coloured solution. At room temperature, CO (g) was bubbled through the solution resulting in a colour change from brown to a yellow-brown. The solution was filtered and the solvent removed *in vacuo* yielding **18$_a$** (8.0 mg, 6.8 x 10^{-6} mol, 27%) as a yellow-brown coloured residue. **^{1}H NMR** δ_H (C_6D_6, 300 MHz) 8.52 (d, *J* = 1.8 Hz, 2H, Ar**H**$_{carb}$), 7.64 (dd, *J* = 5.7 Hz, 3.3 Hz, 1H, Ar**H**$_{Dipp}$), 7.46 (d, *J* = 1.5 Hz, 2H, Ar**H**$_{carb}$), 7.31 – 7.25 (m, 6H, Ar**H**$_{Dipp}$), 6.93 (dd, *J* = 5.7 Hz, 3.3 Hz, 1H, Ar**H**$_{Dipp}$), 3.04 (sept, *J* = 6.8 Hz, 4H, C**H**$(CH_3)_2$), 2.62 (sept, *J* = 6.8 Hz, 4H, C**H**$(CH_3)_2$), 1.55 (d, *J* = 6.9 Hz, 12H, CH(C**H**$_3)_2$), 1.25 (s, 18H, C(C**H**$_3)_3$), 1.16 (d, *J* = 6.9 Hz, 12H, CH(C**H**$_3)_2$), 1.04 (d, *J* = 6.9 Hz, 12H, CH(C**H**$_3)_2$), 0.78 (d, *J* = 6.9 Hz, 12H, CH(C**H**$_3)_2$). **^{13}C NMR** δ_C (C_6D_6, 75 MHz) 195.4 (d, *J* = 70.2 Hz, Rh-**C**O), 173.4 (d, *J* = 41.6 Hz, Rh-**C**$_{Carbene}$), 146.3 (Ar**C**$_q$), 146.1 (Ar**C**$_q$), 144.4 (Ar**C**$_q$), 142.7 (Ar**C**$_q$), 138.2 (Ar**C**$_q$), 137.6 (Ar**C**$_q$), 135.7 (Ar**C**$_q$), 133.4 (Ar**C**$_q$), 131.5 (Ar**C**H), 130.9 (Ar**C**H), 130.8 (Ar**C**H), 129.1 (Ar**C**H), 127.2 (Ar**C**$_q$), 125.4 (Ar**C**H), 124.1 (Ar**C**H), 119.0 (Ar**C**H), 117.1 (Ar**C**H), 111.8 (Ar**C**$_q$), 34.5 (**C**$(CH_3)_3$), 32.3 (C(**C**$H_3)_3$), 29.3 (**C**$H(CH_3)_2$), 29.1

© University of Pretoria

(**C**H(CH$_3$)$_2$), 25.6 (CH(**C**H$_3$)$_2$), 24.8 (CH(**C**H$_3$)$_2$), 24.2 (CH(**C**H$_3$)$_2$), 23.1 (CH(**C**H$_3$)$_2$). **FTIR** (CH_2Cl_2): 1955 cm^{-1}. **HRMS** (FIA-ESI): Calculated for $C_{72}H_{90}N_7RhCO^{2+}$ $[M + H]^{2+}$: 592.8204, found: 592.8197. **Elemental analysis calc.** (%) for $RhC_{73}H_{90}N_7O$: C, 74.02; H, 7.66; N, 8.28. Found: C, 71.87; H, 7.51; N, 7.87.

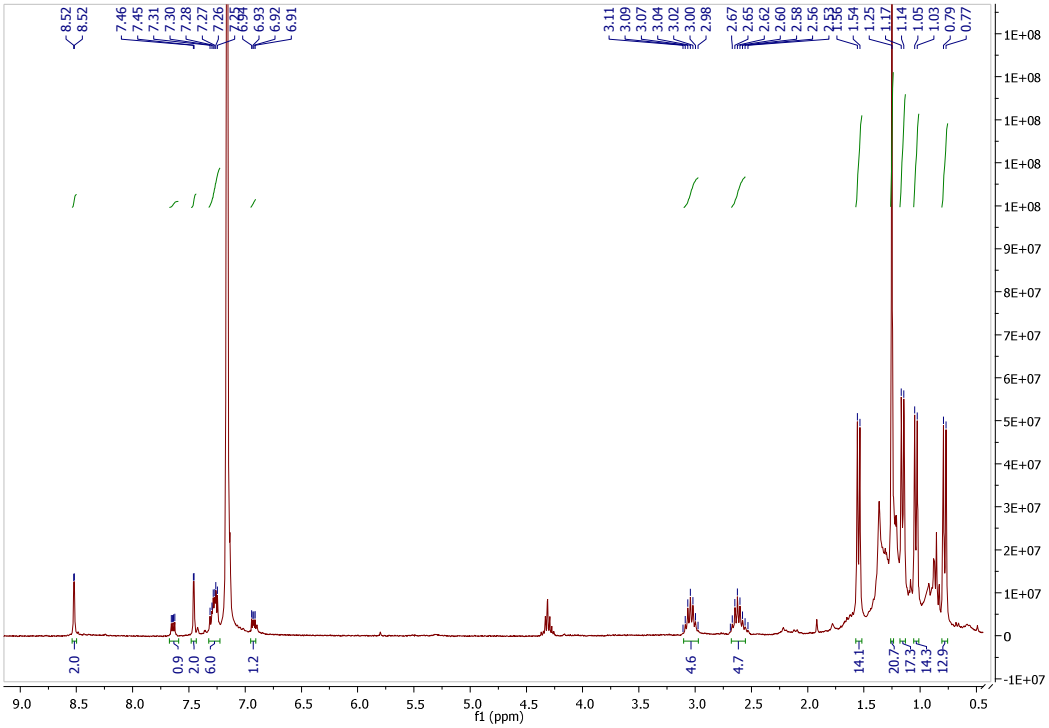

Figure 4.10: ^{1}H NMR spectrum of **18$_a$** in C_6D_6 solvent

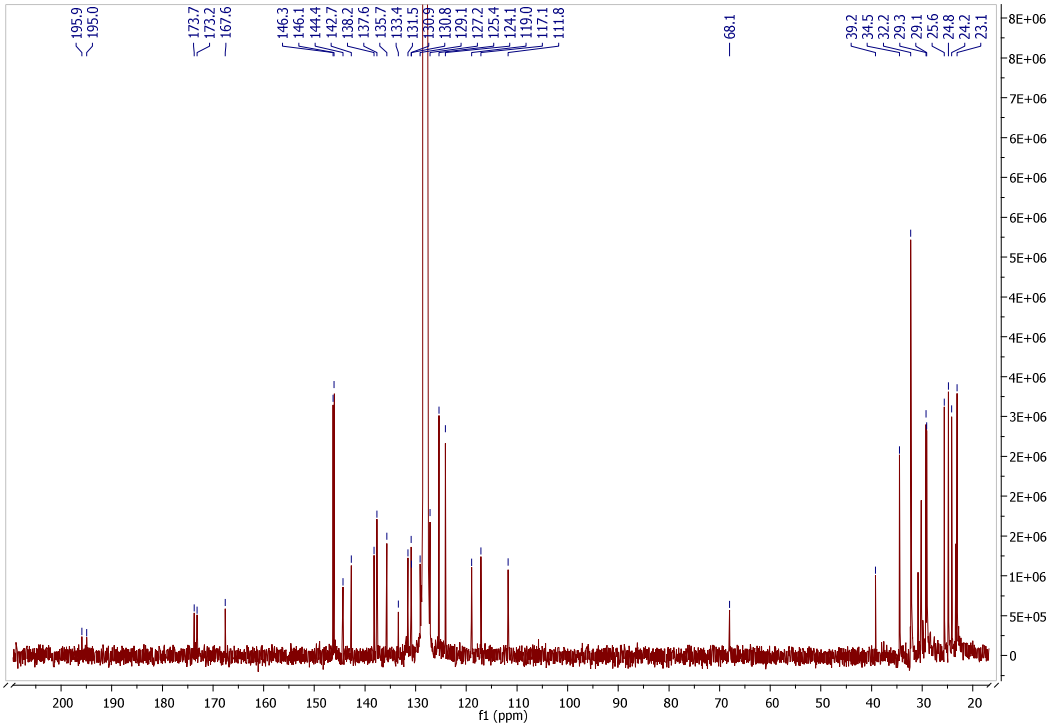

Figure 4.11: ^{13}C NMR spectrum of **18$_a$** in C_6D_6 solvent

© University of Pretoria

4.5.4 Synthesis of (CNC$_{Mes}$)Rh(I)CO (**19$_b$**)

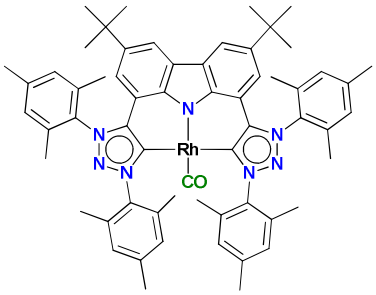

To a flame dried Schlenk tube was added **17$_b$** (25.0 mg, 2.5 x 10^{-5} mol). The reaction vessel was purged with N_2 (g). The brown solid was dissolved by adding hexane (5 mL). Carbon monoxide gas was bubbled through the solution for 5 minutes, resulting in a colour change from dark brown to orange. After filtration, the solvent was removed *in vacuo*, yielding **19$_b$** (8.3 mg, 8.2 x 10^{-6} mol, 33%) as an orange solid. **^{1}H NMR** δ_H (C_6D_6, 300 MHz) 8.67 (d, *J* = 1.8 Hz, 2H, Ar**H**$_{carb}$), 7.42 (d, *J* = 1.8 Hz, 2H, Ar**H**$_{carb}$), 6.84 (s, 4H, Ar**H**$_{Mes}$), 6.73 (s, 4H, Ar**H**$_{Mes}$), 2.40 (s, 12H, ArC**H**$_3$), 2.31 (s, 6H, ArC**H**$_3$), 2.09 (s, 6H, ArC**H**$_3$), 1.78 (s, 12H, ArC**H**$_3$), 1.30 (s, 18H, C(C**H**$_3$)$_3$). **^{13}C NMR** δ_C (C_6D_6, 75 MHz) 194.9 (d, *J* = 71.6 Hz, Rh-**C**O), 173.4 (d, *J* = 41.1 Hz, Rh-**C**$_{Carbene}$), 144.9 (Ar**C**$_q$), 141.3 (Ar**C**$_q$), 140.6 (Ar**C**$_q$), 139.1 (Ar**C**$_q$), 138.3 (Ar**C**$_q$), 138.0 (Ar**C**$_q$), 136.1 (Ar**C**$_q$), 135.7 (Ar**C**$_q$), 135.6 (Ar**C**$_q$), 129.9 (Ar**C**H), 129.0 (Ar**C**H), 127.1 (Ar**C**$_q$), 117.9 (Ar**C**H), 116.9 (Ar**C**H), 112.7 (Ar**C**$_q$), 34.6 (**C**(CH$_3$)$_3$), 32.1 (C(**C**H$_3$)$_3$), 21.5 (Ar**C**H$_3$), 21.0 (Ar**C**H$_3$), 18.7 (Ar**C**H$_3$), 17.3 (Ar**C**H$_3$). **FTIR** (CH_2Cl_2): 1941 cm^{-1}. **HRMS** (FIA-ESI): Calculated for $C_{60}H_{66}N_7RhCO^+$ [M]$^+$: 1015.4384, found: 1015.4407. **Elemental analysis calc.** (%) for $RhC_{61}H_{66}N_7O$: C, 72.10; H, 6.55; N, 9.65. Found: C, 70.37; H, 6.71; N, 9.15.

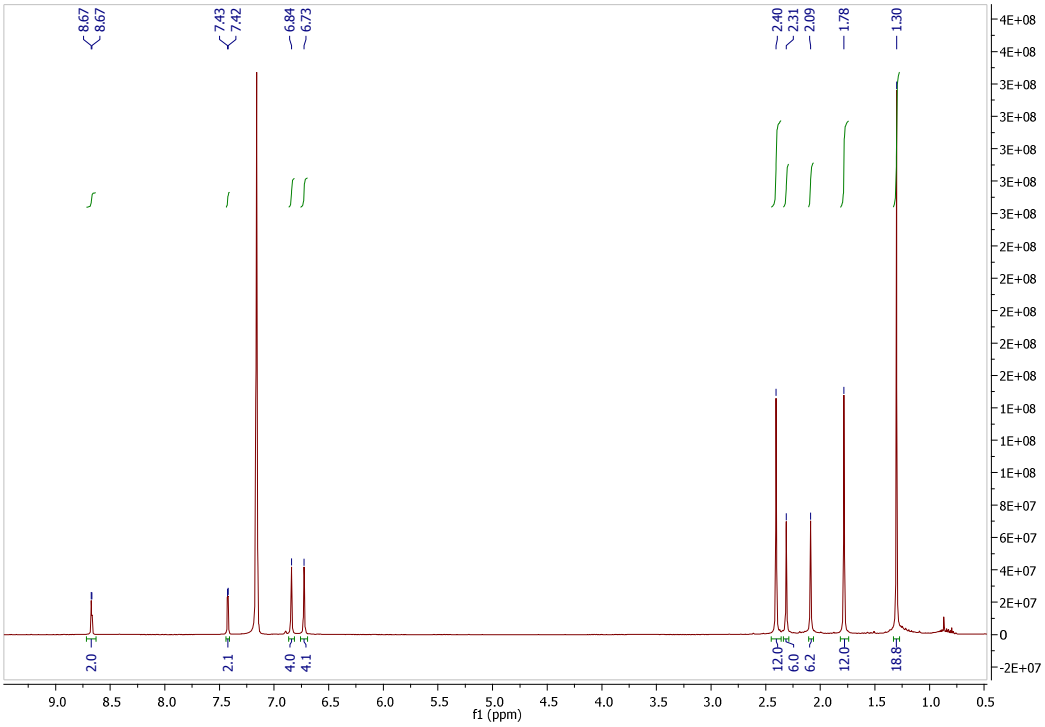

Figure 4.12: ^{1}H NMR spectrum of **19$_b$** in C_6D_6 solvent

© University of Pretoria

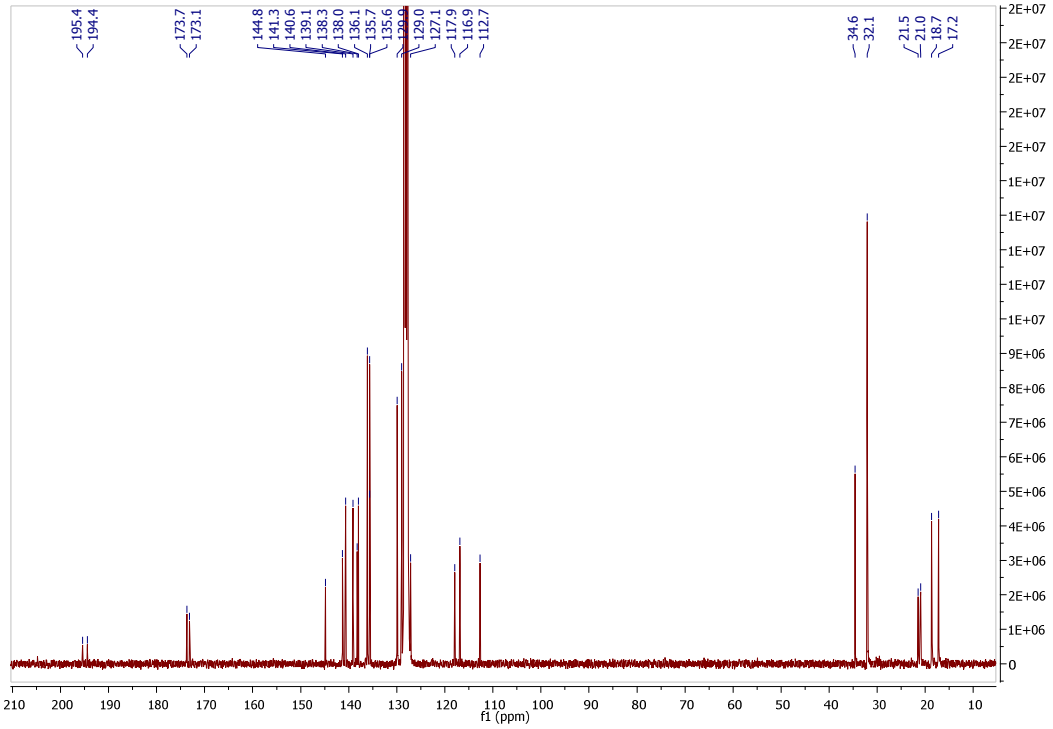

Figure 4.13: ^{13}C NMR spectrum of **19$_b$** in C_6D_6 solvent

4.5.5 Optimization of alkyne dimerization reaction conditions

Standard operating procedure for optimization of dimerization reaction conditions: a high pressure NMR tube with a J. Young valve was charged with one mol % catalyst **17$_b$** (3.6 mg, 3.5 x 10^{-6} mol) or one mol % catalyst **16$_a$** (4.1 mg, 3.5 x 10^{-6} mol) and 0.25 equivalents of internal standard, 1,4-di-*tert*-butylbenzene (16.6 mg, 8.7 x 10^{-5} mol). Catalytic amount of base was added as indicated in Table 4.1. To the mixture was added deuterated benzene (0.5 mL). One equivalent of 1-hexyne (40 µL, 3.5 x 10^{-4} mol) was added, and the NMR tube capped. ^1H NMR spectroscopy was performed at time 10 min after addition of the alkyne. The reaction mixture was heated up to appropriate temperature and reacted for the duration as indicated (see Table 4.1). Upon cooling down to room temperature, ^1H NMR spectroscopy was performed at the final time. Conversion and calculated yields where determined from NMR analysis based on integration of alkyne and product, referenced to the internal standard. Product identity was confirmed by comparison with previously reported NMR spectra.[8]

© University of Pretoria

7-methylene-undec-5-yne

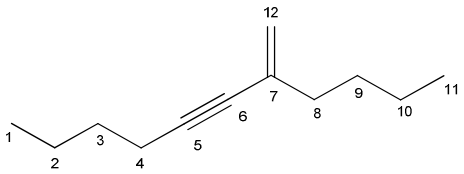

^{1}H NMR δ_H (C_6D_6, 300 MHz) 5.38 (d, *J* = 2.1 Hz, 1H, C=C**H**$_2$), 5.09 (m, 1H, C=C**H**$_2$), 2.16 (m, 8H, **H**$_{4,8}$), 1.59 (tt, *J* = 7.2 Hz, 7.5 Hz, 7.8 Hz, 2H, **H**$_9$), 1.43 - 1.23 (m, 6H, **H**$_{2,3,10}$ overlaps with -C(C**H**$_3$)$_3$ of di-*tert*-butylbenzene), 0.86 and 0.78 (both t, *J* = 7.2 Hz, 6H, **H**$_{1,11}$).

4.5.6 Dimerization of terminal alkynes

Standard operating procedure for dimerization of various alkynes: a high pressure NMR tube with a J. Young valve was loaded with one mol % catalyst **17$_b$** and 0.25 equivalents of internal standard, 1,4-di-*tert*-butylbenzene. To the mixture was added deuterated benzene (0.5 mL). One equivalent of terminal alkyne was added, and the NMR tube capped. ^{1}H NMR spectroscopy was performed at time 10 min after addition of the alkyne. The reaction mixture was heated up to 80 °C and reacted for the duration as indicated (see Table 4.2). Upon cooling down to room temperature, ^{1}H NMR spectroscopy was performed at the final time. Conversion and calculated yields where determined from NMR analysis based on integration of alkyne and product, referenced to the internal standard.

Entry 2, Table 4.2: Dimerization of Phenylacetylene

Experiments were carried out as described above. Amounts of reagents added are as follows: catalyst 1 mol % (3.7 mg, 3.6 x 10^{-6} mol); internal standard 0.25 equivalent (17.3 mg, 9.1 x 10^{-5} mol) and one equivalent phenylacetylene (40 µL, 3.6 x 10^{-4} mol). Product identity was confirmed by comparison with previously reported NMR spectra.[8]

© University of Pretoria

1,3-diphenylbut-1-yn-3-ene

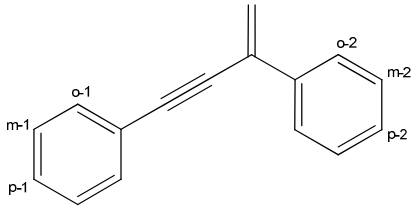

^{1}H NMR δ_H (C_6D_6, 300 MHz) 7.77 - 7.68 (m, 2H, $\mathbf{H}_{o\text{-}1}$), 7.54 - 7.38 (m, 2H, $\mathbf{H}_{o\text{-}2}$, extensive overlap with unreacted phenylacetylene, *E*-enyne, internal standard and residual solvent), 7.09 - 6.87 (m, 6H, $\mathbf{H}_m$ and H_p, extensive overlap with unreacted phenylacetylene, *E*-enyne and internal standard), 5.75 (d, *J* = 0.8 Hz, 1H, C=C$\mathbf{H}_2$), 5.70 (d, *J* = 0.7 Hz, 1H, C=C$\mathbf{H}_2$).

Entry 3, Table 4.2: Dimerization of *N*-Boc-Propargylamine

Experiments were carried out as described above. Amounts of reagents added are as follows: catalyst 1 mol % (2.6 mg, 2.6 x 10^{-6} mol); internal standard 0.25 equivalent (12.3 mg, 6.4 x 10^{-5} mol) and one equivalent *N*-Boc-propargylamine (40 mg, 2.6 x 10^{-4} mol). Product identity was confirmed by comparison with previously reported NMR spectra.[30]

N,N-bis(tert-butyloxycarbonyl)-4-methylenepent-2-yne

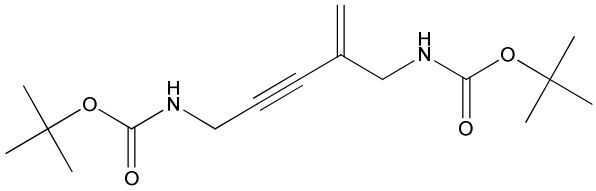

^{1}H NMR δ_H (C_6D_6, 300 MHz) 5.26 (br s, 1H, C=C$\mathbf{H}_2$), 5.15 (d, *J* = 1 Hz, 1H, C=C$\mathbf{H}_2$), 4.57 (br s, 2H, $CH_2N\mathbf{H}$), 3.82 (d, *J* = 2.8 Hz, 2H, C$\mathbf{H}_2$NH), 3.66 (d, *J* = 5.3 Hz, 2H, C$\mathbf{H}_2$NH), 1.42 (s, 9H,-C(C$\mathbf{H}_3$)$_3$), 1.39 (s, 9H,-C(C$\mathbf{H}_3$)$_3$).

Entry 4, Table 4.2: Dimerization of trimethylsilyloxypropyne

Experiments were carried out as described above. Amounts of reagents added are as follows: catalyst 1 mol % (3.3 mg, 3.3 x 10^{-6} mol); internal standard 0.25 equivalent (15.5 mg, 8.1 x 10^{-5} mol) and one equivalent trimethylsilyloxypropyne (50 µL, 3.3 x 10^{-4} mol). Product identity was confirmed by comparison with previously reported NMR spectra.[31]

© University of Pretoria

2-trimethylsiloxymethyl-4-trimethylsiloxy-1-penten-3-yne

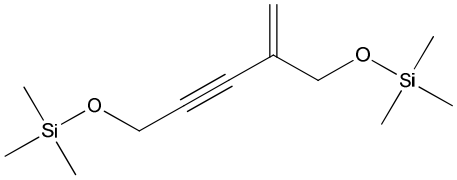

^{1}H NMR δ_H (C_6D_6, 300 MHz) 5.64 (q, *J* = 2.0 Hz, 1H, C=C**H**$_2$), 5.51 (d, *J* = 1.8 Hz, 1H, C=C**H**$_2$), 4.28 (s, 2H, OC**H**$_2$), 4.14 (t, *J* = 1.8 Hz, 2H, OC**H**$_2$), 0.12 (s, 9H, Si(C**H**$_3$)$_3$), 0.06 (s, 9H, Si(C**H**$_3$)$_3$).

Entry 5, Table 4.2: Dimerization of propargylamine

Experiments were carried out as described above. Amounts of reagents added are as follows: catalyst 1 mol % (4.8 mg, 4.7 x 10^{-6} mol); internal standard 0.25 equivalent (22.3 mg, 1.2 x 10^{-4} mol) and one equivalent propargylamine (30 µL, 4.7 x 10^{-4} mol).

4-methylenepent-2-yne-1,5-diamine

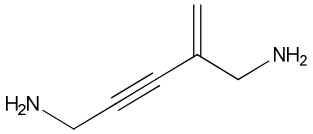

^{1}H NMR δ_H (C_6D_6, 300 MHz) 5.34 (br s, 1H, C=C**H**$_2$), 5.19 (d, *J* = 1.7 Hz, 1H, C=C**H**$_2$), 3.18 (br s, 4H, C**H**$_2$NH$_2$), 0.75 (br s, 4H, CH$_2$N**H**$_2$).

Entry 6, Table 1: Dimerization of *N*,*N*-dimethylaminopropyne

Experiments were carried out as described above. Amounts of reagents added are as follows: catalyst 1 mol % (3.8 mg, 3.7 x 10^{-6} mol); internal standard 0.25 equivalent (17.7 mg, 9.3 x 10^{-5} mol) and one equivalent *N*,*N*-dimethylaminopropyne (40 µL, 3.7 x 10^{-4} mol). Product identity was confirmed by comparison with previously reported NMR spectra.[8]

N,N,N,N-tetramethyl-4-methylenepent-2-yne-1,5-diamine

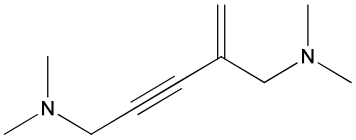

© University of Pretoria

^{1}H NMR δ_H (C_6D_6, 300 MHz) δ 5.50 (d, *J* = 2.1 Hz, 1H, C=C**H**$_2$), 5.38 (m, 1H, C=C**H**$_2$), 3.24 (s, 2H, C**H**$_2$N(CH$_3$)$_2$), 2.90 (s, 2H, C**H**$_2$N(CH$_3$)$_2$), 2.19 (s, 6H, CH$_2$N(C**H**$_3$)$_2$), 2.12 (s, 6H, CH$_2$N(C**H**$_3$)$_2$).

Entry 7, Table 4.2: Dimerization of propargyl alcohol

Experiments were carried out as described above. Amounts of reagents added are as follows: catalyst 1 mol % (4.4 mg, 4.3 x 10^{-6} mol); internal standard 0.25 equivalent (20.4 mg, 1.1 x 10^{-4} mol) and one equivalent propargyl alcohol (25 µL, 4.3 x 10^{-4} mol). Product identity was confirmed by comparison with previously reported NMR spectra of similar enyne alcohol-type compounds.[32]

4-methylenepent-2-yne-1,5-diol

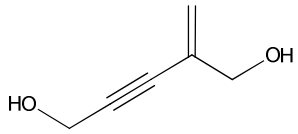

^{1}H NMR δ_H (C_6D_6, 300 MHz) 5.37 (br s, 1H, C=C**H**$_2$), 5.34 (br s, 1H, C=C**H**$_2$), 4.09 (s, 2H, C**H**$_2$OH), 3.96 (s, 2H, C**H**$_2$OH), 2.05 (br s, 2H, CH$_2$O**H**).

Entry 8, Table 4.2: Dimerization of propargyl chloride

Experiments were carried out as described above. Amounts of reagents added are as follows: catalyst 1 mol % (2.8 mg, 2.8 x 10^{-6} mol); internal standard 0.25 equivalent (13.2 mg, 6.9 x 10^{-5} mol) and propargyl chloride, 1 equivalent (20 µL, 2.8 x 10^{-4} mol). Product identity was confirmed by comparison with previously reported NMR spectra of similar enyne chloro-type compounds.[33]

1,5-dichloro-4-methylenepent-2-yne

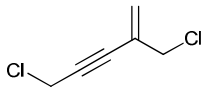

^{1}H NMR δ_H (C_6D_6, 300 MHz) 5.64 (t, *J* = 6.2 Hz, 2H, C=C**H**$_2$), 4.59 (s, 2H, C**H**$_2$Cl), 4.57 (s, 2H, C**H**$_2$Cl).

© University of Pretoria

4.5.7 Optimization of alkyne hydrothiolation reaction conditions

Standard operating procedure for optimization of hydrothiolation reaction conditions. A high pressure NMR tube with a J. Young valve was charged with one mol % catalyst **17$_b$** (4.0 mg, 3.9 x 10^{-6} mol) or one mol % catalyst **16$_a$** (4.7 mg, 3.9 x 10^{-6} mol) and 0.25 equivalents of internal standard, 1,4-di-*tert*-butylbenzene (18.6 mg, 9.8 x 10^{-5} mol). Catalytic amount of base was added as indicated in Table 4.3. To the mixture was added deuterated benzene (0.5 mL). One equivalent of 1-hexyne (45 µL, 3.9 x 10^{-4} mol) and one equivalent of thiophenol (40 µL, 3.9 x 10^{-4} mol) were added, and the NMR tube capped. ^{1}H NMR spectroscopy was performed at time 10 min after addition of the substrates. The reaction mixture was heated up to the appropriate temperature and reacted for the duration as indicated (see Table 4.3). Upon cooling down to room temperature, ^{1}H NMR spectroscopy was performed at the final time. Conversion and calculated yields were determined from NMR analysis based on the integration of substrates and product, referenced to the internal standard. Product identity was confirmed by comparison with previously reported NMR spectra.[34]

2-Phenylthio-1-hexene

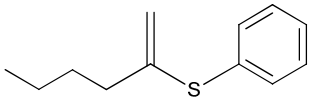

^{1}H NMR δ_H (C_6D_6, 300 MHz) 7.44 - 7.40 (m, 2H, Ar**H**), 7.05 - 6.96 (m, 3H, Ar**H** overlaps with unreacted thiophenol), 5.06 (s, 1H, C=C**H**$_2$), 4.97 (s, 1H, C=C**H**$_2$), 2.20 (t, *J* = 7.6 Hz, 2H, C**H**$_2$), 1.50 (tt, *J* = 7.6 Hz, 7.5 Hz, 2H, C**H**$_2$), 1.26 - 1.16 (m, 2H, C**H**$_2$ overlaps with C(CH_3)$_3$ of internal standard), 0.80 (t, *J* = 7.3 Hz, 3H, C**H**$_3$).

4.5.8 Hydrothiolation of terminal alkynes

Standard operating procedure for hydrothiolation reactions: a high pressure NMR tube with a J. Young valve was loaded with one mol % catalyst **17$_b$** and 0.25 equivalents of internal standard, 1,4-di-*tert*-butylbenzene. To the mixture was added deuterated benzene (0.5 mL). One equivalent of terminal alkyne and thiol was added, and the NMR tube capped. ^{1}H NMR spectroscopy was performed at time 10 min after addition of the substrates. The reaction mixture was heated up to 80 °C and reacted for the

© University of Pretoria

duration as indicated (Table 4.4). Upon cooling down to room temperature, ^{1}H NMR spectroscopy was performed at the final time. Conversion and calculated yields where determined from NMR analysis based on integration of alkyne and product, referenced to the internal standard.

Entry 2, Table 4.4: Hydrothiolation of *N,N*-dimethylaminopropyne with 1-hexanethiol

Experiments were carried out as mentioned. Amounts of reagents added are as follows: 1 mol % catalyst (3.2 mg, 3.2 x 10^{-6} mol); internal standard 0.25 equivalent (15.1 mg, 7.9 x 10^{-5} mol); one equivalent *N,N*-dimethylaminopropyne (34.1 µL, 3.2 x 10^{-4} mol) and one equivalent 1-hexanethiol (45 µL, 3.2 x 10^{-4} mol).

N,N-dimethyl-2-hexylthioprop-2-en-1-amine

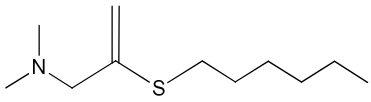

^{1}H NMR δ_H (C_6D_6, 300 MHz) 5.24 (t, *J* = 1.0 Hz, 1H, C=C**H**$_2$), 4.78 (s, 1H, C=C**H**$_2$), 3.00 (s, 2H, C**H**$_2$N(CH$_3$)$_2$), 2.56 (t, *J* = 7.3 Hz, 2H, C**H**$_2$), 2.12 (s, 6H, CH$_2$N(C**H**$_3$)$_2$), 1.53 (tt, *J* = 7.5 Hz, 7.2 Hz, 2H, C**H**$_2$), 1.27 - 1.11 (m, 6H, (C**H**$_2$)$_3$ overlaps with C(CH$_3$)$_3$ of internal standard), 0.82 (t, *J* = 0.8 Hz, 3H, C**H**$_3$). **^{13}C NMR** δ_C (C_6D_6, 75 MHz) 145.7, 106.3, 66.3, 45.1, 31.8, 31.0, 29.2, 28.7, 22.9, 14.2.

© University of Pretoria

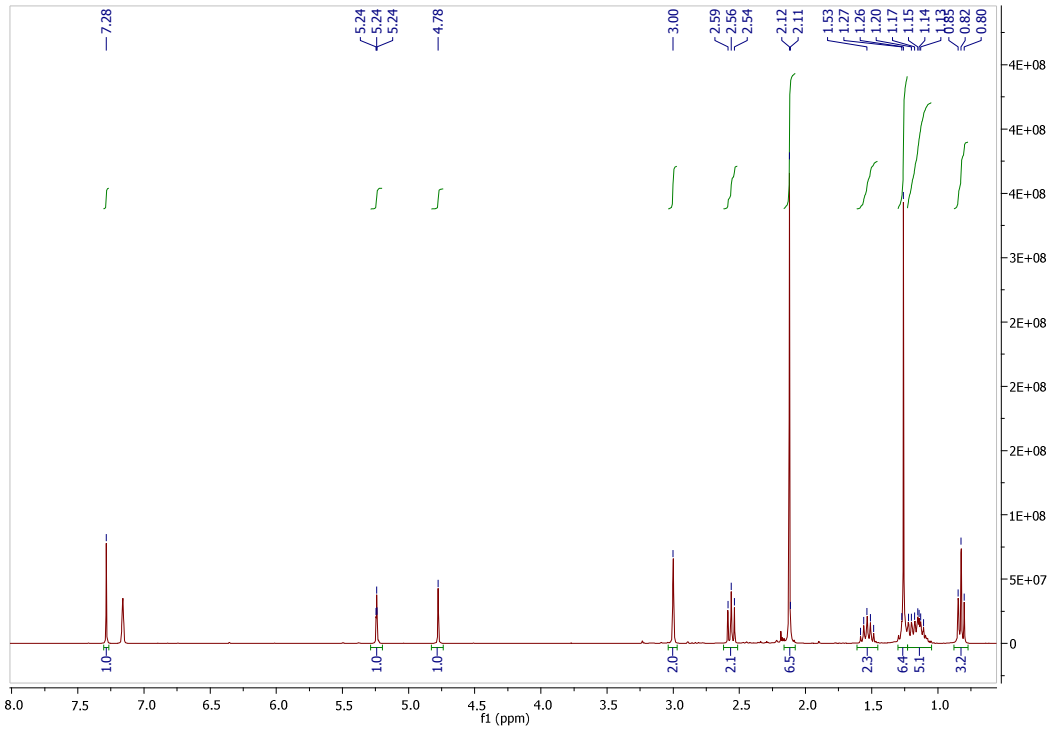

Figure 4.14: ^{1}H NMR spectrum of *N,N*-dimethyl-2-hexylthioprop-2-en-1-amine in C_6D_6

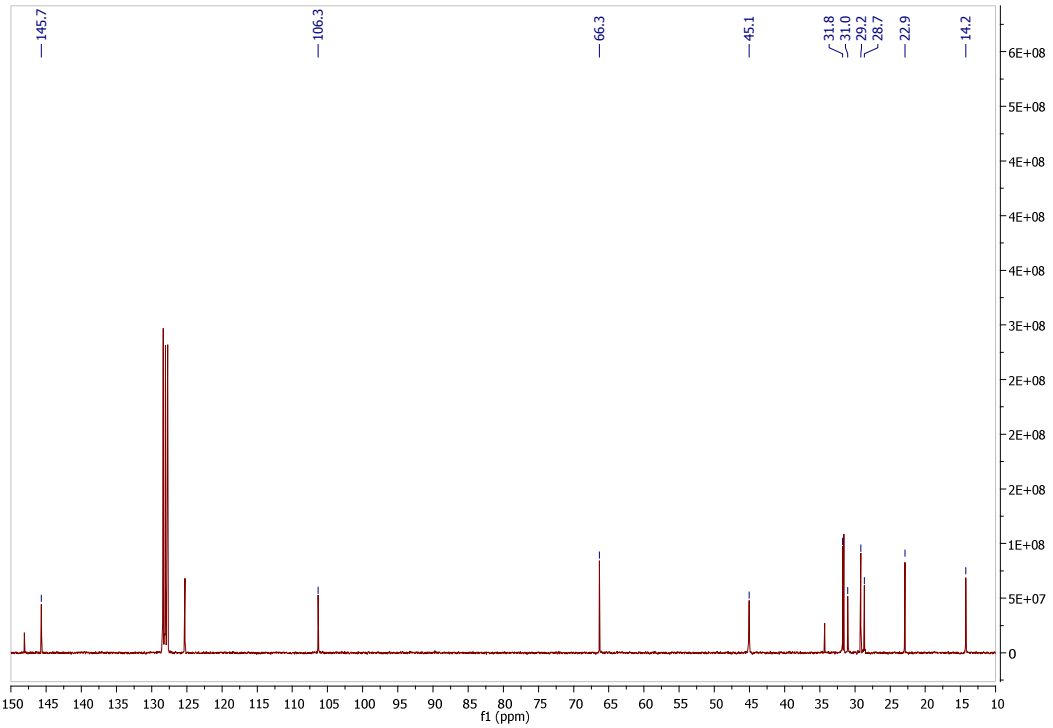

Figure 4.15: ^{13}C NMR spectrum of *N,N*-dimethyl-2-hexylthioprop-2-en-1-amine in C_6D_6

© University of Pretoria

Entry 3, Table 4.4: Hydrothiolation of *N*-Boc-propargylamine with 1-hexanethiol

Experiments were carried out as mentioned. Amounts of reagents added are as follows: 1 mol % catalyst **17$_b$** (3.2 mg, 3.2 x 10^{-6} mol); internal standard 0.25 equivalent (15.1 mg, 7.9 x 10^{-5} mol); one equivalent *N*-Boc-propargylamine (49.1 mg, 3.2 x 10^{-4} mol) and one equivalent 1-hexanethiol (45 µL, 3.2 x 10^{-4} mol).

N-tert-butyloxycarbonyl-2-hexylthioprop-2-en-1-amine

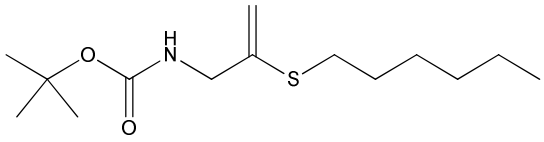

^{1}H NMR δ_H (C_6D_6, 300 MHz) 5.14 (s, 1H, C=C**H**$_2$), 4.77 (s, 1H, C=C**H**$_2$), 4.64 (br s, 1H, CH_2N**H**), 3.82 (d, *J* = 5.9 Hz, 2H, C**H**$_2$NH), 2.45 (t, *J* = 7.3 Hz, 2H, C**H**$_2$), 1.49 - 1.39 (m, 2H, C**H**$_2$ overlaps with OC(CH_3)$_3$), 1.42 (s, 9H, OC(C**H**$_3$)$_3$ overlaps with C**H**$_2$), 1.25 - 1.05 (m, 6H, (C**H**$_2$)$_3$ overlaps with C(CH_3)$_3$ of internal standard), 0.82 (t, *J* = 7.0 Hz, 3H, C**H**$_3$). **^{13}C NMR** δ_C (C_6D_6, 75 MHz) 155.6, 144.0, 108.0, 79.0, 46.1, 31.7, 31.3, 29.0, 28.7, 28.5, 22.9, 14.2.

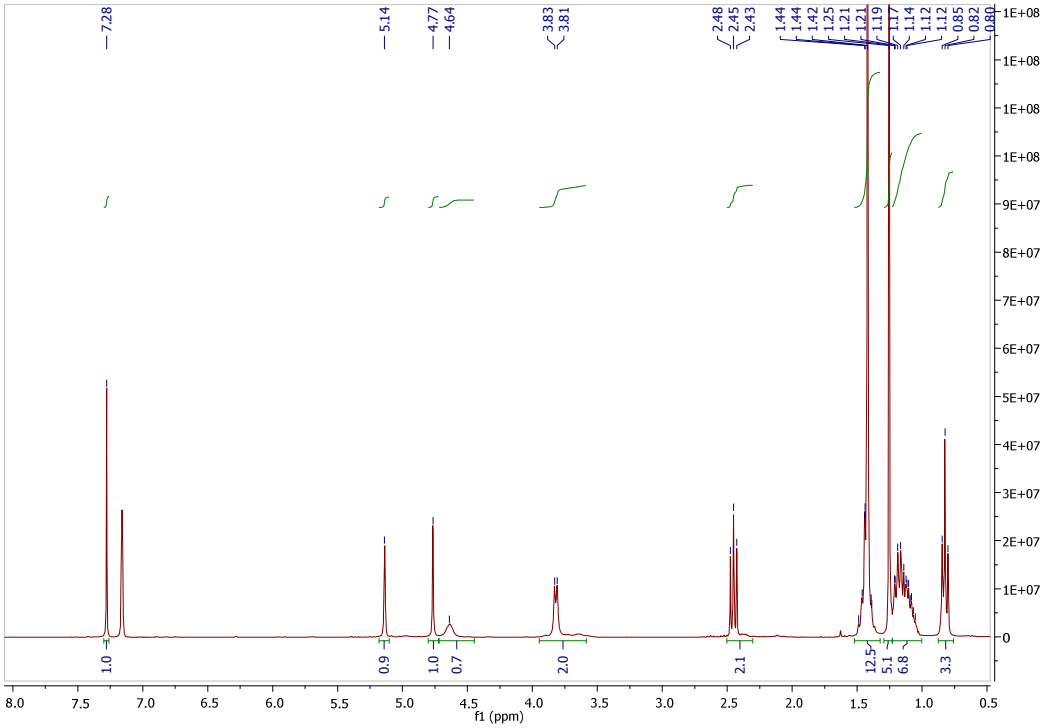

Figure 4.16: ^{1}H NMR spectrum of *N-tert*-butyloxycarbonyl-2-hexylthioprop-2-en-1-amine in C_6D_6

© University of Pretoria

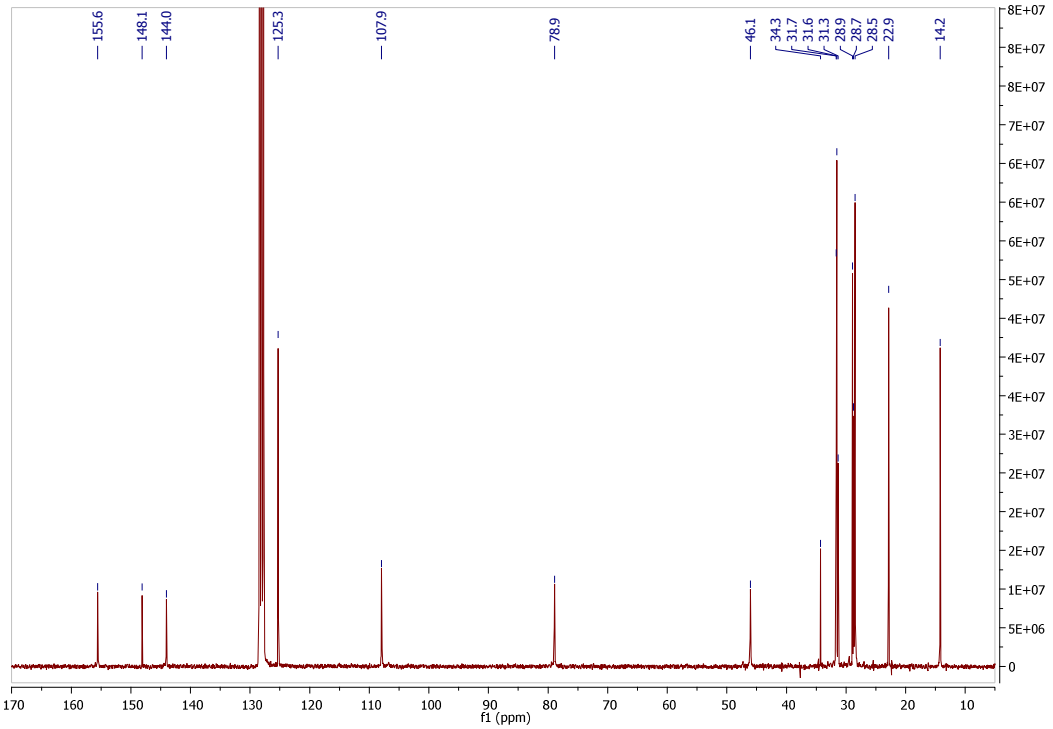

Figure 4.17: ^{13}C NMR spectrum of *N*-*tert*-butyloxycarbonyl-2-hexylthioprop-2-en-1-amine in C_6D_6

Entry 4, Table 4.4: Hydrothiolation of phenylacetylene with thiophenol

Experiments were carried out as mentioned. Amounts of reagents added are as follows: 1 mol % catalyst (3.5 mg, 3.4 x 10^{-6} mol); internal standard 0.25 equivalent (16.3 mg, 8.5 x 10^{-5} mol); one equivalent phenylacetylene (37.6 µL, 3.4 x 10^{-4} mol) and one equivalent thiophenol (35 µL, 3.4 x 10^{-4} mol). Product identity was confirmed by comparison with previously reported NMR spectra.[34]

1-Phenyl-1-phenylthioethene

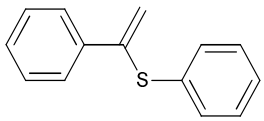

^{1}H NMR δ_H (C_6D_6, 300 MHz) 7.63 - 7.57 (m, 2H, Ar**H** overlaps with *E*- and *Z*-isomers), 7.42 - 7.27 (m, 4H, Ar**H** overlaps with ArH of internal standard and with *E*- and *Z*-isomers), 7.06 - 6.85 (m, 4H, Ar**H** overlaps with *E*- and *Z*-isomers), 5.50 (s, 1H, C=C**H**$_2$), 5.30 (s, 1H, C=C**H**$_2$).

© University of Pretoria

4.5.9 Sequential bis-hydrothiolation

Standard operating procedure for asymmetric bis-hydrothiolation reactions. A high pressure NMR tube with a J. Young valve was charged with two mol % catalyst **17$_b$** and 0.25 equivalents of internal standard, 1,4-di-*tert*-butylbenzene. To the mixture was added deuterated benzene (0.5 mL). One equivalent of terminal alkyne and one equivalent of the dithiol were added, followed by the NMR tube being capped. ^{1}H NMR spectroscopy was performed at time 10 min after addition of the substrates. The reaction mixture was heated up to 80 °C and reacted for the duration as indicated (Table 4.5). ^{1}H NMR spectroscopy confirmed the complete conversion of the substrates to the mono-α-vinyl sulfide product. To the same reaction mixture, in open atmospheric conditions, was added one equivalent of the second terminal alkyne. The NMR tube was capped, a ^{1}H NMR experiment performed, and the tube was subsequently heated up to 80 °C for the duration as indicated in Table 4.5. ^{1}H NMR spectroscopy confirmed the formation of the unsymmetrical bis-α,α'-vinyl sulfide, or unsymmetrical bis-α,β-*E*-vinyl sulfides. Conversion and calculated yields were determined from NMR analysis based on the integration of alkyne and product, referenced to the internal standard.

Entry 1, Table 4.5: Bis-Hydrothiolation of 1-hexyne and *N*,*N*-dimethylaminopropyne with 1,4-butanedithiol (bis-α,α'-vinyl sulfide)

Experiments were carried out as described above. Amounts of reagents added are as follows: **17$_b$** (6.1 mg, 6.0 x 10^{-6} mol); internal standard 0.25 equivalent (14.2 mg, 7.5 x 10^{-5} mol); 1 equivalent of 1-hexyne (34.3 µL, 3.0 x 10^{-4} mol) and one equivalent of 1,4-butanedithiol (35 µL, 3.0 x 10^{-4} mol). Upon completion of the first hydrothiolation reaction, one equivalent of the second alkyne, *N*,*N*-dimethylaminopropyne (32.1 µL, 3.0 x 10^{-4} mol), was added.

bis-α,α'-vinyl sulfide

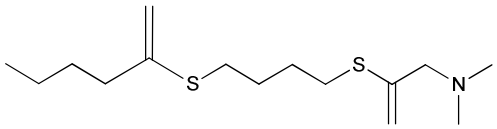

^{1}H NMR δ_H (C_6D_6, 300 MHz) 5.20 (d, *J* = 1.3 Hz, 1H, C=C**H**$_2$), 4.99 (d, *J* = 1.4 Hz, 1H, C=C**H**$_2$), 4.72 (s, 1H, C=C**H**$_2$), 4.65 (s, 1H, C=C**H**$_2$), 2.96 (br s, 2H, C**H**$_2$N(CH$_3$)$_2$), 2.48 - 2.41 (m, 4H, (C**H**$_2$)$_2$), 2.20 (tt, *J* = 7.6 Hz, 4.5 Hz, 2H, C**H**$_2$), 2.10 (s, 6H, CH$_2$N(C**H**$_3$)$_2$), 1.58 - 1.46 (m, 6H, (C**H**$_2$)$_3$), 1.31 - 1.18 (m, 2H, C**H**$_2$ overlaps with

© University of Pretoria

$C(CH_3)_3$ of internal standard), 0.83 (t, *J* = 7.3 Hz, 3H, C**H**$_3$). **^{13}C NMR** δ_C (C_6D_6, 75 MHz) 146.4, 145.2, 106.7, 105.2, 66.3, 45.1, 37.8, 31.4, 30.8, 30.4, 28.0, 27.9, 22.4, 14.1.

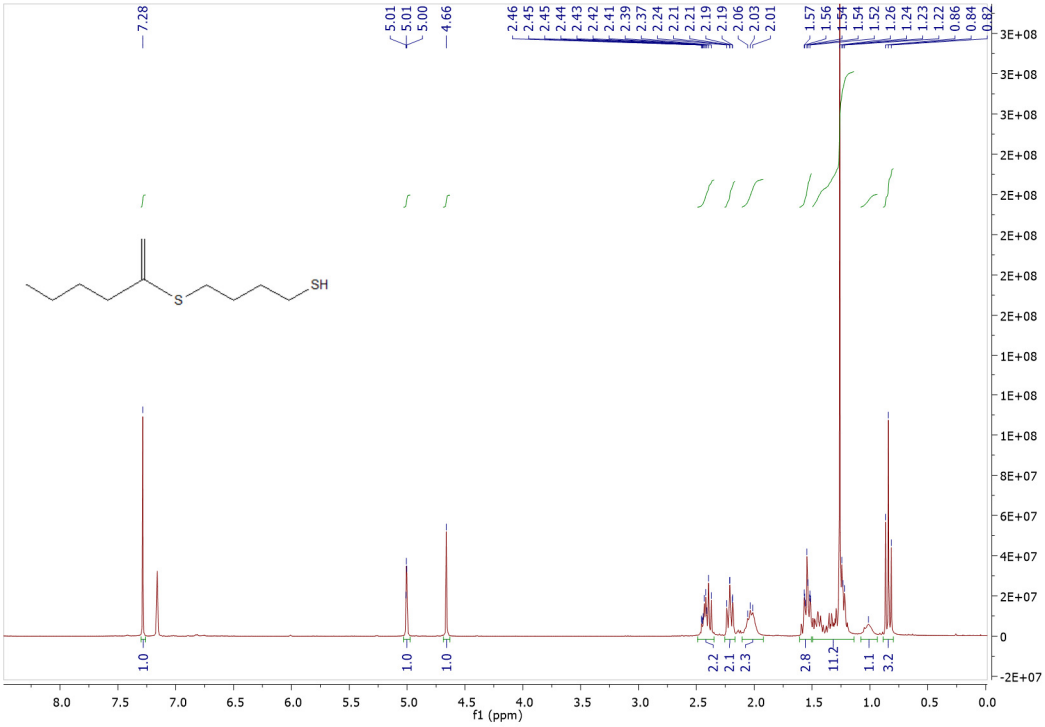

Figure 4.18: ^{1}H NMR spectrum of α-vinyl sulfide intermediate product in C_6D_6

© University of Pretoria

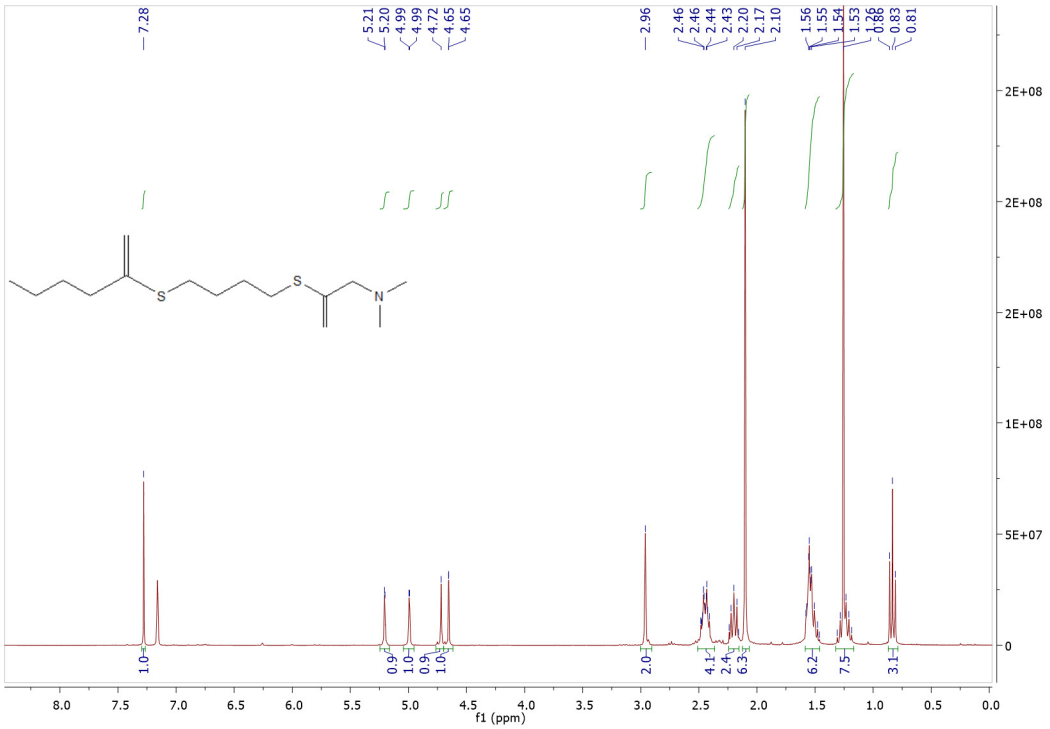

Figure 4.19: ^{1}H NMR spectrum of bis-α,α'-vinyl sulfide in C_6D_6

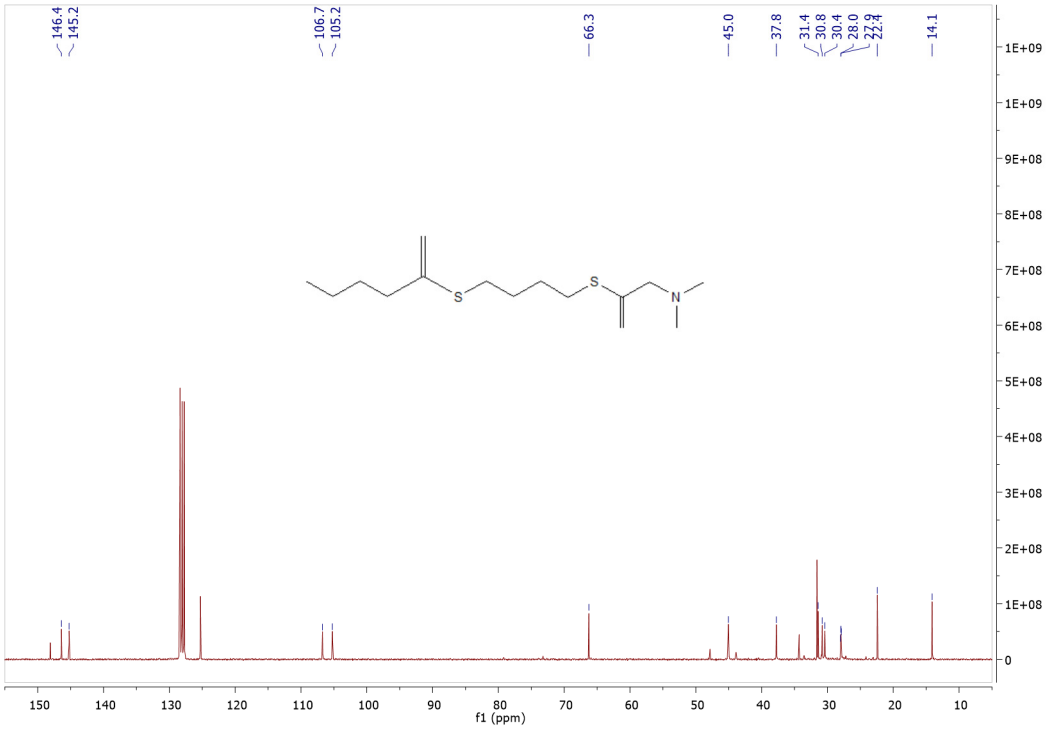

Figure 4.20: ^{13}C NMR spectrum of bis-α,α'-vinyl sulfide in C_6D_6

© University of Pretoria

Entry 2, Table 4.5: Bis-Hydrothiolation of 1-hexyne and 3-hexyne with 1,6-hexanedithiol (bis-α,β-*E*-vinyl sulfide)

Experiments were carried out as mentioned. Amounts of reagents added are as follows: catalyst **17$_b$** (5.3 mg, 5.2 x 10^{-6} mol); internal standard 0.25 equivalent (12.4 mg, 6.5 x 10^{-5} mol); 1 equivalent of 1-hexyne (30.1 µL, 2.6 x 10^{-4} mol) and one equivalent of 1,6-hexanedithiol (40 µL, 2.6 x 10^{-4} mol). Upon completion of the first hydrothiolation reaction, one equivalent of the second alkyne, 3-hexyne (29.7 µL, 2.6 x 10^{-4} mol), was added.

Bis-α,β-*E-vinyl sulfide*

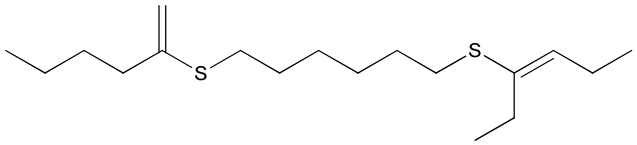

^{1}H NMR δ_H (C_6D_6, 300 MHz) 5.34 (t, *J* = 7.3 Hz, 1H, C=C**H**), 5.02 (d, *J* = 1.1 Hz, 1H, C=C**H**$_2$), 4.70 (s, 1H, C=C**H**$_2$), 2.51 - 2.44 (m, 4H, (C**H**$_2$)$_2$), 2.23 (t, *J* = 7.5 Hz, 2H, C**H**$_2$), 2.21 - 2.13 (m, 2H, C**H**$_2$ overlaps with C**H**$_2$), 1.98 (t, *J* = 7.5 Hz, 2H, C**H**$_2$), 1.61 - 1.50 (m, 2H, C**H**$_2$), 1.50 - 1.40 (m, 4H, (C**H**$_2$)$_2$), 1.33 - 1.12 (m, 6H, (C**H**$_2$)$_3$ overlaps with C(C**H**$_3$)$_3$ of internal standard), 1.11 (t, *J* = 7.5 Hz, 3H, C**H**$_3$), 0.90 (t, *J* = 7.5 Hz, 3H, C**H**$_3$), 0.84 (t, *J* = 7.2 Hz, 3H, C**H**$_3$). **^{13}C NMR** δ_C (C_6D_6, 75 MHz) 146.8, 136.6, 127.1, 104.9, 37.9, 31.5, 31.4, 31.3, 29.0, 28.9, 28.8, 28.5, 25.4, 22.5, 22.2, 14.8, 14.6, 14.1.

© University of Pretoria

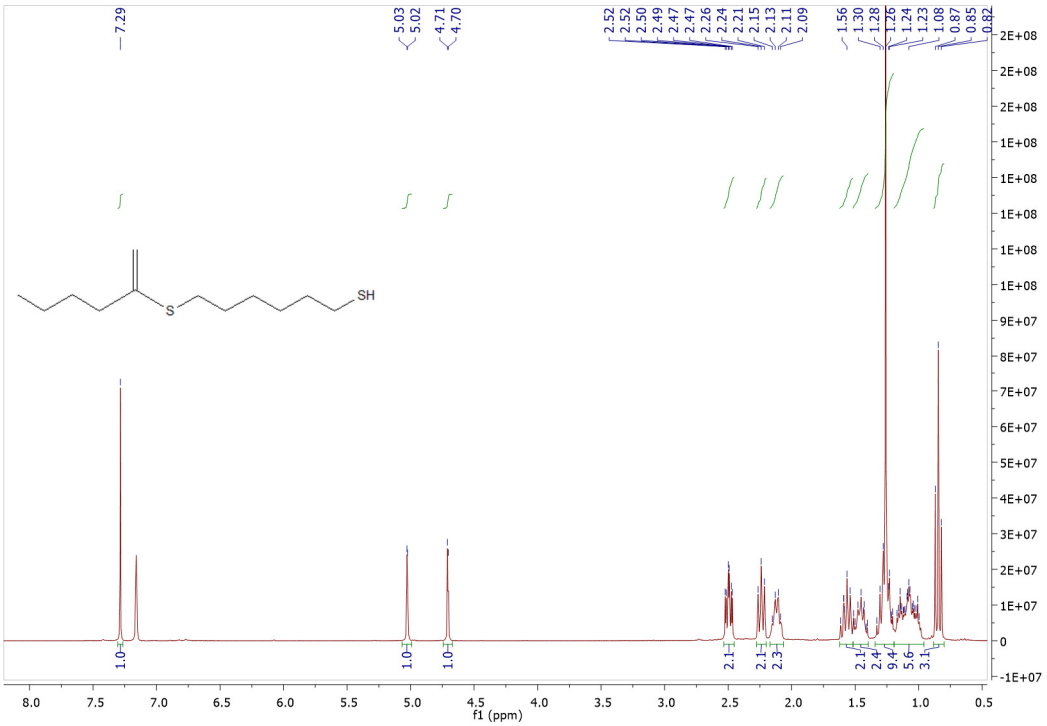

Figure 4.21: ^{1}H NMR spectrum of α-vinyl sulfide intermediate product in C_6D_6

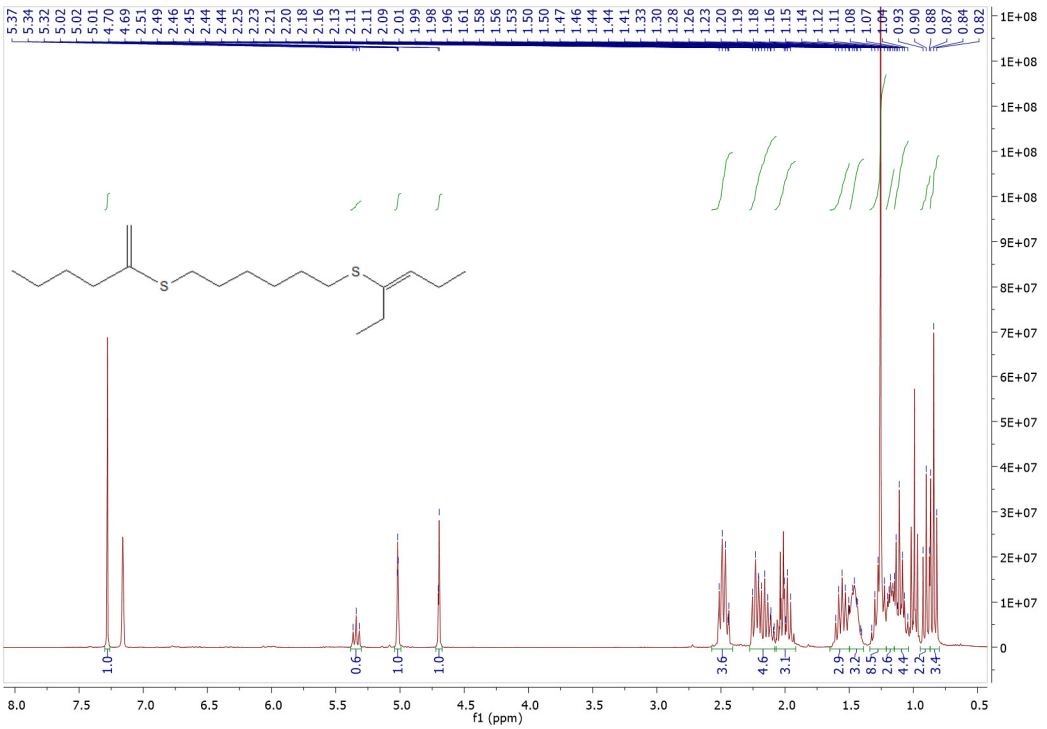

Figure 4.22: ^{1}H NMR spectrum of bis-α,β-*E*-vinyl sulfide and unreacted intermediate product in C_6D_6

© University of Pretoria

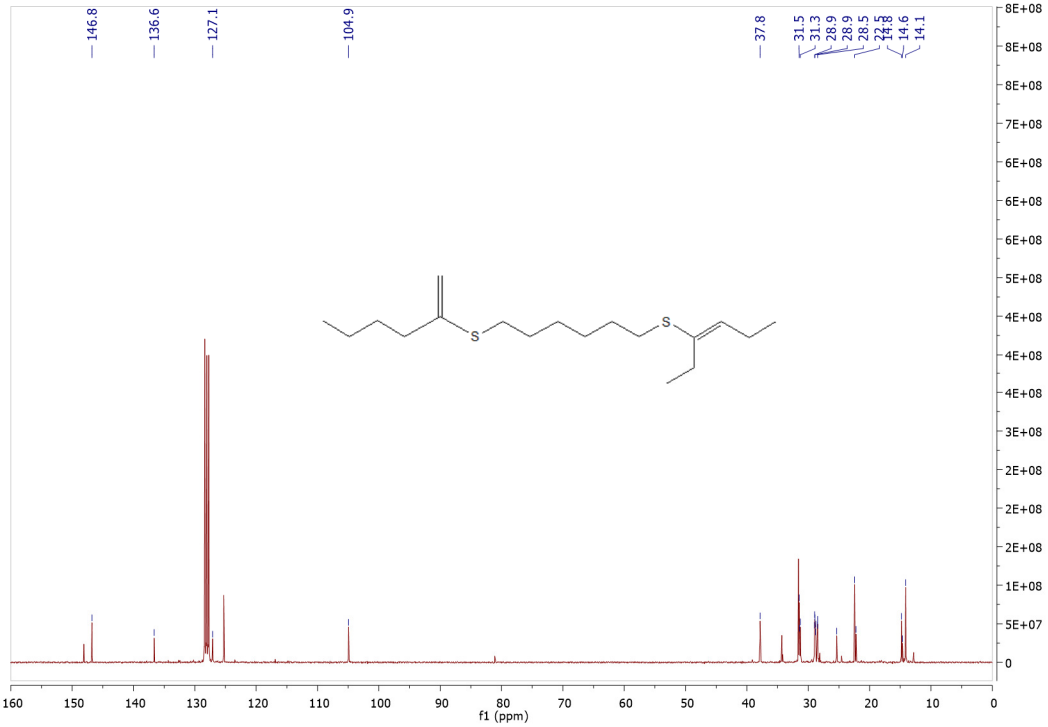

Figure 4.23: ^{13}C NMR spectrum of bis-α,β-*E*-vinyl sulfide and unreacted intermediate product in C_6D_6

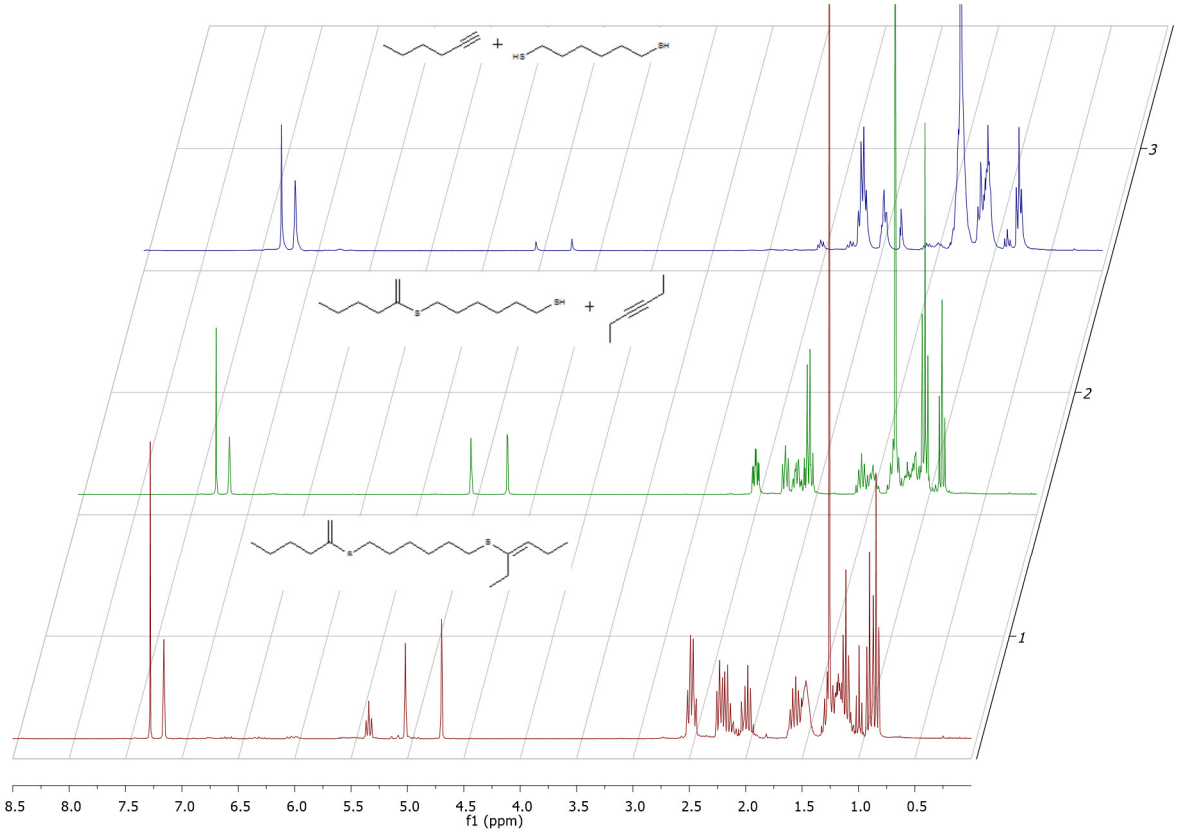

Figure 4.24: Stacked ^{1}H NMR spectra of asymmetric bis-hydrothiolation reaction at initial time (blue spectrum), intermediate step (green spectrum) and final time (red spectrum)

© University of Pretoria

4.5.10 Sequential bis-hydrothiolation under preparative conditions

The reaction reported in Table 4.5, Entry 1 was scaled up tenfold. To a Schlenk tube was added 1-hexyne (343 µL, 2.98 x 10^{-3} mol), 1,4-butanedithiol (350 µL, 2.98 x 10^{-3} mol), catalyst **17$_b$** (116 mg, 5.97 x 10^{-5} mol; 2 mol %) and internal standard 1,4-di-tert-butylbenzene (142 mg, 7.46 x 10^{-4} mol, 0.25 equivalent) in 4 mL solvent C_6D_6. The reaction mixture was heated at 80 °C for 14 hours, where after the reaction mixture was allowed to cool down to room temperature. The second alkyne substrate, dimethylaminopropyne (321 µL, 2.98 x 10^{-3} mol) was added to the reaction mixture and the reaction vessel heated for an additional 30 hours at 80 °C. After a total reaction time of 44 hours, NMR analysis indicated 64% conversion of the substrates, and a calculated overall yield of the bis-α,α'-vinyl sulfide product of 62%. The reaction mixture was thereafter dry-loaded on an aluminium oxide 90 (neutral, activated) plug, and the product eluted with hexane:EtOAc (3:1). The purified bis-α,α'-vinyl sulfide product was isolated with a yield of 406 mg, 47% overall yield.

4.5.11 Sequential alkyne dimerization-hydrothiolation catalytic details

A high pressure NMR tube with a J. Young valve was loaded with 3.5 mol % of catalyst **17$_b$** (11.6 mg, 1.1 x 10^{-5} mol) and 0.25 equivalents of internal standard, 1,4-di-*tert*-butylbenzene (15.4 mg, 8.1 x 10^{-5}mol). To the mixture was added deuterated benzene (0.5 mL). One equivalent of *N*,*N*-dimethylaminopropyne (35 µL, 3.3 x 10^{-4} mol) was added to the solution, and the NMR tube was subsequently capped. ^{1}H NMR spectroscopy was performed at time 10 min after addition of the alkyne. The reaction mixture was heated up to 80 °C and left to react for 3 hours. Upon cooling down to room temperature, ^{1}H NMR spectroscopy confirmed complete conversion of *N*,*N*-dimethylaminopropyne to N^1,N^1,N^5,N^5-tetramethyl-4-methylenepent-2-yne-1,5-diamine. To the same reaction mixture, in open atmospheric conditions, was added 1-hexanethiol (23.1 µL, 1.6 x 10^{-4} mol). The NMR tube was capped, and a ^{1}H NMR experiment performed of the resulting mixture. The reaction mixture was heated up to 60 °C for 48 hours. Upon cooling down to room temperature, a ^{1}H NMR experiment was performed on the resulting mixture. Conversion and calculated yields were determined from NMR analysis based on integration of substrates and product, referenced to the internal standard. Product identity was determined by assignments based on 1D (^{1}H, ^{13}C{^{1}H}, ^{13}C-dept 135) and 2D (COSY, HSQC and HMBC) experiments.

© University of Pretoria

The reaction was scaled up tenfold. To a Schlenk tube was added dimethylaminopropyne (350 µL; 3.25 x 10^{-3} mol), catalyst **17b** (116 mg; 1.14 x 10^{-4} mol; 3.5 mol %) and internal standard 1,4-di-tert-butylbenzene (154 mg, 8.13 x 10^{-4} mol, 0.25 equivalent) in 4 mL solvent C_6D_6. The reaction was heated at 80 °C for 5 hours, where after it was allowed to cool to room temperature. 1-hexanethiol (231 µL; 1.63 x 10^{-3} mol; 0.5 equivalent) was added to the reaction mixture, and the reaction vessel then heated at 60 °C for an additional 43 hours. NMR analysis revealed 60% conversion of the substrates, with calculated yields for the different *gem*-ene-vinyl sulfide product isomers as follows: 1,3-*gem*-ene-β-*E*-vinyl sulfide, 28%; 1,4-*gem*-ene-β-*E*-vinyl sulfide, 19%; and 1,4-*gem*-ene-β-*Z*-vinyl sulfide, 9%, with product distribution: 1,3-*gem*-ene-β-*E*-vinyl sulfide: 1,4-*gem*-ene-β-*E*-vinyl sulfide: 1,4-*gem*-ene-β-*Z*-vinyl sulfide = 50 : 34 : 16. The products were purified by gradient elution with hexane and ethyl acetate after dry loading on an aluminium oxide 90 (neutral, activated) plug to yield all three *gem*-ene-vinyl sulfide products, with an overall crude isolated yield of 180 mg, 6.33 x 10^{-4} mol, 39% yield.

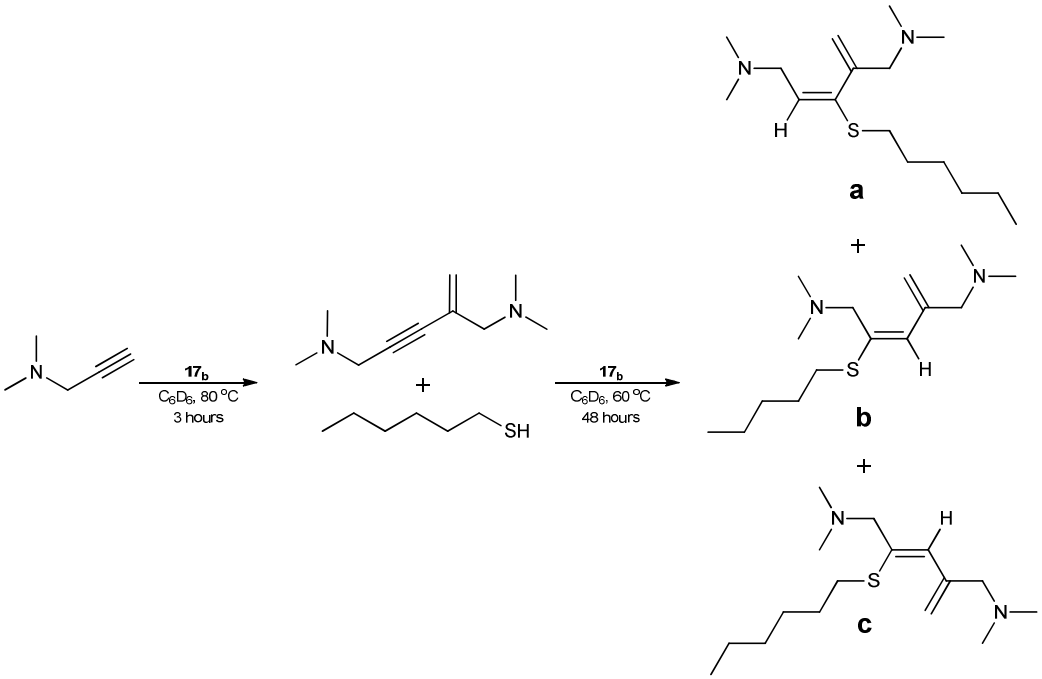

Scheme 4.16: One-pot alkyne dimerization followed by hydrothiolation of the internal alkyne catalyzed by **17b**

© University of Pretoria

(a) 1,3-gem-ene-β-E-vinyl-sulfide

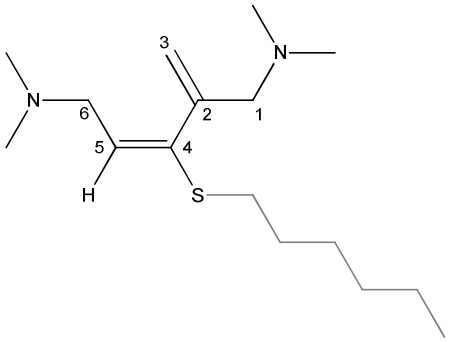

^{1}H NMR δ_H (C_6D_6, 300 MHz) 6.03 (t, *J* = 6.8 Hz, 1H, C5-**H**), 5.44 (dt, *J* = 1.6 Hz, 1.3 Hz, 1H, C3-**H**$_2$), 5.06 (dt, *J* = 1.3 Hz, 1 Hz, 1H, C3-**H**$_2$), 3.10 (t, *J* = 1.3 Hz, 2H, C1-**H**$_2$), 3.03 (d, *J* = 6.8 Hz, 2H, C6-**H**$_2$), 2.18 (s, 6H, C1-N(C**H**$_3$)$_2$), 2.13 (s, 6H, C6-N(C**H**$_3$)$_2$), -S-hexyl moiety (grey scaled) not assigned due to extensive overlap. **^{13}C NMR** δ_C (C_6D_6, 100 MHz) 143.8 (C**2**), 138.6 (C**4**), 129.9 (C**5**), 116.9 (C**3**), 63.8 (C**1**), 58.7 (C**6**), N(CH_3)$_2$ not assigned due to extensive carbon overlap.

(b) 1,4-gem-ene-β-E-vinyl-sulfide

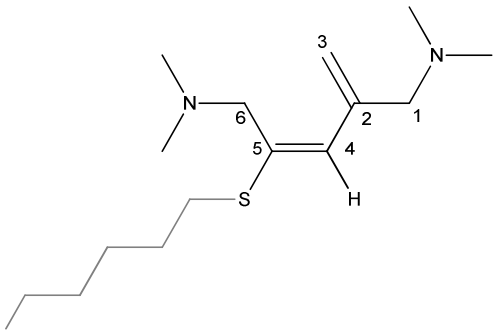

^{1}H NMR δ_H (C_6D_6, 300 MHz) 6.03 (s, 1H, C4-**H**), 5.20 (dt, *J* = 1.3 Hz, 1.2 Hz, 1H, C3-**H**$_2$), 5.13 (d, *J* = 1.5 Hz, 1H, C3-**H**$_2$), 3.35 (d, *J* = 1 Hz, 2H, C6-**H**$_2$), 2.86 (br s, 2H, C1-**H**$_2$), 2.21 (s, 6H, C6-N(C**H**$_3$)$_2$), 2.10 (s, 6H, C1-N(C**H**$_3$)$_2$), -S-hexyl moiety (grey scaled) not assigned due to extensive overlap. **^{13}C NMR** δ_C (C_6D_6, 100 MHz) 143.6 (C**2**), 140.4 (C**5**), 123.3 (C**4**), 115.9 (C**3**), 67.1 (C**1**), 61.2 (C**6**), N(CH_3)$_2$ not assigned due to extensive carbon overlap.

© University of Pretoria

(c) 1,4-gem-ene-β-Z-vinyl-sulfide

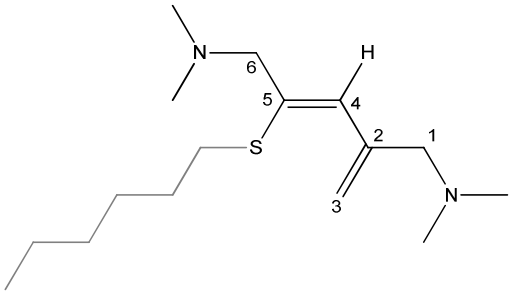

^{1}H NMR δ_H (C_6D_6, 300 MHz) 6.36 (br s, 1H, C4-**H**), 5.12 (d, *J* = 1.3 Hz, 1H, C3-**H**), 5.08 (s, 1H, C3-**H**), 3.23 (s, 2H, C6-**H**), 3.00 (d, *J* = 1.3 Hz, 2H, C1-**H**), 2.16 (s, 6H, C6-N(C**H**$_3$)$_2$), 2.14 (s, 6H, C1-N(C**H**$_3$)$_2$), -S-hexyl moiety (grey scaled) not assigned due to extensive overlap. **^{13}C NMR** δ_C (C_6D_6, 100 MHz) 141.9 (C**2**), 141.7 (C**5**), 128.6 (C**4**), 110.1 (C**3**), 64.1 (C**1**), 57.9 (C**6**), N(CH_3)$_2$ not assigned due to extensive carbon overlap.

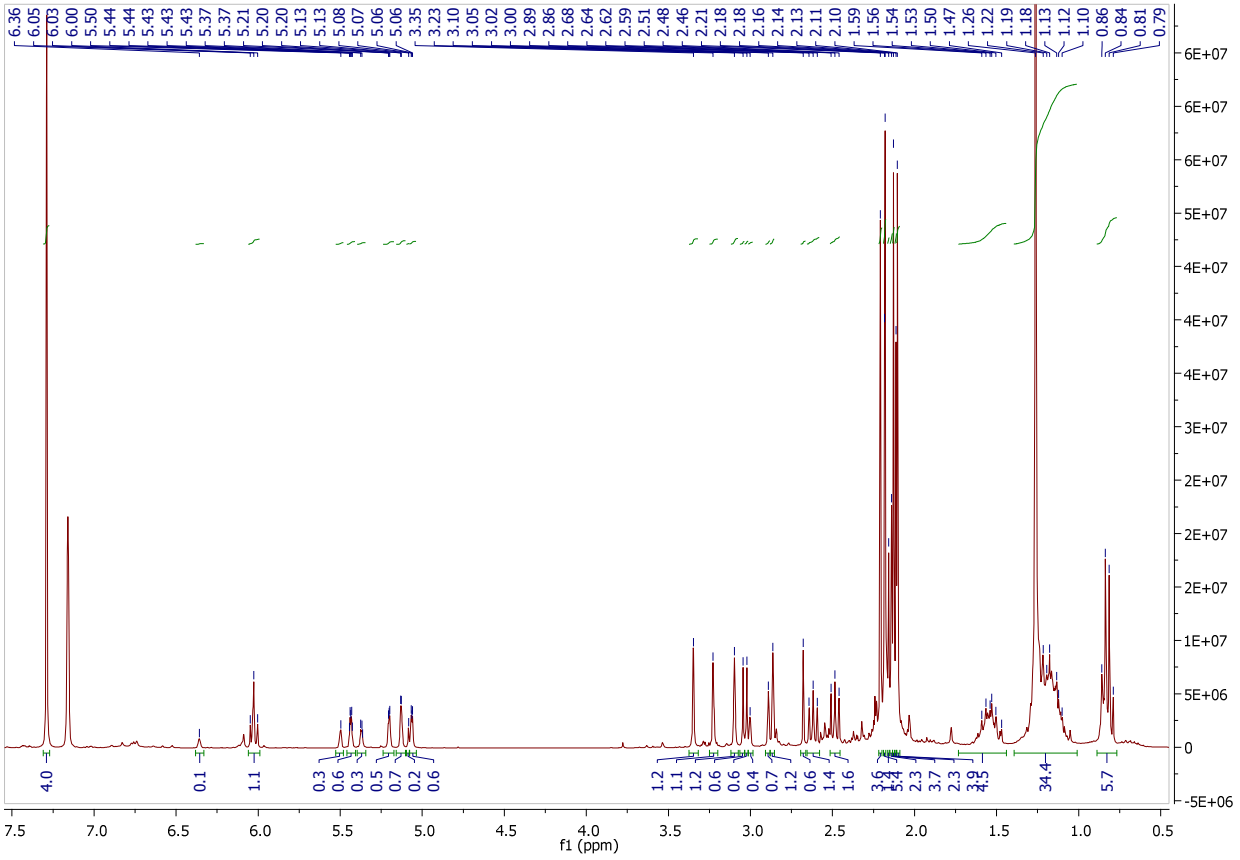

Figure 4.25: ^{1}H NMR spectrum of products obtained after one-pot catalyzed alkyne dimerization followed by hydrothiolation of the internal alkyne by **17$_b$** in C_6D_6

© University of Pretoria

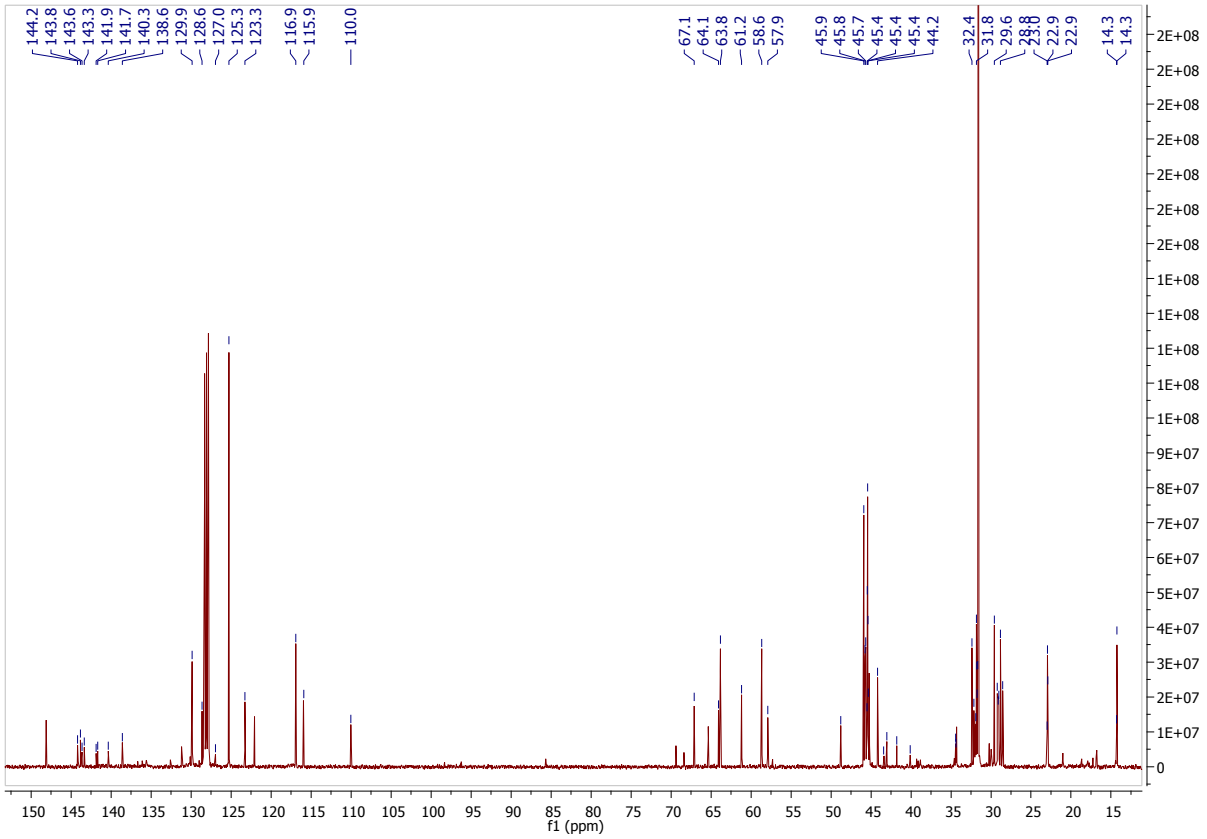

Figure 4.26: ^{13}C NMR spectrum of products obtained after one-pot catalyzed alkyne dimerization followed by hydrothiolation of the internal alkyne by **17ь** in C_6D_6

4.6 References

[1] G. Kleinhans, *MSc Dissertation*, University of Pretoria, **2014**, 106 – 146.

[2] V. P. Ananikov, M. Tanaka, *Top. Organomet. Chem.*, **2013**, *43*, 1 – 367.

[3] See review articles and reference therein: *a*) Y. Zhou, Y. Zhang, J. Wang, *Org. Biomol. Chem.*, **2016**, *14*, 6638 – 6650; *b*) A. H. Cherney, N. T. Kadunce, S. E. Reisman, *Chem. Rev.*, **2015**, *115*, 9587 – 9652; *c*) M. Peña-López, A. Rosas-Hernández, M. Beller, *Angew. Chem. Int. Ed.*, **2015**, *54*, 5006 – 5008; *d*) J. Legros, B. Figadère, *Nat. Prod. Rep.*, **2015**, *32*, 1541 – 1555; *e*) M. Henrion, V. Ritleng, M. J. Chetcuti, *ACS Catal.*, **2015**, *5*, 1283 – 1302; *f*) S. Roscales, A. G. Csákÿ, *Chem. Soc. Rev.*, **2014**, *43*, 8215 – 8225; *g*) R. Chinchilla, C. Nájera, *Chem. Rev.*, **2014**, *114*, 1783 – 1826; *h*) T. Satoh, H. Tsurugi, M. Miura, *Chem. Rec.*, **2008**, *8*, 326 – 336; *i*) E. Barnea, M. S. Eisen, *Coord. Chem. Rev.*, **2006**, *250*, 855 – 899.

[4] See review articles and reference therein: *a*) M. Wathier, J. A. Love, *Eur. J. Inorg. Chem.*, **2016**, 2391 – 2402; *b*) A. Dondoni, A. Marra, *Eur. J. Org. Chem.*, **2014**, 3955 – 3969; *c*) I. P. Beletskaya, V. P. Ananikov, *Chem. Rev.*, **2011**, *111*, 1596 – 1636; *d*) C. J. Weiss, T. J. Marks, *Dalton Trans.*, **2010**, *39*, 6576 – 6588; *e*) I. P. Beletskaya, V. P. Ananikov, *Eur. J. Org. Chem.*, **2007**, 3431 – 3444; *f*) T. Kondo, T.-a. Mitsudo, *Chem. Rev.*, **2000**, *100*, 3205 – 3220; *g*) A. Ogawa, *J. Organomet. Chem.*, **2000**, *611*, 463 – 474.

[5] See review articles and reference therein: *a*) S. A. Shahzad, M. A. Sajid, Z. A. Khan, D. Canseco-Gonzalez, *Synthetic Communications*, **2017**, *47*, 735 – 755; *b*) M. Patel, R. K. Saunthwal, A. K. Verma, *Acc. Chem. Res.*, **2017**, *50*, 240 – 254; *c*) L. C. Wilkins, R. L. Melen, *Coord. Chem. Rev.*, **2016**, *324*, 123 – 139; *d*) V. I. Isaeva, L. M. Kustov, *Top. Catal.*, **2016**, *59*, 1196 – 1206; *e*) M. T. Pirnot, Y.-M. Wang, S. L. Buchwald, *Angew. Chem. Int. Ed.*, **2016**, *55*, 48 – 57; *f*) A. A. Trifonov, I. V. Basalov, A. A. Kissel, *Dalton Trans.*, **2016**, *45*, 19172 – 19193; *g*) V. Rodriguez-Ruiz, R. Carlino, S.

© University of Pretoria

Bezzenine-Lafollée, R. Gil, D. Prim, E. Schulz, J. Hannedouche, *Dalton Trans.*, **2015**, *44*, 12029 – 12059; *h*) A. Dondoni, *Asymmetric Catal.*, **2015**, *2*, 51 – 54; *i*) M. Villa, A. J. von Wangelin, *Angew. Chem. Int. Ed.*, **2015**, *54*, 11906 – 11908; *j*) L. Huang, M. Arndt, K. Gooßen, H. Heydt, L. J. Gooßen, *Chem. Rev.*, **2015**, *115*, 2596 – 2697; *k*) J. Hannedouche, E. Schulz, *Chem. Eur. J.*, **2013**, *19*, 4972 – 4985; *l*) K. D. Hesp, M. Stradiotto, *ChemCatChem.*, **2010**, *2*, 1192 – 1207.

[6] B. M. Trost, *Angew. Chem. Int. Ed. Engl.*, **1995**, *34*, 259 – 281.

[7] Z. A. Werner, *Anorg. Chem.*, **1893**, *3*, 267.

[8] L. Rubio-Pérez, R. Azpíroz, A. D. Giuseppe, V. Polo, R. Castarlenas, J. J. Pérez-Torrente, L. A. Oro, *Chem. Eur. J.*, **2013**, *19*, 15304 – 15314 and references therein.

[9] R. Castarlenas, A. D. Giuseppe, J. J. Pérez-Torrente, L. A. Oro, *Angew. Chem. Int. Ed.*, **2013**, *52*, 211 – 222.

[10] For selected examples of conjugated enynes as building blocks, or use in polymers, biological or photoactive applications, see: *a*) P. Röse, C. C. M. Garcia, F. Pünner, K. Harms, G. Hilt, *J. Org. Chem.*, **2015**, *80*, 7311 – 7316; *b*) O. S. Morozov, A. F. Asachenko, D. V. Antonov, V. S. Kochurov, D. Y. Paraschuk, M. S. Nechaev, *Adv. Synth. Catal.*, **2014**, *356*, 2671 – 2678; *c*) W. P. Forrest, Z. Cao, H. R. Hambrick, B. M. Prentice, P. E. Fanwick, P. S. Wagenknecht, T. Ren, *Eur. J. Inorg. Chem.*, **2012**, 5616 – 5620; *d*) T. H. Jones, R. M. M. Adams, T. F. Spande, H. M. Garraffo, T. Kaneko, T. R. Schultz, *J. Nat. Prod.*, **2012**, *75*, 1930 – 1936; *e*) W. Zhang, S. Zheng, N. Liu, J. B. Werness, I. A. Guzei, W. Tang, *J. Am. Chem. Soc.*, **2010**, *132*, 3664 – 3665; *f*) W. Zhang, H. Xu, H. Xu, W. Tang, *J. Am. Chem. Soc.*, **2009**, *131*, 3832 – 3833; *g*) P. Wessig, G. Müller, *Chem. Rev.*, **2008**, *108*, 2051 – 2063; *h*) H. Katayama, M. Nakayama, T. Nakano, C. Wada, K. Akamatsu, F. Ozawa, *Macromolecules*, **2004**, *37*, 13 – 17; *i*) S. T. Diver, A. J. Giessert, *Chem. Rev.*, **2004**, *104*, 1317 – 1382.

[11] C. J. Pell, O. V. Ozerov, *ACS Catal.*, **2014**, *4*, 3470 – 3480.

[12] T. Chen, C. Guo, M. Goto, L.-B. Han, *Chem. Commun.*, **2013**, *49*, 7498 – 7500.

[13] C. Xu, W. Du, Y. Zeng, B. Dai, H. Guo, *Org. Lett.*, **2014**, *16*, 948 – 951.

[14] B. M. Trost, C. Chan, G. Ruhter, *J. Am. Chem. Soc.*, **1987**, *109*, 3487 – 3488.

[15] O. V. Zatolochnaya, E. G. Gordeev, C. Jahier, V. P. Ananikov, V. Gevorgyan, *Chem. Eur. J.*, **2014**, *20*, 9578 – 9588.

[16] M. Rubina, V. Gevorgyan, *J. Am. Chem. Soc.*, **2001**, *123*, 11107 – 11108.

[17] For selected examples of vinyl sulfides employed as polymers or with biological applications, see: *a*) B. Yao, J. Mei, J. Li, J. Wang, H. Wu, J. Z. Sun, A. Qin, B. Z. Tang, *Macromolecules*, **2014**, *47*, 1325 – 1333; *b*) J. Liu, J. W. Y. Lam, C. K. W. Jim, C. Y. Ng, J. Shi, H. Su, K. F. Yeung, Y. Hong, M. Faisel, Y. Yu, S. Wong, B. Z. Tang, *Macromolecules*, **2011**, *44*, 68 – 79; *c*) Á. Szilágyi, F. Fenyvesi, O. Majercsik, I. F. Pelyvás, I. Bácskay, P. Fehér, J. Váradi, M. Vecsernyés, P. Herczegh, *J. Med. Chem.*, **2002**, *45*, 1767 – 1777; *d*) P. Johannesson, G. Lindeberg, A. Johansson, G. V. Nikiforovich, A. Gogoll, B. Synnergren, M. Le Grèves, F. Nyberg, A. Karlén, A. Hallberg, *J. Med. Chem.*, **2002**, *45*, 1767 – 1777; *e*) C. A. Dvorak, W. D. Schmitz, D. J. Poon, D. C. Pryde, J. P. Lawson, R. A. Amos, A. I. Meyers, *Angew. Chem. Int. Ed.*, **2000**, *39*, 1664 – 1666.

[18] L. Palacios, Y. Meheut, M. Galiana-Cameo, M. J. Artigas, A. D. Giuseppe, F. J. Lahoz, V. Polo, R. Castarlenas, J. J. Pérez-Torrente, L. A. Oro, *Organometallics*, **2017**, *36*, 2198 – 2207.

[19] C. Cao, L. R. Fraser, J. A. Love, *J. Am. Chem. Soc.*, **2005**, *127*, 17614 – 17615.

[20] Y. Misumi, H. Seino, Y. Mizobe, *J. Organomet. Chem.*, **2006**, *691*, 3157 – 3164.

[21] A. D. Giuseppe, R. Castarlenas, J. J. Pérez-Torrente, M. Crucianelli, V. Polo, R. Sancho, F. J. Lahoz, L. A. Oro, *J. Am. Chem. Soc.*, **2012**, *134*, 8171 – 8183.

[22] I. Strydom, G. Guisado-Barrios, I. Fernández, D. C. Liles, E. Peris, D. I. Bezuidenhout, *Chem. Eur. J.*, **2017**, *23*, 1393 – 1401.

[23] E. C. Keske, O. V. Zenkina, A. Asadi, H. Sun, J. M. Praetorius, D. P. Allen, D. Covelli, B. O. Patrick, R. Wang, P. Kennepohl, B. R. James, C. M. Crudden, *Dalton. Trans.*, **2013**, *42*, 7414 – 7423.

[24] See examples: *a*) O. V. Zenkina, E. C. Keske, R. Wang, C. M. Crudden, *Angew. Chem. Int. Ed.*, **2011**, *50*, 8100 – 8104; *b*) J. M. Praetorius, D. P. Allen, R. Wang, J. D. Webb, F. Grein, P. Kennepohl, C. M. Crudden, *J. Am. Chem. Soc.*, **2008**, *130*, 3724 – 3725; *c*) C. M. Frech, L. J. W. Shimon, D. Milstein, *Helv. Chim. Acta.*, **2006**, *89*, 1730 – 1739; *d*) H. L. M. van Gaal, F. L. A. van den Bekerom, *J. Organomet. Chem.*, **1977**, *134*, 237 – 248; *e*) C. Busetto, A. D'Alfonso, F. Maspero, G. Perego, A. Zazzetta, *J. Chem. Soc., Dalton Trans.*, **1977**, 1828 – 1834.

[25] A. Y. Verat, H. Fan, M. Pink, Y.-S. Chen, K. G. Caulton, *Chem. Eur. J.*, **2008**, *14*, 7680 – 7686.

© University of Pretoria

[26] J. Cipot-Wechsler, D. Covelli, J. M. Praetorius, N. Hearns, O. V. Zenkina, E. C. Keske, R. Wang, P. Kennepohl, C. M. Crudden, *Organometallics*, **2012**, *31*, 7306 – 7315.
[27] M. Moser, B. Wucher, D. Kunz, F. Rominger, *Organometallics*, **2007**, *26*, 1024 – 1030.
[28] *a*) S. Kankala, S. Nerella, R. Vadde, C. S. Vassam, *RSC Adv.*, **2013**, *3*, 23582 – 23588; *b*) C. J. Weiss, S. D. Wobser, T. J. Marks, *J. Am. Chem. Soc.*, **2009**, *131*, 2062 – 2063.
[29] *a*) A. Ogawa, T. Ikeda, K. Kimura, T. Hirao, *J. Am. Chem. Soc.*, **1999**, *121*, 5108 – 5114; *b*) J.-E. Bäckvall, A. Ericsson, *J. Org. Chem.*, **1994**, *59*, 5850 – 5851.
[30] H. M. Peng, J. Zhao, X. Li, *Adv. Synth. Catal.*, **2009**, *351*, 1371 – 1377.
[31] M. Akita, H. Yasuda, A. Nakamura, *Bull. Chem. Soc. Jpn.*, **1984**, *57*, 480 – 487.
[32] H.-D. Xu, R.-W. Zhang, X. Li, S. Huang, W. Tang, W.-H. Hu, *Org. Lett.*, **2013**, *15*, 840 – 843.
[33] A. Nishimura, E. Tamai, M. Ohashi, S. Ogoshi, *Chem. Eur. J.*, **2014**, *20*, 6613 – 6617.
[34] C. C. Silveira, P. C. S. Santos, S. R. Mendes, A. L. Braga, *J. Organomet. Chem.*, **2008**, *693*, 3787 – 3790.

© University of Pretoria

Chapter 5

Nucleophilic T-shaped Au(I) pincer complexes: electrophilic oxidation

The syntheses and characterization of the gold(I) complexes **20$_a$** and **21$_b$**, have been previously reported in the MSc dissertation of the author.[1] However, the synthetic methodology has been adapted to obtain the complexes with a higher purity. As such, the syntheses will be reported in this chapter. A brief introduction to the gold relativistic effects and aurophilic interactions was also included in said MSc dissertation,[1] and only certain terms will be highlighted in this thesis chapter for the sake of clarity.

5.1 Background

The exponential surge in the chemistry of gold (over a very short amount of time), has been brought about by the initial utilization of gold mainly as a catalyst towards olefin functionalization. Gold has become an element with a wide range of applications finding use in various fields such as heterogeneous/homogeneous catalysis, biology, photoluminescence, etc.

Gold has witnessed impressive breakthroughs within the field of heterogeneous catalysis, and has successfully been employed in various industrial catalytic reactions, where the issues of catalyst durability and viable catalyst production methods have been addressed.[2] The most recent industrial example includes the hydrochlorination of acetylenes to yield the corresponding vinyl chloride monomer (monomer for PVC). In this reaction, the long used $HgCl_2$/C catalyst is phased out for the more environmentally friendly, $Na_3Au(S_2O_3)_2$ catalyst which also displayed marked catalytic improvement.[3] Other examples include the use of Au-doped Pd-catalysts for the synthesis of vinyl acetate from ethylene instead of employing the more expensive acetylene that has been traditionally used, as well as the oxidative esterification of methacrolein to methyl methacrylate.[2] Additionally, industrial companies such as Mintek are currently manufacturing supported gold catalyst, for trading purposes, ideally for oxidation reactions in the gas and liquid phase. One of the main factors governing the use of gold as an industrial catalyst is not the available amount (gold is more abundant than other platinum group

© University of Pretoria

metals), but its cost - gold remains the most expensive noble metal. However, it is expected that the situation will change in the near future, with gold realizing a prominent role in the industrial sector.[2]

Homogeneous gold catalysis has been dominated by the functionalization of unsaturated carbon substrates, catalyzed by cationic gold complexes (see Figure 5.1 for an example of the cationic gold(I) catalyzed alkyne functionalization reaction mechanism). The well-known catalytic mechanism includes coordination of the olefinic carbon substrate to the cationic gold center, followed by π-activation of the unsaturated carbon substrate towards nucleophilic attack.[4] Nucleophilic addition is followed by protodeauration resulting in the regeneration of the active catalyst, and formation of the targeted product (Figure 5.1). Furthermore, our understanding of gold catalysis has tremendously improved recently thanks to the isolation of species previously considered to be only transient intermediates. These isolated intermediates include, amongst others, π-coordinated complexes, gold-alkyl and gold-vinylic complexes, gold carbenoids, gold-carbonyls, gold-fluorides and also gold-hydrides, to name but a few.[5] As this topic has been a subject of intense research, a number of recent review articles has emerged on their synthesis, properties and importance in catalytic reactions.[5,6,7] As a result, only a few recent examples of reactive organometallic gold complexes, proposed intermediates in catalytic cycles, will be discussed. These examples will appear in the various Sections to follow.

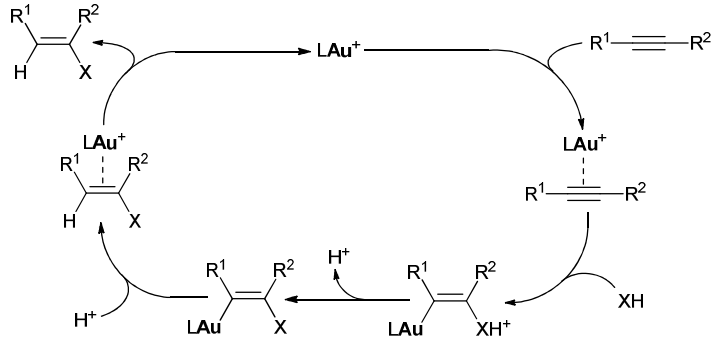

Figure 5.1: Catalytic alkyne functionalization catalyzed by a cationic gold(I) complex[4,7]

The excellent Lewis acidic properties of the cationic gold complexes have been documented as the success behind the gold catalysts.[8] The Lewis acidic properties, in turn, can be attributed to the relativistic effects and the high electronegativity (χ = 2.4) for gold. Contraction of the 6*s*-orbital in gold(I) accounts for both a strengthened L-Au bond and also a low-lying, lowest unoccupied molecular orbital (LUMO). Additionally, the expansion of the 5*d*-orbital creates a scenario in which the electrons experience less electron-electron repulsion as a result of the more diffuse orbital system. The electrons are now attracted more closely to the nucleus and this causes a decrease in the nucleophilic character of

© University of Pretoria

the metal center compared to, for example, copper. It has also been proposed that the diffuse 5*d*-orbitals can accommodate backbonding from the gold to the empty conjugated *p*-orbitals, stabilizing the catalytic intermediates during a catalytic reaction.[8] The carbophilic cationic gold center, with its low-lying LUMO and backbonding to stabilize the catalytic intermediate, can account for the high affinity of the metal towards unsaturated substrates, even in the presence of other, stronger donor functionalities.

The coordination and activation of unsaturated bonds were considered, until very recently, to be the predominant reactivity pattern for gold complexes and the elementary reactions of organometallic chemistry for gold were believed to be highly unfavourable, if not impossible.[6] These elementary organometallic reactions, namely oxidative addition, reductive elimination, transmetallation and migratory insertion reactions are governed by the high redox potential of the Au(I)/Au(III) couple (E^0 = + 1.41 V),[9] and the strong tendency of gold(I) to form linear two coordinate neutral, or cationic complexes.[6] Therefore, the question remains: can the reactivity profile of gold be extended to include the elementary organometallic reactions in order to mimic the platinum group metals? The question was unequivocally answered with a few recent seminal reports. Gold can be manipulated, through appropriate ligand design, control of the coordination environment and under the correct reaction conditions to resemble reactivity patterns reminiscent of the platinum group metals.[6]

5.1.1 Transmetallation

The transmetallation reaction is a well-known transformation process in which the transfer of organic fragments occur; and, with respect to organometallic chemistry, usually between a nucleophilic organometallic species and a transition metal complex. In the case of gold, it has been documented as an active nucleophilic organogold species transferring an organic fragment to a transition metal, usually a Pd-metal complex during stoichiometric and/or catalytic reactions.[10] Recent reviews have summarized these examples, and a few seminal reports will be highlighted to showcase both its significance and elegance. This includes transmetallation reactions between gold and other metal centers, or gold transmetallation with *p*-block elements.[6,10]

The group of Blum described the Au-Pd catalyzed synthesis of butenolides and isocoumarins, structural motifs of active biological compounds.[11] It was proposed that the Lewis acidic gold(I) complex catalyzed the cyclization of starting allenoate, yielding the allyl oxonium intermediate (Scheme 5.1). The reactive oxonium intermediate was subsequently subjected to deallylation, facilitated by the Lewis basic

© University of Pretoria

palladium catalyst to generate the neutral vinyl-gold species and the palladium complex, π-coordinated by the allyl moiety. Transmetallation ensued, releasing the active gold(I) catalyst with formation of the Pd(II) intermediate that continues through a C-C bond forming reductive elimination reaction, which in turn yields the targeted organic product and the Pd(0) starting catalyst. The dual-catalytic C-C bond formation protocol decreases the reaction energy barrier significantly through the allyl oxonium intermediate, in addition to providing an alternative for the classical gold(I) catalyzed reactions, dominated by the protodemetallation step.[11]

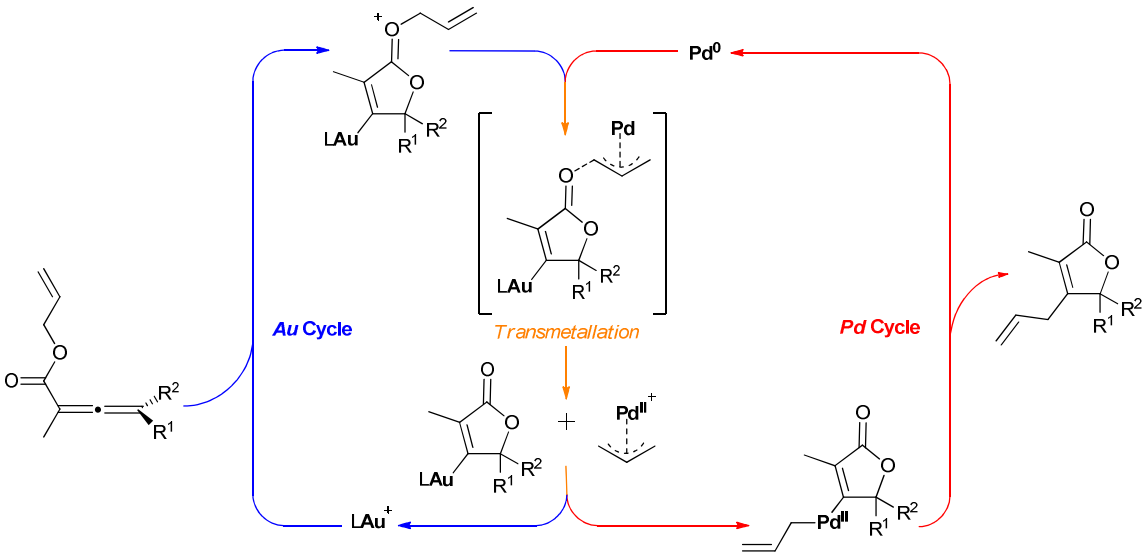

Scheme 5.1: Dual-catalytic C-C bond formation reaction *via* gold-palladium transmetallation step[11]

More recently, Nevado and co-workers unequivocally demonstrated the bimetallic catalyzed protocol as two independent gold and palladium catalyzed cycles that are connected at the transmetallation step (Scheme 5.2).[12] In contrast to the mechanism reported by Blum and co-workers (see Scheme 5.1),[11] the catalytic allyl oxonium gold intermediate is not necessary in order to turn on the palladium catalytic cycle.[12] The synergistic gold-palladium catalyzed reaction incorporated allenoates with aryl and heteroaryl iodides, in addition to exhibiting a wide functional group tolerance, of which the success has been ascribed to the separation of the two catalytic cycles as independent process (Scheme 5.2). Allenoate π-activation and cyclization to yield the zwitterionic vinylgold intermediate is an equilibrium reaction, favoured by excess allenoate. As expected, selective oxidative addition of the aryl and heteroaryl iodides occurred across the short-lived anionic Pd(0) metal center, which was generated by the sequestration of the chlorido co-ligands by CsOAc. The precipitation of CsCl is also highly necessary, as free chloride anions would coordinate to, and deactivate the gold(I) catalyst (Scheme 5.2).[12] The

© University of Pretoria

iodine atom from the Ar-I collapse with the alkyl group from the zwitterionic vinylgold lactone during the transmetallation step yielding, *1)* the active gold(I) catalyst that re-enters the gold cycle, *2)* the Pd(II) intermediate that releases the desired butenolide product and the active Pd(0) catalyst after reductive elimination, and *3)* the alkyl-iodide as a byproduct from the reaction. Finally, no products from protodeauration were detected (Scheme 5.2). This multicomponent catalytic reaction is mild, robust and allows for the preparation of elaborate organic products in a one-pot reaction medium.

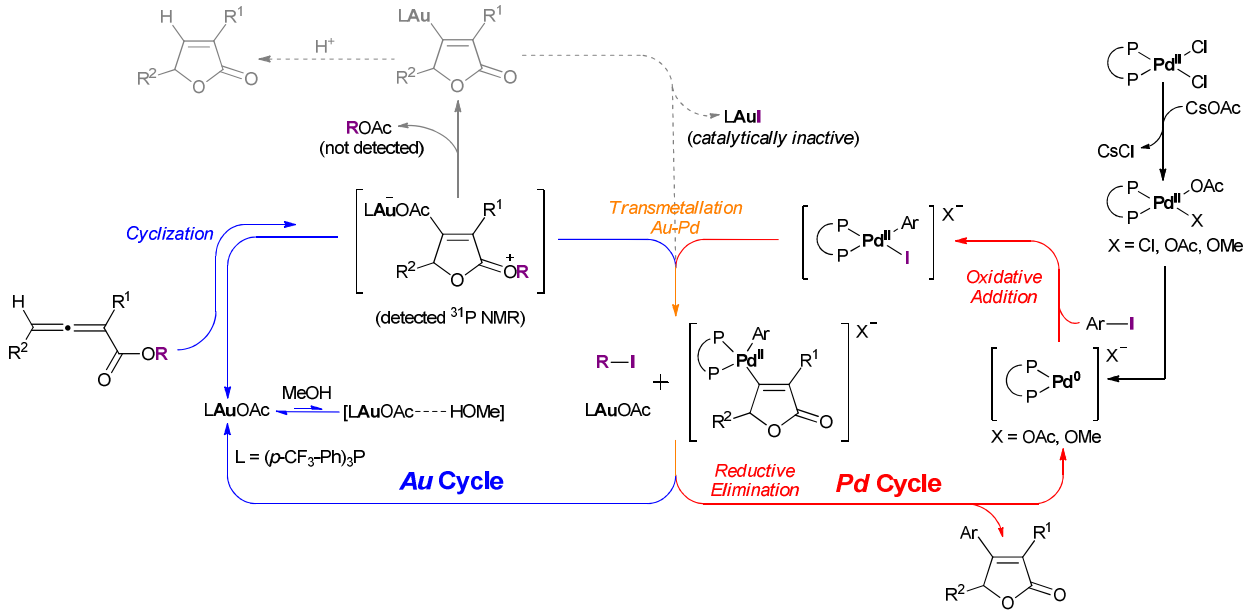

Scheme 5.2: One-pot tandem gold-palladium catalyzed synthesis of butenolides[12]

The extreme electrophilic character of the cationic gold(I) complexes was recently evidenced again, during a transmetallation reaction between an NHC-Au(I) chlorido complex and $NaBArF_{24}$ ($BArF_{24}$ = tetrakis[bis(3,5-trifluoromethyl)phenyl]borate).[13] Immediate precipitation of NaCl was observed and after several days, crystals of the gold(I) complex were obtained and evidenced a C-B bond activation and cleavage reaction (Scheme 5.3). The reactivity of the electrophilic gold(I) cation was compared to that of other proton sources, such as sulfuric acid, with the reactivity being equivalent to only an order of magnitude lesser than that of diethyloxonium etherate. The electrophilic character of cationic gold(I) complexes readily facilitates transmetallation reactions, demonstrating the feasibility of this elementary transformation reaction without the use of additional transition metal complexes.[13]

© University of Pretoria

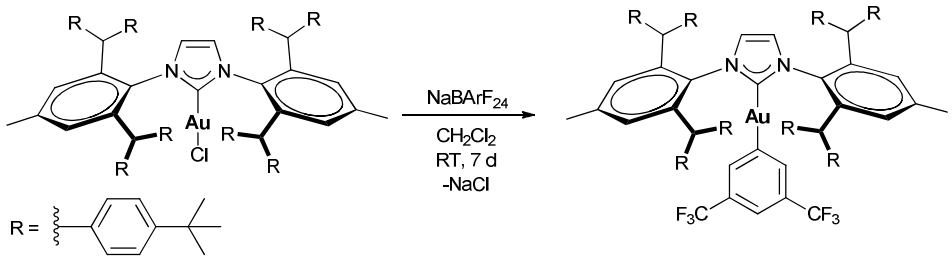

Scheme 5.3: Transmetallation at an electrophilic gold(I) center[13]

Gold(III) transmetallation reactions have also been realized with various gold complexes, mostly as stoichiometric examples.[6] A transmetallation approach reported by Bochmann and co-workers, allowed for easy and mild access to photoluminescent gold(III) complexes (Scheme 5.4).[14] The complexes could be prepared by accommodating high yields through the reaction of the gold(III) hydroxide and the corresponding boronic acids.

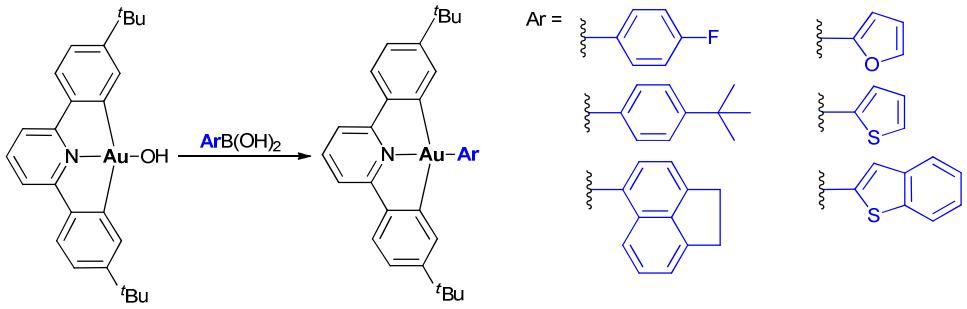

Scheme 5.4: Photoluminescent gold(III) aryl complexes synthesized through a transmetallation approach[14]

5.1.2 Migratory insertion

Migratory insertion is often considered as a possible pathway through which gold-catalyzed functionalization proceeds.[6] Both outer- and inner-sphere mechanisms have been considered for gold-catalyzed olefin activation, with most experimental and theoretical calculations supporting an outer-sphere mechanism (Scheme 5.5).

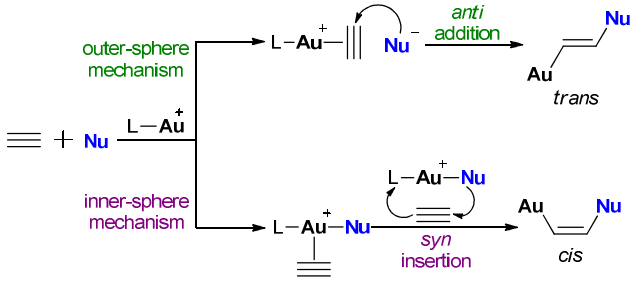

Scheme 5.5: Inner- and outer-sphere migratory insertion reaction facilitated by a gold complex

© University of Pretoria

The group of Sadighi has reported the synthesis and isolation of the first examples of a gold(I) hydride[15] and a gold(I) fluoride complex stabilized by an NHC ligand;[16] complexes believed to be only transient intermediates in catalytic reactions. The robust metal carbene carbon bond with the bulky wingtip substituents allowed for isolation of such reactive species, which provides clear cut evidence for their existence during a catalytic reaction.[5,17] The (NHC)AuH and (NHC)AuF complexes were shown to facilitate migratory insertion reactions, following an outer-sphere mechanism to yield the products of an *anti*-addition reaction. The gold fluoride readily reacted with 1-phenyl-1-propyne affording the product with a *trans*-arrangement of gold and fluorine about the vinylic bond (**I**, Scheme 5.6).[16b] It was stated that displacement of the fluoride ligand by the alkyne forms the cationic gold intermediate, which is followed by nucleophilic attack on the coordinated alkyne by the fluoride nucleophile.[16b] The (NHC)AuH reacted cleanly with dimethyl acetylenedicarboxylate to afford the corresponding vinyl gold(I) complex (**II**, Scheme 5.6).[15] The gold hydride did not react with various other, less reactive alkynes. The results from both studies suggested that gold(I) complexes generally follow an outer-sphere mechanism during a migratory insertion reaction.[6] This is consistent with the fact that two-coordinate gold(I) complexes are very reluctant to coordinate a third ligand. As a result, gold(I) complexes do not follow an inner-sphere migratory insertion reaction mechanism, if the aforementioned complexes are reactive towards unsaturated substrates.[6] The group of Bourissou reported an exception to the general rule, where a phosphine gold(I) silyl complex was able to coordinate an alkyne without dissociation of either the silyl or phosphine co-ligands (**III**, Scheme 5.6).[18] The three coordinate π-intermediate follows an inner-sphere migratory insertion pathway to yield the product of a *syn* insertion reaction, namely the *cis* gold(I) vinyl complex.

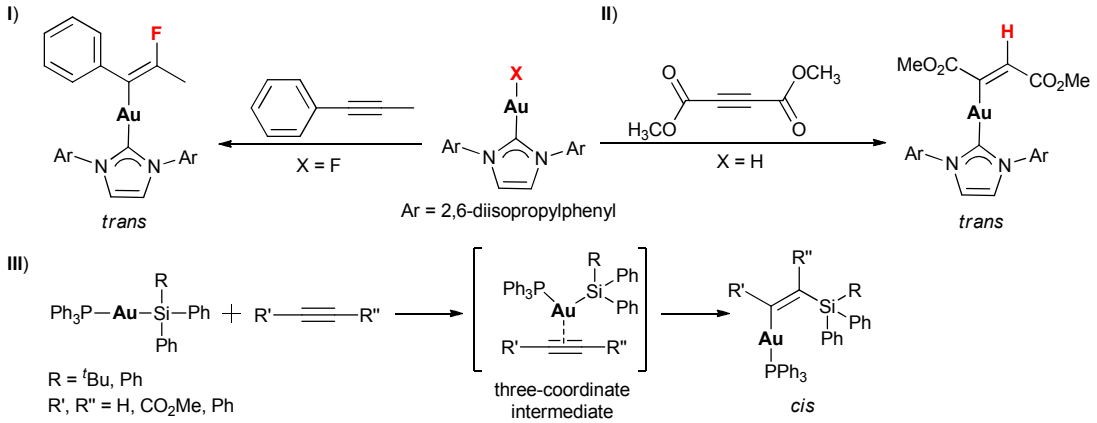

Scheme 5.6: Reactive gold(I) complexes for selective migratory insertion reactions with alkynes

© University of Pretoria

Pincer complex formation demonstrated a high degree of stabilization imparted to the metal, when the first gold(III) hydride was realized by Bochmann et al. in 2012. The pincer gold(III)-hydride complex was accessed through reacting a doubly cyclometallated gold(III) hydroxide with $LiHBEt_3$ (**I**, Scheme 5.7).[19] The hydride was remarkably stable under atmospheric conditions. Again, the isolation of the gold(III)-hydride supports postulated catalytic mechanisms involving *in situ* formation of a gold hydride species, and in this case, a Au(III)-H intermediate. Furthermore, the ligand stabilized the first example of a ''classical'' gold-carbonyl complex (**II**, Scheme 5.7),[20] in addition to stabilizing a range of π-coordinated olefinic gold complexes (**II**, Scheme 5.7).[21] But, with respect to the migratory insertion reaction, it was demonstrated that allenes regioselectively insert across the gold-hydride bond, with formation of the gold(III) vinyl complexes (**I**, Scheme 5.7).[19] The gold hydride complex was unreactive towards ethylene and various other alkynes. However, the gold trifluoroacetato complex (**II**, Scheme 5.7) reacted with ethylene to yield the product of insertion.[21]

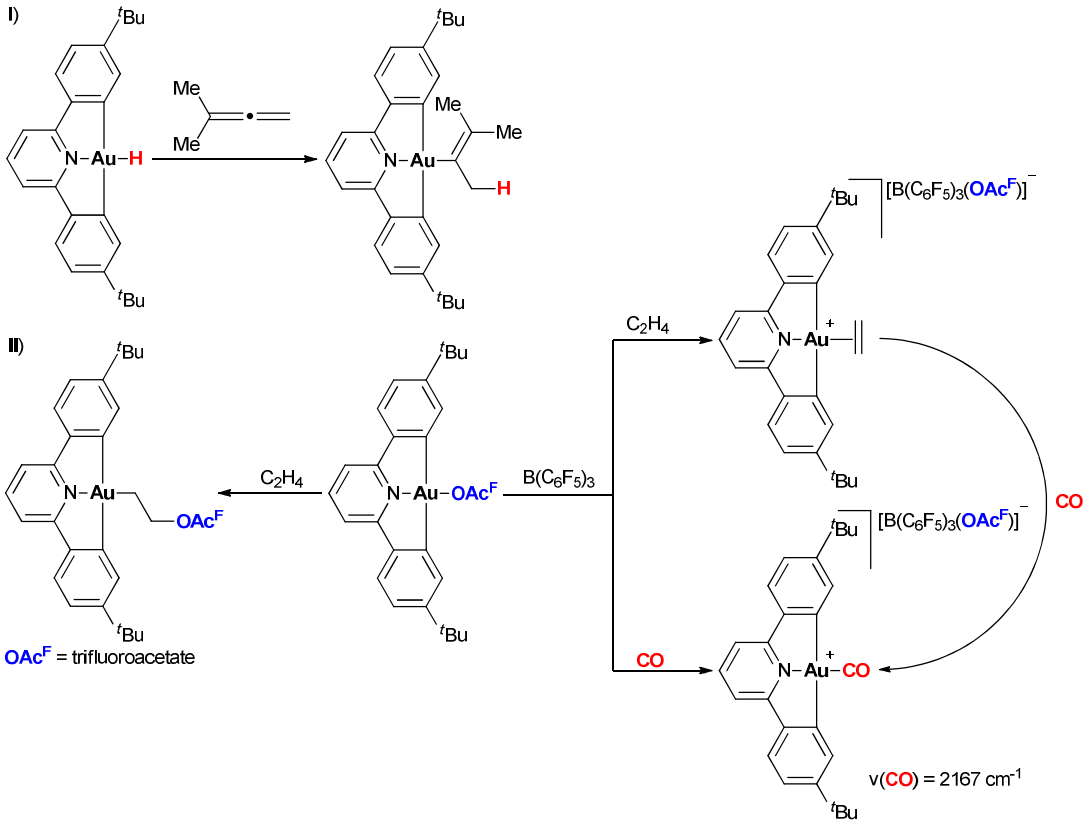

Scheme 5.7: Stabilization of transient gold(III) complexes and their reactivity towards olefins

A comprehensive mechanistic study was reported by the group of Tilset, regarding the insertion of ethylene into a gold(III) oxygen bond.[22] Ethylene insertion occurred *trans* to the nitrogen atom of the

© University of Pretoria

bidentate C,N-ligand (Scheme 5.8). The reaction involved two steps, as was determined from both experimental data and theoretical calculations. First, the trifluoroacetate (OAc^F) ligand *trans* to the nitrogen donor ligand is displaced by ethylene *via* an associative mechanism, forming the π-coordinated ethylene gold(III) cation. This step was reported to be rate-limiting and solvent-dependent.[22] Subsequent *anti*-addition of the free OAc^F ligand to the coordinated ethylene, yields the gold(III) alkyl complex through a migratory reaction following an outer-sphere mechanism.

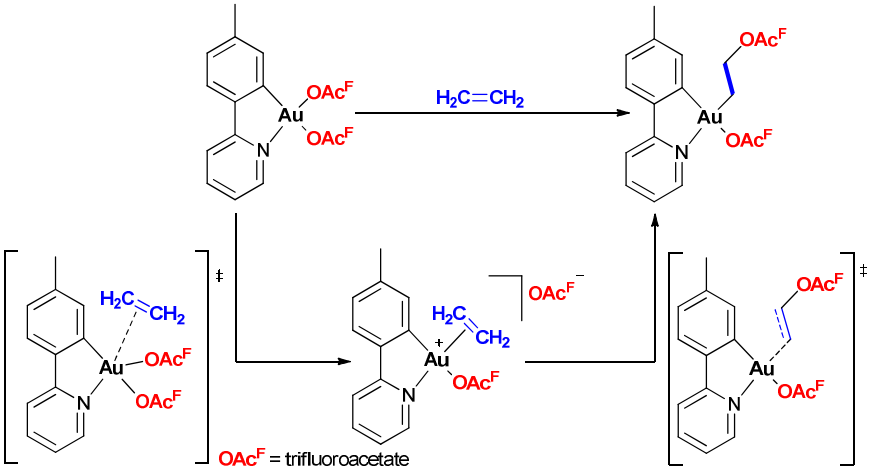

Scheme 5.8: Mechanistic investigation of migratory insertion of ethylene at a gold(III) oxygen bond[22]

A gold(III) dimethyl complex, another complex previously believed to be only a transient intermediate during catalytic reactions, was shown to effectively facilitate the migratory insertion reaction with norbornene.[23] The gold(III) dimethyl complex was readily synthesized through treatment of the diiodogold(III) complex with a Grignard reagent (Scheme 5.9). This was followed by the reaction with excess norbornene in the presence of a strong boron Lewis acid. The reaction proceeded with abstraction of a methyl ligand, followed by coordination of norbornene to the reactive cationic gold(III) complex. A double insertion reaction ensues involving two norbornene units with the reaction proceeding *via* an inner-sphere mechanism (Scheme 5.9). Coordination and insertion accounts for the products of a *syn* addition reaction following an inner-sphere migratory insertion pathway, constituting a rare example of such reactivity observed for gold.[23] Finally, the intermediate cationic gold(III) complex is trapped and stabilized by coordination of either lutidine or pyridine yielding the cationic gold(III) complex, or through quenching the complex with tetrabutylammonium chloride resulting in the isolation of the neutral gold(III) complex (Scheme 5.9).

© University of Pretoria

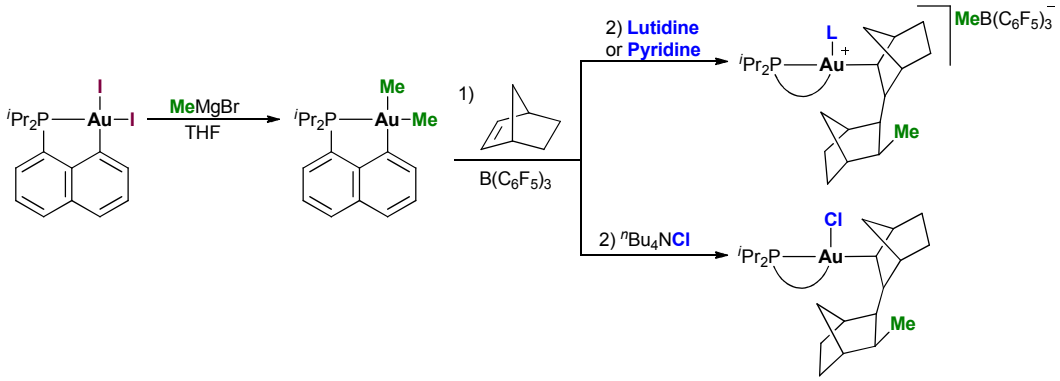

Scheme 5.9: Norbornene insertion across a gold(III)-methyl bond[23]

5.1.3) Reductive elimination

The feasibility of reductive elimination at Au(III) was evident as early on as 1939 as shown by Brain and Gibson,[24] and in 1973 Aresta and Vasapollo demonstrated reductive elimination of a phosphine dibromogold(III) aryl complex to yield the phosphine bromogold(I) complex and the corresponding arylbromide compound (**I**, Scheme 5.10).[25] A mechanistic study by Kochi and co-workers demonstrated that thermal decomposition of the starting tertracoordinated alkyl gold(III) complexes $(Ph_3P)Au(CH_3)_3$ or *cis*-$(Ph_3P)Au(CH_3)_2(X)$, results in the reductive coupling of two methyl-ligands yielding ethane and the $Ph_3PAu(I)X$ (where X = CH_3, OTf, Cl, NO_3, CH_3CO_2) complex (**II**, Scheme 5.10).[6,26] Addition of excess phosphine inhibited the reaction, as the first and rate-determining step was proposed to be dissociation of the phosphine ligand to yield the intermediate, three-coordinate gold-methyl complex that undergoes a fast reductive elimination reaction. Similar to the work done by Kochi et al., Komiya and co-workers also studied the reductive elimination of gold(III) alkyl species, in order to determine the selectivity of the reaction when different hybridized alkyl moieties are substituted at the gold(III) center.[27]

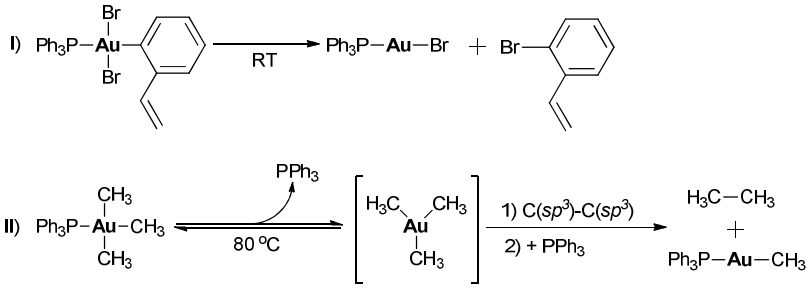

Scheme 5.10: Early evidence of reductive elimination at gold(III)[6,25,26]

© University of Pretoria

Reductive elimination at a gold(III) fluoride complex was investigated by Toste and co-workers. Oxidation of a (IPr)Au(alkyl) (IPr = *N*,*N'*-bis(2,6-diisopropylphenyl)imidazole-2-ylidene) with XeF_2 yielded the *cis*-[(IPr)Au(alkyl)$(F)_2$] complex that could undergo reductive elimination following a dissociative pathway.[28] The product of reduction was the C(sp^3)-F and the (IPr)AuF complex, while the rate of the reaction was dependent on fluoride dissociation yielding the cationic gold(III) intermediate, which is followed by a fast reductive elimination process. Side reactions such as β-hydride elimination or carbocation rearrangements were also noted, and these were in competition with C(sp^3)-F bond formation, but dependent on the nature of the alkyl substituent.[28] The same group again demonstrated the facile reductive elimination of gold(III) complexes; in this case, the reductive coupling of aryl-I or aryl-CF_3 from the corresponding four-coordinate aryl gold(III) complex $(Ph_3P)Au(4\text{-}F\text{-}C_6H_4)(CF_3)(I)$.[29] The gold(III) complex could be prepared by oxidation of the gold(I) with CF_3I (Scheme 5.11). Selective reductive coupling occurs at elevated temperatures yielding the aryl-I compound, even though the aryl- and iodo-substituents occupy the *trans* position with respect to each other, when coordinated to the gold(III) metal. This, and the fact that addition of excess phosphine completely inhibits the decomposition reaction, clearly suggest a dissociative pathway with a three-coordinate intermediate leading to the selective formation of the C(sp^2)-I bond, favoured over the C(sp^2)-CF_3 bond formation.[29] Selectivity for C(sp^2)-CF_3 bond formation was only achieved by the addition of a silver salt as halide scavenger (Scheme 5.11).

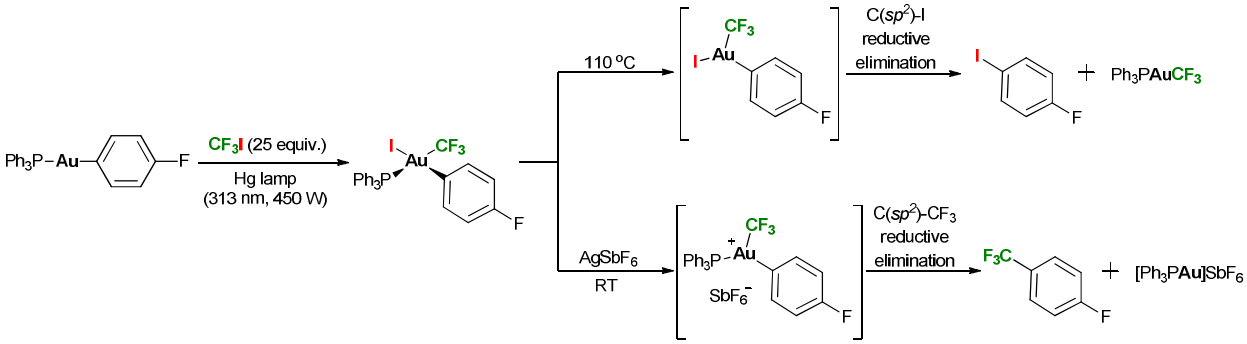

Scheme 5.11: Selective aryl-CF_3 or aryl-I reductive coupling through a gold(III) complex[29]

The feasibility of C(sp^2)-N bond formation upon reductive elimination from the corresponding gold(III) complex, *via* a dissociative mechanism yielding the three-coordinate gold(III) intermediate, was also investigated.[30] Limbach et al. proposed that reduction can occur from a four-coordinate, dichloro(lutidine)phenylgold(III) complex upon treatment with morpholine (Scheme 5.12). Substitution of the lutidine with morpholine was followed by deprotonation of the bound morpholine with NaOAc,

© University of Pretoria

leading to dissociation of a chloride ligand. Fast reductive elimination of the three coordinate intermediate yielded the aryl-morpholine compound, with no competitive side-reactions such as C(sp^2)-Cl bond formation (Scheme 5.12).[30] The various case studies suggest that reductive elimination can occur through ligand dissociation yielding a three-coordinate intermediate, followed by a fast reductive elimination to yield the corresponding gold(I) complex and the coupled organic product. However, this is not the only mechanism of reductive elimination, and a few reports regard the direct reductive process from four-coordinate gold(III) complexes without a three-coordinate intermediate.

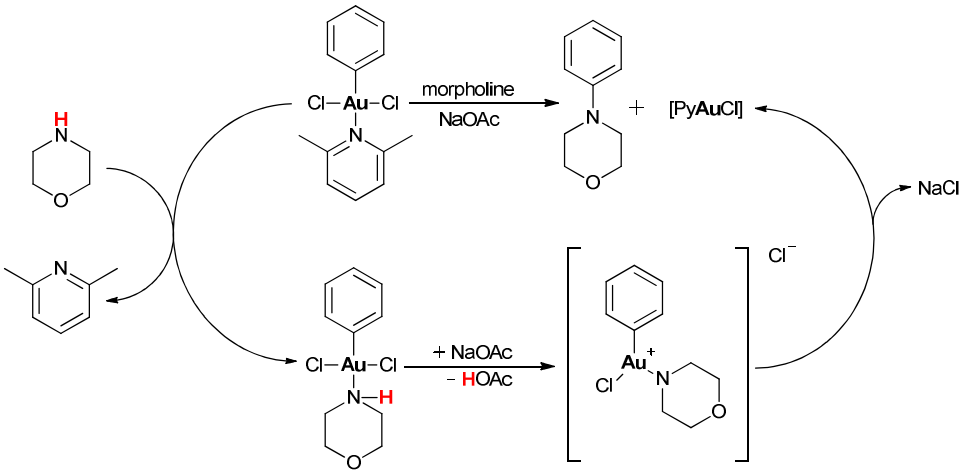

Scheme 5.12: Reductive coupling of a four-coordinate gold(III) lutidine complex[30]

A C(sp^2)-C(sp^2) coupling reaction, via reductive elimination from a four-coordinate gold(III) biphenyl complex, was reported by Toste and co-workers.[31] The reduction reaction was reported as one of the fastest transition-metal-mediated coupling reactions to date. Oxidation of $(PPh_3)(p\text{-}F\text{-}C_6H_4)Au(I)$ with phenyliodoso dichloride yielded, *in situ*, the *cis*-bis(aryl)gold(III) complex after transmetallation with a second equivalent of arylgold(I) at -78 °C (Scheme 5.13). Gold(III) decomposition occurred rapidly at -52 °C, yielding the difluorobiphenyl coupled product and the triphenylphosphine gold(I) chloride. Unlike reductive elimination *via* a three coordinate intermediate, reduction at the four coordinate *cis*-bis(aryl)gold(III) complex is not inhibited by addition of excess phosphine, and in fact, the rate of the reaction is increased. It was proposed that the complex goes through a rapid chlorido-phosphine ligand substitution reaction at the gold center, due to the excess phosphine in solution. This yields a cationic gold(III) intermediate that reduces at increased rates (Scheme 5.13).[31]

© University of Pretoria

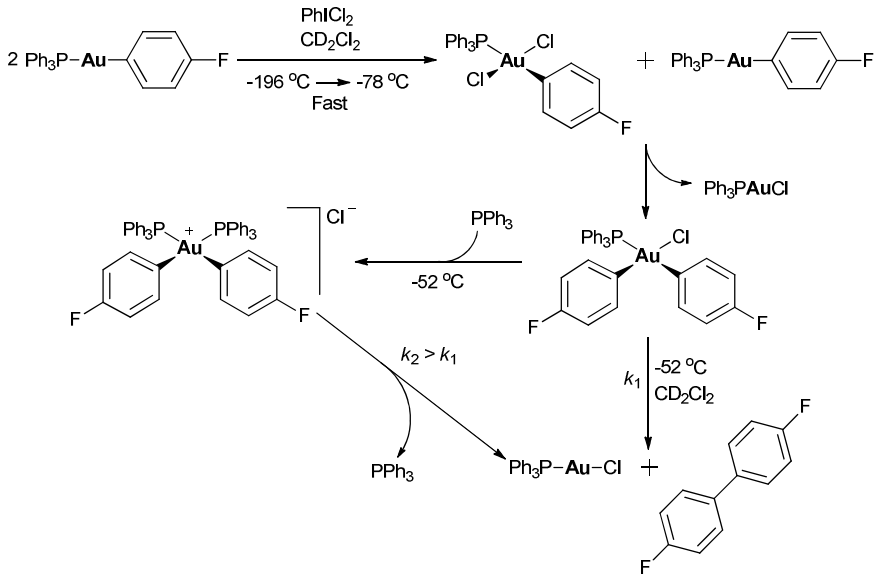

Scheme 5.13: Exceptionally fast reductive coupling yielding difluorobiphenyl and gold(I) species[31]

5.1.4 Oxidative addition

As shown for gold(III) complexes, reductive elimination occurs readily, mainly through *in situ* generation of a reactive intermediate that reductively eliminates to yield the corresponding coupled product and the gold(I) complex. Heuristically, the expectation is therefore that the oxidative addition reaction should be just as accessible. This is not the case, as the various properties of gold discussed in Section 5.1 govern the reactivity of gold towards oxidation reactions employing mild oxidants. Strong oxidants have been used to overcome the high redox potential of the Au(I)/Au(III) couple, and as intuitively expected, such harsh reaction conditions does not allow for broad substrate scope due to low functional group tolerance during a stoichiometric or catalytic reaction, not to mention the high probability of complex decomposition or the occurrence of side reactions. However, a few recent seminal reports have diminished the stigma that gold is oxidatively inert under mild reaction conditions. Appropriate ligand design or choice of substrates employed, as well as fine-tuning of the reaction conditions or the use of light irradiation, leads to adequate manipulation of gold(I) to gold(III) under mild reaction conditions. This allows for new routes to gold(III) complexes previously deemed inaccessible. The various strategies employed towards ***well-defined*** gold(III) complexes *via* ***mild*** oxidative addition across a gold(I) metal center will be briefly discussed. Stoichiometric and/or catalytic reactions involving *in situ* oxidation of a gold(I) precursor with a harsh oxidant such as Selectfluor, will not be discussed.[17]

© University of Pretoria

5.1.4.1 Monocoordinate cationic gold(I)

Bourissou and co-workers recently described the oxidative addition reaction across an unsaturated gold(I) complex, demonstrating that linear gold(I) complexes can in fact facilitate oxidative addition reactions, albeit dependent on the appropriate reaction conditions and choice of substrates.[32] A phosphine coordinated gold(I) chloride complex was treated with $GaCl_3$, followed by addition of a disilane at -90 °C. The authors noted that an oxidative addition event had occurred, yielding the cationic $[(L)(SiMe_2R)_2Au(III)]GaCl_4$ complex (**I**, Scheme 5.14). Unfortunately, the Au(III) complexes were highly reactive and decomposed rapidly above -60 °C. However, they were able to characterize the complex with extensive low-temperature NMR studies. Further support for the structure of the complex was elucidated by computational calculations, which had predicted that the gold species adopts a distorted, three-coordinate Y-shaped geometry.[32] The solution to isolate a stable gold(III) complex through mild oxidative addition at an unsaturated, monocoordinated gold(I) complex, was found by the use of a biphenylene substrate. Oxidative addition of a strained biphenylene to a coordinatively unsaturated $[IPrAu(I)]SbF_6$ complex yielded the gold(III) product coordinated by IPr, the cleaved biphenylene that now coordinates as a C_{sp^2}-C_{sp^2} bidentate ligand, in addition to a weakly coordinating H_2O ligand (**II**, Scheme 5.14).[33] Treatment with $^nBu_4NCl$ substituted the water molecule and formed the neutral gold(III) chloride complex. The coordinating water ligand could also be substituted by *N,N*-dimethylformamide (DMF), which increased the stability of the already benchtop stable gold(III) complex. The reaction mechanism was hypothesized to occur *via* coordination of the biphenylene to the unsaturated gold(I) complex, followed by oxidative addition through C-C bond cleavage of the strained biphenylene generating two gold-aryl bonds. The bond dissociation energy of the strained biphenylene substrate is high, which constitutes for the driving force behind the oxidative addition reaction. It was realized that the gold(III) complex could selectively catalyze a range of organic transformation reactions, which are not accessible employing Au(I) or harsh $AuCl_3$ complexes, in addition to various other sterically demanding Lewis- and Brønsted-acid catalysts. Remarkably, the mild oxidation of the Au(I) complex allowed for a one-pot tandem Au(I)/Au(III) catalyzed reaction (**III**, Scheme 5.14). The Meyer-Schuster rearrangement reaction of propargyl alcohol was first catalyzed by the $[IPrAu(I)]SbF_6$ complex which yielded the unsaturated aldehyde.[33] A Mukaiyama-Michael addition catalyzed reaction between the formed aldehyde and the added ketene silyl acetal yielded the 1,4-/1,2-adducts (≥ 98/2), catalyzed by the *in situ* generated Au(III) complex after the addition of biphenylene to the same reaction mixture. Moreover, the Au(I)/Au(III) tandem reaction allowed for the ring-opening and Mukaiyama-Michael addition reactions. The successive ring-opening Au(I) catalyzed reaction of cyclopropene, which reacted

© University of Pretoria

with excess furan, yielded the conjugated aldehyde that was further catalyzed with added ketene silyl acetal by the *in situ* generated gold(III) catalyst to generate the final product with 98% 1,4-selectivity and 53% isolated yield (**III**, Scheme 5.14).[33]

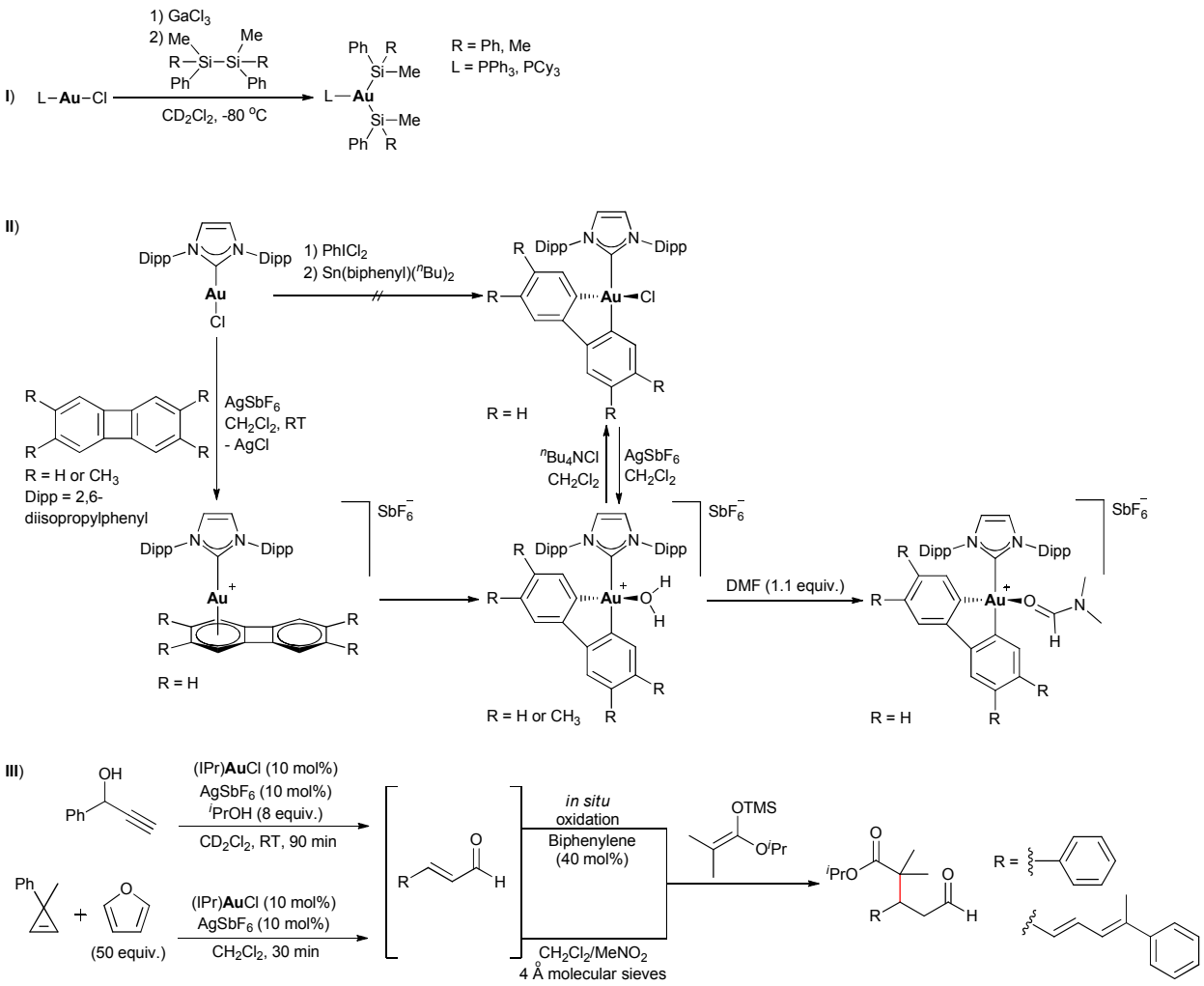

Scheme 5.14: Oxidative addition at monocoordinated cationic gold complexes

The group of Bertrand very recently reported the facile synthesis of a range of cyclic (alkyl)(amino) carbenes (CAACs) featuring various pendant moieties.[34] The (CAAC)gold(I) chloride complex, obtained after deprotonation of the CAAC ligand and subsequent coordination to (tht)AuCl (tht = tetrahydrothiophene), facilitated the oxidative addition of biphenylene when treated with $KB(C_6F_5)_4$ prior to the addition of biphenylene (Scheme 5.15). The hard nitrogen from the imine pendant functionality did not coordinate to the soft gold(I) metal center, but upon oxidation of the cationic $[(CAAC)Au(I)][B(C_6F_5)_4]$ with biphenylene, the imine pendant coordinated and stabilized the corresponding gold(III) complex. Importantly, oxidative addition was not successful when other CAAC-

© University of Pretoria

ligands featuring different functionalities on the side chains were employed, even upon heating the reaction mixtures in question. This illustrates that the imine pendant strongly stabilizes the gold(III) complex favouring Au(I) oxidation (Scheme 5.15).[34] In addition, such hemilabile character could not only stabilize, but also assist the complex during catalytic reactions and therefore function as a non-innocent ligand.

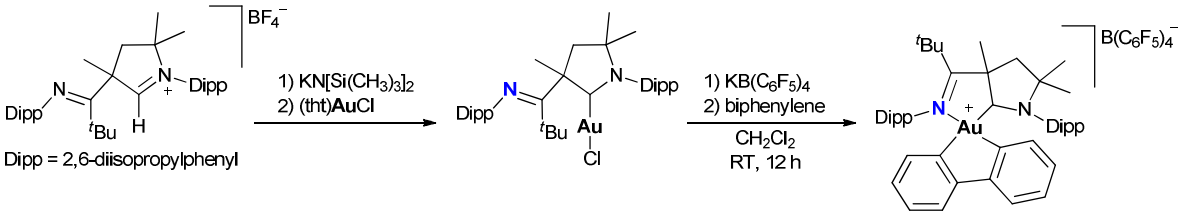

Dipp = 2,6-diisopropylphenyl

Scheme 5.15: Tethering-assisted oxidative addition of biphenylene across a cationic (CAAC)Au(I) complex[34]

5.1.4.2 Neutral two coordinate gold(I) complexes

The use of both aryldiazonium salts acting as oxidizing agents, and visible-light for photoredox processes, has become a widely used technique for stoichiometric and catalytic reactions. The recent success in the field of photoredox promoted gold catalyzed reactions employing aryldiazonium salts has been reviewed.[35] As such, only a few examples of well-defined Au(I) oxidative addition reactions taking advantage of either aryldiazonium salts or light-promoted oxidation reactions will be briefly discussed. Glorius et al. described the facile oxidative addition across a neutral, linear two-coordinate gold(I) complex. The reactivity of diazonium salts in addition to the photoredox properties of the $[Ru(bpy)_3](BF_4)_2$ photocatalyst sufficiently oxidized the gold metal precursor at room temperature.[36] Light irradiation (5 W green LED as light source) excited the photocatalyst, with a subsequent single-electron transfer (SET) event to the diazonium salt (**I**, Scheme 5.16). The aryl radical reacts with the Au(I), generating the intermediate gold(II) that is subjected to a second SET event, to yield the desired gold(III) complex.[36] The route towards gold(III) complexes *via* light promoted oxidative addition across various gold(I) complexes, employing aryldiazonium salts, was reported by Hashmi and co-workers (**II**, Scheme 5.16).[37] The method did not require the use of a photocatalyst, with oxidation readily achieved at room temperature. Parallel to the reports by Glorius and Hashmi, the group of Porcel described the direct oxidative addition of diazonium salts to neutral gold(I) complexes.[38] Their approach involved the *in situ* generation of diazonium salts, exchange of solvent and addition of the gold(I) precursor (**III**, Scheme 5.16). At room temperature, the reaction was slow, but heating up the reaction mixture afforded the gold(III) complexes in less than three hours.[38]

© University of Pretoria

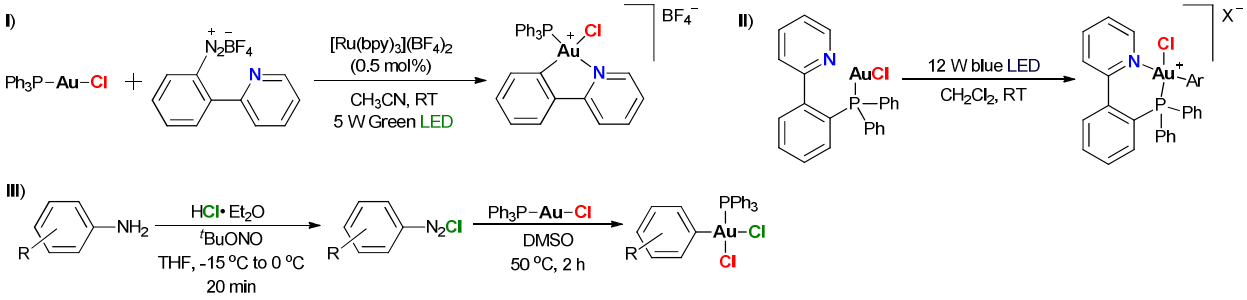

Scheme 5.16: Gold(I) oxidative addition facilitated by photoredox systems or use of diazonium substrates

5.1.4.3 Chelate-assisted oxidative addition

The group of Bourissou developed a series of phosphine ligands, whereby coordination of the phosphine would position the gold(I) metal close to a σ-bond providing a favourable environment for oxidative addition reactions. Coordination of $(Me_2S)AuCl$ to the diphosphine-disilane ligand yielded the intermediate gold(I) complex, followed by spontaneous oxidative addition (Scheme 5.17).[39] The cationic bis(silyl) gold(III) complex, obtained after treatment of the intermediate gold complex with $GaCl_3$, was isolated as a stable complex in high yields. Additionally, a monophosphine-disilane ligand was also coordinated to a gold(I) metal center, which was followed by oxidative addition. However, decomposition ensued above -30 °C, implicating that two phosphine buttresses are not necessary to facilitate oxidative addition but are crucial for stabilization of the formed gold(III) product.[39] Noteworthy is the analogous coinage metals (both Ag and Cu) that coordinated to the diphosphine-disilane ligand, but the products of oxidative addition were not detected.

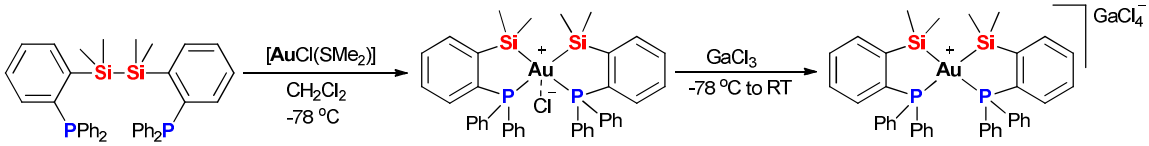

Scheme 5.17: Spontaneous Si-Si bond oxidative addition[39]

The chelate-assisted oxidative addition strategy developed by Bourissou and co-workers proved to be beneficial also with regards to the oxidative addition of C_{sp^2}-X (X = Br, I) bonds across a mononuclear gold(I) metal.[40] Coordination of 8-halo naphthyl phosphines to neutral gold(I) precursors occurred readily. Phosphine coordination was followed by C_{sp^2}-I and C_{sp^2}-Br bond oxidative addition, yielding the corresponding stable gold(III) complexes (**I**, Scheme 5.18). The oxidative addition of the C_{sp^2}-Cl bond across the phosphine gold(I) chloride was not favoured, even after heating the reaction mixture for several days. The seminal report by Bourissou and co-workers further described the facile synthesis of

© University of Pretoria

cyclometallated gold(III) complexes, without the use of organomercury salts or preparative methods involving multistep synthesis. Oxidation and addition of a C_{sp^2}-Br bond was preceded by coordination of two phosphine ligands to a (Me_2S)AuBr metal precursor (**II**, Scheme 5.18).[40] The ensuing gold(III) complex did not show any sign of decomposition, even under atmospheric conditions. The novel oxidative addition strategies paves the way for synthetically useful, well-defined gold(III) complexes not accessible employing classical procedures.

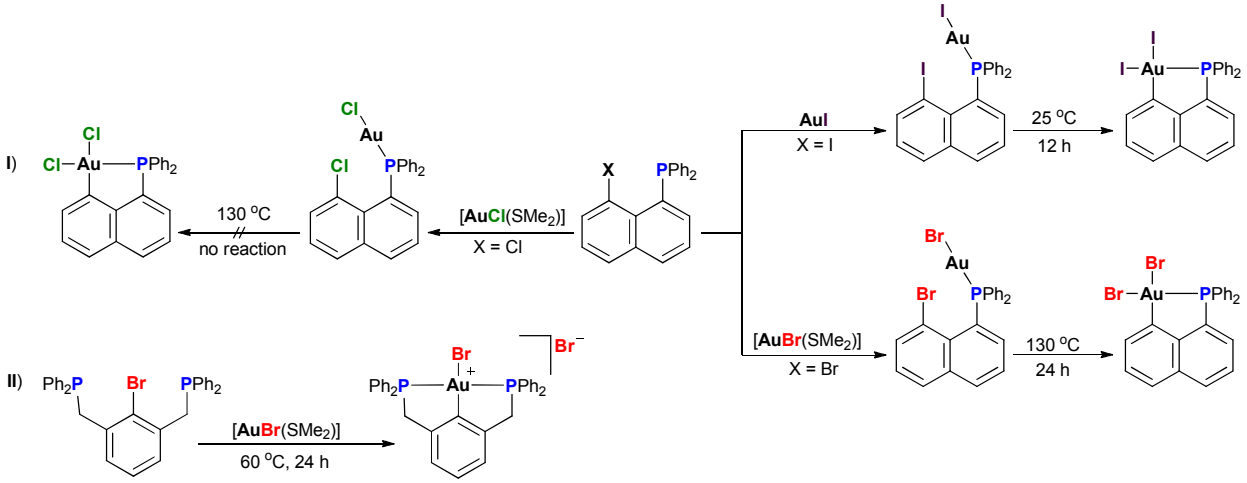

Scheme 5.18: Chelate assisted C_{sp^2}-I and C_{sp^2}-Br bond oxidative addition[40]

5.1.4.4 Bent two-coordinate gold(I) complexes

A different approach to mild gold(I) oxidative addition involved the use of bidentate ligands that, upon coordination, yield a metal complex with a small ligand bite angle. This method is commonly used for the synthesis of reactive Group 10 metals, but has generally not been applied to gold because of the strong prevalence for linear complex formation. However, a gold(I) complex coordinated by a bidentate ligand with a small bite angle was recently reported by the group of Bourissou (Scheme 5.19).[41] The gold(I) triflimidate complex, obtained after chloride abstraction with $AgNTf_2$, coordinated by the carborane diphosphine ligand exhibited an extremely acute P-Au-P bond angle of 100.73(2)° (**I**, Scheme 5.19). The energy of the bent complex had been raised, and the coordination environment was preorganized to accommodate a square-planar geometry after oxidation of the gold(I) metal. The result is rapid and spontaneous oxidative addition of aryl iodides, yielding the corresponding stable gold(III) complexes (**I**, Scheme 5.19). It was additionally shown that various aryl iodides could be used, with electron-rich substrates reacting faster.[41] The group of Bourissou further disclosed the oxidative addition of C-C bonds across the diphosphino-carborane gold(I) complex.[42] The neutral Au(I) complex was first

© University of Pretoria

reacted with $GaCl_3$ and then with biphenylene, resulting to C-C oxidative addition and isolation of the gold(III) product (**II**, Scheme 5.19). More impressive was the selective C-C(O) bond oxidative addition of benzocyclobutenone, yielding the gold(III) acyl complexes (**II**, Scheme 5.19, paths **a** and **b**). The kinetic product was obtained selectively through C(aryl)-C(O) bond activation (**II**, Scheme 5.19, path **a**), while C(alkyl)-C(O) bond oxidative addition yielded the thermodynamic product (**II**, Scheme 5.19, path **b**). Additionally it was discovered that the kinetic product spontaneously reduces to the gold(I) complex in dichloromethane, with concomitant oxidative addition of the C(alkyl)-C(O) bond, at room or elevated temperatures, to yield the thermodynamic product (**II**, Scheme 5.19, path **c**).[42] The results clearly demonstrate that manipulation of the coordination environment allows for the facile oxidative addition, as well as the reductive elimination, at a single and well defined gold center. On a different note, another rare example of a cationic gold(I) carbonyl complex,[43] thought to be only a transient intermediate, was isolated by employing the carborane diphosphine ligand as supporting scaffold.[44] The carbonyl stretching frequency was determined be lower than that of free CO (**III**, Scheme 5.19). Extensive computational calculations predicted a significant Au→CO π-backdonation. The increased backdonation is a direct result of bending, which raises the energetic level of the occupied d_{xz}-orbital at gold. This increases the bonding interaction with the vacant π^*_{CO} orbital. Surprisingly, not only does bending switch on reactivity, but also directly results in the stabilization of reactive intermediates.

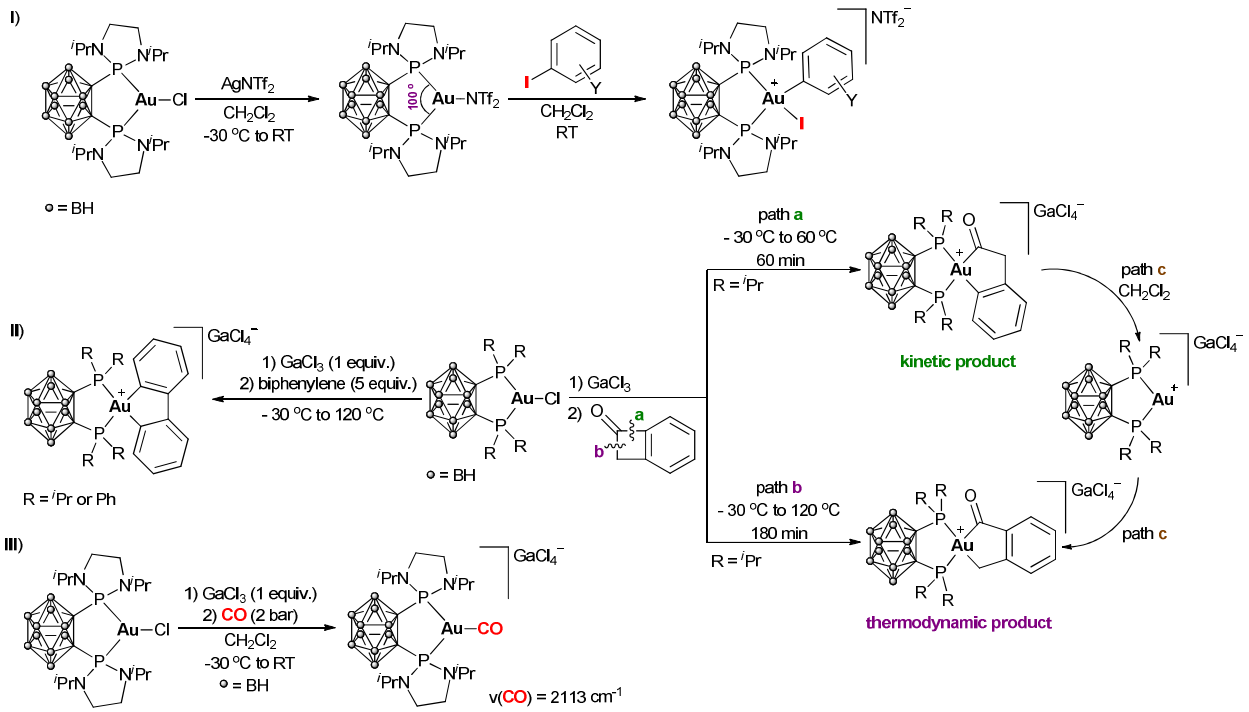

Scheme 5.19: Bending allows for oxidative addition as well as isolation of transient intermediates

© University of Pretoria

5.1.5 The Lewis basic gold question

Around the same time as the question of gold facilitating elementary organometallic reactions arose, another question surfaced. Can gold overcome its rudimentary nature and act as a Lewis base? To clarify the question, the properties of gold need to be considered again from a Lewis basic point of view. In fact, the properties that accounted for the Lewis acid character of gold, can also be used to entertain the notion of a Lewis basic gold center.[45] Gold can accommodate a negative charge and can therefore behave as a halogen, a result originating from golds high electronegativity. The radii of aurates, gold radicals and cations were found to be smaller than that of the iodide anion and similar to the radii of the bromide anion. Also, the strong preference for two-coordinate linear complex formation leaves the gold open for interactions, even if those interactions are very weak. Additionally, with respect to gold clusters, nanoparticles and gold surfaces, the gold can be influenced by an electrical charge, yielding anodic or cathodic gold. The anodic gold could form hydrogen bonding interactions, with an approaching H-bond donor.

Extensive computational studies have been done to show that gold, surprisingly, can act as a hydrogen acceptor, and the term Lewis base was used to describe the gold metal.[46] This is unconventional, as the beginning of the chapter gave an overview of why gold is a strong Lewis acid. It was computationally shown that various gold(I) aurates form hydrogen bonds with various proton donors, including HF, HCN, H_2O, C_2H_2, NH_3 and to a much lesser extent, CH_4. The relativistic effects of gold that give rise to the properties of gold, namely its Lewis acidic character, are also the origin of its Lewis basic character, depending on the metal orbitals involved. Computational analysis taking into account relativistic effects gave clear evidence for Au···H-X (X = atom more electronegative than H) interactions. If relativistic effects were removed from computational calculations, the Au···H-X bonding interaction either decreased considerably or completely disappeared compared to the Au···H-X bonding interaction when relativistic effects were in play. No hydrogen bonding interaction was realized for the Ag and Cu coinage metals, in support of the relativistic effects needed for bonding interactions to exist between the gold metal and a hydrogen bond donor.

© University of Pretoria

5.2 Aim

It was proposed that the use of the CNC pincer ligand scaffold to coordinate to a Au(I) metal center, to yield the corresponding T-shaped (CNC)Au(I) complexes, might facilitate oxidative addition reactions based on the following principals exhibited by the analogues Au(I) complexes. Three coordinate Au(I) complexes are not uncommon, however all known examples display either trigonal or distorted trigonal planar geometries, with no examples of isolated and well-defined T-shaped gold(I) complexes reported to date.[47,48] The synthesis and characterization of the two analogous T-shaped gold(I) complexes was completed during the author's MSc studies.[1] However, the synthesis has since been optimized to yield both complexes with higher purities and as such, the synthetic protocol will be discussed again. Additionally, the strong electron donating ligand gives rise to an electron rich gold metal center. The single crystal X-ray structure of the T-shaped Au(I) complexes (*vide infra*) highlighted the following properties of the complexes **20$_a$** and **21$_b$**: *1)* the gold metal is complexed in a strained environment which raises the energy of the complex; *2)* the Au(I) center is pre-organized to facilitate a square-planar gold(III) coordination after oxidation of the Au(I) complex; *3)* an electron rich metal center would allow oxidative addition processes more readily; and finally *4)* the T-shaped gold complex can be viewed as a coordinatively unsaturated complex, with the position *trans* to the amido nitrogen open/activated towards various substrates.

We had reasoned that these observed structural complex properties could allow for mild Au(I)/Au(III) oxidative addition. The electron rich metal center with the position *trans* to the amido nitrogen being open/activated, could allow for reactivity of the Au(I) complex with electrophilic reagents. This could then lead to an unprecedented mild electrophilic oxidation reaction, were coordination of the electrophile is followed by an oxidation event yielding the cationic gold(III) complex (Scheme 5.20).

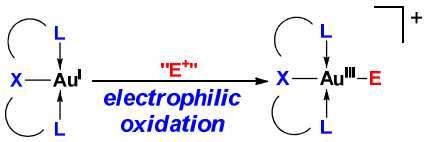

Scheme 5.20: Unprecedented routes to cationic gold(III) complexes

© University of Pretoria

5.3 Results and Discussion

5.3.1 Gold(I) complex formation

One-pot tris-deprotonation of $\mathbf{L_a}$ and $\mathbf{L_b}$ with excess KHMDS followed by addition of (tht)AuCl, yielded the corresponding air-stable dark purple-red pincer Au(I) complexes $\mathbf{20_a}$ and $\mathbf{21_b}$, respectively (Scheme 5.21). Consecutive extractions and filtrations from various solvent systems were necessary in order to isolate the gold(I) complexes with high purity (see Experimental Section 5.5). Single crystals of $\mathbf{20_a}$ and $\mathbf{21_b}$ suitable for X-ray diffraction analysis were obtained by slow evaporation of a toluene solution (Figure 5.2). Both complexes feature the three-coordinate T-shaped geometry around the metal center, with a long Au-N bond distance [$\mathbf{20_a}$, 2.325(2); $\mathbf{21_b}$, 2.412(3) Å]. For the bulkier Au(I) complex $\mathbf{20_a}$, the complex displays a slightly distorted T-shaped geometry. The T-shaped distortion for $\mathbf{21_b}$ is much more significant, with the gold atom deviating out of the plane of the carbazole backbone (Figure 5.2).

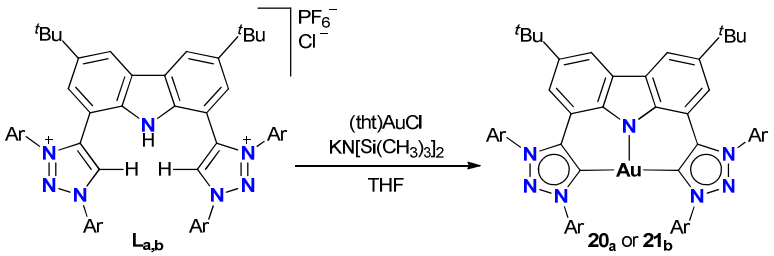

$\mathbf{L_a}$, $\mathbf{20_a}$: Ar = Dipp = 2,6-diisopropylphenyl
$\mathbf{L_b}$, $\mathbf{21_b}$: Ar = Mes = 2,4,6-trimethylphenyl

Scheme 5.21: T-shaped gold(I) complex formation

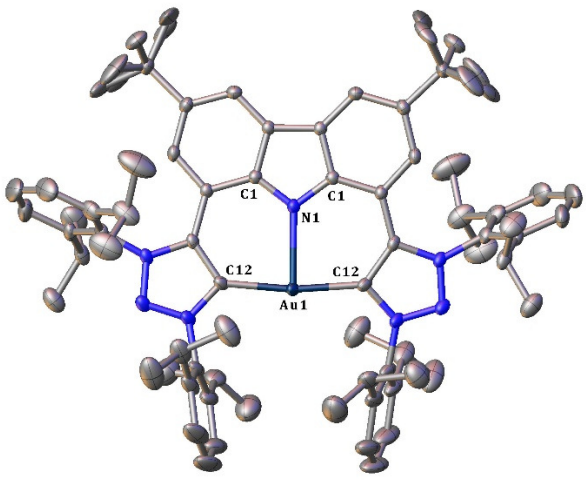

$\mathbf{20_a}$

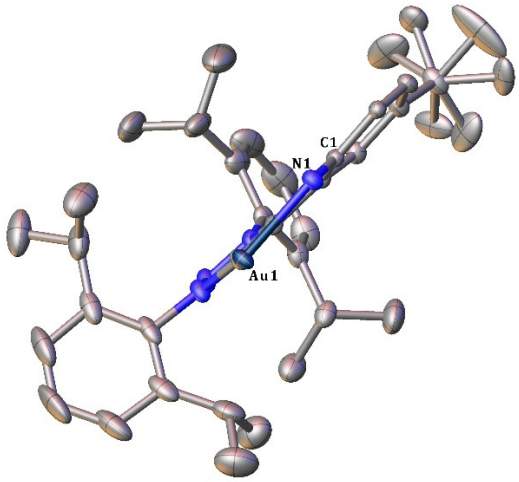

$\mathbf{20_a}$

© University of Pretoria

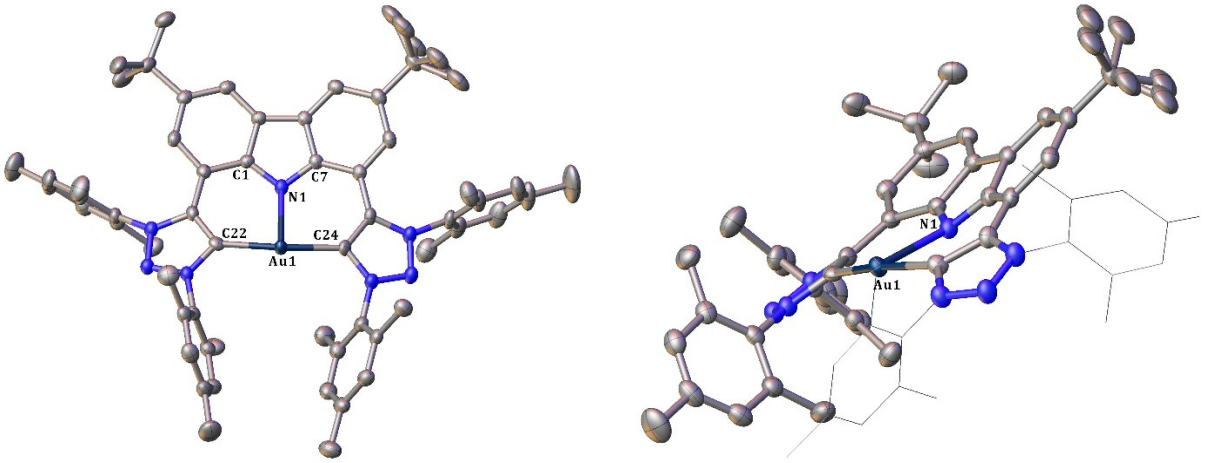

21b **21b**

Figure 5.2: Crystal structure of gold(I) complexes **20a** (top) and **21b** (bottom) with frontal (left) and side-on (right) views (hydrogen atoms and solvent molecules omitted for clarity. The preliminary structures of **20a** and **21b** have previously been reported,[1] but the refined data set is reported here in the experimental section, chapter 8)

Cyclic voltammetry experiments were conducted in order to corroborate our assumption of mild Au(I)/Au(III) oxidation facilitated by the ligand scaffold. The cyclic voltammetric experiments of **20a** were carried out in solvent THF and [^{n}Bu$_4$N][PF$_6$] as supporting electrolyte under inert atmospheric conditions. The cyclic voltammogram of **20a** referenced to ferrocene internal standard (ferrocene cyclic voltammogram is not indicated) is depicted in Figure 5.3. The redox potential of the Au(I)/Au(III) couple was determined to be E_0 = **– 0.39 V**. This clearly substantiate our assumptions of a gold(I) complex that can be oxidized under mild reaction conditions. More surprising was the realization that the gold redox cycle is reversible ($E_{pa} – E_{pc}$ = 97 mV).

© University of Pretoria

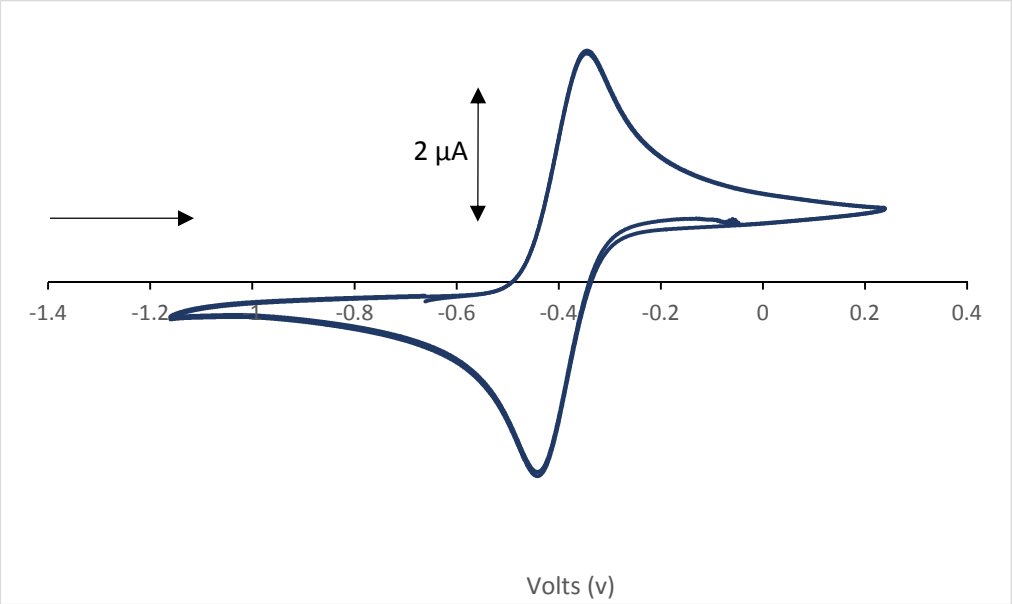

Figure 5.3: Cyclic voltammogram of **20$_a$** referenced to $[Cp^2Fe]^{0/+1}$ in solvent THF

5.3.2 Protonation of T-shaped (CNC)Au(I)

Treatment of **20$_a$** with excess trifluoromethanesulfonic acid (6 equiv.) in THF resulted in a colour change from red-purple to lime-green, and after workup, the cationic Au(III) hydride complex **22$_a$** was isolated with a 35% yield (Scheme 5.22). As was the case with the cyclometallated gold(III) hydride reported by Bochmann,[19] the [(CNC)AuH]TfO complex is air stable both in solution and in the solid state. The carbene carbons of **22$_a$** resonate at $\delta_{Ccarbene}$ 149.8 ppm in the ^{13}C NMR spectrum, which is significantly upfield from the carbene carbon NMR shift of **20$_a$** ($\delta_{Ccarbene}$ 175.1 ppm). The characteristic hydride signal resonates at δ_H -8.34 ppm in the ^1H NMR spectrum. This value is upfield from the only other example of a gold(III) hydride reported at δ_H -6.58 ppm.[19] However, the FT-IR spectrum displays the ν(Au-H) absorption at 2197 cm^{-1}, which varies with a value of less than ten wavenumbers when compared to the ν(Au-H) absorption band reported by Bochmann (2188 cm^{-1}).[19] It was also demonstrated that **20$_a$** readily reacts with weaker acids such as trifluoroacetic acid (Scheme 5.22) and even acetic acid. The reaction of **20$_a$** with acetic acid displayed an interesting reactivity pattern and is discussed later (see Scheme 5.24). The gold hydride **23$_a$** featuring the trifluoroacetate counteranion was characterized spectroscopically. The hydride and carbene carbon NMR shifts were found to be similar to that of **22$_a$**, resonating at δ_H -8.26 ppm and $\delta_{Ccarbene}$ 150.4 ppm, respectively (Scheme 5.22). Interestingly enough, classical gold(I) complexes has been termed as isolobal to H^+.[49] Therefore, the gold(I) complex **20$_a$** can be considered as a Lewis base, which could account for the reactivity observed with the various acids.

© University of Pretoria

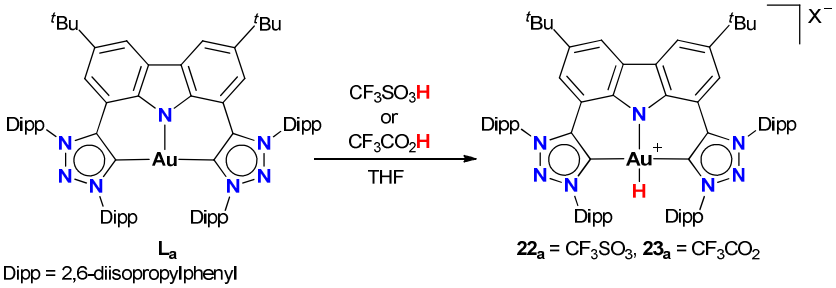

Scheme 5.22: Oxidative protonation of **20**$_a$ yielding the cationic [(CNC)AuH]X complexes (**22**$_a$ = TfO or **23**$_a$ = CF_3CO_2)

The localization of the H atom was unambiguously assigned *via* an X-ray diffraction study of **22**$_a$ (Figure 5.4). The Au(III) complex **22**$_a$ displayed a much shorter Au-N bond distance of 2.051(2) Å compared to the Au-N bond distance of **20**$_a$ at 2.325(2) Å. The other parameters show little deviation from the expected square-planar geometry, with the Au-H bond distance determined to be 1.41(3) Å.

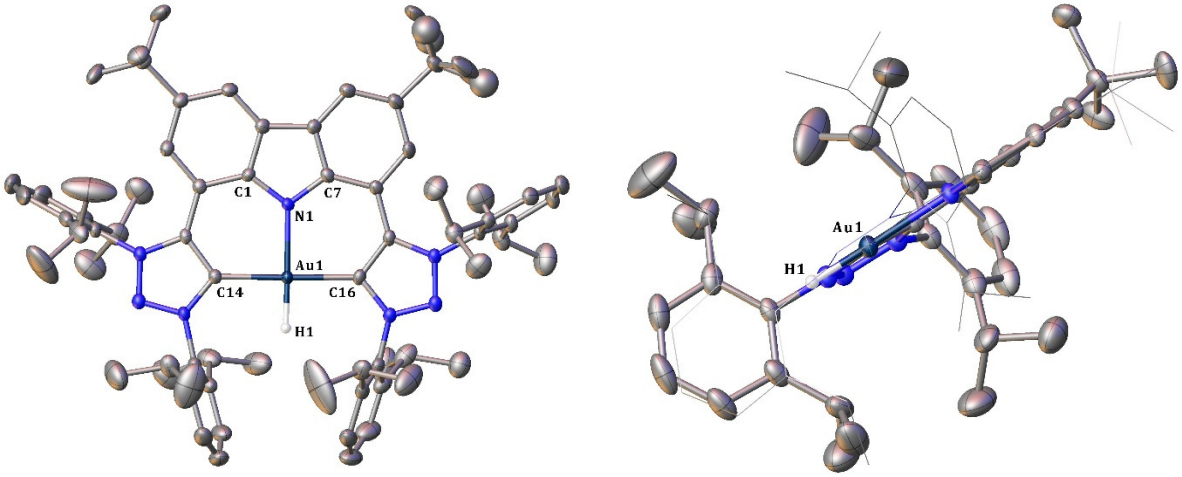

Figure 5.4: X-ray crystal structure of **22**$_a$ (Left: Frontal view and right: side-on view of N-Au-H bond. Counter-anion, solvent molecules and all hydrogens except hydride hydrogen omitted for clarity)

Two postulated mechanisms can account for the formation of the gold(III)-hydride (Scheme 5.23). The first possible route includes direct protonation of the gold center, followed by an oxidation event. This mechanism would illustrate a Lewis basic gold center. The second mechanism would be a two-step process, with protonation of the nucleophilic amido nitrogen followed by a N-H oxidative addition across the Au(I) center. Spectroscopic evidence for protonation of the amido nitrogen was obtained when **20**$_a$ was treated with a stoichiometric amount of trifluoromethanesulfonic acid (TfOH), yielding the protonated nitrogen, cationic gold(I) complex **24**$_a$ (Scheme 5.23). Singlets resonating at δ_H 10.94 ppm and $\delta_{Ccarbene}$ 177.8 ppm in the ^{1}H and ^{13}C NMR spectra, respectively, was accompanied by a colour

© University of Pretoria

change from dark red-purple to light green. The carbene carbon resonance is indicative of a gold center with an oxidation state of +1. Crystals of the complex could not be grown as the intermediate **24$_a$** converted into the cationic gold(III)-hydride over an extended period of time in solution. At first glance, the experimental data suggest an amido nitrogen protonation followed by an N-H oxidative addition in route to **22$_a$** (Scheme 5.23).

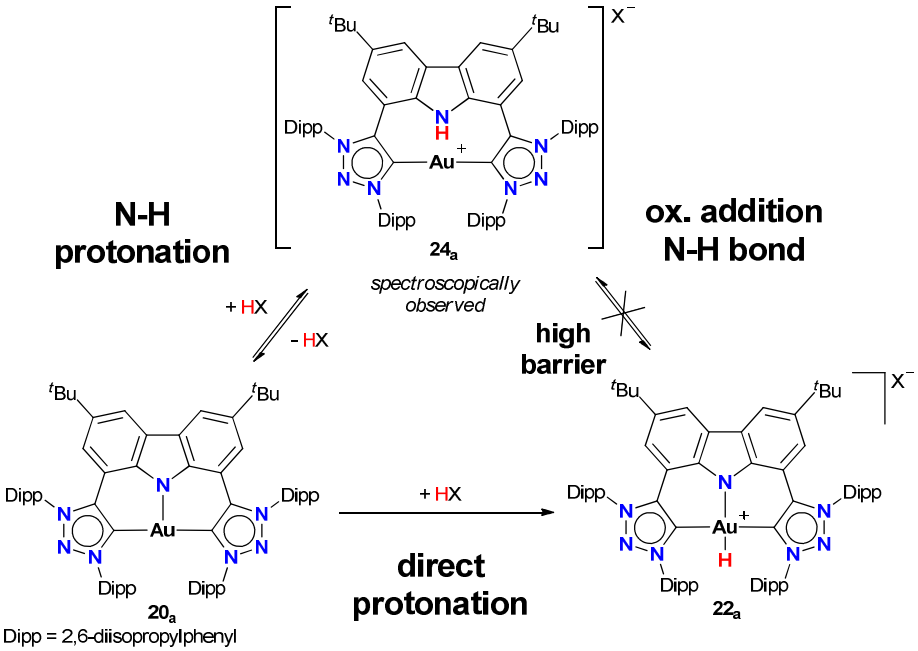

Scheme 5.23: Postulated mechanism for gold(III)-hydride formation

However, computational calculations predicted otherwise. Calculations at the B3PW91-SMD/SDD(Au)-6-31G**(other atoms) level of theory predicted that an N-H oxidative addition reaction is slightly exergonic (ΔG ~ −1 kcal/mol), but is accompanied with a high energy barrier [ΔG‡~50 kcal/mol] which clearly disfavours this mechanism (Scheme 5.23). The high energy barrier can be explained by the fact that the N-H addition requires the hydrogen to migrate *trans* over the gold metal. Therefore, we propose that protonation of **20$_a$** can occur at both the amido nitrogen and the gold metal, with an equilibrium between the protonated and the neutral gold(I) complexes, leading to the formation of the cationic gold(III) hydride. The hypothesis is supported by the visualization of the highest occupied molecular orbital (HOMO) of **20$_a$** (Figure 5.5). Visualization of the HOMO indicates that there is an *anti*-bonding interaction between the amido nitrogen and the gold metal. This in turn results in a significant polarization of the corresponding occupied *d*-orbital at gold, an interaction that can be viewed as a ''remote basicity'' rendering the gold side nucleophilic.[50]

© University of Pretoria

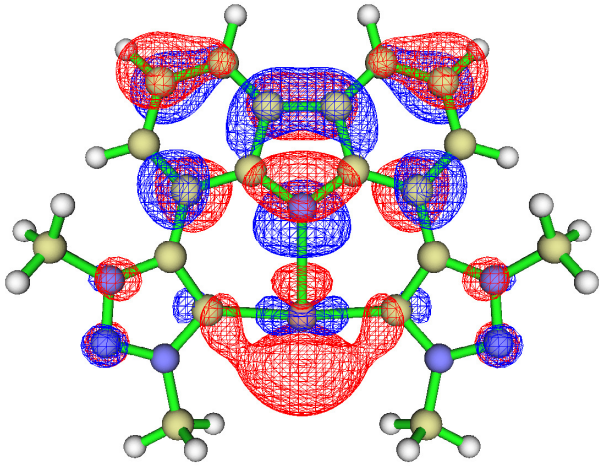

Figure 5.5: Visualization of the HOMO of **20$_a$** at the B3PW91/SDD(Au)-6-31G** (other atoms) level of theory

A solvent dependent redox reaction was noted for the reaction between **20$_a$** and acetic acid (Scheme 5.24). The term solvent dependent redox reaction is used as oxidation of **20$_a$** with acetic acid occurred in dichloromethane solvent, yielding the hydride complex **25$_a$**. Evaporation of the solvent followed by addition of THF to the same reaction vessel resulted in the reduction of the gold(III) hydride to the gold(I) starting complex. The redox cycle was repeated several times through solvent evaporation and addition of the appropriate solvent. The result also agrees with the reversible and low redox Au(I)/Au(III) couple determined for the complex (see Section 5.3.1). The redox cycle at the diphosphino-carborane gold(I) complex discussed in Section 5.1.4.4 was temperature dependent, whereas the redox cycle shown in Scheme 5.24 is controlled through solvent effects and possibly the nature of the counteranion. A possible explanation for the complex behavior could be solvent coordination or lack thereof, as well as the effect of the strength of the acid used. THF will readily coordinate both the acid and the complex while CH_2Cl_2 is a non-coordinating solvent allowing open access for the approaching hydrogen donor to the hydrogen acceptor. Additionally, the oxidizing environment generated by CH_2Cl_2 is known to be higher compared to THF, again attributed to the coordinating properties of the two solvents.[51] Finally, stronger acids will dissociate more readily than weaker acids.

© University of Pretoria

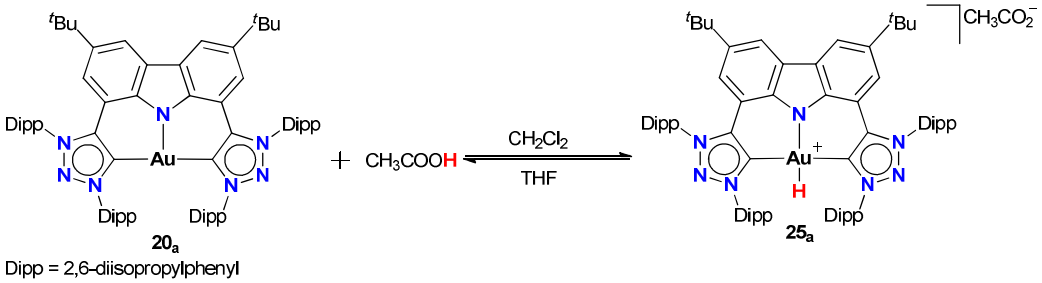

Dipp = 2,6-diisopropylphenyl

Scheme 5.24: Solvent dependent oxidation/reduction reaction of **20$_a$** with acetic acid

The ^{1}H and ^{13}C (small insert displaying the aromatic region) NMR spectra of both reactions clearly demonstrate the Au(III)-H formation and its corresponding reduction to Au(I). The hydride and carbene carbon resonance at δ_H -8.34 ppm and $\delta_{Ccarbene}$ 149.8 ppm (Figure 5.6), respectively, in solvent CD_2Cl_2 correspond to the $[(CNC)AuH]CH_3CO_2$ **25$_a$**. Note the excess of acetic acid in the solution. Addition of *d8*-thf to the same reaction mixture after evaporation of CD_2Cl_2 resulted in reduction of the Au(III)-H (Figure 5.7). The disappearance of the hydride signal and the chemical shift of the carbene carbon resonance from $\delta_{Ccarbene}$ 149.8 to 176.3 ppm unequivocally demonstrate the reduction reaction generating the starting gold complex **20$_a$**, even in the presence of excess acetic acid (Figure 5.7).

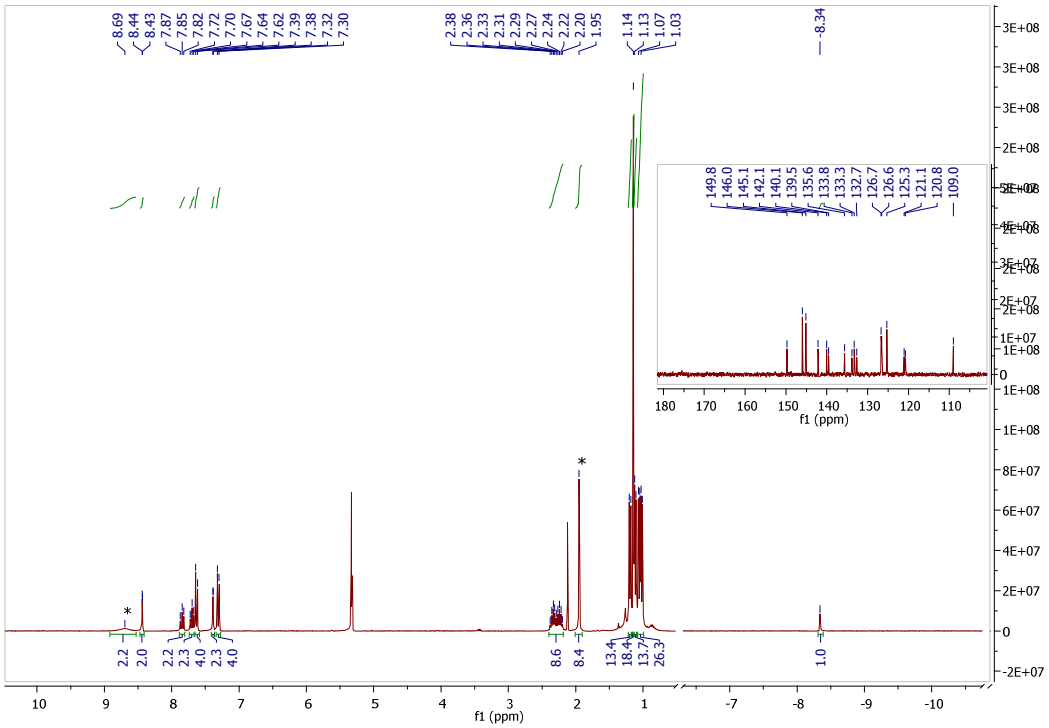

Figure 5.6: ^{1}H NMR spectrum of Au(I) to Au(III)-H oxidation in CD_2Cl_2 (* denotes acetic acid. ^{13}C NMR spectrum insert of aromatic region)

© University of Pretoria

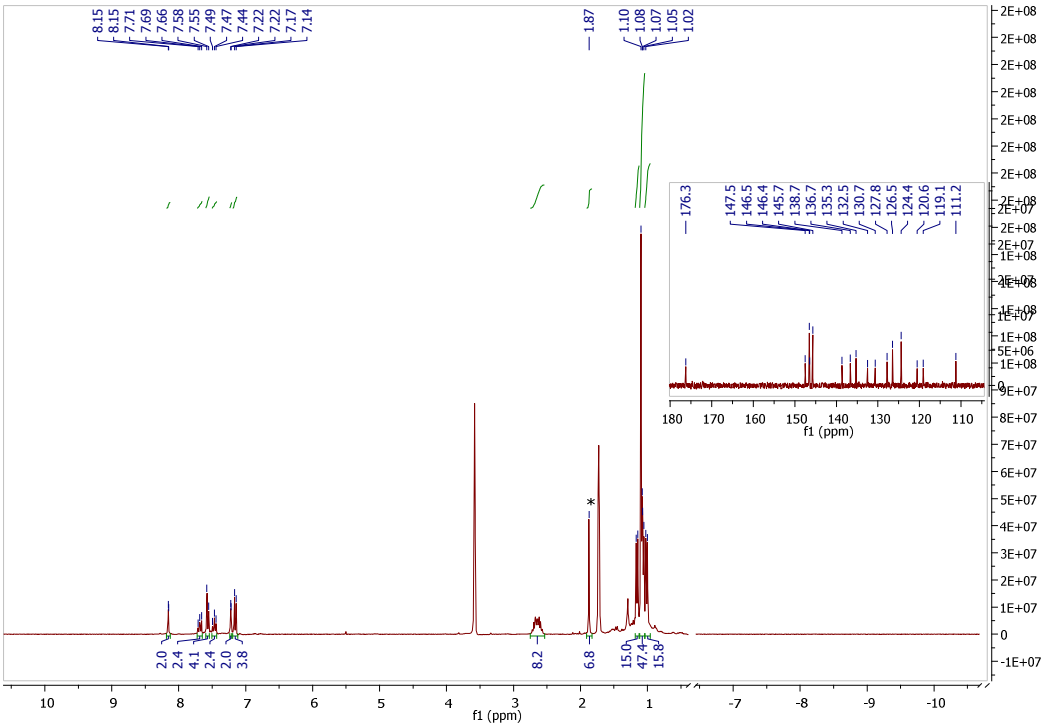

Figure 5.7: ^{1}H NMR spectrum of Au(III)-H to Au(I) reduction in THF (* denotes acetic acid. ^{13}C NMR spectrum insert of aromatic region)

The hydride moiety was further evidenced to be unreactive towards excess strong acids, including HCl and TfOH (Scheme 5.25). The gold(III) hydride **22$_a$** is also unreactive towards excess trifluoroacetic acid, in contrast to the gold(III) hydride reported by Bochmann. The neutral doubly cyclometallated Au(III)-H did not react with acetic acid but readily reacted with trifluoroacetic acid yielding mixtures of various products.[19] The lack of reactivity of **22$_a$** is a result of the strong covalent nature of the gold hydride bond. The hydridic character of the hydride moiety was also probed, through the reaction of **22$_a$** with NaH. Interestingly, the [(CNC)AuH]OTf reacted with NaH at room temperature, regenerating the gold(I) complex **20$_a$** after three days with concomitant release of hydrogen gas (Scheme 5.25). This further corroborates the protic behavior of the hydride functionality. It has to be noted that even though NaH is known as a strong base, it was specifically chosen as it does not feature any reducing properties, especially when compared to other nitrogen-containing bases (amines, amides).

© University of Pretoria

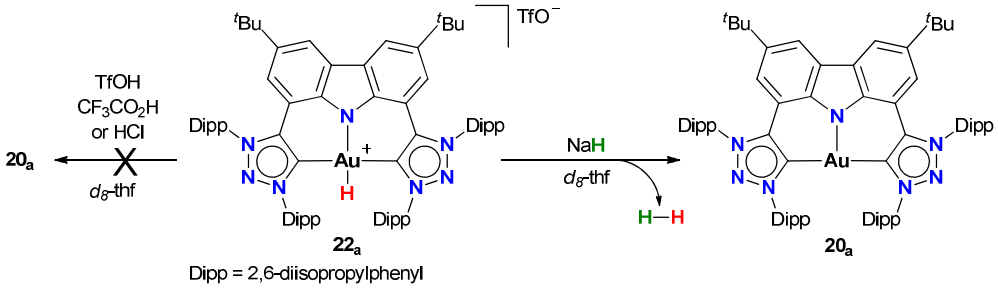

Scheme 5.25: Deprotonation of the cationic gold(III) hydride

The reaction depicted in Scheme 5.25 was monitored by NMR spectroscopy (a high pressure NMR tube was used as the reaction vessel). The reaction was initiated by the addition of *d8*-thf, and after 15 minutes, a small amount of gold(I) product formation was noted (Figure 5.8). At room temperature after 2 days, roughly 85% of the gold(III) hydride had been visibly reduced to gold(I). Finally, complete conversion was substantiated by the disappearance of the hydride signal and the chemical shift of the characteristic carbazole C**H** signal from δ_H 8.58 ppm to δ_H 8.16 ppm (Figure 5.8). Hydrogen gas formation was also detected, with the signal resonating at δ_H 4.54 ppm (this is in accordance with hydrogen gas dissolved in *d8*-thf).[52]

© University of Pretoria

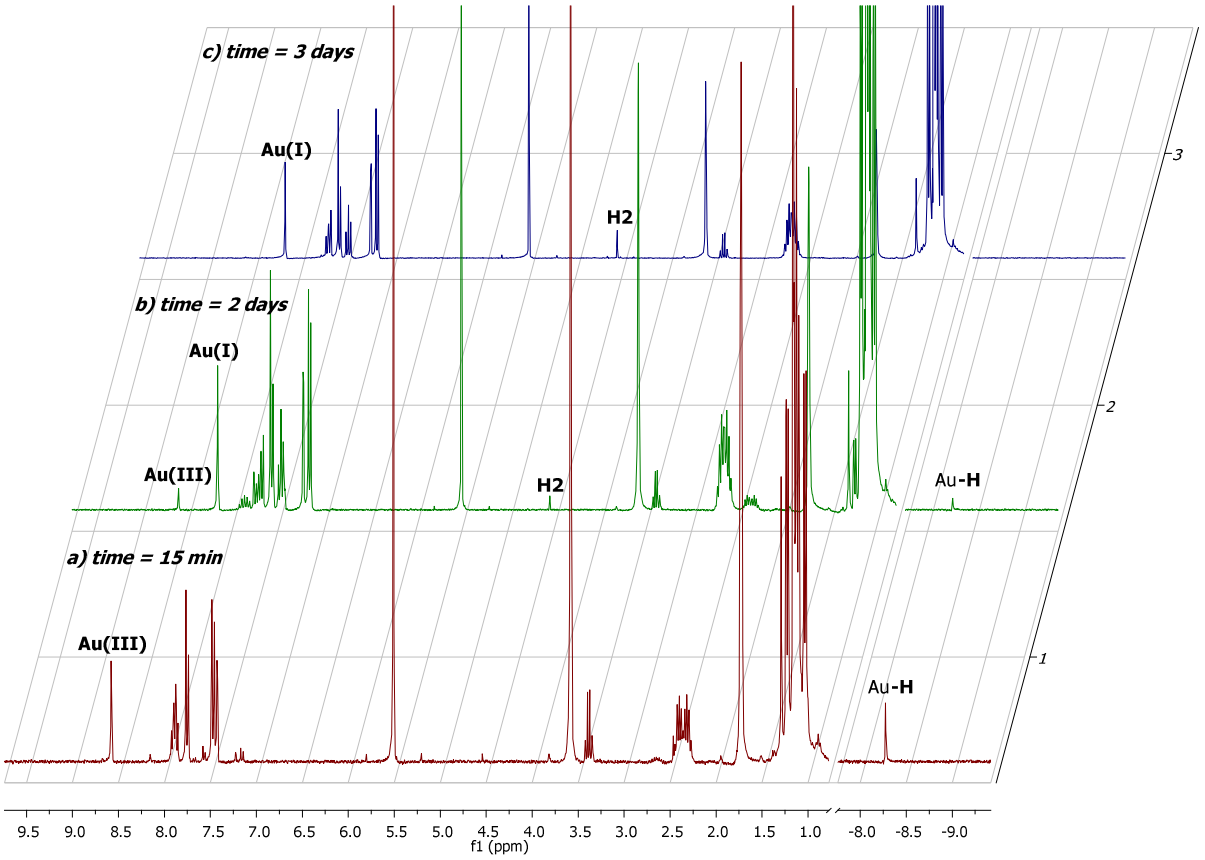

Figure 5.8: Stacked ^{1}H NMR spectra of reaction of **22$_a$** with NaH at time = 15 min (***a***), time = 2 days (***b***) and time = 3 days (***c***) to regenerate **20$_a$**

Again, two mechanistic scenarios were postulated for the reaction depicted in Scheme 5.25. The first involves a direct deprotonation of the hydride at the gold metal accompanied by a reduction event (Scheme 5.26). The second mechanism revolves around a dihydride reductive elimination reaction. Coordination of the second hydride moiety to the vacant site on the gold metal, yields a reactive gold(III) dihydride intermediate (**[AuH$_2$] (intm.)**, Scheme 5.26), that is followed by fast reductive elimination. The mechanistic question was again answered through computational calculations (calculations performed at the B3PW91/SDD(Au)-631G**level of theory). The theoretical data suggested that gold(III) dihydride formation will feature a pentacoordinated complex intermediate. The hydride ligands will subsequently be *trans* with respect to each other, disfavouring a reductive elimination process. The optimized structure of the potential Au-dihydride (B3PW91/SDD(Au)-631G** level of theory) is illustrated in Scheme 5.26 as **[AuH$_2$](intm.)**. Deprotonation of the hydride at the gold metal is therefore more likely, as this is not only the more favoured mechanistic scenario based on theoretical calculations, but is also the

© University of Pretoria

reverse reaction of the postulated gold hydride formation (direct protonation versus direct deprotonation).

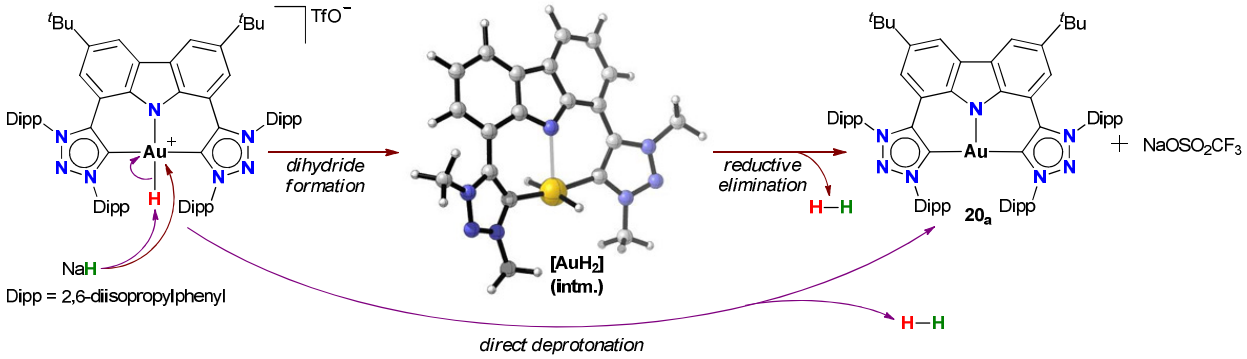

Scheme 5.26: Mechanistic considerations for reduction reaction of **22$_a$** regenerating **20$_a$**. Calculations performed at the B3PW91/SDD(Au)-631G** level of theory

5.3.3 Electrophilic alkylation of T-shaped gold(I) complexes

Our curiosity extended from electrophilic hydrogen to alkyl electrophiles. As such, **20$_a$** was treated with a slight excess of methyl trifluoromethanesulfonate (MeOTf) resulting in a colour change from dark red-purple to lime-green (**26$_a$**, Scheme 5.27). The complex could be isolated with a high purity as a light yellow-green solid. NMR analysis revealed that the amido nitrogen was alkylated, instead of the gold metal center. The methyl hydrogens and carbon resonance at δ_H 2.93 and δ_C 40.3 ppm, respectively, as well as a carbene carbon chemical shift of $\delta_{Ccarbene}$ 177.5 ppm, is in agreement with a cationic gold(I) complex. An X-ray diffraction study unambiguously confirmed alkylation of the amido nitrogen, with cationic gold(I) complex formation (Figure 5.9). The reaction also occurred when using weaker alkylating reagents such as iodomethane, albeit longer reaction times were required (**27$_a$**, Scheme 5.27). No sign of gold(III)-methyl complex formation was noted, even after heating up the reaction to 60 °C for three days. In contrast, the gold(I) complex featuring the mesityl wingtip substituents (ligand from precursor **L$_b$** coordinated), with the distorted ligand backbone and the gold atom deviating out of the plane of the carbazole backbone, reacted immediately with iodomethane at -78 °C. This resulted to clean formation of the cationic gold(III)-methyl product (**28$_b$**, Scheme 5.27). Formation of the alkyl gold(III) complex also occurred readily with methyl trifluoromethanesulfonate, although with accompanying impurities and as a result, the focus was kept on the reaction with iodomethane. It is quite likely that the observed regioselectivity from both reactions is based on steric factors, and contrasting to the protonation of the gold(I) complexes, alkylation is not reversible.

© University of Pretoria

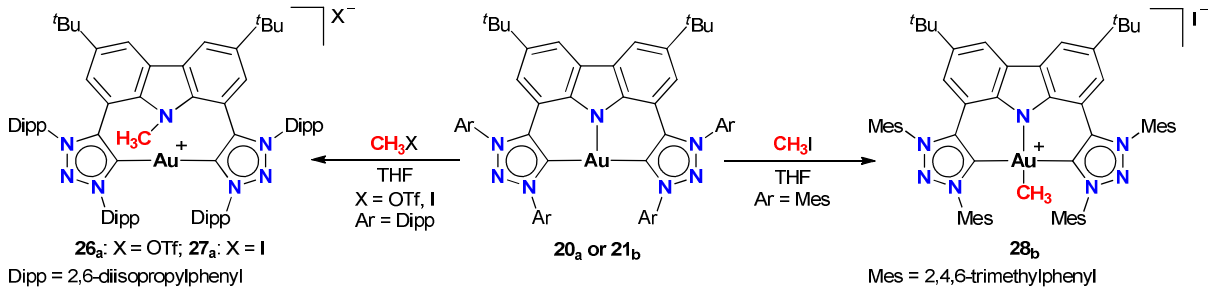

26a: X = OTf; **27a**: X = I
Dipp = 2,6-diisopropylphenyl

20a or 21b

28b
Mes = 2,4,6-trimethylphenyl

Scheme 5.27: Electrophilic alkylation of gold(I) complexes

The crystal structure of **26a** (Figure 5.9) depicts the methyl moiety directed out of the plane of the carbazole backbone, while the carbene-gold-carbene bond angle deviates from the ideal linear geometry (C25-Au-C23 162.35(18)°). The Au···N distance of 2.67(1) Å for **26a** is significantly longer than the Au-N bond distance of 2.325(2) Å for the gold(I) complex **20a**. This could indicate a weak interaction, if any, between the lone electron pair of nitrogen and the cationic gold(I) metal.

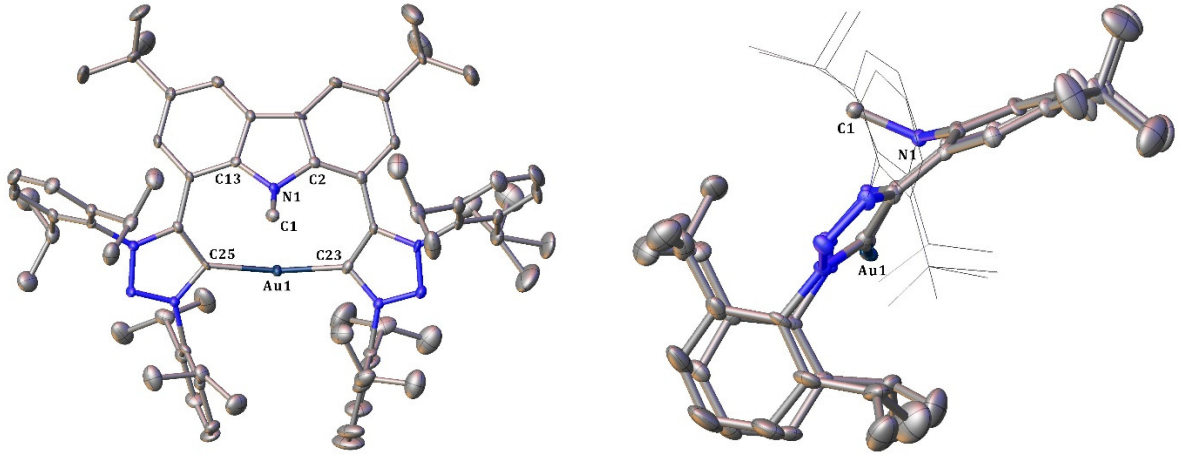

Figure 5.9: X-ray crystal structure of cationic gold(I) complex **26a** with alkylated amido nitrogen (Left: Frontal view and right: side-on view. Counter-anion, solvent molecules and all hydrogens omitted for clarity)

The proton and carbon NMR spectra, Figure 5.10 and Figure 5.11 respectively, of **28b** confirms gold(III)-methyl complex formation. The upfield methyl hydrogen resonance at δ_H 0.20 ppm is indicative of a shielded environment experienced by the methyl moiety. Also, the highfield methyl carbon resonance at δ_C -3.8 ppm further substantiates a methyl functionality bound to the gold metal, while a carbon coupled NMR experiment revealed a quartet splitting pattern owing to the hydrogen-carbon coupling (see insert in Figure 5.11). Both the methyl hydrogens and carbon resonances are in agreement with previously reported values for gold(III) methyl complexes.[23] The carbene carbon NMR shift of $\delta_{Ccarbene}$ 146.3 ppm is in agreement with a gold(III) oxidation state.

© University of Pretoria

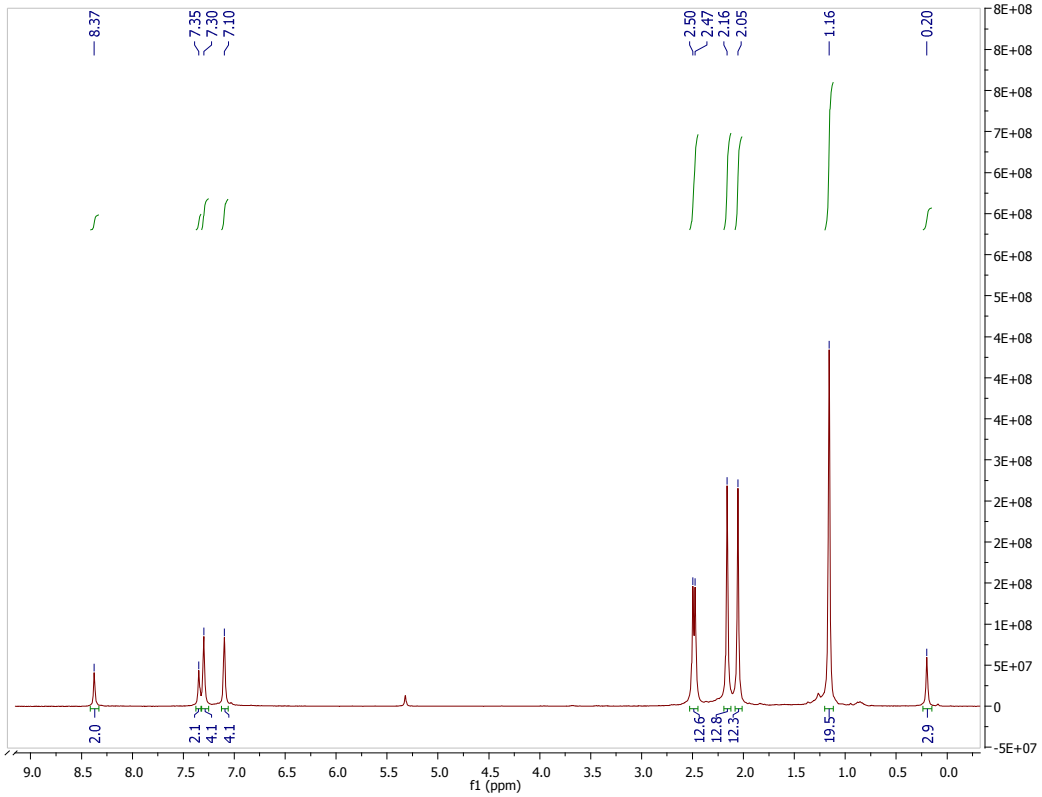

Figure 5.10: ^{1}H NMR spectrum of **28$_b$** in CD_2Cl_2

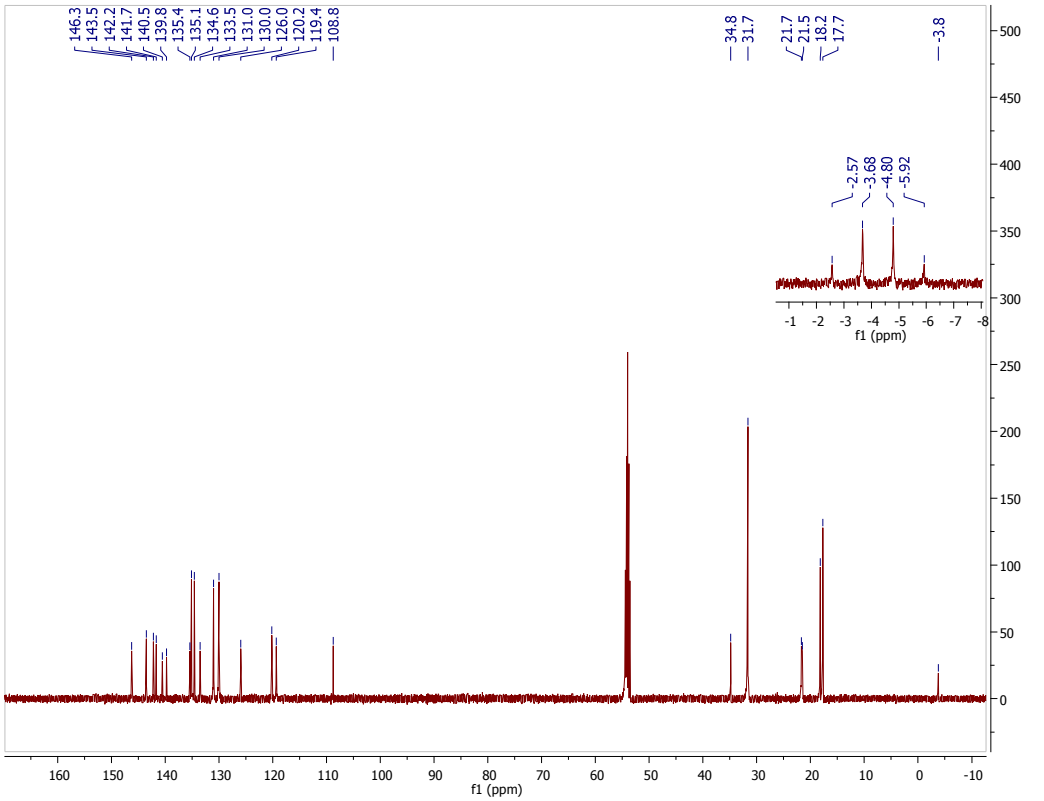

Figure 5.11: ^{13}C NMR spectrum of $[(CNC)AuCH_3]I$ with coupled ^{13}C insert of methyl moiety in CD_2Cl_2

© University of Pretoria

Additional evidence for the influence of steric factors is obtained from the lack of reactivity of **20$_a$** with dichloromethane, whereas the less sterically hindered **21$_b$** readily reacted with CH_2Cl_2 yielding the corresponding chloromethyl gold(III) complex **29$_b$** (Scheme 5.28). NMR spectroscopic characterization again confirmed gold(III) complex formation, with the upfield resonance of $\delta_{Ccarbene}$ 145.7 ppm for both the carbene carbon atoms. Deuteration experiments confirmed the chemical shift of the chloromethyl protons, with a resonance of δ_H 3.03 ppm. It is worth mentioning that a chloromethyl gold complex was previously synthesized *via* a salt metathesis reaction employing a Grignard reagent.[53] Oxidative addition of CH_2X_2 across gold was reported for binuclear gold complexes with concomitant formation of mixed gold(I)/gold(III) complexes.[54]

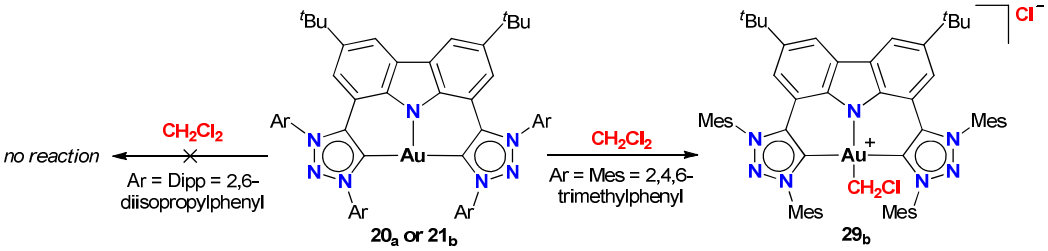

Scheme 5.28: Reactivity of T-shaped gold(I) complexes towards CH_2Cl_2

Crystals suitable for X-ray diffraction analysis were obtained after slow evaporation of a CD_2Cl_2 solution (Figure 5.12). A short Au-N bond distance of 2.078(5) Å for **29$_b$** was noted, similar to the gold(III) hydride complex **22$_a$**. Significant distortion of the ideal square-planar geometry is in all probability a result of excessive steric bulk imparted by the chloromethyl ligand [N-Au-C 166.2(2)°].

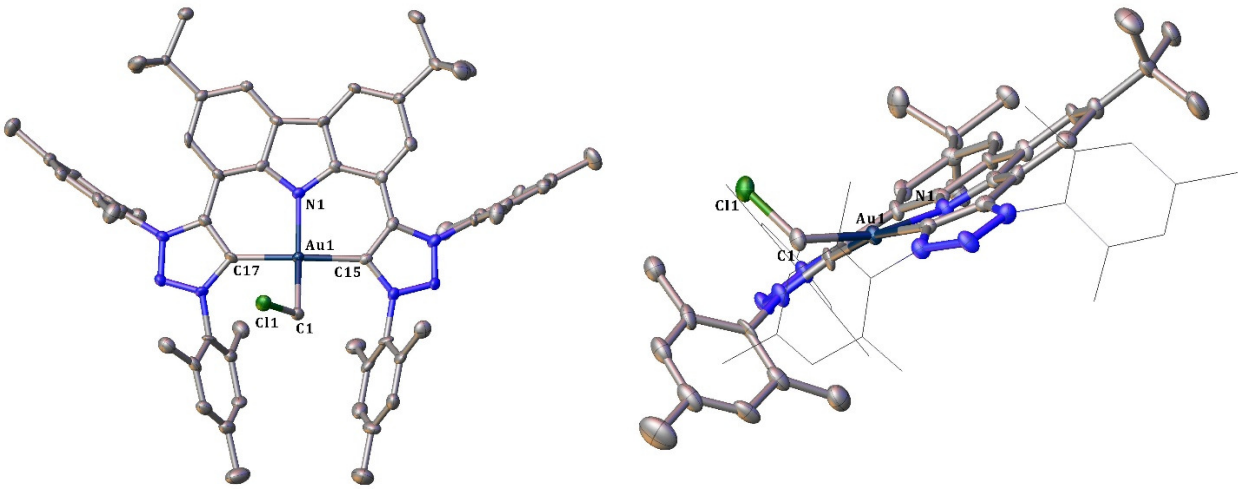

Figure 5.12: X-ray crystal structure of cationic $[(CNC)AuCH_2Cl]Cl$ **29$_b$** (Left: Frontal view and right: side-on view. Counter-anion, solvent molecules and all hydrogens omitted for clarity)

© University of Pretoria

5.3.4 Towards a cationic gold(III) fluoride complex

In an effort to extend the range of reactive gold species stabilized by the CNC-pincer ligand, further justifying the role of these transient intermediates in catalysis,[5] we set out to prepare the first example of a cationic gold(III) fluoride complex. Well defined, isolable gold(III) fluorides have only recently been disclosed by the group of Nevado.[55] A halide exchange reaction, from the corresponding gold(III) chloride complex with AgF, was invoked during the synthesis of the neutral gold(III) fluoride product.[55] The cationic gold(III) fluoride complex **30$_a$** was readily accessed through the oxidation of **20$_a$** with a stoichiometric amount of Selectfluor in THF. The gold(III) fluoride was isolated as a lime green solid, stable under atmospheric conditions. The ^{1}H NMR resonances of **30$_a$** in CD_2Cl_2 as solvent, displayed either upfield or downfield NMR shifts from the corresponding signals of **20$_a$**. However, the disappearance of the gold(I) carbene signal of **20$_a$** indicates an Au(I)/(III) oxidation event. The ^{19}F NMR spectrum portrayed the fluorine resonance at δ_F -299.9 and -153.2 ppm, for the Au**F** and the B**F$_4$** counterion signals, respectively. The fluoride resonance of δ_F -299.9 ppm is significantly upfield from the neutral gold(III) fluoride products, which were reported to be in the range of δ_F -225 ppm.[55] The significant upfield fluoride chemical shift, is in all probability, a result of the cationic gold center compared to the neutral gold complex.

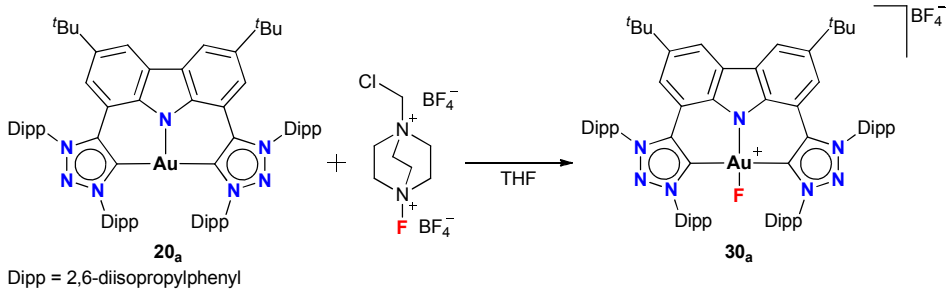

Scheme 5.29: Synthesis of gold(III) fluoride **30$_a$** *via* electrophilic oxidation with Selectfluor

A single crystal X-ray diffraction study unambiguously confirmed the formation of **30$_a$** (Figure 5.13). The Au-N bond distance of 2.001(5) Å resembles the corresponding short bond lengths of the gold(III) products, **22$_a$** and **29$_b$**. The gold-carbene bond distance was determined to be 2.034(4) Å. The Au-F bond length of **30$_a$** was measured at 1.947(5) Å (Figure 5.13), which is comparable to the Au-F bond lengths of the neutral gold(III) fluoride complexes.[55] As is evident from Figure 5.13, the ligand scaffold distorts to accommodate both the increased steric hindrance in the pincer pocket by the fluoride ligand, as well as the near perfect square planar geometry around the gold metal center.

© University of Pretoria

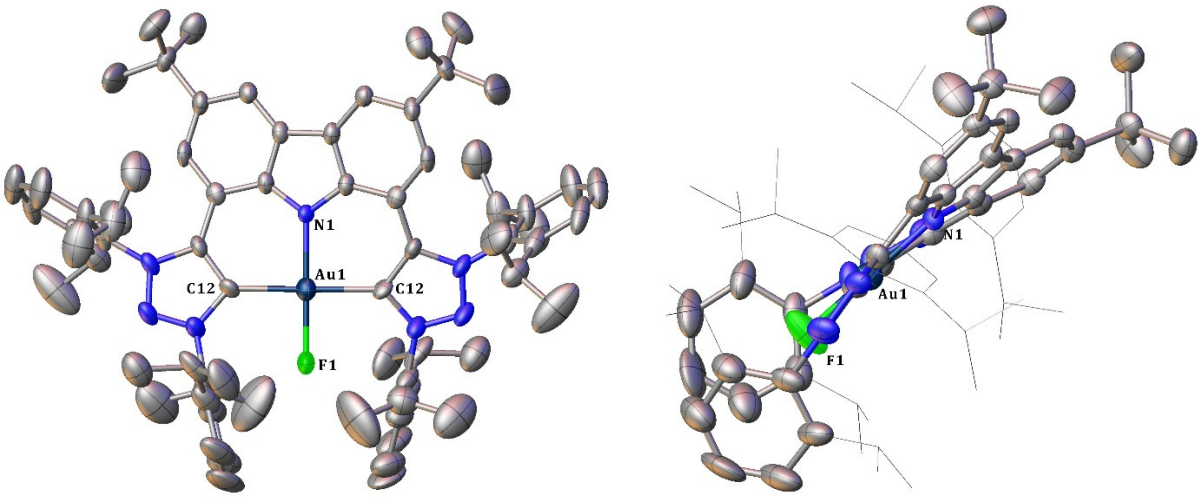

Figure 5.13: X-ray crystal structure of [(CNC)AuF]BF_4 **30b** (Left: Frontal view and right: side-on view. Counter-anion, solvent molecules and all hydrogens omitted for clarity)

5.4 Conclusion

In conclusion, the synthesis of unusual T-shaped (LXL)Au(I) complexes is presented, that reacts with electrophilic reagents which contrast the reactivity of classical gold(I) complexes. The synthesis of the gold(I) complexes was optimized to yield the two analogous complexes with high purity after a more extensive purification procedure. Both gold(I) products displayed unusual three-coordinated T-shaped geometries with deviations from the ideal bond angles and bond lengths. It was proposed that the T-shaped geometries, the strong donor ligands and the coordinatively unsaturated metal center would favour mild oxidation procedure, a postulation supported by the mild redox potential of the Au(I)/Au(III) couple (E_0 = – 0.39 V) which was also confirmed to be reversible by cyclic voltammetric experiments.

The gold(I) complexes were subjected to reactions with a range of electrophiles. Importantly, protonation was accompanied by oxidation leading to the first example of a cationic gold(III)-hydride with protic and not hydridic hydrogen character. The mild oxidation circumvents the use of harsh oxidants, severe reaction conditions and mercury salts to access gold(III) complexes. Computational calculations suggested that the gold(I) metal has Lewis basic character which explained the direct protonation of the metal center. Treatment of the gold(III)-hydride with NaH regenerated the gold(I) complex with concomitant formation of hydrogen gas. The gold(I) complex **20a** was also shown to undergo an oxidation reaction with acetic acid, reversibly; depending on the solvent used.

© University of Pretoria

The reactivity of alkylating electrophiles was demonstrated to be controlled by steric factors, with reactions occurring either at the ligand or at the metal. As such, electrophilic alkylating reagents react either at the amido nitrogen yielding a cationic gold(I) complex, or at the metal which is followed by oxidation to the corresponding gold(III)-methyl complex. The facile oxidation of the complex was again illustrated by the ease of oxidation with dichloromethane across the gold(I) metal featuring the mesityl wingtip substituents on the ligand backbone. The corresponding chloromethyl gold(III) complex was readily obtained with high purity. Electrophilic oxidation permitted the preparation of the first example of a cationic gold(III) fluoride through treatment of **20$_a$** with stoichiometric amounts of Selectfluor. The strongly donating and bulky ligand readily stabilizes the highly electrophilic gold metal center.

The facile redox event of the two analogous gold(I) metal complexes is currently being exploited in various stoichiometric and catalytic reactions. In addition, the reactivity of the synthesized gold(III) complexes, especially the gold(III)-hydrides and gold(III)-fluoride, is under investigation. This includes various stoichiometric investigations which, if successful, could be extrapolated to catalytic reactions.

5.5 Experimental

5.5.1 Synthesis of (CNC$_{Dipp}$)Au(I) (20$_a$)

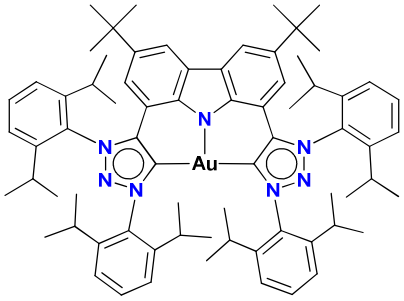

Compound **20$_a$** was synthesized by adaptation of a previously disclosed method.[1] A flame dried Schlenk tube was loaded with **L$_a$** (400 mg, 3.2 x 10^{-4} mol), (tht)AuCl (145 mg, 4.5x 10^{-4} mol) and KN[Si(CH$_3$)$_3$]$_2$ (322 mg, 1.6 x 10^{-3} mol). The reaction vessel was evacuated, purged with Ar (g) and cooled down to -78 °C. The solids were dissolved by the addition of THF (60 mL) which was also cooled down to -78 °C. The solution was stirred for one hour at -78 °C, at which point, the reaction was slowly heated up to RT followed by stirring the solution for two days. The solvent was evaporated under reduced pressure and the residue was extracted with hexanes (4 x 150 mL), followed by toluene (2 x 60 mL) in the absence of light. The solvent of the two fractions were evaporated *in vacuo*, yielding purple residues which were each re-dissolved in Et$_2$O (150 mL) and stirred at RT for two days, in the absence of light. Evaporation of the solvent from both fractions under reduced pressure yielded dark red-orange residues, which were both washed with hexanes (4 x 150 mL) followed by extraction of the product with

© University of Pretoria

Et_2O (3 x 80 mL). The two fractions were combined and the solvent removed under reduced pressure. The residue was finally washed with pentanes (3 x 20 mL), and the solid dried *in vacuo*, which yielded **20$_a$** (102 mg, 8.2 x 10^{-5} mol, 25%) as a dark red-orange solid. Crystallization from toluene yielded single crystals suitable for XRD analysis. **^{1}H NMR** δ_H (C_6D_6, 300 MHz) 8.62 (d, *J* = 1.5 Hz, 2H, Ar**H**$_{carb}$), 7.43 (d, *J* = 1.5 Hz, 2H, Ar**H**$_{carb}$), 7.37 (t, *J* = 7.8 Hz, 2H, Ar**H**$_{Dipp}$), 7.29 (dd, *J* = 8.4 Hz, 6.9 Hz, 2H, Ar**H**$_{Dipp}$), 7.17 (d, 4H, Ar**H**$_{Dipp}$ overlaps with C_6H_6), 7.11 (d, *J* = 7.8 Hz, 4H, Ar**H**$_{Dipp}$), 2.95 (sept, *J* = 6.9 Hz, 4H, C**H**$(CH_3)_2$), 2.70 (sept, *J* = 6.9 Hz, 4H, C**H**$(CH_3)_2$), 1.29 (s, 18H, C(C**H**$_3)_3$), 1.18 (d, *J* = 6.6 Hz, 12H, CH(C**H**$_3)_2$), 1.15 (d, *J* = 6.9 Hz, 12H, CH(C**H**$_3)_2$), 1.05 (d, *J* = 6.9 Hz, 12H, CH(C**H**$_3)_2$), 0.84 (d, *J* = 6.6 Hz, 12H, CH(C**H**$_3)_2$). **^{13}C NMR** δ_C (C_6D_6, 75 MHz) 176.0 (**C**$_{Carbene}$), 147.5 (Ar**C**$_q$), 146.7 (Ar**C**$_q$), 145.9 (Ar**C**$_q$), 145.3 (Ar**C**$_q$), 138.2 (Ar**C**$_q$), 135.9 (Ar**C**$_q$), 135.1 (Ar**C**$_q$), 131.5 (Ar**C**H), 130.0 (Ar**C**H), 125.5 (Ar**C**H), 123.8 (Ar**C**H), 120.6 (Ar**C**H), 119.2 (Ar**C**H), 111.1 (Ar**C**$_q$), 34.7 (**C**$(CH_3)_3$), 32.6 (C(**C**$H_3)_3$), 29.2 (**C**$H(CH_3)_2$), 29.0 (**C**$H(CH_3)_2$), 25.2 (CH(**C**$H_3)_2$), 24.9 (CH(**C**$H_3)_2$), 24.3 (CH(**C**$H_3)_2$), 22.9 (CH(**C**$H_3)_2$). **^{1}H NMR** δ_H (CD_2Cl_2, 300 MHz) 8.21 (d, *J* = 1.5 Hz, 2H, Ar**H**$_{carb}$), 7.69 (t, *J* = 7.8 Hz, 2H, Ar**H**$_{Dipp}$), 7.52 (d, *J* = 7.8 Hz, 4H, Ar**H**$_{Dipp}$), 7.49 (t, *J* = 7.8 Hz, 2H, Ar**H**$_{Dipp}$), 7.22 (d, *J* = 1.8 Hz, 2H, Ar**H**$_{carb}$), 7.15 (d, *J* = 7.8 Hz, 4H, Ar**H**$_{Dipp}$), 2.67 - 2.49 (m, 8H, C**H**$(CH_3)_2$), 1.14 (d, *J* = 6.9 Hz, 12H, CH(C**H**$_3)_2$), 1.09 (s, 18H, C(C**H**$_3)_3$), 1.08 (d, *J* = 6.9 Hz, 12H, CH(C**H**$_3)_2$), 1.06 (d, *J* = 6.9 Hz, 12H, CH(C**H**$_3)_2$), 0.99 (d, *J* = 6.9 Hz, 12H, CH(C**H**$_3)_2$). **^{13}C NMR** δ_C (CD_2Cl_2, 75 MHz) 175.1 (**C**$_{Carbene}$), 146.9 (Ar**C**$_q$), 146.0 (Ar**C**$_q$), 145.4 (Ar**C**$_q$), 145.3 (Ar**C**$_q$), 137.8 (Ar**C**$_q$), 136.1 (Ar**C**$_q$), 135.8 (Ar**C**$_q$), 132.1 (Ar**C**H), 130.4 (Ar**C**H), 126.7 (Ar**C**$_q$), 126.0 (Ar**C**H), 124.1 (Ar**C**H), 120.6 (Ar**C**H), 118.8 (Ar**C**H), 111.0 (Ar**C**$_q$), 34.8 (**C**$(CH_3)_3$), 32.4 (C(**C**$H_3)_3$), 29.4 (**C**$H(CH_3)_2$), 29.2 (**C**$H(CH_3)_2$), 25.5 (CH(**C**$H_3)_2$), 25.1 (CH(**C**$H_3)_2$), 24.2 (CH(**C**$H_3)_2$), 23.4 (CH(**C**$H_3)_2$). **^{1}H NMR** δ_H (*d8*-thf, 300 MHz) 8.15 (d, *J* = 1.5 Hz, 2H, Ar**H**$_{carb}$), 7.68 (dd, *J* = 8.4 Hz, 6.9 Hz, 2H, Ar**H**$_{Dipp}$), 7.57 (d, *J* = 7.5 Hz, 4H, Ar**H**$_{Dipp}$), 7.47 (t, *J* = 7.8 Hz, 2H, Ar**H**$_{Dipp}$), 7.22 (d, *J* = 1.8 Hz, 2H, Ar**H**$_{carb}$), 7.15 (d, *J* = 7.8 Hz, 4H, Ar**H**$_{Dipp}$), 2.72 - 2.57 (m, 8H, C**H**$(CH_3)_2$), 1.16 (d, *J* = 6.6 Hz, 12H, CH(C**H**$_3)_2$), 1.10 (s, 18H, C(C**H**$_3)_3$), 1.08 (d, *J* = 8.7 Hz, 12H, CH(C**H**$_3)_2$ overlaps with C$(CH_3)_3$), 1.07 (d, *J* = 6.9 Hz, 12H, CH(C**H**$_3)_2$), 1.01 (d, *J* = 6.9 Hz, 12H, CH(C**H**$_3)_2$). **^{13}C NMR** δ_C (*d8*-thf, 75 MHz) 176.3 (**C**$_{Carbene}$), 147.5 (Ar**C**$_q$), 146.5 (Ar**C**$_q$), 146.4 (Ar**C**$_q$), 145.7 (Ar**C**$_q$), 138.7 (Ar**C**$_q$), 136.7 (Ar**C**$_q$), 135.3 (Ar**C**$_q$), 132.5 (Ar**C**H), 130.7 (Ar**C**H), 127.8 (Ar**C**$_q$), 126.5 (Ar**C**H), 124.4 (Ar**C**H), 120.6 (Ar**C**H), 119.1 (Ar**C**H), 111.2 (Ar**C**$_q$), 35.2 (**C**$(CH_3)_3$), 32.8 (C(**C**$H_3)_3$), 30.0 (**C**$H(CH_3)_2$), 29.7 (**C**$H(CH_3)_2$), 25.7 (CH(**C**$H_3)_2$), 25.2 (CH(**C**$H_3)_2$), 24.5 (CH(**C**$H_3)_2$), 23.8 (CH(**C**$H_3)_2$). **HRMS** (FIA-ESI): Calculated for $C_{72}H_{90}N_7Au^+$ $[M + H]^+$: 1250.7001, found: 1250.7035.

© University of Pretoria

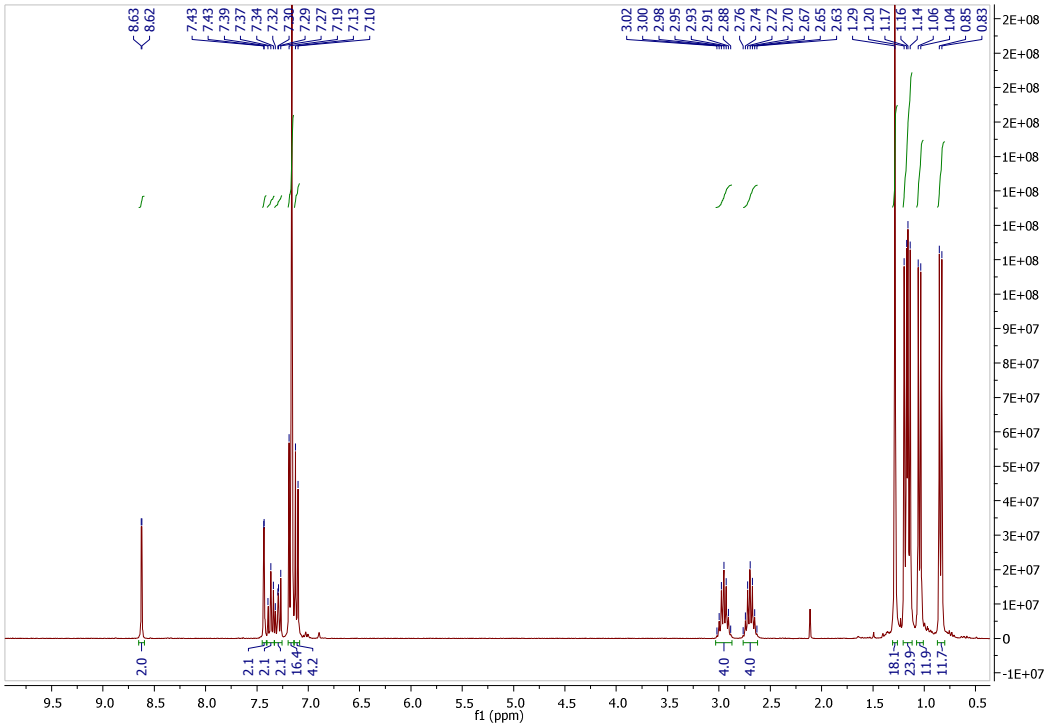

Figure 5.14: ^{1}H NMR spectrum of **20$_a$** in C_6D_6

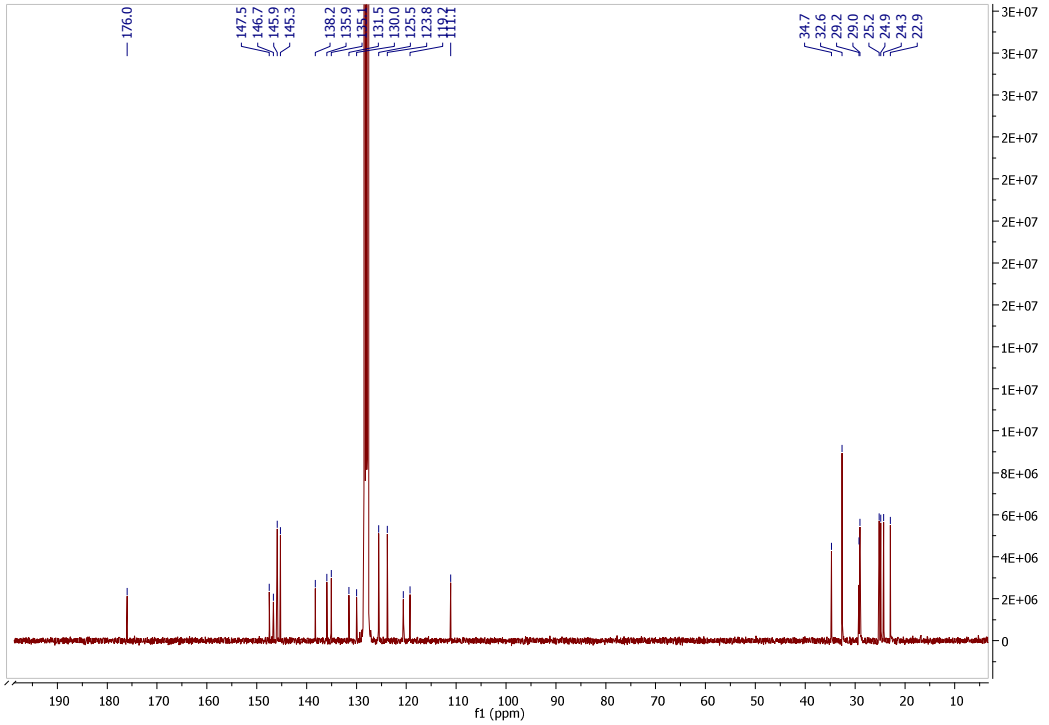

Figure 5.15: ^{13}C NMR spectrum of **20$_a$** in C_6D_6

© University of Pretoria

5.5.2 Synthesis of (CNC$_{Mes}$)Au(I) (**21$_b$**)

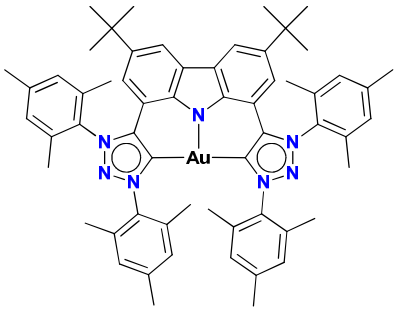

Compound **21$_b$** was synthesized based on a similar procedure employed for the synthesis of **20$_a$**, from ligand precursor **L$_b$** (400 mg, 3.7 x 10^{-4} mol), (tht)AuCl (168 mg, 5.2 x 10^{-4} mol) and KN[Si(CH$_3$)$_3$]$_2$ (373 mg, 1.9 x 10^{-4} mol) in 40 mL THF. The reaction vessel was evacuated, purged with Ar (g), and cooled down to -78 °C. The solids were dissolved by the addition of THF (40 mL) which was also cooled down to -78 °C. The solution was stirred for one hour at -78 °C, at which point, the reaction was slowly warmed up to RT followed by stirring the solution for two days. The solvent was evaporated under reduced pressure and the residue was extracted with hexanes (4 x 150 mL) followed by toluene (2 x 60 mL) in the absence of light. The solvent of the two fractions were evaporated *in vacuo*, yielding purple residues which were each re-dissolved in Et$_2$O (150 mL) and stirred at RT for two days, in the absence of light. Evaporation of the solvent from both fractions under reduced pressure yielded dark pink residues, which were both washed with hexanes (4 x 150 mL) followed by extraction of the product with Et$_2$O (3 x 80 mL). The two fractions were combined and the solvent removed under reduced pressure. The residue was finally washed with pentanes (3 x 20 mL), and the solid dried *in vacuo*, which yielded **21$_b$** (55 mg, 5.1 x 10^{-5} mol, 14%) as a dark pink solid. Crystals suitable for XRD analysis were obtained through slow evaporation of a toluene solution. **^{1}H NMR** δ_H (C_6D_6, 300 MHz) 8.72 (d, *J* = 1.5 Hz, 2H, Ar**H**$_{carb}$), 7.37 (d, *J* = 1.8 Hz, 2H, Ar**H**$_{carb}$), 6.73 (s, 4H, Ar**H**$_{Mes}$), 6.71 (s, 4H, Ar**H**$_{Mes}$), 2.30 (s, 6H, ArC**H**$_3$), 2.14 (s, 12H, ArC**H**$_3$), 2.07 (s, 6H, ArC**H**$_3$), 1.88 (s, 12H, ArC**H**$_3$), 1.32 (s, 18H, C(C**H**$_3$)$_3$). **^{13}C NMR** δ_C (C_6D_6, 75 MHz) 175.8 (**C**$_{Carbene}$), 147.5 (Ar**C**$_q$), 147.3 (Ar**C**$_q$), 140.6 (Ar**C**$_q$), 138.5 (Ar**C**$_q$), 138.3 (Ar**C**$_q$), 135.8 (Ar**C**$_q$), 135.4 (Ar**C**$_q$), 135.2 (Ar**C**$_q$), 134.8 (Ar**C**$_q$), 130.0 (Ar**C**H), 128.9 (Ar**C**H), 127.5 (Ar**C**$_q$), 119.8 (Ar**C**H), 118.9 (Ar**C**H), 111.8 (Ar**C**$_q$), 34.8 (**C**(CH$_3$)$_3$), 32.5 (C(**C**H$_3$)$_3$), 21.5 (Ar**C**H$_3$), 21.5 (Ar**C**H$_3$), 21.0 (Ar**C**H$_3$), 21.0 (Ar**C**H$_3$), 18.3 (Ar**C**H$_3$), 18.3 (Ar**C**H$_3$), 17.7 (Ar**C**H$_3$), 17.6 (Ar**C**H$_3$). **HRMS** (FIA-ESI): Calculated for $C_{60}H_{66}N_7Au^+$ $[M + H]^+$: 1082.5123, found: 1082.5104.

© University of Pretoria

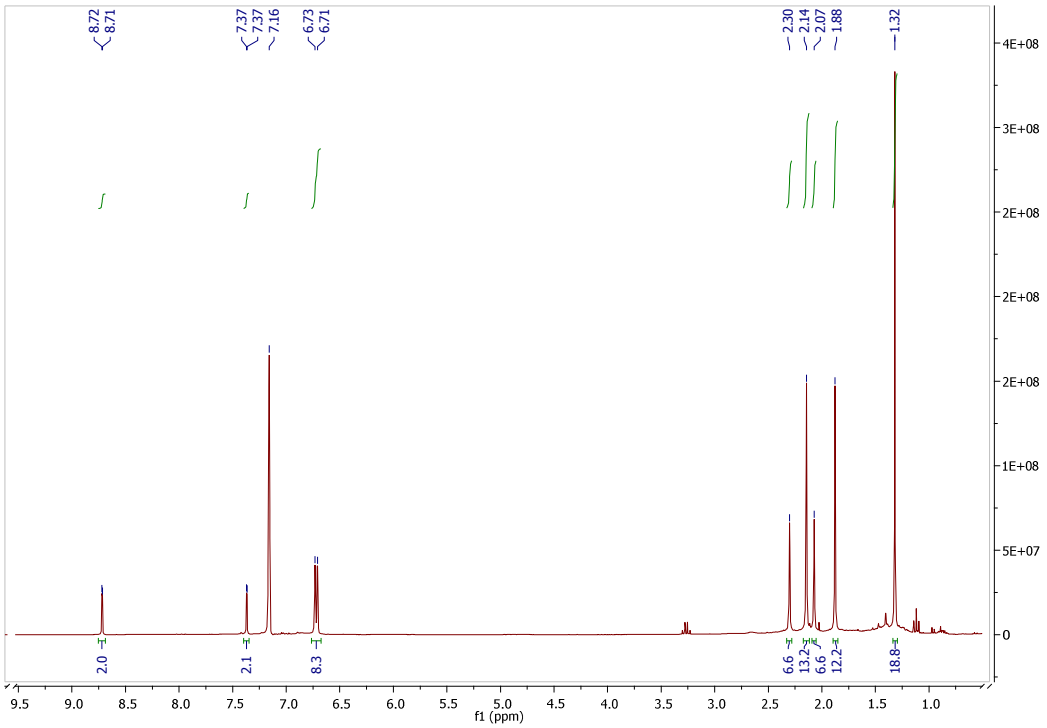

Figure 5.16: ^{1}H NMR spectrum of **21$_b$** in C_6D_6

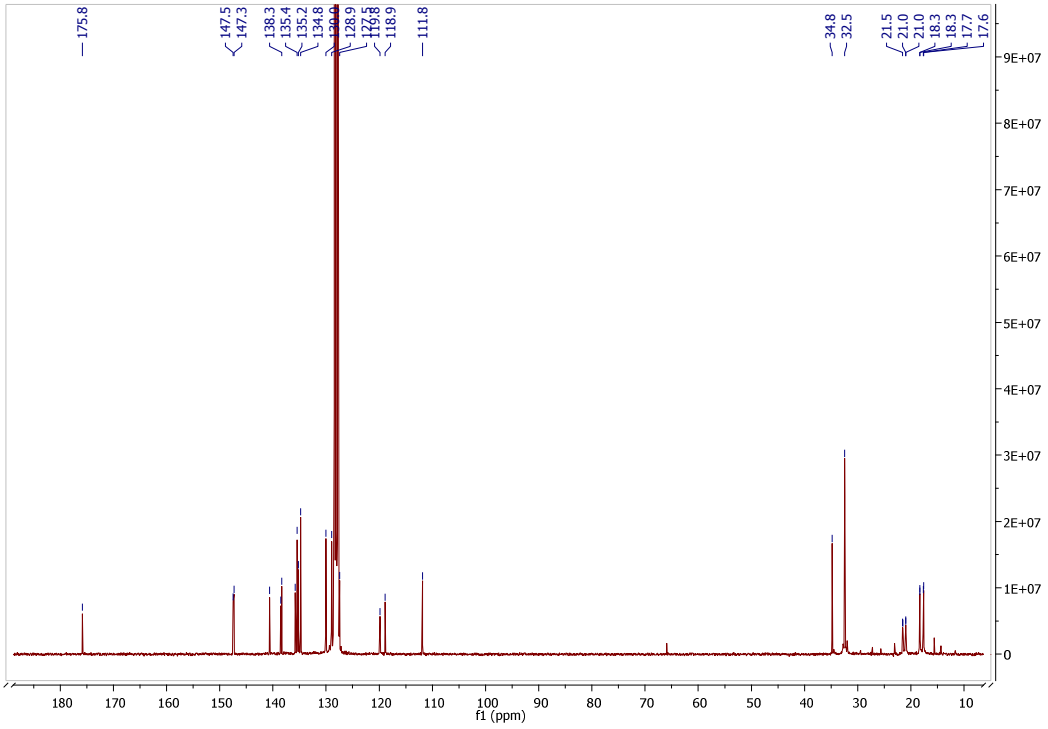

Figure 5.17: ^{13}C NMR spectrum of **21$_b$** in C_6D_6

© University of Pretoria

5.5.3 Synthesis of [(CNC$_{Dipp}$)Au(III)H]OTf (22$_a$)

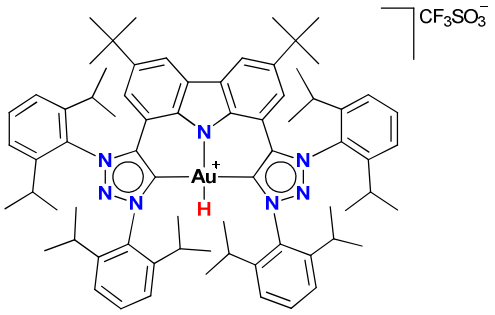

A Schlenk tube was evacuated and purged with Ar (g) after being charged with **20$_a$** (40.0 mg, 3.2 x 10^{-5} mol). The solid was dissolved by adding THF (15 mL) to the reaction vessel. The solution was cooled down to -78 °C followed by the addition of excess (6 equivalents) trifluoromethanesulfonic acid (TfOH) (17.0 µL, 1.9 x 10^{-4} mol). The reaction was warmed to RT after being stirred, in the absence of light, at -78 °C for 15 minutes. The light green solution was stirred an additional 2 hours, before the solvent was removed under reduced pressure. The green residue was first washed with hexanes (4 x 20 mL), and subsequently with toluene (4 x 20 mL). The product was extracted with dichloromethane (3 x 15 mL) and solvent evaporated *in vacuo*, to yield **22$_a$** (15.5 mg, 1.1 x 10^{-5} mol, 35%) as a lime green solid. Slow evaporation of a deuterated THF solution yielded crystals suitable for XRD analysis. **^{1}H NMR** δ_H (CD_2Cl_2, 300 MHz) 8.44 (d, *J* = 1.5 Hz, 2H, Ar**H**$_{carb}$), 7.85 (t, *J* = 7.8 Hz, 2H, Ar**H**$_{Dipp}$), 7.71 (t, *J* = 7.8 Hz, 2H, Ar**H**$_{Dipp}$), 7.63 (d, *J* = 7.8 Hz, 4H, Ar**H**$_{Dipp}$), 7.39 (d, *J* = 1.5 Hz, 2H, Ar**H**$_{carb}$), 7.32 (d, *J* = 7.8 Hz, 4H, Ar**H**$_{Dipp}$), 2.34 (sept, *J* = 6.9 Hz, 4H, C**H**$(CH_3)_2$), 2.25 (sept, *J* = 6.9 Hz, 4H, C**H**$(CH_3)_2$), 1.20 (d, *J* = 6.6 Hz, 12H, CH$(C\mathbf{H}_3)_2$), 1.15 (s, 18H, C$(C\mathbf{H}_3)_3$), 1.12 (d, *J* = 6.9 Hz, 12H, CH$(C\mathbf{H}_3)_2$), 1.06 (d, *J* = 6.9 Hz, 12H, CH$(C\mathbf{H}_3)_2$), 1.02 (d, *J* = 6.9 Hz, 12H, CH$(C\mathbf{H}_3)_2$), -8.34 (s, 1H, Au**H**). **^{13}C NMR** δ_C (CD_2Cl_2, 75 MHz) 149.8 (**C**$_{Carbene}$), 146.0 (Ar**C**$_q$), 145.1 (Ar**C**$_q$), 142.1 (Ar**C**$_q$), 140.0 (Ar**C**$_q$), 139.5 (Ar**C**$_q$), 135.6 (Ar**C**$_q$), 133.8 (Ar**C**$_q$), 133.3 (Ar**C**H), 132.7 (Ar**C**H), 126.7 (Ar**C**H), 126.6 (Ar**C**$_q$), 125.3 (Ar**C**H), 121.1 (Ar**C**H), 120.8 (Ar**C**H), 109.1 (Ar**C**$_q$), 35.0 (**C**$(CH_3)_3$), 31.9 (C$(\mathbf{C}H_3)_3$), 29.9 (**C**H$(CH_3)_2$), 29.7 (**C**H$(CH_3)_2$), 25.8 (CH$(\mathbf{C}H_3)_2$), 25.1 (CH$(\mathbf{C}H_3)_2$), 23.9 (CH$(\mathbf{C}H_3)_2$), 23.6 (CH$(\mathbf{C}H_3)_2$). **^{19}F NMR** δ_F (CD_2Cl_2, 282 MHz) -78.9 ($C\mathbf{F}_3SO_3$). **^{1}H NMR** δ_H (*d8*-thf, 300 MHz) 8.57 (d, *J* = 1.5 Hz, 2H, Ar**H**$_{carb}$), 7.89 (t, *J* = 7.8 Hz, 2H, Ar**H**$_{Dipp}$), 7.80 (t, *J* = 7.8 Hz, 2H, Ar**H**$_{Dipp}$), 7.74 (d, *J* = 7.8 Hz, 4H, Ar**H**$_{Dipp}$), 7.43 (d, *J* = 7.8 Hz, 4H, Ar**H**$_{Dipp}$ overlaps with Ar**H**$_{carb}$), 7.42 - 7.41 (m, 2H, Ar**H**$_{carb}$ overlaps with Ar**H**$_{Dipp}$), 2.44 - 2.24 (m, 8H, C**H**$(CH_3)_2$), 1.21 (d, *J* = 6.6 Hz, 12H, CH$(C\mathbf{H}_3)_2$), 1.15 (s, 18H, C$(C\mathbf{H}_3)_3$), 1.12 (d, *J* = 6.9 Hz, 12H, CH$(C\mathbf{H}_3)_2$), 1.09 (d, *J* = 6.9 Hz, 12H, CH$(C\mathbf{H}_3)_2$), 1.02 (d, *J* = 6.9 Hz, 12H, CH$(C\mathbf{H}_3)_2$), -8.28 (s, 1H, Au**H**). **^{13}C NMR** δ_C (*d8*-thf, 75 MHz) 150.3 (**C**$_{Carbene}$), 146.4 (Ar**C**$_q$), 145.4 (Ar**C**$_q$), 142.3 (Ar**C**$_q$), 140.6 (Ar**C**$_q$), 140.2 (Ar**C**$_q$), 136.0 (Ar**C**$_q$), 134.5, 133.8, 133.7, 127.5, 127.4, 126.1, 123.7, 121.8, 121.1, 119.5, 109.2, 35.4 (**C**$(CH_3)_3$), 32.1 (C$(\mathbf{C}H_3)_3$), 30.4 (**C**H$(CH_3)_2$), 30.2 (**C**H$(CH_3)_2$), 26.4 (CH$(\mathbf{C}H_3)_2$), 25.0 (CH$(\mathbf{C}H_3)_2$), 23.8 (CH$(\mathbf{C}H_3)_2$), 23.4 (CH$(\mathbf{C}H_3)_2$). **^{19}F NMR** δ_F (d_8-thf, 282 MHz) -79.5 ($C\mathbf{F}_3SO_3$). **FTIR** (CH_2Cl_2): 2197 cm^{-1}. **HRMS** (ESI-TOF): Calculated for $C_{72}H_{91}N_7Au^+$ $[M]^+$: 1250.6996, found: 1250.6993.

© University of Pretoria

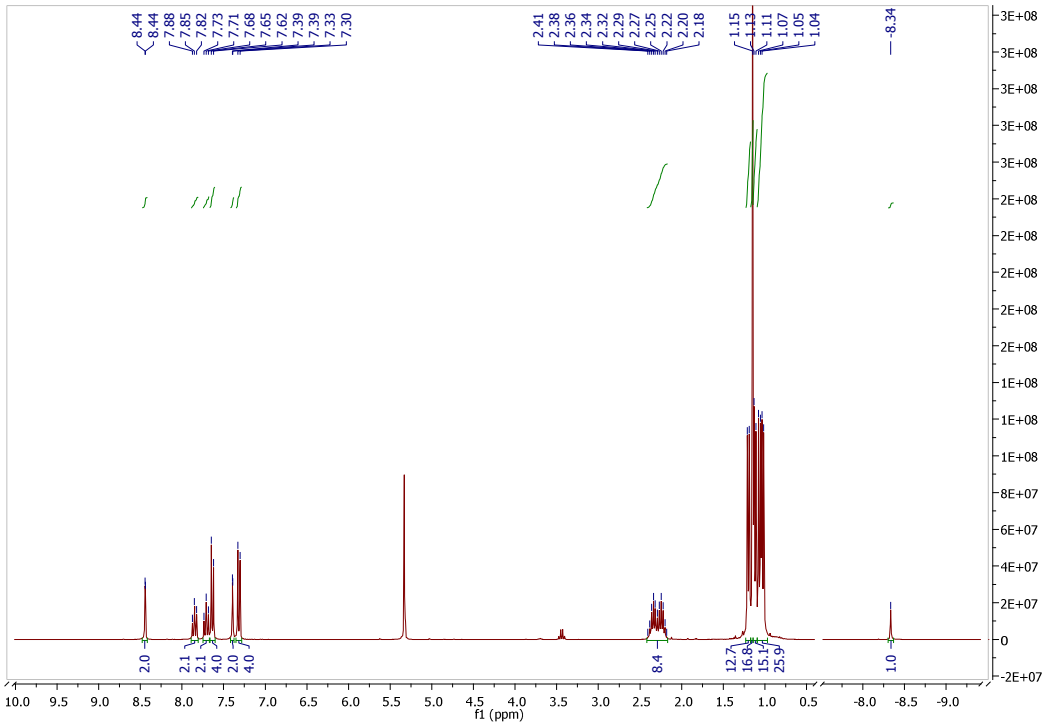

Figure 5.18: ^{1}H NMR spectrum of **22$_a$** in CD_2Cl_2

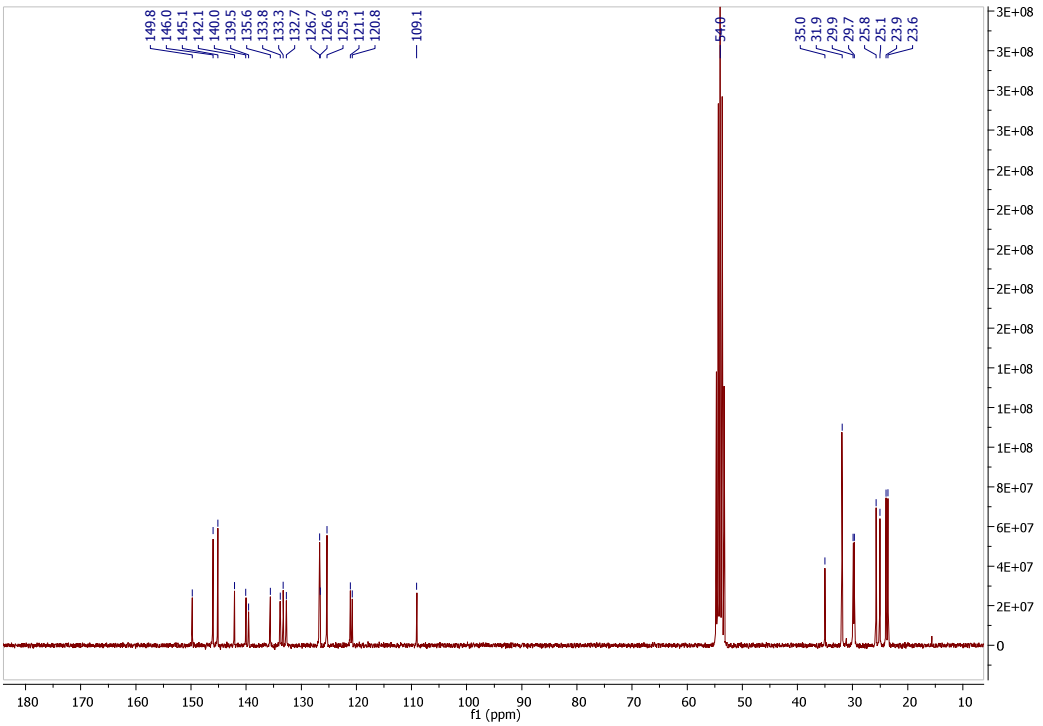

Figure 5.19: ^{13}C NMR spectrum of **22$_a$** in CD_2Cl_2

© University of Pretoria

5.5.4 Synthesis of [(CNC$_{Dipp}$)Au(III)H]OAc^{F} (23$_a$)

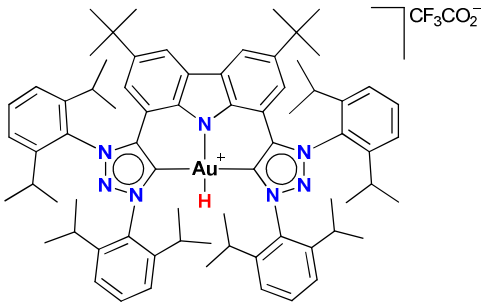

A NMR tube was charged with **20$_a$** (15.0 mg, 1.2 x 10^{-5} mol) in the glove box. The solid was dissolved through addition of *d8*-thf (0.4 mL). To the purple solution was added trifluoroacetic acid (HOAc^{F}) (5.5 µL, 7.2 x 10^{-5} mol). The reaction was monitored with ^{1}H NMR analysis. A colour change occurred from purple to lime green, with quantitative conversion of **20$_a$** to **23$_a$**, as determined by NMR analysis. The product was not isolated. **^{1}H NMR** δ_H (*d8*-thf, 300 MHz) 8.58 (d, *J* = 1.5 Hz, 2H, Ar**H**$_{carb}$), 7.90 (t, *J* = 7.8 Hz, 2H, Ar**H**$_{Dipp}$), 7.80 (t, *J* = 7.8 Hz, 2H, Ar**H**$_{Dipp}$), 7.75 (d, *J* = 7.8 Hz, 4H, Ar**H**$_{Dipp}$), 7.44 (d, *J* = 7.5 Hz, 4H, Ar**H**$_{Dipp}$ overlaps with Ar**H**$_{carb}$), 7.43 - 7.42 (m, 2H, Ar**H**$_{carb}$ overlaps with Ar**H**$_{Dipp}$), 2.44 - 2.28 (m, 8H, C**H**(CH$_3$)$_2$), 1.23 (d, *J* = 6.9 Hz, 12H, CH(C**H**$_3$)$_2$), 1.16 (s, 18H, C(C**H**$_3$)$_3$), 1.14 (d, *J* = 6.9 Hz, 12H, CH(C**H**$_3$)$_2$), 1.11 (d, *J* = 6.9 Hz, 12H, CH(C**H**$_3$)$_2$), 1.03 (d, *J* = 6.6 Hz, 12H, CH(C**H**$_3$)$_2$), -8.26 (s, 1H, Au**H**). **^{13}C NMR** δ_C (*d8*-thf, 75 MHz) 150.4 (**C**$_{carbene}$), 146.5, 145.5, 142.4, 140.7, 140.3, 136.1, 134.5, 133.9, 133.7, 127.6, 127.4, 126.1, 121.8, 121.2, 109.3, 35.4 (**C**(CH$_3$)$_3$), 32.1 (C(**C**H$_3$)$_3$), 30.5 (**C**H(CH$_3$)$_2$), 30.3 (**C**H(CH$_3$)$_2$), 25.1 (CH(**C**H$_3$)$_2$), 23.9 (CH(**C**H$_3$)$_2$), 23.5 (CH(**C**H$_3$)$_2$). **^{19}F NMR** δ_F (*d8*-thf, 282 MHz) -76.8 (C**F**$_3$SO$_3$). **^{1}H NMR** δ_H (CD_2Cl_2, 300 MHz) 8.44 (d, *J* = 1.5 Hz, 2H, Ar**H**$_{carb}$), 7.85 (t, *J* = 7.8 Hz, 2H, Ar**H**$_{Dipp}$), 7.70 (t, *J* = 7.8 Hz, 2H, Ar**H**$_{Dipp}$), 7.63 (d, *J* = 8.1 Hz, 4H, Ar**H**$_{Dipp}$), 7.39 (d, *J* = 1.8 Hz, 2H, Ar**H**$_{carb}$), 7.31 (d, *J* = 7.8 Hz, 4H, Ar**H**$_{Dipp}$), 2.34 (sept, *J* = 6.9 Hz, 4H, C**H**(CH$_3$)$_2$), 2.25 (sept, *J* = 6.9 Hz, 4H, C**H**(CH$_3$)$_2$), 1.20 (d, *J* = 6.6 Hz, 12H, CH(C**H**$_3$)$_2$), 1.15 (s, 18H, C(C**H**$_3$)$_3$), 1.12 (d, *J* = 6.6 Hz, 12H, CH(C**H**$_3$)$_2$), 1.06 (d, *J* = 6.9 Hz, 12H, CH(C**H**$_3$)$_2$), 1.03 (d, *J* = 6.6 Hz, 12H, CH(C**H**$_3$)$_2$), -8.33 (s, 1H, Au**H**). **^{13}C NMR** δ_C (CD_2Cl_2, 75 MHz) 149.8 (**C**$_{carbene}$), 146.0 (Ar**C**$_q$), 145.2 (Ar**C**$_q$), 142.2 (Ar**C**$_q$), 140.1 (Ar**C**$_q$), 139.6 (Ar**C**$_q$), 135.7 (Ar**C**$_q$), 133.8 (Ar**C**H), 133.3 (Ar**C**$_q$), 132.7 (Ar**C**H), 126.7 (Ar**C**H), 126.6 (Ar**C**$_q$), 125.3 (Ar**C**H), 121.1 (Ar**C**H), 120.8 (Ar**C**H), 109.1 (Ar**C**$_q$), 35.0 (**C**(CH$_3$)$_3$), 31.9 (C(**C**H$_3$)$_3$), 29.9 (**C**H(CH$_3$)$_2$), 29.7 (**C**H(CH$_3$)$_2$), 25.8 (CH(**C**H$_3$)$_2$), 25.1 (CH(**C**H$_3$)$_2$), 23.9 (CH(**C**H$_3$)$_2$), 23.6 (CH(**C**H$_3$)$_2$). **^{19}F NMR** δ_F (CD_2Cl_2, 282 MHz) -76.4 (C**F**$_3$SO$_3$).

© University of Pretoria

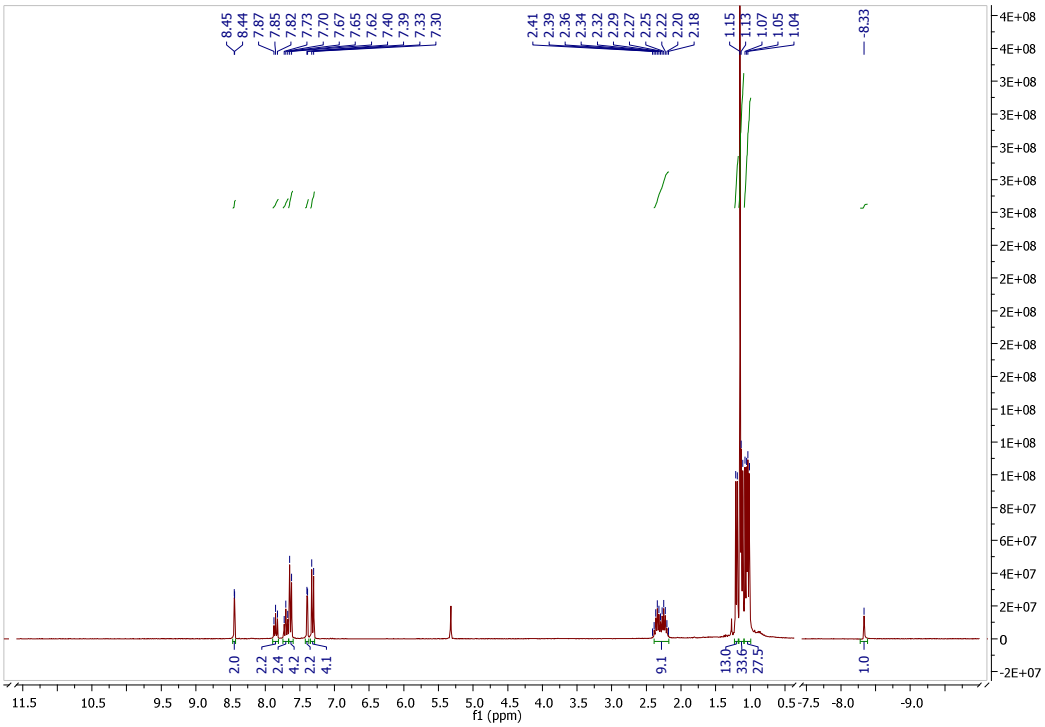

Figure 5.20: ^{1}H NMR spectrum of **23$_a$** in CD_2Cl_2

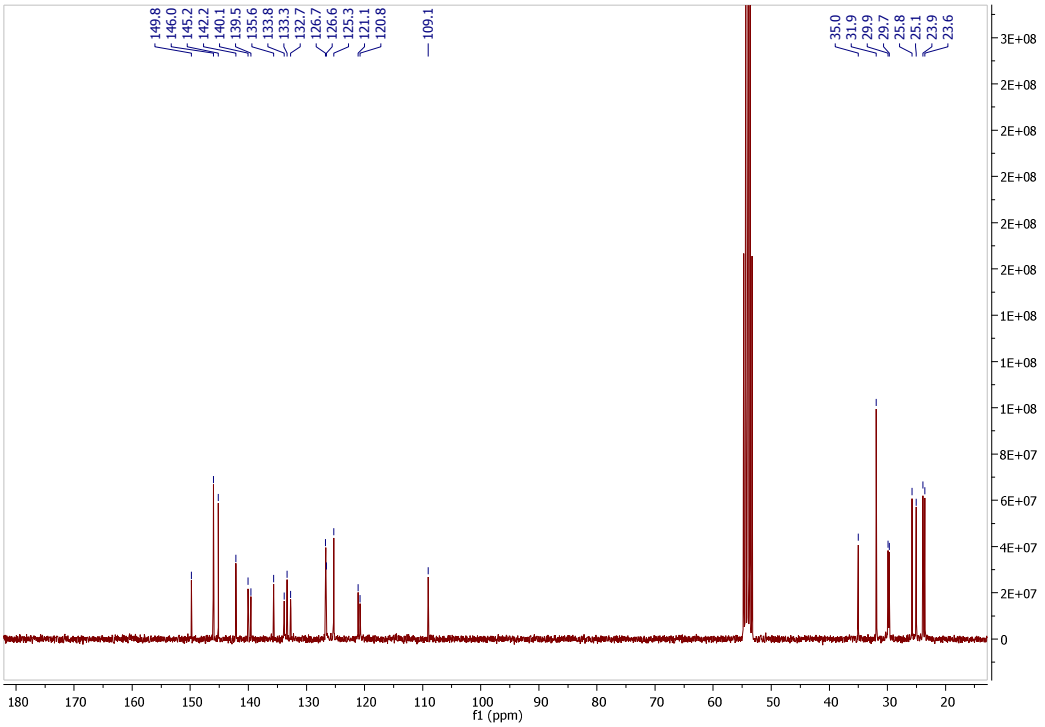

Figure 5.21: ^{13}C NMR spectrum of **23$_a$** in CD_2Cl_2

© University of Pretoria

5.5.5 Synthesis of [(CNHC$_{Dipp}$)Au(I)]OTf (24$_a$)

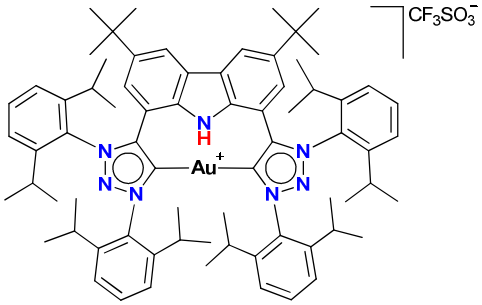

A Schlenk tube was evacuated and purged with Ar (g) followed by addition of THF (10 mL), after being charged with **20$_a$** (20.0 mg, 1.6 x 10^{-5} mol). 1.1 equivalents of trifluoromethanesulfonic acid (TfOH) (1.6 µL, 1.8 x 10^{-5} mol) was then added to the solution that was cooled down to -78 °C. The reaction was warmed to RT after being stirred, in the absence of light, at -78 °C for 15 minutes. The light green solution was stirred an additional 20 hours, before the solvent was removed under reduced pressure. The light green residue was further dried under vacuum for 24 hours. ^{1}H NMR analysis of the crude residue indicated quantitative conversion of **20$_a$** to the intermediate **24$_a$**. However, over an extended period of time (> 4 weeks), **24$_a$** converted in the NMR solvent into product **22$_a$** (*vide infra*), and crystals isolated from the NMR sample were proven to be product **22$_a$**. Compound **24$_a$**: **^{1}H NMR** δ_H (d_8-thf, 300 MHz) 10.94 (s, 1H, N**H**), 8.15 (br s, 2H, Ar**H**$_{carb}$), 7.68 (dd, *J* = 8.1 Hz, 7.8 Hz, 2H, Ar**H**$_{Dipp}$), 7.56 (d, *J* = 7.5 Hz, 4H, Ar**H**$_{Dipp}$), 7.50 (dd, *J* = 8.1 Hz, 7.8 Hz, 2H, Ar**H**$_{Dipp}$), 7.20 (d, *J* = 7.8 Hz, 4H, Ar**H**$_{Dipp}$), 7.02 (br s, 2H, Ar**H**$_{carb}$), 2.91 (sept, *J* = 6.9 Hz, 4H, C**H**(CH$_3$)$_2$), 2.72 (sept, *J* = 6.9 Hz, 4H, C**H**(CH$_3$)$_2$), 1.15 (d, *J* = 6.9 Hz, 12H, CH(C**H**$_3$)$_2$), 1.12 (d, *J* = 6.6 Hz, 12H, CH(C**H**$_3$)$_2$), 1.09 (s, 18H, C(C**H**$_3$)$_3$), 1.04 (d, *J* = 6.3 Hz, 12H, CH(C**H**$_3$)$_2$ overlaps with CH(C**H**$_3$)$_2$), 1.04 (d, *J* = 6.9 Hz, 12H, CH(C**H**$_3$)$_2$ overlaps with CH(C**H**$_3$)$_2$). **^{13}C NMR** δ_C (d_8-thf, 75 MHz) 177.8 (**C**$_{Carbene}$), 147.9, 146.9, 146.3, 143.4, 138.1, 137.6, 134.4, 133.0, 131.5, 128.0, 126.7, 125.0, 123.6, 119.3, 113.4, 35.4 (**C**(CH$_3$)$_3$), 32.2 (C(**C**H$_3$)$_3$), 29.7 (**C**H(CH$_3$)$_2$), 29.6 (**C**H(CH$_3$)$_2$), 26.2 (CH(**C**H$_3$)$_2$ and additional CH(**C**H$_3$)$_2$ resonance overlaps with d_8-thf), 24.4 (CH(**C**H$_3$)$_2$), 22.9 (CH(**C**H$_3$)$_2$). **^{19}F NMR** δ_F (d_8-thf, 282 MHz) -78.7 (C**F**$_3$SO$_3$).

© University of Pretoria

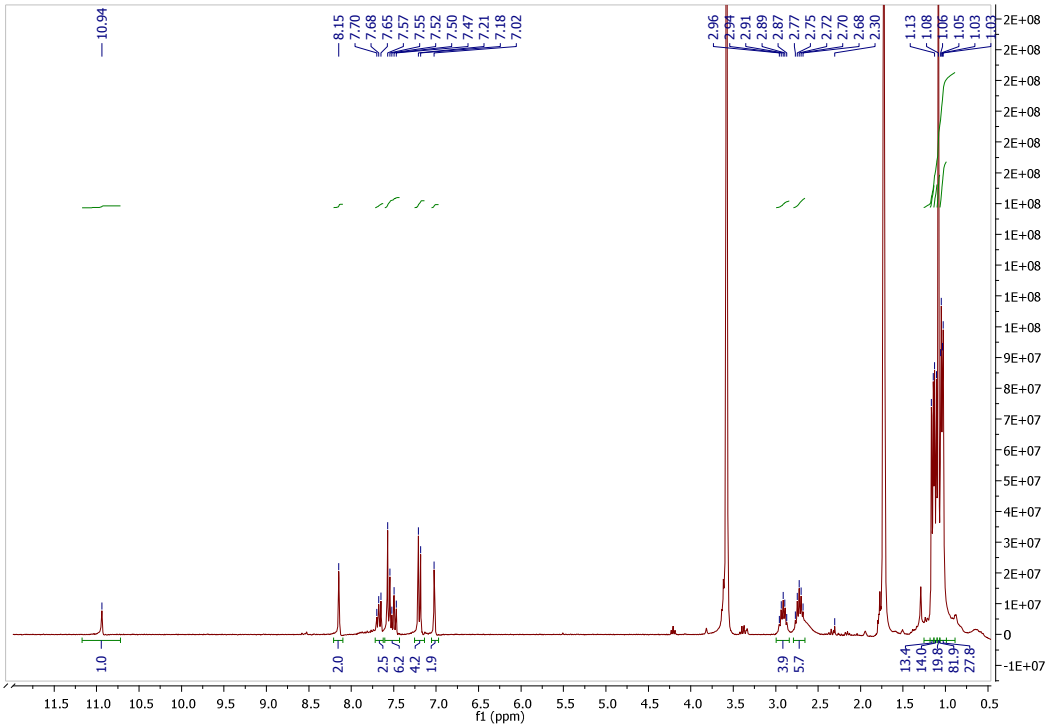

Figure 5.22: ^{1}H NMR spectrum of **24$_a$** in *d8*-thf

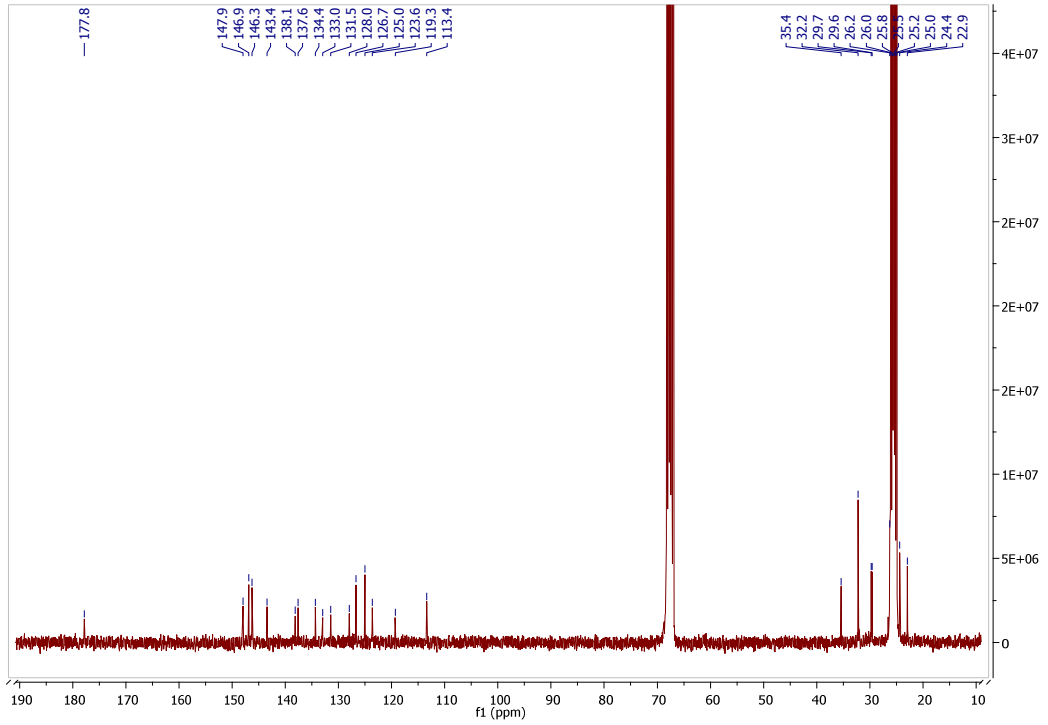

Figure 5.23: ^{13}C NMR spectrum of **24$_a$** in *d8*-thf

© University of Pretoria

5.5.6 Synthesis of [(CNMeC$_{Dipp}$)Au(I)]OTf (26$_a$)

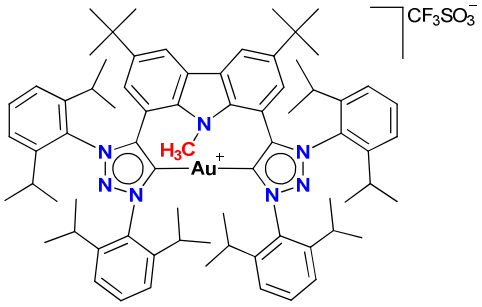

A flame dried Schlenk tube was loaded with **20$_a$** (40.0 mg, 3.2 x 10^{-5} mol). The reaction vessel was evacuated and purged with Ar (g). To the reaction vessel was added THF (15 mL), followed by cooling the purple solution down to -78 °C. To the reaction mixture was added methyl trifluoromethanesulfonate (MeOTf) (4.7 µL, 4.2 x 10^{-5} mol). The reaction was stirred at -78 °C for 15 minutes, before being warmed up to room temperature, with subsequent stirring of the solution overnight. The solvent was removed under reduced pressure. The green residue was first washed with hexanes (4 x 20 mL), then with toluene (4 x 20 mL) and finally with Et_2O (3 x 10 mL). The product was subsequently extracted with dichloromethane (2 x 10 mL) and the solvent evaporated *in vacuo* to yield **26$_a$** (15.0 mg, 1.1 x 10^{-5} mol, 33%) as a light yellow-green solid. Slow evaporation of a deuterated THF solution yielded crystals suitable for XRD analysis. **^{1}H NMR** δ_H (CD_2Cl_2, 300 MHz) 8.01 (d, *J* = 1.8 Hz, 2H, Ar**H**$_{carb}$), 7.73 (t, *J* = 7.8 Hz, 2H, Ar**H**$_{Dipp}$), 7.62 (dd, *J* = 8.0 Hz, 1.5 Hz, 2H, Ar**H**$_{Dipp}$), 7.55 (t, *J* = 7.8 Hz, 2H, Ar**H**$_{Dipp}$), 7.44 (dd, *J* = 7.7 Hz, 1.5 Hz, 2H, Ar**H**$_{Dipp}$), 7.21 (d, *J* = 7.8 Hz, 4H, Ar**H**$_{Dipp}$), 6.90 (d, *J* = 1.5 Hz, 2H, Ar**H**$_{carb}$), 2.93 (s, 3H, NC**H**$_3$), 2.59 - 2.43 (m, 6H, C**H**$(CH_3)_2$), 2.31 (sept, *J* = 6.9 Hz, 2H, C**H**$(CH_3)_2$), 1.34 (d, *J* = 6.9 Hz, 6H, CH(C**H**$_3)_2$), 1.26 (d, *J* = 6.6 Hz, 6H, CH(C**H**$_3)_2$), 1.14 (d, *J* = 6.6 Hz, 6H, CH(C**H**$_3)_2$), 1.12 (d, *J* = 6.6 Hz, 6H, CH(C**H**$_3)_2$), 1.11 (d, *J* = 6.9 Hz, 6H, CH(C**H**$_3)_2$), 1.09 (d, *J* = 6.3 Hz, 6H, CH(C**H**$_3)_2$), 1.08 (s, 18H, C(C**H**$_3)_3$), 1.02 (d, *J* = 6.9 Hz, 6H, CH(C**H**$_3)_2$), 0.84 (d, *J* = 6.6 Hz, 6H, CH(C**H**$_3)_2$). **^{13}C NMR** δ_C (CD_2Cl_2, 75 MHz) 177.5 (**C**$_{Carbene}$), 147.8 (Ar**C**$_q$), 146.4 (Ar**C**$_q$), 145.9 (Ar**C**$_q$), 145.5 (Ar**C**$_q$), 145.1 (Ar**C**$_q$), 144.6 (Ar**C**$_q$), 144.4 (Ar**C**$_q$), 136.3 (Ar**C**$_q$), 133.2 (Ar**C**H), 132.5 (Ar**C**$_q$), 131.7 (Ar**C**H), 131.2 (Ar**C**$_q$), 126.5 (Ar**C**H), 126.3 (Ar**C**H), 124.9 (Ar**C**H), 124.8 (Ar**C**H), 119.6 (Ar**C**H), 119.6 (Ar**C**H), 115.1 (Ar**C**$_q$), 40.3 (N**C**H_3), 35.3 (**C**$(CH_3)_3$), 31.7 (C(**C**$H_3)_3$), 30.1 (**C**$H(CH_3)_2$), 29.9 (**C**$H(CH_3)_2$), 29.8 (**C**$H(CH_3)_2$), 29.3 (**C**$H(CH_3)_2$), 26.1 (CH(**C**$H_3)_2$), 25.4 (CH(**C**$H_3)_2$), 25.0 (CH(**C**$H_3)_2$), 24.9 (CH(**C**$H_3)_2$), 24.3 (CH(**C**$H_3)_2$), 23.7 (CH(**C**$H_3)_2$), 23.2 (CH(**C**$H_3)_2$), 22.7 (CH(**C**$H_3)_2$). **^{19}F NMR** δ_F (CD_2Cl_2, 282 MHz) -78.9 (CF_3SO_3). **^{1}H NMR** δ_H (*d*$_8$-thf, 300 MHz) 8.23 (d, *J* = 1.8 Hz, 2H, Ar**H**$_{carb}$), 7.78 - 7.68 (m, 4H, Ar**H**$_{Dipp}$), 7.61 - 7.53 (m, 4H, Ar**H**$_{Dipp}$), 7.30 - 7.24 (m, 4H, Ar**H**$_{Dipp}$), 6.94 (d, *J* = 1.8 Hz, 2H, Ar**H**$_{carb}$), 3.10 (s, 3H, NC**H**$_3$), 2.70 - 2.52 (m, 6H, C**H**$(CH_3)_2$), 2.48 - 2.34 (m, 2H, C**H**$(CH_3)_2$), 1.38 (d, *J* = 6.9 Hz, 6H, CH(C**H**$_3)_2$), 1.27 (d, *J* = 6.6 Hz, 6H, CH(C**H**$_3)_2$), 1.20 (d, *J* = 6.9 Hz, 6H, CH(C**H**$_3)_2$), 1.16 (d, *J* = 7.5 Hz, 6H, CH(C**H**$_3)_2$), 1.13 (d, *J* = 6.9 Hz, 6H, CH(C**H**$_3)_2$), 1.11 (d, *J* = 7.5 Hz, 6H, CH(C**H**$_3)_2$ overlaps with C(C**H**$_3)_3$), 1.09 (s, 18H, C(C**H**$_3)_3$ overlaps with CH(C**H**$_3)_2$), 1.03 (d, *J* = 6.6 Hz, 6H, CH(C**H**$_3)_2$), 0.89 (d, *J* = 6.6 Hz, 6H, CH(C**H**$_3)_2$). **^{13}C NMR** δ_C (*d*$_8$-thf, 75 MHz) 178.3 (**C**$_{Carbene}$), 147.6, 147.1,

© University of Pretoria

146.4, 146.2, 146.2, 145.6, 145.3, 137.0, 133.7, 133.2, 132.3, 131.8, 127.2, 126.8, 125.6, 125.2, 124.9, 120.4, 115.4, 42.0 (N**C**H_3), 35.7 (**C**(CH_3)$_3$), 32.0 (C(**C**H_3)$_3$), 30.7 (**C**H(CH_3)$_2$), 29.8 (**C**H(CH_3)$_2$), 25.1 (CH(**C**H_3)$_2$), 23.9 (CH(**C**H_3)$_2$), 23.3 (CH(**C**H_3)$_2$), 22.7 (CH(**C**H_3)$_2$). **^{19}F NMR** δ_F (*d*$_8$-thf, 282 MHz) -78.9 (C**F**$_3$$SO_3$). **HRMS** (ESI-TOF): Calculated for $C_{73}H_{93}N_7Au^+$ [M]$^+$: 1264.7152, found: 1264.7153.

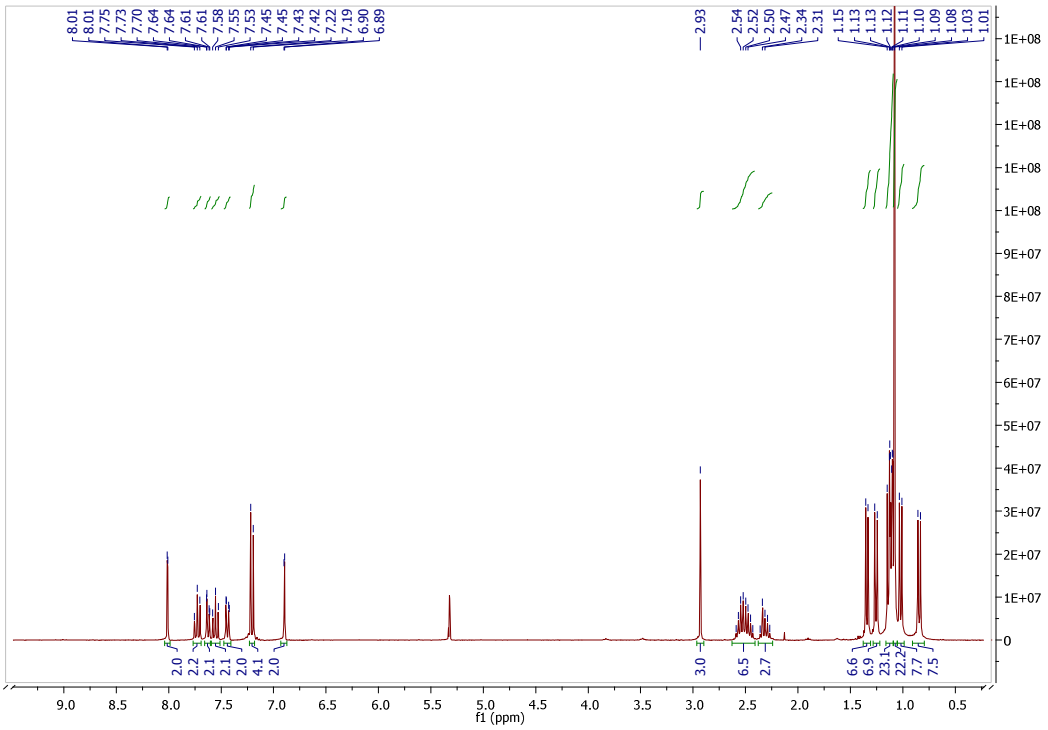

Figure 5.24: ^{1}H NMR spectrum of **26$_a$** in solvent CD_2Cl_2

© University of Pretoria

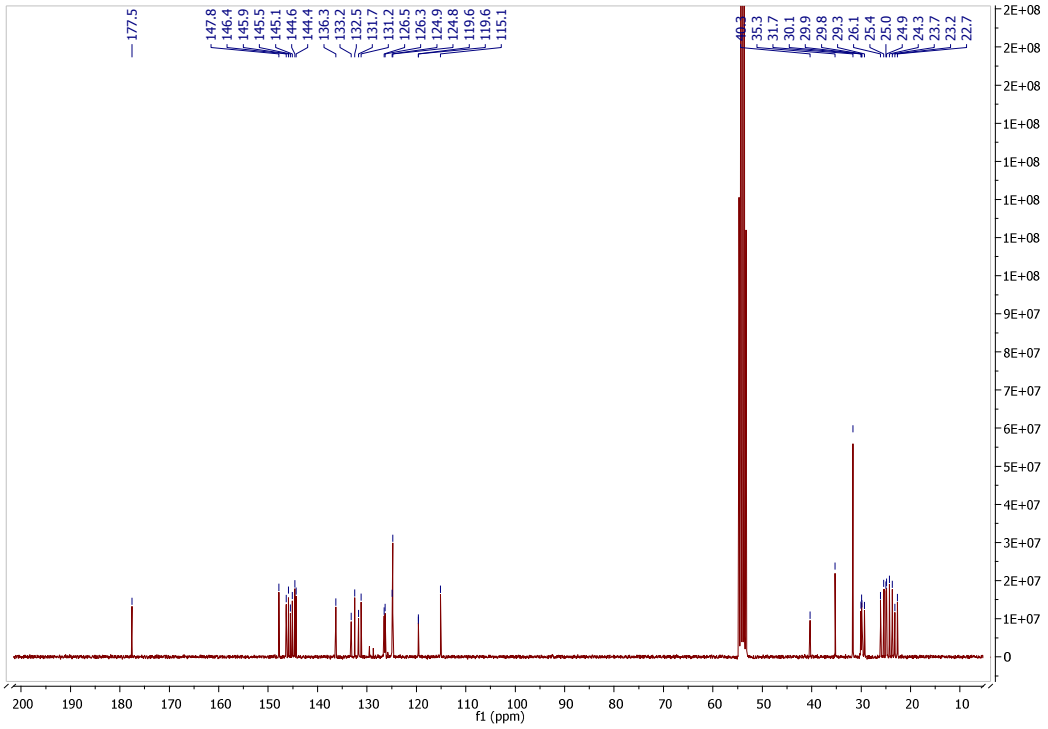

Figure 5.25: ^{13}C NMR spectrum of **26$_a$** in CD_2Cl_2

5.5.7 Synthesis of [(CNMeC$_{Dipp}$)Au(I)]I (27$_a$)

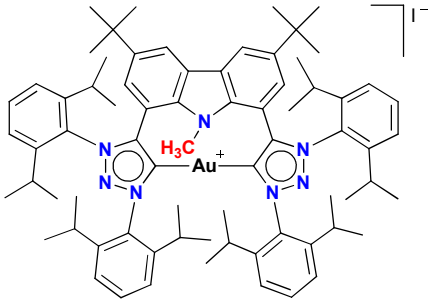

To a Schlenk tube charged with **20$_a$** (30.0 mg, 2.4 x 10^{-5} mol) and THF (15 mL), was added iodomethane (MeI) (1.6 µL, 2.5 x 10^{-5} mol) at -78 °C. The reaction was stirred at -78 °C for 20 minutes, before being warmed up to room temperature. Stirring was continued for four days at room temperature and in the absence of light. The solvent was removed under reduced pressure. The yellow residue was first washed with hexanes (4 x 15 mL), then with toluene (4 x 10 mL) and finally with Et_2O (3 x 5 mL). The product was subsequently extracted with dichloromethane (2 x 10 mL) and the solvent evaporated *in vacuo* to yield **27$_a$** (6.5 mg, 4.7 x 10^{-6} mol, 20%) as a yellow solid. **^{1}H NMR** δ_H (CD_2Cl_2, 300 MHz) 8.02 (d, *J* = 1.5 Hz, 2H, Ar**H**$_{carb}$), 7.73 (t, *J* = 7.8 Hz, 2H, Ar**H**$_{Dipp}$), 7.63 (dd, *J* = 7.8 Hz, 1.5 Hz, 2H, Ar**H**$_{Dipp}$), 7.56 (t, *J* = 7.8 Hz, 2H, Ar**H**$_{Dipp}$), 7.44 (dd, *J* = 7.8 Hz, 1.2 Hz, 2H, Ar**H**$_{Dipp}$), 7.21 (d, *J* = 7.8 Hz, 4H, Ar**H**$_{Dipp}$), 6.90 (d, *J* = 1.5 Hz, 2H, Ar**H**$_{carb}$), 2.93 (s, 3H, NC**H**$_3$), 2.59 - 2.43 (m, 6H, C**H**$(CH_3)_2$), 2.36 - 2.25 (m, 2H, C**H**$(CH_3)_2$, overlaps with residual toluene C**H**$_3$ resonance), 1.34 (d, *J* = 6.6Hz, 6H, CH(C**H**$_3)_2$), 1.26 (d, *J* = 6.6 Hz, 6H, CH(C**H**$_3)_2$), 1.14 (d, *J* = 6.9 Hz, 6H, CH(C**H**$_3)_2$), 1.12 (d, *J* = 6.6 Hz, 6H, CH(C**H**$_3)_2$), 1.11 (d, *J* = 6.9 Hz, 6H, CH(C**H**$_3)_2$), 1.09 (d, *J* = 5.7 Hz, 6H, CH(C**H**$_3)_2$ overlaps with C(C**H**$_3)_3$), 1.08 (s, 18H, C(C**H**$_3)_3$

© University of Pretoria

overlaps with CH(C**H**$_3$)$_2$), 1.02 (d, *J* = 6.9 Hz, 6H, CH(C**H**$_3$)$_2$), 0.85 (d, *J* = 6.6 Hz, 6H, CH(C**H**$_3$)$_2$). **^{13}C NMR** δ_C (CD_2Cl_2, 75 MHz) 177.5 (**C**$_{Carbene}$), 147.8 (Ar**C**$_q$), 146.3 (Ar**C**$_q$), 145.9 (Ar**C**$_q$), 145.4 (Ar**C**$_q$), 145.0 (Ar**C**$_q$), 144.6 (Ar**C**$_q$), 144.3 (Ar**C**$_q$), 136.3 (Ar**C**$_q$), 133.2 (Ar**C**H), 132.5 (Ar**C**$_q$), 131.7 (Ar**C**H), 131.2 (Ar**C**$_q$), 126.5 (Ar**C**H), 126.3 (Ar**C**H), 124.9 (Ar**C**H), 124.7 (Ar**C**H), 119.6 (Ar**C**H), 119.6 (Ar**C**H), 115.1 (Ar**C**$_q$), 40.3 (N**C**H$_3$), 35.3 (**C**(CH$_3$)$_3$), 31.7 (C(**C**H$_3$)$_3$), 30.0 (**C**H(CH$_3$)$_2$), 29.9 (**C**H(CH$_3$)$_2$), 29.8 (**C**H(CH$_3$)$_2$), 29.3 (**C**H(CH$_3$)$_2$), 26.0 (CH(**C**H$_3$)$_2$), 25.4 (CH(**C**H$_3$)$_2$), 25.0 (CH(**C**H$_3$)$_2$), 24.8 (CH(**C**H$_3$)$_2$), 24.3 (CH(**C**H$_3$)$_2$), 23.7 (CH(**C**H$_3$)$_2$), 23.2 (CH(**C**H$_3$)$_2$), 22.7 (CH(**C**H$_3$)$_2$). **HRMS** (ESI-TOF): Calculated for $C_{73}H_{93}N_7Au^+$ [M]$^+$: 1264.7152, found: 1264.7147.

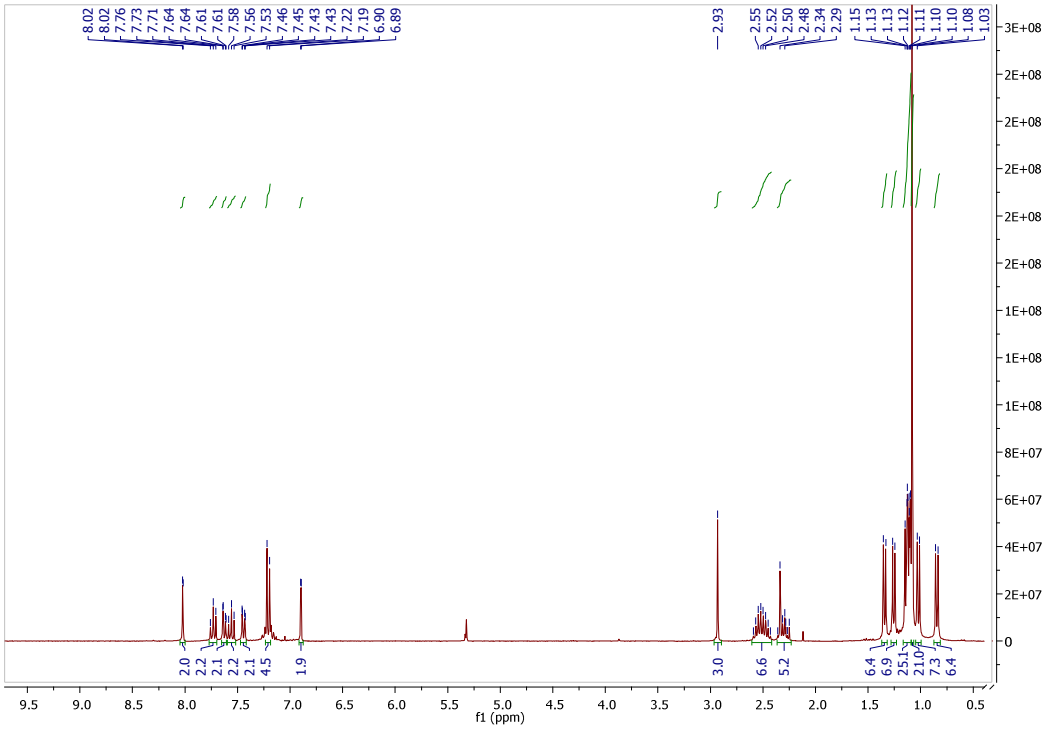

Figure 5.26: ^{1}H NMR spectrum of **27$_a$** in CD_2Cl_2

© University of Pretoria

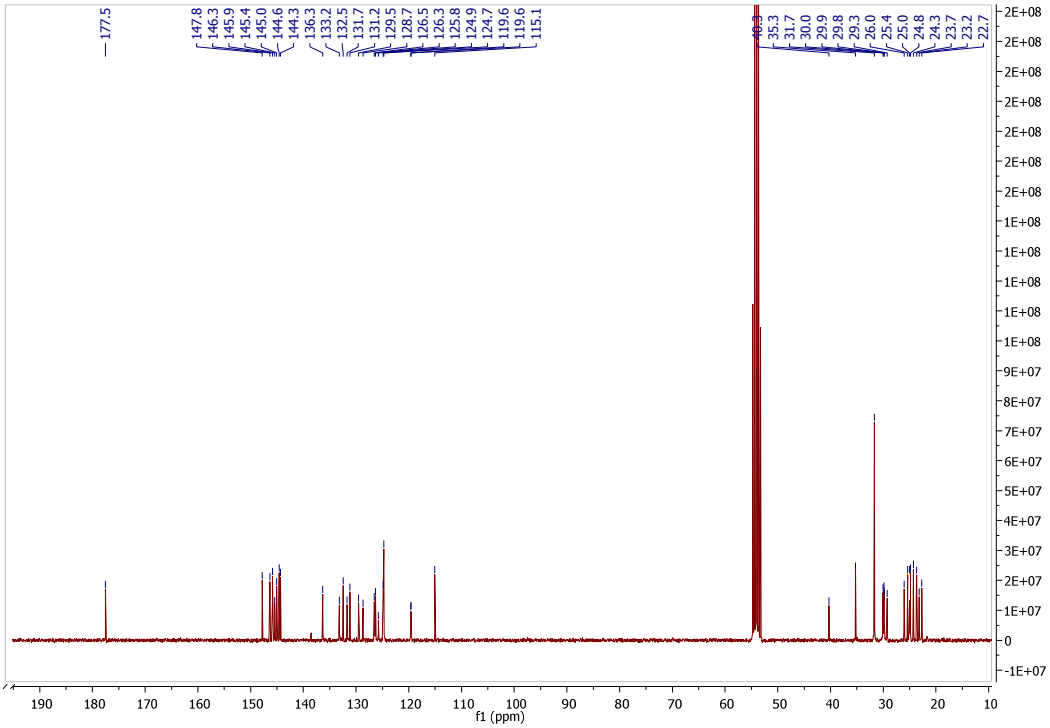

Figure 5.27: ^{13}C NMR spectrum of **27$_a$** in CD_2Cl_2

5.5.8 Synthesis of [(CNC$_{Mes}$)Au(III)CH$_3$]I (28$_b$)

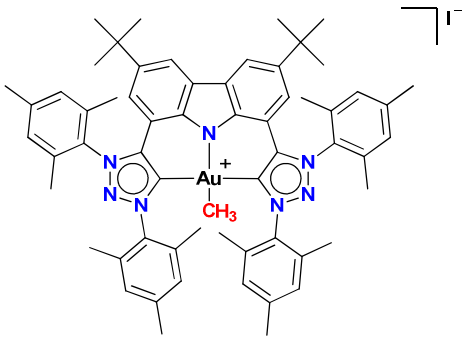

To a Schlenk tube charged with **21$_b$** (50.0 mg, 4.6 x 10^{-5} mol) and THF (15 mL), was added iodomethane (0.1 mL, 1.6 x 10^{-3} mol) at -78 °C. Upon addition the colour of the solution instantaneously changed from dark pink to yellow. The reaction was stirred at -78 °C for 1 h and then warmed up to room temperature and stirred for an additional 2 h to give a yellow suspension. The solvent was removed under vacuum, the remaining solid washed with hexanes (2 x 15 mL) and Et_2O (10 mL) to give **28$_b$** as a yellow solid (35 mg, 2.9 x 10^{-5} mol, 62% yield). **^{1}H NMR** δ_H (CD_2Cl_2, 500 MHz) 8.37 (d, *J* = 1.8 Hz, 2H, Ar**H**$_{carb}$), 7.34 (d, *J* = 1.8 Hz, 2H, Ar**H**$_{carb}$), 7.29 (s, 4H, Ar**H**$_{Mes}$), 7.09 (s, 4H, Ar**H**$_{Mes}$), 2.49 (s, 6H, ArC**H**$_3$), 2.47 (s, 6H, ArC**H**$_3$), 2.15 (s, 12H, ArC**H**$_3$), 2.05 (s, 12H, ArC**H**$_3$), 1.15 (s, 18H, C(C**H**$_3$)$_3$), 0.19 (s, 3H, Au-CH$_3$). **^{13}C NMR** δ_C (CD_2Cl_2, 125 MHz) 146.3 (**C**$_{Carbene}$), 143.5 (Ar**C**$_q$), 142.2 (Ar**C**$_q$), 141.7 (Ar**C**$_q$), 140.5 (Ar**C**$_q$), 139.8 (Ar**C**$_q$), 135.4 (Ar**C**$_q$), 135.1 (Ar**C**$_q$), 134.6 (Ar**C**$_q$), 133.5 (Ar**C**$_q$), 131.0 (Ar**C**H), 130.0 (Ar**C**H), 126.0 (Ar**C**$_q$), 120.2 (Ar**C**H), 119.4 (Ar**C**H), 108.8 (Ar**C**$_q$), 34.9 (**C**(CH$_3$)$_3$), 31.7 (C(**C**H$_3$)$_3$), 21.7 (Ar**C**H$_3$), 21.5 (Ar**C**H$_3$), 18.2 (Ar**C**H$_3$), 17.7 (Ar**C**H$_3$), -3.8 (Au-**C**H$_3$). See Figures 5.11 and 5.12 for ^{1}H and ^{13}C NMR spectra, respectively.

© University of Pretoria

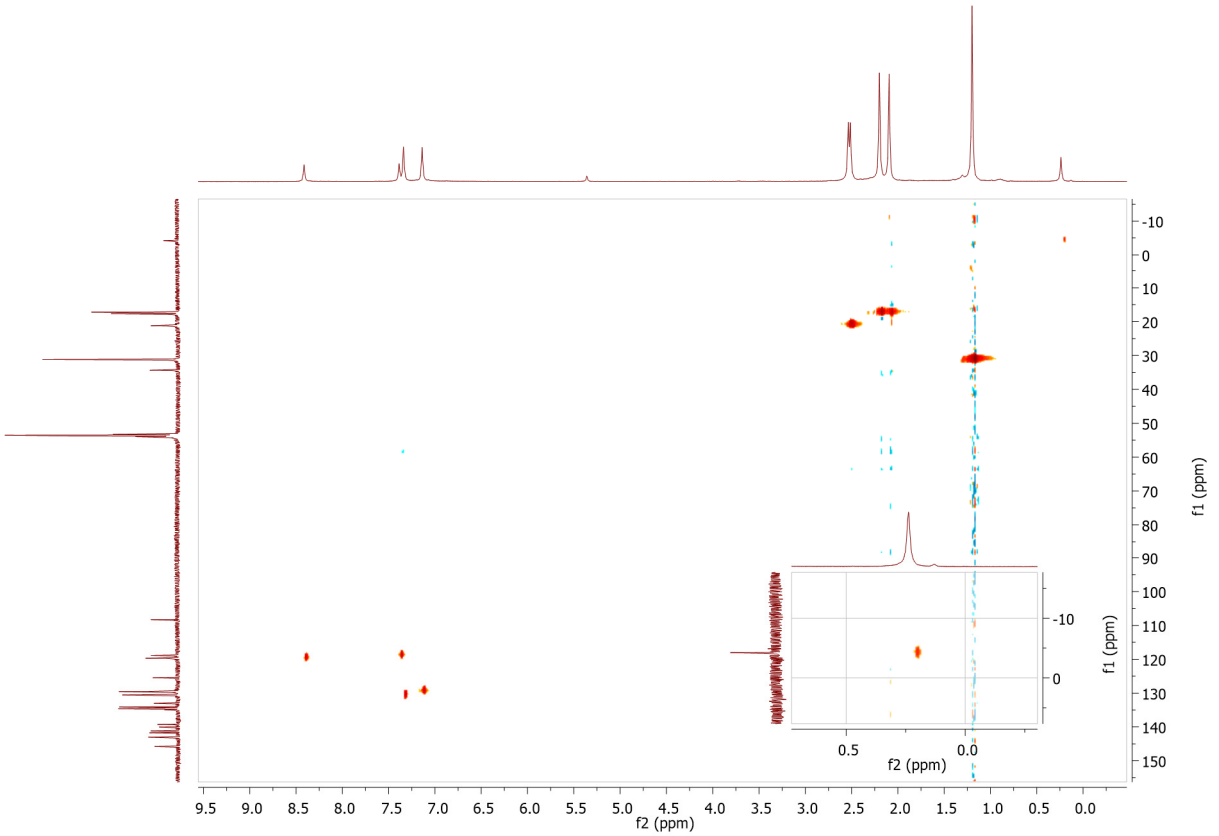

Figure 5.28: ^{1}H-^{13}C HSQC NMR spectrum of **28$_b$** in CD_2Cl_2

5.5.9 Synthesis of [(CNC$_{Mes}$)Au(III)CH$_2$Cl]Cl (29$_b$)

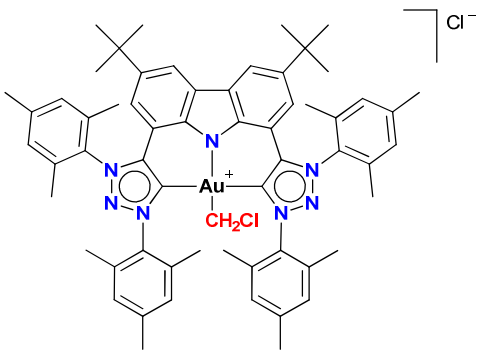

A Schlenk tube was loaded with **21$_b$** (60.0 mg, 5.5 x 10^{-5} mol), evacuated and purged with Ar (g). To the residue was added CH_2Cl_2 (20 mL). The reaction, which changed colour from dark pink to yellow during the course of the reaction, was stirred for 2 days at room temperature in the absence of light. The solvent was evaporated, and the resulting residue was first washed with hexanes (4 x 20 mL), followed by Et_2O (3 x 10 mL). The compound was extracted with CH_2Cl_2 (2 x 10 mL), with subsequent evaporation of the solvent under reduced pressure to yield **29$_b$** (16.0 mg, 1.4 x 10^{-5} mol, 25%) as a yellow-brown solid. **^{1}H NMR** δ_H (CD_2Cl_2, 300 MHz) 8.40 (d, *J* = 1.8 Hz, 2H, Ar**H**$_{carb}$), 7.36 (d, *J* = 1.8 Hz, 2H, Ar**H**$_{carb}$), 7.31 (br s, 4H, Ar**H**$_{Mes}$), 7.17 (s, 4H, Ar**H**$_{Mes}$), 3.03 (s, 2H, AuC**H**$_2$Cl), 2.51 (s, 6H, ArC**H**$_3$), 2.50 (s, 6H, ArC**H**$_3$), 2.25 (s, 12H, ArC**H**$_3$ overlaps with ArC**H**$_3$), 2.35 - 1.80 (br s, 12H, ArC**H**$_3$ overlaps with ArC**H**$_3$), 1.17 (s, 18H, C(C**H**$_3$)$_3$). **^{13}C NMR**

© University of Pretoria

δ_C (CD_2Cl_2, 75 MHz) 145.7 (**C**$_{Carbene}$), 143.7 (Ar**C**$_q$), 142.8 (Ar**C**$_q$), 142.2 (Ar**C**$_q$), 140.3 (Ar**C**$_q$), 139.6 (Ar**C**$_q$), 135.2 (Ar**C**$_q$), 134.6 (Ar**C**$_q$), 133.4 (Ar**C**$_q$), 131.1 (Ar**C**H), 130.4 (Ar**C**H), 126.3 (Ar**C**$_q$), 120.4 (Ar**C**H), 119.5 (Ar**C**H), 108.6 (Ar**C**$_q$), 34.9 (**C**$(CH_3)_3$), 31.6 (C(**C**$H_3)_3$), 25.1 (Au**C**H_2Cl), 21.7 (Ar**C**H_3), 21.7 (Ar**C**H_3), 21.5 (Ar**C**H_3), 21.5 (Ar**C**H_3), 18.6 (Ar**C**H_3), 17.7 (Ar**C**H_3). **HRMS** (ESI-TOF): Calculated for $C_{61}H_{68}N_7AuCl^+$ $[M]^+$: 1130.4885, found: 1130.4882.

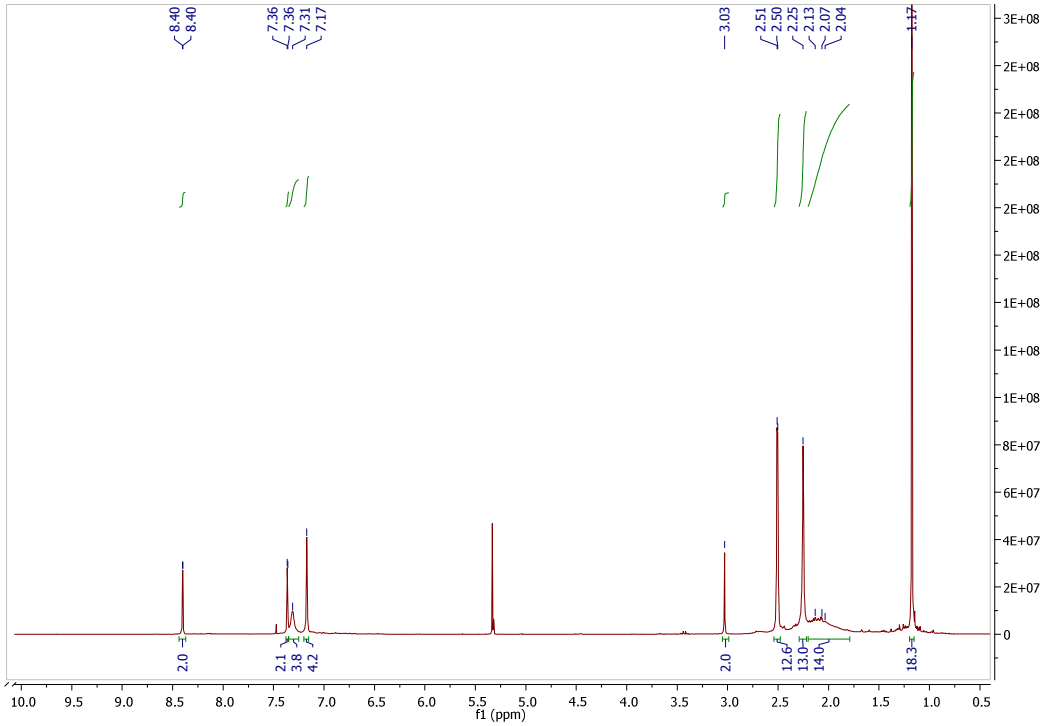

Figure 5.29: ^{1}H NMR spectrum of **29$_b$** in CD_2Cl_2

© University of Pretoria

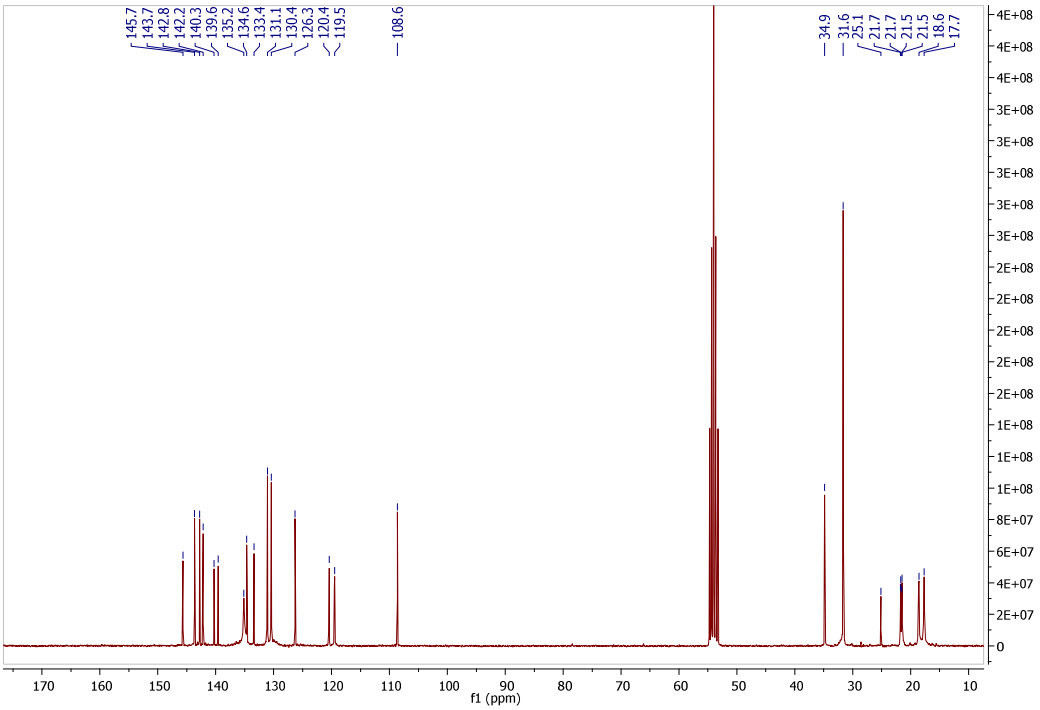

Figure 5.30: ^{13}C NMR spectrum of **29b** in CD_2Cl_2

5.5.10 Synthesis of [(CNC$_{Dipp}$)Au(III)F]BF$_4$ (30$_a$)

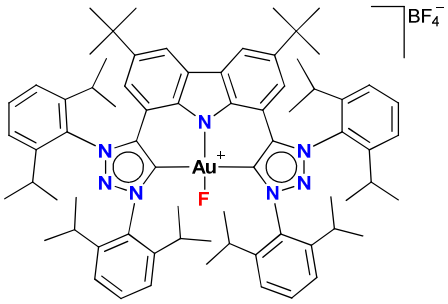

A Schlenk tube was loaded with **20$_a$** (120.0 mg, 9.6 x 10^{-5} mol), Selectfluor (35.7 mg, 1.0 x 10^{-5} mol), evacuated and purged with Ar (g). The solids were cooled down to -78 °C. To the vessel was added THF (15 mL) which was also cooled down to -78 °C. The reaction was stirred at this temperature for 10 minutes, before being gradually warmed up to room temperature whilst stirring in the absence of light. The solution was stirred overnight. The lime green solution was filtered and the solvent evaporated under reduced pressure. The lime green residue was washed with toluene (4 x 10 mL) and then with Et_2O (4 x 10 mL). The product was extracted with a mixture of CH_2Cl_2 and toluene in a 1:2 ratio (2 x 10 mL), respectively. The solvent was evaporated under reduced pressure. The residue was washed with hexanes (4 x 10 mL) and the solid was dried *in vacuo*, to yield **30$_a$** (48.0 mg, 3.5 x 10^{-5} mol, 37%) as a light green solid. Crystals suitable for X-ray diffraction analysis was obtained through slow evaporation of a CD_2Cl_2 solution of **30$_a$**. **^{1}H NMR** δ_H (CD_2Cl_2, 400 MHz) 8.37 (d, *J* = 1.6 Hz, 2H, Ar**H**$_{carb}$), 7.85 (t, *J* = 8.0 Hz, 2H, Ar**H**$_{Dipp}$), 7.62 (d, *J* = 8.0 Hz, 4H, Ar**H**$_{Dipp}$), 7.49 (t, *J* = 8.0 Hz, 2H, Ar**H**$_{Dipp}$), 7.28 (d, *J* = 1.6 Hz, 2H, Ar**H**$_{carb}$), 7.17 (d, *J* = 8.0 Hz, 4H, Ar**H**$_{Dipp}$), 2.33 (sept, *J* = 6.8 Hz, 4H, C**H**$(CH_3)_2$), 2.23 (sept, *J* =

© University of Pretoria

6.8 Hz, 4H, C**H**$(CH_3)_2$), 1.20 (d, *J* = 6.8 Hz, 12H, CH(C**H**$_3)_2$), 1.13 (s, 18H, C(C**H**$_3)_3$), 1.11 (d, *J* = 7.2 Hz, 12H, CH(C**H**$_3)_2$ overlaps with CH$(CH_3)_2$), 1.09 (d, *J* = 7.8 Hz, 12H, CH(C**H**$_3)_2$ overlaps with CH$(CH_3)_2$), 1.03 (d, *J* = 6.8 Hz, 12H, CH(C**H**$_3)_2$). **^{13}C NMR** δ_C (CD_2Cl_2, 100 MHz) n.o. (**C**$_{carbene}$), 146.0 (Ar**C**$_q$), 145.0 (Ar**C**$_q$), 144.9 (Ar**C**$_q$), 143.8 (Ar**C**$_q$), 141.9 (Ar**C**$_q$), 138.1 (Ar**C**$_q$), 136.5 (Ar**C**$_q$), 134.6 (Ar**C**$_q$), 134.5 (Ar**C**$_q$), 134.0 (Ar**C**H), 132.7 (Ar**C**$_q$), 131.6 (Ar**C**H), 126.7 (Ar**C**H), 126.0 (Ar**C**$_q$), 124.0 (Ar**C**H), 121.1 (Ar**C**H), 120.5 (Ar**C**H), 108.3 (Ar**C**$_q$), 35.0 (**C**$(CH_3)_3$), 31.8 (C(**C**$H_3)_3$), 29.9 (**C**H$(CH_3)_2$), 25.4 (CH(**C**$H_3)_2$), 25.1 (CH(**C**$H_3)_2$), 24.4 (CH(**C**$H_3)_2$), 23.6 (CH(**C**$H_3)_2$). **^{19}F NMR** δ_F (CD_2Cl_2, 282 MHz) -299.9 (Au**F**), -153.2 (B**F**$_4$). **HRMS** (ESI-TOF): Calculated for $C_{72}H_{90}N_7AuF^+$ $[M]^+$: 1268.6907, found: 1268.6650.

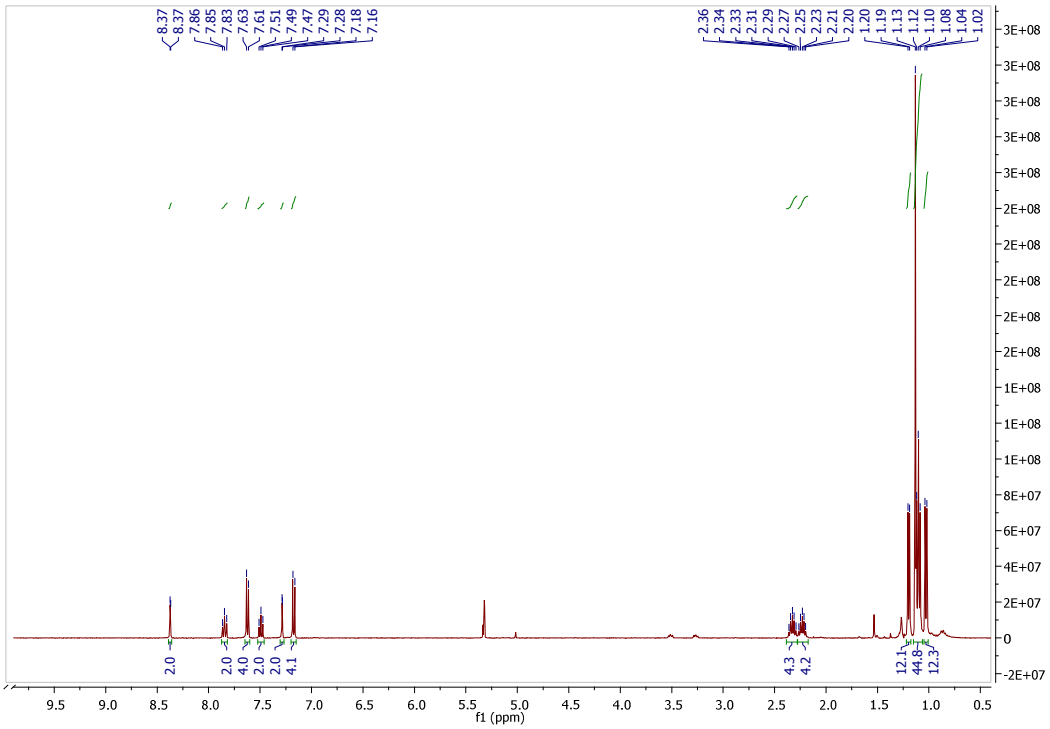

Figure 5.31: ^{1}H NMR spectrum of **30$_a$** in CD_2Cl_2

© University of Pretoria

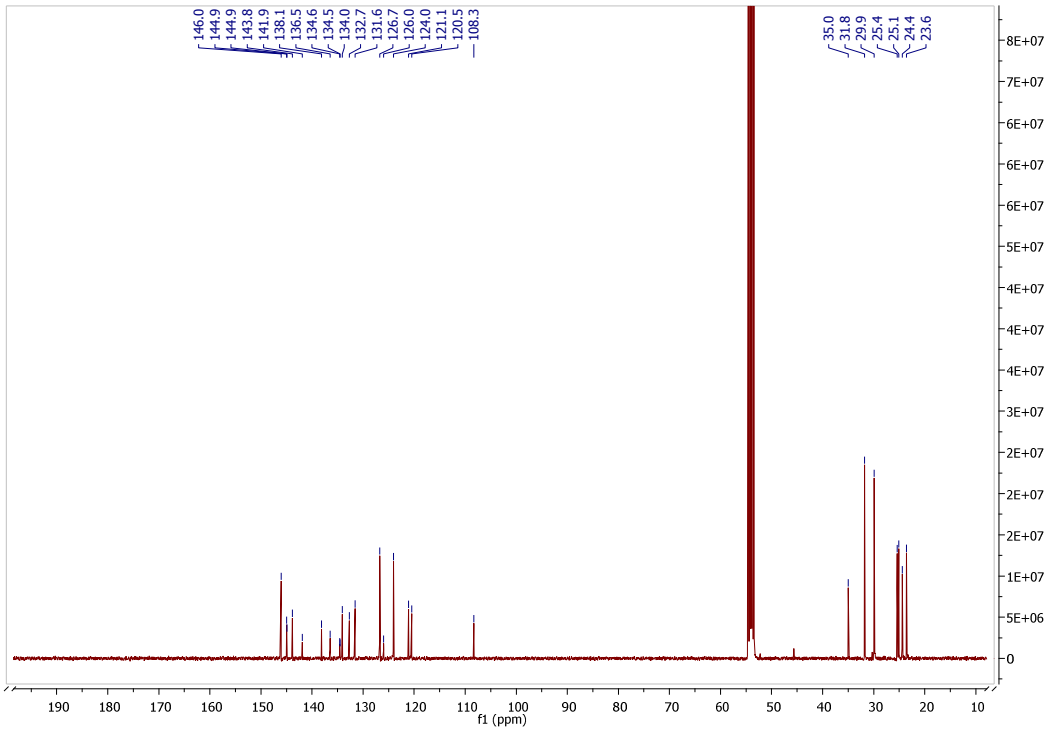

Figure 5.32: ^{13}C NMR spectrum of **30$_a$** in CD_2Cl_2

5.5.11 Solvent dependent redox reaction of 20$_a$ with acetic acid

See Scheme 5.24. A high pressure NMR tube was loaded with **20$_a$** (40.0 mg, 3.2 x 10^{-5} mol) followed by the addition of 6 equivalents of glacial acetic acid (AcOH) (11.0 µL, 1.9 x 10^{-4} mol) in 0.4 mL CD_2Cl_2 to yield yellow-green solution of **25$_a$**. The solvent CD_2Cl_2 solvent was then evaporated, and the yellow-green solid was observed to darken to red-orange. Subsequently, the NMR tube was loaded with d_8-thf (0.4 mL), and the solution changed colour from yellow to red. The reaction was followed with NMR analysis, and reductive elimination of acetic acid, and quantitative regeneration of compound **20$_a$** was observed.

© University of Pretoria

5.5.12 Deprotonation and reduction of 22_a with sodium hydride

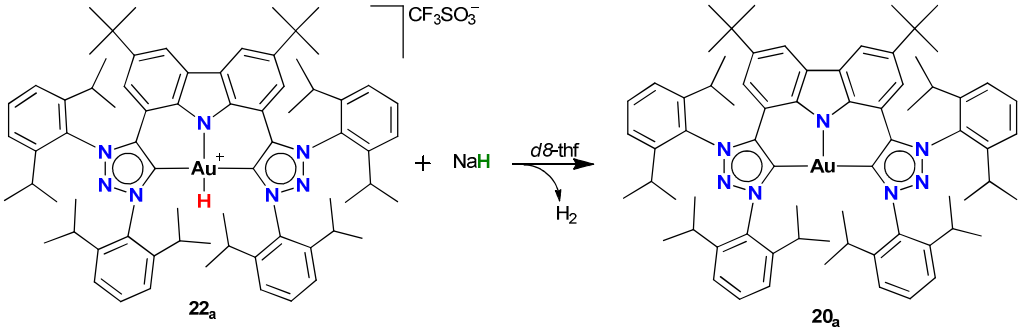

Scheme 5.30: Reaction of **22_a** with NaH

A high pressure NMR tube was loaded with **22_a** (15.5 mg, 1.1 x 10^{-5} mol) and NaH (1.0 mg, 4.2 x 10^{-5} mol) in a glove box. The reaction was initiated by the addition of d_8-thf (0.4 mL). The reaction progress was monitored by ^{1}H NMR spectroscopy. The reaction slowly changed colour from lime green to purple, with quantitative conversion of **22_a** to **20_a**, after three days at room temperature. See Figure 5.8 for stacked ^{1}H NMR spectra representing reaction progress.

5.5.13 Reaction of 22_a with hydrochloric acid (1M in Et_2O)

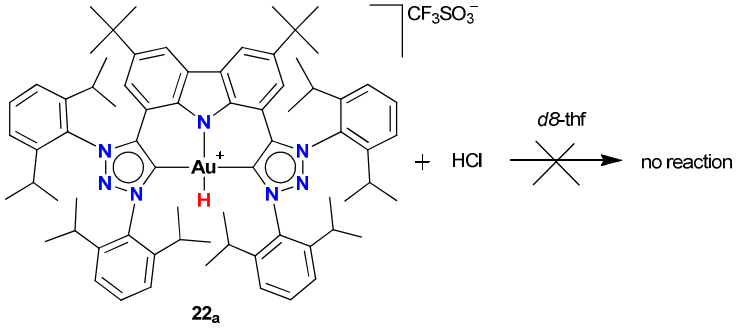

Scheme 5.31: Reaction of **22_a** with HCl

A high pressure NMR tube was loaded with **22_a** (9.0 mg, 6.4 x 10^{-6} mol) in a glove box. To the vessel was added d_8-thf (0.4 mL) and 1M HCl (32.1 µL, 3.2 x 10^{-5} mol) in Et_2O. The reaction was followed with ^{1}H NMR analysis. No reaction occurred.

© University of Pretoria

5.6 References

[1] G. Kleinhans, *MSc Dissertation*, *University of Pretoria*, **2014**, 147 – 185.
[2] R. Ciriminna, E. Falletta, C. D. Pina, J. H. Teles, M. Pagliaro, *Angew. Chem. Int. Ed.*, **2016**, *55*, 14210 – 14217.
[3] P. Johnston, N. Carthey, G. J. Hutchings, *J. Am. Chem. Soc.*, **2015**, *137*, 14548 – 14557.
[4] H. G. Raubenheimer, H. Schmidbaur, *J. Chem. Educ.*, **2014**, *91*, 2024 – 2036.
[5] T. Lauterbach, A. M. Asiri, A. S. K. Hashmi, *Advances in Organometallic Chemistry*, **2014**, *62*, 261 – 297.
[6] M. Joost, A. Amgoune, D. Bourissou, *Angew. Chem. Int. Ed.*, **2015**, *54*, 15022 – 15045.
[7] For selected reviews and references therein, see: *a*) R. Kumar, C. Nevado, *Angew. Chem. Int. Ed.*, **2017**, *56*, 1994 – 2015; *b*) D.-A. Roşca, J. A. Wright, M. Bochmann, *Dalton Trans.*, **2015**, *44*, 20785 – 20807; *c*) M. Rudolph, A. S. K. Hashmi, *Chem. Commun.*, **2011**, *47*, 6536 – 6544; *d*) A. S. K. Hashmi, *Angew. Chem. Int. Ed.*, **2010**, *49*, 5232 – 5241; *e*) A. Fürstner, *Chem. Soc. Rev.*, **2009**, *38*, 3208 – 3221; *f*) Z. Li, C. Brouwer, C. He, *Chem. Rev.*, **2008**, *108*, 3239 – 3265; *g*) A. Arcadi, *Chem. Rev.*, **2008**, *108*, 3266 – 3325; *h*) E. Jiménez-Núñez, A. M. Echavarren, *Chem. Rev.*, **2008**, *108*, 3326 – 3350; *i*) D. J. Gorin, B. D. Sherry, F. D. Toste, *Chem. Rev.*, **2008**, *108*, 3351 – 3378; *j*) A. Fürstner, P. A. Davies, *Angew. Chem. Int. Ed.*, **2007**, *46*, 3410 – 3449; *k*) A. S. K. Hashmi, G. J. Hutchings, *Angew. Chem. Int. Ed.*, **2006**, *45*, 7896 – 7936.
[8] D. J. Gorin, F. D. Toste, *Nature*, **2007**, *446*, 395 – 403.
[9] M. N. Hopkinson, A. D. Gee, V. Gouverneur, *Chem. Eur. J.*, **2011**, *17*, 8248 – 8262.
[10] See review articles and references therein: *a*) D. R. Pye, N. P. Mankind, *Chem. Sci.*, **2017**, *8*, 1705 – 1718; *b*) M. H. Pérez-Temprano, J. A. Casares, P. Espinet, *Chem. Eur. J.*, **2012**, *18*, 1864 – 1884; *c*) J. J. Hirner, Y. Shi, S. A. Blum, *Acc. Chem. Res.*, **2011**, *44*, 603 – 613.
[11] Y. Shi, K. E. Roth, S. D. Ramgren, S. A. Blum, *J. Am. Chem. Soc.*, **2009**, *131*, 18022 – 18023.
[12] P. García-Domínguez, C. Nevado, *J. Am. Chem. Soc.*, **2016**, *138*, 3266 – 3269.
[13] S. G. Weber, D. Zahner, F. Rominger, B. F. Straub, *Chem. Commun.*, **2012**, 11325 – 11327.
[14] D.-A. Roşca, D. A. Smith, M. Bochmann, *Chem. Commun.*, **2012**, *48*, 7247 – 7249.
[15] E. Y. Tsui, P. Müller, J. P. Sadighi, *Angew. Chem. Int. Ed.*, **2008**, *47*, 8937 – 8940.
[16] For synthesis and characterization of (NHC)AuF, see *a*) D. S. Laitar, P. Müller, T. G. Gray, J. P. Sadighi, *Organometallics*, **2005**, *24*, 4503 – 4505; for reactivity studies including catalysis, see *b*) J. A. Akana, K. X. Bhattacharyya, P. Müller, J. P. Sadighi, *J. Am. Chem. Soc.*, **2007**, *129*, 7736 – 7739.
[17] J. Miró, C. del Pozo, *Chem. Rev.*, **2016**, *116*, 11924 – 11966.
[18] *a*) M. Joost, P. Gualco, S. Mallet-Ladeira, A. Amgoune, D. Bourissou, *Angew. Chem. Int. Ed.*, **2013**, *52*, 7160 – 7163; *b*) M. Joost, L. Estévez, S. Mallet-Ladeira, K. Miqueu, A. Amgoune, D. Bourissou, *J. Am. Chem. Soc.*, **2014**, *136*, 10373 – 10382.
[19] D.-A. Roşca, D. A. Smith, D. L. Hughes, M. Bochmann, *Angew. Chem. Int. Ed.*, **2012**, *51*, 10643 – 10646.
[20] D.-A. Roşca, J. Fernandez-Cestau, J. Morris, J. A. Wright, M. Bochmann, *Sci. Adv.*, **2015**, *1*, e1500761.
[21] N. Savjani, D.-A. Roşca, M. Schormann, M. Bochmann, *Angew. Chem. Int. Ed.*, **2013**, *52*, 874 – 877.
[22] E. Langseth, A. Nova, E. A. Tråseth, F. Rise, S. Øien, R. H. Heyn, M. Tilset, *J. Am. Chem. Soc.*, **2014**, *136*, 10104 – 10115.
[23] F. Rekhroukh, R. Brousses, A. Amgoune, D. Bourissou, *Angew. Chem. Int. Ed.*, **2015**, *54*, 1266 – 1269.
[24] F. H. Brain, C. S. Gibson, *J. Chem. Soc. Resumed*, **1939**, 762 – 767.
[25] M. Aresta, G. Vasapollo, *J. Organomet. Chem.*, **1973**, *50*, C51 – C53.
[26] *a*) A. Tamaki, S. A. Magennis, J. K. Kochi, *J. Am. Chem. Soc.*, **1974**, *96*, 6140 – 6148; *b*) S. Komiya, T. A. Albright, R. Hoffmann, J. K. Kochi, *J. Am. Chem. Soc.*, **1976**, *98*, 7255 – 7265; *c*) S. Komiya, J. K. Kochi, *J. Am. Chem. Soc.*, **1976**, *98*, 7599 – 7607.
[27] *a*) S. Komiya, A. Shibue, *Organometallics*, **1985**, *4*, 684 – 687; *b*) S. Komiya, S. Ozaki, A. Shibue, *J. Chem. Soc. Chem. Commun.*, **1986**, 1555 – 1556.
[28] N. P. Mankad, F. D. Toste, *Chem. Sci.*, **2012**, *3*, 72 – 76.
[29] M. S. Winston, W. J. Wolf, F. D. Toste, *J. Am. Chem. Soc.*, **2014**, *136*, 7777 – 7782.
[30] S. Lavy, J. J. Miller, M. Pažický, A.-S. Rodrigues, F. Rominger, C. Jäkel, D. Serra, N. Vinokurov, M. Limbach, *Adv. Synth. Catal.*, **2010**, *352*, 2993 – 3000.
[31] W. J. Wolf, M. S. Winston, F. D. Toste, *Nat. Chem.*, **2014**, *6*, 159 – 164.

© University of Pretoria

[32] M. Joost, P. Gualco, Y. Coppel, K. Miqueu, C. E. Kefalidis, L. Maron, A. Amgoune, D. Bourissou, *Angew. Chem. Int. Ed.,* **2014**, *53*, 747 – 751.
[33] C.-Y. Wu, T. Horibe, C. B. Jacobsen, F. D. Toste, *Nature*, **2015**, *517*, 449 – 454.
[34] J. Chu, D. Munz, R. Jazzar, M. Melaimi, G. Bertrand, *J. Am. Chem. Soc.*, **2016**, *138*, 7884 – 7887.
[35] M. N. Hopkinson, A. Tlahuext-Aca, F. Glorius, *Acc. Chem. Res.*, **2016**, *49*, 2261 – 2272.
[36] A. Tlahuext-Aca, M. N. Hopkinson, C. G. Daniliuc, F. Glorius, *Chem. Eur. J.*, **2016**, *22*, 11587 – 11592.
[37] L. Huang, F. Rominger, M. Rudolph, A. S. K. Hashmi, *Chem. Commun.*, **2016**, *52*, 6435 – 6438.
[38] E. O. Asomoza-Solís, J. Rojas-Ocampo, R. A. Toscano, S. Porcel, *Chem. Commun.,* **2016**, *52*, 7295 – 7298.
[39] P. Gualco, S. Ladeira, K. Miqueu, A. Amgoune, D. Bourissou, *Angew. Chem. Int. Ed.*, **2011**, *50*, 8320 – 8324.
[40] J. Guenther, S. Mallet-Ladeira, L. Estévez, K. Miqueu, A. Amgoune, D. Bourissou, *J. Am. Chem. Soc.*, **2014**, *136*, 1778 – 1781.
[41] M. Joost, A. Zeineddine, L. Estévez, S. Mallet-Ladeira, K. Miqueu, A. Amgoune, D. Bourissou, *J. Am. Chem. Soc.*, **2014**, *136*, 14654 – 14657.
[42] M. Joost, L. Estévez, K. Miqueu, A. Amgoune, D. Bourissou, *Angew. Chem. Int. Ed.*, **2015**, *54*, 5236 – 5240.
[43] *a*) J. Schaefer, A. Kraft, S. Reininger, G. Santiso-Quinones, D. Himmel, N. Trapp, U. Gellrich, B. Breit, I. Krossing, *Chem. Eur. J.*, **2013**, *19*, 12468 –12485; *b*) M. A. Celik, C. Dash, V. A. K. Adiraju, A. Das, M. Yousufuddin, G. Frenking, H. V. R. Dias, *Inorg. Chem.*, **2013**, *52*, 729 – 742; *c*) H. V. R. Dias, C. Dash, M. Yousufuddin, M. A. Celik, G. Frenking, *Inorg. Chem.*, 2011, *50*, 4253 – 4255; *d*) C. Dash, P. Kroll, M. Yousufuddin, H. V. R. Dias, *Chem. Commun.*, **2011**, *47*, 4478 – 4480; *e*) S. Martínez-Salvador, J. Forniés, A. Martín, B. Menjón, *Angew. Chem. Int. Ed.*, **2011**, *50*, 6571 – 6574; *f*) D. B. Dell' Amico, F. Calderazzo, *Gold Bull.*, **1997**, *30*, 21 – 24.
[44] M. Joost, L. Estévez, S. Mallet-Ladeira, K. Miqueu, A. Amgoune, D. Bourissou, *Angew. Chem. Int. Ed.*, **2014**, *53*, 14512 – 14516.
[45] H. Schmidbaur, H. G. Raubenheimer, L. Dobrzańska, *Chem. Soc. Rev.*, **2014**, *43*, 345 – 380.
[46] *a*) F. Groenewald, H. G. Raubenheimer, J. Dillen, C. Esterhuysen, *Dalton Trans*., **2017**, *46*, 4960 – 4967; *b*) F. Groenewald, J. Dillen, H. G. Raubenheimer, C. Esterhuysen, *Angew. Chem. Int. Ed.*, **2016**, *55*, 1694 – 1698.
[47] Au-complexes featuring a biarylphosphane ligand also exhibit short C(ipso)-Au contacts resembling a T-shaped geometry at gold; see for example: *a*) A.S.K. Hashmi, B. Bechem, A. Loos, M. Hamzic, F. Rominger, H. Rabaa, *Aust. J. Chem*., **2014**, *67*, 481 – 499; *b*) M. Touil, B. Bechem, A.S.K. Hashmi, B. Engels, M. A. Omary, H. J. Rabaâ, *Mol. Struct.: THEOCHEM,* **2010**, *957*, 21 – 25; *c*) D. V. Partyka, J. B. Updegraff III, M. Zeller, A. D. Hunter, T. G. Gray, *Organometallics,* **2009**, *28*, 1666 – 1674; *d*) D. V. Partyka, T. J. Robilotto, M. Zeller, A. D. Hunter, T. G. Gray, *Organometallics,* **2008**, *27*, 28 – 32; *e*) M. C. Gimeno, A. Laguna, *Chem. Rev.*, **1997**, *97*, 511 – 522.
[48] Note that Au(I) compounds bearing two phosphine ligands in nearly linear arrangement exist in which the halogen counter-anion is "bond" in a T-shape fashion based on electrostatic interaction; see for example: A.-M. Larsonneur, R. Turpin, P. Castan, G. Bernardinelli, *Inorg. Chim. Acta*, **1994**, *227*, 85 – 90.
[49] A. S. K. Hashmi, *Chem. Rev.*, **2007**, *107*, 3180 – 3211.
[50] This is in agreement with the reported donor ability of Au(I) complexes in the presence of tethered Z-ligands *a*) H. Yang, F. P. Gabbaï, *J. Am. Chem. Soc.*, **2015**, *137*, 13425 – 13432; *b*) I.-S. Ke, F. P. Gabbaï, *Inorg. Chem.*, **2013**, *52*, 7145 – 7151; *c*) P. Gualco, M. Mercy, S. Ladeira, Y. Coppel, L. Maron, A. Amgoune, D. Bourissou, *Chem. Eur. J.*, **2010**, *16*, 10808 – 10817; *d*) P. Gualco, T.-P. Lin, M. Sircoglou, M. Mercy, S. Ladeira, G. Bouhadir, L. M. Pérez, A. Amgoune, L. Maron, F. P. Gabbaï, D. Bourissou, *Angew. Chem. Int. Ed.*, **2009**, *48*, 9892 – 9895; *e*) M. Sircoglou, S. Bontemps, M. Mercy, N. Saffon, M. Takahashi, G. Bouhadir, L. Maron, D. Bourissou, *Angew. Chem. Int. Ed.*, **2007**, *46*, 8583 – 8586.
[51] N. G. Connelly, W. E. Geiger, *Chem. Rev.*, **1996**, *96*, 877 – 910.
[52] G. R. Fulmer, A. J. M. Miller, N. H. Sherden, H. E. Gottlieb, A. Nudelman, B. M. Stoltz, J. E. Bercaw, K. I. Goldberg, *Organometallics*, **2010**, *29*, 2176 – 2179.
[53] D. Steinborn, S. Becke, R. Herzog, M. Günther, R. Kircheisen, H. Stoeckli-Evans, C. Bruhn, *Z. Anorg. Allg. Chem.*, **1998**, *624*, 1303 – 1307.
[54] *a*) H. H. Murray III, J. P. Fackler Jr., D. A. Tocher, *J. Chem. Soc., Chem. Commun*., **1985**, *0*, 1278 – 1280; *b*) H. H. Murray III, J. P. Fackler Jr., A. M. Mazany, *Organometallics*, **1984**, *3*, 1310 – 1311.
[55] *a*) R. Kumar, A. Linden, C. Nevado, *J. Am. Chem. Soc.*, **2016**, *138*, 13790 – 13793; *b*) R. Kumar, A. Linden, C. Nevado, *Angew. Chem. Int. Ed.*, **2015**, *54*, 14287 – 14290.

© University of Pretoria

Chapter 6

An exploratory study towards the first yttrium triazolylidene complex

6.1 Background

Whilst ruthenium carbene complexes have prevailed in alkene metathesis reactions, catalysis involving σ-bond metathesis has been dominated by complexes substituted with hard Lewis acidic metals. This includes both *f*-block elements and early transition metals. With regards to the lanthanide *f*-block elements, their large ionic radii and hard Lewis acid character permit the activation of small molecules featuring inert bonds.[1] The mentioned reactivity, in addition to the higher abundance of the inexpensive elements compared to the late transition metals, brand lanthanides as attractive alternatives to the above-mentioned. This is one of the reasons for the steady increase in the frequency of reported lanthanide complexes, however there are still far less examples compared to their late transition metal counterparts. One of the arguments for this is the higher instability of lanthanide complexes, generally resulting in the fast decomposition of the targeted product.[1,2] Synthesis and manipulation of the organometallic lanthanide complexes are therefore not trivial, with the use of advanced inert synthetic skills a prerequisite towards the handling of the aforementioned complexes. Nonetheless, appropriate ligand design has allowed for the preparation of relatively stable lanthanide-containing complexes,[1,2,3] which have displayed very promising results in various homogeneous catalyzed reactions.[4] The catalytic reaction mechanism generally involves σ-bond metathesis and not the cornerstone two-electron processes of classical catalysts, namely oxidative addition and reductive elimination.[1,4] This paves the way towards catalytic reactions generally not accessible by transition metal catalysts.

The σ-bond metathesis reaction is the workhorse of catalyzed polymerization processes, and as such, the reaction mechanism is well-known.[1] The reaction generally proceeds through a four-centered transition state, without a change in the oxidation state of the metal (**I**, Figure 6.1). It can therefore be argued that the energy of the catalyzed reaction is lower compared to classical two-electron catalyzed

© University of Pretoria

processes. Lanthanide catalysts can also mediate substrate activation through 1,2-addition or H-atom abstraction reactions (**II**-**III**, Figure 6.1). For a 1,2-addition reaction, a metal substrate double bond is required, which coordinates to two substrate atoms, yielding an intermediate four-membered metallacycle leading to substrate activation (**II**, Figure 6.1). This route is generally considered for imido-substituted Lewis acidic metals. Hydrogen atom abstraction is commonly facilitated by a metal substituted with a hard basic donor ligand, such as an amido- or oxo-functionality, leading to homolytic bond scission with subsequent radical formation (**III**, Figure 6.1).[1] Oxidative addition across a single well-defined metal center is currently only considered for uranium complexes with low oxidation states, such as U(III) and U(IV), but examples of such reactivity has yet to be reported (**IV**, Figure 6.1).

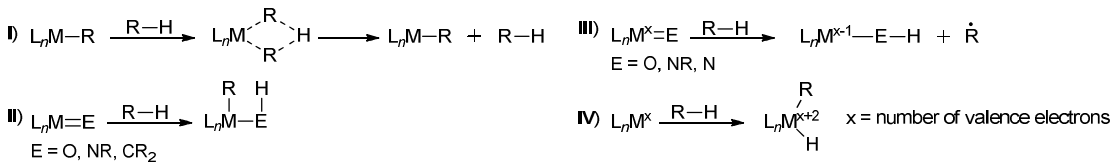

Figure 6.1: Bond activation strategies considered for lanthanide catalysts[1]

As a general rule, lanthanides form weak covalent bonds to ligands.[5] This is largely attributed to *f*-orbital contraction that is further shielded by the 5*s*-, 5*p*- and 6*s*-orbitals. Ionic metal-ligand bond formation becomes the preferred bonding scenario, yielding more stable organometallic lanthanide complexes.[5] This is one of the main reasons behind the large scale use of hard anionic oxygen and nitrogen donor ligands during lanthanide complex formation, which has also been paramount in advancing the organometallic lanthanide discipline.[3,6] Ligand design taking into account hard donor coordinating moieties will resultantly yield more stable organo-lanthanide complexes, through ionic bond formation with the hard Lewis acidic metal. It could therefore be speculated that coordination of soft basic donor ligands to lanthanides would be highly unfavourable with a small probability of complex development due to weak covalent bond formation. Since the first reported examples of lanthanide carbene complexes, the speculation has been firmly contradicted.[7] Even though the soft-hard mismatch could disfavour lanthanide carbene complex formation, the strongly donating character of the carbene ligand prevails over this shortcoming to yield a complex with a relatively stable M-$C_{Carbene}$ bond. Moreover, incorporation of additional anchoring functionalities during appropriate ligand design can coordinate and further stabilize the lanthanide carbene complex.[7,8] This has resulted in the synthesis of a range of NHC-supported lanthanide complexes exhibiting interesting reactivity patterns, with a number of these complexes being active in various catalytic reactions.

© University of Pretoria

The lanthanide carbene bonding situation has been theoretically investigated by Bourissou and co-workers.[9] There results demonstrated that the main bonding contribution arises from the carbene-to-metal σ-donation. The σ-bond was accompanied with negligible, if any, bonding contribution from π-donation of the carbene to the metal (Figure 6.2). As can be expected from the electropositive metals, no carbene π-backdonation is found. The involvement of ancillary ligand stabilization of the carbene moiety was a notable realization. With a favourable metal geometry, the ancillary ligand can donate π-electron density into the vacant carbene π-orbital (Figure 6.2).[9] This imparts increased stabilization to the carbene complex, even though the M-$C_{Carbene}$ bond length increases slightly. Substitution of a chloride with an amido ancillary ligand markedly improved the stabilization through stronger π-donation into the vacant carbene orbital (Figure 6.2).[9] Finally, both reports disclosed the formation of stronger metal-carbene bonds when employing imidazole-4-ylidene as carbene donor ligand. This is attributed to the stronger donor properties of aNHC (abnormal *N*-heterocyclic carbene) compared to their classical imidazole-2-ylidene counterparts.

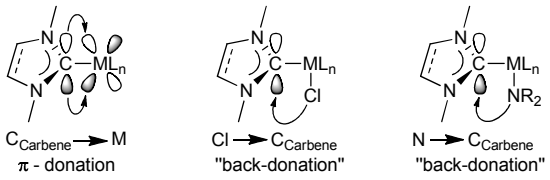

Figure 6.2: Probable secondary bonding interactions[9]

The study of lanthanide organometallic complexes is further complicated by the fact that only a handful of lanthanides are diamagnetic. Resultantly, NMR characterization cannot be used during product elucidation, leaving X-ray diffraction analysis as the only viable tool towards confirming formation of the air and moisture sensitive complexes. Yttrium is diamagnetic and cheaper than the other diamagnetic lanthanide metals, such as scandium and lutetium. These advantages render yttrium an attractive substitute during the investigation of organo-lanthanide complexes. NMR characterization is especially useful during the synthesis of yttrium-carbene complexes. Carbene coordination is unequivocally evidenced by NMR characterization of the downfield carbene resonance featuring a distinctive doublet due to coupling between the ^{89}Y and ^{13}C nuclei.

© University of Pretoria

6.1.1 Yttrium carbenes

Yttrium carbene complexes have been documented since the onset of Ln-$C_{Carbene}$ (Ln = lanthanide) complexes. The first reported example was, not surprisingly, from Arduengo and co-workers who readily coordinated a free NHC to $Y(thd)_3$ (thd = tetramethylheptanedioate) yielding the desired complex (Figure 6.3).[10] Anwander et al. later reported the facile preparation of mono- and biscarbene yttrium complexes *via* substitution of the coordinated THF molecules with the corresponding free carbenes (Figure 6.3).[11]

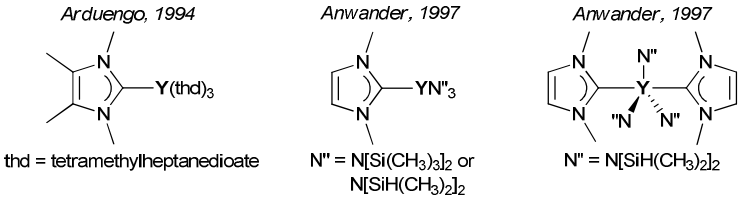

Figure 6.3: Early examples of yttrium carbene complexes

The coordination of Y(III) to tridentate pincer ligands featuring carbene moieties has been documented, but is vastly underexplored compared to the mono- and bidentate supported yttrium carbene complexes. Only a handful of examples exist, some of which are discussed in this Section (*vide infra*). However, the elegant study by the group of Arnold on the preparation and reactivity of tethered yttrium carbene complexes warrant consideration.[8] Facile preparation of the tethered yttrium carbene complexes was accomplished through transamination of $Y[N(SiMe_3)_2]_3$ with the lithium fee carbene salt (**I**, Scheme 6.1).[12] Ligand redistribution reactions are inhibited by tethering, which anchors the ligand to the metal, therefore simplifying the investigation of the reactivity of the metal carbene carbon bond.[12] As such, it was reported that the M-$C_{Carbene}$ bond can either accommodate heterolytic cleavage reactions with polar bonds or simple ligand substitution reactions with neutral donor substrates (**II**, Scheme 6.1).[13]

© University of Pretoria

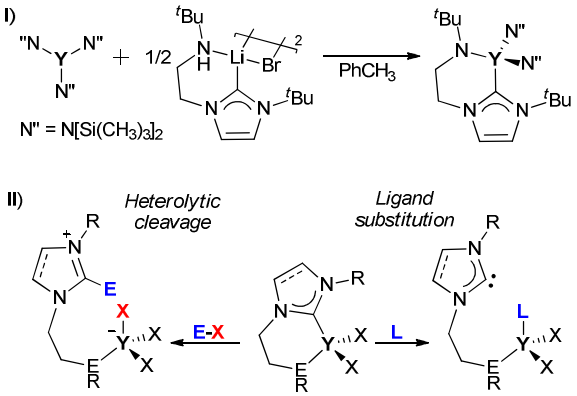

Scheme 6.1: Synthesis of **I**) amido-tethered yttrium carbene complex and the generic **II**) reactivity of the Y-$C_{Carbene}$ bond[12,13]

Substitution of the carbene ligand by neutral donor ligands was successfully demonstrated with tetramethylethylenediamine (TMEDA) and triphenylphosphine oxide;[12] as well as BH_3, CO_2, $Ph_3P{=}S$ and $[W(CO)_5(coe)]$ (coe = cyclooctene), albeit as unpublished results due to problematic complex elucidation (**I**, Scheme 6.2).[7,8] As is evident from Scheme 6.2, substitution results in complex formation with bifunctional character, exhibiting the required reactivity sites needed for a Lewis acid (lanthanide metal) and Lewis base (free carbene) catalytic reaction.[12] A different reactivity pattern is noted upon treatment of the saturated NHC yttrium complex with polar E-X (E =$SiMe_3$, PPh_2, $^nBu_3Sn$ or BBN; with X = Cl, I or N_3) (BBN = 9-borabicyclo[3.3.1]nonane) substrates (**II**, Scheme 6.2).[14] The polar substrates readily inserted across the M-$C_{Carbene}$ bond, yielding the substituted cationic NHC fragment and an anodic metal center. The insertion reactions were also proven to be reversible. This non-innocent ligand can therefore react with a substrate and initiate a catalytic reaction across a redox neutral complex, as was the case for the catalysts discussed in chapters 3 and 4.

© University of Pretoria

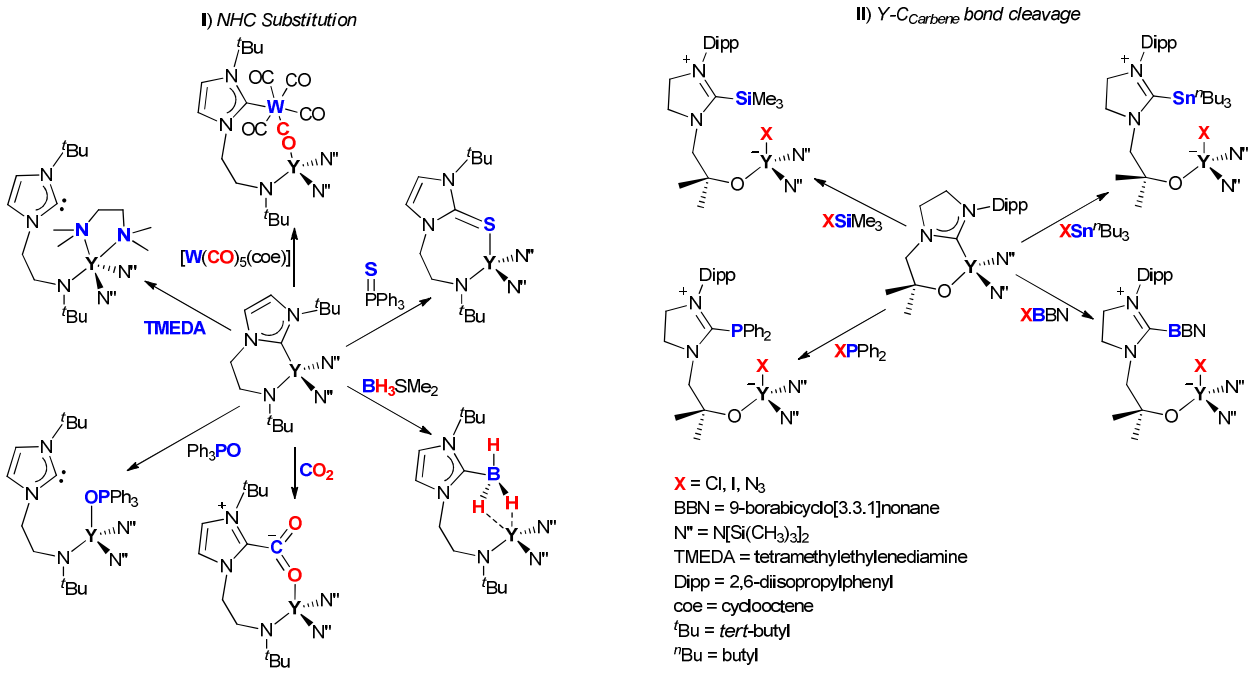

Scheme 6.2: Y-$C_{Carbene}$ bond reactivity towards **I**) neutral and **II**) polar substrates[7,8,12,14]

Yttrium pincer complex formation is in most cases accompanied with at least one hard X-donor ligand to anchor the ligand and allow for coordination of the carbene moiety/moieties. This was illustrated first by Arnold et al. who reacted the anionic CNC-pincer free carbene ligand with $Y[N(SiMe_3)_2]_3$ in a transamination reaction, yielding the yttrium biscarbene complex (Scheme 6.3).[15] Various characterization techniques confirmed yttrium carbene complex formation, including ^{13}C NMR analysis depicting the carbene signal as a doublet resonating at $\delta_{Ccarbene}$ 194.3 ppm (J_{YC} = 48 Hz). Catalysis with the yttrium biscarbene complex was not reported. Additionally, the yttrium pincer product was treated with stoichiometric amounts of triphenylphosphine oxide resulting in decomposition of the carbene complex.[15]

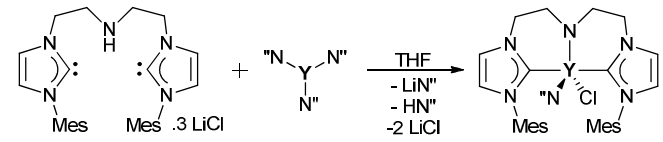

N" = N[Si(CH3)3]2
Mes = 2,4,6-trimethylphenyl

Scheme 6.3: Anionic CNC-yttrium pincer complex formation[15]

The group of Cui reported a range of CCC-pincer supported lanthanide complexes.[16] The meridional yttrium biscarbene product was one of the complexes amongst the range of products reported. The

© University of Pretoria

targeted pincer yttrium bis(NHC) complex was obtained through a one-pot deprotonation and metallation reaction of the ligand with YCl_3 (Scheme 6.4).[16] The product was isolated in moderate yields, contrasting with the complex isolated by Arnold in low yields (see Scheme 6.3 above). Again, the diamagnetic nature of yttrium allowed for the NMR spectroscopic characterization of the carbene carbon (Scheme 6.4), which resonated at $\delta_{Ccarbene}$ 192.4 ppm (no doublet reported).[16] The complex mediated the isoprene polymerization catalyzed reaction, with moderate catalytic activity at 25 °C and excellent selectivity for the *cis*-1,4 isomer (> 99%).

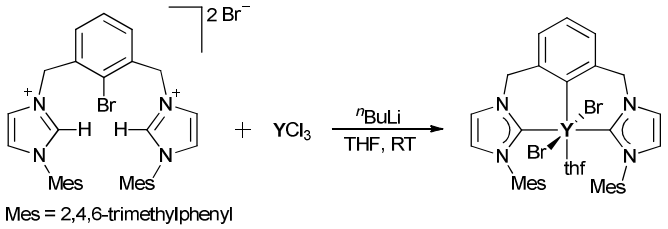

Mes = 2,4,6-trimethylphenyl

Scheme 6.4: CCC-tridentate coordination to Y(III)[16]

The addition reaction of the terminal alkyne C-H bond across carbodiimides was catalyzed, at room temperature, by an yttrium biscarbene complex supported by an anionic CNC-tridentate ligand.[17] Various ligand-to-metal complexation procedures were attempted, and found to be ineffective towards the preparation of the targeted pincer complex. It was only when the ligand precursor salt was reacted with five equivalents of $NaN[Si(CH_3)_3]_2$ in THF, followed by the addition of one equivalent YCl_3, that the targeted product could be isolated (Scheme 6.5). After purification *via* crystallization, the complex was isolated with only a 20% yield. Product formation was validated by a range of complex characterization techniques, including ^{13}C NMR analysis which revealed the carbene carbon signals, resonating at $\delta_{Ccarbene}$ 192.0 and 192.5 ppm.[17] The complex catalyzed the aforementioned reaction with a high catalytic activity, constituting the first example of such a reaction being catalyzed by an organo-rare earth metal complex.

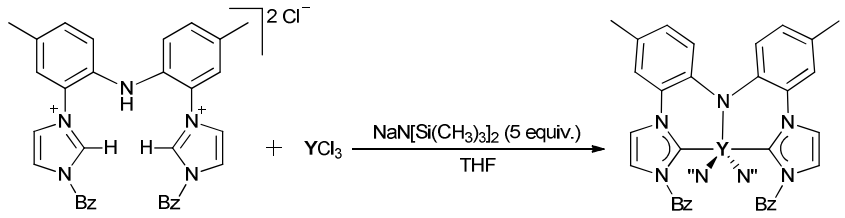

N" = $N[Si(CH_3)_3]_2$
Bz = benzyl

Scheme 6.5: Yttrium biscarbene amido complex formation[17]

© University of Pretoria

6.1.2 Lanthanides for efficient catalysis

It is not surprising that organo-lanthanide complexes have been cemented as prominent homogeneous catalysts.[4] The high reactivity of the lanthanide organometallic complexes readily promotes the hydroamination and hydrophosphination catalyzed reactions, in addition to hydrogenation, hydroboration, hydrothiolation and hydrosilylation of olefins, as well as various polymerization catalyzed processes. In most cases, the catalyzed processes involve activation of inert bonds across the reactive lanthanide-alkyl bonds. The atom-economical reactions can selectively be catalyzed by the organo-lanthanide complexes with appropriate ligand design and choice of reaction conditions, in some cases requiring the addition of co-catalysts and additives to further enhance the selectivity outcome. The air and moisture sensitive organo-lanthanide complexes are generally highly susceptible to oxygen, limiting catalytic substrate scope in addition to the choice of solvent, with ether solvents generally not used for fear of oxygen-alkyl bond cleavage leading to catalyst poisoning. Nevertheless, glovebox and Schlenk-line techniques, and the use of alkane or no solvents (during neat catalyzed reactions) have permitted the investigation of these highly reactive catalysts, with some catalysts displaying exceptional catalytic activity and selectivity (*vide supra*).

The well-known polymerization reaction is catalyzed by organo-lanthanides following the general mechanism encountered for early transition metal catalysts. This involves formation of the active catalyst, coordination of the olefin substrate, insertion across the reactive metal-ligand bond which is followed by coordination of another substrate olefin to the vacant site left after the insertion process. The hydroelementation reaction of polar E-H bonds (E = NH, PH, PR, SR) also follows a similar reaction mechanism.[4] Scheme 6.6 depicts the general mechanism of the hydroelementation reaction of olefins (in particular, the mechanism illustrates the hydroelementation of a double bond, but unsaturated alkyne substrates can also be catalyzed *via* the same reaction mechanism). The presence of reactive metal-alkyl or metal-amido ancillary ligands significantly affects the catalytic activity, with the catalyzed reaction being initiated *via* exothermic σ-bond metathesis of the incoming polar substrate with the aforementioned ligand (**i**, Scheme 6.6). This yields the active catalyst that can subsequently coordinate the olefinic substrate (**ii**, Scheme 6.6). The product is formed and the active catalyst regenerated after bond rearrangement (**iii**, Scheme 6.6) and metal-alkyl protonolysis by an additional polar substrate (**iv**, Scheme 6.6).[4] The saturated product is obtained if the olefinic substrate employed features a double bond, while the use of alkyne substituted substrates yields the corresponding alkene product. As is evident from the hydroelementation reaction mechanism, the catalyzed process does not involve

© University of Pretoria

oxidative addition and reductive elimination across the metal center, contrasting to the transition metal catalyzed processes discussed in chapter 4.

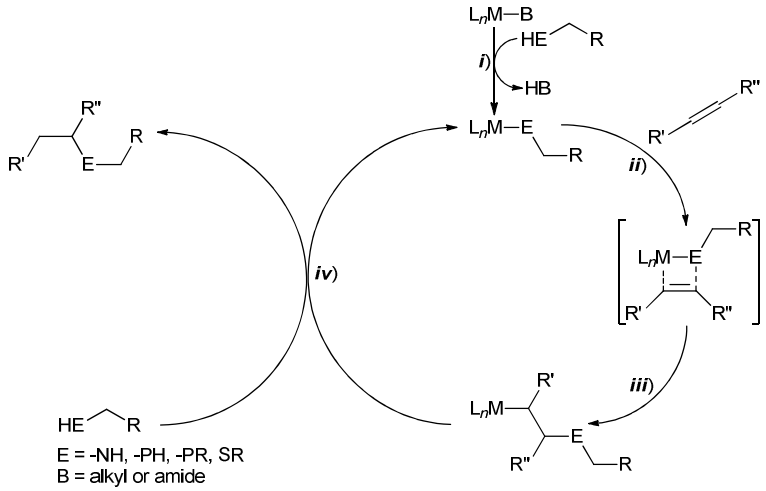

Scheme 6.6: Lanthanide-catalyzed hydroelementation reaction of olefins with polar E-H bonds (E = NH, Ph, PR, S,)

A few recent examples of organo-lanthanide catalyzed hydrophosphination reactions are worth mentioning. In an ongoing investigation of lanthanide complexes for various catalytic applications such as the hydrophosphination process,[18] the group of Trifonov developed a multidentate ligand which was coordinated to an ytterbium metal (**I**, Scheme 6.7).[19] The ytterbium catalyst demonstrated excellent catalytic activity and near to complete selectivity for the anti-Markovnikov isomer during the hydrophosphination reaction of phenylphosphine with styrene. A styrene phenylphosphine substrate ratio of 1:1 lead to the formation of the secondary phosphine, accompanied with formation of a small amount of tertiary phosphine. A 2:1 ratio of styrene to phenylphosphine was catalyzed by the ytterbium complex yielding the tertiary phosphine quantitatively and selectively. The ability of the catalyst to add styrene in a step-wise controlled mode was exploited for the preparation of unsymmetrical tertiary phosphines.[19] Hydrophosphination of styrene with phenylphosphine yielded the targeted secondary phosphine, which was further reacted with a non-equivalent styrene derivative to generate the unsymmetrical tertiary phosphine (**II**, Scheme 6.7). This route allows for the selective preparation of unsymmetrical tertiary phosphines, which can be extremely useful in organic chemistry as well as organometallic chemistry where novel phosphine ligands are required for coordination and subsequent formation of a desired organometallic complex.

© University of Pretoria

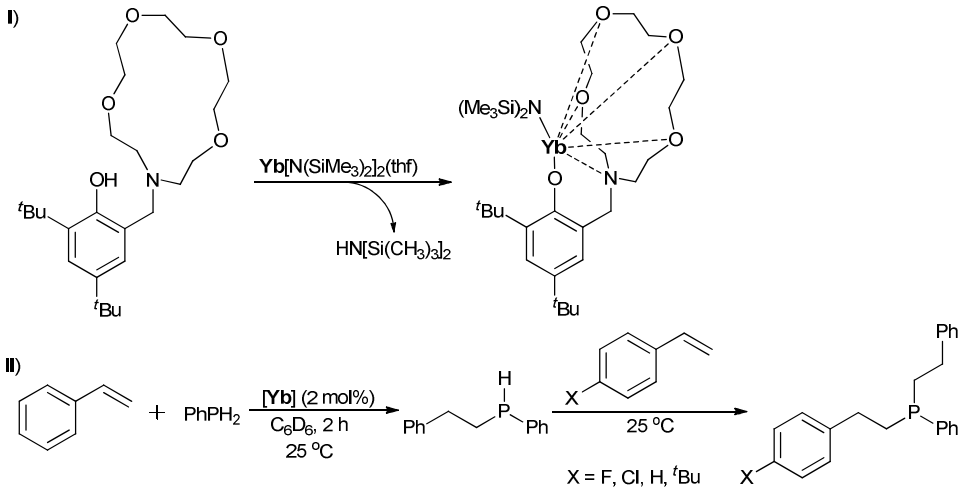

Scheme 6.7: Ytterbium-catalyzed stepwise hydrophosphination of phenylphosphine with styrene derivatives[19]

Another seminal report with regards to the hydrophosphination catalyzed reaction, described the synthesis of an NHC-supported ytterbium complex for catalytic phosphination endeavors.[20] Substitution of two coordinated THF molecules for two NHC ligands ensued readily at room temperature (**I**, Scheme 6.8). The tetramethyl substituted NHC (IMe_4) ligand metal complex was reacted with two equivalents of diphenylphosphine yielding the first example of an NHC-lanthanide phosphide complex (**II**, Scheme 6.8). It was proposed that the complex had formed through a ligand redistribution reaction of the intermediate biscarbene complex to yield the isolated triscarbene product (**II**, Scheme 6.8). The $(IMe_4)_2Yb[N(SiMe_3)_2]_2$ complex demonstrated a high catalytic activity during the hydrophosphination catalyzed reaction, with exclusive formation of the anti-Markovnikov isomer. More surprising was the high functional group tolerance displayed by the catalyst during the catalysis of various styrene derivatives, which included ether-substituted styrenic substrates. The authors attributed the high functional group tolerance to the strongly donating NHC ligand that, upon coordination to the metal, renders the lanthanide ion less acidic and therefore more inert towards various functional groups such as oxygen-containing ether functionalities.[20] In addition to the high functional group tolerance, the catalyst also mediated the hydrophosphination of diphenylphosphine with terminal alkynes, *gem*-alkenes and even isoprene. The most prominent feature of the catalyst however, is the fact that it is easily recyclable. After four cycles (catalysis and recovery represents one cycle), the complex's catalytic activity had only slightly decreased from 98% to 95% conversion. A plausible reaction mechanism was elucidated from stoichiometric reactions and kinetic studies (**III**, Scheme 6.8). Reaction of the amido ligands with diphenylphosphine generates the active catalyst. Olefin insertion occurs across the Yb-PPh_2 bond leading to the formation of a reactive metal-carbon bond that readily reacts with another

© University of Pretoria

diphenylphosphine substrate, yielding the targeted phosphine product and regenerating the active catalyst. Upon total consumption of the diphenylphosphine substrate, the reactive Yb-C bond is cleaved by residual $HN[Si(CH_3)_3]_2$, forming the tertiary phosphine product and the starting pre-catalyst.[20] This report again demonstrates the prominent role played by carbene ligands within the realm of homogeneous catalysis, where the NHC ligand not only stabilizes the lanthanide catalyst towards a range of functional groups, but also alters the properties of the aforementioned complex to allow for catalyst regeneration.

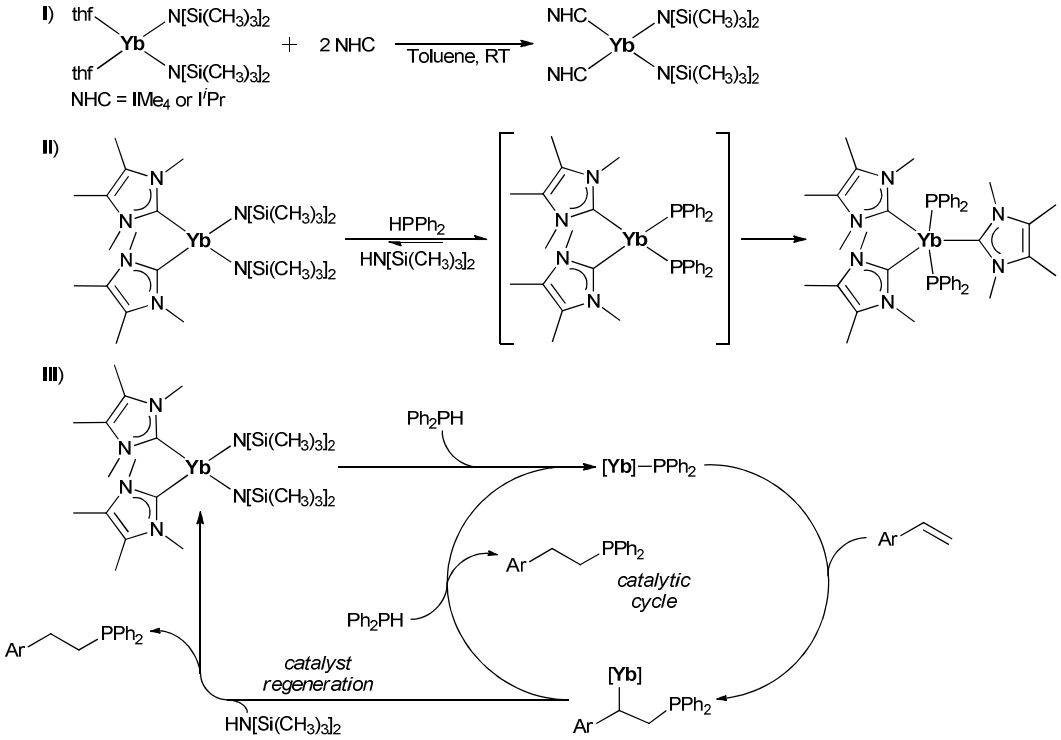

Scheme 6.8: Preparation of biscarbene ytterbium complex for the catalyzed hydrophosphination of styrene[20]

6.2 Aim

Developing our understanding of organo-lanthanide complexes is warranted, as this would shed light on the rich and elegant chemistry hiding behind those large lanthanide orbitals. In particular, the possibility of combining lanthanides with our continued interest in CNC-pincer triazolylidene ligands, piqued our curiosity in exploring various routes towards synthesizing the first example of a triazolylidene-supported lanthanide complex. The properties and reactivity of such a hypothesized complex could be markedly different from that of NHC supported lanthanide complexes. For instance, triazolylidenes form stronger bonds with lanthanides compared to their NHC counterparts. This would decrease the tendency of

© University of Pretoria

carbene substitution. If the (*trz*)Ln complex is found to be catalytically active, the stronger metal carbene bond would be more resistant towards substitution by the added substrate, leading to increased functional group tolerance as well as catalytic applications.

For this study, we directed our attention to yttrium as the choice of lanthanide metal to be used. It can be proposed that coordination of the ligands generated from $\mathbf{L_a}$ and/or $\mathbf{L_b}$ could be favoured by anchoring the yttrium metal to the ligand through an anionic bond with the amido moiety. The carbene carbons can then coordinate to the metal, *via* formation of covalent bonds stronger than the NHC lanthanide bonds. Complex formation could then be confirmed through both NMR and XRD characterization techniques.

With an yttrium triazolylidene complex in hand, a range of catalytic reactions can be scrutinized against the synthesized product. Specifically, the isoprene polymerization and olefin hydrophosphination catalyzed reactions are envisaged. If the olefin functionalization reaction proves successful, other catalytic reactions such as the hydroamination and hydrosilylation of olefins could also be attempted.

6.3 Results and Discussion

The route towards the first example of an yttrium triazolylidene complex started through the one-pot deprotonation and metallation reaction of the ligand salt $\mathbf{L_a}$. Deprotonation of $\mathbf{L_a}$ with five equivalents of KHMDS or (trimethylsilyl)methyllithium followed by metallation with YCl_3 or $YCl_3(thf)_n$ (n = 2 or 3) did not yield the desired complex, only the mono-deprotonated ligand salt $\mathbf{1_a}$. It was proposed that a salt elimination reaction between the corresponding free carbene lithium adduct and the yttrium chloride precursor would be a cleaner reaction with a higher probability of product formation. For this, the lithium salt of $\mathbf{L_a}$ first had to be isolated. As such, the ligand salt $\mathbf{L_a}$ was reacted with five equivalents of ^{n}BuLi, (trimethylsilyl)methyllithium or lithium diisopropylamide (LDA) in either toluene or benzene (Scheme 6.9). It was determined that the reaction of $\mathbf{L_a}$ with LDA in benzene yielded the targeted product with the highest purity after work-up, compared with the other bases or solvent systems employed.

© University of Pretoria

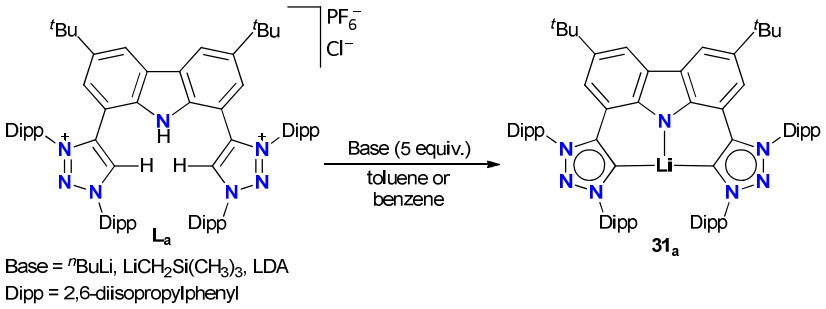

Scheme 6.9: Synthesis of lithium free carbene adduct **31a**

The ^{1}H NMR spectrum confirms deprotonation of all three acidic protons (Figure 6.4). The carbene carbon resonance was not detected in the ^{13}C NMR spectrum (Figure 6.5), but ^{7}Li NMR analysis (insert, Figure 6.5) indicates lithium coordination (δ_{Li} = 4.94 ppm).

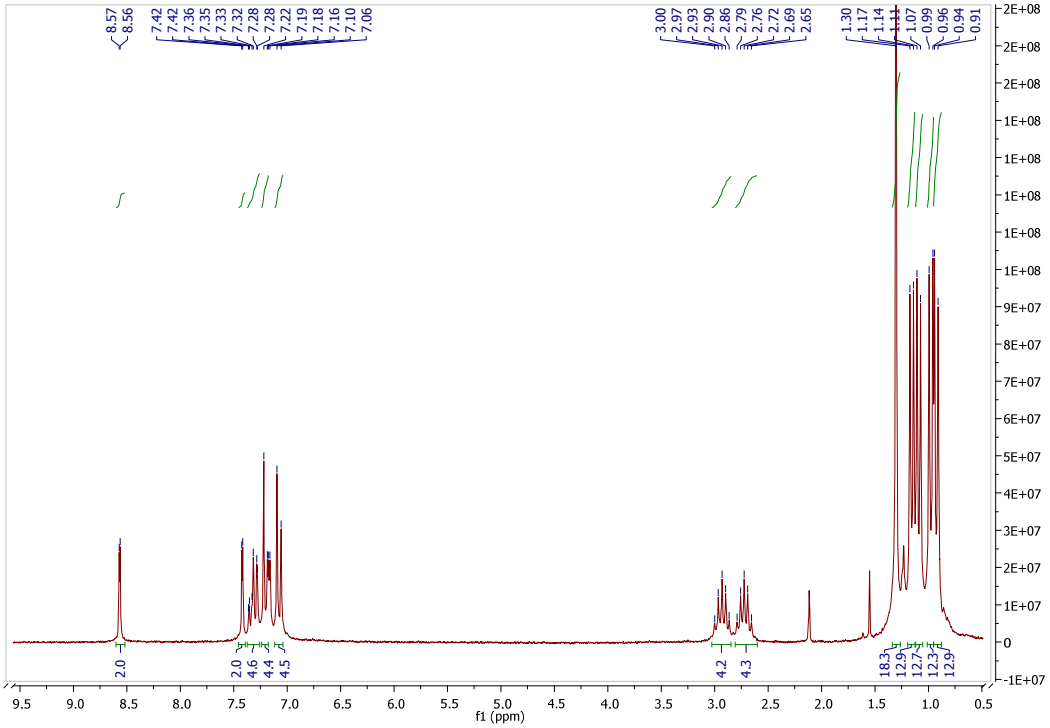

Figure 6.4: ^{1}H NMR spectrum of (CNC$_{Dipp}$)Li salt **31a** in solvent C_6D_6

© University of Pretoria

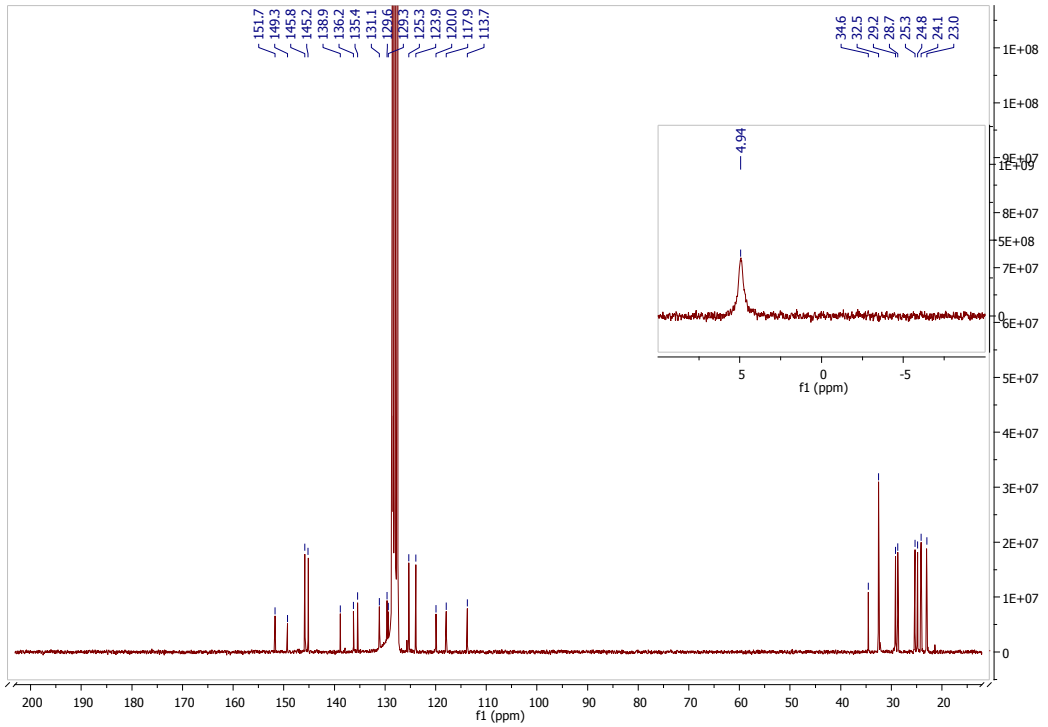

Figure 6.5: ^{13}C and ^{7}Li (insert) NMR spectra of (CNC_{Dipp})Li salt **31$_a$** in solvent C_6D_6

The salt elimination reaction between the lithium adduct **31$_a$** and an yttrium(III) chloride precursor could now be investigated. Treatment of **31$_a$** with YCl_3 in either THF, Et_2O or benzene only lead to the isolation of decomposition products. However, substitution of YCl_3 with the more reactive $YCl_3(thf)_n$ (n= 2 or 3) precursor displayed promising results during the NMR scale salt elimination reaction in C_6D_6 (Scheme 6.10). From both the ^{1}H (Figure 6.6) and ^{7}Li NMR (insert, Figure 6.6) spectra, it could be speculated that the postulated complex **32$_a$** had formed, while the ^{13}C NMR spectra was inconclusive. The reaction was also attempted under preparative conditions in benzene, with the accompanying colour change from lime green to orange. Again, decomposition products were isolated during product purification procedures, even when working under strictly inert conditions.

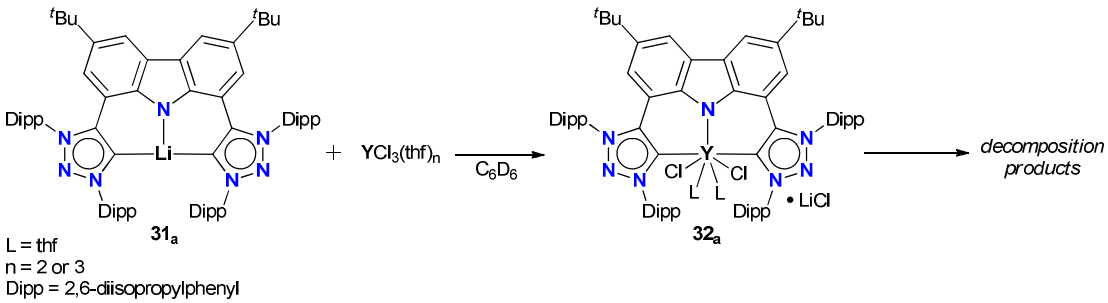

Scheme 6.10: Speculated complex formation *via* salt elimination reaction

© University of Pretoria

The aromatic carbazole C**H** proton of **32$_a$** resonates upfield at δ_H 8.42 ppm (Figure 6.6) compared to the corresponding aromatic proton of **31$_a$**, with a resonance of δ_H 8.57 ppm (Figure 6.4). More important is the detection of a lithium resonance, as precipitation of the inorganic LiCl salt would have resulted to an NMR silent spectrum. The ^{7}Li NMR spectrum (insert, Figure 6.6) further validates that a reaction had occurred, with the lithium resonance of **32$_a$** (δ_{Li} 0.70 ppm) upfield from that of the lithium salt **31$_a$** (δ_{Li} 4.94 ppm). This could point towards the formation of a complex intermediate with coordinated LiCl, that collapses back to YCl_3 and various decomposition products upon attempted purification of the product (*vide infra*). Unfortunately, no crystals suitable for X-ray diffraction analysis could be obtained.

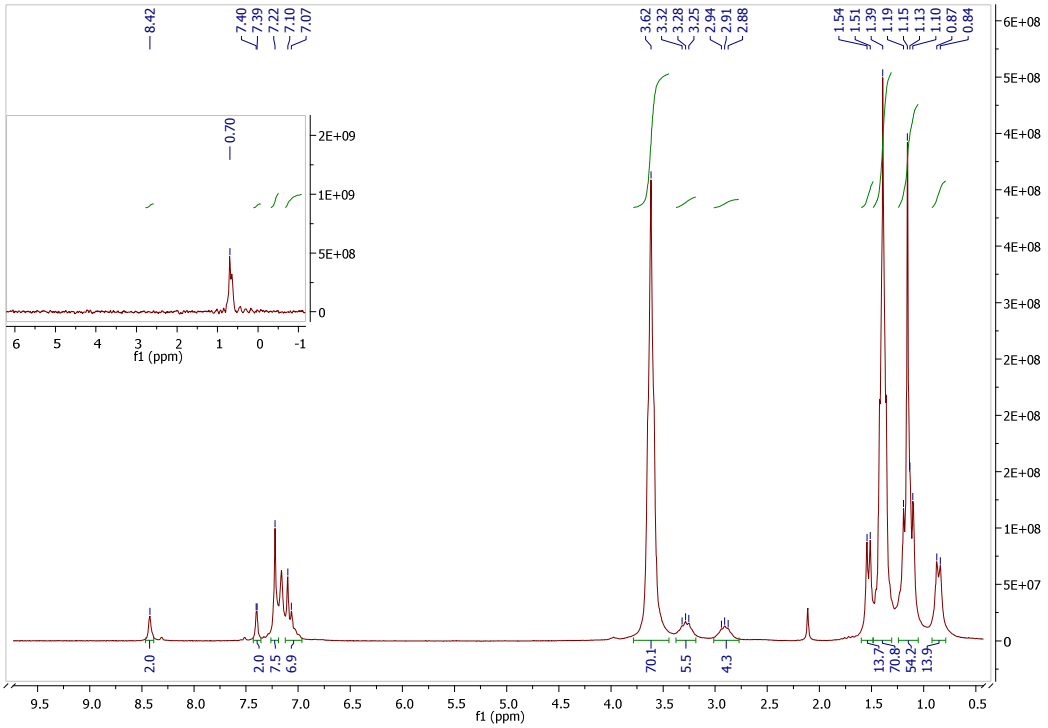

Figure 6.6: ^{1}H and ^{7}Li (insert) spectra of salt elimination reaction between **31$_a$** and $YCl_3(thf)_n$ in solvent C_6D_6

The results obtained prompted the question: could the increased steric bulk of **L$_a$** be a contributing factor in the decrease of the complex stability observed after metallation of **31$_a$** with an yttrium metal precursor? As such, the ligand was changed to the less sterically demanding ligand salt **L$_b$**. Based on the results obtained from the reactions of **L$_a$**, one-pot deprotonation and metallation reactions were not attempted. Instead, deprotonation of **L$_b$** with LDA in benzene yielded the precursor lithium adduct **33$_b$** for the salt elimination reaction with various yttrium chloride metal precursors (Scheme 6.11).

© University of Pretoria

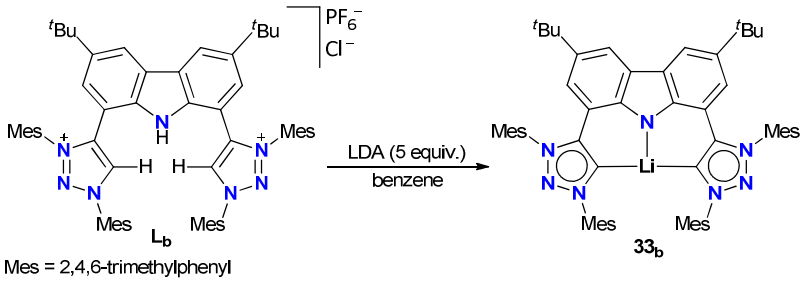

Scheme 6.11: Synthetic protocol towards **33b**

The ^{1}H (Figure 6.7), ^{13}C (Figure 6.8) and ^{7}Li (insert, Figure 6.8) NMR spectra confirms deprotonation of all three acidic protons and Li-$C_{Carbene}$ bond formation. The carbene carbon resonance was not detected during the ^{13}C NMR experiment, but the resonance of the lithium counterion is similar to that of **31a**, verifying the coordination of the carbene carbon to the lithium ion.

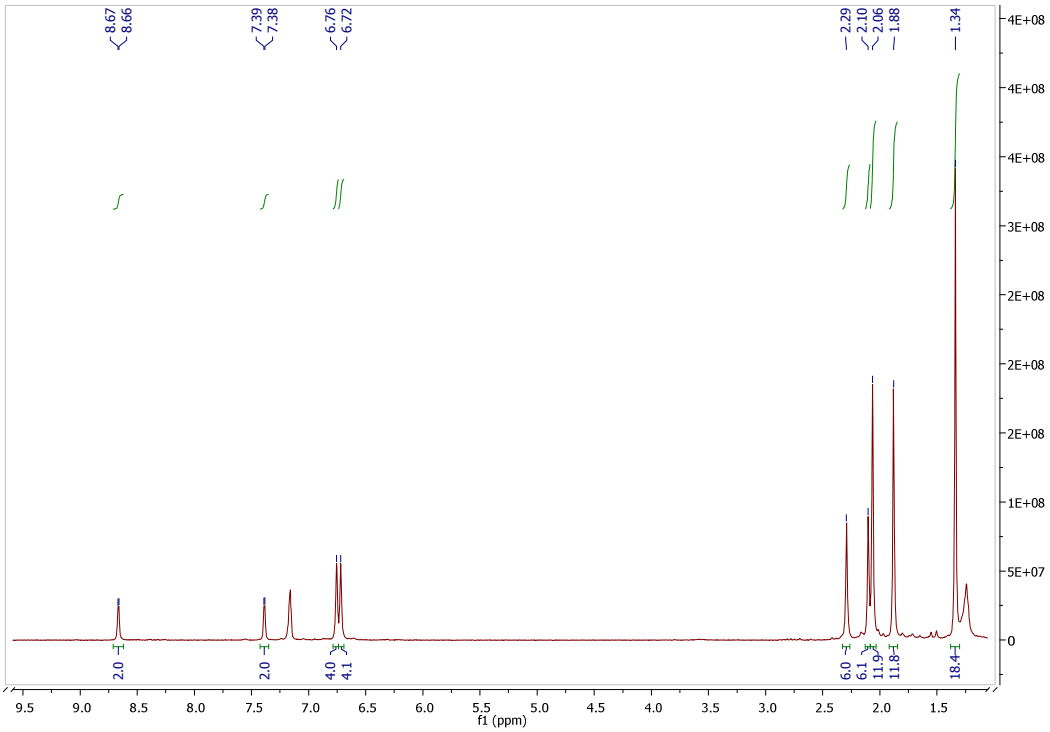

Figure 6.7: ^{1}H NMR spectrum of **33b** in solvent C_6D_6

© University of Pretoria

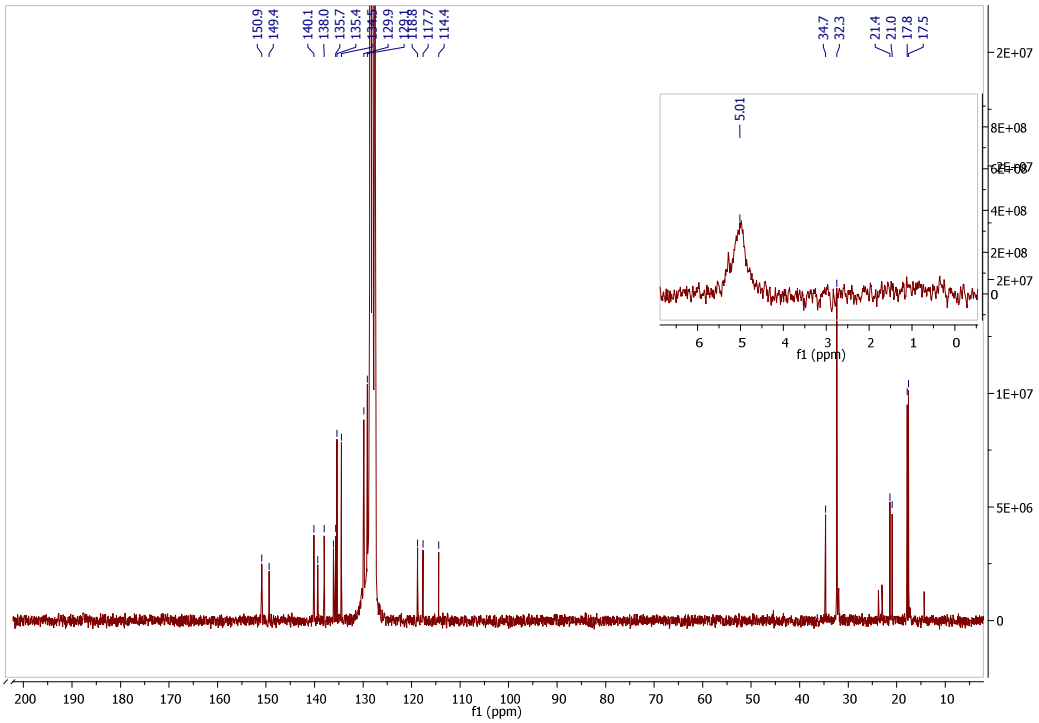

Figure 6.8: ^{13}C and ^{7}Li (insert) NMR spectra of **33$_b$** in solvent C_6D_6

With the lithium salt **33$_b$** in hand, the salt metathesis reactions with yttrium(III) chloride precursors ensued. As was the case for **31$_a$**, the reaction of **33$_b$** with YCl_3 in benzene was unsuccessful. It was determined, *via* NMR analysis, that only a small amount of product had formed initially, but quickly resulted in decomposition yielding various impurities, one of which being the mono-deprotonated salt. Fortunately, changing the yttrium precursor from YCl_3 to $YCl_3(thf)_n$ (n = 2 or 3) in C_6D_6 resulted in the formation of the proposed product, as was determined through NMR analysis of the NMR scale reaction (Scheme 6.12). The reaction was also accompanied with a colour change from lime green to orange. The ^{1}H and ^{7}Li (insert) NMR spectra are depicted in Figure 6.9. Again, no viable ^{13}C NMR spectrum could be obtained. However, the proton chemical shifts (aromatic C**H** proton of the carbazole backbone of **32$_b$** resonate upfield with 0.2 ppm compared to **34$_b$**) point towards yttrium coordination, while the lithium chemical resonance of **34$_b$** (δ_{Li} = 0.34 ppm) is upfield from the ^{7}Li chemical shift of **33$_b$** (δ_{Li} 5.01 ppm) and similar to that of **32$_a$**. Attempts at synthesizing and purifying the complex under preparative conditions were met with complex decomposition and the proposed product **34$_b$** could not be isolated.

© University of Pretoria

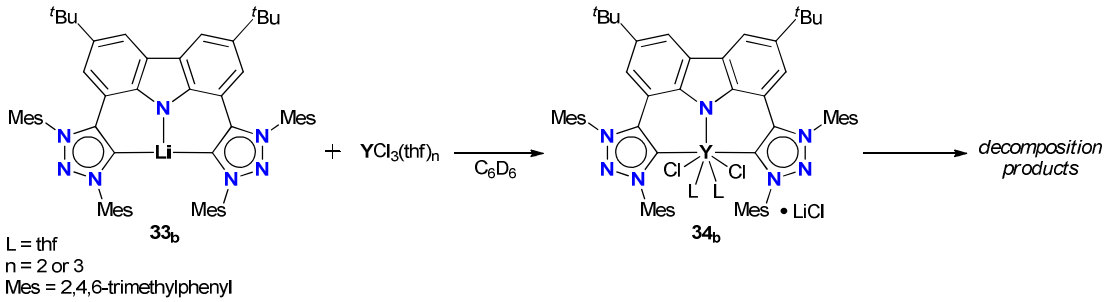

Scheme 6.12: Salt metathesis reaction between **33b** and $YCl_3(thf)_n$ yielding **34b**

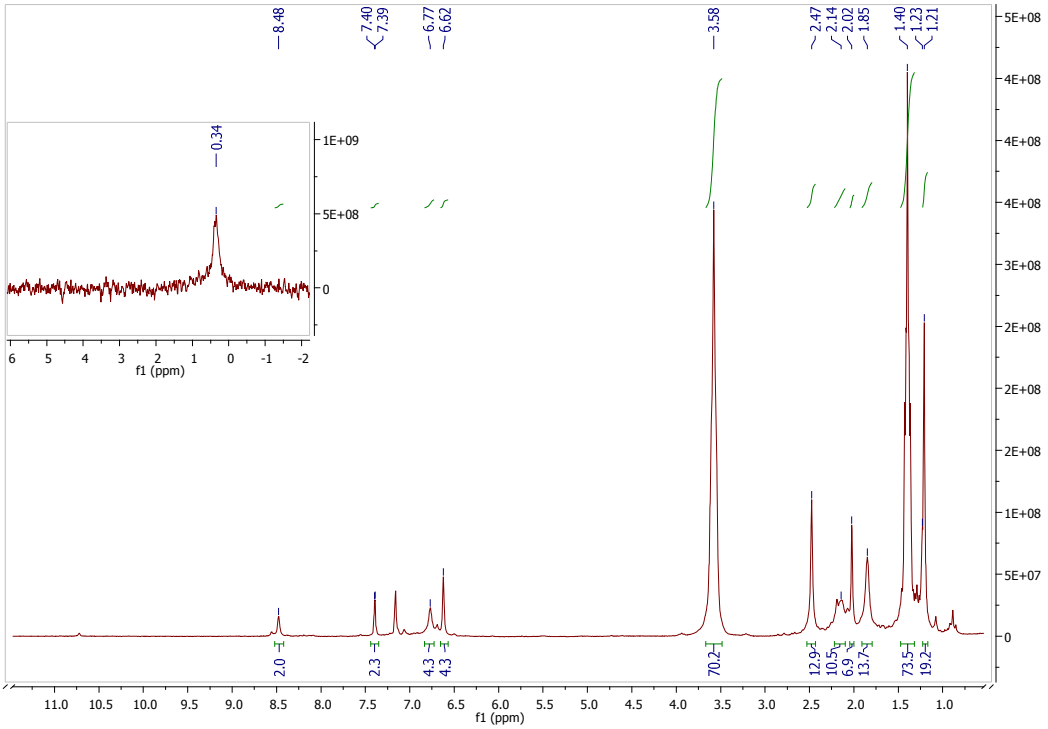

Figure 6.9: ^{1}H and ^{7}Li NMR spectra of postulated complex **34b** in solvent C_6D_6

The observations up to this point suggested that either steric factors or the choice of yttrium metal precursor greatly affect the outcome of the reaction. The YCl_3 metal is unreactive, while the $YCl_3(thf)_n$ precursor yields a complex too reactive to isolate under preparative conditions. This could be due to *1*) the harsh Lewis acidic character of the yttrium chloride metal that does not form a stable bond with the soft Lewis basic carbenes; *2*) or simply inadequate stabilization imparted by the ligand on the reactive metal center. These factors either inhibit product formation or yield a reactive complex that decomposes during manipulation of the aforementioned complex, even under strict inert conditions. It was therefore proposed to change the yttrium reagent to a 'softer' metal precursor and react it with the lithium salt of the sterically less demanding ligand **Lb**. As such, the yttrium bisalkyl chloride precursor

© University of Pretoria

was synthesized through an adapted procedure as reported by Okuda et al.[21] A slurry of YCl_3 in THF was reacted with two equivalents of (trimethylsilyl)methyllithium, to yield the targeted product after solvent evaporation and crystallization from hexane (Scheme 6.13).

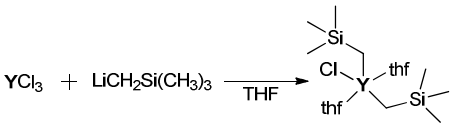

Scheme 6.13: Synthesis of $[YCl(CH_2SiMe_3)_2(thf)_2]$

The reaction between the synthesized yttrium bisalkyl chloride precursor and the lithium salt **33b** was first attempted in an NMR tube. Therefore, an NMR vessel was loaded with **33b** and $[YCl(CH_2SiMe_3)_2(thf)_2]$ under negative pressure, followed by the addition of C_6D_6 that was accompanied with an immediate colour change from lime green to dark red-brown, in addition to the precipitation of a small amount of white solid (Scheme 6.14). The reaction could also be repeated under preparative conditions, and to our delight, allowed for the isolation of the product as a brown solid stable indefinitely under strict inert conditions.

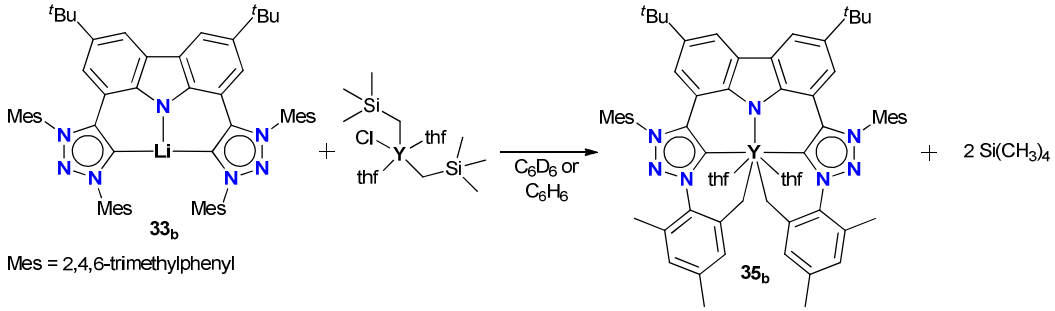

Scheme 6.14: Salt elimination reaction towards preparation of a stable yttrium triazolylidene complex **35b**

The ^1H and ^{13}C NMR spectra of the reaction depicted in Scheme 6.14, are given in Figure 6.10 and Figure 6.11, respectively. It can be deduced from the ^1H NMR spectrum (Figure 6.10) that the reaction portrayed in Scheme 6.14 is complete, as the lithium salt **33b** has been consumed (complete disappearance of carbazole C**H** signal at δ_H 8.67 ppm) while the $Si(CH_3)_4$ resonance (analogous to free and not coordinated tetramethylsilane) integrates to 24 hydrogens, corresponding to protonation of both yttrium (trimethylsilyl)methyl moieties. As is also evident from the proton spectrum of **35b**, the resonance of the methyl moieties substituted on the 2,4,6-trimethylphenyl wingtip groups integrates to 34 hydrogens, and not the expected 36. The benzylic protons resonate as a broad singlet at δ_H 2.32 ppm with an integration of 4. No lithium ion was detected in the ^7Li NMR spectrum, confirming LiCl

© University of Pretoria

precipitation. The ^{13}C NMR spectrum (Figure 6.11) unequivocally validates Y-$C_{Carbene}$ bond formation. The carbene doublet has a resonance of $\delta_{Ccarbene}$ 182.6 ppm, with an ^{89}Y-^{13}C coupling constant of 35.8 Hz. These values fall within the range reported for yttrium carbene complexes.[15,16,17] Formation of the Y-CH_2 bonds are supported by the carbon doublet at δ_C 50.5 ppm, the value of which is commonly encountered for yttrium benzylic bonds (*vide infra*). The ^{89}Y-^{13}C coupling constant for the benzylic protons is 19.4 Hz. The NMR spectra of the reaction performed under preparative conditions was different only in the disappearance of the $Si(CH_3)_4$ signal, as a result of *in vacuo* evaporation of the solvent. Unfortunately, crystals suitable for X-ray diffraction analysis could not be obtained, even after attempting various crystallization techniques with different solvent systems. Also, due to the extreme sensitivity of complex **35$_b$** towards air and moisture, mass spectrometric or infrared spectroscopic characterization techniques were not possible.

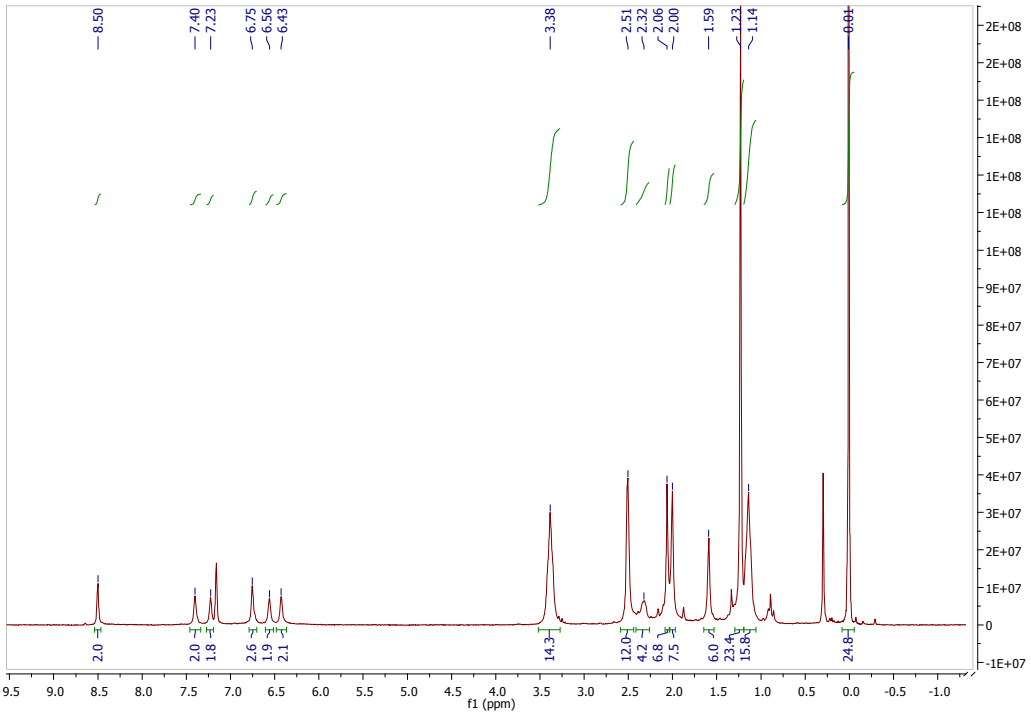

Figure 6.10: ^1H NMR spectrum of **35$_b$** in solvent C_6D_6

© University of Pretoria

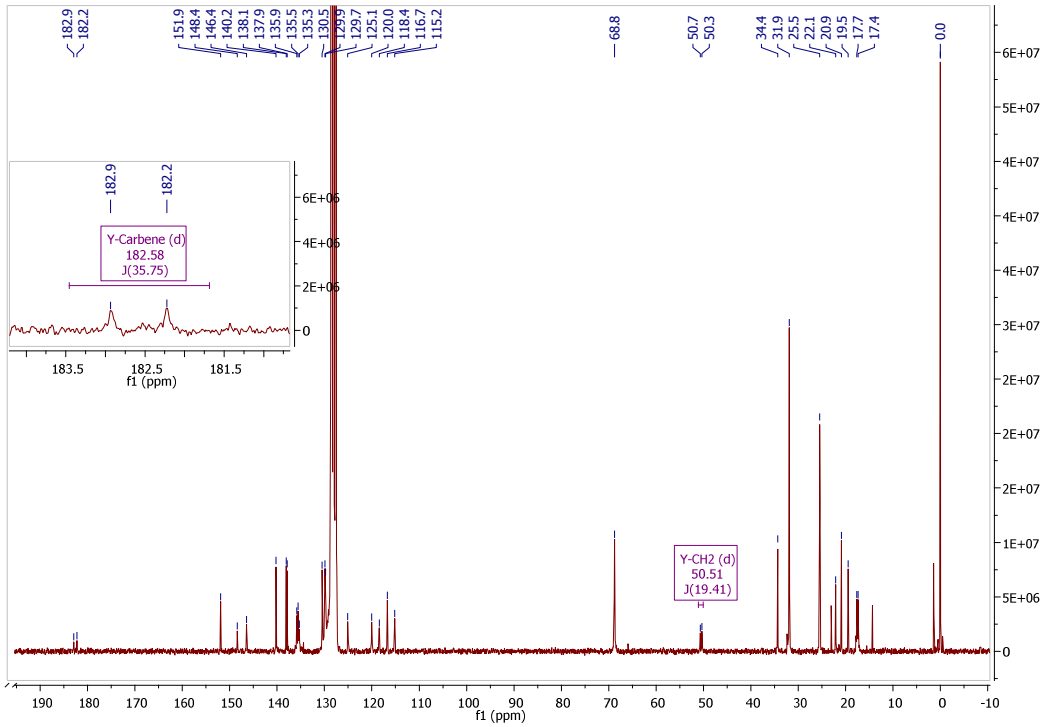

Figure 6.11: ^{13}C NMR spectrum of **35b** (insert displays carbene carbon doublet) in solvent C_6D_6

Intramolecular C-H bond activation is not a new concept, especially in the area of lanthanide chemistry where reactive ancillary ligands are frequently encountered.[22] These reactive alkyl or hydrido ligands react with the ligand backbone, with elimination of a free molecule (usually hydrogen or alkane) and formation of a cyclometallated complex. The product formed is thermodynamically favoured, lowering the energy and yielding a more stable and robust complex. A recent example of an unexpected cyclometallation reaction through C-H bond activation involved an yttrium complex coordinated by an NHC ligand, also featuring 2,4,6-trimethylphenyl wingtip substituents on the nitrogens.[23] Metallation of the NHC ligand with an yttrium trisalkyl precursor resulted in C-H bond activation of the methyl moiety substituted on the wingtip group (Scheme 6.15). A new metal carbon bond had formed, in addition to carbene carbon coordination to the yttrium metal. Evidence for the formation of the Y-CH_2 methylene bond was unequivocally provided by NMR and X-ray characterization methods. The ^{13}C NMR spectra depicted the Y-CH_2 carbon as a doublet resonating at δ_C 46.2 ppm with a coupling constant of J_{YCH_2} 17.3 Hz. The carbene carbon resonance was also detected, resonating at $\delta_{Ccarbene}$ 194.0 ppm and featuring a coupling constant of J_{YC} 37.3 Hz (Scheme 6.15). The corresponding NMR chemical shifts of **35b**, in addition to the observed reaction outcome, are very similar to that of the reaction and complex mentioned.

© University of Pretoria

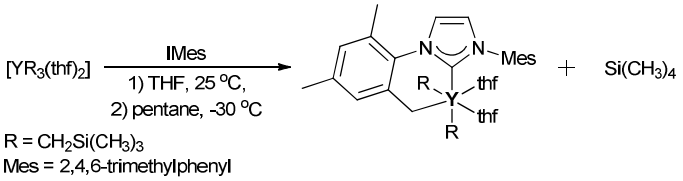

Scheme 6.15: Cyclometallation of an NHC ligand substituted with 2,4,6-trimethylphenyl wingtips[23]

In order to further validate **35$_b$** complex formation (to be more specific, Y-CH_2 bond formation), the complex **35$_b$** was reacted with phenylacetylene (Scheme 6.16). The benzylic carbons are more basic compared to the carbene carbons. Consequently, the acidic alkyne C**H** proton would preferentially react with the benzylic carbons instead of the carbene carbons. As such, addition of two equivalents phenylacetylene to **35$_b$** dissolved in C_6D_6 was accompanied with an immediate colour change from dark red-brown to dark green (Scheme 6.16).

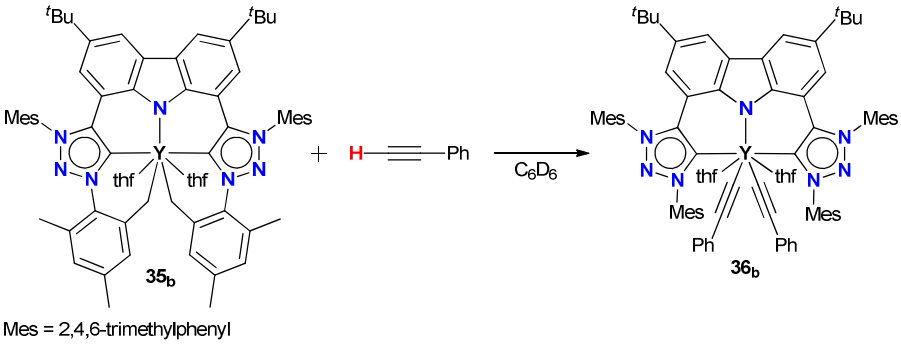

Scheme 6.16: Protonation of the benzylic carbons with phenylacetylene

Again, the ^{13}C NMR spectrum was inconclusive. However, the ^{1}H NMR spectrum depicted in Figure 6.12 provides clear cut evidence for protonation of the benzylic carbons, to yield the proposed yttrium bis-acetylide complex **36$_b$**. All of the 36 protons of the 2,4,6-trimethylphenyl wingtip substituents are accounted for. The carbazole aromatic C**H** proton of **36$_b$** resonates at δ_H 8.53 ppm, only 0.3 ppm downfield from the corresponding aromatic protons of **35$_b$**, but is still significantly upfield from the equivalent proton of **33$_b$** (δ_H 8.67 ppm). This would illustrate that the complex remains essentially unchanged after the addition of phenylacetylene to **35$_b$**, except in the case of the Y-CH_2 moieties which were protonated (decoordination or protonation of the carbene carbons would have had a greater impact on the carbazole backbone, whilst substitution of an alkyl with an alkyl acetylide bond would not

© University of Pretoria

amount to a drastic change in the chemical environment of the ligand backbone).

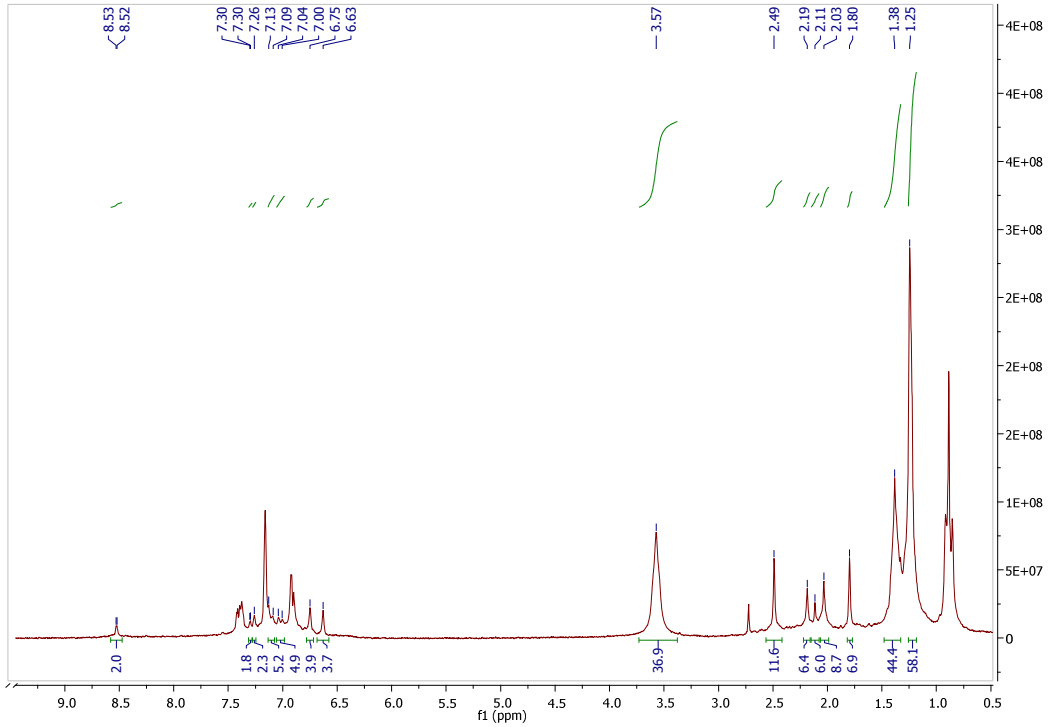

Figure 6.12: ^{1}H NMR spectrum of the reaction of phenylacetylene with **36$_b$** in solvent C_6D_6

The reaction depicted in Scheme 6.14 was repeated, but the lithium salt of **L$_a$** was used instead of the lithium adduct **33$_b$**. The yttrium bisalkyl chloride precursor was reacted with **31$_a$** in an NMR tube, with C_6D_6 as solvent (Scheme 6.17). As was determined by NMR analysis of the sample over several days, no reaction occurred. The colour of the reaction mixture also remained the same and did not change from lime green to dark red-brown or orange.

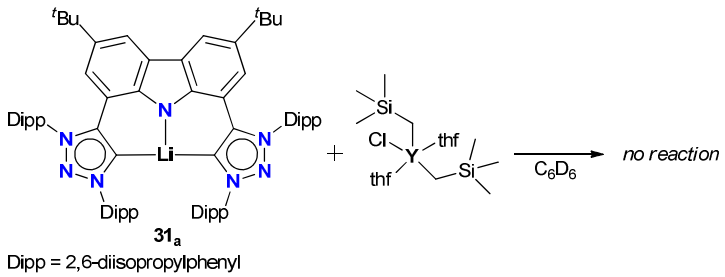

Scheme 6.17: Reactivity of **31$_a$** towards the yttrium bisalkyl chloride precursor

The reactivity of **35$_b$** towards a range of catalytic reactions was investigated, as a proof of concept. The catalyst **35$_b$** was found to be inactive in both the isoprene polymerization reaction and the C-C coupling reaction between 2,6-lutidine and styrene, even in the presence of $[(C_6H_5)_3C][B(C_6F_5)_4]$. Gratifyingly, the

© University of Pretoria

hydrophosphination reaction of diphenylphosphine with styrene was determined to be successful. The *anti*-Markovnikov product was isolated with > 95% selectivity and 87% conversion after 20 hours at 80 °C in a neat reaction (Scheme 6.18). Reaction optimization and substrate variation was not completed as a result of time constraints, but is envisaged as a future endeavour.

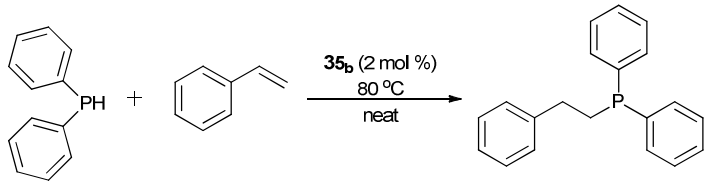

Scheme 6.18: Hydrophosphination of styrene with diphenylphosphine catalyzed by **35b**

Based on the hydroelementation reactions discussed above (Section 6.1.2), and in particular the hydrophosphination catalyzed reaction portrayed in Scheme 6.8, a catalytic mechanism for the reaction depicted in Scheme 6.18 is postulated (Scheme 6.19). The first step involves formation of the active catalyst. The basic yttrium benzylic carbons will deprotonate the diphenylphosphine substrate, yielding the yttrium phosphide active catalyst with re-formation of the 2,4,6-trimethylphenyl wingtip substituent (Scheme 6.19). Another possibility could also involve the deprotonation of two diphenylphosphine substrates and protonation of both wingtip functionalities. This would yield the bis-phosphide active catalyst. Styrene coordination, metallacycle formation and bond rearrangement would yield the reactive Y-C complex intermediate. Deprotonation of another diphenylphosphine substrate releases the tertiary phosphine product and yields the active catalyst (Scheme 6.19).

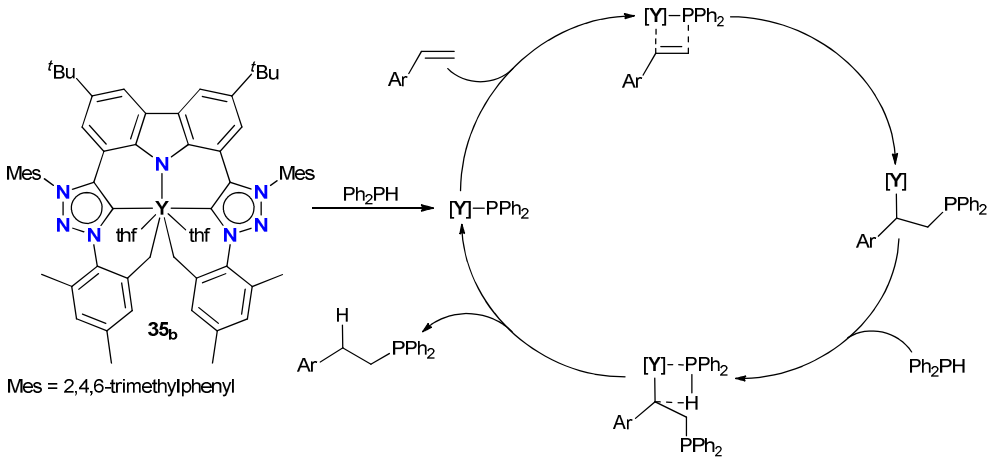

Scheme 6.19: Postulated hydrophosphination reaction mechanism catalyzed by **35b**

© University of Pretoria

6.4 Conclusion

To conclude this exploratory study, the first example of a lanthanide/yttrium triazolylidene complex has been synthesized and spectroscopically characterized. The non-trivial route towards **35$_b$** involves a salt elimination reaction between the lithium free carbene adduct **33$_b$** and the yttrium bisalkyl chloride metal precursor. Double C-H bond activation leads to stabilization and therefore permits the isolation of the biscarbene complex **35$_b$**. The complex was characterized by NMR spectroscopy, while all attempts at obtaining crystals suitable for X-ray diffraction analysis were unsuccessful.

It was determined, throughout the study, that either steric congestion (or lack thereof) and the choice of metal precursor greatly affects the reaction outcome. Contradicting chemical intuition, the bulkier ligand derived from **L$_a$** yields a reactive intermediate complex and does not stabilize the metal center and therefore leads to complex decomposition. The less sterically demanding lithium salt **33$_b$** is also inefficient at stabilizing the reactive metal center upon metallation with an YCl_3 precursor. It is only when an yttrium metal precursor with reactive alkyl ancillary ligands is introduced, that a stable complex is obtained. Two factors permit the isolation of **35$_b$**. The less bulky ligand obtained from the precursor **L$_b$** features the correct geometry for C-H bond activation leading to stabilization of the complex through cyclometallation, while the metal precursor with reactive alkyl ancillary ligands can mediate the aforementioned bond activation. Both ligand geometry and metal precursor are required for complex formation.

The yttrium triazolylidene complex **35$_b$** mediates the hydrophosphination catalyzed reaction of diphenylphosphine with styrene, yielding the anti-Markovnikov product with > 95% selectivity and 87% conversion. Further investigation of the hydrophosphination reaction catalyzed by **35$_b$** is warranted, which includes probing the stability and reactivity of **35$_b$** towards a range of functional groups. Changing the phosphine substrates from secondary to primary and also from aromatic to alkyl substituted phosphines is also envisaged during the catalytic investigations. It could be postulated that the ligand complex would demonstrate promising reactivity patterns towards alkyl substituted phosphines and olefins, as was the case for the rhodium catalyst discussed in chapter 4. Finally, the catalytic activity of **35$_b$** will also be scrutinized against other hydroelementation reactions such as the hydrosilylation, hydrothiolation and hydroamination of olefins.

© University of Pretoria

6.5 Experimental

6.5.1 Synthesis of (CNC_{Dipp})Li (31_a)

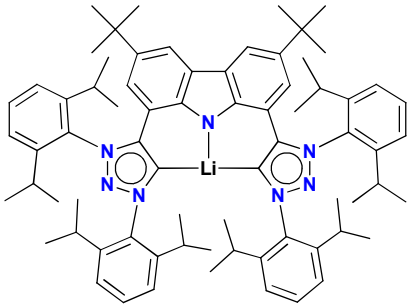

To a solid mixture of $\mathbf{L_a}$ (468.1 mg, 3.8 x 10^{-4} mol) and LDA (202.7 mg, 1.9 x 10^{-3} mol) in a tube under vacuum, was added benzene (15mL) or toluene (15mL). The tube was sealed off and the reaction was allowed to warm up to room temperature. The reaction was shaken until a homogeneous fluorescent lime green solution was obtained. The reaction mixture was centrifuged and the mother liquor decanted. Solvent was evaporated under reduced pressure until about 2 mL of solvent remained. Hexane (20 mL) was condensed to the concentrated solution. The resultant mixture was stirred at room temperature for 20 minutes. The tube was centrifuged and the mother liquor decanted. The solids were dried under vacuum to yield $\mathbf{31_a}$ (244.3 mg, 2.3 x 10^{-4} mol, 61%) as a yellow solid. **^{1}H NMR** δ_H (C_6D_6, 200 MHz) 8.57 (d, *J* = 1.6 Hz, 2H, Ar**H**$_{carb}$), 7.42 (d, *J* = 1.8 Hz, 2H, Ar**H**$_{carb}$), 7.33 (dd, *J* = 8.8 Hz, 6.4Hz, 2H, Ar**H**$_{Dipp}$ overlaps with ArH$_{Dipp}$), 7.32 (t, *J* = 7.6 Hz, 2H, Ar**H**$_{Dipp}$ overlaps with ArH$_{Dipp}$), 7.20 (d, *J* = 6.8 Hz, 4H, Ar**H**$_{Dipp}$), 7.08 (d, *J* = 7.8 Hz, 4H, Ar**H**$_{Dipp}$), 2.93 (sept, *J* = 6.8 Hz, 4H, C**H**$(CH_3)_2$), 2.72 (sept, *J* = 6.8 Hz, 4H, C**H**$(CH_3)_2$), 1.30 (s, 18H, C(C**H**$_3)_3$), 1.16 (d, *J* = 7.0 Hz, 12H, CH(C**H**$_3)_2$), 1.09 (d, *J* = 7.0 Hz, 12H, CH(C**H**$_3)_2$), 0.98 (d, *J* = 6.8 Hz, 12H, CH(C**H**$_3)_2$), 0.93 (d, *J* = 6.8 Hz, 12H, CH(C**H**$_3)_2$). **^{13}C NMR** δ_C (C_6D_6, 50 MHz) n.o. (not observed) (Li-**C**$_{Carbene}$), 151.7 (Ar**C**$_q$), 149.3 (Ar**C**$_q$), 145.8 (Ar**C**$_q$), 145.2 (Ar**C**$_q$), 138.9 (Ar**C**$_q$), 136.2 (Ar**C**$_q$), 135.4 (Ar**C**$_q$), 131.1 (Ar**C**H), 129.6 (Ar**C**H), 129.3 (Ar**C**$_q$), 125.3 (Ar**C**H), 123.9 (Ar**C**H), 120.0 (Ar**C**H), 117.9 (Ar**C**H), 113.7 (Ar**C**$_q$), 34.6 (**C**$(CH_3)_3$), 32.5 (C(**C**$H_3)_3$), 29.2 (**C**$H(CH_3)_2$), 28.7 (**C**$H(CH_3)_2$), 25.3 (CH(**C**$H_3)_2$), 24.8 (CH(**C**$H_3)_2$), 24.1 (CH(**C**$H_3)_2$), 23.0 (CH(**C**$H_3)_2$). **^{7}Li NMR** δ_{Li} (C_6D_6, 77 MHz) 4.94.

6.5.2 Synthesis of [(CNC_{Dipp})$YCl_2(thf)_2$](LiCl) (32_a)

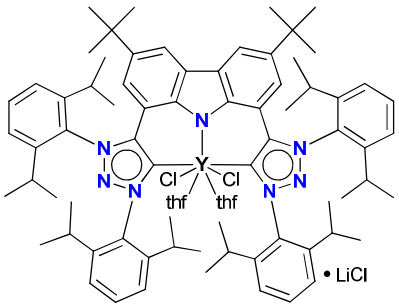

An NMR tube was loaded with YCl_3 (14.3 mg, 7.3 x 10^{-5} mol), followed by the addition of THF (0.5 mL). The mixture was heated up to 50 °C for 45 minutes. The solvent was evaporated under reduced pressure, followed by the addition of $\mathbf{31_a}$ (51.8 mg, 4.9 x 10^{-5} mol). C_6D_6 (0.5 mL) was condensed into the NMR tube. The tube was sealed and warmed up to room temperature. A colour change from

© University of Pretoria

lime green to orange was noted. The reaction was monitored with NMR spectroscopy. The proposed product could not be isolated, as a result of complex decomposition upon purification attempts. **^{1}H NMR** δ_H (C_6D_6, 200 MHz) 8.42 (s, 2H, Ar**H**$_{carb}$), 7.40 (d, *J* = 1.6 Hz, 2H, Ar**H**$_{carb}$), 7.22 (br s, 6H, Ar**H**$_{Dipp}$ overlaps with C_6D_6), 7.08 (d, *J* = 6.8 Hz, 6H, Ar**H**$_{Dipp}$ overlaps with C_6D_6 and ArH$_{Dipp}$), 3.62 (br s, η-C_4**H**$_8$O, overlapping with uncoordinated thf), 3.35 – 3.25 (br m, 4H, C**H**$(CH_3)_2$ overlaps with C_4H_8O), 2.91 (sept, *J* = 5.8 Hz, 4H, C**H**$(CH_3)_2$), 1.53 (d, *J* = 6.6 Hz, 12H, CH(C**H**$_3)_2$), 1.39 (br s, η-C_4**H**$_8$O, overlapping with uncoordinated thf), 1.17 (d, *J* = 7.6 Hz, 12H, CH(C**H**$_3)_2$ overlaps with C$(CH_3)_3$), 1.16 (s, 18H, C(C**H**$_3)_3$ overlaps with CH$(CH_3)_2$), 1.12 (d, *J* = 6.0 Hz, 12H, CH(C**H**$_3)_2$ overlaps with C$(CH_3)_3$), 0.86 (d, *J* = 6.4 Hz, 12H, CH(C**H**$_3)_2$). **^{7}Li NMR** δ_{Li} (C_6D_6, 77 MHz) 0.70.

6.5.3 Synthesis of (CNC$_{Mes}$)Li (33$_b$)

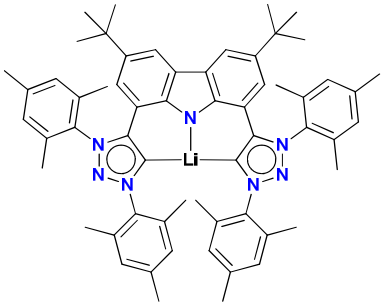

Benzene (15 mL) was condensed into an ampule loaded with **L$_b$** (273.7 mg, 2.6 x 10^{-4} mol) and LDA (137.2 mg, 1.3 x 10^{-3} mol). The tube was sealed off and the reaction was allowed to warm till room temperature. The mixture was shaken until a homogeneous lime green solution was obtained. The solution was centrifuged and the mother liquor decanted. The solvent was evaporated *in vacuo* until ca. 2 mL of solvent remained. Hexane (25 mL) was condensed into the product containing ampule. The mixture was stirred at room temperature for 30 minutes. The mixture was centrifuged followed by decanting the mother liquor. The solvent was evaporated and the solids were dried under vacuum to yield **33$_b$** (143.2 mg, 1.6 x 10^{-4} mol, 63%) as a yellow solid. **^{1}H NMR** δ_H (C_6D_6, 200 MHz) 8.66 (d, *J* = 1.6 Hz, 2H, Ar**H**$_{carb}$), 7.39 (d, *J* = 1.6 Hz, 2H, Ar**H**$_{carb}$), 6.76 (s, 4H, Ar**H**$_{Mes}$), 6.72 (s, 4H, Ar**H**$_{Mes}$), 2.29 (s, 6H, ArC**H**$_3$), 2.10 (s, 6H, ArC**H**$_3$), 2.06 (s, 12H, ArC**H**$_3$), 1.88 (s, 12H, ArC**H**$_3$), 1.34 (s, 18H, C(C**H**$_3)_3$). **^{13}C NMR** δ_C (C_6D_6, 50 MHz) n.o. (Li-**C**$_{Carbene}$), 150.9 (Ar**C**$_q$), 149.4 (Ar**C**$_q$), 140.1 (Ar**C**$_q$), 139.3 (Ar**C**$_q$), 138.0 (Ar**C**$_q$), 136.1 (Ar**C**$_q$), 135.7 (Ar**C**$_q$), 135.4 (Ar**C**$_q$), 134.5 (Ar**C**$_q$), 129.9 (Ar**C**H), 129.1 (Ar**C**H), 118.8 (Ar**C**H), 117.7 (Ar**C**H), 114.4 (Ar**C**$_q$), 34.7 (**C**$(CH_3)_3$), 32.3 (C(**C**$H_3)_3$), 21.4 (Ar**C**H_3), 21.0 (Ar**C**H_3), 17.8 (Ar**C**H_3), 17.5 (Ar**C**H_3). **^{7}Li NMR** δ_{Li} (C_6D_6, 77 MHz) 5.01.

© University of Pretoria

6.5.4 Synthesis of [(CNC$_{Mes}$)YCl$_2$(thf)$_2$](LiCl) (34$_b$)

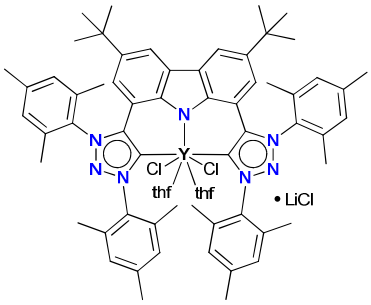

An NMR tube was charged with YCl_3 (13.4 mg, 6.9 x 10^{-5} mol), followed by the addition of THF (0.5 mL). The tube was sealed and the mixture was heated up to 50 °C for 45 minutes. The solvent was evaporated under reduced pressure. To the white solid was added **33$_b$** (38.2 mg, 4.3 x 10^{-5} mol) under negative pressure, followed by the addition of C_6D_6 (0.5 mL). The reaction mixture was warmed up to room temperature after the NMR tube had been sealed off. The reaction, which was accompanied by a colour change from lime green (indicative of **33$_b$**) to orange, was monitored with NMR spectroscopy. The proposed product could not be isolated, as a result of complex decomposition upon purification and isolation attempts. **^{1}H NMR** δ_H (C_6D_6, 200 MHz) 8.48 (br s, 2H, Ar**H**$_{carb}$), 7.39 (d, *J* = 1.8 Hz, 2H, Ar**H**$_{carb}$), 6.77 (s, 4H, Ar**H**$_{Mes}$), 6.62 (s, 4H, Ar**H**$_{Mes}$), 3.58 (br s, , η-C$_4$**H**$_8$O, overlapping with uncoordinated thf), 2.47 (s, 12H, ArC**H**$_3$), 2.14 (br s, 6H, ArC**H**$_3$ overlaps with unidentified impurity), 2.02 (s, 6H, ArC**H**$_3$), 1.85 (s, 12H, ArC**H**$_3$), 1.40 (br s, η-C$_4$**H**$_8$O, overlapping with uncoordinated thf), 1.21 (s, 18H, C(C**H**$_3$)$_3$). **^{7}Li NMR** δ_{Li} (C_6D_6, 77 MHz) 0.34.

6.5.5 Synthesis of [(CNC$_{Mes}$)Y(thf)$_2$] (35$_b$)

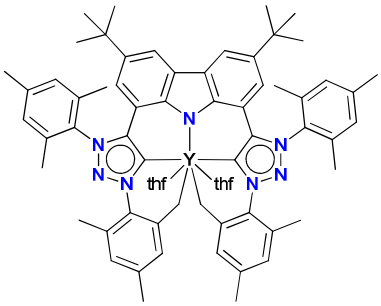

An ampule was charged with **33$_b$** (161.7 mg, 1.8 x 10^{-4} mol) and [YCl(CH$_2$SiMe$_3$)$_2$(thf)$_2$] (160.6 mg, 3.6 x 10^{-4} mol) under negative pressure. Benzene (15 mL) was condensed into the ampule and the vessel was subsequently sealed off. The reaction was warmed up and stirred at room temperature for 2 days. The dark red-brown solution was centrifuged and the mother liquor decanted. The solvent was evaporated *in vacuo*, and the solid residue washed with hexanes (2 x 5 mL). The solid was dried under reduced pressure to yield **35$_b$** (126.7 mg, 1.1 x 10^{-4} mol, 62%) as a brown solid. **^{1}H NMR** δ_H (C_6D_6, 200 MHz) 8.50 (br s, 2H, Ar**H**$_{carb}$), 7.40 (br s, 2H, Ar**H**$_{carb}$), 7.23 (s, 2H, Ar**H**$_{Mes}$), 6.75 (s, 2H, Ar**H**$_{Mes}$), 6.56 (s, 2H, Ar**H**$_{Mes}$), 6.43 (s, 2H, Ar**H**$_{Mes}$), 3.38 (br s, 8H, η-C$_4$**H**$_8$O), 2.51 (s, 12H, ArC**H**$_3$), 2.32 (br s, 4H, YC**H**$_2$), 2.06 (s, 6H, ArC**H**$_3$), 2.00 (s, 6H, ArC**H**$_3$), 1.59 (s, 6H, ArC**H**$_3$), 1.23 (s, 18H, C(C**H**$_3$)$_3$), 1.14 (br s, 8H, η-C$_4$**H**$_8$O). **^{13}C NMR** δ_C (C_6D_6, 50 MHz) 182.6 (d, *J* = 35.8 Hz, Y-**C**$_{Carbene}$), 151.9 (Ar**C**$_q$), 148.4 (Ar**C**$_q$), 146.4 (Ar**C**$_q$), 140.2 (Ar**C**$_q$), 138.1 (Ar**C**$_q$), 137.9 (Ar**C**$_q$), 135.9 (Ar**C**$_q$), 135.5 (Ar**C**$_q$), 135.3 (Ar**C**$_q$), 130.5 (Ar**C**$_q$), 129.9 (Ar**C**H),

© University of Pretoria

129.7 (Ar**C**H), 125.1 (Ar**C**H), 120.0 (Ar**C**H), 118.4 (Ar**C**H), 116.7 (Ar**C**H), 115.2 (Ar**C**$_q$), 68.8 (η-**C**$_4$H$_8$O), 50.5 (d, *J* = 19.4 Hz, Y-**C**H$_2$), 34.4 (**C**(CH$_3$)$_3$), 31.9 (C(**C**H$_3$)$_3$), 25.5 (η-**C**$_4$H$_8$O), 22.1 (Ar**C**H$_3$), 20.9 (Ar**C**H$_3$), 19.5 (Ar**C**H$_3$), 17.7 (Ar**C**H$_3$), 17.4 (Ar**C**H$_3$).

6.5.6 Synthesis of [(CNC$_{Mes}$)Y(C$_8$H$_5$)$_2$(thf)$_2$] (36$_b$)

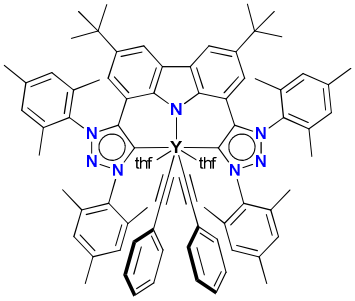

An NMR tube was loaded with **35$_b$** (16.3 mg, 1.5 x 10^{-5} mol) and the brown solid dissolved through the addition of C_6D_6 (0.5 mL). To the dark red-brown solution was added C_8H_6 (3.8 x 10^{-5} mol). The NMR tube was sealed off under negative pressure. The reaction was warmed up to room temperature with an accompanying colour change to dark green. The reaction was monitored with NMR spectroscopy. **^{1}H NMR** δ_H (C_6D_6, 200 MHz) 8.52 (d, *J* = 1.8 Hz, 2H, Ar**H**$_{carb}$), 7.30 (d, *J* = 1.2 Hz, 2H, Ar**H**$_{carb}$), 7.26 (br s, 2H, *p*-C$_6$**H**$_4$), 7.13 – 7.09 (br m, 4H, C$_6$**H**$_4$ overlaps with C_6D_6), 7.04 – 7.00 (br m, 4H, C$_6$**H**$_4$ overlaps with C_6D_6), 6.75 (br s, 4H, Ar**H**$_{Mes}$), 6.63 (br s, 4H, Ar**H**$_{Mes}$), 3.57 (br s, η-C$_4$**H**$_8$O, overlapping with uncoordinated thf), 2.49 (s, 12H, ArC**H**$_3$), 2.19 (s, 6H, ArC**H**$_3$), 2.11 (s, 6H, ArC**H**$_3$), 2.03 (s, 6H, ArC**H**$_3$), 1.80 (s, 6H, ArC**H**$_3$), 1.38 (br s, η-C$_4$**H**$_8$O, overlapping with uncoordinated thf), 1.25 (s, 18H, C(C**H**$_3$)$_3$ overlaps with C$_4$H$_8$O and hexane).

6.5.7 Catalytic hydrophosphination of styrene with diphenylphosphine

To a Schlenk tube was added **35$_b$** (5.6 mg, 5.0 x 10^{-6} mol), diphenylphosphine (43 µL, 2.5 x 10^{-4} mol) and styrene (29 µL, 2.5 x 10^{-4} mol). The vessel was sealed off and the reaction heated to 80 °C for 20 hours. To the mixture was added $CDCl_3$ (0.5 mL). From ^{1}H and ^{31}P NMR analysis, it was determined that the reaction was catalyzed with > 95% selectivity for the anti-Markovnikov product, with 80% conversion after 20 hours.

6.6 References

[1] P. L. Arnold, M. W. McMullon, J. Rieb, F. E. Kühn, *Angew. Chem. Int. Ed.*, **2015**, *54*, 82 – 100.
[2] *a*) G. R. Giesbrecht, J. C. Gordon, *Dalton Trans.*, **2004**, 2387 – 2393; *b*) F. T. Edelmann, D. M. M. Freckmann, H. Schumann, *Chem. Rev.*, **2002**, *102*, 1851 – 1896.

© University of Pretoria

[3] See review articles and references therein: *a*) A. A. Trifonov, D. M. Lyubov, *Coord. Chem. Rev.*, **2017**, *340*, 10 – 61; *b*) F.-F. Chen, Z.-Q. Chen, Z.-Q. Bian, C.-H. Huang, *Coord. Chem. Rev.*, **2010**, *254*, 991 – 1010; *c*) C. E. Willans, *J. Organomet. Chem.*, **2010**, *36*, 1 – 28; *d*) S. Mishra, *Coord. Chem. Rev.*, **2008**, *252*, 1996 – 2025; *e*) P. M. Zeimentz, S. Arndt, B. R. Elvidge, J. Okuda, *Chem. Rev.*, **2006**, *106*, 2404 – 2433; *f*) S. Arndt, J. Okuda, *Chem. Rev.*, **2002**, *102*, 1953 – 1976.

[4] See selected review articles and references therein: *a*) H. Pellissier, *Coord. Chem. Rev.*, **2017**, *336*, 96 – 151; *b*) A. A. Trifonov, I. V. Basalov, A. A. Kissel, *Dalton Trans.*, **2016**, *45*, 19172 – 19193; *c*) M. Nishiura, F. Guo, Z. Hou, *Acc. Chem. Res.*, **2015**, *48*, 2209 – 2220; *d*) B. D. Ward, L. H. Gade, *Chem. Commun.*, **2012**, *48*, 10587 – 10599; *e*) A. L. Reznichenko, K. C. Hultzsch, *Top. Organomet. Chem.*, **2011**, *43*, 51 – 114; *f*) D. McGuinness, *Dalton Trans.*, **2009**, 6915 – 6923; *g*) C. WenQi, W. FoSong, *Sci. China Ser. B-Chem.*, **2009**, *52*, 1520 – 1543; *h*) S. Hong, T. J. Marks, *Acc. Chem. Res.*, **2004**, *37*, 673 – 686; *i*) G. A. Molander, J. A. C. Romero, *Chem. Rev.*, **2002**, *102*, 2161 – 2185; *j*) H. C. Aspinall, *Chem. Rev.*, **2002**, *102*, 1807 – 1850.

[5] J.-C. G. Bünzli, *J. Coord. Chem.*, **2014**, *67*, 3706 – 3733.

[6] See compilation of review articles by Frank T. Edelmann, and references therein: *a*) F. T. Edelmann, *Coord. Chem. Rev.*, **2017**, *338*, 27 – 140; *b*) F. T. Edelmann, *Coord. Chem. Rev.*, **2016**, *318*, 29 – 130; *c*) F. T. Edelmann, *Coord. Chem. Rev.*, **2016**, *306*, 346 – 419; *d*) F. T. Edelmann, *Coord. Chem. Rev.*, **2015**, *284*, 124 – 205; *e*) F. T. Edelmann, *Coord. Chem. Rev.*, **2014**, *261*, 73 – 155; *f*) F. T. Edelmann, *Coord. Chem. Rev.*, **2013**, *257*, 1122 – 1231; *g*) F. T. Edelmann, *Coord. Chem. Rev.*, **2012**, *256*, 2641 – 2740; *h*) F. T. Edelmann, *Coord. Chem. Rev.*, **2012**, *256*, 1151 – 1228; *i*) F. T. Edelmann, *Coord. Chem. Rev.*, **2011**, *255*, 1834 – 1920; *j*) F. T. Edelmann, *Coord. Chem. Rev.*, **2009**, *253*, 2515 – 2587; *k*) F. T. Edelmann, *Coord. Chem. Rev.*, **2009**, *253*, 343 – 409; *l*) F. T. Edelmann, *Coord. Chem. Rev.*, **2007**, *251*, 142 – 202; *m*) F. T. Edelmann, *Coord. Chem. Rev.*, **2006**, *250*, 2511 – 2564; *n*) F. T. Edelmann, *Coord. Chem. Rev.*, **2006**, *250*, 2347 – 2410; *o*) F. T. Edelmann, *Coord. Chem. Rev.*, **2005**, *249*, 2787 – 2844.

[7] See review articles and references therein: *a*) P. L. Arnold, I. J. Casely, *Chem. Rev.*, **2009**, *109*, 3599 – 3611; *b*) P. L. Arnold, S. T. Liddle, *Chem. Commun.*, **2006**, 3959 – 3971.

[8] See citing article and references therein: S. T. Liddle, I. S. Edworthy, P. L. Arnold, *Chem. Soc. Rev.*, **2007**, *36*, 1732 – 1744.

[9] *a*) L. Maron, D. Bourissou, *Organometallics*, **2009**, *28*, 3686 – 3690; *b*) L. Maron, D. Bourissou, *Organometallics*, **2007**, *26*, 1100 – 1103.

[10] A. J. Arduengo III, M. Tamm, S. J. McLain, J. C. Calabrese, F. Davidson, W. J. Marshall, *J. Am. Chem. Soc.*, **1994**, *116*, 7927 – 7928.

[11] W. A. Herrmann, F. C. Munck, G. R. J. Artus, O. Runte, R. Anwander, *Organometallics*, **1997**, *16*, 682 – 688.

[12] P. L. Arnold, S. A. Mungur, A. J. Blake, C. Wilson, *Angew. Chem. Int. Ed.*, **2003**, *42*, 5981 – 5984.

[13] P. L. Arnold, Z. R. Turner, A. I. Germeroth, I. J. Casely, G. S. Nichol, R. Bellabarba, R. P. Tooze, *Dalton Trans.*, **2013**, *42*, 1333 – 1337.

[14] Z. R. Turner, R. Bellabarba, R. P. Tooze, P. L. Arnold, *J. Am. Chem. Soc.*, **2010**, *132*, 4050 – 4051.

[15] I. S. Edworthy, A. J. Blake, C. Wilson, P. L. Arnold, *Organometallics*, **2007**, *26*, 3684 – 3689.

[16] K. Lv, D. Cui, *Organometallics*, **2010**, *29*, 2987 – 2993.

[17] X. Gu, X. Zhu, Y. Wei, S. Wang, S. Zhou, G. Zhang, X. Mu, *Organometallics*, **2014**, *33*, 2372 – 2379.

[18] *a*) I. V. Basalov, O. S. Yurova, A. V. Cherkasov, G. K. Fukin, A. A. Trifonov, *Inorg. Chem.*, **2016**, *55*, 1236 – 1244; *b*) A. A. Kissel, T. V. Mahrova, D. M. Lyubov, A. V. Cherkasov, G. K. Fukin, A. A. Trifonov, I. D. Rosal, L. Maron, *Dalton Trans.*, **2015**, *44*, 12137 – 12148; *c*) I. V. Basalov, S. Claudiu Roşca, D. M. Lyubov, A. N. Selikhov, G. K. Fukin, Y. Sarazin, J.-F. Carpentier, A. A. Trifonov, *Inorg. Chem.*, **2014**, *53*, 1654 – 1661.

[19] *a*) I. V. Basalov, B. Liu, T. Roisnel, A. V. Cherkasov, G. K. Fukin, J.-F. Carpentier, Y. Sarazin, A. A. Trifonov, *Organometallics*, **2016**, *35*, 3261 – 3271; *b*) I. V. Basalov, V. Dorcet, G. K. Fukin, J.-F. Carpentier, Y. Sarazin, A. A. Trifonov, *Chem. Eur. J.*, **2015**, *21*, 6033 – 6036.

[20] J. Yuan, H. Hu, C. Cui, *Chem. Eur. J.*, **2016**, *22*, 5778 – 5785.

[21] K. C. Hultzsch, P. Voth, K. Beckerle, T. P. Spaniol, J. Okuda, *Organometallics*, **2000**, *19*, 228 – 243.

[22] K. R. D. Johnson, P. G. Hayes, *Chem. Soc. Rev.*, **2013**, *42*, 1947 – 1960.

[23] W. Fegler, T. P. Spaniol, J. Okuda, *Dalton Trans.*, **2010**, *39*, 6774 – 6779.

© University of Pretoria

Chapter 7

Conclusion

The stability, reactivity and catalytic activity of the novel bis(1,2,3-triazol-5-ylidene)carbazolide ligands, synthesized during an MSc study by the author, have been successfully exploited throughout this study. The aforementioned achievements could only be accessed *via* appropriate ligand design, which has been stated as a crucial part of complex preparation during the course of this project. It was noted that the central amido moiety of the CNC pincer ligand fulfills multiple roles, such as that of an adequate *trans* donor ligand that imparts unique reactivity properties on various metals, in addition to serving as an anchor to lock the metal in the pincer pocket. The triazolylidene side-arm donor ligands increased the nucleophilic character of the metal, whilst adequately stabilizing metals in low and high oxidation states. The rigid carbazole backbone enforced specific complex geometry, whilst the bulkier 2,6-diisopropylphenyl wingtip substituents (from ligand salt $\mathbf{L_a}$) conferred additional steric stabilization around the metal center. The smaller 2,4,6-trimethylphenyl wingtip substituents (of ligand precursor $\mathbf{L_b}$) also provided a certain degree of stability, but more importantly, allowed for improved catalytic performance due to increased access of the substrate to the active catalyst.

In the second chapter, activation of carbon dioxide was achieved by a nickel hydride complex supported by the CNC pincer ligand. It was demonstrated that the nickel hydride complex $\mathbf{8_a}$ cleaved the carbon oxygen double bond with concomitant insertion of CO_2 across the metal hydrogen bond, at room temperature, yielding the nickel formate product $\mathbf{10_a}$. This is surprising as nickel hydride complexes featuring an anionic nitrogen donor *trans* to the hydride ligand are generally unreactive towards CO_2. However, the combined donor strength of the ligand allows for the facile activation of CO_2, while the ligand bulk stabilizes the nickel hydride complex towards atmospheric conditions. It was discovered that the CO_2 insertion is a reversible process. Evaporation of the solvent under reduced pressure at room temperature yielded the nickel hydride complex $\mathbf{8_a}$. The nickel acetate complex $\mathbf{11_a}$ was also prepared, to elucidate the bonding situation of the nickel formate $\mathbf{10_a}$. The formate anion was trapped with the addition of TMSCl or tetrabutylammonium chloride, leading to the isolation of the nickel chloride complex. The trapping experiments confirmed the formation of complex $\mathbf{10_a}$, and therefore reversible CO_2 insertion at room temperature. The nickel chloride product $\mathbf{12_a}$ was independently prepared

© University of Pretoria

through the addition of HCl to the nickel hydride complex, to confirm nickel chloride preparation during the formate trapping experiments with the chloride containing reagents.

Coordination of the ligand scaffolds to metals that are well known for their excellent performance in catalysis was also realized in chapter 3. As such, coordination of the ligand derived from $\mathbf{L_b}$ to a ruthenium metal precursor yielded the ruthenium dicarbonyl chloride complex $\mathbf{13_b}$, which was found to be an active catalyst in the transfer hydrogenation reaction of acetophenone, yielding the corresponding alcohol whilst utilizing *iso*-propanol as sacrificial hydrogen donor. The catalytic activity in the hydrogenation catalyzed reaction was unsatisfactory, in all probability due to the absence of reactive donor moieties in addition to coordination of two carbonyl ligands. The corresponding ruthenium dicarbonyl hydride complex $\mathbf{15_b}$ coordinated by deprotonated $\mathbf{L_b}$ was prepared, in order to access a complex with a more reactive hydrido ligand. This hydride analogue was prepared through the one-pot deprotonation and metallation reaction of $\mathbf{L_b}$ with $[Ru(H)(Cl)(CO)(AsPh_3)_3]$, yielding the intermediated triphenylarsine coordinated complex $\mathbf{14_b}$. Treatment of $\mathbf{14_b}$ with CO (g) resulted to the formation of the targeted hydride complex $\mathbf{15_b}$. The catalytic activity of $\mathbf{15_b}$ is yet to be investigated.

Both ligand scaffolds $\mathbf{L_a}$ and $\mathbf{L_b}$ were also coordinated, after being deprotonated with excess base, to a rhodium metal precursor, another renowned player in the field of homogeneous catalysis. The corresponding atmospherically stable rhodium oxygen adducts $\mathbf{16_a}$ and $\mathbf{17_b}$ were isolated, respectively. The rhodium carbonyl complexes $\mathbf{18_a}$ and $\mathbf{19_b}$ were obtained after treating the rhodium oxygen adducts with CO (g). The carbonyl stretching frequencies were determined to be of low frequency in the FT-IR spectra, attributable to the strong donor properties of the ligands. The rhodium oxygen adducts were scrutinized as possible candidates for the catalytic alkyne hydroelementation reactions, as they are nucleophilic metals stabilized by the weakly coordinating molecular oxygen. Correspondingly, the rhodium complex $\mathbf{17_b}$ was found to catalyze the alkyne homo-dimerization reaction, with excellent selectivity for the *gem*-enyne isomer, by means of 1 mol % catalyst loading at 80 °C. The complex $\mathbf{16_a}$ did not catalyze the aforementioned reaction, in all probability due to the increased steric bulk around the metal center inhibiting catalysis. However, both rhodium oxygen adducts did mediate the alkyne hydrothiolation catalyzed reaction. As can be expected, the catalytic activity of $\mathbf{17_b}$ was superior compared to $\mathbf{16_a}$. Similar to the alkyne dimerization catalyzed reaction, no additives were required during the hydrothiolation reaction employing 1 mol % catalyst loading at 80 °C. In addition, the catalyst displayed complete selectivity for the α-vinyl sulfide isomer, if aliphatic substituted substrates were used while a decrease in selectivity was noted when phenyl substituted substrates were employed.

© University of Pretoria

More pleasing was the first example of unsymmetrical bis-vinyl sulfide preparation through the hydrothiolation of a dithiol with different alkyne equivalents. Complex **17$_b$** selectively catalyzed the double hydrothiolation reaction yielding the bis-α,α'-vinyl sulfide, if two non-equivalent terminal alkynes were added in a step-wise manner to the reaction mixture containing 2 mol % of **17$_b$** and one equivalent of a dithiol. The bis-α,β-*E*-vinyl sulfide product could be accessed through the addition of an internal alkyne, as the second non-equivalent alkyne. Finally, both alkyne functionalization reactions were combined in a one-pot tandem catalyzed reaction. First, the alkyne dimerization reaction with 3.5 mol % **17$_b$** yielded the *gem*-enyne isomer. To the same reaction mixture was added hexanethiol, followed by heating up the solution to 60 °C. It was determined that the catalyst mediated the *syn* addition of the thiol across the internal alkyne, yielding the 1,3-*gem*-ene-β-*E*-vinyl sulfide and the 1,4-*gem*-ene-β-*E*-vinyl sulfide products in a 1:1 ratio. A small amount of the 1,4-*gem*-ene-β-*Z*-vinyl sulfide isomer was also obtained, in all probability due to isomerization of the β-*E*- to the β-*Z*- product, but the reaction could be shown to be scalable to preparative quantities.

Gold complexes coordinated by the ligands obtained from salts **L$_a$** or **L$_b$** were prepared through a one-pot deprotonation and metallation reaction with (tht)AuCl, resulting in the isolation of the unique T-shaped gold(I) complexes **20$_a$** and **21$_b$**, respectively. It was determined, through cyclic voltammetry, that the gold(I) complex **20$_a$** displayed a redox potential for the Au(I)/Au(III) couple at values negative relative to that of ferrocene, which was further validated to be reversible. The facile oxidation was attributed to the unique T-shaped structure of the complex, which lowers the deformation energy required during a gold(I) oxidation event and also pre-organizes the complex to accommodate a square-planar gold(III) geometry after oxidation. The facile oxidation of **20$_a$** was exploited during the preparation of the first example of a cationic gold(III) hydride complex. Treatment of **20$_a$** with excess triflic acid resulted to the immediate electrophilic oxidation of the Au(I) complex to **22$_a$**. The gold(III) hydride complex **22$_a$** was subsequently reacted with sodium hydride, liberating molecular hydrogen and regenerating **20$_a$**. This illustrated that the hydrogen of **22$_a$** has protic and not hydridic character, which was further justified by the lack of reactivity of **22$_a$** with a range of strong acids. Oxidation of **20$_a$** with trifluoroacetic acid also lead to the isolation of the gold(III) hydride complex **23$_a$**. Furthermore, **20$_a$** was oxidized to the gold(III) hydride **25$_a$** through the addition of acetic acid in DCM, but reduced back to **20$_a$** after removal of the DCM solvent and redissolving the solid in THF. Computational analysis suggested that the gold(I) complex features Lewis basic character, unlike classical gold(I) species. This explains the reactivity of **20$_a$** with electrophilic reagents. Concurrently, the range of electrophiles were expanded from electrophilic hydrogen reagents to alkyl and even fluoride electrophiles. Hence, the gold(I) complex **20$_a$** was reacted

© University of Pretoria

with an alkylating reagent, but to our surprise, did not lead to oxidation to the corresponding gold(III) complex as was expected. Instead, alkylation of the amido moiety had occurred, yielding the cationic gold(I) complexes **26$_a$** and **27$_a$**. However, the reaction of **21$_b$** with iodomethane immediately resulted to oxidation of Au(I) to the corresponding gold(III) methyl complex **28$_b$**. The substantial reactivity of **21$_b$** was again evidenced when the complex readily oxidized in neat DCM to the analogous chloromethyl gold(III) complex **29$_b$**. Finally, the first example of a cationic gold(III) fluoride complex **30$_a$** was accessed through the oxidation of **20$_a$** with Selectfluor. The reactivity of the gold(I) complexes towards electrophiles exemplifies that coordination of gold to an appropriate ligand, can significantly alter the properties of gold in order to resemble the platinum group metals.

The preparation of the first example of a lanthanide triazolylidene complex was also envisaged. However, the exploratory study proved non-trivial, as reactivity of the complexes complicated the preparation of a triazolylidene supported lanthanide complexes. The sterically encumbered lithium salt **31$_a$** did not yield isolable products after being reacted with various yttrium metal precursors. Fortunately, a triazolylidene supported yttrium complex could be synthesized and isolated with appreciable yields, employing the less bulky lithium salt **33$_b$**. Reaction of **33$_b$** with $YCl_3(thf)_n$ ensued to yield **34$_b$** which decomposed as in the case of **32$_a$**. But, when **33$_b$** was reacted with the softer $[YCl(CH_2SiMe_3)_2(thf)_2]$ precursor, the yttrium complex **35$_b$** was isolated as a brown solid. Formation of the yttrium benzyl bonds observed in the coordination sphere of **35$_b$** was validated through reacting **35$_b$** with two equivalents of phenylacetylene, leading to the cleavage of the aforementioned bonds and preparation of the bisacetylide complex **36$_b$**. This exemplified the necessity of the specific ligand geometry of **L$_b$** to enhance the stability of the yttrium triazolylidene product upon coordination. It was further realized that the yttrium complex **35$_b$** facilitated the hydrophosphination of styrene with diphenylphosphine. The complex catalyzed the reaction with a high selectivity for the anti-Markovnikov product, with 80% conversion after 20 hours.

The results obtained signify the importance of appropriate ligand design that can render the corresponding metal complex with a range of key properties, be it stability or reactivity. The rudimentary properties are accessed with the ligand salts **L$_a$** and **L$_b$**. Consequently, an expanded investigation of the ligands and the resulting metal complexes is certainly warranted as it could generate both thought-provoking, fundamental chemical knowledge, as well as providing new and useful applications in both catalysis (syntheses of organic compounds) and template reactions (metal-mediated stoichiometric transformations).

© University of Pretoria

Future Perspectives

Instead of preparing a range of ligand analogues, the synthesis of a range of novel non-noble metal complexes such as cobalt, iron and even manganese is rather envisaged. This would add to the existing library of 3*d*-transition metal complexes supported by the two ligand classes. This could lead to the preparation of earth abundant metal complexes with catalytic applications, even exhibiting photophysical properties. This is validated by the reactivity of the nickel hydride complex towards CO_2. Complementary and additional reactivity studies of the nickel hydride complex towards CO_2, including formate trapping experiments, are intended. The range of reactivity studies will also be expanded to other small molecules, such as CO, O_2 and NH_3. The reactivity of the nickel hydride complexes towards CO_2 will then be exploited during catalytic attempts towards formate and even methanol preparation.

As the ruthenium chloride catalyst featured unsatisfactory catalytic activity, the more reactive ruthenium hydride complex will be screened as an alternative to the chlorido catalyst. Additionally, the coordination environment around the ruthenium complex will be varied to feature one or no carbonyl supporting ligands. The planned catalytic reactions with the modified ruthenium complexes will not only be limited to the transfer hydrogenation reaction, but will also include amination catalyzed reactions.

Due to the high selectivity of the rhodium catalyst in the alkyne functionalization catalyzed reactions, the range of alkyne hydroelementation reactions will be expanded. This specifically includes the silylation catalyzed reaction. However, due to the high functional group tolerance of the rhodium oxygen adduct, it is speculated that catalyst poisoning will not occur in the presence of phosphines. As such, the hydrophosphination catalyzed reaction will also be attempted.

The range of electrophiles will be expanded even further, in the electophilic oxidation of the gold(I) complexes. This includes the reaction of the gold(I) complexes with various boron reagents, to either yield a Lewis acid-base pair or result to oxidation and formation of a gold boron bond. The facile and reversible oxidation, especially in the case of the gold(I) complex featuring the 2,4,6-trimethylphenyl wingtip substituents, will be exploited during a catalytic investigation. Also, the photophysical properties of the various gold complexes presented in this thesis is currently being investigated.

Preparation of the analogous lanthanide complexes supported by the triazolylidene ligands, is currently being investigated. This includes coordination of the ligands to scandium and ytterbium metal precursors. If successfully isolated and characterized, their catalytic activity will be scrutinized. This also

© University of Pretoria

includes further investigation of the catalytic hydrophosphination reaction catalyzed by the CNC-pincer supported yttrium complex discussed in chapter 6.

© University of Pretoria

Chapter 8

Experimental

8.1 Standard operating procedures

8.1.1 Method

All synthetic manipulations, unless otherwise stated, were performed under an N_2 gas or Ar gas atmosphere using oven or flame dried glassware and standard Schlenk or vacuum line techniques. Air sensitive solids were handled and stored in a PureLab HE glove box under a N_2 gas atmosphere, or under a constant negative pressure. Preparation of NMR and crystallization samples that also require an inert atmosphere was done in the glove box, or under a constant vacuum.

8.1.2 Materials

Unless otherwise stated, only anhydrous solvents were used during experimental procedures. Anhydrous THF and Et_2O were obtained after distillation over a sodium and benzophenone ketyl, under a N_2 gas atmosphere. Anhydrous PhMe and hexane were obtained after distillation over sodium under a N_2 gas atmosphere. Anhydrous CH_2Cl_2 and CH_3CN were obtained after distillation over calcium hydride, also under an N_2 gas atmosphere. All solvents were degassed through several freeze-thaw cycles under N_2 or Ar gas before use. Deuterated benzene was dried over sodium and distilled under an Ar gas atmosphere. Deuterated dichloromethane and tetrahydrofuran were used as purchased. Deuterated acetonitrile was dried over calcium hydride and distilled under an Ar gas atmosphere.

The following ligands and reagents were prepared as previously reported: ligands $\mathbf{L_a}$[1] and $\mathbf{L_b}$;[2] ^{t}BuOCl;[3] $[RuCl(H)(AsPh_3)_3(CO)]$[4] and $[YCl(CH_2SiMe_3)_2(thf)_2]$.[5] All other reagents were obtained from commercial sources and were used without any further purification.

© University of Pretoria

8.2 Characterization techniques

8.2.1 Nuclear magnetic resonance spectroscopy

Nuclear magnetic resonance (NMR) spectra were obtained using a range of different NMR spectrometers, namely a Bruker AVANCE-III-300 operating at 300.13 MHz for ^{1}H, 75.47 MHz for ^{13}C, 121.49 MHz for ^{31}P and 282.40 MHz for ^{19}F; or both Bruker AVANCE-III-400 or DRX-400 operating at 400.21 MHz for ^{1}H, 100.64 MHz for ^{13}C, 162.01 MHz for ^{31}P and 376.57 MHz for ^{19}F. A Varian Inova 500 spectrometer was used which operated at 499.83 MHz for ^{1}H and 125.76 MHz for ^{13}C, while a Bruker DPX 200 was used, operating at 200.13 MHz for ^{1}H and 50.32 MHz for ^{13}C. ^{1}H chemical shifts are reported as δ (ppm) values downfield from Me_4Si and chemical shifts were referenced to residual non deuterated solvents peaks (CD_3CN, 1.94 ppm; *d8*-thf, 3.58; CD_2Cl_2, 5.32 ppm; $CDCl_3$, 7.26 ppm; C_6D_6, 7.16 ppm). ^{13}C chemical shifts are also reported as δ (ppm) values downfield from Me_4Si and chemical shifts were referenced to residual non deuterated solvents peaks (CD_3CN, 1.32 ppm; CD_2Cl_2, 54.00 ppm; *d8*-thf, 67.57; $CDCl_3$, 77.16 ppm; C_6D_6, 128.06 ppm). Proton coupling constants (*J*) are given in Hz. The spectral coupling patterns are designated as follows: s/S - singlet; d/D - doublet; t/T - triplet; q/Q - quartet; sept - septet; m - multiplet; br - broad signal. Quaternary carbons are designated as C_q.

Signal assignment in the ^{1}H NMR spectra is based on first-order analysis and when required were confirmed by two-dimensional (2D) (^{1}H-^{1}H) homonuclear chemical shift correlation (COSY) experiments. The ^{13}C shifts were obtained from proton-decoupled ^{13}C NMR spectra. Where necessary, the multiplicities of the ^{13}C signals were deduced from proton-decoupled DEPT-135 spectra or proton-coupled ^{13}C NMR experiments. The signals of the proton-bearing carbon atoms were correlated with specific proton resonances using 2D (^{13}C-^{1}H) heteronuclear single-quantum coherence (HSQC) and heteronuclear multiple bond correlation (HMBC) experiments. Standard Bruker pulse programs were used in the experiments.

8.2.2 Fourier-transform infrared spectroscopy

Solution IR spectra were recorded on a Bruker AlLPHA FT-IR spectrometer, or on a Perkin-Elmer Spectrum RXI FT-IR spectrophotometer, or on a JASCO FT/IR-6200 spectrometer with a NaCl cell, using solvent as indicated, or as a KBr pellet. The range of absorption was measured from 4000 – 600 cm^{-1}.

© University of Pretoria

8.2.3 Mass Spectroscopy

8.2.3.1 Nickel complex (12_a), ruthenium complexes (13_b and 15_b) and gold complex (30_a)

Electrospray mass spectra (ESI-MS) were recorded on a Micromass Quatro LC instrument or on a Bruker QTOF Mass spectrometer with positive electron spray as the ionization techniques; nitrogen was employed as drying and nebulizing gas at a flow of 4 L/min. The m/z values were measured in the range of 100–1500 with acetonitrile as solvent. Accurate mass measurements were performed by use of a Q-TOF premier mass spectrometer with electrospray source (Waters, Manchester, UK) operating at a resolution of ca. 16000 (fwhm).

8.2.3.2 Gold (22_a, 26_a, 27_a, 29_b) complexes

Mass spectral analyses were performed on a Waters Synapt G2 HDMS by direct infusion at 5µL/min with positive electron spray as the ionization technique. The *m/z* values were measured in the range of 400-1500 with acetonitrile as solvent. Prior to analysis, a 5 mM sodium formate solution was used to calibrate the instrument in resolution mode. An Agilent 6230 accurate mass time of flight mass spectrometer was employed for high resolution mass spectrometry (HR-MS) analysis using positive ion mode electrospray ionization as the ion source.

8.2.4 X-Ray diffraction analysis

Preliminary crystal structures of complexes **16_a**, **20_a** and **21_b** were previously reported in the MSc study preceding this thesis.[6] However, the refined datasets and single crystal X-ray structures of these compounds are reported in this thesis for the first time.

CIF files for the single crystal X-ray structural analysis are appended as supplementary information on a compact disc accompanying this thesis.

© University of Pretoria

8.2.4.1 Ruthenium (13_b)

A single crystal of **13_b** was selected and mounted on a SuperNova, Dual, Cu at zero, Atlas diffractometer. The crystal was kept at 293 (2) K during data collection. Using OLEX2,[7] the structure was solved with the XS structure solution program using Direct Methods and refined with the SHELXL refinement package using Least Squares minimization.[8]

Crystal Data for **13_b**: $C_{63}H_{68}Cl_3N_7O_2Ru$ (M = 1162.66 g/mol): triclinic, space group P1 (No. 2), a = 11.68915(13) Å, b = 14.9965 (2) Å, c = 19.5138(3) Å, α = 69.4553(14)°, β = 81.5229(11)°, γ = 68.4617(12)°, V = 2978.81(8) Å^3, Z = 2, T = 293(2) K, μ(Mo Kα) = 0.446 mm^{-1}, *Dcalc* = 1.296 g/cm^3, 58667 reflections measured (5.666° ≤ 2Θ ≤ 52°), 11710 unique (R_{int} = 0.0423, R_{sigma} = 0.0284) which were used in all calculations. The final R_1 was 0.0338 (I > 2σ(I)) and wR_2 was 0.0939 (all data). CCDC 1547961.

8.2.4.2 Rhodium (16_a)

Single crystal X-ray diffraction data were collected on a Bruker Apex II-CCD detector using Mo-Kα radiation (λ = 0.71073 Å). Crystals were selected under oil, mounted on nylon loops then immediately placed in a cold stream of N_2 at 150 K. Structures were solved and refined using Olex2[7] and SHELXTL.[8] A satisfactory refinement of the crystal structure after squeeze methodology was applied in order to eliminate residual electronic density of the solvent that could be refined otherwise.

Crystal Data for **16_a**: $C_{72}H_{84}N_7O_2Rh$ (M =1182.37 g/mol): triclinic, space group P-1 (no. 2), a = 10.8323(5) Å, b = 15.4988(8) Å, c = 24.8410(13) Å, α = 103.4480(14)°, β = 97.0590(13)°, γ = 107.0370(13)°, V = 3795.4(3) Å^3, Z = 2, T = 150.15 K, μ(MoKα) = 0.267 mm^{-1}, *Dcalc* = 1.035 g/cm^3, 84650 reflections measured (4.428° ≤ 2Θ ≤ 51.56°), 14487 unique (R_{int} = 0.1099, R_{sigma} = 0.0978) which were used in all calculations. The final R_1 was 0.0610 (I > 2σ(I)) and wR_2 was 0.1727 (all data). CCDC 1435498.

8.2.4.3 Gold

Single crystal X-ray diffraction data were collected on a Bruker D8 Venture kappa geometry diffractometer using I μS micro source Mo-Kα radiation (λ = 0.71073 Å), a Photon 100 CMOS detector and APEX2 (**20_a**, **21_b** and **22_a**) or Apex3 (**26_a**, **29_b** and **30_a**) control software.[9] Crystals were selected under oil, mounted on nylon loops and then immediately placed in a cold stream of N_2 at 150 K. Data reductions were performed using *SAINT*[9] and multi-scan absorption corrections were applied using

© University of Pretoria

SADABS[9]. Structures were solved using SHELXTS[10] and refined using SHELXTL and SHELXL-2014/7.[11] For **22$_a$** an electron density maxima was observed for the H bonded to Au and the position was refined. The crystal structures of **22$_a$**, **26$_a$**, and **29$_b$** contained badly disordered solvent molecules. The contributions of these disordered molecules to the structure factors in both structures were calculated using PLATON SQUEEZE[12] (For further details, including those related to checkCIFs, see "*Refinement special details*" below for **26$_a$** and **29$_b$**, as well as related CIF files).

Crystal Data for **20$_a$**: $C_{72}H_{90}AuN_7$ (*M* = 1250.47 g/mol): monoclinic, space group C2/c (no. 15), *a* = 25.5229(13) Å, *b* = 15.3460(8) Å, *c* = 16.4106(8)Å, β = 100.7610(15)°, *V* = 6314.6(6) Å^3, *Z* = 4, *T* = 150(2) K, μ(MoKα) = 2.377 mm^{-1}, *Dcalc* = 1.315 g/cm^3, 109310 reflections measured (2.527° ≤ Θ ≤ 26.372°), 6466 unique (6117 with I > 2σ(I)) (R_{int} = 0.0404, R_{sigma} = 0.0146) which were used in all calculations. The final R_1 was 0.0197 (I > 2σ(I)) and wR_2 was 0.0496 (all data). CCDC 1513409.

Crystal Data for **21$_b$**: $C_{63}H_{72}AuN_7$ (*M* =1124.24 g/mol): monoclinic, space group C2/c (no. 15), *a* = 27.4209(14) Å, *b* = 18.0706(8) Å, *c* = 23.4524(12) Å, β = 108.7689(15)°, *V* = 11003.0(9) Å^3, *Z* = 8, *T* = 150(2) K, μ(MoKα) = 2.720 mm^{-1}, *Dcalc* = 1.357 g/cm^3, 246113 reflections measured (4.508° ≤ 2Θ ≤ 51.494°), 10529 unique (R_{int} = 0.0841, R_{sigma} = 0.0285) which were used in all calculations. The final R_1 was 0.0319 (I > 2σ(I)) and wR_2 was 0.0784 (all data). CCDC 1513410.

Crystal Data for **22$_a$**: $C_{82.10}H_{91}AuCl_{0.14}D_{18.48}F_{2.59}N_7O_{4.90}S_{0.86}$ (*M* =1570.00 g/mol): monoclinic, space group P21/n (no. 14), *a* = 16.7934(11) Å, *b* = 23.5581(12) Å, *c* = 20.6319(15) Å, β = 99.142(2)°, *V* = 8058.7(9) Å^3, *Z* = 4, *T* = 150(2) K, μ(MoKα) = 1.911 mm^{-1}, *Dcalc* = 1.294 g/cm^3, 341617 reflections measured (2.260° ≤ Θ ≤ 27.254°), 17964 unique (14486 with I > 2σ(I)) (R_{int} = 0.0644, R_{sigma} = 0.0251) which were used in all calculations. The final R_1 was 0.0288 (I > 2σ(I)) and wR_2 was 0.0729 (all data). CCDC 1513411

Crystal Data for **26$_a$**: $C_{264.36}H_{279}Au_3Cl_{0.14}D_{85}F_{8.57}N_{21}O_{19.20}S_{2.86}$ (*M* = 5079.34 g/mol): monoclinic, space group C2/c (no. 15), *a* = 60.923(9) Å, *b* = 15.369(2) Å, *c* = 54.439(8) Å, β = 99.142(2)°, *V* = 49549(13) Å^3, *Z* = 8, *T* = 150(2) K, μ(MoKα) = 1.871 mm^{-1}, *Dcalc* = 1.362 g/cm^3, 640847 reflections measured (2.120° ≤ Θ ≤ 27.103°), 54623 unique (43114 with I > 2σ(I)) (R_{int} = 0.1056, R_{sigma} = 0.0629) which were used in all calculations. The final R_1 was 0.0594 (I > 2σ(I)) and wR_2 was 0.1157 (all data). CCDC 1513412. The crystal

© University of Pretoria

structure of **26$_a$** included 2 full and one partial (0.86) trifluromethanesulfonate anions and (0.14) of a chloride anion distributed over 2 positions approximately within the same volume of space occupied by the partial trifluromethanesulfonate anion. The asymmetric unit also contained a number of badly disordered deutero-THF molecules. The contributions of these disordered molecules to the structure factors were calculated using PLATON SQUEEZE (A.L. Spek, Acta Cryst, (2015), C71, 9-18) and the electron count amounted to 10.625 deutero-THF molecules. (Note: checkcif calculates the formula based only on the refined model so there are discrepancies between it's calculated formula weight, density and F000 and the true values which also include the squeezed solvents giving an *CHEMW03_ALERT_2_A* alert). Reported chemical formula weight 4227.73 corresponds to the C221.86 H279 Au3 Cl0.14 F8.58 N21 O8.57 S2.86. Calculated chemical formula weight 5079.34 corresponds to C264.36 H279 Au3 Cl0.14 D85 F8.57 N21 O19.20 S2.86, which is consistent with the molecular structure lacking the corresponding deuterated THF solvent molecules.

Crystal Data for **29$_b$**: $C_{164}H_{184}Au_2Cl_4N_{14}$ (*M* =2886.97 g/mol): orthorhombic, space group $Pna2_1$ (no. 33), *a* = 35.530(3) Å, *b* = 12.8815(10) Å, *c* = 29.850(3) Å, *V* = 13662.1(19) Å^3, *Z* = 4, *T* = 150(2) K, μ(MoKα) = 2.283 mm^{-1}, *Dcalc* = 1.404 g/cm^3, 404106 reflections measured (4.332° ≤ 2Θ ≤ 52.996°), 28116 unique (R_{int} = 0.1059, R_{sigma} = 0.0408) which were used in all calculations. The final R_1 was 0.0310 (I > 2σ(I)) and wR_2 was 0.0731 (all data). CCDC 1513413. The crystal structure of **29$_b$** was refined as a 2-component inversion twin. The asymmetric unit contains 2 chloride anions disordered over 7 sites. The crystal structure included 6 toluene disordered solvate molecules, one of which is sandwiched between the 2 complex molecules was reasonably well defined. The contributions of the 5 toluene solvate molecules to the structure factors were calculated using PLATON SQUEEZE (A.L. Spek, Acta Cryst, (2015), C71, 9-18). (Note: checkcif calculates the formula based only on the refined model so there are discrepancies between its calculated formula weight, density and F000 and the true values which also include the squeezed solvents giving a *CHEMW03_ALERT_2_A* alert). Reported chemical formula weight 2426.44 corresponds to the C129 H144 Au2 Cl4 N14. Calculated chemical formula weight 2886.97 corresponds to C164 H184 Au2 Cl4 N14, which is consistent with the molecular structure lacking 5 toluene solvate molecules.

© University of Pretoria

Crystal Data for **30$_a$**: $C_{76}H_{98}AuBCl_8F_5N_7$ (M = 1704.03 g/mol): monoclinic, space group C2/c (no. 15), a = 25.550(2) Å, b = 23.099(2) Å, c = 15.3633(14) Å, β = 110.607(3), V = 8487.0(13) Å^3, Z = 4, T = 150(2) K, μ(MoKα) = 2.039 mm^{-1}, *Dcalc* = 1.334 g/cm^3, 146191 reflections measured (4.524° ≤ 2Θ ≤ 55.758°), 9970 unique (R_{int} = 0.0876, R_{sigma} = 0.0403) which were used in all calculations. The final R_1 was 0.0658 (I > 2σ(I)) and wR_2 was 0.1667 (all data).

8.2.5 Elemental analysis

Microanalyses (%C, H, N) were performed using a ThermoScientific Flash 2000 elemental analyzer or, a EuroEA3000 Eurovector Analyzer.

8.3 Computational details

All calculations were performed with the Gaussian09 program package (version g09, rev.d01).[13] The theoretical approach is based on density functional theory (DFT).[14] A benchmark of various basis-sets such as Dunning's correlation consistent basis-sets,[15] and Pople basis sets,[16] was performed (*vide infra*, Table 8.1). Gold was treated with the Stuttgart-Dresden relativistic pseudopotential[17] at the corresponding cc-pVDZ/TZ/QZ level of theory.[18] A benchmark of three different functionals including B3LYP, M06-2X and B3PW91 was performed (Table 8.1). The B3PW91/SMD(Au)-6-31G** level of theory has previously shown to perform very good in related gold complexes.[19] All transition states and ground states were fully optimized without constraints at the corresponding level of theory and uniquely characterized by occurrence of one or none imaginary frequency respectively and verified by the corresponding frequency calculation. The imaginary frequencies for the transition state calculations can be found together with the optimized x,y,z coordinates. Transition states were located by using the quadratic synchronous transit (QST3) algorithm developed by Schlegel et al.[20] The connection of all transition states with the related ground states was verified by following the intrinsic reaction coordinate (IRC).[21] Gibbs free reaction energies and enthalpies were calculated for standard conditions (p = 1 atm, T = 298 K) and are unscaled. Solvent effects were taken into account using the Truhlar's SMD solvation model for THF.[22,23] Grimme's D3 dispersion correction with Becke-Johnson damping was used in order to take dispersion effects into account.[24] For the visualization of optimized structures CYLview was used.[25]

© University of Pretoria

Table 8.1: Benchmark of functionals/basis-sets with the experimentally obtained bond parameters (X-ray)

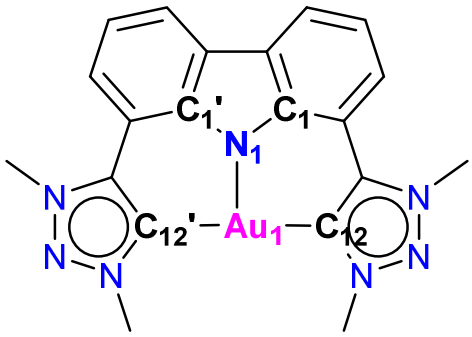

Entry		Au-N_1 [Å]	Au-C_{12} [Å]	C_{12}-Au-$C_{12'}$ [°]	N-Au-C_{12} [°]	C_{12}-Au-N-C_1 [°]
1	**1a**	**2.325(2)**	**2.0147(17)**	**171.16(11)**	**85.58(5)**	**175.32(11)**
2	**1b**	**2.412(3)**	**2.040(4)**	**167.30(16)**	**86.78(12)**	**167.4(3)**
3	B3LYP-D3BJ/SDD(Au)-cc-pVDZ	2.455	2.044	166.8	84.6	163.6
4	B3LYP-D3BJ-SMD(THF)/SDD(Au)-cc-pVDZ	2.457	2.049	166.8	84.7	163.7
5	M06-2X-D3/SDD(Au)-cc-pVDZ	2.505	2.054	164.6	83.7	162.2
6	M06-2X-D3-SMD(THF)/SDD(Au)-cc-pVDZ	2.513	2.057	164.8	83.7	161.8
7	**B3PW91/SDD(Au)-6-31G****	**2.423**	**2.035**	**167.5**	**85.2**	**164.1**
8	B3PW91-D3/SDD(Au)-6-31G**	2.449	2.033	166.5	84.7	162.9
9	B3PW91-SMD(THF)/SDD(Au)-6-31G**	2.425	2.038	167.6	85.2	164.1
10	B3PW91-SMD(THF)/SDD(Au/pVTZ)-6-31G**	2.421	2.035	167.7	85.3	164.0

© University of Pretoria

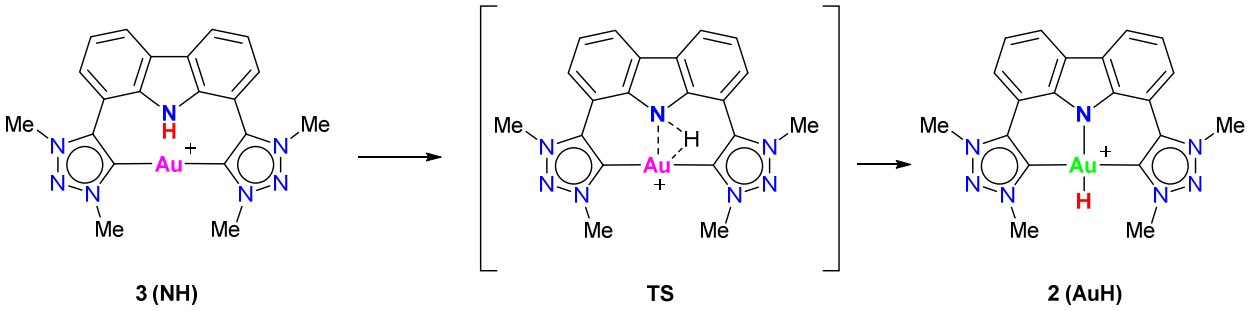

Scheme 8.1: Potential N-H *trans*-insertion reaction

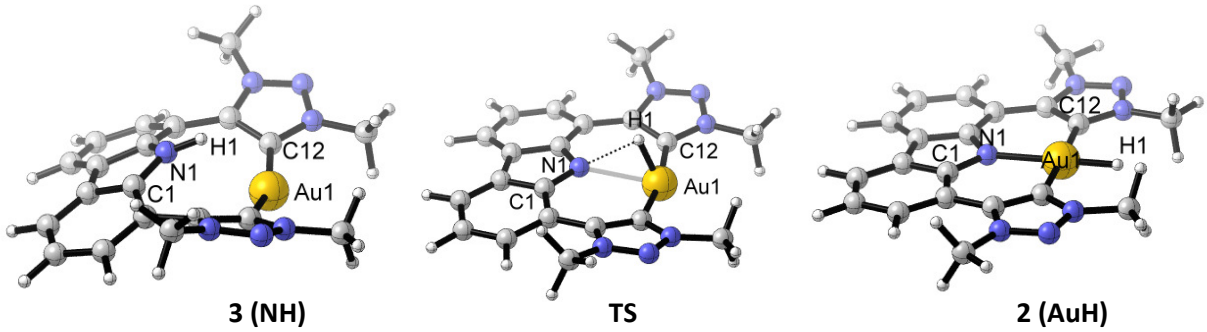

Scheme 8.2: Optimized geometries for a *trans*-insertion process (B3PW91/SDD(Au)-6-31G**)

Table 8.2: Calculated geometries at the B3PW91/SDD(Au)-6-31G** level of theory

Entry	Au-N_1 [Å]	Au-H_1 [Å]	N_1-H_1 [Å]	Au-C_{12} [Å]	C_{12}-Au-$C_{12'}$ [°]	N-Au-C_{12} [°]	C_{12}-Au-N-C_1 [°]
N-H	2.813	2.221	1.001	2.052	159.7	81.4	156.4
TS	2.378	1.547	2.100	2.040	170.2	85.4	172.1
Au-H	2.058	1.558	-----	2.027	179.6	89.8	180.0
(Au-H; x-ray)	2.051(2)	1.41(3)	-----	2.026(3)	178.8(1)	89.6(1)	179.6(2)

Table 8.3: N-H protonation *vs*. Au-protonation

Entry	method	$\Delta G^{\ddagger}$(TS) [kcal/mol]	ΔG [kcal/mol]
1	B3LYP-D3BJ/cc-pVDZ	+ 55.2	+ 3.7

© University of Pretoria

2	B3PW91/SDD(Au/pVDZ)-6-31G**	+ 55.3	+ 2.7
3	B3PW91-SMD(THF)/SDD(Au/pVDZ)-6-31G**	+51.5	+ 1.0
4	B3PW91-SMD(THF)/SDD(Au/pVTZ)-6-31G**	---	- 0.2
5	B3PW91-SMD(THF)/SDD(Au/pVQZ)-6-31G**	---	- 1.0

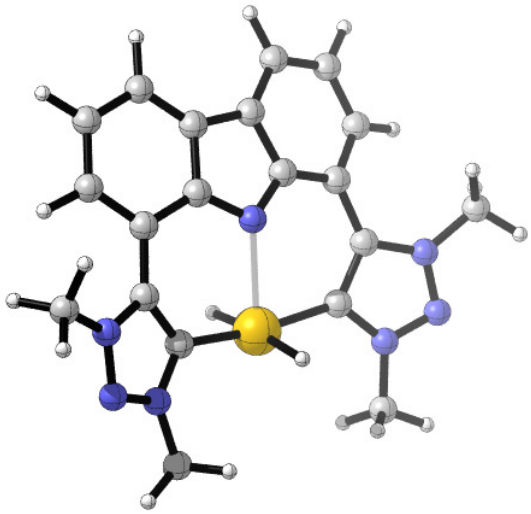

Figure 8.1: Optimized structure of a potential Au-dihydride (B3PW91/SDD(Au)-631G** level)

Optimized x,y,z Coordinates

1 (B3PW91/SDD(Au)-6-31G**)

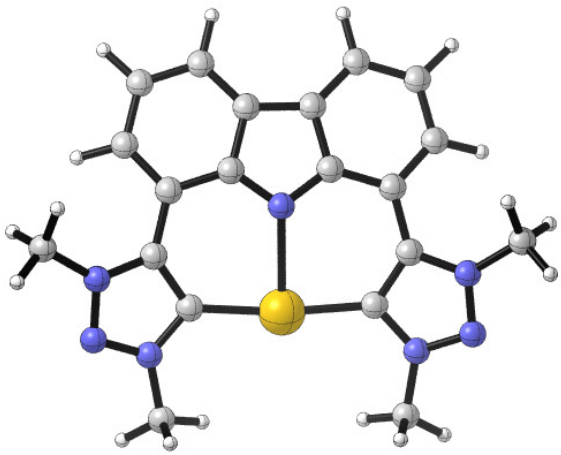

© University of Pretoria

scf done:	-1291.581266
Zero-point correction=	0.360670 (Hartree/Particle)
Thermal correction to Energy=	0.384312
Thermal correction to Enthalpy=	0.385257
Thermal correction to Gibbs Free Energy=	0.307480
Sum of electronic and zero-point Energies=	-1291.220596
Sum of electronic and thermal Energies=	-1291.196954
Sum of electronic and thermal Enthalpies=	-1291.196009
Sum of electronic and thermal Free Energies=	-1291.273786

N	10.202086	14.454313	11.853482
C	11.558266	14.629376	11.995723
C	11.900098	13.930921	13.181547
N	10.691895	13.471556	13.611824
N	9.660592	13.759784	12.839741
C	12.387433	15.419832	11.086366
C	13.787899	15.190772	10.998121
C	14.628806	16.051725	10.212384
C	14.075738	17.087522	9.466698
C	12.699466	17.305983	9.538896
C	11.884959	16.506276	10.347842
C	15.970986	15.608111	10.496915
C	15.805488	14.523907	11.425813
N	14.501885	14.255010	11.663556
C	16.930550	13.918222	12.049464
C	18.192320	14.421521	11.684924
C	18.350612	15.438115	10.736861
C	17.243453	16.040515	10.138217
Au	13.757657	13.369501	13.792893
C	15.665094	12.686559	13.979662
C	16.751343	12.912984	13.096671
N	17.697152	11.977123	13.442639
N	17.333772	11.223747	14.466692
N	16.129261	11.674475	14.764622
C	18.959810	11.636849	12.809009
C	15.415209	11.022968	15.848927
C	10.443615	12.666011	14.794825
C	9.314796	14.824658	10.763923
H	12.252416	18.132747	8.994557
H	19.083794	14.065886	12.190009
H	17.380903	16.855681	9.431245
H	10.842441	16.789864	10.442943
H	14.701595	17.741260	8.863267
H	19.351704	15.786200	10.499478
H	9.525126	13.010060	15.272699
H	10.344184	11.614789	14.513740
H	11.303796	12.787572	15.452098
H	9.872559	14.789828	9.827929
H	8.498934	14.102253	10.748398
H	8.908336	15.828181	10.911706
H	14.612801	11.693862	16.153458
H	14.989606	10.079446	15.498813
H	16.109675	10.834326	16.668983
H	19.149617	10.582045	13.006751
H	18.875085	11.814361	11.736766
H	19.778094	12.235567	13.216514

3 (NH) (B3PW91/SDD(Au)-6-31G**)

© University of Pretoria

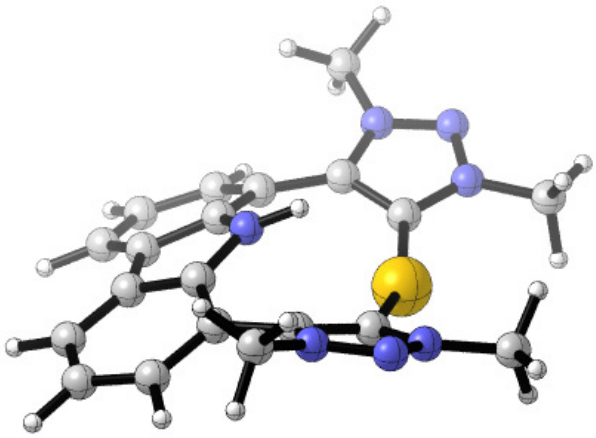

scf done:	-1292.021470
Zero-point correction=	0.374398 (Hartree/Particle)
Thermal correction to Energy=	0.398291
Thermal correction to Enthalpy=	0.399236
Thermal correction to Gibbs Free Energy=	0.321399
Sum of electronic and zero-point Energies=	-1291.647072
Sum of electronic and thermal Energies=	-1291.623178
Sum of electronic and thermal Enthalpies=	-1291.622234
Sum of electronic and thermal Free Energies=	-1291.700070

N	10.330789	15.038850	12.416198
C	11.612820	14.699580	12.057114
C	11.855373	13.447453	12.664457
N	10.668657	13.187298	13.286558
N	9.749316	14.119708	13.152765
C	12.425192	15.499461	11.126062
C	13.830065	15.526372	11.196212
C	14.645066	15.998019	10.135512
C	14.045946	16.628504	9.045244
C	12.656142	16.704275	8.999636
C	11.866651	16.116457	9.992914
C	15.994764	15.546957	10.426440
C	15.920161	14.827904	11.646747
N	14.649801	14.970682	12.146668
C	16.951930	13.986679	12.101833
C	18.135806	14.021329	11.344261
C	18.270907	14.827823	10.209916
C	17.199964	15.574421	9.725093
Au	13.638259	12.482470	12.981745
C	15.609232	12.193039	13.473744
C	16.734253	12.988081	13.161077
N	17.728322	12.566734	14.010739
N	17.346359	11.580987	14.790411
N	16.090146	11.375652	14.455359
C	19.078647	13.084641	14.204610
C	15.363147	10.327935	15.160231
C	10.330098	12.009748	14.075114
C	9.575908	16.260245	12.156346
H	12.169937	17.166500	8.146791
H	18.953040	13.353861	11.595437
H	17.294501	16.130249	8.797173
H	10.793906	16.080677	9.836707
H	14.643421	17.016258	8.225740
H	19.208550	14.814218	9.663992
H	9.274184	12.071387	14.334872
H	10.522470	11.115060	13.482215
H	10.939786	11.991026	14.980050
H	8.963912	16.148259	11.259095
H	8.930936	16.439016	13.015929
H	10.276345	17.084861	12.029624
H	14.571902	10.777226	15.762759
H	14.928201	9.642657	14.432062
H	16.069465	9.801067	15.800346
H	19.330828	12.963359	15.257472
H	19.792820	12.529664	13.592970
H	19.092461	14.138760	13.930183

© University of Pretoria

H 14.333197 14.591195 13.027085

3 (NH) (B3LYP-D3BJ/cc-pVDZ)

scf done:	-1292.653506
Zero-point correction=	0.371190 (Hartree/Particle)
Thermal correction to Energy=	0.395247
Thermal correction to Enthalpy=	0.396191
Thermal correction to Gibbs Free Energy=	0.317335
Sum of electronic and zero-point Energies=	-1292.282316
Sum of electronic and thermal Energies=	-1292.258259
Sum of electronic and thermal Enthalpies=	-1292.257315
Sum of electronic and thermal Free Energies=	-1292.336171

N	10.335170	15.067081	12.469872	C	19.090115	13.039377	14.182690
C	11.606788	14.717730	12.074419	C	15.321784	10.314900	15.127516
C	11.851203	13.451468	12.655966	C	10.366971	12.010788	14.108550
N	10.678104	13.192320	13.310092	C	9.578874	16.294140	12.224810
N	9.764709	14.141387	13.213460	H	12.153005	17.221517	8.166788
C	12.418434	15.519732	11.138292	H	18.969676	13.341987	11.561997
C	13.827687	15.536602	11.202143	H	17.281979	16.138247	8.766027
C	14.641874	16.013407	10.133698	H	10.774691	16.144289	9.874443
C	14.039618	16.654891	9.046918	H	14.641381	17.041026	8.222111
C	12.645838	16.744088	9.015181	H	19.212502	14.807761	9.620884
C	11.854807	16.157597	10.015506	H	9.300522	12.040999	14.358144
C	15.996217	15.550251	10.412613	H	10.598234	11.114138	13.521129
C	15.925686	14.819044	11.634182	H	10.972682	12.020601	15.024616
N	14.654470	14.964216	12.142499	H	9.006562	16.207447	11.291929
C	16.960183	13.966294	12.073514	H	8.894247	16.429800	13.069302
C	18.144122	14.006811	11.310710	H	10.278014	17.135166	12.162200
C	18.271997	14.820308	10.173949	H	14.832814	9.665256	14.391729
C	17.197473	15.575167	9.697330	H	16.024289	9.739113	15.740286
Au	13.632119	12.456689	12.941562	H	14.563748	10.791241	15.763639
C	15.611834	12.164759	13.429771	H	19.366493	12.846192	15.225085
C	16.742846	12.960624	13.131697	H	19.784986	12.518723	13.510840
N	17.730479	12.536639	13.992106	H	19.102279	14.115572	13.978481
N	17.333649	11.551292	14.771116	H	14.335389	14.555128	13.012785
N	16.077038	11.344796	14.420934				

3 (NH) (B3PW91-SMD(THF)/SDD(Au/pVDZ)-6-31G**)

scf done:	-1292.093435
Zero-point correction=	0.374346 (Hartree/Particle)
Thermal correction to Energy=	0.398132
Thermal correction to Enthalpy=	0.399076
Thermal correction to Gibbs Free Energy=	0.321644
Sum of electronic and zero-point Energies=	-1291.719089
Sum of electronic and thermal Energies=	-1291.695303

© University of Pretoria

Sum of electronic and thermal Enthalpies=	-1291.694359
Sum of electronic and thermal Free Energies=	-1291.771791

N	10.350660	15.065887	12.471365	C	19.070397	13.054465	14.185257
C	11.616826	14.714548	12.078984	C	15.335424	10.311585	15.117085
C	11.858626	13.450185	12.659948	C	10.359292	12.013750	14.093277
N	10.685802	13.193647	13.305225	C	9.601088	16.294947	12.238978
N	9.777670	14.142302	13.208139	H	12.155127	17.214886	8.182084
C	12.425181	15.514052	11.140870	H	18.952542	13.338324	11.559833
C	13.832298	15.528616	11.197265	H	17.282841	16.130324	8.774365
C	14.641623	16.003493	10.131522	H	10.785090	16.133513	9.881151
C	14.037318	16.648628	9.051318	H	14.631698	17.037757	8.229543
C	12.647630	16.738309	9.024277	H	19.199857	14.803621	9.629794
C	11.860735	16.149071	10.021905	H	9.296109	12.047225	14.329275
C	15.990706	15.541788	10.408794	H	10.586961	11.121987	13.508791
C	15.919321	14.814369	11.626211	H	10.947078	12.015439	15.013290
N	14.654295	14.957597	12.133334	H	8.996211	16.205361	11.334778
C	16.950985	13.965170	12.071052	H	8.953134	16.452335	13.100621
C	18.131865	14.002797	11.310768	H	10.301529	17.123665	12.142604
C	18.262859	14.816421	10.178290	H	14.851282	9.662999	14.386573
C	17.192704	15.568618	9.699775	H	16.042292	9.739695	15.717461
Au	13.634380	12.462938	12.941864	H	14.583839	10.771951	15.761376
C	15.604724	12.168322	13.430103	H	19.327579	12.902862	15.233075
C	16.732500	12.963963	13.130572	H	19.776521	12.515422	13.550997
N	17.718766	12.544686	13.986140	H	19.086257	14.117373	13.947241
N	17.327689	11.559023	14.760534	H	14.341520	14.572864	13.014441
N	16.074756	11.349823	14.413365				

3 (NH) (B3PW91-SMD(THF)/SDD(Au/pVTZ)-6-31G**)

scf done:	-1292.097559
Zero-point correction=	0.374355 (Hartree/Particle)
Thermal correction to Energy=	0.398115
Thermal correction to Enthalpy=	0.399060
Thermal correction to Gibbs Free Energy=	0.321687
Sum of electronic and zero-point Energies=	-1291.723204
Sum of electronic and thermal Energies=	-1291.699443
Sum of electronic and thermal Enthalpies=	-1291.698499
Sum of electronic and thermal Free Energies=	-1291.775872

N	10.351225	15.064495	12.470306	C	14.037977	16.651907	9.052659
C	11.617820	14.713863	12.078895	C	12.648136	16.739189	9.024530
C	11.861022	13.450189	12.661442	C	11.861298	16.147799	10.020945
N	10.687790	13.193763	13.306932	C	15.991454	15.544619	10.409881
N	9.779015	14.141261	13.208142	C	15.919435	14.815579	11.626292
C	12.425738	15.512994	11.140081	N	14.654906	14.960221	12.134445
C	13.832826	15.529633	11.197358	C	16.950183	13.964699	12.070160
C	14.642347	16.006302	10.132556	C	18.131064	14.002246	11.309799

© University of Pretoria

C	18.263006	14.817748	10.178760
C	17.193752	15.571982	9.701380
Au	13.635195	12.467526	12.945358
C	15.602400	12.169853	13.430547
C	16.731310	12.963992	13.130066
N	17.717898	12.543568	13.984652
N	17.326121	11.558602	14.759595
N	16.072811	11.350986	14.413940
C	19.070259	13.051862	14.183068
C	15.332754	10.313711	15.118508
C	10.362188	12.014652	14.096690
C	9.600320	16.292493	12.236273
H	12.155549	17.215749	8.182372
H	18.951274	13.336862	11.557910
H	17.284679	16.135193	8.776960
H	10.785787	16.131144	9.879373
H	14.632348	17.042839	8.231731
H	19.200152	14.805047	9.630513
H	9.298977	12.047576	14.332559
H	10.590449	11.122204	13.513392
H	10.949968	12.018096	15.016747
H	8.996213	16.201342	11.331723
H	8.951476	16.449723	13.097265
H	10.299840	17.121992	12.139897
H	14.847240	9.665526	14.388485
H	16.039461	9.740944	15.718208
H	14.582338	10.775110	15.763480
H	19.328194	12.898680	15.230461
H	19.775310	12.512840	13.547600
H	19.086852	14.115070	13.946425
H	14.337228	14.554932	13.005151

3 (NH) (B3PW91-SMD(THF)/SDD(Au/pVQZ)-6-31G**)

scf done:	-1292.099690
Zero-point correction=	0.374347 (Hartree/Particle)
Thermal correction to Energy=	0.398097
Thermal correction to Enthalpy=	0.399042
Thermal correction to Gibbs Free Energy=	0.321677
Sum of electronic and zero-point Energies=	-1291.725342
Sum of electronic and thermal Energies=	-1291.701592
Sum of electronic and thermal Enthalpies=	-1291.700648
Sum of electronic and thermal Free Energies=	-1291.778012

N	10.351082	15.063810	12.470024
C	11.618438	14.714535	12.079567
C	11.862803	13.451369	12.662697
N	10.689388	13.193713	13.307612
N	9.779573	14.140073	13.207720
C	12.425958	15.513679	11.140504
C	13.833023	15.530149	11.197627
C	14.642417	16.006562	10.132606
C	14.038007	16.652004	9.052649
C	12.648139	16.739363	9.024643
C	11.861381	16.148177	10.021259
C	15.991545	15.544895	10.409957
C	15.919487	14.816158	11.626553
N	14.655200	14.961593	12.135223
C	16.950265	13.965456	12.070592
C	18.131125	14.002684	11.310181
C	18.263091	14.817951	10.178962
C	17.193812	15.572104	9.701419
Au	13.636169	12.471207	12.946689
C	15.601341	12.172024	13.431235
C	16.731002	12.964999	13.130574
N	17.717670	12.542932	13.984383
N	17.325147	11.557938	14.758862
N	16.071369	11.351961	14.413976
C	19.070737	13.049614	14.182171
C	15.330107	10.315266	15.118203
C	10.365143	12.014330	14.097588
C	9.598959	16.290894	12.235052
H	12.155475	17.215896	8.182518
H	18.951438	13.337573	11.558678
H	17.284719	16.135190	8.776922
H	10.785828	16.131822	9.880002
H	14.632358	17.042805	8.231646
H	19.200278	14.805201	9.630789
H	9.301654	12.045204	14.332404
H	10.595778	11.122098	13.514858
H	10.952091	12.019358	15.018192
H	8.995473	16.198659	11.330185

© University of Pretoria

H	8.949436	16.447896	13.095572
H	10.297664	17.121095	12.138719
H	14.842811	9.668729	14.387876
H	16.036186	9.740573	15.716769
H	14.581021	10.777474	15.764174
H	19.329246	12.895828	15.229333
H	19.774748	12.509995	13.546036
H	19.088355	14.112895	13.945896
H	14.336650	14.552869	13.004413

TS (B3PW91/SDD(Au)-6-31G**)

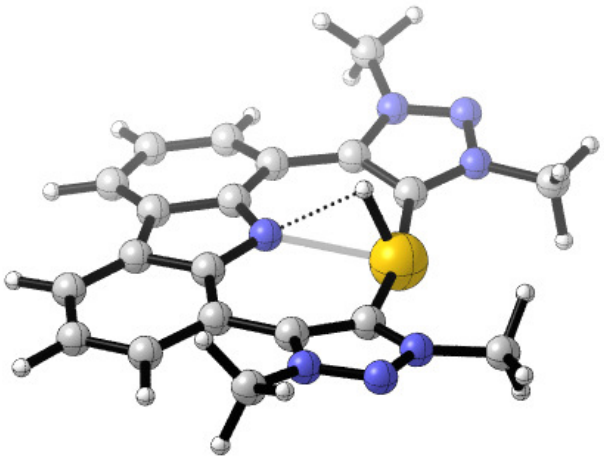

scf done:	-1291.926668
Imaginary frequency:	-689.0 cm^{-1} (Int. 14.9)
Zero-point correction=	0.368281 (Hartree/Particle)
Thermal correction to Energy=	0.391958
Thermal correction to Enthalpy=	0.392903
Thermal correction to Gibbs Free Energy=	0.314708
Sum of electronic and zero-point Energies=	-1291.558388
Sum of electronic and thermal Energies=	-1291.534710
Sum of electronic and thermal Enthalpies=	-1291.533766
Sum of electronic and thermal Free Energies=	-1291.611961

N	4.138806	-0.788019	0.700517
C	2.791690	-0.490659	0.805187
C	2.142796	-1.734208	0.599246
N	3.174683	-2.607097	0.415513
N	4.364576	-2.064928	0.477801
C	2.249718	0.836373	1.079407
C	0.878858	1.132632	0.859182
C	0.322448	2.412413	1.166198
C	1.123891	3.420963	1.678490
C	2.474604	3.140921	1.909262
C	3.014890	1.887846	1.631418
N	-0.086510	0.274882	0.431321
C	-1.276026	0.934193	0.464438
C	-1.098649	2.281547	0.905874
C	-2.561347	0.393331	0.198088
C	-3.644710	1.274576	0.411473
C	-3.467180	2.593754	0.820812
C	-2.193805	3.115443	1.070735
Au	0.158595	-2.085609	0.279935
C	-1.839891	-2.100966	-0.130326
C	-2.728631	-0.999015	-0.206058
N	-3.877699	-1.526243	-0.767994
N	-3.781259	-2.815063	-1.014401
N	-2.569643	-3.136081	-0.636766
C	-5.115323	-0.893783	-1.215319
C	-2.151111	-4.523194	-0.786518
C	3.087737	-4.040758	0.173165
C	5.322066	0.067376	0.696663

© University of Pretoria

H	-2.079878	4.139842	1.413957	H	2.479370	-4.216105	-0.714875
H	-4.342735	3.216120	0.975218	H	4.098981	-4.415755	0.022161
H	-4.662887	0.925453	0.310755	H	-5.586745	-1.581563	-1.915864
H	4.048036	1.727625	1.906473	H	-4.880284	0.046578	-1.714064
H	3.115228	3.902910	2.341411	H	-5.785927	-0.719004	-0.371823
H	0.717424	4.397440	1.926383	H	5.611106	0.330527	1.715952
H	-2.961393	-5.065931	-1.271202	H	5.115140	0.967037	0.116957
H	-1.248609	-4.559407	-1.397786	H	6.123321	-0.503205	0.229255
H	-1.947220	-4.949295	0.197141	H	0.311462	-1.217406	-0.991003
H	2.629760	-4.527810	1.035578				

TS (B3LYP-D3BJ/cc-pVDZ)

scf done:	-1292.488165
Imaginary frequency:	-680.0 cm^{-1} (Int. 10.5)
Zero-point correction=	0.365540 (Hartree/Particle)
Thermal correction to Energy=	0.389220
Thermal correction to Enthalpy=	0.390164
Thermal correction to Gibbs Free Energy=	0.311991
Sum of electronic and zero-point Energies=	-1292.122625
Sum of electronic and thermal Energies=	-1292.098946
Sum of electronic and thermal Enthalpies=	-1292.098001
Sum of electronic and thermal Free Energies=	-1292.176175

N	4.156559	-0.795957	0.728363	N	-2.578581	-3.145183	-0.647811
C	2.802799	-0.493141	0.814282	C	-5.160601	-0.911276	-1.157846
C	2.153026	-1.737327	0.590232	C	-2.141650	-4.527793	-0.822626
N	3.188391	-2.614114	0.408618	C	3.092547	-4.045786	0.136206
N	4.382164	-2.074746	0.493188	C	5.346577	0.056309	0.766922
C	2.259482	0.837343	1.083703	H	-2.076662	4.160183	1.393549
C	0.884596	1.131539	0.867216	H	-4.351461	3.240719	0.938060
C	0.325697	2.419128	1.163491	H	-4.677732	0.944431	0.274148
C	1.128578	3.435116	1.664520	H	4.071199	1.750105	1.876827
C	2.485644	3.158112	1.889365	H	3.131967	3.929854	2.308916
C	3.028820	1.901432	1.617925	H	0.718047	4.417543	1.905499
N	-0.089080	0.268793	0.448410	H	-2.977718	-5.090848	-1.251049
C	-1.283932	0.931843	0.469973	H	-1.275897	-4.547065	-1.496630
C	-1.101872	2.287665	0.901981	H	-1.857778	-4.943343	0.152661
C	-2.572006	0.392420	0.198644	H	2.562122	-4.536322	0.962326
C	-3.655173	1.285915	0.393513	H	2.537026	-4.195941	-0.798155
C	-3.473372	2.609357	0.797759	H	4.111307	-4.438034	0.047563
C	-2.195703	3.128989	1.055559	H	-5.670289	-1.627184	-1.810964
Au	0.164745	-2.101476	0.254336	H	-4.943737	0.015476	-1.701519
C	-1.845575	-2.105550	-0.142255	H	-5.786813	-0.698436	-0.281923
C	-2.741602	-1.003715	-0.201374	H	5.576676	0.348007	1.799708
N	-3.902407	-1.538092	-0.747926	H	5.174562	0.947250	0.152009
N	-3.801102	-2.828327	-1.005872	H	6.171306	-0.536716	0.358252

© University of Pretoria

H 0.314630 -1.202473 -1.015806

TS (B3PW91-SMD(THF)/SDD(Au/pVDZ)-6-31G**)

scf done:	-1292.004820
Imaginary frequency:	-744.7 cm^{-1} (Int. 167.4)
Zero-point correction=	0.368128 (Hartree/Particle)
Thermal correction to Energy=	0.391792
Thermal correction to Enthalpy=	0.392736
Thermal correction to Gibbs Free Energy=	0.315070
Sum of electronic and zero-point Energies=	-1291.636692
Sum of electronic and thermal Energies=	-1291.613028
Sum of electronic and thermal Enthalpies=	-1291.612084
Sum of electronic and thermal Free Energies=	-1291.689750

N	4.122320	-0.776060	0.618741
C	2.784014	-0.486470	0.778697
C	2.134401	-1.736590	0.647168
N	3.157621	-2.610605	0.446053
N	4.346420	-2.058638	0.430066
C	2.247403	0.849036	1.056617
C	0.879033	1.154270	0.822301
C	0.315614	2.418730	1.192348
C	1.119198	3.410182	1.746052
C	2.468324	3.124694	1.964958
C	3.010273	1.875785	1.647270
N	-0.072894	0.317642	0.335497
C	-1.267044	0.956642	0.429169
C	-1.102678	2.288123	0.932537
C	-2.553444	0.406936	0.177168
C	-3.643907	1.263015	0.428318
C	-3.478121	2.577098	0.875654
C	-2.211338	3.103480	1.135944
Au	0.139459	-2.120995	0.402184
C	-1.848602	-2.103376	-0.082463
C	-2.713001	-0.992679	-0.228280
N	-3.835905	-1.508916	-0.839098
N	-3.748896	-2.804119	-1.052886
N	-2.564076	-3.137504	-0.602084
C	-5.040257	-0.858023	-1.343596
C	-2.146241	-4.527656	-0.716982
C	3.059599	-4.048262	0.236658
C	5.291837	0.093438	0.549103
H	-2.104756	4.116203	1.516971
H	-4.361493	3.183209	1.054027
H	-4.658284	0.900055	0.326924
H	4.042608	1.701302	1.920805
H	3.110582	3.871297	2.422805
H	0.708254	4.375248	2.032274
H	-2.976488	-5.095956	-1.134549
H	-1.279385	-4.589546	-1.376790
H	-1.890011	-4.909553	0.272112
H	2.543785	-4.501255	1.084324
H	2.505605	-4.240995	-0.683430
H	4.070118	-4.447049	0.156293
H	-5.466371	-1.515786	-2.100231
H	-4.770146	0.097907	-1.791860
H	-5.761978	-0.712400	-0.537468
H	5.646160	0.338152	1.552349
H	5.032168	1.000583	0.003792
H	6.065855	-0.453806	0.012316
H	0.302386	-1.328102	-0.885811

2 (Au-H) (B3PW91/SDD(Au)-6-31G**)

© University of Pretoria

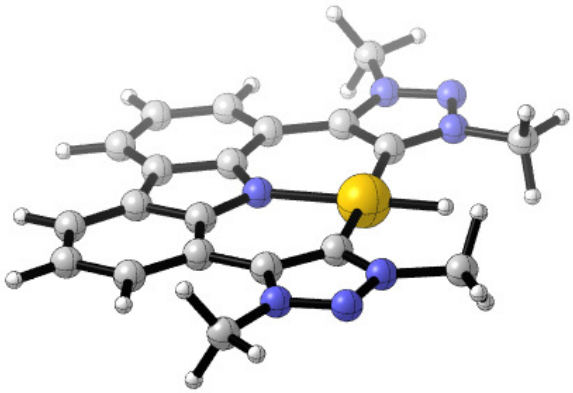

scf done:	-1292.015603
Zero-point correction=	0.373058 (Hartree/Particle)
Thermal correction to Energy=	0.396171
Thermal correction to Enthalpy=	0.397116
Thermal correction to Gibbs Free Energy=	0.319779
Sum of electronic and zero-point Energies=	-1291.642545
Sum of electronic and thermal Energies=	-1291.619431
Sum of electronic and thermal Enthalpies=	-1291.618487
Sum of electronic and thermal Free Energies=	-1291.695824

Au	10.142024	14.753771	12.077179
C	12.162456	14.662414	11.949497
C	13.035529	13.933578	12.767497
N	14.291921	14.205997	12.271181
N	14.258518	15.024009	11.239140
N	12.986748	15.286044	11.060368
N	10.192910	13.475648	13.689906
C	9.102657	13.018444	14.400191
C	9.529527	12.153202	15.444403
C	10.964008	12.091279	15.350065
C	11.323368	12.922564	14.254133
C	8.616855	11.558156	16.307792
C	7.262861	11.825791	16.131911
C	6.834010	12.671885	15.112193
C	7.723687	13.295251	14.215781
C	12.685018	13.081028	13.889459
C	13.627448	12.378634	14.665431
C	13.264574	11.566757	15.737249
C	11.927260	11.415280	16.090107
H	6.527344	11.375697	16.790363
C	7.303987	14.181153	13.144554
C	8.121928	14.836963	12.215323
N	7.245072	15.534170	11.438182
N	5.989843	15.381342	11.783236
N	6.021563	14.563340	12.815339
C	7.516745	16.405487	10.301906
C	4.723524	14.231853	13.391929
C	15.620906	13.760938	12.674872
C	12.644643	16.183819	9.964427
H	10.103513	15.720985	10.856712
H	14.681501	12.453969	14.443068
H	11.644532	10.782087	16.925968
H	5.770316	12.838605	15.029074
H	8.951036	10.898313	17.103068
H	14.038501	11.051550	16.296470
H	6.559769	16.780576	9.942461
H	8.148925	17.234718	10.621546
H	8.015518	15.835826	9.516948
H	4.679940	14.561362	14.431236
H	3.976062	14.765450	12.806750
H	4.545868	13.157499	13.322367
H	12.133292	17.062493	10.359264
H	13.575034	16.477313	9.480764
H	12.000408	15.663510	9.254718
H	16.328439	14.231458	11.993793
H	15.828323	14.079782	13.697590
H	15.694874	12.675682	12.588946

© University of Pretoria

2 (AuH) (B3LYP-D3BJ/cc-pVDZ)

Zero-point correction=	0.370303 (Hartree/Particle)
Thermal correction to Energy=	0.393502
Thermal correction to Enthalpy=	0.394446
Thermal correction to Gibbs Free Energy=	0.316690
Sum of electronic and zero-point Energies=	-1292.204564
Sum of electronic and thermal Energies=	-1292.181365
Sum of electronic and thermal Enthalpies=	-1292.180421
Sum of electronic and thermal Free Energies=	-1292.258178

N	4.159037	-0.521579	0.064677	C	-5.481221	0.127331	0.100068
C	2.881778	0.004319	0.007898	C	-2.586382	-3.598301	0.013441
C	2.031381	-1.114212	-0.016911	C	2.574685	-3.608047	0.019092
N	2.888110	-2.180677	0.022065	C	5.471435	0.118177	0.149466
N	4.158854	-1.844054	0.072585	H	3.795028	4.588861	-0.066292
C	2.499936	1.405987	-0.010619	H	-0.006012	-2.692999	-0.100206
C	1.124272	1.760929	0.001195	H	-4.477768	2.295416	0.008919
C	0.731256	3.131921	-0.003369	H	-1.337791	5.207551	-0.001468
C	1.678629	4.153873	-0.023646	H	4.491665	2.267708	-0.061665
C	3.031744	3.810711	-0.044115	H	1.369026	5.200325	-0.029810
C	3.426637	2.471367	-0.037898	H	-3.767812	4.611011	0.004513
C	-0.714225	3.135246	0.009061	H	3.525639	-4.150884	0.033154
C	-1.115722	1.765710	0.016461	H	1.981825	-3.852322	0.909571
N	0.002808	0.946811	0.009704	H	2.006955	-3.854378	-0.885963
C	-2.492642	1.417888	0.017639	H	5.508292	0.766301	1.034030
C	-3.411832	2.490369	0.012647	H	6.207882	-0.686619	0.241476
C	-3.009133	3.828158	0.008823	H	5.668269	0.703240	-0.757693
C	-1.654462	4.163137	0.006135	H	-1.952134	-3.830837	0.877133
Au	-0.002212	-1.124803	-0.052851	H	-3.534377	-4.142647	0.077901
C	-2.039986	-1.104309	-0.002073	H	-2.061225	-3.856357	-0.914573
C	-2.886143	0.016996	0.018473	H	-6.219785	-0.680112	0.136317
N	-4.165810	-0.509841	0.053136	H	-5.560675	0.750372	0.999489
N	-4.169927	-1.831769	0.048433	H	-5.634435	0.736409	-0.799452
N	-2.899905	-2.170909	0.017864				

2 (AuH) (B3PW91-SMD(THF)/SDD(Au/pVDZ)-6-31G**)

scf done:	-1292.090247
Zero-point correction=	0.372982 (Hartree/Particle)
Thermal correction to Energy=	0.396083
Thermal correction to Enthalpy=	0.397027
Thermal correction to Gibbs Free Energy=	0.319978
Sum of electronic and zero-point Energies=	-1291.717266
Sum of electronic and thermal Energies=	-1291.694165
Sum of electronic and thermal Enthalpies=	-1291.693220
Sum of electronic and thermal Free Energies=	-1291.770269

© University of Pretoria

Au	10.141916	14.757292	12.073227
C	12.162395	14.665172	11.946260
C	13.035560	13.936661	12.763224
N	14.290884	14.206471	12.269827
N	14.255432	15.023425	11.239559
N	12.984052	15.288372	11.057772
N	10.193063	13.471502	13.694946
C	9.103983	13.015588	14.403978
C	9.529349	12.149253	15.450445
C	10.964629	12.087233	15.356006
C	11.322302	12.919734	14.258018
C	8.613476	11.554511	16.314175
C	7.261387	11.825999	16.132853
C	6.833558	12.674096	15.109847
C	7.724172	13.295586	14.215361
C	12.684499	13.081254	13.888986
C	13.627750	12.380510	14.662797
C	13.266142	11.566520	15.737742
C	11.931103	11.411149	16.095877
H	6.521305	11.378177	16.789227
C	7.303670	14.184316	13.140353
C	8.121803	14.839734	12.212097
N	7.247589	15.536211	11.435193
N	5.992887	15.380415	11.783188
N	6.022448	14.563686	12.813821
C	7.521589	16.406981	10.299858
C	4.726972	14.229742	13.392408
C	15.617396	13.759280	12.675935
C	12.639733	16.185861	9.963121
H	10.103580	15.720814	10.858004
H	14.681119	12.457988	14.437284
H	11.649816	10.777579	16.932618
H	5.770325	12.843045	15.023610
H	8.946317	10.894410	17.110512
H	14.044488	11.053075	16.294199
H	6.565657	16.783215	9.937964
H	8.152858	17.236044	10.621760
H	8.020435	15.835930	9.515949
H	4.686531	14.561113	14.431231
H	3.976095	14.761652	12.809149
H	4.553041	13.154934	13.320793
H	12.129499	17.064221	10.360123
H	13.568879	16.480684	9.477228
H	11.995505	15.664189	9.254399
H	16.328425	14.227974	11.996451
H	15.821659	14.080160	13.698631
H	15.687513	12.673920	12.588350

2 (AuH) (B3PW91-SMD(THF)/SDD(Au/pVTZ)-6-31G**)

scf done:	-1292.096025
Zero-point correction=	0.372910 (Hartree/Particle)
Thermal correction to Energy=	0.396012
Thermal correction to Enthalpy=	0.396956
Thermal correction to Gibbs Free Energy=	0.319892
Sum of electronic and zero-point Energies=	-1291.723115
Sum of electronic and thermal Energies=	-1291.700013
Sum of electronic and thermal Enthalpies=	-1291.699069
Sum of electronic and thermal Free Energies=	-1291.776133

Au	10.141991	14.755616	12.075461
C	12.160386	14.664669	11.947214
C	13.034906	13.936635	12.763275
N	14.289906	14.206682	12.269534
N	14.253443	15.023736	11.239399
N	12.981976	15.288209	11.058348
N	10.193038	13.471927	13.694277
C	9.104102	13.015556	14.403907
C	9.529355	12.149379	15.450283
C	10.964612	12.087360	15.355846
C	11.322173	12.919714	14.257964
C	8.613522	11.554610	16.314103
C	7.261470	11.826053	16.132839
C	6.833629	12.674133	15.109803
C	7.724297	13.295509	14.215354
C	12.684369	13.081189	13.888998
C	13.627677	12.380559	14.662769
C	13.266062	11.566583	15.737743
C	11.931056	11.411250	16.095811
H	6.521433	11.378238	16.789273
C	7.304320	14.184231	13.140315
C	8.123869	14.839051	12.212778

© University of Pretoria

N	7.249699	15.535845	11.435474	H	6.568642	16.783110	9.938048
N	5.994856	15.380532	11.782749	H	8.155682	17.235565	10.622299
N	6.023394	14.563821	12.813407	H	8.023170	15.835425	9.516330
C	7.524348	16.406594	10.300204	H	4.686846	14.561627	14.430236
C	4.727590	14.230224	13.391428	H	3.977032	14.762251	12.807867
C	15.616697	13.759785	12.675013	H	4.553510	13.155433	13.319795
C	12.637022	16.185752	9.963863	H	12.126729	17.064011	10.361081
H	10.103662	15.719457	10.860039	H	13.565937	16.480896	9.477753
H	14.681045	12.458133	14.437249	H	11.992823	15.663969	9.255156
H	11.649597	10.777755	16.932542	H	16.327383	14.228655	11.995293
H	5.770404	12.843169	15.023551	H	15.821259	14.080622	13.697671
H	8.946538	10.894569	17.110408	H	15.686958	12.674435	12.587338
H	14.044373	11.053153	16.294268				

2 (AuH) (B3PW91-SMD(THF)/SDD(Au/pVQZ)-6-31G**)

scf done:	-1292.098911
Zero-point correction=	0.372866 (Hartree/Particle)
Thermal correction to Energy=	0.395971
Thermal correction to Enthalpy=	0.396915
Thermal correction to Gibbs Free Energy=	0.319822
Sum of electronic and zero-point Energies=	-1291.726045
Sum of electronic and thermal Energies=	-1291.702940
Sum of electronic and thermal Enthalpies=	-1291.701996
Sum of electronic and thermal Free Energies=	-1291.779089

Au	10.142061	14.754089	12.077532	N	7.251874	15.535649	11.435512
C	12.158886	14.664232	11.948061	N	5.996806	15.380809	11.782084
C	13.034266	13.936576	12.763413	N	6.024306	14.564166	12.812777
N	14.288950	14.207083	12.269008	C	7.527900	16.406195	10.300415
N	14.251459	15.024235	11.239034	C	4.728174	14.230958	13.390257
N	12.979821	15.288249	11.058710	C	15.616019	13.760470	12.673843
N	10.193033	13.471851	13.694260	C	12.633516	16.185748	9.964610
C	9.104152	13.015369	14.404041	H	10.103742	15.718080	10.862120
C	9.529350	12.149224	15.450427	H	14.681081	12.458274	14.437255
C	10.964624	12.087215	15.355997	H	11.649742	10.777679	16.932674
C	11.322125	12.919543	14.258115	H	5.770372	12.843218	15.023488
C	8.613426	11.554511	16.314209	H	8.946403	10.894478	17.110537
C	7.261395	11.825989	16.132891	H	14.044467	11.053179	16.294375
C	6.833588	12.674074	15.109829	H	6.572751	16.783331	9.937445
C	7.724384	13.295343	14.215465	H	8.159550	17.234733	10.623025
C	12.684285	13.081057	13.889140	H	8.027032	15.834641	9.517010
C	13.627721	12.380553	14.662834	H	4.687128	14.562482	14.429024
C	13.266143	11.566568	15.737828	H	3.977913	14.763037	12.806364
C	11.931159	11.411169	16.095925	H	4.553963	13.156175	13.318700
H	6.521349	11.378192	16.789330	H	12.122924	17.063576	10.362413
C	7.304963	14.184100	13.140356	H	13.561830	16.481595	9.477788
C	8.125422	14.838472	12.213417	H	11.989055	15.663628	9.256378

© University of Pretoria

H	16.326379	14.229482	11.993882	H	15.686402	12.675124	12.586098
H	15.820895	14.081277	13.696457				

Potential dihydride (B3PW91/SDD(Au)-631G**)

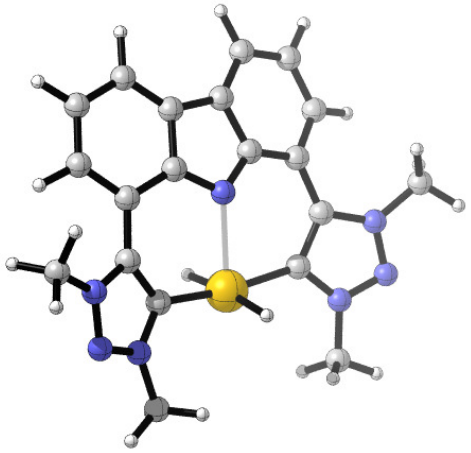

scf done:	-1292.724619
Zero-point correction=	0.376443 (Hartree/Particle)
Thermal correction to Energy=	0.400516
Thermal correction to Enthalpy=	0.401460
Thermal correction to Gibbs Free Energy=	0.323737
Sum of electronic and zero-point Energies=	-1292.348176
Sum of electronic and thermal Energies=	-1292.324104
Sum of electronic and thermal Enthalpies=	-1292.323159
Sum of electronic and thermal Free Energies=	-1292.400883

N	2.923098	-2.197688	0.175257	C	2.450884	1.380765	-0.018864
C	2.035064	-1.181414	0.289215	C	-2.773219	-0.043278	-0.025779
C	2.802614	-0.039164	-0.029098	N	-4.017061	-0.539581	-0.336056
N	4.046801	-0.533647	-0.340907	N	-4.108266	-1.851608	-0.200730
N	4.140034	-1.845574	-0.205901	N	-2.890361	-2.201946	0.178999
Au	0.015935	-1.329246	0.455356	C	-2.003630	-1.184387	0.291717
N	0.013736	1.002072	-0.311393	C	-5.186973	0.134407	-0.873753
C	-1.068770	1.792031	-0.139785	C	-2.612596	-3.611480	0.381169
C	-0.707724	3.173697	0.027941	C	5.215142	0.142073	-0.879834
C	0.732412	3.174749	0.027106	C	2.647497	-3.607654	0.377377
C	1.095290	1.793609	-0.141048				
C	-1.687620	4.141119	0.227762				
C	-3.019245	3.738608	0.325684				
C	-3.369362	2.386720	0.234578				
C	-2.423601	1.377177	-0.016015				
C	1.711104	4.143617	0.225804				
C	3.043436	3.743078	0.322174				
C	3.395438	2.391710	0.230637				

© University of Pretoria

H	1.446036	5.191954	0.343748
H	3.818898	4.478200	0.516631
H	4.430023	2.130741	0.424527
H	-4.403336	2.124225	0.429672
H	-3.795565	4.472586	0.521040
H	-1.423971	5.189847	0.345403
H	3.583073	-4.154439	0.263328
H	2.235317	-3.752781	1.376826
H	1.913755	-3.934220	-0.362434
H	-1.878535	-3.937030	-0.358770
H	-2.199965	-3.755954	1.380534
H	-3.547390	-4.159657	0.267409
H	5.770501	-0.588402	-1.467776
H	5.852167	0.524365	-0.078656
H	4.884661	0.967106	-1.511012
H	-4.858373	0.959957	-1.505231
H	-5.823736	0.515703	-0.071891
H	-5.741846	-0.596868	-1.461161
H	0.016656	-0.833263	2.012948
H	0.015642	-2.020124	-1.042516

© University of Pretoria

8.4 References

[1] D. I. Bezuidenhout, G. Kleinhans, G. Guisado-Barrios, D. C. Liles, G. Ung, G. Bertrand, *Chem. Commun.*, **2014**, *50*, 2431 – 2433.
[2] G. Kleinhans, G. Guisado-Barrios, D. C. Liles, G. Bertrand, D. I. Bezuidenhout, *Chem. Commun.*, **2016**, *52*, 3504 – 3507.
[3] M. J. Mintz, C. Walling, *Organic Synthesis, Coll.*, 1973, **5**, 184.
[4] D. Spasyuk, S. Smith, D. G. Gusev, *Angew. Chem. Int. Ed.*, **2012**, *51*, 2772 – 2775.
[5] K. C. Hultzsch, P. Voth, K. Beckerle, T. P. Spaniol, J. Okuda, *Organometallics*, **2000**, *19*, 228 – 243.
[6] G. Kleinhans, *MSc Dissertation*, University of Pretoria, **2014**.
[7] O. V. Dolomanov, L. J. Bourhis, R. J. Gildea, J. A. K. Howard, H. Puschmann, *J. Appl. Cryst.*, **2009**, *42*, 339.
[8] G. M. Sheldrick, *Acta Cryst.*, **2008**, *A64*, 112.
[9] Bruker AXS Inc., Madison, WI, 2015–2016.
[10] G. M. Sheldrick, *ActaCrystallogr*., *Sect. A: Fundam. Crystallogr*. **2015**, *71*, 3.
[11] G. M. Sheldrick, *ActaCrystallogr*., *Sect. C: Cryst*. *Struct. Commun.* **2015**, *71*, 3.
[12] A. L. Spek, *ActaCrystallogr*., *Sect. C: Cryst*. *Struct. Commun.* **2015**, *71*, 9.
[13] Gaussian 09, Revision D.01, M. J. Frisch, G. W. Trucks, H. B. Schlegel, G. E. Scuseria, M. A. Robb, J. R. Cheeseman, G. Scalmani, V. Barone, B. Mennucci, G. A. Petersson, H. Nakatsuji, M. Caricato, X. Li, H. P. Hratchian, A. F. Izmaylov, J. Bloino, G. Zheng, J. L. Sonnenberg, M. Hada, M. Ehara, K. Toyota, R. Fukuda, J. Hasegawa, M. Ishida, T. Nakajima, Y. Honda, O. Kitao, H. Nakai, T. Vreven, J. A. Montgomery Jr., J. E. Peralta, F. Ogliaro, M. Bearpark, J. J. Heyd, E. Brothers, K. N. Kudin, V. N. Staroverov, T. Keith, R. Kobayashi, J. Normand, K. Raghavachari, A. Rendell, J. C. Burant, S. S. Iyengar, J. Tomasi, M. Cossi, N. Rega, J. M. Millam, M. Klene, J. E. Knox, J. B. Cross, V. Bakken, C. Adamo, J. Jaramillo, R. Gomperts, R. E. Stratmann, O. Yazyev, A. J. Austin, R. Cammi, C. Pomelli, J. W. Ochterski, R. L. Martin, K. Morokuma, V. G. Zakrzewski, G. A. Voth, P. Salvador, J. J. Dannenberg, S. Dapprich, A. D. Daniels, O. Farkas, J. B. Foresman, J. V. Ortiz, J. Cioslowski, D. J. Fox, Gaussian, Inc., Wallingford CT, **2013**.
[14] *a*) P. Hohenberg, W. Kohn, *Phys. Rev. B.*, **1964**, *136*, B864; *b*) W. Kohn, L. J. Sham, *Phys. Rev.*, **1965**, *140*, A1133.
[15] T. H. Dunning Jr., *J. Chem. Phys.*, **1989**, *90*, 1007.
[16] W. J. Hehre, R. Ditchfield, J. A. Pople, *J. Chem. Phys.*, **1972**, *56*, 2257.
[17] D. Figgen, G. Rauhut, M. Dolg, H. Stoll, *Chem. Phys.*, **2005**, *311*, 227.
[18] K. A. Peterson, C. Puzzarini, *Theor. Chem. Acc.*, **2005**, *114*, 283.
[19] See for example: M. Sircoglou, S. Bontemps, M. Mercy, N. Saffon, M. Takahashi, G. Bouhadir, L. Maron, D. Bourissou, *Angew. Chem. Int. Ed.*, **2007**, *46*, 8583
[20] *a*) C. Peng, H. B. Schlegel, *Israel J. of Chem.,* **1993**, *33*, 449; *b*) C. Peng, P. Y. Ayala, H. B. Schlegel, M. J. Frisch, *J. Comp. Chem.*, **1996**, *17*, 49.
[21] *a*) K. Fukui, *Acc. Chem. Soc.*, **1981**, *12*, 363; *b*) C. Gonzalez, H. B. Schlegel, *J. Chem. Phys.*, **1989**, *90*, 2154; *c*) C. Gonzalez, H. B. Schlegel, *J. Phys. Chem.*, **1990**, *94*, 5523.
[22] A. V. Marenich, C. J. Cramer, D. G. Truhlar, *J. Phys. Chem. B*, **2009**, *113*, 6378.
[23] J. Tomasi, B. Mennucci, R. Cammi, *Chem. Rev.*, **2005**, *105*, 2999.
[24] *a*) S. Grimme, S. Ehrlich, L. Goerigk, *J. Comp. Chem*., **2011**, *32*, 1456; *b*) S. Grimme, J. Antony, S. Ehrlich, H. Krieg, *J. Chem. Phys.*, **2010**, *132*, 154104.
[25] CYLview, 1.0b; Legault, C. Y., Université de Sherbrooke, 2009 (http://www.cylview.org).

© University of Pretoria